frontiers | Research Topics

From preparation to faulting: multidisciplinary investigations on earthquake processes, volume II

Edited by
Fuqiong Huang, Galina Kopylova, Jie Liu, Paresh Nath Singha Roy, Giovanni Martinelli and Mohammad Mokhtari

Published in
Frontiers in Earth Science

FRONTIERS EBOOK COPYRIGHT STATEMENT

The copyright in the text of individual articles in this ebook is the property of their respective authors or their respective institutions or funders. The copyright in graphics and images within each article may be subject to copyright of other parties. In both cases this is subject to a license granted to Frontiers.

The compilation of articles constituting this ebook is the property of Frontiers.

Each article within this ebook, and the ebook itself, are published under the most recent version of the Creative Commons CC-BY licence. The version current at the date of publication of this ebook is CC-BY 4.0. If the CC-BY licence is updated, the licence granted by Frontiers is automatically updated to the new version.

When exercising any right under the CC-BY licence, Frontiers must be attributed as the original publisher of the article or ebook, as applicable.

Authors have the responsibility of ensuring that any graphics or other materials which are the property of others may be included in the CC-BY licence, but this should be checked before relying on the CC-BY licence to reproduce those materials. Any copyright notices relating to those materials must be complied with.

Copyright and source acknowledgement notices may not be removed and must be displayed in any copy, derivative work or partial copy which includes the elements in question.

All copyright, and all rights therein, are protected by national and international copyright laws. The above represents a summary only. For further information please read Frontiers' Conditions for Website Use and Copyright Statement, and the applicable CC-BY licence.

ISSN 1664-8714
ISBN 978-2-8325-5569-9
DOI 10.3389/978-2-8325-5569-9

About Frontiers

Frontiers is more than just an open access publisher of scholarly articles: it is a pioneering approach to the world of academia, radically improving the way scholarly research is managed. The grand vision of Frontiers is a world where all people have an equal opportunity to seek, share and generate knowledge. Frontiers provides immediate and permanent online open access to all its publications, but this alone is not enough to realize our grand goals.

Frontiers journal series

The Frontiers journal series is a multi-tier and interdisciplinary set of open-access, online journals, promising a paradigm shift from the current review, selection and dissemination processes in academic publishing. All Frontiers journals are driven by researchers for researchers; therefore, they constitute a service to the scholarly community. At the same time, the *Frontiers journal series* operates on a revolutionary invention, the tiered publishing system, initially addressing specific communities of scholars, and gradually climbing up to broader public understanding, thus serving the interests of the lay society, too.

Dedication to quality

Each Frontiers article is a landmark of the highest quality, thanks to genuinely collaborative interactions between authors and review editors, who include some of the world's best academicians. Research must be certified by peers before entering a stream of knowledge that may eventually reach the public - and shape society; therefore, Frontiers only applies the most rigorous and unbiased reviews. Frontiers revolutionizes research publishing by freely delivering the most outstanding research, evaluated with no bias from both the academic and social point of view. By applying the most advanced information technologies, Frontiers is catapulting scholarly publishing into a new generation.

What are Frontiers Research Topics?

Frontiers Research Topics are very popular trademarks of the *Frontiers journals series*: they are collections of at least ten articles, all centered on a particular subject. With their unique mix of varied contributions from Original Research to Review Articles, Frontiers Research Topics unify the most influential researchers, the latest key findings and historical advances in a hot research area.

Find out more on how to host your own Frontiers Research Topic or contribute to one as an author by contacting the Frontiers editorial office: frontiersin.org/about/contact

From preparation to faulting: multidisciplinary investigations on earthquake processes, volume II

Topic editors

Fuqiong Huang — China Earthquake Networks Center, China

Galina Kopylova — Kamchatka Branch of the Geophysical Survey of the Russian Academy of Sciences, Russia

Jie Liu — Sun Yat-sen University, Zhuhai Campus, China

Paresh Nath Singha Roy — Indian School of Mines, India

Giovanni Martinelli — National Institute of Geophysics and Volcanology, Section of Palermo, Italy

Mohammad Mokhtari — International Inst. earthquake Engineering and seismology, Iran

Citation

Huang, F., Kopylova, G., Liu, J., Singha Roy, P. N., Martinelli, G., Mokhtari, M., eds. (2024). *From preparation to faulting: multidisciplinary investigations on earthquake processes, volume II*. Lausanne: Frontiers Media SA.

doi: 10.3389/978-2-8325-5569-9

Table of contents

05 Editorial: From preparation to faulting: multidisciplinary investigations on earthquake processes, volume II
Fuqiong Huang, Jie Liu, Galina Kopylova, Giovanni Martinelli, Mohammad Mokhtari and Paresh Nath Singha Roy

09 The apparent focal depth, emergence angle, and take-off angle of seismic wave measured by YRY-4-type borehole strainmeter as one kind of strain seismograph
Lei Tang, Zehua Qiu, Junyi Fan and Zhigang Yin

21 Probabilistic seismic hazard function based on spatiotemporal earthquake likelihood simulation and Akaike information criterion: The PSHF study around off the west coast of Sumatra Island before large earthquake events
Wahyu Triyoso

31 Statistical analysis of ionospheric vertical total electron content anomalies before global Mw≥6.0 shallow earthquakes during 2000–2020
Yifang Ma, Xiaohui Zhou, Yilin Yang, Leyin Hu, Hongyan Dong and Rui Yan

46 Seismic Rigoletto: Hazards, risks and seismic roulette applications
James Bela, Vladimir Kossobokov and Giuliano Panza

74 The 3-D shallow velocity structure and sedimentary structure of 2017 Ms6.6 Jinghe earthquake source area derived from dense array observations of ambient noise
Ming Zhou, Xiaofeng Tian, Zhuoxin Yang, Qiaoxia Liu and Zhanyong Gao

88 Micro-seismic events detection and its tectonic implications in Northeastern Hainan Province
Zeyu Ma, Hongyi Li, Min Liu, Yafen Huang, Shengzhong Zhang and Yuejun Lv

98 Characteristic identification of seismogenic electromagnetic anomalies based on station electromagnetic impedance
Ye Fan, Wenbao Hu, Bing Han, Ji Tang, Xiao Wang and Qing Ye

115 Sensitivity limits for strain detection of hypothetical remote fluid-induced earthquakes ($M_w \geq 4$): a case study in Taiwan
Alexandre Canitano

127 Research on thermal infrared anomaly characteristics of moderate strong earthquakes in northeast China
Mengying Li, Zhihong Zhang, Shichao Yang, Xiangrui Kong and Mingruo Jiao

139 Influence of the Yucatan earthquake event
Changcheng Li

147 Groundwater trace element changes were probably induced by the ML3.3 earthquake in Chaoyang district, Beijing
Yuxuan Chen and Jianbo Liu

160 Geofluids as a possible unconventional tool for seismic hazard assessment
Giovanni Martinelli, Lisa Pierotti, Gianluca Facca and Fabrizio Gherardi

169 Crustal heterogeneity effects on coseismic deformation: numerical simulation of the 2008 M_w 7.9 Wenchuan earthquake
Mingqian Shi, Sichen Meng, Caibo Hu and Yaolin Shi

183 Stable isotopes and hydrogeochemical evolutions of groundwater from a typical seismic fault zone in the Mt. Lushan region, Eastern China
Zhicheng Bao, Le Hu, Jian Xiao, Xiaohui Zha, Jian Lv and Ying Zhao

194 Spatio-temporal characteristics of seismic strain anomalies reveal seismic risk zones along the Longmenshan fault zone and adjacent areas
Guofu Luo, Yingcai Xu, Hengzhi Luo, Fenghe Ding and Wenjun Li

frontiers | Frontiers in Earth Science

TYPE Editorial
PUBLISHED 20 September 2024
DOI 10.3389/feart.2024.1467641

Check for updates

OPEN ACCESS

EDITED AND REVIEWED BY
Jeroen van Hunen,
Durham University, United Kingdom

*CORRESPONDENCE
Fuqiong Huang,
hfqiong126@126.com
Giovanni Martinelli,
giovanni.martinelli15@gmail.com

RECEIVED 20 July 2024
ACCEPTED 08 August 2024
PUBLISHED 20 September 2024

CITATION
Huang F, Liu J, Kopylova G, Martinelli G, Mokhtari M and Singha Roy PN (2024) Editorial: From preparation to faulting: multidisciplinary investigations on earthquake processes, volume II.
Front. Earth Sci. 12:1467641.
doi: 10.3389/feart.2024.1467641

COPYRIGHT
© 2024 Huang, Liu, Kopylova, Martinelli, Mokhtari and Singha Roy. This is an open-access article distributed under the terms of the Creative Commons Attribution License (CC BY). The use, distribution or reproduction in other forums is permitted, provided the original author(s) and the copyright owner(s) are credited and that the original publication in this journal is cited, in accordance with accepted academic practice. No use, distribution or reproduction is permitted which does not comply with these terms.

Editorial: From preparation to faulting: multidisciplinary investigations on earthquake processes, volume II

Fuqiong Huang[1,2,3]*, Jie Liu[4], Galina Kopylova[5], Giovanni Martinelli[6,7]*, Mohammad Mokhtari[8] and Paresh Nath Singha Roy[9]

[1]China Earthquake Networks Center, Beijing, China, [2]Institute of Disaster Prevention, Beijing, China, [3]North China Institute of Science and Technology, Beijing, China, [4]School of Earth Sciences and Engineering, Sun Yat-sen University, Zhuhai, Guangdong, China, [5]Kamchatka Branch of the Geophysical Survey of the Russian Academy of Sciences (KB GS RAS), Petropavlovsk-Kamchatsky, Russia, [6]INGV National Institute of Geophysics and Volcanology, Palermo, Italy, [7]Institute of Eco-Environment and Resources, Chinese Academy of Sciences, Lanzhou, China, [8]International Institute of Earthquake Engineering and Seismology, Tehran, Iran, [9]Department of Geology and Geophysics, Indian Institute of Technology, Kharagpur, India

KEYWORDS

earthquake preparation process, physics of earthquake sources, evidence for risk evaluation and forecasting, monitoring systems of networks, multidisciplinary approaches

Editorial on the Research Topic
From preparation to faulting: multidisciplinary investigations on earthquake processes, volume II

1 Aims and content of this Research Topic

This Research Topic "From Preparation to Faulting: Multidisciplinary Investigations on Earthquake Processes - Volume II" is in the series of the research topic "From Preparation to Faulting: Multidisciplinary Investigations on Earthquake Processes," so the two research topics shared the similar aims and contents (Huang et al., 2023a). Recent research progress provides state-of-the-art studies on earthquake processes via multidisciplinary approaches coming from geophysical, geochemical, geodetical, and geological routes, which were mostly exchanged at the annual conference of the China Earthquake Prediction Forum (Huang et al., 2023a; Huang et al., 2023b; Huang et al., 2024). As we have noted (Huang et al., 2023a), in seismically active areas, the best disaster mitigation method is to enhance risk evaluation and prediction skills. Over the last few decades, multidisciplinary studies from small-scale fractures in the laboratory to real seismogenic structures in field test sites have given us opportunities to understand the nature of earthquake processes from preparation to faulting. Pre-earthquake observations, methods, and perspectives can provide an up-to-date view in our knowledge of processes preceding earthquake occurrence in China; modeling, which can be employed to set up earthquake forecasting experiments, aims to verify test site areas, whether large or small, even across the world.

2 Overview on published contributions

There are 15 articles collected for this Research Topic volume II, mostly involving precursors from space view (two articles) and from ground base observation techniques and monitoring networks (2 articles for bore hole strain meter, 2 articles for chemistry of groundwater, 1 article for electromagnetism, 1 article for seismicity, respectively), involving earthquake hazard risk assessment through conventional (two articles) and unconventional (1 article) approaches, involving the seismogenic structure and fault geometry of seismic source (2 article) and numerical modeling (1 article), and specifically involving seismic wave effects of an historical event for the scale of tectonic plate (1 article).

2.1 Precursors of multidisciplinary monitoring networks: from ground base to space view observation techniques

Extracting anomalous changes relevant to earthquake processes from observation systems is the key step for routine earthquake prediction. In the past, research results mainly came from ground-based conventional observation approaches. Nowadays, supported by advanced space science and technology, anomalies from satellite measurements provide space views on earthquake precursors.

Conventional approaches are ground-based observation systems including groundwater measurements, seismograph measurements, deformation measurements, and electromagnetism measurements. Anomalies from hydro-geochemistry of groundwater measurements are generally considered short-term indicators of earthquake occurrence (Chen and Liu, *Groundwater trace element changes were probably induced by the ML3.3 earthquake in Chaoyang district, Beijing*). Through systematically measuring the chemical components from the surface water to groundwater, scientists can trace the chemical evolution of water and obtain clues as to the mechanisms of earthquake precursors (Bao et al., *Stable isotopes and hydrogeochemical evolutions of groundwater from a typical seismic fault zone in the Mt. Lushan region, Eastern China*). By way of the three-dimensional numerical simulation method and the field component composition method, the response of low-frequency pre-earthquake electromagnetic radiation was calculated; the seismogenic resistivity anomaly and pre-earthquake electromagnetic radiation are obtained (Fan et al., *Characteristic identification of seismogenic electromagnetic anomalies based on station electromagnetic impedance*). By using the conventional method of orthogonal expansion in climate change to seismicity data analysis in an innovative way, the research results showed that the temporal indicators from long-term to short-term stages are process-dependent, and the epicenter indicator of future strong earthquakes is closely related to the fault position and the seismic strain contour (Luo et al., *Spatio-temporal characteristics of seismic strain anomalies reveal seismic risk zones along the Longmenshan fault zone and adjacent areas*). From the satellite data on *China's geostationary meteorological satellite FY-2E/G* for weather forecasting, the characteristics of thermal infrared radiation (TIR) anomalous changes prior to deep and shallow earthquakes in Northeast China have been found to be an short-term indicator (Li et al., *Research on thermal infrared anomaly characteristics of moderate strong earthquakes in northeast China*). From satellite data, scientists also derived the pre-earthquake vertical total electron content (VTEC) variations and statistically researched the characteristics of VTEC before 1,522 shallow (≤60 km) strong (Mw ≥ 6.0) earthquakes in the global area, which occurred between 2000 and 2020, and then declaimed the short-term anomalies within decade-days before earthquake occurrence (Ma et al. , *Statistical analysis of ionospheric vertical total electron content anomalies before global Mw ≥ 6.0 shallow earthquakes between 2000–2020*).

2.2 New views from conventional observation data: borehole strain meter

The borehole strain meter is widely used to observe the strain changes so that the stress-related earthquake precursors can be derived. The co-seismic oscillations of borehole observation data had been neglected due to the low-frequency sampling observation techniques. With high-frequency sampling data, scientists have found a new approach to infer the parameters of the seismic source (Tang et al., *The apparent focal depth, emergence angle, and take-off angle of seismic wave measured by YRY-4-type borehole strainmeter as one kind of strain seismograph*). This result provides support of the comparison of a fiber seismogram with a conventional seismogram, which promotes the conventional techniques for seeking precursors to new application views. In addition to borehole strain meter observation, through the hypothesis of fluid flow, the mechanisms of remote triggering can be understood (Canitano, *Sensitivity limits for strain detection of hypothetical remote fluid-induced earthquakes (Mw ≥ 4): a case study in Taiwan*). This is the first attempt to analyze strain time-series for detecting pre-earthquake strain anomalies related to fluid-induced earthquakes and illustrate the challenges in detecting and characterizing intermediate-to far-afield earthquake precursors caused by the fluid flow in active regions.

2.3 From seismogenic structure and fault geometry to co-seismic deformation of the seismic source: useful arrays and powerful modeling techniques

Fault geometry and movement are the main objectives which can be used in prediction models. With a dense array of seismometers and ambient noise or micro-seismic events, the fault structure of the seismic source can be detected (Zhou et al., *The 3-D shallow velocity structure and sedimentary structure of 2017 Ms6.6 Jinghe earthquake source area derived from dense array observations of ambient noise;* Ma et al., *Micro-seismic events detection and its tectonic implications in Northeastern Hainan Province*). With the finite element method and clear material heterogeneity and geometric complexity, the co-seismic deformation of earthquakes can be inferred through numerical modeling (Shi et al., *Crustal heterogeneity effects on coseismic deformation: numerical simulation of the 2008 MW 7.9 Wenchuan earthquake*). This supplies an approach

suitable to understand the mechanism of earthquake processes and is a significant step forward for the road map of numerical earthquake prediction in China (Huang et al., 2017a).

2.4 Models for earthquake risk assessment: from conventional to unconventional approaches

With the model of probabilistic seismic hazard analysis (PSHA), a global seismic hazard map was created to be widely used in the social economy. This is a kind of expression of long-term forecasting where the earthquake potential model plays a crucial role. The probabilistic seismic hazard function (PSHF) of the model is region-dependent due to the regional data quality based on the regional research level of tectonic settings and seismic events recorded. The map will be modified after regional strong events. Here, we collected one article on PSHF for Sumatra Island (Triyoso, *Probabilistic seismic hazard function based on spatiotemporal earthquake likelihood simulation and Akaike information criterion: The PSHF study around off the west coast of Sumatra Island before large earthquake events*). The neo-deterministic seismic hazard assessment (NDSHA) is the new multi-disciplinary scenario and physics-based approach for the evaluation of seismic hazard and safety—guaranteeing "prevention rather than cure." We collected a review article introducing this new model (Bela et al., *Seismic Rigoletto: Hazards, risks and seismic roulette applications*). They are conventional approaches to the seismic hazard mostly based on earthquake catalogs. Some scientists have found an unconventional approach to the hazard map mainly based on the areas characterized by the occurrence of thermal waters and/or by the release of deep-seated gases, as traced by the isotope composition of associated helium (see Martinelli et al. , *Geofluids as a possible unconventional tool for seismic hazard assessment*).

Based on seismological methods, the impact of seismic wave effects generated by meteorite impacts over 66 million years ago on the solid Earth itself has been quantitatively explored. The research results show that this event promoted the formation of the Indian Ocean plate, which is of great significance for improving our understanding of spatial distribution patterns of the global disaster risk from outer space, as well as for the development of plate tectonics theory (C. LI, *Influence of the Yucatan earthquake event*).

All the above progress in this Research Topic volume is largely based on advanced observation techniques and monitoring systems from ground to space which currently operate.

3 Discussion and perspectives

The progress of geosciences sinks its roots in advanced observation techniques. Through advanced laboratory experiment techniques, various scientists have reported that earthquakes are accompanied by possible precursors that can be used for prediction (e.g., Ma, 2016). The long-term cumulated precursors have supplied opportunities to understand the preparation processes of strong earthquakes (Huang et al., 2017b; Martinelli et al., 2021). By way of co-seismic oscillations observed from the borehole strain meter, seismic source parameters can be extracted (see the works of Tang et al. in this volume), the mechanisms of remote triggering can be explained based on the fluid flow hypothesis (see the works of Canitano in this volume). Based on comprehensive analysis of parameters related to geofluids, the stress evolution, and the global seismicity, an unconventional approach of geofluids can be added to the list of fundamental geological parameters to be considered in the hazard assessment (see the works of Martinelli et al. in this volume). Many innovative ideas are included in the articles of this volume, which will play a role in understanding the nature of earthquake processes.

The question as to how can machine learning techniques be used for extracting the precursors from long-term cumulated observation data is raised. The time for earthquake precursors (e.g., Pritchard et al., 2020) is now ripe! Let us broaden our perspectives and make it happen!

Author contributions

FH: writing–original draft, writing–review and editing, conceptualization, and investigation. JL: writing–original draft and writing–review and editing. GK: writing–original draft and writing–review and editing. GM: writing–original draft and writing–review and editing. MM: writing–original draft and writing–review and editing. PS: writing–original draft and writing–review and editing.

Funding

The author(s) declare that no financial support was received for the research, authorship, and/or publication of this article.

Acknowledgments

This Research Topic originates from and expands on the annual conference on the *China Earthquake Prediction Forum* sponsored by the Earthquake Prediction Committee of Seismological Society of China and co-sponsored and partly supported by the Department of Earthquake Monitoring and Prediction of China Earthquake Administration. The editors wish to thank all the authors who contributed their manuscripts and reviewers who contributed their time, expertise, and patience to reviewing the manuscripts and interacting with the authors, which has helped significantly improve the quality of the articles for this Research Topic.

Conflict of interest

The authors declare that the research was conducted in the absence of any commercial or financial relationships that could be construed as a potential conflict of interest.

Publisher's note

All claims expressed in this article are solely those of the authors and do not necessarily represent those of their affiliated organizations, or those of the publisher, the editors, and the reviewers. Any product that may be evaluated in this article, or claim that may be made by its manufacturer, is not guaranteed or endorsed by the publisher.

References

Huang, F. Q., Zhang, X. D., Cao, Z. X., Li, J. P., and Li, S. H. (2017a). The roadmap of numerical earthquake prediction in China. *Recent Dev. World Seismol.* 460 (4), 4–10. (in Chinese).

Huang, F. Q., Li, M., Ma, Y. C., Han, Y. Y., Tian, L., Yan, W., et al. (2017b). Studies on earthquake precursors in China: a review for recent 50 years. *Geod. Geodyn.* 8, 1–12. doi:10.1016/j.geog.2016.12.002

Huang, F., Yao, H., Liu, J., Yang, H., and Martinelli, G. (2023a). Editorial: From preparation to faulting: multidisciplinary investigations on earthquake processes. *Front. Earth Sci.* 11, 1220232. doi:10.3389/feart.2023.1220232

Huang, F. Q., Liu, J., Yao, H., Shao, Z. G., Wang, Q., Liu, J., Shao, Y. X., Yan, R., De, J., et al. (2023b). Introduction to the special issue of 2022 annual conference on China Earthquake Prediction Forum (CEPF) (in Chinses). *Seismological and Geomagnetic Observation and Research* 01. doi:10.3969/j.issn.1003-3246.2022.S1.001

Huang, F. Q., Liu, J., and Yao, H. J. (2024). Introduction to the special issue of 2023 annual conference on China Earthquake Prediction Forum (CEPF) (in Chinses). *Seismol. Geomagn. Obs. Res.* doi:10.3969/j.issn.1003-3246.2023.S1.001

Ma, J. (2016). On "Whether earthquake precursors help for prediction do exist?" (in Chinese). *Chin Sci Bull* 61, 409–414. doi:10.1360/N972015-01239

Martinelli, G., Ciolini, R., Facca, G., Fizio, F., Gherardi, F., Heinicke, J., and Pierotti, L. (2021). Tectonic-related geochemical and hydrological anomalies in Italy during the last fifty years. *Minerals* 11, 107. doi:10.3390/min11020107

Pritchard, M. E., Allen, R. M., Becker, T. W., Behn, M. D., Brodsky, E. E., Bürgmann, R., Ebinger, C., Freymueller, J. T., Gerstenberger, M., Haines, B., et al. (2020). New Opportunities to Study Earthquake Precursors. *Seismol. Res. Lett.* 91 (5), 2444–2447. doi:10.1785/0220200089

frontiers | Frontiers in Earth Science

TYPE Original Research
PUBLISHED 20 March 2023
DOI 10.3389/feart.2023.1036797

Check for updates

OPEN ACCESS

EDITED BY
Jie Liu,
School of Earth Sciences and Engineering, Sun Yat-sen University, China

REVIEWED BY
Wanpeng Feng,
School of Earth Sciences and Engineering, Sun Yat-sen University, China
Lingyun Ji,
The Second Monitoring and Application Center, China Earthquake Administration, China

*CORRESPONDENCE
Lei Tang,
tanglei06@seis.ac.cn

SPECIALTY SECTION
This article was submitted to Solid Earth Geophysics, a section of the journal Frontiers in Earth Science

RECEIVED 05 September 2022
ACCEPTED 09 March 2023
PUBLISHED 20 March 2023

CITATION
Tang L, Qiu Z, Fan J and Yin Z (2023), The apparent focal depth, emergence angle, and take-off angle of seismic wave measured by YRY-4-type borehole strainmeter as one kind of strain seismograph.
Front. Earth Sci. 11:1036797.
doi: 10.3389/feart.2023.1036797

COPYRIGHT
© 2023 Tang, Qiu, Fan and Yin. This is an open-access article distributed under the terms of the Creative Commons Attribution License (CC BY). The use, distribution or reproduction in other forums is permitted, provided the original author(s) and the copyright owner(s) are credited and that the original publication in this journal is cited, in accordance with accepted academic practice. No use, distribution or reproduction is permitted which does not comply with these terms.

The apparent focal depth, emergence angle, and take-off angle of seismic wave measured by YRY-4-type borehole strainmeter as one kind of strain seismograph

Lei Tang[1]*, Zehua Qiu[2], Junyi Fan[1] and Zhigang Yin[3]

[1]China Earthquake Networks Center, China Earthquake Administration, Beijing, China, [2]National Institute of Natural Hazards, Ministry of Emergency Management of China, Beijing, China, [3]Shanxi Earthquake Agency, Taiyuan, China

Introduction: In theory, the observation objects and principles of strain seismograph and traditional pendulum seismograph are different, and the characteristics of observed signals should also be dissimilar. The observation results of pendulum seismograph show that seismic waves in inhomogeneous media will undergo refraction, reflection, and attenuation. Then, what signal characteristics can be detected by strain seismograph is great significance for understanding and explaining the observation results.

Methods: Using YRY-4 type four-gauge borehole strainmeter as one kind of strain seismograph to detect the strain tensor change of the plane seismic wave emitted from the surface, a five-site strain seismograph observation network was built in Shanxi Province, with continuous observation for 2 years at a sampling rate of 100 Hz. In this paper, two local events occurring in the area covered by the strain seismograph observation network are taken as examples. We systematically studied the characteristics of seismic wave signals recorded by strain seismographs at five sites, inverted for the focal depth of the two local earthquakes and the relationship between the wave velocity and the wave velocity gradient of the focal depth, and calculated the apparent focal depth, the emergence angle and the take-off angle of seismic waves.

Results: These results show stable uniqueness and apparent regularity, especially since the inverted focal depths are basically consistent with the seismic solutions based on those traditional pendulum seismographs. The observations from this study show that the strain seismograph can be used as an effective supplement to the pendulum seismograph.

Discussion: In the future, we will continue to study the rupture process and focal mechanism of moderate-strong earthquakes and teleseismic earthquakes by combining two kinds of observations.

KEYWORDS

strain seismograph, seismic reaction, emergence angle, focal depth, take-off angle

1 Introduction

Since the 1960s, relative stress observations have been carried out in the United States, China, Japan and other countries (Sacks et al., 1971; Gladwin, 1984; Ishii, 2001); borehole strain observation is a vital observation method gradually developed from relative stress observation. Scholars in mainland China have developed RZB-type four-component borehole strainmeter (Ouyang, 1977), TJ-type borehole volume strainmeter (Su, 1982), and YRY-type four-component borehole strainmeter (Chi et al., 2009), and continuously improved the observation technology. It has developed to more than 130 stations equipped with borehole strainmeters. These borehole strain observations can record clear solid tides and play an essential role in the field of earthquake monitoring and prediction in mainland China (Huang et al., 2017).

Unlike GTSM strainmeter such as the United States, which can produce high frequency data of 20 Hz, the data sampling rate of strainmeter in mainland China is minute sampling due to data storage and transmission technology. Using these minute data, scholars in mainland China have carried out a lot of research, including the tidal Variation and calibration technology (Qiu et al., 2015), abnormal changes of different earthquakes (Qiu et al., 2010; Liu et al., 2014), co-seismic strain steps (Gong et al., 2019; Li et al., 2020), free oscillation of the earth excited by large earthquakes (Tang et al., 2007; Tang et al., 2008; Qiu, 2017), and also studied and analyzed the influence of water level, air pressure, rainfall and other factors on borehole strain, and studied the data processing methods to identify and eliminate these influencing factors (Zhou et al., 2008; Zhang and Huang, 2011; Zhang et al., 2015). However, these studies are limited to longer period signals because of the low sampling rate.

Numerous studies have shown that the borehole strainmeter can be used for seismic wave observation (Byerly, 1926; Johnston et al., 1986; Borcherdt and Glassmoyer, 1989; Borcherdt et al., 2006; Johnston et al., 2006; Blum et al., 2010; Barbour and Agnew, 2012; Qiu et al., 2015; Barbour and Crowell, 2017; Canitano et al., 2017; Cao et al., 2018; Farghal et al., 2020; Barbour et al., 2021). This initially realized seismologists' expectations of strain seismographs (Benioff et al., 1961; Aki and Richards, 2002). Although the current horizontal component borehole strainmeter can only detect the two-dimensional strain variation in the horizontal plane, the seismic wave is usually approximated as a plane wave, and both have only three independent components, which can convert to each other. Therefore, this instrument can still be used to observe and analyze the strain variation of seismic waves.

Notably, strain seismographs are different from traditional pendulum seismographs. The traditional pendulum seismograph measures a vector (displacement), while the strain seismograph detects a tensor (displacement gradient). The strain seismograph can provide new information that can be used to carry out further research. One of the most critical research directions is the inversion of focal mechanism with strain seismic observation. Theoretically, the source moment tensor (Qiu et al., 2020) can be converted from the data of at least two strain observation points in different directions. Solving the focal mechanisms of local earthquakes by strain seismic observation can be used as supplementary information for pendulum seismograph observation.

The determination of the focal mechanism by seismic strain observation is theoretically based on the assumption of an ideal homogeneous medium, but the actual crustal strata are inhomogeneous. Figure 1 shows the geometrical interpretation of seismic wave propagation in homogeneous and inhomogeneous media. In a homogeneous medium, the angle (take-off angle) i_e between the seismic wave ray from the hypocenter and the normal direction of the ground remains unchanged when the seismic wave propagates linearly, which is equal to the emergence angle i_0 when reaching the ground. Seismic waves propagating in non-uniform strata can reflect and refract, and the rays are not straight lines. When the focal depth cannot be ignored, the emergence angle i is generally not equal to the take-off angle, i_e. This makes it difficult to solve the focal mechanism by seismic strain observation. The crust is separated from the mantle by the Moho surface, and it can be considered that there is no similar interface within the crust (Wyllie PJ, 1963). However, crustal rock is not a homogeneous medium. Basically, the wave velocity generally linearly increases with depth. As a first-order approximation, it can be considered that the gradient of wave velocity of crustal rocks with depth is a constant; this is defined as a constant velocity gradient model (Stein and Wysession, 2003; Wan, 2016). Under this condition, for local earthquakes, when the observation site is very close to the epicenter (within tens of kilometers), because the seismic waves only propagate in the crust, the initial motion is a direct wave, so the situation becomes relatively simple.

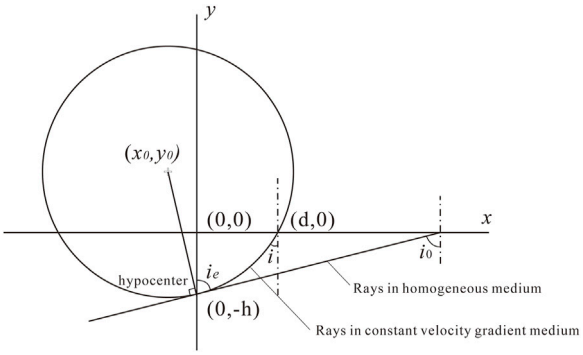

FIGURE 1
The geometry of the constant velocity gradient model. i_e: take-off angle; i: emergence angle for constant velocity gradient medium; i_0: emergence angle for homogeneous medium; (d, 0): site coordinates; (0, h): focal coordinates.

As the technical management and planning team of the borehole strain network in Mainland China, we have upgraded and updated the high-sampling data collectors of 10 four-component borehole strainmeters which are producing high frequency data of 100 Hz since 2017, only one site could produce high-frequency data before. Using these data, the ability of four-component borehole strainmeters to record strain seismic waves of earthquakes of different magnitudes has been studied (Qiu et al., 2015; Tang et al., 2022), the study of determining the strain magnitude of seismic surface wave based on borehole strain seismic wave is carried out (Li et al., 2020), Shi et al. (2021) studied the direct observation of co-seismic static stress deviation changes consistent with the theoretical prediction. These sites can record the seismic waves of earthquakes with M6.0 or above in the world (Tang et al., 2022), and can also record the local earthquakes in the area where the site is located. In this article, two earthquakes are experimentally examined through seismic strain observation using a high-density borehole strainmeter network in Xinzhou, Shanxi Province, China. The results show that there is an obvious rule that

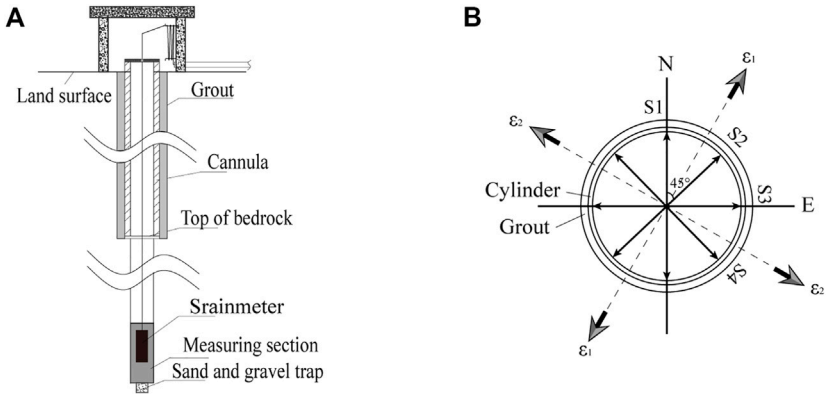

FIGURE 2
(A) The overall composition diagram of a standard borehole strain observation; **(B)** Schematic diagram of a standard borehole strainmeter, S1, S2, S3, S4 sensors in 4 directions,ε_1 and ε_2 represent the maximum and minimum principal strains, respectively.

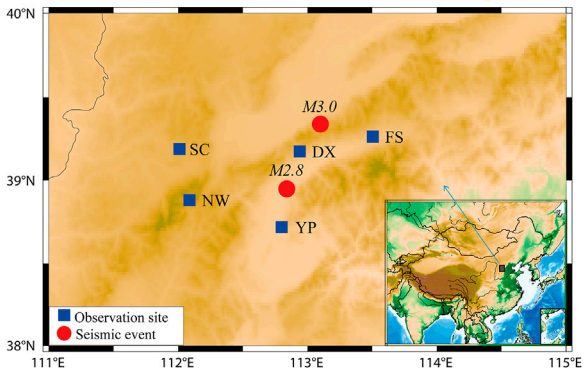

FIGURE 3
Map of the observation sites and the two local events.

the emergence angle of seismic waves reaching the observation sites varies with the epicentral distance, which can be simulated by the crustal wave velocity structure model with constant velocity gradient. On this basis, not only the focal depth can be calculated, the take-off angle of seismic wave rays arriving at each observation site can be determined.

2 Data

YRY-4 type of four-gauge borehole strainmeter (FGBS) is an important instrument for crustal deformation observation in china; the overall composition of the borehole observation (Tang et al., 2020) was designed by us as the drafters for the construction of the seismic industry standard borehole strain stations in mainland China and the four sensors of the YRY-4- type FGBS (Qiu et al., 2013; Li et al., 2021) are shown in Figure 2. The four gauges are arranged at 45° intervals, S*i* (*i* =1, 2, 3, 4) is the measurement obtained from each of the four gauges; it directly measure the change in diameter in the corresponding azimuth that results from changes in strain state. Since 2012, the YRY-4 -type FGBS has been used in Xinzhou area of Shanxi Province, and the sites such as Shenchi (SC), Fanshi (FS), Yuanping (YP), Daixian (DX), and Ningwu (NW) have been successively established, forming a high-density local observation network, as shown in Figure 3, and the measurement information of 5 sites are in Table 1. In 2018, we conducted an earthquake monitoring experiment using this observation network with a sampling rate of 100 Hz. Presently, more than 2 years of data have been accumulated. We have been very fortunate to capture two small local seismic events (YP M2.8 and DX M3.0) within the observation network (Figure 3), Table 2 gives the parameters of the two local events calculated by traditional pendulum seismograph, which are provided by the China Seismic Network.

YRY-4-type FGBS has good observation performance and has achieved great success in the study of geodynamic problems (Chi et al., 2009; Qiu et al., 2013; Liu et al., 2014). Some scholars have also studied the theoretical issues and feasibility of using the observed seismic strain waves (Zhang et al., 2019; Zhang et al., 2020; Zhang et al., 2021), but there has been no actual observation to verify the results. For the two earthquakes, the *P* and *S* waves of seismic strain waves recorded by the YRY-4-type FGBS at all the sites are apparent in Figure 4.

Based on NW in Figure 4, Figure 5 shows the more apparent seismic wave curve of YP *M*2.8 earthquake recorded at the NW site. For such local earthquakes, the first pulse (direct wave P_g and S_g) reaching the observation site is the most direct reflection of the earthquake hypocenter, which is extremely valuable for examining the focal mechanism. In this article, the extreme value (wave peak or trough) of this pulse is called the initial motion. The arrow in Figure 5 indicates the selection time of direct strain wave observation data.

It should be noted that the observation curve in Figure 5 does not show the real strain variation. The borehole strainmeter directly measures the relative diameter change of the probe sleeve, which requires calibration and conversion to obtain the strain variation in the rock layer (Qiu et al., 2013). The long-period signals, such as hydrological and tidal effects have no effect on high-frequency seismic wave signals, so it is reasonable to remove the linear trend of the observed record only by fitting. Table 3 and Table 4 show the observed strains of the initial motions of *P* and *S* waves of the two earthquakes in Table 2. ε_{11}, ε_{12}, and ε_{22} are three strain

TABLE 1 Measurement information of 5 sites.

Site	Lon. (°)	Lat. (°)	Measuring depth (*m*)	Lithology	Azimuth of S1
SC	112.01	39.19	32.0	Limestone	N24°W
FS	113.51	39.26	43.0	Granite	N26°W
YP	112.81	38.72	44.7	Granite	N56°W
DX	112.94	39.18	45.8	Granite	N60°E
NW	112.09	38.88	42.3	Granite	N9°E

TABLE 2 Parameters of the two local events provided by the China Seismic Network.

Seismic event	Date	Time	Lon. (°)	Lat. (°)	Magnitude (*M*)	Depth (*km*)
YP *M*2.8	2019-02-04	10:33:55	112.83	38.95	2.8	8
DX *M*3.0	2019-09-13	03:29:00	113.10	39.34	3.0	5

components in the horizontal plane of the geographic coordinate system obtained by calibration and conversion.

3 Methods and models

3.1 Strain conversion of emergent wave

3.1.1 Hypothesis

To discuss the evaluation of actual seismic wave strain using the observed horizontal strain, there are some hypotheses: Firstly, it is assumed that the epicenter location is known. Since Shanxi Province has a relatively dense pendulum seismograph observation network, it can be considered that this epicenter location is reliable. Secondly, the seismic wave near the earthquake hypocenter must not be an ideal plane wave, but the seismic wave reaching the observation site can be treated as a plane wave. Finally, the local earthquake events are discussed here, so it can be assumed that the path deviations of the *P* wave and *S* wave from the source to the observation site are small, which can be regarded as approximate values (Qiu et al., 2020). Practical calculations also confirm these hypotheses.

3.1.2 Fundamental formula

In the geographic coordinate system shown in Figure 6, the strain tensor of the seismic waves arriving at the observation site is denoted as

$$\varepsilon_G = \begin{bmatrix} \varepsilon_{11} & \varepsilon_{12} & \varepsilon_{13} \\ \varepsilon_{12} & \varepsilon_{22} & \varepsilon_{23} \\ \varepsilon_{13} & \varepsilon_{23} & \varepsilon_{33} \end{bmatrix} \tag{1}$$

However, the current borehole strainmeter can only observe symmetrical horizontal strain variation, i.e., only the three independent strain components (ε_{11}, ε_{12}, and ε_{22}) shown in the dashed frame of Eq. 1, the vertical strain components (ε_{13}, ε_{23}, and ε_{33}) are not considered.

According to the above assumptions, the seismic waves reaching the observation site can be regarded as plane waves. In the seismic ray coordinate system shown in Figure 6, where the seismic waves propagate along the x'_1 axis, the strain tensor should be written as (Qiu, 2017)

$$\begin{aligned} \varepsilon_R &= \varepsilon_R^P + \varepsilon_R^{SH} + \varepsilon_R^{SV} \\ &= \begin{bmatrix} \varepsilon'_{11} & 0 & 0 \\ 0 & 0 & 0 \\ 0 & 0 & 0 \end{bmatrix} + \begin{bmatrix} 0 & \varepsilon'_{12} & 0 \\ 0 & 0 & 0 \\ 0 & 0 & 0 \end{bmatrix} + \begin{bmatrix} 0 & 0 & \varepsilon'_{13} \\ 0 & 0 & 0 \\ 0 & 0 & 0 \end{bmatrix}, \\ &= \begin{bmatrix} \varepsilon'_{11} & \varepsilon'_{12} & \varepsilon'_{13} \\ 0 & 0 & 0 \\ 0 & 0 & 0 \end{bmatrix} \end{aligned} \tag{2}$$

where ε_R^P is the *P* wave strain, ε_R^{SH} is the *SH* wave strain, and ε_R^{SV} is the *SV* wave strain. It should be noted that $\varepsilon'_{12}$is parallel to the ground, while ε'_{13} is perpendicular to the ground. It is also noteworthy that ε_R is asymmetric.

The relationship between the horizontal strain detected at the observation site and the actual plane seismic wave strain should conform to the following coordinate transformation equation:

$$\varepsilon_G = l_{GR}\varepsilon_R l_{GR}^T \tag{3}$$

where the direction chord matrix is defined as follows:

$$l_{GR} = \begin{bmatrix} l_{11} & l_{12} & l_{13} \\ l_{21} & l_{22} & l_{23} \\ l_{31} & l_{32} & l_{33} \end{bmatrix} \tag{4}$$

The column vectors of l_{GR} are the direction vectors of the axes of the seismic wave ray coordinate system (x'_1, x'_2, x'_3) in the geographic coordinate system (x_1, x_2, x_3).

In fact, *P* and *S* waves propagate separately, while *SH* and *SV* waves propagate together. For *P* waves, for the strain component that can be observed by the borehole strainmeter, Eq. 3 can be written as follows:

$$\begin{cases} \varepsilon_{11}^P = \varepsilon'_{11} {l_{11}}^2 \\ \varepsilon_{22}^P = \varepsilon'_{11} {l_{21}}^2 \\ \varepsilon_{12}^P = \varepsilon'_{11} l_{11} l_{21} \end{cases} \tag{5}$$

The ε'_{11} of the observation site can be calculated by Eq. 5. For *S* wave, Eq. 3 can be written as

$$\begin{cases} \varepsilon_{11}^S = 2\varepsilon'_{12} l_{11} l_{12} + 2\varepsilon'_{13} l_{13} l_{11} \\ \varepsilon_{22}^S = 2\varepsilon'_{12} l_{21} l_{22} + 2\varepsilon'_{13} l_{23} l_{21} \\ \varepsilon_{12}^S = \varepsilon'_{12}(l_{11} l_{22} + l_{12} l_{21}) + \varepsilon'_{13}(l_{13} l_{21} + l_{11} l_{23}) \end{cases} \tag{6}$$

ε'_{12} and ε'_{13} of the observation site can be calculated from Eq. 6.

10.3389/feart.2023.1036797

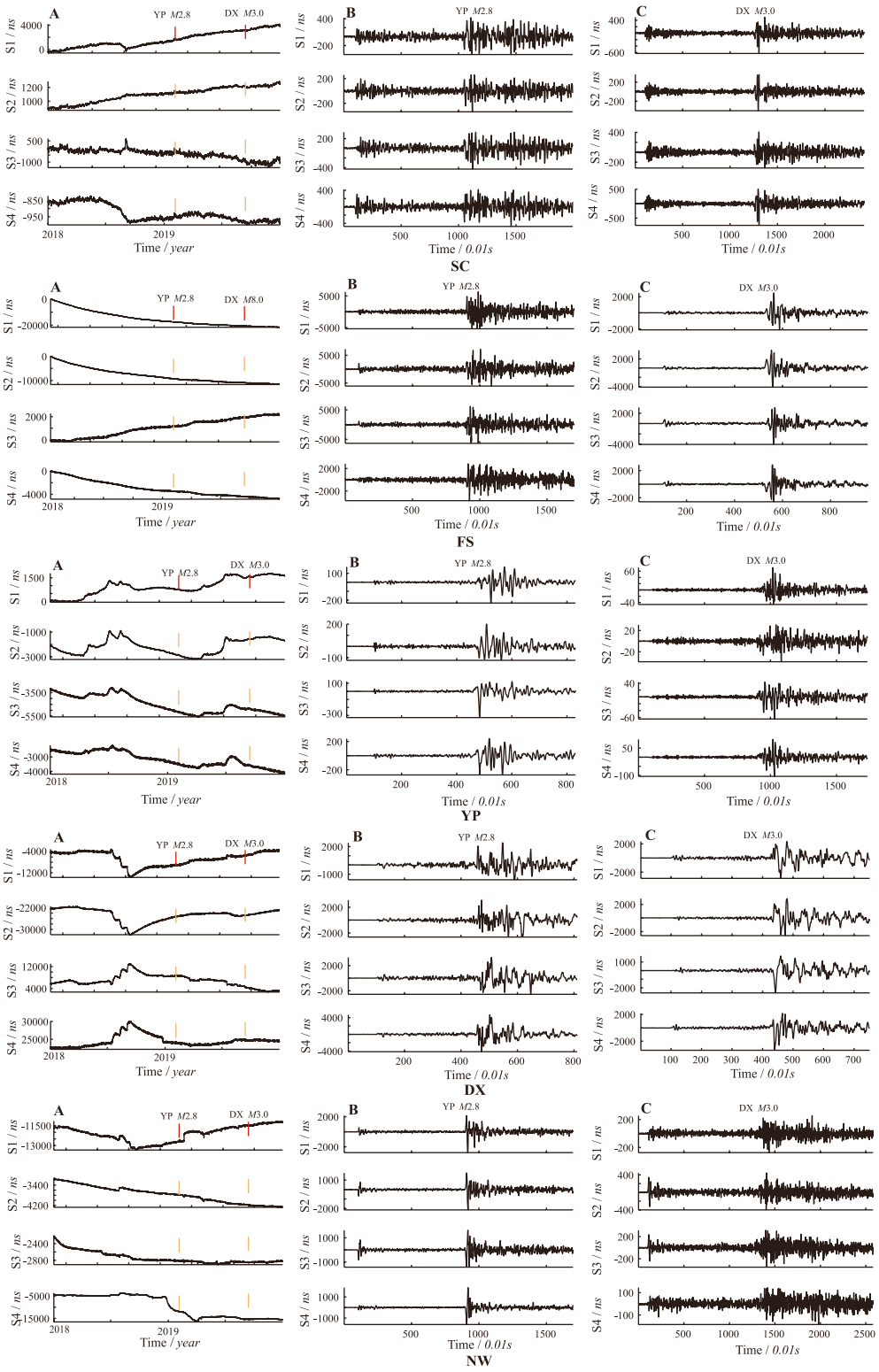

FIGURE 4
(A) Observation curves recorded by 5 sites in 2018-2019; **(B)** *P* and *S* waves of YP *M*2.8 event observed at 5 sites; **(C)** *P* and *S* waves of DX *M*3.0 event observed at 5 sites.

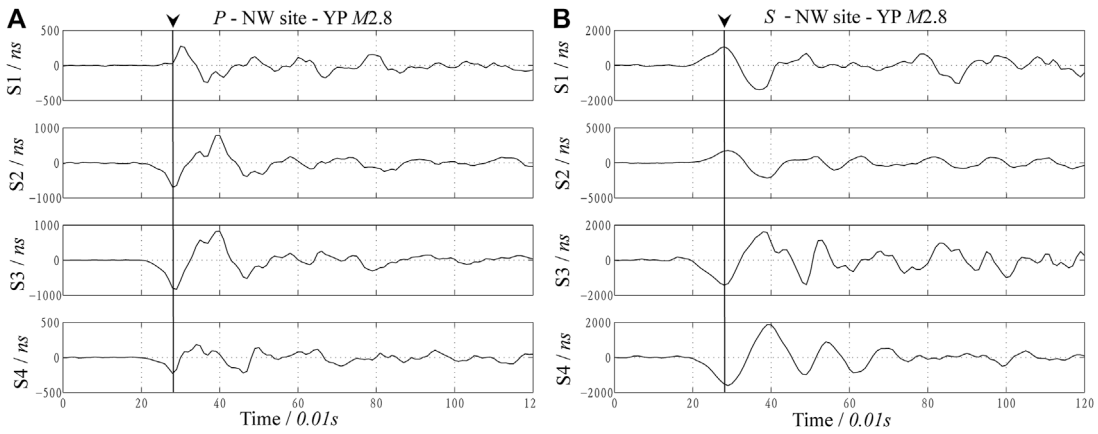

FIGURE 5
P **(A)** and *S* **(B)** waves of the *M*2.8 event were observed at the NW site.

TABLE 3 Observed strains of the initial motions of *P* and *S* waves for the *M*2.8 event.

Site	Epicentral distance (*km*)	*P* wave strain (10 μs)			*S* wave strain (10 μs)		
		ε_{11}^{P}	ε_{22}^{P}	ε_{12}^{P}	ε_{11}^{S}	ε_{22}^{S}	ε_{12}^{S}
SC	76	−0.4279	−0.7521	0.3176	−0.9617	−1.2507	0.9431
FS	67	0.5575	0.1510	0.2124	1.1606	−0.4319	−0.6266
YP	26	−0.7733	−0.5425	−0.0309	4.4307	6.0956	1.2608
DX	26	0.2868	0.1726	0.0180	2.1731	1.5789	1.1088
NW	66	−1.0526	−2.8689	−0.1171	1.0185	−1.5087	3.1583

TABLE 4 Observed strains of the initial motions of *P* and *S* waves for the *M*3.0 event.

Site	Epicentral distance (*km*)	*P* wave strain (10 μs)			*S* wave strain (10 μs)		
		ε_{11}^{P}	ε_{22}^{P}	ε_{12}^{P}	ε_{11}^{S}	ε_{22}^{S}	ε_{12}^{S}
SC	95	0.2889	0.4486	−0.0719	0.2977	0.5873	0.3213
FS	36	1.1503	1.6837	0.9323	4.7661	−1.9321	1.2547
YP	74	−0.0785	−0.0531	−0.0219	−0.3770	0.3770	0.0226
DX	23	0.2550	0.2044	0.1121	−2.8276	0.0711	−0.0870
NW	101	0.4559	1.0147	0.2115	0.2697	0.0244	0.1864

As shown in Figure 6, the emergence angle is expressed as $i = \pi - \theta$. The components of l_{GR} can be expressed by azimuth angle φ and emergence angle i:

$$\begin{cases} l_{11} = \sin i \cos\varphi \\ l_{21} = \sin i \sin\varphi \\ l_{31} = -\cos i \\ l_{12} = -\sin\varphi \\ l_{22} = \cos\varphi \\ l_{32} = 0 \\ l_{13} = -\cos i \cos\varphi \\ l_{23} = -\cos i \sin\varphi \\ l_{33} = \sin i \end{cases} \tag{7}$$

3.1.3 Practical algorithm

In addition to the known observations, the azimuth φ can be calculated from the epicenter position for an observation site. In other words, we are facing with an overdetermined problem; four unknowns need to be solved by Eqs 5, 6: $\varepsilon_{11}^{'}$, $\varepsilon_{12}^{'}$, $\varepsilon_{13}^{'}$, and the emergence angle i.

In a homogeneous medium, if the epicentral distance d and focal depth h are known, the emergence angle i can be easily calculated. However, on the one hand, although the epicentral distance d is generally reliable, the focal depth h given by the existing methods is not reliable; on the other hand, the crustal strata are not a homogeneous medium. Therefore, the emergence angle i cannot be given in advance.

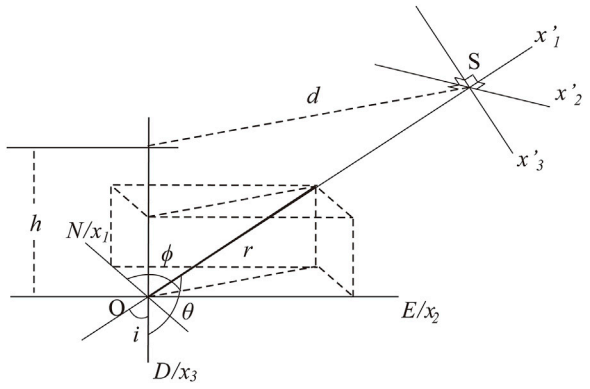

FIGURE 6
Geographical coordinates (x_1, x_2, x_3) and ray coordinates (x'_1, x'_2, x'_3). "O" represents the seismic focus; "S" represents the seismographic site.

Here, the apparent focal depth at each observation site is defined as

$$h_i = \frac{d}{\tan i} \tag{8}$$

We first calculate the apparent focal depth h_i rather than the emergence angle i. Because the focal depth is not a high-precision quantity, it is generally accurate to the km level. Therefore, we use the enumeration method, where all the values from 1 km to 300 km are tried, and the optimal value is selected as the apparent focal depth; the error does not exceed 1 km.

For an observation site, we proposed a specific algorithm to determine the focal depth as follows. Firstly, for the attempted h_i, three ε'_{11} are obtained by using Eq. 5, and the standard deviation $std(\varepsilon'_{11})$ is calculated. Secondly, for the attempted h_i, three ε'_{12} and three ε'_{13} are obtained by using Eq. 6, and the corresponding standard deviations $std(\varepsilon'_{12})$ and $std(\varepsilon'_{13})$ are calculated. Thirdly, the objective function is established as follows:

$$F_{std} = \log\left[std\left(\varepsilon'_{11}\right) + std\left(\varepsilon'_{12}\right) + std\left(\varepsilon'_{13}\right)\right] \tag{9}$$

Finally, all h_i are tested, and the minimum target function h_i is selected as the apparent focal depth of the observation point. Further, the corresponding ε'_{11}, ε'_{12} and ε'_{13} are selected as the strain component value of the plane seismic wave reaching the observation site.

For the two earthquakes, Figure 7 shows the calculated apparent focal depth of the five observation sites. There are two notable points. First, the objective function can reach the obvious minimum extreme point; second, as shown in the sub-graphs at the lower right corner of Figures 7A, B, compared with Figure 3 and Table 3, and Table 4, the apparent focal depth of each observation site shows linear behavior: when the epicentral distance is larger, the apparent focal depth is also larger. These two points prove the reliability of the observation data as well as the accuracy of the calculation results. Further, the calculation results validate the feasibility of the above-mentioned assumptions.

3.2 Constant velocity gradient model

The two earthquakes recorded by our experimental network occurred in the crust. In a homogeneous medium, seismic waves should propagate linearly. If the crust is a homogeneous medium, the apparent focal depth calculated at all the observation sites should be equal to the actual focal depth when the seismic wave emitted by the hypocenter reaches different observation sites. However, actually, the apparent focal depths of each observation site are different, indicating that the crust may not be homogeneous medium.

The variation in the wave velocity of crustal rocks with depth is very complex, but the primary feature of the crustal structure is that the wave velocity increases with depth. As a first-order approximation, we can consider that the wave velocity steadily increases with depth, which is called the constant velocity gradient model (Stein and Wysession, 2003; Wan, 2016). When the epicentral distance is larger, the observed phenomenon that the focal depth is larger can be explained by this model.

The constant wave velocity gradient model is usually established on the premise that the hypocenter is located on the surface. To examine the seismic wave rays of local earthquakes, the constant velocity gradient model with a certain depth is considered, as shown in Figure 1. Assuming that the wave velocity gradient is k, the variation in the wave velocity with depth can be expressed as follows:

$$v = v_e - k(y + h) = v_0 - ky \tag{10}$$

where v_e is the wave velocity at the focal depth, and $v_0 = v_e - kh$ is the wave velocity near the surface. In a homogeneous medium, the rays emitted from the take-off angle i_e propagate in a straight line, and the emergence angle $i_0 = i_e$ reaches the surface. In the medium, where the wave velocity steadily increases with depth, the emergence angle $i \neq i_e$ reaches the surface.

The characteristic of the rays emitted from the emergence angle i_e is that the radius of curvature ρ remains constant (Wan, 2016), which can be written as

$$\rho = \frac{1}{pk} \tag{11}$$

where p is the ray parameter, which conforms to Snell's law as follows:

$$p = \frac{\sin i_e}{v_e} \tag{12}$$

According to the previous assumptions, the path of P and S waves is the same, i.e., p is the same. Substituting Eq. 12 into Eq. 11, we get

$$\rho = \frac{H}{\sin i_e} \tag{13}$$

where $H = \frac{v_e}{k}$, H reflects the relationship between wave velocity gradient and wave velocity at the focal depth.

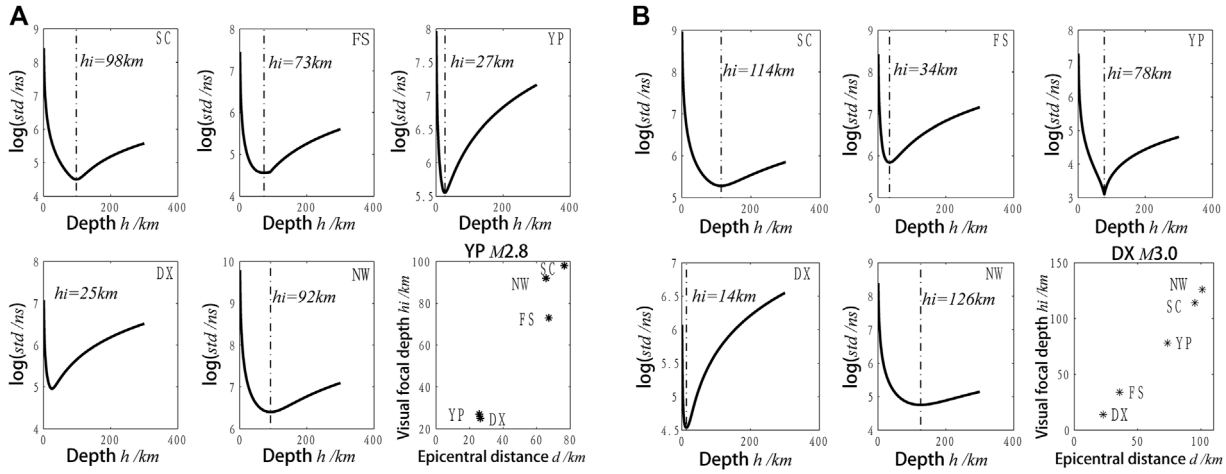

FIGURE 7
Optimal estimations of the apparent focal depths (indicated by the dash-dotted lines) for the two events: **(A)** YP *M*2.8, **(B)** DX *M*3.0.

3.3 Formula of take-off angle

As mentioned above, in a constant velocity gradient medium, the equation of the circle (Figure 1) of the seismic wave rays emitted from the source is as follows:

$$(x - x_0)^2 + (y - y_0)^2 = \rho^2 \tag{14}$$

where

$$\begin{cases} x_0 = -\rho \cos i_e \\ y_0 + h = \rho \sin i_e \end{cases} \tag{15}$$

On the ground, y = 0. Substituting Eq. 15 into Eq. 14 and simplifying it, we get

$$x^2 + 2x\rho \cos i_e + h^2 - 2h\rho \sin i_e = 0 \tag{16}$$

Then, inserting Eq. 13 with Eq. 16, we obtain

$$x^2 + 2x\frac{H}{\tan i_e} + h^2 - 2hH = 0 \tag{17}$$

Thus, the take-off angle can be expressed as

$$i_e = \arctan\frac{2Hx}{2Hh - h^2 - x^2} \tag{18}$$

where x is the epicentral distance, which can also be denoted by d.

Using Eqs 14, 15 we get

$$y = \pm\sqrt{\rho^2 - (x + \rho \cos i_e)^2} + \rho \sin i_e - h \tag{19}$$

Then, the actual seismic wave ray equation can be written as

$$\begin{aligned} y &= -\sqrt{\rho^2 - (x + \rho \cos i_e)^2} + \rho \sin i_e - h \\ &= -\sqrt{\frac{H^2}{\sin^2 i_e} - \left(x + \frac{H}{\tan i_e}\right)^2} + H - h \end{aligned} \tag{20}$$

Using Eq. 20, seismic wave rays with different departure angles can be obtained. Differentiating the above equation to x and substituting Eq. 13 into it, we get

$$\frac{dy}{dx} = \frac{x + \rho \cos i_e}{\sqrt{\rho^2 - (x + \rho \cos i_e)^2}} \tag{21}$$

Finally, using Eqs 13, 18, we get

$$\frac{dy}{dx} = \frac{2h(H - h) + x^2}{2(H - h)x} \tag{22}$$

The emergence angle of seismic waves reaching the observation site is expressed as

$$i = \frac{\pi}{2} - \arctan\frac{dy}{dx} \tag{23}$$

4 Results and discussion

4.1 Fitting results

The feasibility of using the constant velocity gradient model to explain the actual observation results depends on whether the emergence angle of each observation site can be approximately fitted with Eq. 22. The observation Eq. 22 and related Eqs 21, 18 involve two quantities with clear physical significance: focal depth h and take-off angle, i_e, which are the quantities to be determined through the fitting.

Equation 22 gives the emergence angle i corresponding to different epicentral distances x. To explain our experimental results, we must determine two parameters in Eq. 22: h and H, where the focal depth h has a more significant application value.

This problem is non-linear, and the enumeration method is still used for inversion. For the focal depth h, all the integer values from 1 *km* to 100 *km* are traversed, and the error does not exceed 1 *km*. Since v_e generally does not exceed 8 *km/s* in the crust, assuming that the wave velocity near the surface is 5 *km/s* and the crustal thickness is 30 *km*, then k is approximately *0.1/s*, and the corresponding H is equal to 80 *km*. Based on this analysis, the variation range of H is selected as 1-200 *km*, and all the integer values are traversed with an

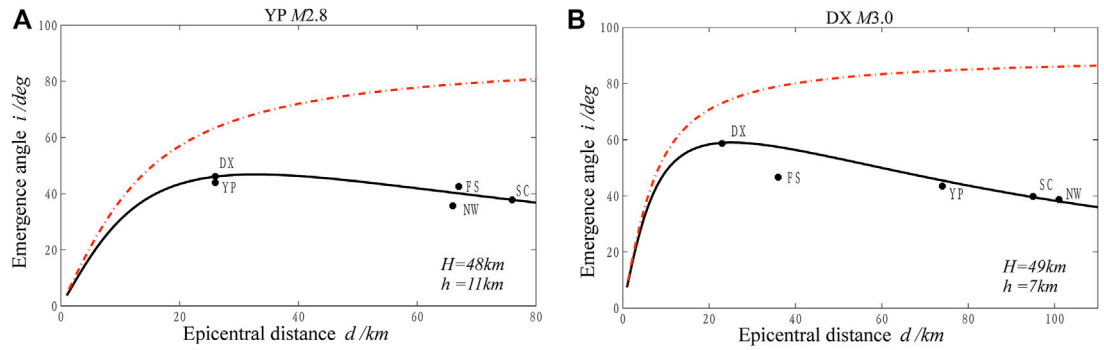

FIGURE 8
Calculated emergence angle (*i*) vs. epicentral distance (*d*) of the two events: **(A)** YP *M*2.8, **(B)** DX *M*3.0.

error of less than 1 *km*. The specific algorithm is as follows. Firstly, the given h and H values are substituted into Eq. 22 to establish the *x-i* relation. Secondly, the epicentral distance of each observation site of j is replaced into the established *x-i* relationship; the emergence angle $i_j^{'}$ is calculated and compared with the actual observed emergence angle i_j. Thirdly, the objective function: $F = \sum_{j=1}^{5} |i_j - i_j^{'}|$, is established. Finally, all the h and H values are traversed, and the h and H values that minimize the objective function F are selected as the solution. The corresponding *x-i* relationship is considered as the criterion.

Figure 8 shows the fitting results of two earthquakes. Here, the dash-dotted curve shows the variation in the emergence angle with the epicentral distance in the homogeneous medium under the same focal depth. The solid curve is the *x-i* relationship obtained by the constant velocity gradient model. Obviously, the observed *x-i* relationship does not conform to the homogeneous medium model, but it is in good agreement with the constant velocity gradient model. The inversion results of h and H are also shown in Figure 8, which shows that the focal depths h of the two earthquakes is 11*km* and 7 *km* respectively, which are consistent with the results of 8*km* and 5 *km* given by the pendulum seismograph (Table 2). It is noteworthy that the H of the two local events is 48 *km* and 49 *km*, respectively, and the results are largely consistent; this also explains that the medium structure should also be consistent results for two earthquakes in the same area.

Red dash-dotted line: homogeneous medium; solid line: constant velocity gradient medium.

Once h and H are determined, seismic wave rays can be plotted for different take-off angles, as shown in Figure 9 (solid lines). It is also necessary to give the take-off angle corresponding to each observation site to plot the seismic wave rays at each observation site, which are shown by red dash-dotted lines in Figure 9.

Eq. 21 can be rewritten as

$$\cot i = \frac{x + \rho \cos i_e}{\sqrt{\rho^2 - (x + \rho \cos i_e)^2}} \tag{24}$$

Squaring and expanding both sides of Eq. 24, we obtain

$$\rho^2 \cot^2 i = (1 + \cot^2 i)(x + \rho \cos i_e)^2 \tag{25}$$

Using trigonometric function relation, we get

$$\frac{\cot^2 i}{1 + \cot^2 i} = \cos^2 i \tag{26}$$

Substituting Eq. 14 into Eq. 25 ($y = 0$ on the ground), we have

$$\rho^2 \cos^2 i = \rho^2 - (\rho \sin i_e - h)^2 \tag{27}$$

Then,

$$\rho^2 \sin^2 i = (\rho \sin i_e - h)^2 \tag{28}$$

Squaring both sides of Eq. 28 and substituting in Eq. 13, we get

$$\frac{\sin i}{\sin i_e} = \pm \frac{H - h}{H} = \pm \frac{v_e - kh}{v_e} \tag{29}$$

Using Eq. 29, the following expression of Snell's law can be obtained:

$$\frac{\sin i_e}{v_e} = \pm \frac{\sin i}{v_0} \tag{30}$$

When h and H are known, $\frac{H-h}{H}$ can be calculated, and then the take-off angle, i_e is calculated from the emergence angle i according to Eq. 29. According to Figure 6, $i_e < 90^\circ$ corresponds to the usual Snell's law, where Eq. 30 takes a positive sign on the right. When $i_e > 90^\circ$, the seismic waves emitted from the source are downward, and the negative sign should be taken. At the same time, the obtained negative take-off angle should be added to 180°. Eq. 18 shows that when $i_e = 90^\circ$, the epicentral distance is expressed as follows:

$$x_{90} = \sqrt{2Hh - h^2} \tag{31}$$

Therefore, the epicentral distance is positive when $x < x_{90}$, and it is negative when $x > x_{90}$. In fact, the take-off angle can be directly calculated using Eq. 18. The two methods give the same results and substantiate each other. Table 5 shows the calculation results.

It can be seen from Figure 9 that all the seismic wave rays represented by the dash-dotted lines do not exceed the depth of 30 *km*, and they should not exceed the crust range and are propagated in the crust.

4.2 Discussion

Most of the seismic sites and borehole strainmeter sites in mainland China are planned and constructed separately, so there

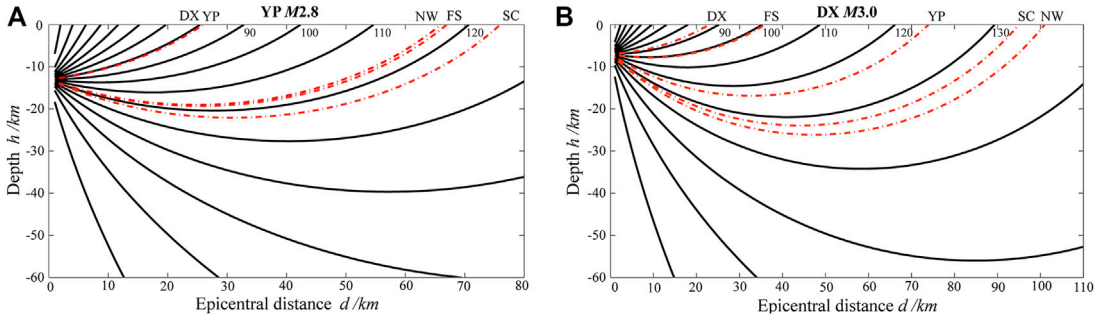

FIGURE 9
Ray paths of the two events according to constant velocity gradient model: **(A)** YP *M*2.8, **(A)** DX *M*3.0.

TABLE 5 Calculated emergence angles and take-off angles for the two local events.

Site	YP *M*2.8			DX *M*3.0		
	Epicentral distance *d* (*km*)	Emergence angle *i* (°)	Take-off angle, i_e (°)	Epicentral distance *d* (*km*)	Emergence angle *i* (°)	Take-off angle, i_e (°)
SC	76	37.8	122.8	95	39.6	132.0
FS	67	40.1	117.9	36	57.4	100.6
YP	26	46.0	80.8	74	45.5	123.7
DX	26	46.0	80.8	23	58.9	87.3
NW	66	40.4	117.3	101	38.1	134.0

are few sites where the two observations are co-located. Although Shanxi Province has a relatively dense pendulum seismograph observation network, there are only three seismic stations in the study area of this paper, and only the NW site is co-located. Seismic observation is a velocity observation optimized by frequency band; the strain observed by the four-component borehole strainmeter is a vector. The results of the two observations may be different. Therefore, the research in this paper did not carry out a detailed comparative analysis with seismic observations; only the hypocenter parameters given by the seismic network were compared. With continuous observation, the number of local earthquakes recorded has increased. In the future, we will use the sites where seismic and borehole strainmeters are co-located to carry out a comparative analysis of the two observations through a large number of earthquakes.

This study is part of our research on solving the focal mechanism solution with strain seismic observation, which broadens the application field of four-component borehole strain observation. The results can provide a practical basis for further development of the four-component borehole strainmeter in mainland China in the future. Other than that, some recent studies show that strain seismographs could help provide unique constraints for local earthquakes, which then further strengthening the efficiency of the local earthquake warning system (Juhel et al., 2018; Canitano et al., 2021). Based on the research in this paper, how to apply these high sampling sites to the earthquake early warning system in mainland China will be a meaningful study.

5 Conclusion

The apparent focal depth, the emergence angle, and the take-off angles of seismic waves given in this study for five sites of two local events have stable uniqueness and apparent regularity. In particular, the inverted focal depths are basically consistent with the interpretation results of the traditional pendulum seismograph, which shows the reliability of the research results. This provides another important application direction of the YRY-4 type four-gauge borehole strainmeter. The accuracy of the YRY-4 type four-gauge borehole strainmeter was the prerequisite for this study. The *H* values of the two earthquakes (*H* is the reflection of the relationship between wave velocity gradient and wave velocity at focal depth) are consistent, which also verifies the applicability of the crustal model with constant gradient wave velocity. The observation results suggest that the constant velocity gradient model is more realistic than the homogeneous medium crust model.

Currently, the research on solving focal mechanisms by seismic strain observation is limited to local earthquakes. Especially, in the range of direct wave with initial motion, the seismic moment is generally less than 100 km. At present, there is no good way to solve the problem that the emergence of the first wave and mantle

reflection wave in a larger range can cause greater errors in the inversion. However, the research in this paper gives a method to determine the emergence angle, which clears a major obstacle for further solving the focal mechanism of local earthquakes by strain seismographs. It should be noted that this method of determining the emergence angle requires more observation sites. We will continue to study the rupture process and focal mechanism of moderate-strong earthquakes and teleseismic earthquakes by combining two kinds of observations.

Strain seismographs and pendulum seismographs are different with distinct advantages and disadvantages. The research in this paper shows that the strain seismograph can be used as an effective supplement to the pendulum seismograph, especially in areas with fewer measuring sites of pendulum seismographs. Using strain seismographs and seismographs for co-site or co-hole observation will be one of the development directions of seismic observation in China.

Data availability statement

The original contributions presented in the study are included in the article/Supplementary Material, further inquiries can be directed to the corresponding author.

Author contributions

LT: Conceptualization, methodology, visualization, formal analysis, writing–Original draft. ZQ: Conceptualization, methodology, writing–Reviewing and editing. JF: Methodology, formal analysis, investigation. ZY: Methodology, data curation.

Funding

This work was supported by the National Natural Science Foundation of China (No. 41974018), and the Research Grant (Grant Nos. ZDJ 2018-09, ZDJ 2017-10) from National Institute of Natural Hazards, Ministry of Emergency Management of China.

Acknowledgments

We thank www.scimj.com for its linguistic assistance during the preparation of this manuscript. Parameters of the two local events are provided by the China Seismic Network. Figures were plotted using the Generic Mapping Tools (Wessel et al., 2013). The authors also gratefully acknowledge editors and two reviewers for their useful reviews and constructive comments that helped improve the article.

Conflict of interest

The authors declare that the research was conducted in the absence of any commercial or financial relationships that could be construed as a potential conflict of interest.

Publisher's note

All claims expressed in this article are solely those of the authors and do not necessarily represent those of their affiliated organizations, or those of the publisher, the editors and the reviewers. Any product that may be evaluated in this article, or claim that may be made by its manufacturer, is not guaranteed or endorsed by the publisher.

Supplementary material

The Supplementary Material for this article can be found online at: https://www.frontiersin.org/articles/10.3389/feart.2023.1036797/full#supplementary-material

References

Aki, K., and Richards, P. G. (2002). *Quantitative seismology: Theory and methods*. San Francisco: W. H. Freeman.

Barbour, A. J., and Agnew, D. C. (2012). Detection of seismic signals using seismometers and strainmeters. *Bull. Seismol. Soc. Am.* 102 (6), 2484–2490. doi:10.1785/0120110298

Barbour, A. J., and Crowell, B. W. (2017). Dynamic strains for earthquake source characterization. *Seismol. Res. Lett.* 88 (2), 354–370. doi:10.1785/0220160155

Barbour, A. J., Langbein, J. O., and Farghal, N. S. (2021). Earthquake magnitudes from dynamic strain. *Bull. Seismol. Soc. Am.* 111 (3), 1325–1346. doi:10.1785/0120200360

Benioff, H., Press, F., and Smith, S. (1961). Excitation of the free oscillations of the Earth by earthquakes. *J. Geophys. Res.* 66 (2), 605–619. doi:10.1029/JZ066i002p00605

Blum, J., Igel, H., and Zumberge, M. (2010). Observations of Rayleigh-wave phase velocity and coseismic deformation using an optical fiber, interferometric vertical strainmeter at the SAFOD borehole, California. *Bull. Seismol. Soc. Am.* 100 (5A), 1879–1891. doi:10.1785/0120090333

Borcherdt, R. D., and Glassmoyer, G. (1989). An exact anelastic model for the free-surface relfection of P and S-I waves. *Bull. Seismol. Soc. Am.* 79 (3), 842–859. doi:10.1785/BSSA0790030842

Borcherdt, R. D., Johnston, M., Glassmoyer, G., and Dietel, C. (2006). Recordings of the 2004 parkfield earthquake on the general earthquake observation system array: Implications for earthquake precursors, fault rupture, and coseismic strain changes. *Bull. Seismol. Soc. Am.* 96, S73–S89. doi:10.1785/0120050827

Byerly, P. (1926). The Montana earthquake of June 28, 1925 GMCT. *Bull. Seismol. Soc. Am.* 16 (4), 209–265. doi:10.1785/bssa0160040209

Canitano, A., Hsu, Y. J., Lee, H. M., Linde, A. T., and Sacks, S. (2017). A first modeling of dynamic and static crustal strain field from near-field dilatation measurements: Example of the 2013 $$M_w$$ M w 6.2 ruisui earthquake, taiwan. *J. Geod.* 91 (1), 1–8. doi:10.1007/s00190-016-0933-6

Canitano, A., Mouyen, M., Hsu, Y. J., Linde, A., Sacks, S., and Lee, H. M. (2021). Fifteen years of continuous high-resolution borehole strainmeter measurements in eastern taiwan: An overview and perspectives. *GeoHazards* 2, 172–195. doi:10.3390/geohazards2030010

Cao, Y., Mavroeidis, G. P., and Ashoory, M. (2018). Comparison of observed and synthetic near-fault dynamic ground strains and rotations from the 2004 Mw 6.0 Parkfield, California, earthquake. *Bull. Seismol. Soc. Am.* 108 (3A), 1240–1256. doi:10.1785/0120170227

Chi, S. L., Chi, Y., Deng, T., Liao, C. W., Tang, X. L., and Chi, L. (2009). The necessity of building national strain-observation network from the strain abnormality before wenchuan earthquake. *Recent Dev. World Seismol.* 1, 1–13.

Farghal, N., Baltay, A., and Langbein, J. (2020). Strain-estimated ground motions associated with recent earthquakes in California. *Bull. Seismol. Soc. Am.* 110 (6), 2766–2776. doi:10.1785/0120200131

Gladwin, M. T. (1984). High precision multi-component borehole deformation monitoring. *Rev. Sci. Instru.* 55, 2011–2016. doi:10.1063/1.1137704

Gong, Z., Jing, Y., Li, H. B., Li, L., Fan, X. Y., and Liu, Z. (2019). Static-dynamic strain response to the 2016 M6.2 Hutubi earthquake (eastern Tien Shan, NW China) recorded in a borehole strainmeter network. *J. Asian Earth Sci.* 183, 103958. doi:10.1016/j.jseaes.2019.103958

Huang, F. Q., Li, M., Ma, Y. C., Han, Y. Y., Tian, L., Yan, W., et al. (2017). Studies on earthquake precursors in China: A review for recent 50 years. *Geodesy Geodyn.* 8 (1), 1–12. doi:10.1016/j.geog.2016.12.002

Ishii, H. (2001). Development of new multi-component borehole instrument. *Rep. Tono Res. Inst. Earthq. Sci.* 6, 5–10.

Johnston, M. J. S., Borcherdt, R. D., Linde, A. T., and Gladwin, M. T. (2006). Continuous borehole strain and pore pressure in the near field of the 28 September 2004 *M* 6.0 Parkfield, California, earthquake: Implications for nucleation, fault response, earthquake prediction, and tremor. *Bull. Seismol. Soc. Am.* 96, S56–S72. doi:10.1785/0120050822

Johnston, M. J. S., Borcherdt, R. D., and Linde, A. T. (1986). Short-period strain (0.1-10^5 s): Near-source strain field for an earthquake (ML 3.2) near San Juan Bautista, California. *J. Geophys. Res.* 91 (11), 11497–11502. doi:10.1029/JB091iB11p11497

Juhel, K., Ampuero, J. P., Barsuglia, M., Bernard, P., Chassande-Mottin, E., Fiorucci, D., et al. (2018). Earthquake early warning using future generation gravity strainmeters. *J. Geophys. Res. Solid Earth* 123 (12), 2018JB016698–10902. doi:10.1029/2018JB016698

Li, F. Z., Zhang, H., Tang, L., and Shi, Y. L. (2021). Determination of seismic surface wave strain magnitude based on borehole strain seismic wave records. *Chin. J. Geophys.* 64 (5), 1620–1631. doi:10.6038/cjg2021O0366

Li, Y., Zhang, H., Tang, L., Chen, L., and Jing, Y. (2020). Seismogenic faulting of the 2016 Mw 6.0 Hutubi earthquake in the northern Tien Shan region: Constraints from near-field borehole strain step observations and numerical simulations. *Front. Earth Sci.* 8, 588304. doi:10.3389/feart.2020.588304

Liu, X. Y., Wang, Z. Y., Fang, H. F., Huang, S. M., and Wang, L. (2014). Analysis of 4-component borehole strain observation based on strain invariant. *Chin. J. Geophys.* 57 (10), 3332–3346. doi:10.6038/cjg20141020

Ouyang, Z. X. (1977). RDB-1 type electric capacity strainmeter. *Sel. Pap. Natl. Conf. stressmeasurement* 2, 337–348.

Qiu, Z. H. (2017). *Borehole strain observation, theory and application*. Beijing: Seismological Press.

Qiu, Z. H., Chi, S. L., Wang, Z. M., Carpenter, S., Tang, L., Guo, Y. P., et al. (2015). The strain seismograms of P-and S-Waves of a local event recorded by Four-Gauge Borehole Strainmeter. *Earthq. Sci.* 28, 209–214. doi:10.1007/s11589-015-0120-5

Qiu, Z. H., Tan, L., Zhao, S, X., and Guo, Y. P. (2020). Fundamental principle to determine seismic source moment tensor using strain seismographs. *Chin. J. Geophys.* 63 (2), 551–561. doi:10.6038/cjg2020M0609

Qiu, Z. H., Tang, L., Zhang, B. H., and Guo, Y. P. (2013). *In-situ* calibration of and algorithm for strain monitoring using four-gauge borehole strainmeters (FGBS). *J. Geophys. Res. Solid Earth* 118, 1609–1618. doi:10.1002/jgrb.50112

Qiu, Z. H., Zhang, B. H., Chi, S. L., Tang, L., and Song, M. (2010). Abnormal strain changes observed at Guza before the Wenchuan earthquake. *Sci. China Earth Sci.* 40 (08), 233–240. doi:10.1007/s11430-010-4057-1

Sacks, I. S., Suyehiro, S., and Evertson, D. W. (1971). Sacks–Evertson strainmeter, its installation in Japan and some preliminary results concerning strain steps. *Proc. Jpn. Acad.* 47, 707–712. doi:10.2183/pjab1945.47.707

Shi, Y. L., Yin, D., Ren, T. X., Qiu, Z. H., and Chi, S. L. (2021). The variation of coseismic static stress deviation consistent with theoretical prediction was observed for the first time-Observation of borehole strain of the Yuanping ML4.7 earthquake in Shanxi on April 7, 2016. *Chin. J. Geophys.* 64 (6), 1937–1948. doi:10.6038/cjg2021O0398

Stein, S., and Wysession, M. (2003). *An introduction to seismology, earthquakes, and earth structure*. Oxford: Blackwell Publishing.

Su, K. Zh (1982). Working principle of liquid level volumetric strain gauge. *Seismol. Res.* 04, 57.

Tang, L., Qiu, Z. H., Fan, J. Y., and Luo, Z. H. (2022). Characteristic analysis of coseismic variation of 4-component borehole strain observation with different sampling rates. *J. Geodesy Geodyn.* 42 (11), 1196–1201. doi:10.14075/j.jgg.2022.11.018

Tang, L., Qiu, Z. H., and Kan, B. X. (2008). An analysis on shear strain orientation of the Earth's torsional oscillation excited by twice Indonesia earthquake. *J. Geodesy Geodyn.* 28 (2), 56–60.

Tang, L., Qiu, Z. H., and Kan, B. X. (2007). Earth's spheroidal oscillations observed with China borehole dilatometer network. *J. Geodesy Geodyn.* 27 (6), 37–44.

Tang, L., Qiu, Z. H., Lu, P. J., Wu, Y., Li, Z. Y., Du, R. L., et al. (2020). *DB/T 8.2-2020: Specification for the construction of seismic station - crustal deformation station - Part 2: Crustal tilt and strain observatory in borehole*. China: Chinese Industry Standard.

Wan, Y. G. (2016). *Introduction to seismology*. Beijing: Science Press.

Wessel, P., Smith, W. H. F., Scharroo, R., Luis, J., and Wobbe, F. (2013). Generic mapping tools:improved version released. *Eos.Transactions Am. Geophys. Union* 94 (45), 409–410. doi:10.1002/2013EO450001

Wyllie, P. J. (1963). The nature of the Mohorovicic Discontinuity, a compromise. *J. Geophys. Res.* 68 (15), 4611–4619. doi:10.1029/jz068i015p04611

Zhang, K. H., Tian, J. Y., and Hu, Z. F. (2021). Can seismic strain waves Be measured quantitatively by borehole tensor strainmeters? *Seismol. Res. Lett.* 92 (6), 3602–3609. doi:10.1785/0220200114

Zhang, K. H., Tian, J. Y., and Hu, Z. F. (2020). The influence of the expansive grout on theoretical bandwidth for the measurement of strain waves by borehole tensor strainmeters. *Appl. Sci.* 10 (9), 3199. doi:10.3390/app10093199

Zhang, K. H., Tian, J. Y., and Hu, Z. F. (2019). Theoretical frequency response and corresponding bandwidth of an empty borehole for the measurement of strain waves in borehole tensor strainmeters. *Bull. Seismol. Soc. Am.* 109, 2459–2469. doi:10.1785/0120180264

Zhang, Y., Fu, L. Y., Huang, F. Q., and Chen, X. Z. (2015). Coseismic water-level changes in a well induced by teleseismic waves from three large earthquakes. *Tectonophysics* 651, 232–241. doi:10.1016/j.tecto.2015.02.027

Zhang, Y., and Huang, F. Q. (2011). Mechanism of different Co-seismic water-level changes in wells with similar epicentral distances of intermediate field. *Bull. Seismol. Soc. Am.* 101, 1531–1541. doi:10.1785/0120100104

Zhou, L. S., Qiu, Z. H., and Tang, L. (2008). The response of crustal strain field to short-period Atmospheric pressure variation. *Prog. Geophys.* 23 (06), 1717–1726.

frontiers | Frontiers in Earth Science

TYPE Original Research
PUBLISHED 12 April 2023
DOI 10.3389/feart.2023.1104717

Check for updates

OPEN ACCESS

EDITED BY
Fuqiong Huang,
China Earthquake Networks Center, China

REVIEWED BY
Paresh Nath Singha Roy,
Indian School of Mines, India
Xiaoqing Wang,
Institute of Earthquake Forecasting, China Earthquake Administration, China

*CORRESPONDENCE
Wahyu Triyoso,
wtriyoso@gmail.com

SPECIALTY SECTION
This article was submitted to Solid Earth Geophysics, a section of the journal Frontiers in Earth Science

RECEIVED 21 November 2022
ACCEPTED 27 March 2023
PUBLISHED 12 April 2023

CITATION
Triyoso W (2023), Probabilistic seismic hazard function based on spatiotemporal earthquake likelihood simulation and Akaike information criterion: The PSHF study around off the west coast of Sumatra Island before large earthquake events.
Front. Earth Sci. 11:1104717.
doi: 10.3389/feart.2023.1104717

COPYRIGHT
© 2023 Triyoso. This is an open-access article distributed under the terms of the Creative Commons Attribution License (CC BY). The use, distribution or reproduction in other forums is permitted, provided the original author(s) and the copyright owner(s) are credited and that the original publication in this journal is cited, in accordance with accepted academic practice. No use, distribution or reproduction is permitted which does not comply with these terms.

Probabilistic seismic hazard function based on spatiotemporal earthquake likelihood simulation and Akaike information criterion: The PSHF study around off the west coast of Sumatra Island before large earthquake events

Wahyu Triyoso*

Faculty of Mining and Petroleum Engineering, Institut Teknologi Bandung, Bandung, Indonesia

The probabilistic seismic hazard function (PSHF) before large earthquake events based on the hypothesis earthquake forecast algorithm using the Akaike information criterion (AIC) is performed in this study. The motivation for using the AIC is to better understand the reliability model used to construct the PSHF. The PSHF as the function of the b-value is calculated based on a 5-year window length with a 1-year moving window (instantaneous PSHF) before a large earthquake event. The AIC is calculated based on the likelihood of success and failure using shallow earthquake catalog data around the west coast of Sumatra Island. The probability of occurrence defines the success criteria as more significant than the average probability of greater than or equal to the given magnitude; otherwise, it is defined as failure. Seismic potency has been determined based on the likelihood of an earthquake occurring in several decades or a hundred years. The seismicity rate model is developed based on the integrated data of pre-seismic shallow crustal movement data and the shallow crustal earthquake catalog data. Furthermore, the AIC is calculated based on the likelihood of success and failure as a function of b(t). The b(t) is the change in the b-value as a time function estimated based on shallow earthquake data from 1963 to 2016. In addition, the AIC before M7.9 of 2000, M8.5 of 2007, and M7.8 of 2010 is assessed. The δAIC is then introduced as a function of (AIC_{model}–$AIC_{reference}$) during the observation time. The positive δAIC implies that the likelihood of having a large earthquake is more significant; otherwise, it is smaller. By plotting the time of observation *versus* δAIC and the PSHF estimated as the function of b(t), we could identify a large positive gradient and increase the PSHF at each certain probability exceedance (PE) level before the great earthquake event. It consistently happened for the three events that were evaluated. It suggested that the results of this study might be very beneficial for probabilistic seismic hazard analysis (PSHA) and seismic mitigation realization.

KEYWORDS

AIC, likelihood of success and failure, seismic potency, b-value, PSHF

1 Introduction

The island of Sumatra moved separately between segments, which was caused by the convergence of the Indo-Australian Plate, which was subducting toward the Eurasian plate (Fitch, 1972; Jarrard, 1986). Sieh and Natawidjaja (2000) and Bradley et al. (2017) clarified that the subduction plate movement is along the Sunda Trench in the southwest part of Sumatra Island with low-obliquity subduction and right-lateral shear fault, near the southwest coast of Sumatra Island, parallel to the trough. It is called the Sumatran fault zone (SFZ) (Sieh and Natawidjaja, 2000). The orientation and magnitude of the relative plate movement velocity vectors vary along plate boundaries (Sieh and Natawidjaja, 2000). They are 52 mm/yr in the northern, 57 mm/yr in the middle, and 60 mm/yr in the southern part, and they are caused by the curved shape of the plate boundary (Sieh and Natawidjaja, 2000). The oblique subduction and Sumatran shear faults produced the complexity of Sumatra's stress, strain, and deformation patterns. According to Zachariasen et al. (2000), relatively high convergent plate movement of about 49 mm/year causes a relatively very high annual rate of earthquakes. For the last 250 years, Megawati and Pan (2009) clarified that five major earthquakes ($M_w \geq 8.0$) have occurred along the Sumatran megathrust. McClosky et al. (2005) noted that subsequent earthquakes often follow earthquakes that occur in subduction zones. It implies that the stress interaction can affect the forearc area's seismicity, as Pollitz et al. (2006) and Triyoso and Sahara (2021) suggested. An obvious example is that the 2004 Sumatra–Andaman earthquake caused changes in seismic activity in the Andaman Sea (Sevilgen et al., 2012) and produced earthquakes in 2005 in Nias and the northern part of the Sumatra fault zone (McClosky et al., 2005; Pollitz et al., 2006; Rafie et al., 2021; Triyoso and Sahara, 2021).

The change in the b-value in time and space can be related to stress levels before a large earthquake in a seismotectonic area (Hirata, 1989; Öncel et al., 1995; Caneva and Smirnov, 2004; Roy et al., 2011). Thus, the b-value as the function of space and time could be used to better understand the possible existence of the stress interaction that can affect the potential future seismicity. Other workers have proposed some suggestions. For example, a decrease in the b-value is interpreted as an increase in stress before a seismic event (Scholz, 1968; Wyss et al., 2004). Therefore, lower b-values can be expected near the area of possible future earthquakes.

The correspondence between low b-values and the evidence of large earthquakes around the Sumatra subduction zone has been noted by Nuannin and Kulhánek (2012) and Nuannin et al. (2012). Their study focuses on determining the b-value as a function of time and space for events in the Andaman–Sumatra region and assessing its potential as a seismic precursor. The results showed that large earthquakes occur when b-values decrease before a large earthquake. The phenomenon is clear enough, as they showed in the diagrams for each catalog data they used. The most critical of their finding (Nuannin et al., 2012) shows that about fifteen largest earthquakes, $M_w \geq 7$, occurred between 2000 and 2010 in the Andaman–Sumatra region; all events occurred within areas of low b and were preceded by significant decrease in b-values—about 15 most considerable observed correspondence between low b before the occurrence of large earthquakes. The temporal variations revealed significant decreases in the b-value, which happened before the time of occurrence of the two large earthquakes ($M_s \geq 7$) in 2002 and the M_w = 9.2 event in 2004 (Nuannin et al., 2012). The spatial distribution exhibits low b around the epicenters of the 2002 and 2004 events. This finding implies that the b-value as a function of time could be employed for the PSHA study and seismic mitigation of future earthquake potency (Triyoso et al., 2021; 2022).

Pailoplee and Choowong (2014) evaluated the a and b values of the magnitude–frequency distribution and fractal dimension (D_C) simultaneously for the 13 recognized seismic source zones in mainland Southeast Asia, including northern Sumatra, using a complete earthquake dataset. They found a relationship between D_C-b and D_C-(a/b) and suggested that the Sumatra–Andaman interplate and intraslab, Andaman Basin, and Sumatra fault zones are areas of high tectonic stress that may risk producing major future earthquakes. Triyoso et al. (2022) evaluated the possible correlation between D_C and seismic moment rate based on GPS and late-quarter active fault and shallow earthquake data on the island of Sumatra. The result can characterize a reasonable correlation between two seismotectonic parameters: D_C—b. The most important finding is that relatively high D_C coincides with high seismic hazard function (SHF) curves and high seismic moment rates derived from pre-seismic GPS data (Triyoso et al., 2022). Their findings align with Pailoplee and Choowong (2014) results. Therefore, it is reasonable to conclude that regions with relatively high D_C or low b-values overlap with high seismic moment loading rates, implying high tectonic stress loading, which could risk generating significant future earthquake hazards.

Two earthquakes happened on 12 September 2007 around the Mentawai region, where large earthquakes of M_w 8.8 occurred in 1797 and M_w 9.0 in 1833. Konca et al. (2008) studied them and concluded that earthquakes with M_w 8.4 and M_w 7.9 were only a small part of the fracture area in 1833 and other patches of megathrust that remained locked in the interseismic period. According to Konca et al. (2008), the same section of a megathrust may rupture in different patterns depending on whether the asperities rupture as isolated seismic events or work together to produce a more significant collapse.

Triyoso and Shimazaki (2012) noted that an earthquake potential model plays a crucial role in seismic hazard analysis. Moreover, it has long been realized that evaluating a potential source model is essential to accurate earthquake forecasting. Still, learning this technique has required many decades—until data on an adequate number of large earthquakes were available for evaluation.

Vere-Jones (1995) clarified that very small volumes of earthquakes in space could be considered completely random. As a result, earthquake events can be considered a point process and can be regarded as a realization of a point process by applying the Poisson distribution. Console (1998) introduced an algorithm to test the earthquake forecasting hypothesis by formulating the probability of realization of success and failure. Finally, Triyoso and Shimazaki (2012) noted that when the study area is gridded into cells. In each cell, the expected number of events is known, and we know that at least one event (event) or no event (no event) occurred based on the historical earthquake catalog. Thus, using historical catalog data as a reference, Triyoso and Shimazaki (2012) adopted the formulation of the probability of the realization of success and failure and gridded the study area. Since the number of expected events is known in each cell or grid, at least one event (event) or no event (no event) occurs in every cell. Then, considering the seismicity level, Triyoso and Shimazaki (2012) introduced an adjustment factor of *k*. The factor *k* is constant, and the expected rate of occurrence can be

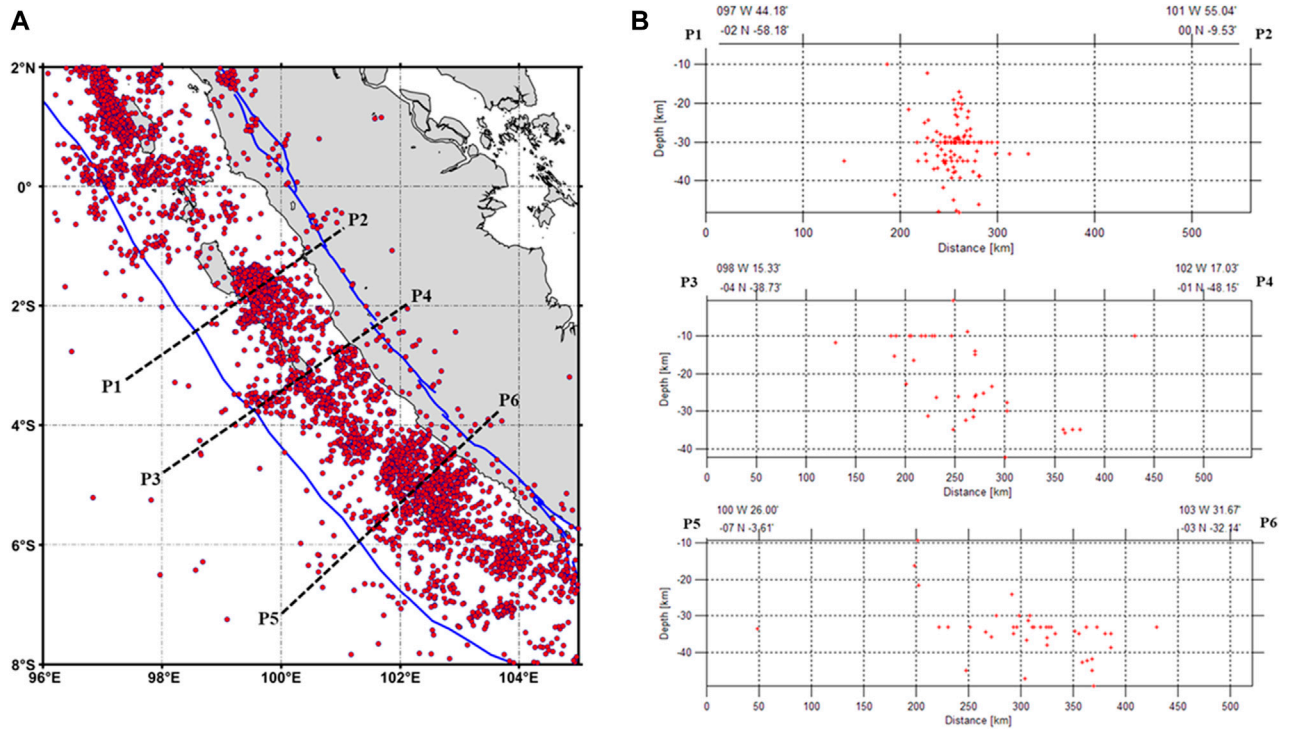

FIGURE 1
Distribution of shallow earthquakes with depths less than 50 km from 1963 to 2016 (The 2017 PuSGen, 2017) and the cross-sections using a width of 10 km **(B)**. They are cross-sections P1–P2, P3–P4, and P5–P6.

multiplied by k to maximize the logarithm of the probability function. Maximizing the logarithm likelihood function with respect to k, we can adjust the level of seismic activity. Thus, the factor k in this study is the variable used to maximize the likelihood function. With this optimizing factor k, we need to use the AIC (Akaike, 1974). We select the most reliable seismicity rate and pattern based on the comparison of the AIC values of each of them. The model that gives the minimum AIC is chosen as the most reliable. Usually, a difference more prominent than 2 in the AIC is considered statistically very significant. By replacing the historical earthquake catalog of Triyoso and Shimazaki (2012) as a reference with the probability of occurrence above the mean value, we then adopt the algorithm to evaluate the AIC *versus* the time before a significant earthquake event addressed for probabilistic seismic hazard and mitigation.

The aim of this study is to evaluate the PSHF before large earthquake events based on the hypothesis earthquake forecast algorithm using the AIC. The AIC is used to better understand the reliability model used to realize the seismic hazard analysis from the viewpoint of probability. In addition, the purpose is to better understand the reliability of the 5-year window of the PSHF as a function of the b-value calculated based on a 5-year window length with a 1-year moving window (instantaneous PSHF) before a large earthquake event. The area of the study is chosen by following the suggestion of Natawidjaja et al. (2006), Konca et al. (2008), Shamim et al. (2019), and Álvarez et al. (2021). It is around the west coast of Sumatra Island.

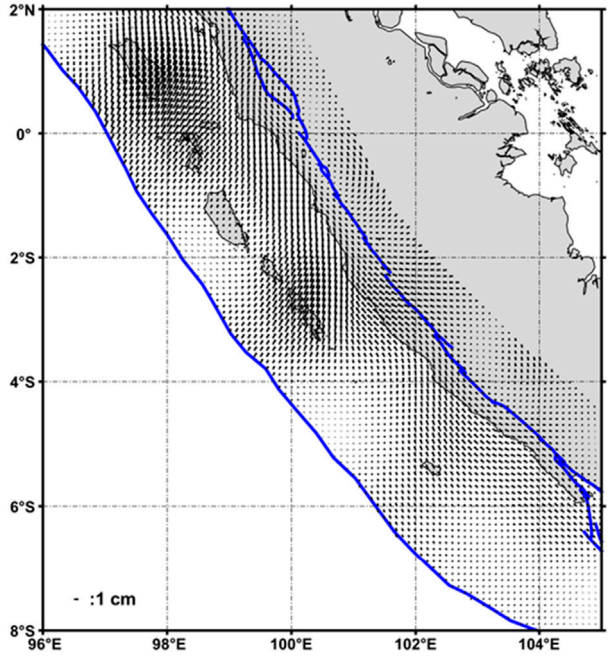

FIGURE 2
The pre-seismic GPS data model was derived based on Triyoso et al. (2020) and Triyoso et al. (2022).

2 Data and method

2.1 Data

This study's shallow crustal earthquake data are based on PuSGeN 2017 (The 2017 PuSGen, 2017). The selected area is around the west coast of Sumatra Island, with the selected data of $M_w \geq 4.7$ with a maximum depth of 50 km from 1963 to 2016. The pre-seismic surface displacement data are based on Triyoso et al. (2022). Figure 1A shows the distribution of shallow earthquakes with depths less than 50 km from 1963 to 2016 (The PuSGen, 2017) and the cross-sections using a width of 10 km (B). They are cross-sections P1–P2, P3–P4, and P5–P6. Figure 2 shows that the pre-seismic GPS model was derived based on Triyoso et al. (2020) and Triyoso et al. (2022).

2.2 The b-value

The b-value of the Gutenberg–Richter equation (Gutenberg and Richter, 1944) is an important parameter, and it correlates with the possible size of the scaling properties of earthquake seismicity. According to Frohlich and Davis (1993), the average b-value on a regional scale is usually ~ 1. In estimating the b-value, the maximum likelihood is the most robust method for calculating the b-value (Aki, 1965). Following Utsu (1978), the formula for the b-value could be written as follows:

$$b = \frac{\log_{10}(e)}{(\bar{M} - M_c + 0.05)}, \quad (1)$$

where $\bar{M}$ is the average magnitude value greater than or equal to M_c and M_c is the magnitude completeness. M_c is determined based on the maximum curvature method of the Gutenberg–Richter law of earthquake magnitude distribution (Wiemer, 2001). The 0.05 in Eq. 1 is a correction constant. In this study, the b-value is calculated as a function of time in which the time window is 5 years, with a 1-year moving window. In this study, it is denoted by $b_5(t)$. Furthermore, the b_5 is estimated using a constant number with a radius of 150 km, referring to the observation point. The number of events calculating b_5 refers to Triyoso and Yuninda (2022).

2.3 Geodetic modeling: SH_{max} rate estimation

In this study, to obtain the geodetic modeling data, the horizontal displacement field of each observation point over the entire seismogenic depth is assumed to be homogeneous and isotropic. Furthermore, the horizontal displacement in E–W and N–S direction components is denoted by *u* and *v*, respectively. Referring to El-fiky et al. (1999), an assumption is needed to determine which signals *u* and *v* are not correlated. The study area was gridded into 10 × 10 km cell sizes, and the surface strain rate was estimated. First, we calculated each cell's horizontal crustal strain rate using previous studies' procedures (Triyoso et al., 2020; Triyoso et al., 2021; 2022; Triyoso and Sahara, 2021; Triyoso and Suwondo, 2022) and the least square collocation (LSC) method. Then, the local covariance functions based on the horizontal surface displacement data are used to estimate the horizontal surface displacement of each grid or cell in the study area. Finally, the horizontal crustal strain was used as the input to estimate the maximum shear strain over the entire study area. Following El-fiky et al. (1999), the formula used in this study to calculate the maximum shear strain (SH_{max}) is as follows:

$$SH_{max} = \sqrt{\left((\varepsilon_{uu} - \varepsilon_{vv})^2 + 0.25\left((\varepsilon_{uv} + \varepsilon_{vu})^2\right)\right)}, \quad (2)$$

where SH_{max} is the maximum shear strain and ε_{ij} is the strain component.

Based on the corrected displacement data, this study's pre-seismic GPS data were used after large earthquakes. It means that the post-seismic effect of the previous large earthquake events is removed. Therefore, the GPS data before the large earthquakes are based on Triyoso et al. (2020), and after the large earthquakes, they are based on Yusfania et al. (2014), Khaerani et al. (2018), and Triyoso et al. (2022). They are addressed to estimate the strain rate over a more extended period.

2.4 Statistical background

2.4.1 Likelihood function

If the occurrence of an event is described as a uniform random process and $\boldsymbol{\lambda}$ is the expected number of events in the realization of a test that could be conducted as many times as we could imagine, the probability that in a single realization, the number of events is **n** is given by the Poisson distribution is as follows:

$$p(n|\lambda) = \frac{e^{-\lambda}\lambda^n}{n!}. \quad (3)$$

From Eq. 3, the probability of no event is

$$p(0|\lambda) = e^{-\lambda}. \quad (4)$$

The probability of at least one event is

$$p(n \geq 1|\lambda) = 1 - e^{-\lambda}. \quad (5)$$

For the combination of events, there are the rules of the probability theory. Thus, the probability that a series of **n** tests come out with a pre-determined realization of at least one event (**n′** times) and no event (**n″** times) is given by the following product, with $\mathbf{n} = \mathbf{n}' + \mathbf{n}''$:

$$\begin{aligned} L &= p\left(0|\lambda_i; i = 1, \ldots n'; n \geq 1|\lambda_j, j = 1, \ldots n''\right) \\ &= \prod_{i=1}^{n'} p(0|\lambda_i).\prod_{j=1}^{n''} p\left(n \geq 1|\lambda_j\right) = e^{-\sum_{i=1}^{n'}\lambda_i}.\prod_{j=1}^{n''}\left(1 - e^{-\lambda_j}\right). \end{aligned} \quad (6)$$

Eq. 6 is the likelihood of the realization of the tests. The values for Eq. 6 depend on the test results and are a function of the parameters used to determine probabilities. Accordingly, the term likelihood function emerges. The likelihood functions may assume very small values, especially when the number of single tests is large and the probabilities connected with them are small. For this reason, it is practical to use the logarithm of this function (log-likelihood); thus, by referring to Triyoso and Shimazaki (2012), we may write the equation as follows (Kagan and Jackson, 1995; Jackson and Kagan, 1999):

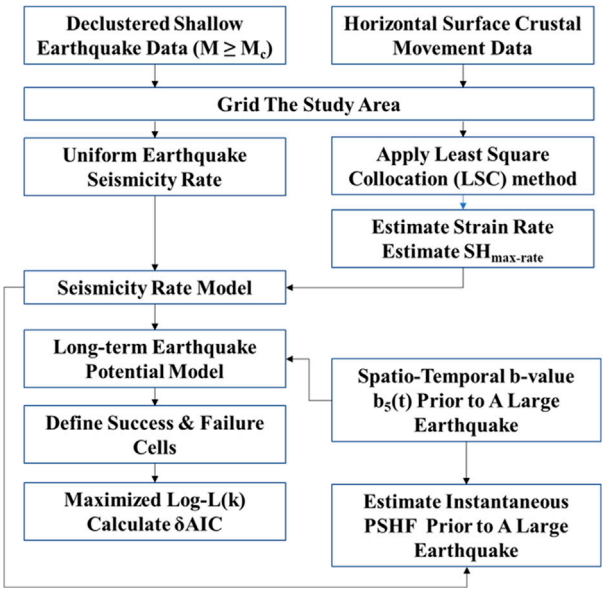

FIGURE 3
The proposed workflow is used in this study.

$$\log L = \sum_{i=1}^{n} (c_i \log(p_i) + (1 - c_i)\log(1 - p_i)) = \sum_{i=1}^{n} \left(c_i . \log \frac{p_i}{1 - p_i} + \log(1 - p_i) \right), \tag{7}$$

where n is the total number of cells, pi is the occurrence rate at cell i, and c_i is equal to 1 when a historically large earthquake used as a reference occurred in cell i and 0 when not (Kagan and Jackson, 1995; Jackson, 1996).

2.4.2 Akaike information criterion

Referring to Triyoso and Shimazaki (2012), in which the historical catalog is used to evaluate the reliability of the earthquake potential model, the adjustment factor k is introduced. The purpose is to consider the possibility that the historical data are incomplete. However, Triyoso and Shimazaki (2012) focused on the spatial distribution of the occurrence rate, not the absolute value of the rate. In other words, we cannot perform an "N-test" (the number test) (Kagan and Jackson, 1995) because the observed earthquake frequency may be underestimated due to historically missing events. Thus, the probability p_i is not used directly, but its relative magnitude kp_i is used by introducing a scaling factor k. Therefore, Eq. 7 could be written as follows:

$$\log L = \sum_{i=1}^{n} (c_i \log(kp_i) + (1 - c_i)\log\ (1 - kp_i)). \tag{8}$$

Maximizing the log-likelihood function with respect to k, we may write the AIC (Akaike, 1974) as follows:

$$\mathrm{AIC} = -2.\mathrm{Log}\, L_{\max} + 2p, \tag{9}$$

where p is the number of parameters used to maximize the log-likelihood function. p equals 1 as the factor k is the only parameter, and $L_{\max}$ is the maximized log-likelihood. It should be noted that the minus sign in the aforementioned equation means that the better model has a smaller AIC value. For the purpose of model comparison, Triyoso and Shimazaki (2012) introduced δAIC as

$$\delta\mathrm{AIC} = -(\mathrm{AIC}_{\mathrm{model}} - \mathrm{AIC}_{\mathrm{reference}}). \tag{10}$$

$\mathrm{AIC}_{\mathrm{model}}$ is the AIC of the specific model, and $\mathrm{AIC}_{\mathrm{reference}}$ is calculated based on the uniform background seismicity model. In this study, the success cell based on the historical earthquake catalog of Triyoso and Shimazaki (2012) as a reference is replaced by cells with the probability of occurrence above the mean value over the entire 150 km radius of the large earthquake event that is evaluated. Because the place of the success cell is treated as at least one earthquake is expected, adjustment factor k and maximizing L_{max} with respect to k is then applied. The 150 km radius refers to the radius of the b-value calculation. Thus, the $\mathrm{AIC}_{\mathrm{model}}$ is calculated based on the cell with the probability of occurrence above the mean value. The positive δAIC implies that the likelihood of having a large earthquake is more significant, and otherwise, it is smaller.

3 Probabilistic seismic hazard function estimation

3.1 Seismicity rate modeling: Potential source area and rate formulation

As this study is intended to evaluate the PSHF before large earthquake events based on the hypothesis earthquake forecast algorithm using the AIC, the primary purpose is to better understand the reliability of the instantaneous PSHF as the function of the b-value with time before a large earthquake event. Then, the modified seismicity rate model of Triyoso et al. (2020) by the following formulation is proposed. The potential

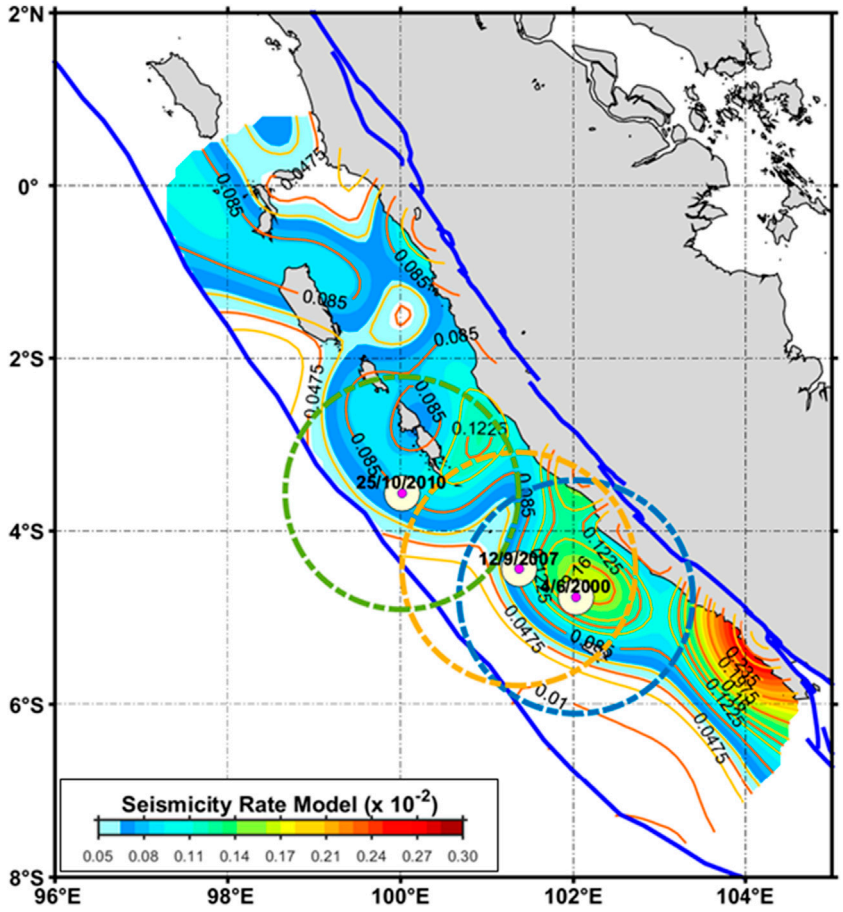

FIGURE 4
Seismicity rate model overlaid with earthquakes of M7.9 in 2000, M8.5 in 2007, M7.8 in 2010, and the three-point observation placed in the position epicenter. The seismicity rate model is constructed based on the uniform background of the declustered shallow earthquake data from 1963 to 2016 and then weighted by the normalized maximum shear strain rate deduced by the pre-seismic GPS data model that was derived based on (Triyoso et al., 2020; Triyoso et al., 2022).

earthquake occurrence rate above or equal to magnitude completeness as a reference (M_{ref}) in the particular grid *i* is modeled by using the uniform background seismicity rate ($A_{background}$) weighted by the normalized maximum shear strain rate ($SH_{max\text{-}rate}$). The formulation could be written as follows:

$$v_i(\geq M_c) \approx \left(A_{background} \frac{SH_{max-rate}}{\text{maximum}\ (SH_{max-rate})} \right) = A_{SH\,max-rate}, \tag{11}$$

where $A_{background}$ is uniform background seismicity with magnitude ≥ M_{ref} in grid *i*, the $SH_{max\text{-}rate}$ is the maximum shear strain rate estimated at the grid of *i*, and the maximum ($SH_{max\text{-}rate}$) is the maximum value of the $SH_{max\text{-}rate}$ over the entire study area. v_i represents the likelihood estimation seismicity rate (annual of the 10^a) with a magnitude greater than or equal to a given earthquake magnitude reference (M_{ref}).

Furthermore, by substituting 10^a of Eq. 11 in the frequency–magnitude of the Guttenberg–Richter equation (Guttenberg and Richter, 1944), we may write the following equation:

$$v_i(\geq m) \approx \frac{A_{SHmax-rate}}{b\ln(10)}\, 10^{bm}\left(1 - 10^{b(m-M_{max})}\right). \tag{12}$$

$A_{SHmax\text{-}rate}$ is the estimated seismicity rate above or equal to M_{ref}, a magnitude greater than or equal to magnitude completeness (M_c). The b is the b-value.

3.2 Probabilistic seismic hazard function estimation: Ground motion prediction equation (GMPE) and probability exceedance (PE)

The SHF is constructed by cross-plotting between the probability of exceedance (PE) and peak ground acceleration (PGA) of a given magnitude reference (M_{ref}) and a distance between the source and a site of observation. The PE formulation of the annual earthquake rate with a magnitude greater than or equal to M_{ref}, which is the estimated maximum ground acceleration denoted by *a*, is calculated using GMPE at an observation point because the earthquake source on the grid *k* can be written as

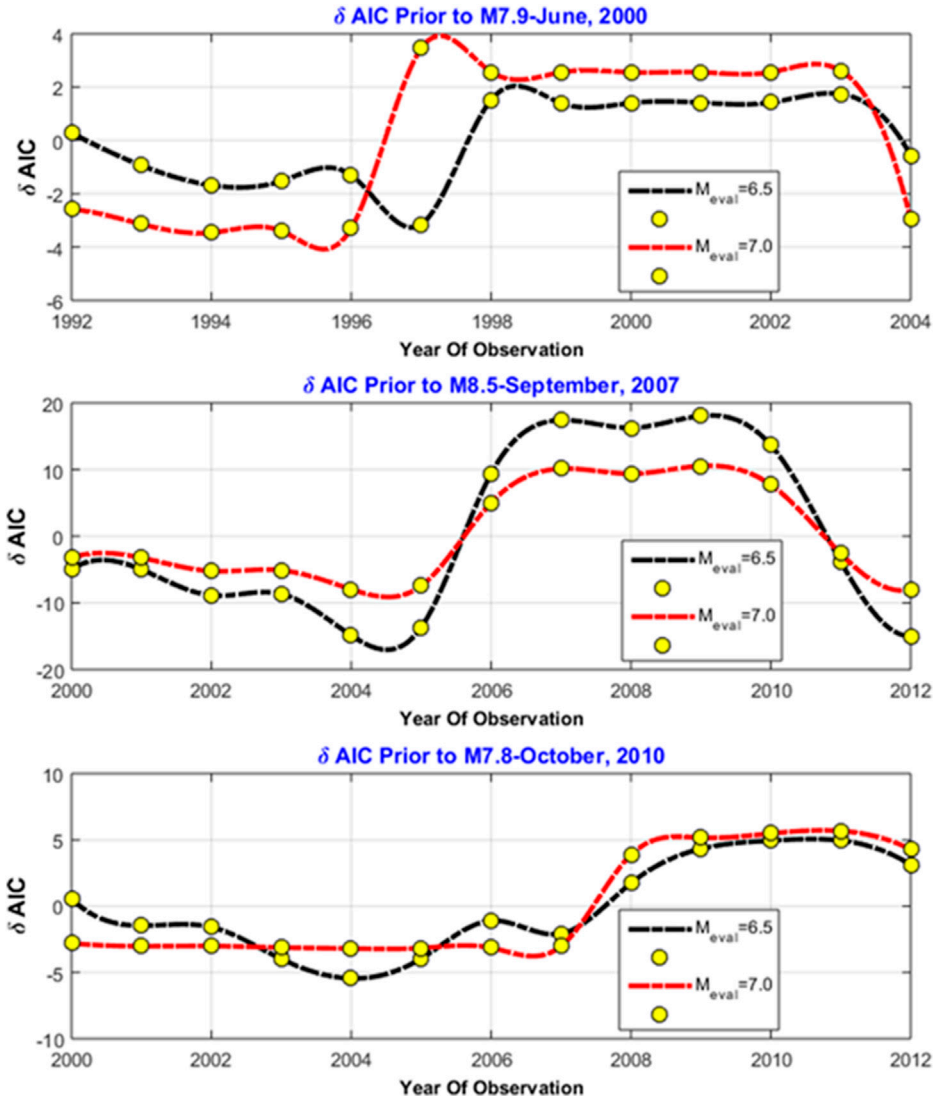

FIGURE 5
Plot of the time of observation *versus* δAIC with M_{ref} of 6.5 and 7.0. The δAIC was calculated before the large earthquake of M7.9 in 2000, M8.5 in 2007, and M7.8 in 2010. The result shows a significant positive gradient before the large earthquake event. It consistently happened for the three events that were evaluated.

$$P(a \geq a_o) = P_k(m \geq m(a_o, R_k)) = 1 - e^{(-v_k(\geq m(a_o, R_k)))}, \quad (13)$$

where P_k ($m \geq m$ (a_o, R_k)) is the annual PE of earthquakes in the kth grid or cell, $m(a_o, R_k)$ is the magnitude in the ith source grid that would produce a PGA estimated of a_o or larger at the site, and R_k is the distance between the site and the source grid. The PSHF parameter calculation is based on Triyoso and Suwondo (2022), where the starting locking depth at the top is 5 km (The 2017 PuSGen, 2017). Following Triyoso and Suwondo (2022), the focal depth value is estimated from half the seismogenic thickness of about 10 km; thus, the focal depth used is 15 km. The function $m(a_o, R_k)$ is the GMPE relation. The following equation determined the total PE distribution of PGA at the site:

$$P(a \geq a_o) = 1 - \prod P_k(m \geq m(a_o, R_k)). \quad (14)$$

Thus, by substituting the GMPE in Eq. 16, we could calculate the annual PE of the particular PGA as follows:

$$P(a \geq a_o) = 1 - \prod e^{(-v_k(\geq m(a_o, R_k)))} = 1 - e^{-\Sigma v_k(\geq m(a_o, R_k))}. \quad (15)$$

For a given specified time of observation of T, the PE could be calculated as follows:

$$P(a \geq a_o) = 1 - \prod e^{(-Tv_k(\geq m(a_o, R_k)))} = 1 - e^{-\Sigma Tv_k(\geq m(a_o, R_k))}. \quad (16)$$

The annual PE of each grid or cell of specified ground motion is calculated using Eq. 15. For a time duration of T, the PE of specified ground motions is computed using Eq. 16.

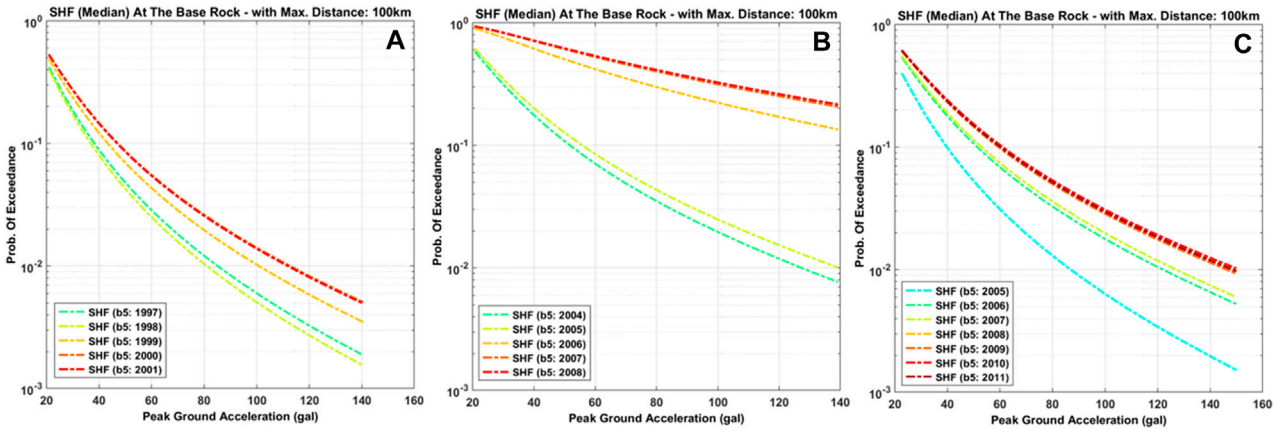

FIGURE 6
PSHF before M7.9 of 2000 **(A)**, M8.5 of 2007 **(B)**, and M7.8 of 2010 **(C)** as a function of b(t). It shows the consistency between a large positive gradient of δAIC and an increase in the PSHF at each certain probability exceedance (PE) level before the great earthquake event. It consistently happened for the three events that were evaluated.

4 Results and discussion

This study is motivated to evaluate the PSHF before large earthquake events based on the hypothesis earthquake forecast algorithm using the AIC. The primary purpose is to better understand the 5-year window length's reliability to estimate PE of the SHF with a 1-year moving window (instantaneous PSHF) as the function of the b-value with time before a large earthquake. The shallow earthquake catalog data are based on PusGen 2017 (The 2017 PuSGen, 2017) around the west coast of Sumatra Island. The area has become the main area of interest as Konca et al. (2008) clarified that the potential megathrust events in the Mentawai area, as suggested by Natawidjaja et al. (2006), remain significant. Thus, the likelihood of the remaining earthquake potency around the Mentawai area needs to be understood more deeply. For earthquake mitigation purposes, the reliability of the spatiotemporal of the b-value and correlation dimension (D_C) as the precursor to forecast the possible future large earthquake needs to be evaluated.

The declustering process is used to apply the earthquake catalog to develop the model. First, the seismicity rate model is constructed based on the uniform background of the declustered shallow earthquake data from 1963 to 2016 and then weighted by the normalized maximum shear strain rate deduced by the pre-seismic GPS data model (Triyoso et al., 2020; 2022). The purpose of declustering is to get the independent earthquake events with approximate to constant rates using ZMAP software (Wiemer, 2001). Figure 3 shows the proposed workflow used in this study.

Triyoso and Shimazaki (2012) proposed using the historical catalog as the reference used to define the success cell to select the most reliable model based on the AIC that will be used to estimate hazards. In this study, the probability of occurrence defines the success criteria if the probability occurrence of the earthquake with a magnitude larger than or equal to a given magnitude reference (M_{ref}) is larger than the average probability; otherwise, it is defined as failure. In addition, the seismic potency has been determined based on the likelihood of an earthquake occurring in several decades or a hundred years.

As clarified by the previous study, the correspondence between low b before the evidence of large earthquakes has been noted (Nuannin et al., 2012; Nuannin and Kulhánek, 2012; Triyoso and Yuninda, 2022). Moreover, the b-value as a function of time and space before large earthquake events has been used as a seismic precursor. Since the earthquake potency and the PSHF are functions of the b-values, applying the proposed method, we could measure how reliable the b-value is as the precursor before a large earthquake from the viewpoint of PSHA.

The previous studies have suggested that we can characterize a reasonable correlation between two seismotectonic parameters, D_C–b (Pailoplee and Choowong, 2014; Triyoso et al., 2022). The critical finding is that relatively high D_C coincides with high SHF curves (Triyoso et al., 2022). The finding aligns with Pailoplee and Choowong (2014) results. As we may find the relationship of the Dc with the b-value and it can be used to estimate the possible future earthquake hazards, thus applying the proposed method, we could measure the reliability of D_C and the b-value before a large earthquake for the PSHA.

Figure 4 shows this study's seismicity rate model and the three-point observation. The seismic potency has been determined based on the likelihood of an earthquake occurring in over two hundred years. The probability of occurrence of the cells defines the success criteria as larger than the average probability of greater than or equal to the given magnitude; otherwise, it is defined as failure cells.

Furthermore, the AIC is calculated based on the likelihood of success and failure as a function of b(t) using a constant number with a radius of 150 km, referring to the point of observation. The event number of at least approximately 25 events is used in this study. The reason is that the event number is at least 25 events (Triyoso and Yuninda, 2022) due to comparing the b-value of the various events, at least 25, 50, 75, and 100 events. Therefore, comparison with the mean shows that at least 25 events or more tend to be reliable enough. The $b_5(t)$ is the change in the b-value as a time function estimated using 5-

year time windows, with the 1-year moving window using the shallow earthquake data from 1963 to 2016 as the input. Furthermore, the AIC before M7.9 of 2000, M8.5 of 2007, and M7.8 of 2010 is assessed. The δAIC is then introduced as a function of (AIC_{model}−$AIC_{reference}$) during the observation time. The positive δAIC implies that the likelihood of having a large earthquake is more significant; otherwise, it is smaller. By plotting the observation time *versus* δAIC, we could identify the gradient before the large earthquake event. The difference of δAIC ≥ 2 is supposed to be significant.

Figure 5 shows the plotting of the time of observation *versus* δAIC with M_{ref} of 6.5 and 7.0, and we could identify a large positive gradient before the large earthquake. Furthermore, it consistently happened for the three events that were evaluated. A large positive δAIC could be found before the large earthquake with M_w8.5 compared to M_w7 class. δAIC before M_w 7.8 and M_w 7.9 were almost similar. The result showed a quantity of δAIC with respect to M_w size or class. Therefore, it implies that we can probably use the δAIC to evaluate the reliability of using spatiotemporal b-value and DC as a precursor before a large earthquake.

Furthermore, the PSHF before large earthquake events is estimated at the three-point observation as a function of b(t). The PSHF parameter calculation is based on Triyoso and Suwondo (2022), where the starting locking depth at the top is 5 km (The 2017 PuSGen, 2017). In this study, the probabilistic seismic hazard is calculated by referring to the GMPE recommendation results of Triyoso and Suwondo (2022) in which, based on our present knowledge, the GMPE Zhao et al. (2006) tends to fit better, especially for the Sumatra subduction zone; thus, we refer to it. Referring to Triyoso and Suwondo (2022), the maximum radius distance of about 100 km with a magnitude range of 6.0–9.0 is used in PSHF estimation. The instantaneous PSHF is estimated based on the time windows, the same as the b(t) time length estimation, which is approximately 5 years.

Figure 6 shows the PSHF before M7.9 of 2000 (A), M8.5 of 2007 (B), and M7.8 of 2010 (C) as a function of b(t). It shows the consistency between a large positive gradient of δAIC and an increase in the PSHF at each certain probability exceedance (PE) level before the great earthquake event. It consistently happened for the three events that were evaluated. The results are consistent with the high reliability of the spatiotemporal b-value to estimate the PSHF around the study area. A different large δAIC has been shown before a large earthquake compared to the δAIC of starting observation time. In this study, we can find a similar behavior of the PSHF and the δAIC. The result showed that the SHF changed drastically with respect to M_w size or class. Therefore, it implies that using spatiotemporal b-value before a large earthquake for instantaneous PSHF seems to be reliable enough. Based on the finding, it is suggested that the result of this study might be very beneficial for PSHA and seismic mitigation realization.

5 Conclusion

An algorithm to better understand the reliability of the PSHF before large earthquake events has been proposed. The algorithm is based on the hypothesis earthquake forecast that is based on the AIC. This study found that the reliability of the use of b-value (D_C) as a function of time and space before large earthquake events has been used as a seismic precursor could be evaluated. Furthermore, this study showed a quantity of δAIC with respect to M_w size or class. Therefore, a drastic change in the PSHF is found when δAIC is large enough. Furthermore, as the earthquake potency and PSHF are functions of the b-values (D_C), applying the proposed method, we could measure how reliable the b-value (D_C) is as the precursor before a large earthquake from the viewpoint of PSHA. The result of this study might be very beneficial for PSHA and seismic mitigation realization.

Data availability statement

The datasets presented in this study can be found in online repositories. The names of the repository/repositories and accession number(s) can be found in the article/supplementary material.

Author contributions

WT developed the main idea and algorithm and analyzed and prepared the figures and the manuscript.

Funding

This research was partly supported by the Riset P3MI ITB 2022 grant funded by the Research and Community Services program (LPPM), Institute of Technology, Bandung (ITB), Indonesia.

Acknowledgments

The author thanks the Global Geophysics Group, the Faculty of Mining and Petroleum Engineering, and the Bandung Institute of Technology for their support in producing this paper.

Conflict of interest

The authors declare that the research was conducted in the absence of any commercial or financial relationships that could be construed as a potential conflict of interest.

Publisher's note

All claims expressed in this article are solely those of the authors and do not necessarily represent those of their affiliated organizations or those of the publisher, the editors, and the reviewers. Any product that may be evaluated in this article, or claim that may be made by its manufacturer, is not guaranteed or endorsed by the publisher.

References

Akaike, H. (1974). A new look at the statistical model identification. *IEEE Trans. Autom. Control* 19, 716–723. doi:10.1109/tac.1974.1100705

Aki, K. (1965). Maximum likelihood estimate of b in the formula log N = a bM and its confidence limits-. *Bull. Earthq. Res. Inst. Tokyo Univ.* 43, 237–239.

Álvarez, O., Pechuan Canet, S., Gimenez, M., and Folguera, A. (2021). Megathrust slip behavior for great earthquakes along the Sumatra- andaman subduction zone mapped from satellite GOCE gravity field derivatives. *Front. Earth Sci.* 8, 581396. doi:10.3389/feart.2020.581396

Bradley, K. E., Feng, L., Hill, E. M., Natawidjaja, D. H., and Sieh, K. (2017). Implications of the diffuse deformation of the Indian Ocean lithosphere for slip partitioning of oblique plate convergence in Sumatra. *J. Geophys Res. Solid Earth* 122, 572–591. doi:10.1002/2016jb013549

Caneva, A., and Smirnov, V. (2004). Using the fractal dimension of earthquake distributions and slope of the recurrence curve to forecast earthquakes in Colombia. *Earth Sci. Res. J.* 8, 3–9.

Console, R. (1998). *Computer algorithms for testing earthquake forecasting hypotheses, ERI*. The University of Tokyo.

El-fiky, G. S. A., Kato, T., and Oware, E. N. (1999). Crustal deformation and interplate coupling in the Shikoku district, Japan, as seen from continuous GPS observation. *Tectonophysics* 314 (1999), 387–399. doi:10.1016/s0040-1951(99)00226-7

Fitch, T. J. (1972). Plate convergence, transcurrent faults, and internal deformation adjacent to southeast Asia and the Western Pacific. *J. Geophys. Res.* 77, 4432–4460. doi:10.1029/jb077i023p04432

Frohlich, C., and Davis, S. (1993). Teleseismic b-values: Or, much ado about 1.0-. *J. Geophys. Res.* 98 (B1), 631–644. doi:10.1029/92jb01891

Gutenberg, B., and Richter, C. F. (1944). Frequency of earthquakes in California*. *Bull. Seismol. Soc. Am.* 34, 185–188. doi:10.1785/bssa0340040185

Hirata, T. (1989). Correlation between the b-value and the fractal dimension of earthquakes. *J. Geophys. Res.* 94, 7507–7514.

Jackson, D. D., and Kagan, Y. Y. (1999). Testable earthquake forecasts for 1999. *SRL* 70 (4), 393–403. doi:10.1785/gssrl.70.4.393

Jarrard, R. D. (1986). Terrane motion by strike-slip faulting of forearc slivers. *Geology* 14, 780–783. doi:10.1130/0091-7613(1986)14<780:tmbsfo>2.0.co;2

Kagan, Y. Y., and Jackson, D. D. (1995). New seismic gap hypothesis: Five years after. *J. Geoph. Res.* 100, 3943–3959. doi:10.1029/94jb03014

Khaerani, D., Meilano, I., Sarsito, D. A., and Susilo, D. (2018). "Deformation of West Sumatra due to the 2016 earthquake (M7.8) based on continuous GPS data," in Proceedings of the 2018 IEEE Asia-Pacific Conference on Geoscience, Electronics and Remote Sensing Technology (AGERS), Jakarta, Indonesia, September 18–19, 2018.

Konca, A. O., Avouac, J. P., Sladen, A., Meltzner, A. J., Sieh, K., Fang, P., et al. (2008). Partial rupture of a locked patch of the Sumatra megathrust during the 2007 earthquake sequence. *Nature* 456 (7222), 631–635. doi:10.1038/nature07572

McClosky, J., Nalbant, S., and Steacy, S. (2005). Indonesian earthquake: Earthquake risk from co-seismic stress. *Nature* 434, 291. doi:10.1038/434291a

Megawati, K., and Pan, T. (2009). Regional seismic hazard posed by the mentawai segment of the sumatran megathrust. *Bull. Seismol. Soc. Am.* 99, 566–584. doi:10.1785/0120080109

Natawidjaja, D. H., Sieh, K., Chlieh, M., Galetzka, J., Suwargadi, B. W., Cheng, H., et al. (2006). Source parameters of the great Sumatran megathrust earthquakes of 1797 and 1833 inferred from coral microatolls. *J. Geophys. Res. Solid Earth* 111 (B6). doi:10.1029/2005jb004025

Nuannin, P., and Kulhánek, O. (2012). A study of b-value precursors applied to the andaman-sumatra region. *J. Earth Sci. Eng.* 2 (2012), 166–188.

Nuannin, P., Kulhánek, O., and Persson, L. (2012). Variations of b-values preceding large earthquakes in the Andaman–Sumatra subduction zone. *J. Asian Earth Sci.* 61, 237–242. doi:10.1016/j.jseaes.2012.10.013

Öncel, A. O., Alptekin, Ö., and Main, I. (1995). Temporal variations of the fractal properties of seismicity in the Western part of the North Anatolian fault zone: Possible artifacts due to improvements in station coverage. *Nonlinear Process. Geophys.* 2, 147–157.

Pailoplee, S., and Choowong, M. (2014). Earthquake frequency-magnitude distribution and fractal dimension in mainland Southeast Asia. *Earth. Planets. Space.* 66, 8.

Rafie, M. T., Cummins, P. R., Sahara, D. P., Widiyantoro, S., Triyoso, W., and Nugraha, A. D. (2021). Variations in forearc stress and changes in principle stress orientations caused by the 2004–2005 megathrust earthquakes in Sumatra, Indonesia. *Front. Earth Sci.* 9, 712144. doi:10.3389/feart.2021.712144

Roy, S., Ghosh, U., Hazra, S., and Kayal, J. R. (2011). Fractal dimension and b-value mapping in the Andaman-Sumatra subduction zone. *Nat. Hazards.* 57, 27–37.

Scholz, C. H. (1968). The frequency-magnitude relation of microfracturing in rock and its relation to earthquakes. *Bull. Seism. Soc. Am.* 58, 399–415. doi:10.1785/bssa0580010399

Sevilgen, V., Stein, R. S., and Pollitz, F. F. (2012). Stress imparted by the great 2004 Sumatra earthquake shut down transforms and activated rifts up to 400 km away in the Andaman Sea. *Proc. Natl. Acad. Sci.* 109 (38), 15152–15156. doi:10.1073/pnas.1208799109

Shamim, S. K., Khana, P. K., and Mohanty, S. P. (2019). Stress reconstruction and lithosphere dynamics along the Sumatra subduction margin. *J. Asian Earth Sci.* 170 (2019), 174–187. doi:10.1016/j.jseaes.2018.11.008

Sieh, K., and Natawidjaja, D. H. (2000). Neotectonics of the Sumatran Fault, Indonesia. *J. Geophys. Res.* 105, 28295–28326. doi:10.1029/2000jb900120

Tim Pusat Studi Gempa Nasional-2017 (The 2017 PuSGen) (2017). *Peta sumber dan bahaya gempa Indonesia tahun 2017*. Jakarta: Kementrian Pekerjaan Umum dan Perumahan Rakyat. (In Indonesian).

Triyoso, W., and Sahara, D. P. (2021). Seismic hazard function mapping using estimated horizontal crustal strain off West Coast Northern Sumatra, *Front. Earth Sci.* 28. doi:10.3389/feart.2021.558923

Triyoso, W., Sahara, D. P., Sarsito, D. A., Natawidjaja, D. H., and Sukmono, S. (2022). Correlation dimension in Sumatra island based on active fault, earthquake data, and estimated horizontal crustal strain to evaluate seismic hazard functions (SHF). *GeoHazards, MDPI*, 3, 227–241. doi:10.3390/geohazards3020012

Triyoso, W., and Shimazaki, K. (2012). Testing various seismic potential models for hazard estimation against a historical earthquake catalog in Japan. *Earth Planets Space* 64, 673–681. doi:10.5047/eps.2011.02.003

Triyoso, W., and Suwondo, A. (2022). From the geodynamic aspect to earthquake potential hazard analysis of Liwa city and its surrounding. *Nat. Hazards* 116, 1329–1344. doi:10.1007/s11069-022-05705-0

Triyoso, W., Suwondo, A., Sahara, D. P., and Sarsito, D. A. (2021). Earthquake potential hazard around off coast the West sumatra-bengkulu: Application spatial correlation between estimated SHmax and correlation dimension. Proceedings of the 18th Annual Meeting of the Asia Oceania Geosciences Society (AOGS 2021), August 1-6, 2021, Singapore.

Triyoso, W., Suwondo, A., Yudistira, T., and Sahara, D. P. (2020). Seismic hazard function (SHF) study of coastal sources of Sumatra island: SHF evaluation of padang and bengkulu cities, *Geosci. Lett.* 7:2. doi:10.1186/s40562-020-00151-x

Triyoso, W., and Yuninda, O. (2022) Seismic hazard function (SHF) study prior to large earthquake event of the year 1994 and 2006 off coast of the java island: The SHF analysis based on the change of the b-value. Proceedings of the 19th Annual Meeting of the Asia Oceania Geosciences Society (AOGS 2021), August 1-5, 2022, Singapore.

Utsu, T. (1978). Estimation of parameters in formulas for frequency-magnitude relation of earthquake occurrence. *Zisin* 31, 367–382. doi:10.4294/zisin1948.31.4_367

Vere-Jones, D. (1995). Forecasting earthquakes and earthquake risk, *Int. J. Forecast.*, 11, 503–538. doi:10.1016/0169-2070(95)00621-4

Wiemer, S. (2001). A software package to analyze seismicity: Zmap. *Seismol. Res. Lett.* 72 (2), 373–382. doi:10.1785/gssrl.72.3.373

Wyss, M., Sammis, C. G., Nadeau, R. M., and Wiemer, S. (2004). Fractal dimension and b-value on creeping and locked patches of the san andreas fault near parkfield, californiafield, California. *Bull. Seism. Soc. Am.* 94, 410–421. doi:10.1785/0120030054

Yusfania, M., Meilano, I., and Sarsito, D. A. (2014). "The utilization of spatial filtering for tectonic strain study based on SUGAR (SUMATRAN GPS ARRAY) data 2006–2008 study case: The September 2007 Bengkulu earthquake, (7226)," in FIG Congress 2014 Engaging the Challenges—Enhancing the Relevance.

Zachariasen, J., Sieh, K., Taylor, F. W., and Hantoro, W. S. (2000). Modern vertical deformation above the sumatran subduction zone: Paleogeodetic insights from coral microatolls. *Bull. Seismol. Soc. Am.* 90, 897–913. doi:10.1785/0119980016

Zhao, J. X., Zhang, J., Asano, A., Ohno, Y., Oouchi, T., Takahashi, T., et al. (2006). Attenuation relations of strong ground motion in Japan using site classification based on predominant period. *Bull. Seismol. Soc. Am.* 96, 898–913. doi:10.1785/0120050122

frontiers | Frontiers in Earth Science

TYPE Original Research
PUBLISHED 14 April 2023
DOI 10.3389/feart.2023.1137177

Check for updates

OPEN ACCESS

EDITED BY
Giovanni Martinelli,
National Institute of Geophysics and Volcanology, Italy

REVIEWED BY
Patricl Taylor,
National Aeronautics and Space Administration (NASA), United States
Angelo De Santis,
Istituto Nazionale di Geofisica e Vulcanologia (INGV), Italy
Funchun Chen,
Chinese Academy of Sciences (CAS), China

*CORRESPONDENCE
Xiaohui Zhou,
xhzhou@sgg.whu.edu.cn

RECEIVED 04 January 2023
ACCEPTED 03 April 2023
PUBLISHED 14 April 2023

CITATION
Ma Y, Zhou X, Yang Y, Hu L, Dong H and Yan R (2023), Statistical analysis of ionospheric vertical total electron content anomalies before global Mw≥6.0 shallow earthquakes during 2000–2020.
Front. Earth Sci. 11:1137177.
doi: 10.3389/feart.2023.1137177

COPYRIGHT
© 2023 Ma, Zhou, Yang, Hu, Dong and Yan. This is an open-access article distributed under the terms of the Creative Commons Attribution License (CC BY). The use, distribution or reproduction in other forums is permitted, provided the original author(s) and the copyright owner(s) are credited and that the original publication in this journal is cited, in accordance with accepted academic practice. No use, distribution or reproduction is permitted which does not comply with these terms.

Statistical analysis of ionospheric vertical total electron content anomalies before global Mw≥6.0 shallow earthquakes during 2000–2020

Yifang Ma[1], Xiaohui Zhou[2]*, Yilin Yang[3], Leyin Hu[1], Hongyan Dong[1] and Rui Yan[1]

[1]Beijing Earthquake Agency, Beijing, China, [2]School of Geodesy and Geomatics, Wuhan University, Wuhan, China, [3]Nordic Volcanological Center, Institute of Earth Sciences, University of Iceland, Reykjavík, Iceland

To quantitatively investigate the relationship between earthquakes and ionospheric anomalies, this paper presents a statistical study of pre-earthquake vertical total electron content (VTEC) variations. A total of 1522 shallow (≤60 km) strong (Mw≥6.0) earthquakes in the global area during 2000-2020 are selected, and classified according to different magnitudes, latitudes and focal depths. A quartile-based process with different lengths of sliding windows, equaling 10 days, 15 days and 27 days, respectively, has been utilized to detect VTEC anomalies. The abnormal level is first defined, and then VTEC anomalies occurrence probabilities (P_O) and occurrence rates (P_E) within 1-10 days before 1522 earthquakes have been calculated. Besides, VTEC anomalies occurrence rates of the background days (PN) are also calculated. The results show that the significant correlation between Po and epicentral latitudinal locations could be observed within 1-10 days before earthquakes. The values of Po increase with larger magnitudes in the equatorial and low-latitude regions, but decrease with greater magnitudes in the mid- and high-latitude regions to some degree. Within 1-5 days before earthquakes, the overall trend of P_E shows an increase with larger magnitudes, but the correlation between the values of P_E and magnitudes is relatively weak in the southern mid- and high-latitude regions. There is no evident causality between PN and the magnitude, and most of the values of P_E/P_N are larger than 1, indicating that VTEC anomalies within a few days before earthquakes are probably related with the forthcoming earthquakes. Moreover, when the abnormal level exceeds 60%, different sliding window lengths have a significant impact on the values of P_O and P_E in the mid- and high-latitude regions. In particular, there are obvious systematic deviations between the values of P_O obtained from different sliding windows in the southern mid- and high-latitude regions. However, the selection of the optimal sliding window needs to be further studied.

KEYWORDS

shallow strong earthquakes, seismo-ionospheric anomaly, VTEC, statistical analysis, different lengths of sliding window

1 Introduction

The seismic process is not only confined to the lithosphere, but also has impacts on the troposphere, ionosphere and even magnetosphere through the electromagnetic fields effect. The ionospheric anomalies within a few days before the earthquakes are relatively stable at short time scales, and have been studied widely in the field of earthquake prediction (Pulinets and Boyarchuk, 2004; Liperovsky et al., 2008; Pulinets and Ouzounov, 2011). A large number of studies have shown that ionospheric perturbations before many earthquakes could be identified (e.g., Liu et al., 2001; Le et al., 2011; Zhu et al., 2014; Tang et al., 2015; Sun et al., 2016; Parrot and Li, 2018; Pulinets et al., 2021). The possible earthquake-related NmF2 (F2 layer peak electron density) and TEC anomalies have been widely discussed in recent decades (e.g., Nishihashi et al., 2009; Ma et al., 2014). Especially, because of the development of the Global Navigation Satellite system (GNSS), GNSS VTEC have attracted more and more attention in the investigation of the ionospheric variations prior to large earthquakes (Liu et al., 2004; Shah and Jin, 2015). For the first time, Liu et al. (2001) used GNSS(GPS) VTEC to study the ionospheric disturbance before the Chi-Chi earthquake, and found that the VTEC over the epicenter decreased significantly 1, 3 and 4 days before the earthquake. Later on, more and more scientists began to focus on GNSS VTEC variations before earthquakes, aiming to detect the potential ionospheric anomalies related to the forthcoming earthquakes. For example, Yao et al. (2012) analyzed ionospheric variations prior to the 2011 Mw9.0 Japan earthquake, and indicated that ionospheric anomalies occurring on 8 March might be a precursor of the earthquake; Ho et al. (2013) showed that TEC increased 9–19 days before the 2010 M8.8 Chile earthquake and specifically over the epicenter; Su et al. (2013) investigated ionospheric TEC variations before the Hector Mine earthquake, and found that ionospheric disturbance appeared just above the epicenter 5 days before the earthquake. These studies show that the GNSS TEC anomalies appear a few days before the earthquake with different magnitude and focal depth.

Over about 50 years of research, no consensus in the scientific community has been formed on the existence of ionospheric earthquake precursors (Rishbeth, 2006; Dautermann et al., 2007; Masci, 2012; Ovalle et al., 2013; Masci and Thomas, 2014; Zolotov et al., 2019). Dautermann et al. (2007) indicated that there was no statistically significant correlation between TEC anomalies and earthquakes in Southern California during 2003–2004; Kon et al. (2011) selected M≥6.0 earthquakes in Japan during 1998–2010, and found that significant positive TEC anomalies within 1000 km above the epicenter appeared within 1–5 days before the earthquakes. According to Masci (2012), the analysis of Kon et al. (2011) was not reliable because of the influence of global geomagnetic events. Ovalle et al. (2013) concluded that it remained controversial whether the observed NmF2 and TEC anomalies were unambiguously related to the 2010 M8.8 Chile earthquake. Background geomagnetic events may impact revealing the relationship between TEC anomalies and earthquakes.

To validate the relationship between ionospheric anomalies and earthquakes in response to the controversy, many scientists have undertaken a multitude of studies on the physical mechanism of generating ionospheric anomalies. Firstly, the morphological characteristics of ionospheric anomalies before a large number of earthquakes are summarized. For instance, Liu et al. (2004) analyzed Ms5.0+ earthquakes in Taiwan from 1999 to 2002, and found that obvious negative TEC anomalies occurred 5 days before the

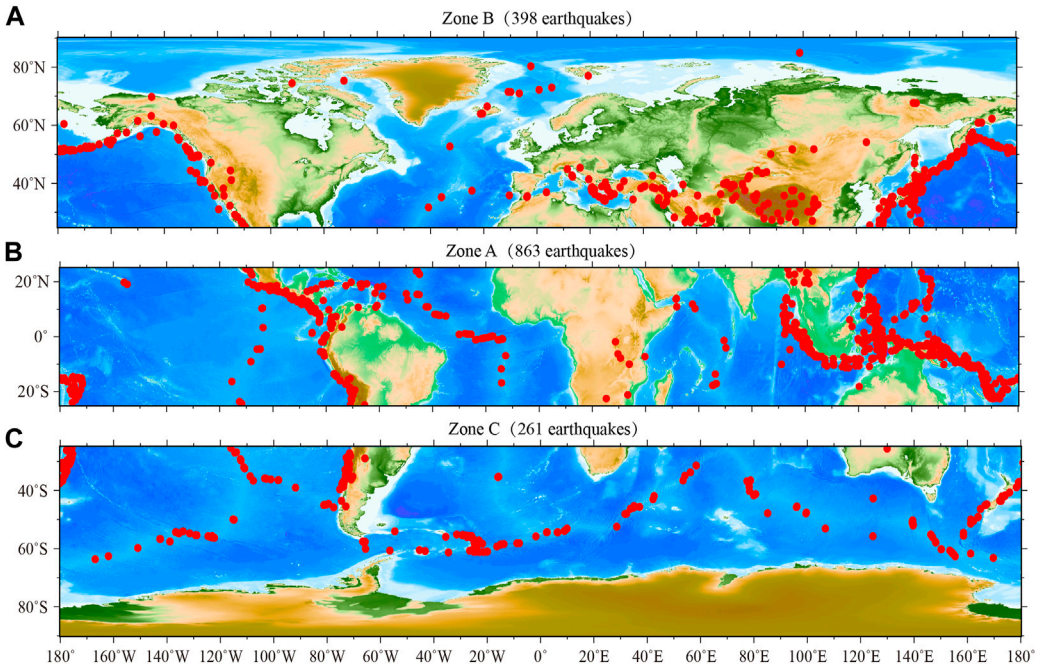

FIGURE 1
Locations of global 1522 Mw≥6.0 earthquakes during 2000–2020.

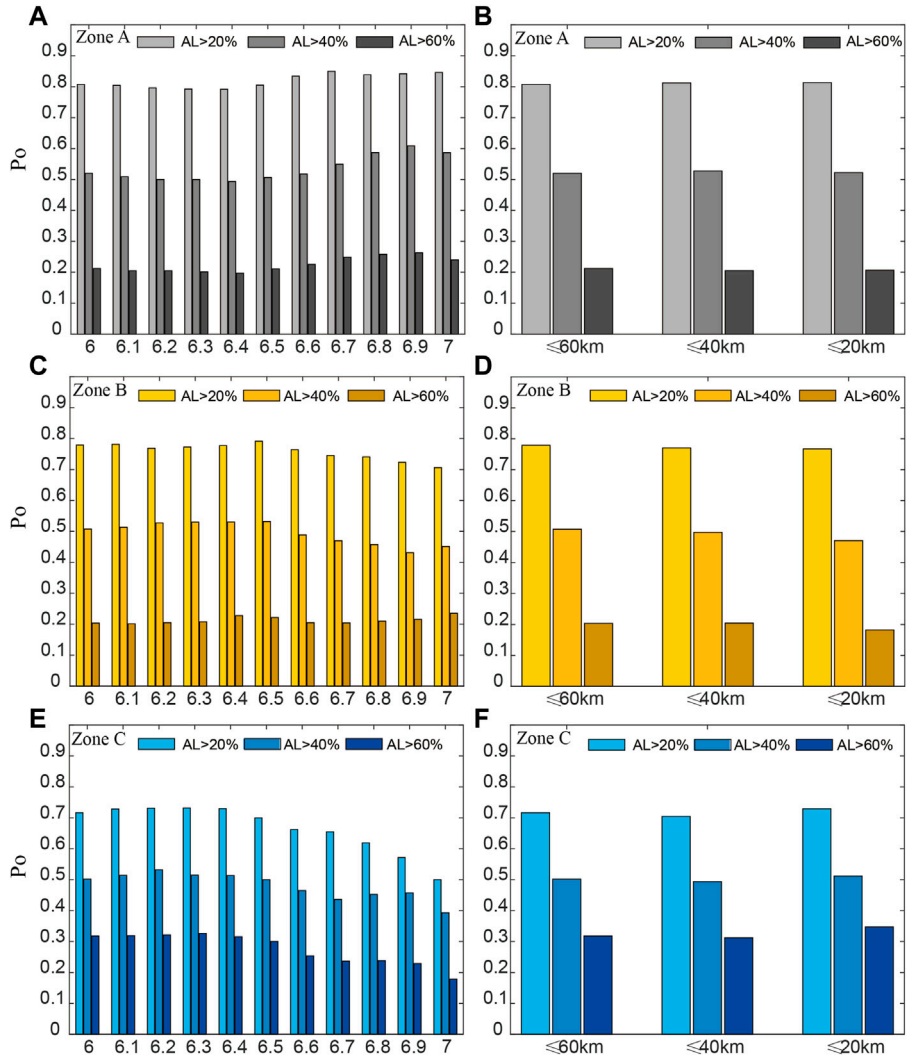

FIGURE 2
Seismo-ionospheric anomalies occurrence probabilities of AL>20%, 40%, and 60% with different magnitudes **(A, C, E)** and depths **(B, D, F)**, respectively (15-day sliding window). **(A, C)** are the results in Zone A. **(C, D)** are the results in Zone B. **(E, F)** are the results in Zone C.

earthquakes. Le et al. (2011) made a statistical study of global 736 M≥6.0 earthquakes during 2002–2010, and proposed that occurrence rates of abnormal days are larger for earthquakes with greater magnitude and lower depth. De Santis et al. (2019) analyzed the electron density and magnetic field data from 3 Swarm satellites to detect possible anomalies associated with 1312 M≥5.5 shallow earthquakes from January 2014 to August 2018, and the results showed that anomalies occurred between a few days and 80 days before the earthquakes with larger peaks at around 10, 20 and 80 days, and supported the Lithosphere-Atmosphere-Ionosphere Coupling (LAIC) with clear statistical significance. Shah et al. (2020) studied the ionospheric anomalies before the global Mw≥5.0 earthquakes from 1998 to 2019, and the results revealed that prominent ionospheric anomalies appeared within 5 days before and after the earthquakes. Based on the characteristics of ionospheric anomalies prior to a large number of earthquakes, the physical mechanisms of seismic LAIC have been extensively studied (Freund, 2011; Klimenko et al., 2012; Pulinets, 2012; Zolotov et al., 2012). For example, Freund (2011) proposed that positive holes released by stressed rocks are highly mobile and can reach the Earth's surface, and then ionize the atmosphere and change the vertical electric field between the ground and the lower edge of the ionosphere. In addition, a large number of studies have shown that anomalous atmospheric electric field variations in the earthquake preparation zone are likely to be the main cause of ionospheric disturbance (Zhang et al., 2014; Jiang et al., 2017; Pulinets and Davidenko, 2018; Davidenko and Pulinets, 2019). For example, Namgaladze et al. (2009) proposed that vertical plasma motion in the ionospheric F2 region under the action of the zonal electric field is the main disturbance formation factor, and ionospheric anomalies before strong earthquakes at middle and low latitudes verified this mechanism. Liu et al. (2010) studied the crest of equatorial ionization anomaly (EIA) variations before 150 M≥5.0 earthquakes in Taiwan, and the results implied that the weak atmospheric electric field a few days before the earthquakes may cause the EIA crest anomalies.

TABLE 1 The difference of disturbed days based on Dst and AE before 51 Earthquakes at high latitudes.

No	Date		Location of epicenter		Magnitude (Mw)	Place	Disturbed days based on Dst (Doy)	Disturbed days based on AE > 500 nT (Doy)
	Year	Doy	Latitude (°)	Longitude (°)				
1	2014	198	60.42	−140.31	6	Zone B		190–191;193
2	2010	120	60.45	−177.71	6.5	Zone B		112–114;119
3	2006	142	60.86	165.81	6.6	Zone B		132–134;138–141
4	2006	110	60.89	167.05	7.6	Zone B	100–109	100;103–108
5	2018	334	61.49	−150.02	7.1	Zone B		329;331
6	2020	9	62.27	171	6.4	Zone B		3;8
7	2002	307	63.23	−144.89	7.8	Zone B	297–306	297–304;306
8	2008	150	63.92	−21.17	6.3	Zone B		142–144;146;149
9	2000	169	63.99	−20.47	6.5	Zone B	160–165	159–160;162–168
10	2020	173	66.46	−18.72	6	Zone B		
11	2013	45	67.65	142.51	6.7	Zone B		35;38–39;43–44
12	2008	174	67.71	141.43	6.1	Zone B	167–170	166–170;172
13	2018	224	69.74	−144.78	6.4	Zone B		215;219;223
14	2011	29	70.99	−6.65	6.2	Zone B		19–20;28
15	2012	243	71.44	−9.84	6.7	Zone B		233;235–239
16	2018	313	71.51	−10.81	6.8	Zone B	309–312	308–312
17	2009	232	72.22	0.84	6	Zone B		231
18	2012	145	73.01	5.59	6.3	Zone B	137–144	135;137;139;141;143–144
19	2017	8	74.44	−92.06	6.1	Zone B		366;1–7
20	2009	188	75.33	−72.49	6	Zone B		179–181
21	2008	52	77.02	19.28	6.1	Zone B		42–47;49–50
22	2009	65	80.33	−2.32	6.5	Zone B		55;58
23	2005	65	84.93	98.69	6.3	Zone B	55	55–61;64
24	2004	214	−63.65	−166.92	6	Zone C	204–213	204–211;213
25	2016	31	−63.14	169.7	6	Zone C	21–25	21–24;28
26	2014	107	−62.65	155.43	6.2	Zone C		97;101–103
27	2013	15	−62.6	−161.94	6.1	Zone C		13
28	2020	336	−61.97	154.9	6.1	Zone C		326–328;330–334
29	2007	102	−61.72	161.2	6	Zone C	92–94	92–94;100
30	2017	281	−61.56	154.32	6.2	Zone C	271–274	271–276;278–279
31	2019	204	−61.31	154.26	6.1	Zone C		194;196;198;202–203
32	2006	232	−61.27	−34.52	7	Zone C	222	224;229–231
33	2011	196	−61.12	−22.85	6	Zone C	186–189	186–188;190–193;195
34	2006	2	−61.12	−21.39	7.4	Zone C	357–361	360–363;365
35	2013	196	−61.05	−23.51	7.3	Zone C	187–195	186–195
36	2008	41	−61.05	−25.01	6.5	Zone C	33–36	31–35;38
37	2007	118	−61.04	−20.12	6.1	Zone C		113–117

(Continued on following page)

TABLE 1 (*Continued*) **The difference of disturbed days based on Dst and AE before 51 Earthquakes at high latitudes.**

No	Date		Location of epicenter		Magnitude (Mw)	Place	Disturbed days based on Dst (Doy)	Disturbed days based on AE > 500 nT (Doy)
	Year	Doy	Latitude (°)	Longitude (°)				
38	2014	306	−61.03	153.88	6	Zone C	296	296–301
39	2009	59	−61.03	−24.39	6.3	Zone C		54–55;58
40	2014	70	−61.01	−19.92	6.4	Zone C	60–62	60;69
41	2020	208	−60.97	−25.01	6.3	Zone C	198–199	198;206–207
42	2003	216	−60.8	−43.21	7.6	Zone C	207–215	206–215
43	2009	106	−60.71	−26.55	6.7	Zone C		99–101
44	2012	283	−60.65	153.39	6.6	Zone C	274–279;282	274–275;280;282
45	2012	15	−60.62	−56.47	6.6	Zone C		5;10
46	2019	239	−60.54	−25.82	6.6	Zone C		238
47	2013	321	−60.49	−45.32	7.8	Zone C	311–320	311;313–315;319–320
48	2018	58	−60.23	150.18	6	Zone C		48–50;52–55;57
49	2000	64	−60.2	150.21	6.3	Zone C	61–63	54–59;61–62
50	2009	300	−60.05	−65.54	6	Zone C	296–299	295–298
51	2001	103	−60.04	−24.37	6.2	Zone C	93–102	94–102

Both the characteristics of ionospheric anomalies and the physical mechanisms of lithosphere-atmosphere-ionosphere coupling present diversity and complexity, and the influence factors may include magnitudes, focal depths, latitude and longitude of the epicenter, focal mechanisms, the weather, the season, solar and geomagnetic activity and so on. However, many studies focused on a single large earthquake, and there are relatively few statistical results based on a large number of earthquakes. The corresponding characteristics of the ionospheric anomalies are still not fully understood. In addition, a quartile-based process is the most common method for extracting ionospheric VTEC anomalies, but different authors use different numbers of days as the lengths of the sliding windows, such as, 10 days (e.g., Zhou et al., 2009; Zhu et al., 2014), 15 days (e.g., Liu et al., 2010; Ke et al., 2016; Liu and Xu, 2017), 27 days (e.g., Xu et al., 2011; Guo et al., 2015), etc. It should be noted that the effects of different sliding windows on the ionospheric anomalies are rarely studied (Zolotov et al., 2019). To solve the above problems, this study uses GIM VTEC to carry out a statistical analysis by studying the VTEC anomalies within 1–10 days before 1522 global shallow (≤60 km) Mw≥6.0 earthquakes during 2000–2020. The factors, including the magnitude, focal depth and the latitude of the epicenter are considered for all the earthquakes, and the effects of different sliding windows on ionospheric anomalies are investigated. Moreover, ionospheric anomalies during background days are also analyzed to compare with those prior to the earthquakes. This study aims at helping the research on the physical mechanisms of lithosphere-atmosphere-ionosphere coupling by summarizing the characteristics of ionospheric anomalies comprehensively, and determining whether different lengths of sliding windows affect ionospheric anomalies features.

2 Data and method

2.1 Data source

The worldwide Mw≥6.0 earthquakes during 2000–2020 are selected to analyze ionospheric anomalies in this study. The data are retrieved from the Global Centroid Moment Tensor (CMT) Project (http://www.globalcmt.org/). The earthquakes selected in this study are declustered from aftershocks following the method of Michael (2011), and the earthquakes occurring at the similar location but with the short interval (<10 days) from the previous ones are also excluded to avoid possible confounded effects from adjacent earthquakes. Finally, 1522 shallow (≤60 km) earthquakes are selected, and Figure 1 illustrates epicenter locations of these earthquakes.

The GIM VTEC is derived using the observations from hundreds of global GNSS stations (Hernández-Pajares et al., 2009). The GIM covers ± 87.5° latitude and ± 180° longitude ranges with spatial resolutions of 2.5° and 5°, respectively, and the time interval of the VTEC is 2 h. For each earthquake, the cell including the epicenter was selected as the point to analyze ionospheric VTEC anomalies. According to Dobrovolsky, (1979), the radius of the M6.0 earthquake preparation zone is about 380 km, corresponding to 3.5°. Therefore, the spatial resolution of GIM VTEC is sufficient to extract ionospheric anomalies using the nearest grid to the epicenter.

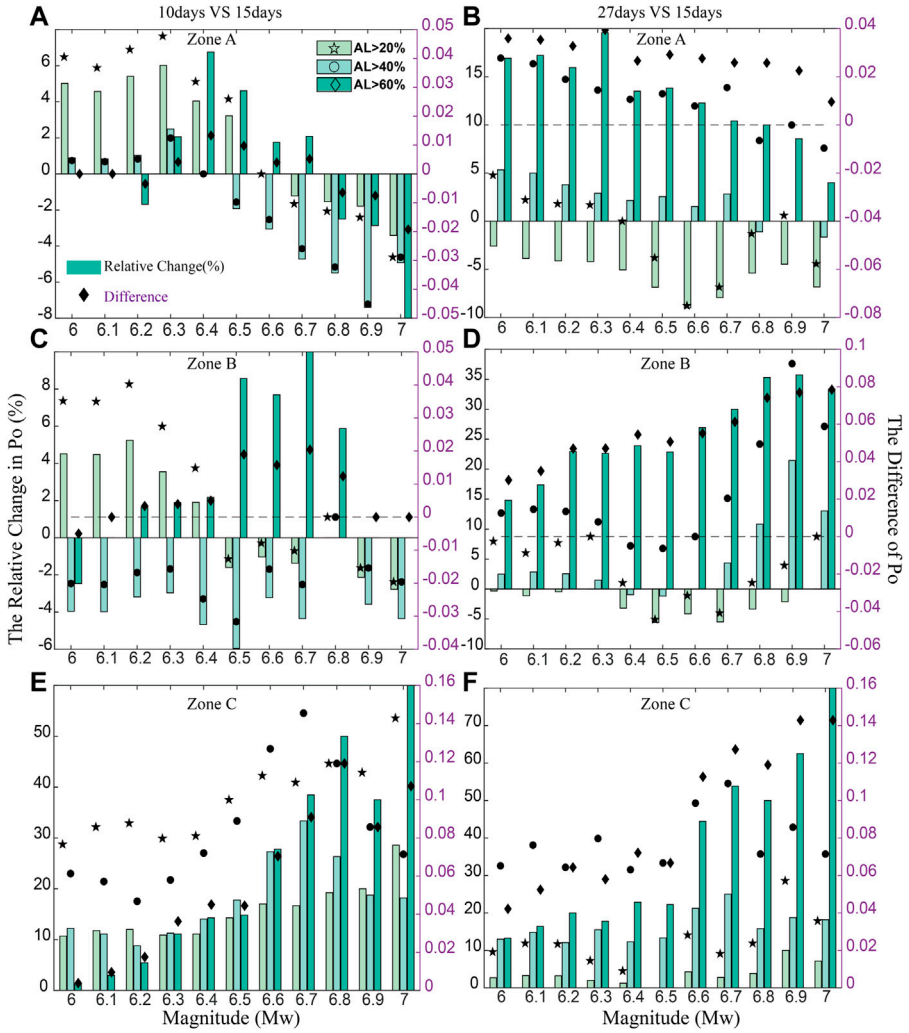

FIGURE 3
The differences and relative changes of seismo-ionospheric anomalies occurrence probabilities between the results of different sliding windows. **(A, C, E)** show the difference between the results of 10-day and 15-day sliding windows in Zone A, Zone B and Zone C, respectively. **(B, D, F)** show the difference between the results of 27-day and 15-day sliding windows in Zone A, Zone B and Zone C, respectively.

The equatorial geomagnetic activity index (Dst) data provided by the World Data Center for Geomagnetism, Kyoto (https://wdc.kugi.kyoto-u.ac.jp/) are used to represent the geomagnetic activity.

2.2 Statistical method

In this study, a quartile-based process is performed to detect ionospheric VTEC anomalies within 1–10 days prior to each earthquake. As the length of sliding window is limited by the seasonal variability of the ionosphere at longer timescales, 10, 15, and 27 days are chosen as the candidate lengths of sliding windows based on the previous studies. At each time point on any day, the median $\bar{x}$ is computed using the VTEC at the same time point within 10, 15, and 27 days before this day as the background value, respectively, and the associated inter-quartile range IQR is also obtained to construct the upper or lower bound $\bar{x} \pm 1.5IQR$. If VTEC continuously exceeds the associated upper or lower bounds for at least 6 h during a day, this day would be considered as an anomalous day. Moreover, the abnormal level (AL) is defined as the percentage of the largest deviation from the median (Le et al., 2011). Ionospheric anomalies with AL<20% are regarded as the daily effects of solar activities (Le et al., 2011, Personal Communication), therefore, only ionospheric anomalies with AL>20% are analyzed in this study. In addition, the ionospheric anomalies with AL>40% and AL>60% (i.e., $n \times AL, n = 1, 2, 3$ with $AL = 20\%$) are also checked for the purpose of studying whether the characteristics of ionospheric anomalies are similar with different AL. If a day with Dst≤−40 nT or Dst≥40nT, this day and the following 3 days are excluded to avoid the interference of the magnetic disturbed activity. After removing the effects of daily solar activity and geomagnetic disturbance, ionospheric

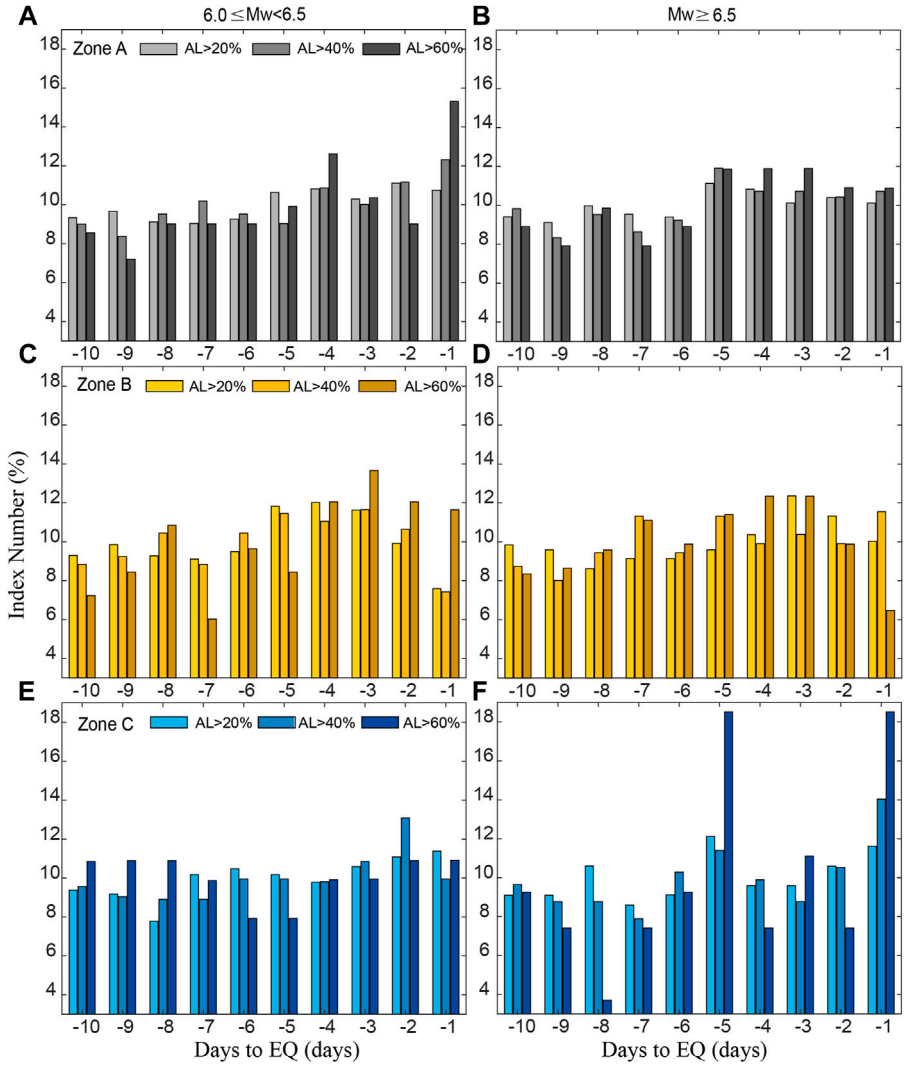

FIGURE 4
The Index Numbers of the seismo-ionospheric anomalies within 1-10 days before the global earthquakes during 2000-2020 (15-day sliding window). **(A, C, E)** are the results of 6.0≤Mw<6.5 in Zone A, Zone B and Zone C, respectively. **(B, D, F)** are the results of Mw≥6.5 in Zone A, Zone B and Zone C, respectively.

anomalies occurring on 1 day are recorded as the seismo-ionospheric anomalies.

After the analysis of seismo-ionospheric anomalies for each event, 1522 earthquakes are divided into three different latitudinal zones (as shown in Figure 1), and VTEC anomalies occurrence probabilities (P_o) and occurrence rates (P_E) will be investigated respectively. For each zone, the earthquakes are firstly classified by magnitudes in increments of 0.1 or by depths in increments of 20km, and then we calculate P_o and P_E of each group. P_o can be computed as the ratio of the number of earthquakes with seismo-ionospheric anomalies and the total number of earthquakes (Fujiwara et al., 2004), as shown in Eq. 1. In this equation, No_{AL} and No_{Total} are the number of earthquakes with seismo-ionospheric anomalies and the total number of all the earthquakes in each group, respectively. For example, in the group (Mw ≥ 6.5 in Zone A with AL>20%), P_o is the number of earthquakes with seismo-ionospheric anomalies divided by the total number of earthquakes.

$$P_o = \frac{No_{AL}}{No_{Total}} \tag{1}$$

The occurrence rates for the n th earthquake P_{En} can be calculated as the ratio of the number of the seismo-ionospheric abnormal days and the total quiet days: $N^n_{AL,T}/(T - \Delta S_n)$, and P_E is defined as the mean of P_{En}, as shown in Eq. 2, derived from Le et al. (2011). In this equation, K is the number of earthquakes in each group (for example, Mw ≥ 6.5 in Zone A with AL>20%); $N^n_{AL,T}$ is the number of seismo-ionospheric days with different AL (for example, AL>20%) within the T days before the n th earthquake, and $T = 1, 2, 3, ..., 10$; ΔS_n is the number of magnetic disturbed days during the 1–10 days before the n th earthquake; $N^n_{AL,T}/(T - \Delta S_n)$ is the number of the seismo-ionospheric

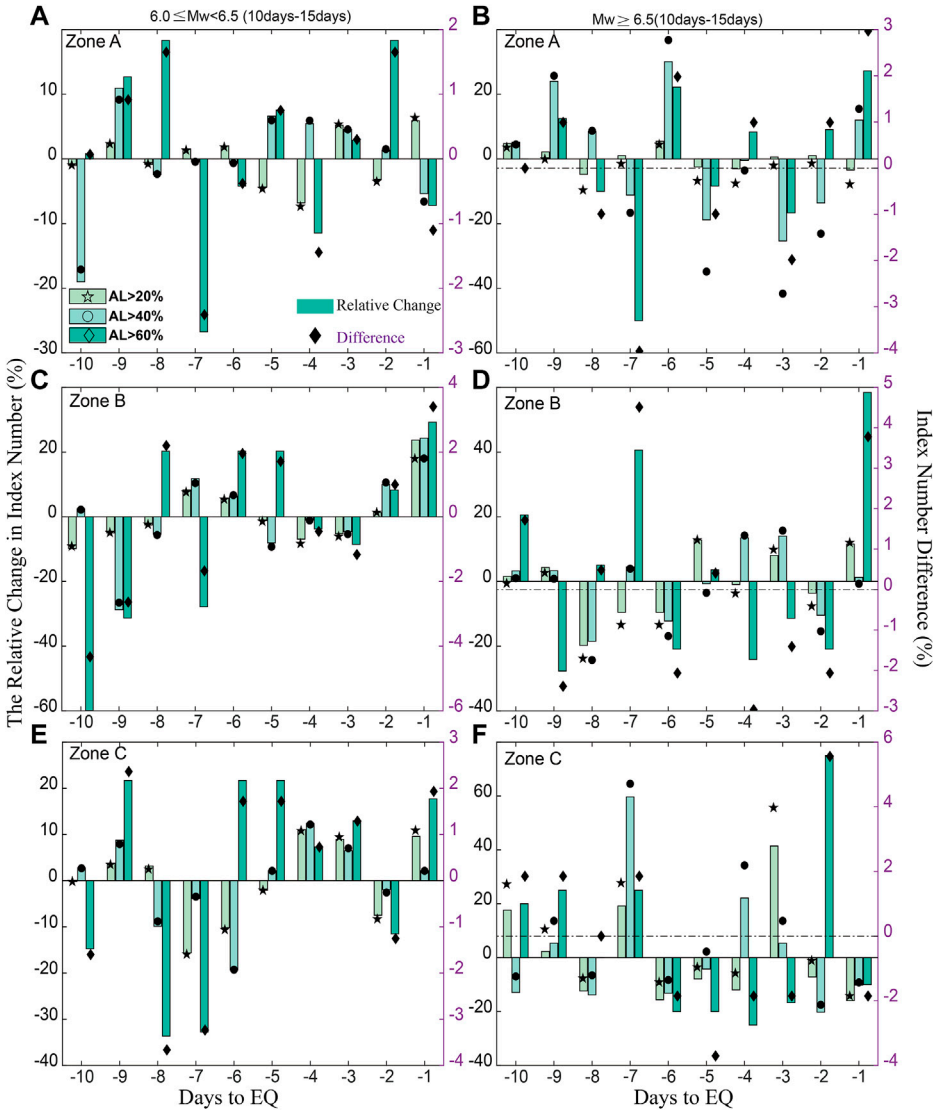

FIGURE 5
The differences and relative changes of the Index Numbers of the seismo-ionospheric anomalies between the results of 10-day and 15-day sliding windows. **(A, C, E)** represent the results of 6.0≤Mw<6.5 in Zone A, Zone B and Zone C, respectively. **(B, D, F)** represent the results of Mw≥6.5 in Zone A, Zone B and Zone C, respectively.

abnormal days divided by the number of the total quiet days before the n th earthquake.

$$PE = \frac{1}{K}\sum_{n=1}^{K}\frac{N^{n}_{AL,T}}{T-\Delta S_{n}} \times 100\% \quad (2)$$

3 Results and discussions

3.1 Seismo-ionospheric anomalies occurrence probabilities

According to the method described above, we calculated P_o for earthquakes with different magnitudes and depths. Figure 2 shows P_o with AL > 20%, 40%, and 60% within 1–10 days before different magnitude earthquakes with the depth ≤20, ≤40, and ≤60 km, respectively. It can be seen from Figure 2 (left), there is no significant correlation between the values of P_o and the magnitude for the earthquakes of 6.0≤Mw < 6.5 in all three zones. There are larger values of P_o in Zone A for larger magnitude earthquakes of Mw≥6.5, but the values of P_o decrease with the magnitudes increasing in Zone B and C for Mw≥6.5 earthquakes to some extent. The values of P_o in Zone A are higher than those in the other zones for Mw≥6.7 earthquakes, and all the results in Zone A are larger than those in the other zones with AL>20% and AL>40%. Ionospheric enhancements in equatorial regions may be the main reason (Liu et al., 2010; Shah et al., 2020). However, the results in Zone C for 6.0≤Mw < 6.7 earthquakes are higher than those in the other two zones with AL>60%. It needs to note that for the earthquakes in the mid-

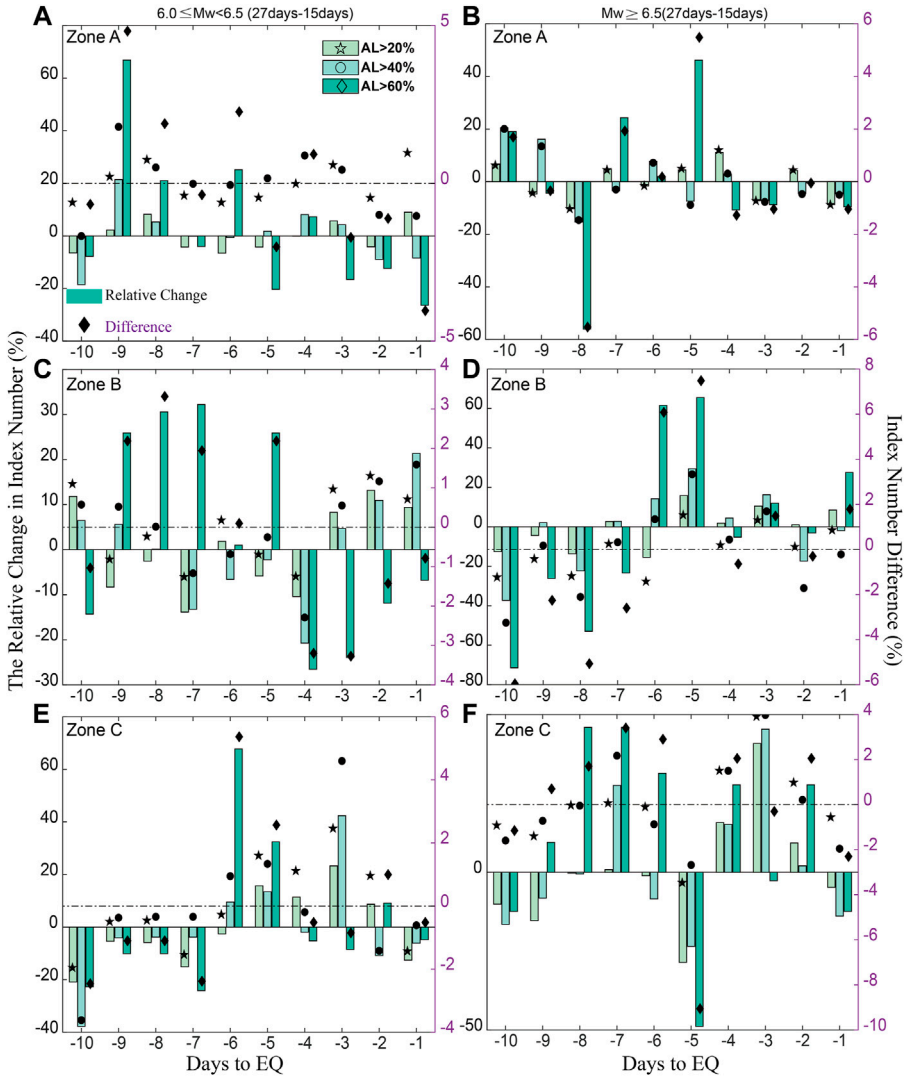

FIGURE 6
The differences and relative changes of the Index Numbers of the seismo-ionospheric anomalies between the results of 27-day and 15-day sliding windows. **(A, C, E)** represent the results of 6.0≤Mw<6.5 in Zone A, Zone B and Zone C, respectively. **(B, D, F)** represent the results of Mw≥6.5 in Zone A, Zone B and Zone C, respectively.

and high-latitude regions, other magnetic indices are not considered except the Dst index. So we compared the variations of the Kp index and Dst index, and found that if Kp=4 is chosen as the threshold value, the impact of not considering Kp can be ignored. But for the earthquakes in the high-latitude regions (as shown in Table 1), the number of disturbed day based on the AE index (>500 nT) is larger than that based on Dst. That is, external magnetic fields contamination is still probably not excluded in this study for these 51 earthquakes in Zone B and Zone C. However, the most of values of P_o in Zone A are still higher than those in other zones. It indicates that the latitude of the epicenter has a significant influence on the P_o, that is, the results of the low-latitude and equatorial regions are higher than those of the mid- and high-latitude regions. To a certain extent, P_o increases with the magnitude increasing in the low-latitude and equatorial region, while P_o decreases with the magnitude increasing in the mid- and high-latitude region.

According to Figure 2 (right), one can find that the values of P_o decrease in Zone A and C, and increase in Zone B slightly, with depths increasing. The maximum difference of P_o between different depths in Zone A, B and C was 0.0075, 0.0372 and 0.0291, respectively. Therefore, it reveals that for shallow earthquakes (≤60 km), the influence of depths on P_o could be ignored. For the case of AL>20% or AL>40%, the results of Zone A are the largest, followed by those of Zone B. For the case of AL>60%, the results of Zone C are the largest, while the rest two zones have no significant difference. Therefore, selecting different AL has an obvious impact on P_o in different zones with different magnitudes and depths. Considering that all the earthquakes in this study are shallow

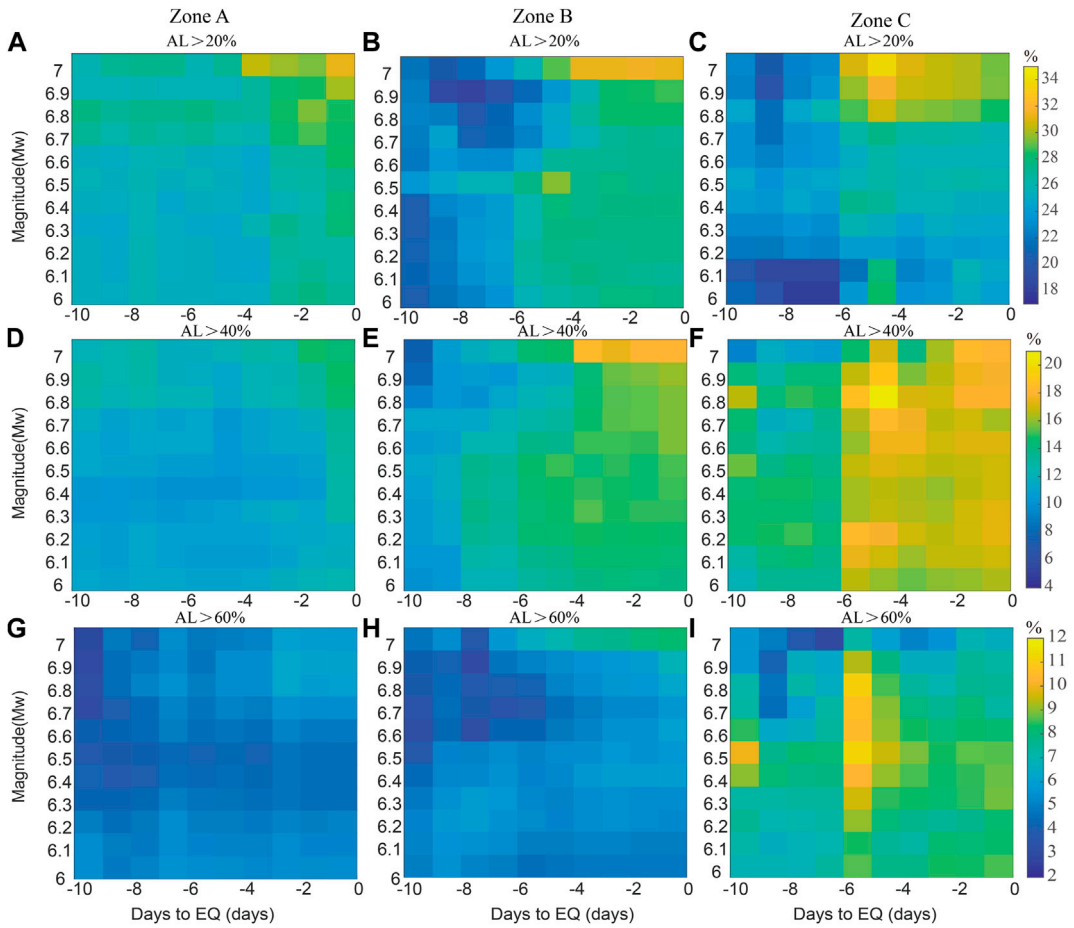

FIGURE 7
Seismo-ionospheric anomalies occurrence rates of AL>20%, 40%, and 60% within 1-10 days before earthquakes of Zone A **(A, D, G)**, Zone B **(B, E, H)**, and Zone C **(C, F, I)**, respectively (15-day sliding window).

earthquakes, the impact of different depths will not be further investigated in the following sections.

To study the effects of different lengths of the sliding windows on P_o, Figure 3 shows the differences between the results of different sliding windows, indicating the effect of sliding window length on latitudinal zones, that is, the most affected zones are Zone C, B and A in decreasing order. For the earthquakes in the southern mid- and high-latitude region (Zone C), compared with the results of 15-day sliding window: 1) the results of 10-day or 27-day sliding window are systematically increased, and the differences are larger using 27-day sliding window; 2) For the cases of AL>20% or AL>40%, most of the relative changes are less than 20%, while the maximum difference and relative change can reach 0.16% and 80%, respectively with AL>60%. Moreover, the differences increase with the increase of the magnitude selecting AL>60%.

For the earthquakes in the northern mid- and high-latitude region (Zone B), compared with the results of 15-day sliding window: 1) most differences are random, and are also greater using 27-day sliding window; 2) For the cases of AL>20% or AL>40%, most relative changes are between −6% and 10%. For the cases of AL>60%, the 27-day results increase systematically, and the maximum difference and relative change can reach 0.092% and 35.71%, respectively.

For the earthquakes in the low-latitude and equatorial region (Zone A), compared with the results of 15-day sliding window: 1) the results vary systematically using the 27-day sliding window; 2) For the cases of AL> 20% or AL>40%, most relative changes are between −8% and 8%. For the cases of AL>60%, the 27-day results increase systematically and the differences decrease with the magnitude increasing, with the maximum difference and relative change reaching 0.039% and 19.59%, respectively.

When AL > 20% or AL > 40% is selected to extract seismo-ionospheric anomalies, most of the relative changes of different sliding window are under 20%. In this study, GIM produced by the Jet Propulsion Laboratory (JPL) is used, and the error of VTEC estimation during the creating process of global maps by JPL is about 10%–17% (Zakharenkova et al., 2008). Therefore, for the case of AL > 20% or AL > 40%, different lengths of sliding windows have a statistically insignificant influence on P_o. When AL>60% is selected, different lengths of sliding windows have non-negligible impacts on P_o in the mid- and high-latitude region, particularly in the southern

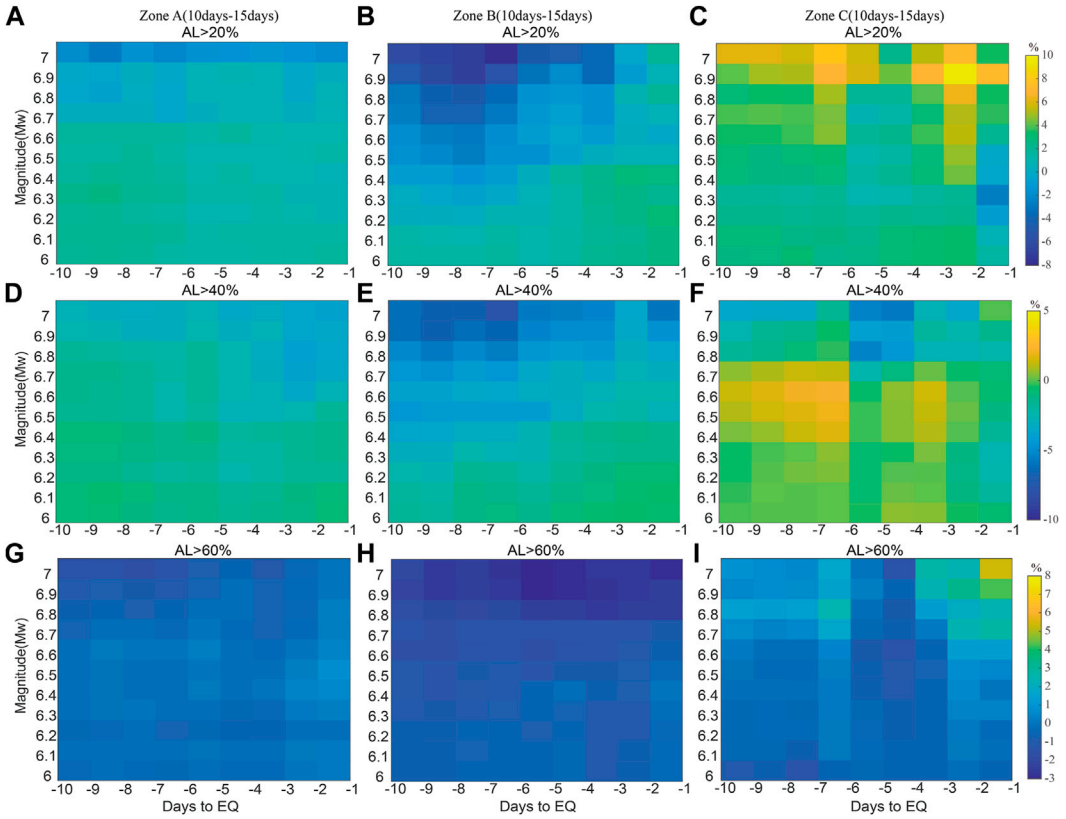

FIGURE 8
The differences of seismo-ionospheric anomalies occurrence rates between the results of 10-day and 15-day sliding windows. **(A, D, G)** represent the results in Zone A. **(B, E, H)** represent the results in Zone B. **(C, F, I)** represent the results in Zone C.

Hemisphere where there are obvious systematic deviations between the results of different sliding windows. The reasons for the observed systematic deviations may include: 1) the real effects of different lengths of sliding windows; 2) the number of GNSS stations in the southern Hemisphere is smaller than those in the northern Hemisphere, resulting in larger error of VTEC in the southern Hemisphere; 3) the number of earthquakes in Zone C is the smallest. 4) external magnetic fields contamination is still probably not excluded in this study for some earthquakes in Zone B and Zone C (Table 1). However, it can be noted that in Zone A, there are also obvious systematic deviations between the results of 15-day and 27-day sliding windows, indicating the influence of different sliding window lengths cannot be ignored.

Figure 4 shows the Index Number in percentage of the seismo-ionospheric anomalies within 1–10 days before the earthquakes. The Index Number is calculated as the ratio of the cumulative number of seismo-ionospheric anomalies in a single day and the total number of seismo-ionospheric anomalies (Shah et al., 2020). The Index Number enhances within 5 days before the earthquakes in all the three zones, especially in Zone A and B. Figures 5, 6 show the differences and relative changes between the results of different sliding windows. It can be seen that the differences between the results of different sliding windows are random, and are larger between the results of 15-day and 27-day sliding windows. The differences are smallest in Zone A, followed by Zone B. The differences raise with AL increasing. For the case of AL>20% or AL>40%, compared with the results of 15-day sliding window, the most of relative changes are between −20% and 25%. For the case of AL > 60%, the differences are more significant, as the relative changes can exceed 50% in all the three zones. So when AL>60% is selected, the impacts of different sliding windows on the Index Number can not be neglected.

3.2 Seismo-ionospheric anomalies occurrence rates

According to Eq. 2, seismo-ionospheric anomalies occurrence rates P_E are obtained for all the three zones. Figure 7 shows P_E with AL>20%, AL>40% and AL>60% within 1–10 days before different magnitude earthquakes. We found that the larger magnitude of earthquakes and the closer prior to the earthquake occurrence, the larger values of P_E. For instance, the value of P_E increases from 26.82% for Mw≥6.0 earthquakes to 31.29% for Mw≥7.0 earthquakes 1 day before the earthquakes. It can be seen that the correlation is not obvious between the values of P_E in Zone C and the magnitude with AL>60%. It needs to be taken into account with the time (for example, 1–5 days prior to the earthquakes) and the latitude of the epicenter (for example, in the low-latitude and equatorial region) that the values of P_E increase with the magnitude increasing. In addition, as

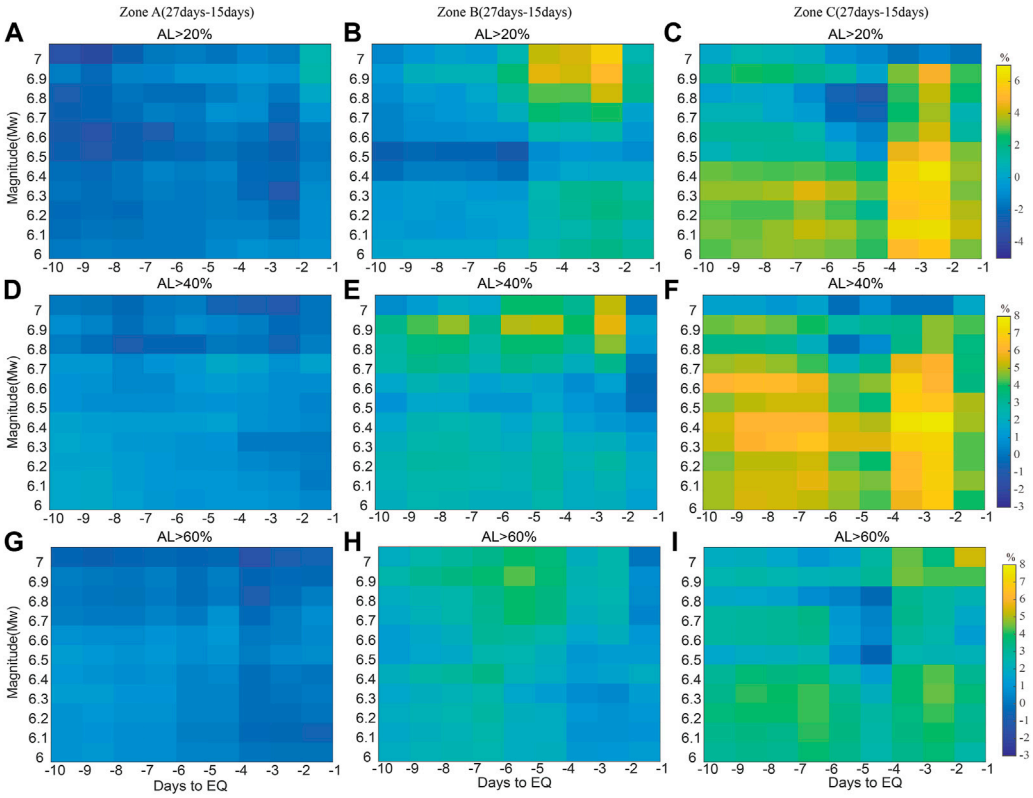

FIGURE 9
The differences of seismo-ionospheric anomalies occurrence rates between the results of 27-day and 15-day sliding windows. **(A, D, G)** represent the results in Zone A. **(B, E, H)** represent the results in Zone B. **(C, F, I)** represent the results in Zone C.

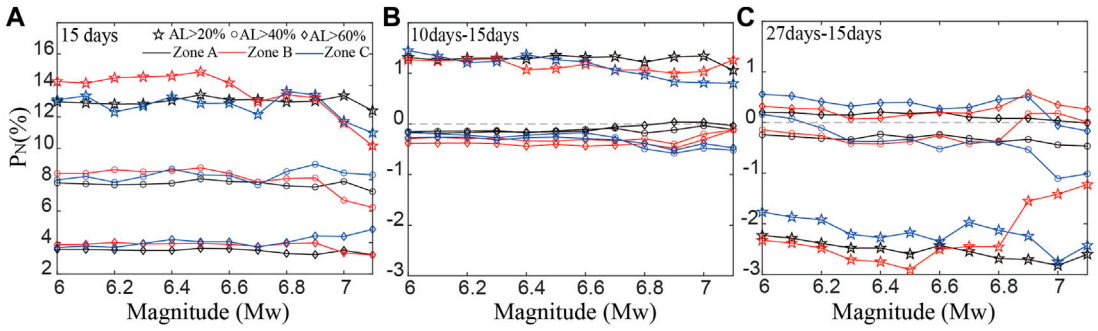

FIGURE 10
(A) Ionospheric anomalies occurrence rates of A >20%, 40%, and 6% during background days; **(B)** The differences of ionospheric anomalies occurrence rates between the results of 10-day and 15-day sliding windows; **(C)** The differences of ionospheric anomalies occurrence rates between the results of 27-day and 15-day sliding windows.

mentioned in the previous section, the number of earthquakes is smaller and the errors of VTEC are larger in Zone C, so the results in Zone C could be biased to some extent. Besides, the effects of external magnetic fields contamination for some earthquakes in Zone B and Zone C may not be excluded, which would also bias the results.

Figures 8, 9 represent the P_E differences of the results using different sliding windows. For Zone A, different sliding window lengths have little influence. For Zone B, compared with the results of the 15-day sliding window, the values of P_E significantly increase for Mw≥6.7 earthquakes using 27-day sliding window. For Zone C, the differences of the results of different sliding windows are larger than those in the other zones without systematic pattern. Therefore, it indicates that the impacts of sliding window lengths are related to the latitude of the epicenter. Different sliding windows should be selected to investigate the earthquakes in different zones. For Zone A, 10-day, 15-day and 27-day sliding windows may be selected

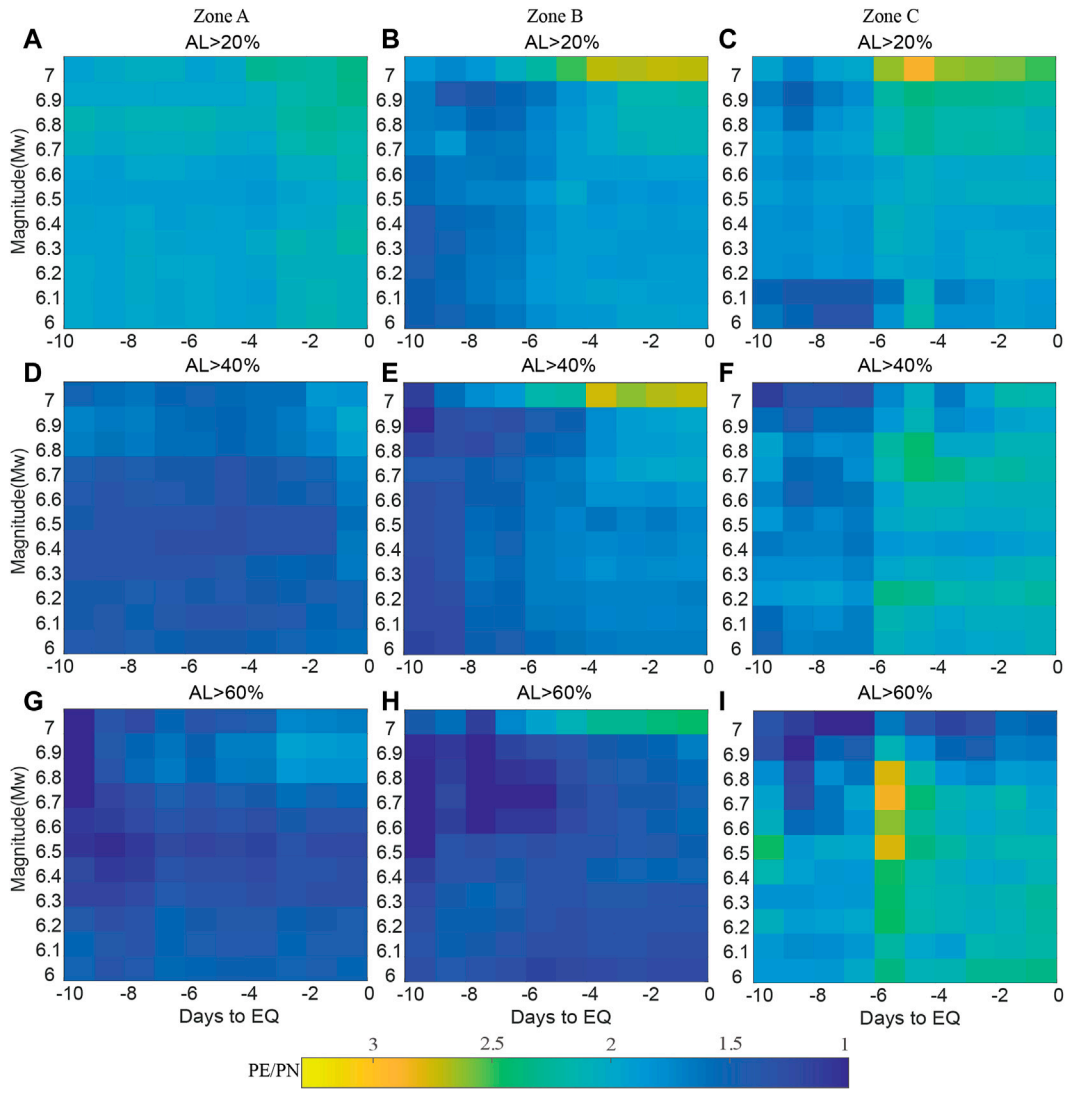

FIGURE 11
The ratio of the seimo-ionospheric anomalies occurrence rates within 1-10 days before the earthquakes to the ionospheric anomalies occurrence rates during background days (15-day sliding window). **(A, D, G)** represent the results in Zone A. **(B, E, H)** represent the results in Zone B. **(C, F, I)** represent the results in Zone C.

arbitrarily. For Zone B, 27-day sliding window may be a better choice. But the selection of the optimal sliding window for Zone C still needs further research in the future.

To compare the difference between the seimo-ionospheric anomalies a few days before the earthquakes and the day-to-day ionospheric variation, the ionospheric anomalies occurrence rates during background days P_N, as shown in Eq. 3, derived from Le et al. (2011), are also calculated. For each earthquake, 61–300 days before this earthquake are selected as the background days, and disturbed days ΔW by geomagnetic storms and by the Mw≥6.0 earthquakes at the adjacent places are also excluded.

$$P_N = \frac{\sum_{n=1}^{K} N_{AL}^n}{K \times 240 - \Delta W} \quad (3)$$

In this equation, K is the number of earthquakes in each group (for example, Mw ≥ 6.5 in Zone A with AL>20%); N_{AL}^n is the number of seismo-ionospheric days with different AL (for example, AL>20%) during the 61–300 days before the n th earthquake; ΔW is the number of disturbed days.

Figure 10A shows the values of P_N for different magnitude earthquakes. The results are smaller than those of P_E, and seem to decrease very slightly with the magnitude increasing. The effects of different latitudinal locations and AL on the values of P_N is insignificant. Figures 10B, C) presents the differences of P_N derived from different sliding window lengths are obviously systematic, and are related to AL. For example, when AL > 20% is assumed, all the results of 27-day sliding window are reduced compared with those of 15-day sliding window. Therefore, different sliding window lengths have a systematic effect on the values of P_N.

Figure 11 shows the ratio of P_E and P_N with different magnitude using 15-day sliding window. The results show that most of the

values of P_E/P_N are larger than 1, indicating large differences of the occurrence rates between the days prior to earthquakes and the background days.

4 Conclusion

Both the latitude of the epicenter and the magnitude can affect the characteristics of seismo-ionospheric anomalies before shallow earthquakes. In terms of seismo-ionospheric anomalies occurrence probabilities P_o, ionospheric enhancement in the low-latitude and equatorial region is more significant (Zone A), and their P_o are larger with the magnitude increasing, especially for Mw≥6.6 earthquakes; in the mid- and high-latitude region (Zone B and C), a slight negative correlation is presented between the values of P_o and the magnitude. In terms of seismo-ionospheric anomalies occurrence rates P_E, the values of P_E increase with the magnitude increasing in all the three zones, but the correlation between the values of P_E and the magnitude is faint in Zone C. Because of the small number of earthquakes and the low accuracy of VTEC in Zone C, the reliability of the results still needs to be further studied and confirmed.

Both the number of days before earthquakes and the AL can affect the characteristics of seismo-ionospheric anomalies before shallow earthquakes. The number of seismo-ionospheric anomalies within 1–5 days before the earthquakes increases significantly in all the three zones, and the positive correlation between the values of P_E and the magnitude is more strong within 1–5 days before the earthquakes. For the case of AL>20% and AL>40%, the values of P_o in the low-latitude and equatorial region are higher than those in the mid- and high-latitude region; For the case of AL>60%, the values of P_o in the southern mid- and high-latitude region are higher than those in the other zones before 6.0≤Mw < 6.7 earthquakes. Therefore, when seismo-ionospheric anomalies in different regions are analyzed, the choice of AL may affect the outcome significantly.

For the mid- and high-latitude region, the effects of different lengths of sliding windows on seismo-ionospheric anomalies can not be ignored. For the case of AL>60%, different sliding windows have a significant impact on the values of P_o and $P_{E,}$ and there are systematic deviations between the values of P_o using different sliding windows in the southern mid- and high-latitude region. However, the selection of the optimal sliding window needs to be further studied, especially for the Zone C.

Moreover, there are large differences between the seismo-ionospheric anomalies occurrence rates P_E 1–10 days prior to the earthquakes and ionospheric anomalies occurrence rates P_N during the background days, indicating that the seismo-ionospheric anomalies within just a few days before the earthquakes are probably related with the forthcoming earthquakes. The 1522 earthquakes in this study are divided into multiple groups, resulting in the small number of earthquakes in some groups, and the accuracy of VTEC in different regions is uneven, which may bias the results in this study. Although the earthquakes occurring at the similar location but with the short interval (<10 days) from the previous ones are excluded, some earthquakes occurring close to their boundaries in two confining zones may also have some confounded effects on the results. Besides, whether a pixel of $2.5^\circ \times 5^\circ$ is appropriate for the earthquakes larger than Mw6.0 needs to be further studied.

Data availability statement

The raw data supporting the conclusion of this article will be made available by the authors, without undue reservation.

Author contributions

MY and ZX contributed to conception of the study. Data were collected by HL, DH, and YR. MY, ZX, and YY performed the experimental analysis. MY wrote the first draft of the manuscript. ZX revised the manuscript. All authors read and approved the final manuscript.

Funding

This work was supported by Beijing Natural Science Foundation Grant Numbers 8224094.

Acknowledgments

We are grateful to the World Data Center for Geomagnetism, Kyoto providing Dst index, the Global CMT Project providing parameters of earthquakes, and IGS providing GIM.

Conflict of interest

The authors declare that the research was conducted in the absence of any commercial or financial relationships that could be construed as a potential conflict of interest.

Publisher's note

All claims expressed in this article are solely those of the authors and do not necessarily represent those of their affiliated organizations, or those of the publisher, the editors and the reviewers. Any product that may be evaluated in this article, or claim that may be made by its manufacturer, is not guaranteed or endorsed by the publisher.

References

Dautermann, T., Calais, E., Haase, J., and Garrison, J. (2007). Investigation of ionospheric electron content variations before earthquakes in southern California, 2003-2004. *J. Geophys. Res.* 112, 1074–1086. doi:10.1029/2006JB004447

Davidenko, D. V., and Pulinets, S. A. (2019). Deterministic variability of the ionosphere on the eve of strong (M≥6) earthquakes in the regions of Greece and Italy according to long-term measurements data. *Geomagn. Aeron.* 59 (4), 493–508. doi:10.1134/S001679321904008X

De Santis, A., Marchetti, D., Pavón-Carrasco, F. J., Cianchini, G., Perrone, L., Abbattista, C., et al. (2019). Precursory worldwide signatures of earthquake occurrences on Swarm satellite data. *Sci. Rep.* 9, 20287. doi:10.1038/s41598-019-56599-1

Dobrovolsky, I. P., Zubkov, S. I., and Miachkin, V. I. (1979). Estimation of the size of earthquake preparation zones. *Pure Appl. Geophys.* 117 (5), 1025–1044. doi:10.1007/BF00876083

Freund, F. (2011). Pre-earthquake signals: Underlying physical processes. *J. Asian Earth Sci.* 41 (4-5), 383–400. doi:10.1016/j.jseaes.2010.03.009

Fujiwara, H., Kamogawa, M., Ikeda, M., Liu, J. Y., Sakata, H., Chen, Y. I., et al. (2004). Atmospheric anomalies observed during earthquake occurrences. *Geophys. Res. Lett.* 31, L17110. doi:10.1029/2004GL019865

Guo, J., Li, W., Yu, H., Liu, Z., Zhao, C., and Kong, Q. (2015). Impending ionospheric anomaly preceding the Iquique Mw8.2 earthquake in Chile on 2014 April 1. *Geophys. J. Int.* 203 (3), 1461–1470. doi:10.1093/gji/ggv376

Hernández-Pajares, M., Juan, J., Sanz, J., Orus, R., Garcia-Rigo, A., Feltens, J., et al. (2009). The IGS VTEC maps: A reliable source of ionospheric information since 1998. *J. Geod.* 83 (3-4), 263–275. doi:10.1007/s00190-008-0266-1

Ho, Y. Y., Jhuang, H. K., Su, Y. C., and Liu, J. Y. (2013). Seismo-ionospheric anomalies in total electron content of the GIM and electron density of DEMETER before the 27 February 2010 M8.8 Chile earthquake. *Adv. Space Res.* 51 (12), 2309–2315. doi:10.1016/j.asr.2013.02.006

Jiang, W., Ma, Y., Zhou, X., Li, Z., An, X., and Wang, K. (2017). Analysis of ionospheric vertical total electron content before the 1 April 2014 Mw 8.2 Chile earthquake. *J. Seismol.* 21 (6), 1599–1612. doi:10.1007/s10950-017-9684-y

Ke, F., Wang, Y., Wang, X., Qian, H., and Shi, C. (2016). Statistical analysis of seismo-ionospheric anomalies related to Ms>5.0 earthquakes in China by GPS TEC. *J. Seismol.* 20 (1), 137–149. doi:10.1007/s10950-015-9516-x

Klimenko, M. V., Klimenko, V. V., Zakharenkova, I. E., and Pulinets, S. A. (2012). Variations of equatorial electrojet as possible seismo-ionospheric precursor at the occurrence of TEC anomalies before strong earthquake. *Adv. Space Res.* 49 (3), 509–517. doi:10.1016/j.asr.2011.10.017

Kon, S., Nishihashi, M., and Hattori, K. (2011). Ionospheric anomalies possibly associated with M ≥ 6.0 earthquakes in the Japan area during 1998–2010: Case studies and statistical study. *J. Asian Earth Sci.* 41 (4), 410–420. doi:10.1016/j.jseaes.2010.10.005

Le, H., Liu, J. Y., and Liu, L. (2011). A statistical analysis of ionospheric anomalies before 736 M6.0+ earthquakes during 2002-2010. *J. Geophys. Res.* 116 (A2), A02303. doi:10.1029/2010JA015781

Liperovsky, V. A., Pokhotelov, O. A., Meister, C. V., and Liperovskaya, E. V. (2008). Physical models of coupling in the lithosphere-atmosphere-ionosphere system before earthquakes. *Geomagn. Aeron.* 48, 795–806. doi:10.1134/S0016793208060133

Liu, J. Y., Chen, C. H., Chen, Y. I., Yang, W. H., Oyama, K. I., and Kuo, K. W. (2010). A statistical study of ionospheric earthquake precursors monitored by using equatorial ionization anomaly of GPS TEC in Taiwan during 2001–2007. *J. Asian Earth Sci.* 39 (1), 76–80. doi:10.1016/j.jseaes.2010.02.012

Liu, J. Y., Chen, Y. I., Chuo, Y. J., and Tsai, H. F. (2001). Variations of ionospheric total electron content during the Chi-Chi earthquake. *Geophys. Res. Lett.* 28 (7), 1383–1386. doi:10.1029/2000GL012511

Liu, J. Y., Chuo, Y. J., Shan, S. J., Tsai, Y. B., Chen, Y. I., Pulinets, S. A., et al. (2004). Pre-earthquake ionospheric anomalies registered by continuous GPS TEC measurements. *Ann. Geophys.* 22 (5), 1585–1593. doi:10.5194/angeo-22-1585-2004

Liu, W., and Xu, L. (2017). Statistical analysis of ionospheric TEC anomalies before global Mw≥7.0 earthquakes using data of CODE GIM. *J. Seismol.* 21 (4), 759–775. doi:10.1007/s10950-016-9634-0

Ma, X., Lin, Z., and Chen, H. (2014). Analysis on ionospheric perturbation of TEC and NmF2 based on GPS and COSMIC data before and after the Wenchuan earthquake. *Chin. J. Geophys* 57 (8), 2415–2422. doi:10.6038/cjg20140803

Masci, F. (2012). The study of ionospheric anomalies in Japan area during 1998–2010 by Kon et al.: An inaccurate claim of earthquake-related signatures? *J. Asian Earth Sci.* 57, 1–5. doi:10.1016/j.jseaes.2012.06.009

Masci, F., and Thomas, J. (2014). Comment on "Temporal and spatial precursors in ionospheric total electron content of the 16 October 1999 M_w 7.1 Hector Mine earthquake" by Su et al. (2013). *J. Geophys. Res.* 119, 6994–6997. doi:10.1002/2014JA019896

Michael, A. J. (2011). Random variability explains apparent global clustering of large earthquakes. *Geophys. Res. Lett.* 38, L21301. doi:10.1029/2011GL049443

Namgaladze, A. A., Klimenko, M. V., Klimenko, V. V., and Zakharenkova, I. E. (2009). Physical mechanism and mathematical modeling of earthquake ionospheric precursors registered in total electron content. *Geomagn. Aeron.* 49 (2), 252–262. doi:10.1134/S0016793209020169

Nishihashi, M., Hattori, K., Jhuang, H. K., and Liu, J. Y. (2009). Possible spatial extent of ionospheric GPS-TEC and NmF2 anomalies related to the 1999 Chi-Chi and Chia-Yi earthquakes in Taiwan. *Terr. Atmos. Ocean. Sci.* 20, 779–789. (T). doi:10.3319/tao.2009.01.22.01(t)

Ovalle, E., Villalobos, C., Bravo, M., and Foppiano, A. (2013). Maximum electron concentration and total electron content of the ionosphere over Concepción, Chile, prior to the 27 February 2010 earthquake. *Adv. Space Res.* 52, 1274–1288. doi:10.1016/j.asr.2013.07.005

Parrot, M., and Li, M. (2018). "Statistical analysis of the ionospheric density recorded by DEMETER during seismic activity," In *pre-earthquake processes: a multidisciplinary approach to earthquake prediction studies (geophysical monograph 234)*. Editors D. Ouzounov, S. Pulinets, K. Hattori, and P. Taylor (Washington, DC: American Geophysical Union John Wiley and Sons, Inc.).

Pulinets, S. A., and Boyarchuk, K. (2004). *Ionospheric precursors of earthquakes*. Berlin: Springer Press.

Pulinets, S. A., and Davidenko, D. V. (2018). The nocturnal positive ionospheric anomaly of electron density as a short-term earthquake precursor and the possible physical mechanism of its formation. *Geomagn. Aeron.* 58, 559–570. doi:10.1134/s0016793218040126

Pulinets, S. A., Krankowski, A., Hernandez-Pajares, M., Marra, S., Budnikov, P., Zakharenkova, I., et al. (2021). Ionosphere sounding for pre-seismic anomalies identification (INSPIRE): Results of the Project and perspectives for the short-term earthquake forecast. *Front. Earth Sci.* 9, 610193. doi:10.3389/feart.2021.610193

Pulinets, S. (2012). Low-latitude atmosphere-ionosphere effects initiated by strong earthquakes preparation process. *Int. J. Geophys* 2012, 1–14. doi:10.1155/2012/131842

Pulinets, S., and Ouzounov, D. (2011). Lithosphere-Atmosphere-Ionosphere Coupling (LAIC) model-An unified concept for earthquake precursors validation. *J. Asian Earth Sci.* 41 (4), 371–382. doi:10.1016/j.jseaes.2010.03.005

Rishbeth, H. (2006). Ionoquakes: Earthquake precursors in the ionosphere? *Eos. Trans. Am. Geophys. Union* 87, 316. doi:10.1029/2006EO320008

Shah, M., Ahmed, A., Ehsan, M., Khan, M., Tariq, M. A., Calabia, A., et al. (2020). Total electron content anomalies associated with earthquakes occurred during 1998-2019. *Acta Astronaut.* 175, 268–276. doi:10.1016/j.actaastro.2020.06.005

Shah, M., and Jin, S. (2015). Statistical characteristics of seismo-ionospheric GPS TEC disturbances prior to global Mw≥5.0 earthquakes (1998–2014). *J. Geodyn.* 92, 42–49. doi:10.1016/j.jog.2015.10.002

Su, Y. C., Liu, J. Y., Chen, S. P., Tsai, H. F., and Chen, M. Q. (2013). Temporal and spatial precursors in ionospheric total electron content of the 16 october 1999M_w7.1 hector mine earthquake: Ionoquack OF*M*7.1 hector mine earthquake. *J. Geophys. Res.* 118 (10), 6511–6517. doi:10.1002/jgra.50586

Sun, Y., Liu, J., Lin, C., Tsai, H. F., Chang, L. C., Chen, C. Y., et al. (2016). Ionospheric f2 region perturbed by the 25 april 2015 Nepal earthquake: Ionosphere perturbed by Nepal earthquake. *J. Geophys. Res.* 121, 5778–5784. doi:10.1002/2015JA022280

Tang, J., Yao, Y., and Zhang, L. (2015). Temporal and spatial ionospheric variations of 20 April 2013 earthquake in Yaan, China. *IEEE Geosci. Remote Sens. Lett.* 12, 2242–2246. doi:10.1109/LGRS.2015.2463081

Xu, T., Chen, Z., Li, C., Wu, J., Hu, Y., and Wu, Z. (2011). GPS total electron content and surface latent heat flux variations before the 11 March 2011 M9.0 Sendai earthquake. *Adv. Space Res.* 48 (8), 1311–1317. doi:10.1016/j.asr.2011.06.024

Yao, Y., Chen, P., Wu, H., Zhang, S., and Peng, W. (2012). Analysis of ionospheric anomalies before the 2011 Mw 9.0 Japan earthquake. *Chin. Sci. Bull.* 57, 500–510. doi:10.1007/s11434-011-4851-y

Zakharenkova, I. E., Shagimuratov, I. I., Tepenitzina, N. Y., and Krankowski, A. (2008). Anomalous modification of the ionospheric total electron content prior to the 26 September 2005 Peru earthquake. *J. Atmos. Sol-terr. Phy.* 70 (15), 1919–1928. doi:10.1016/j.jastp.2008.06.003

Zhang, X., Shen, X., Zhao, S., Yao, L., Ouyang, X., and Qian, J. (2014). The characteristics of quasistatic electric field perturbations observed by DEMETER satellite before large earthquakes. *J. Asian Earth Sci.* 79 (2), 42–52. doi:10.1016/j.jseaes.2013.08.026

Zhou, Y., Wu, Y., Qiao, X., and Zhang, X. (2009). Ionospheric anomalies detected by ground-based GPS before the Mw7.9 Wenchuan earthquake of May 12, 2008, China. *J. Atmos. Sol-terr. Phy.* 71, 959–966. doi:10.1016/j.jastp.2009.03.024

Zhu, F., Zhou, Y., Lin, J., and Su, F. (2014). A statistical study on the temporal distribution of ionospheric TEC anomalies prior to M7.0+ earthquakes during 2003-2012. *Astrophys. Space Sci.* 350, 449–457. doi:10.1007/s10509-014-1777-2

Zolotov, O. V., Knyazeva, M. A., and Romanovskaya, Y. V. (2019). Computer analysis of total electron content in the Earth's ionosphere in problems of searching for and detection of earthquake precursors: Current problems and challenges. *Russ. J. Phys. Chem. B* 13 (4), 681–684. doi:10.1134/S1990793119040146

Zolotov, O. V., Namgaladze, A. A., Zakharenkova, I. E., Martynenko, O. V., and Shagimuratov, I. I. (2012). Physical interpretation and mathematical simulation of ionospheric precursors of earthquakes at midlatitudes. *Geomagn. Aeron.* 52 (3), 390–397. doi:10.1134/S0016793212030152

frontiers | Frontiers in Earth Science

TYPE Review
PUBLISHED 20 April 2023
DOI 10.3389/feart.2023.1136472

Check for updates

OPEN ACCESS

EDITED BY
Giovanni Martinelli,
National Institute of Geophysics and Volcanology, Italy

REVIEWED BY
Boyko Ranguelov,
University of Mining and Geology "Saint Ivan Rilski", Bulgaria
Zhenming Wang,
University of Kentucky, United States

*CORRESPONDENCE
Vladimir Kossobokov,
volodya@mitp.ru

SPECIALTY SECTION
This article was submitted to Solid Earth Geophysics, a section of the journal Frontiers in Earth Science

RECEIVED 03 January 2023
ACCEPTED 10 March 2023
PUBLISHED 20 April 2023

CITATION
Bela J, Kossobokov V and Panza G (2023), Seismic Rigoletto: Hazards, risks and seismic roulette applications. *Front. Earth Sci.* 11:1136472. doi: 10.3389/feart.2023.1136472

COPYRIGHT
© 2023 Bela, Kossobokov and Panza. This is an open-access article distributed under the terms of the Creative Commons Attribution License (CC BY). The use, distribution or reproduction in other forums is permitted, provided the original author(s) and the copyright owner(s) are credited and that the original publication in this journal is cited, in accordance with accepted academic practice. No use, distribution or reproduction is permitted which does not comply with these terms.

Seismic Rigoletto: Hazards, risks and seismic roulette applications

James Bela[1,2], Vladimir Kossobokov[1,3]* and Giuliano Panza[1,4,5,6,7,8]

[1]International Seismic Safety Organization (ISSO), Arsita, Italy, [2]Oregon Earthquake Awareness, Portland, OR, United States, [3]Institute of Earthquake Prediction Theory and Mathematical Geophysics, Russian Academy of Sciences (IEPT RAS), Moscow, Russia, [4]Accademia Nazionale dei Lincei, Rome, Italy, [5]Institute of Geophysics, China Earthquake Administration, Beijing, China, [6]Accademia Nazionale Delle Scienze detta dei XL, Rome, Italy, [7]Beijing University of Civil Engineering and Architecture (BUCEA), Beijing, China, [8]Associate to the National Institute of Oceanography and Applied Geophysics - OGS, Trieste, Italy

Neo-Deterministic Seismic Hazard Assessment (NDSHA), dating back to the turn of the Millennium, is the new multi-disciplinary scenario- and physics-based approach for the evaluation of seismic hazard and safety–guaranteeing "prevention rather than cure." When earthquakes occur, shaking certainly does not depend on sporadic occurrences within the study area, nor on anti-seismic (earthquake-resistant) design parameters scaled otherwise to *probabilistic* models of earthquake return-period and likelihood — as adopted in the widespread application of the model-driven Probabilistic Seismic Hazard Analysis (PSHA). Therefore, from a policy perspective of *prevention,* coherent and compatible with the most advanced theories in Earth Science, it is essential that at least the infrastructure installations and public structures are designed so as to resist future strong earthquakes. Evidences and case histories detailed in the newly published book *Earthquakes and Sustainable Infrastructure* present a new paradigm for Reliable Seismic Hazard Assessment (RSHA) and seismic safety — comprehensively detailing in one volume the 'state-of-the-art' scientific knowledge on earthquakes and their related seismic risks, and actions that can be taken to ensure greater safety and sustainability. The book is appropriately dedicated to the centenary of Russian geophysicist Vladimir Keilis-Borok (1921–2013), whose mathematical-geophysical insights have been seminal for the innovative paradigm of Neo-deterministic seismic hazard assessment. This review focuses on Hazards, Risks and Prediction initially discussed in the introductory Chapter 1 — an understanding of which is essential in the applications of the state-of-the-art knowledge presented in the book's 29 following chapters.

KEYWORDS

complex dynamical systems, earthquake disaster, hazard analysis, pattern recognition applications, risk analysis, scenario simulation

Introduction

Newly published *Earthquakes and Sustainable Infrastructure* (Panza et al., 2021) presents a new paradigm for seismic safety — comprehensively detailing in one volume the 'state-of-the-art' scientific knowledge on earthquakes and their related seismic risks, and the actions that can be taken to reliably ensure greater safety and sustainability. This book is appropriately dedicated to the centenary of Russian geophysicist Vladimir Keilis-Borok (1921–2013), whose mathematical insights have been seminal for the innovative paradigm of Neo-Deterministic Seismic Hazard Assessment (NDSHA). Dating back to the turn of the Millennium, NDSHA is the new multi-disciplinary scenario- and physics-based approach

for the evaluation of seismic hazard and safety — guaranteeing "prevention rather than cure."

When earthquakes occur with a given magnitude (M), the shaking certainly does not depend on sporadic occurrences within the study area, nor on anti-seismic (earthquake resistant) design parameters scaled otherwise to *probabilistic* models of earthquake return period and likelihood — as adopted in the widespread application of the model-driven Probabilistic Seismic Hazard Analysis (PSHA), e.g., by the Global Earthquake Model (GEM) project and its recent spinoff Modello di Pericolosità Sismica (MPS19) for Italy.

An earthquake compatible with the *seismogenic* characteristics of a certain area, even if sporadic and therefore labelled as "unlikely", can occur at any time, and the anti-seismic design parameters must take into account the magnitude values defined according to both the *seismic history* and the *seismotectonics*. Therefore, from a policy perspective of prevention, coherent and compatible with the most advanced theories in Earth Science, it is essential that at least the infrastructure installations and public structures are designed so as to resist (or sustain) future strong earthquakes and continue operation in their original capacities.

Thirty chapters of the book provide comprehensive reviews and updates of NDSHA research and applications so far in Africa, America, Asia and Europe — a collection of evidences and case histories that hopefully will persuade responsible people and authorities to consider these more reliable procedures for seismic hazard analyses and risk evaluation. Providing awareness that the use of PSHA may result in the design of unsafe buildings, NDSHA evaluations must be considered in the next versions of earthquake-resistant design standards and explicitly taken as the reference approach for both safety and sustainability.

The book fulfils essential needs of geophysicists, geochemists, seismic engineers, and all those working in disaster preparation and prevention; and is the only book to cover earthquake prediction and civil preparedness measures from a Neo-Deterministic (NDSHA) approach. In this review we focus on the lead chapter: Hazard, Risks, and Prediction by Vladimir Kossobokov (2021) — an understanding of which is essential in the applications of the state-of-the-art knowledge presented in the book's 29 following chapters.

Science should be able to warn people of looming Disaster

> « Science should be able to warn people of looming disaster, Vladimir Keilis-Borok believes."My main trouble," he says, "is my feeling of responsibility." »
>
> (Los Angeles Times, 9 July 2012)

Nowadays, in our Big Data World, Science can disclose Natural Hazards, assess Risks, and deliver the state-of-the-art Knowledge of Looming Disasters in advance of catastrophes, along with useful Recommendations on the level of risks for decision-making with regard to engineering design, insurance, and emergency management. Science cannot remove, yet, people's favor for fable and illusion regarding reality, as well as political denial, sincere ignorance, and conscientious negligence among decision-makers. The general conclusion above is confirmed by application and testing against Earthquake Reality, that the innovative methodology of Neo-Deterministic Seismic Hazard Assessment (NDSHA) "Guarantees Prevention Rather Than Cure." NDSHA results are based on reliable seismic evidence, Pattern Recognition of Earthquake Prone Areas (PREPA), implications of the Unified Scaling Law for Earthquakes (USLE), and exhaustive scenario-based modeling of ground shaking.

The UN World Conference on Disaster Reduction, held January 18–22, 2005 in Kobe, Hyogo, Japan, formally adopted the Hyogo Framework for Action 2005–2015: "Building the Resilience of Nations and Communities to Disasters", just days following the 26 December 2004, M_W 9.2 Great Indian Ocean mega-earthquake and tsunami. During the Conference, a Statement (Kossobokov, 2005a) at the "Special Session on the Indian Ocean Disaster: risk reduction for a safer future" was urging or insistent on a possibility of a few mega-earthquakes of about the same magnitude M_W 9.0 occurring globally within the next 5–10 years. This *prediction* was confirmed, unfortunately, by both the 27 February 2010, M_W 8.8 mega-thrust offshore Maule, Chile and the 11 March 2011, M_W 9.1 mega-thrust and tsunami off the Pacific coast of Tōhoku, Japan (Kossobokov, 2011; Ismail-Zadeh and Kossobokov, 2020).

An opportunity to reduce the impacts from both these earthquakes and tsunami disasters was missed. Davis et al. (2012) showed how the prediction information on expected world's largest earthquakes provided by the M8 and MSc algorithms (Keilis-Borok and Kossobokov, 1990; Kossobokov et al., 1990), although limited to the *intermediate-term* span of years and *middle-range* location of a thousand km, can be used to reduce future impacts from the world's largest earthquakes.

The primary reasons for having not used the prediction for improving preparations in advance of the Tōhoku earthquake "included: 1) inadequate links between emergency managers and the earthquake prediction information; and 2) no practiced application of existing methodologies to guide emergency preparedness and policy development on *how* to make important public safety decisions based on information provided for an *intermediate-term* and *middle-range* earthquake prediction having limited but known accuracy." The Tōhoku case-study exemplifies how reasonable, prudent, and cost-effective decisions can be made to reduce damaging effects in a region, when given a reliable Time of Increased Probability (TIP) for the occurrence of a large earthquake and associated phenomena like tsunami, landslides, liquefaction, floods, fires, *etc.*

The Sendai Framework for Disaster Risk Reduction 2015–2030, a successor of the Hyogo Framework for Action, is a set of agreed-upon commitments to *proactively* ensure the prevention of "new" Disasters — through the timely implementation of integrated economic, structural, legal, social, health, cultural, educational, environmental, technological, political, and institutional measures (Briceño, 2014; Mitchell, 2014). Years after the 2005 Hyogo and 2015 Sendai Frameworks for Disaster Risk Reduction, countries are now following a range of different approaches and mitigation strategies, due to the variety of both societal systems and hazards. However, Gilbert White's (2005) observation from the tragic tsunami beginnings of this heightened awareness that it was "important to recognize that no country in the world has achieved

a completely effective policy for dealing with the *rising tide* of costs from natural hazards" is still largely true today.

Our beliefs in models, myths can contradict real-world observations

Moreover, the ongoing COVID-19 pandemic is an itchy and troubling global example of how public policies based on presumably both "the best science available" and also *data of high quality* nonetheless appear to be extremely difficult, uneven, and may sometimes lead to *Disaster* even in those countries that were supposedly well-prepared for such an emergency. In fact, the pandemic (https://coronavirus.jhu.edu/map.html), with a rapidly growing less-than-a-year death toll of 1,820,841 and 83,579,767 global cases reported on 1 January 2021, as of 13 February 2021, had the numbers alarmingly already raised to 2,385,203 and 108,289,000 respectively — and thereby sheds a sobering shower on our existing unperturbed and unchallenged *myths* about disasters (Mitchell, 2014). As of 2 September 2021, the totals had more than *doubled*, rising to 4,702,119 and 229,159,687 despite enormous efforts on vaccination. JHU has stopped collecting data as of March 10, 2023 when the death toll reached 6,881,955; total cases reached 676,609,955; and total vaccine doses administered reached 13,338,833,198.

In one disastrous outcome, "the *anzen shinwa* ("safety myth") image portrayed by the Japanese government and electric power companies tended to stifle honest and open discussion of the risks" from nuclear power, in the years leading up to the 2011 Fukushima disaster (Nöggerath et al., 2011). Kaufmann and Penciakova (2011) illustrate how "countries with good governance"— for example, Chile in 2010, "can better prepare for and mitigate the devastating effects of natural disasters" through leadership and transparency. In exploring "Japan's governance in an international context and its impact on the country's crisis response," they reveal how *failures* in the nuclear plant regulatory environment (including *regulatory capture* — wherein "the rulemaking process also appears to be riddled with conflict of interest") led to an unmitigated disaster that was totally avoidable. See also (Saltelli et al., 2022).

Can nothing be done to stop the increasing number of disasters?

Is there any reason, when estimating long-term trends, for *inventing* the Myth that now "fewer people are dying in disasters" (Mitchell, 2014), if a pandemic like COVID-19 (or even a single deadly event like the 2004 Great Indian Ocean mega-earthquake and tsunami that killed 227,898 people) can push up significantly the *expected average* rate of death tolls? Is Climate Change now the biggest cause of disasters, since both vulnerable populations and infrastructures presently exist widespread in the areas exposed to extreme catastrophic events of different kinds?

Is it true that *nothing* can be done to stop the increasing number of disasters, if, *alternatively*, a country can radically reduce its risks from disasters by *appropriate investments*, *incentives*, and *political leadership?* Unlike 30 years ago, Science presently does have the know-how to reduce damage from even the major hazardous events to the level of incidents rather than disasters.

Evidently, we do not live in a black-and-white disaster world, and our beliefs, i.e., our *mental models,* or the "conceptualizations" that we "bring to the task" (pages 2–3 in Chu, 2014) in "initial basic principles" may unfortunately lead us to rather prefer models that *contradict* with our *real-world* observations. We know quite well the famous quotation that "all models are wrong, but some are useful" from George Box (1979), but too often we forget that *some models are useless* and *some others are really harmful*, especially, when viewed as complete substitutes for the original natural phenomenon (Gelfand, 1991).

Nowadays, in our Big Data World, where the global information storage capacity routinely surpasses a level of more than 6 Zettabytes ($6 \times 10^{+21}$ in optimally compressed bytes) per year, "open data", together with the enormous amount of available pretty fast user-friendly software, provide unprecedented opportunities for the development and enhancement of *pattern recognition* studies — in particular, those studies applied to Earth System processes. However, a Big Data World alternatively opens up as well many wide avenues, narrow pathways, and even *rabbit holes* for finding and/or imagining *deceptive* associations (i.e., Quixote-like patterns that are not really there) in both inter- and trans-disciplinary data — therein then subsequently inflicting *misleading* inventions, predictions, and, regretfully, *wrong* decisions that eventually may lead to different kinds of disasters.

The core seed of disaster is risk

The "common language vocabulary" by itself is oftentimes confusing to common peoples' understandings of well-intentioned messaging conveying importance of dangers and their likelihood, even though generally being both thought-provoking and pretty much instructive: see Cambridge Dictionary for Disaster; Hazard; Risk; Vulnerability; and Prediction (https://dictionary.cambridge.org/us/).

"Although 'hazard' and 'risk' are commonly regarded as synonyms, it is useful to distinguish between them. Hazard can be thought of as the possibility that a dangerous phenomenon might occur, whereas risk is a measure of the loss to society that would result from the occurrence of the phenomenon. More concisely, 'risk is a measure of the probability and severity of adverse effects' (Lowrance, 1976; Peterson, 1988)." Seismic hazard refers to the natural phenomenon of earthquakes, ground motion in particular, which can cause harm. Seismic risk refers to the possibility of loss or injury caused by a seismic hazard.

We are all living in a risky world, and Figure 1 illustrates further our appetite for all the essential intertwined loops of Risk: defined in common language as "the chance of injury, damage, or loss." The figure complements with the fifth basic component of *Time* the four components presented by Boissonnade and Shah (1984), who define Risk "as the likelihood of loss". In insurance studies: a) the Exposure is defined as "the value of structures and contents, business interruption, lives, *etc.*"; and b) Vulnerability as the sensitivity to Hazard(s) at certain Location(s) — i.e., "the position of the exposure relative to the hazard." Since Hazard is likely to cause damage and losses sometimes, the origin Time and duration of any hazardous event may become critical in its transformation to Disaster, as illustrated later.

FIGURE 1
A knot that symbolically intertwines hazard, location, time, exposure, and vulnerability — all around Risk.

Natural hazards

In the natural hazard realm, these dangerous and damaging phenomena may include earthquake, tsunami, flood, landslide, volcanic eruption, hurricane, tornado, wildfire, *etc.* Hazards (or possibilities that dangerous phenomena might occur) are especially "risky" when they are only thought of in terms of the *perceived* probabilities for their occurrence (i.e., low hazard or high hazard) — because here we really need to consider the components of Location, Time, and Exposure *versus* Vulnerability as well.

We also know quite well from experience that hazardous events may cascade — where (under certain circumstances) a *primary* event may initiate or cause further secondary, tertiary, *etc.* damages, disruptions, and losses — such as the recent August 26 2021 Hurricane Ida, a Category 4 storm that blasted ashore in Louisiana midday "knocking out power to all of New Orleans, blowing roofs off buildings and reversing the flow of the Mississippi River as it rushed from the Louisiana coast into one of the nation's most important industrial corridors" in the middle of increasing *Delta Variant* infections/hospitalizations due to the ongoing COVID-19 pandemic. Thus, depending on both the particular risky situation and our response, a hazardous event scenario may either cause or not cause a Disaster.

Can uncertainty be computed?

While Risk can be computed, uncertainty cannot. So regretfully, the following statement, originally attributed to seismic hazard assessment some four decades ago, has not lost its relevance today, and still applies appropriately to present day situations we face in analyzing other potential damages and losses — for the timely implementation of integrated economic, structural, legal, social, health, cultural, educational, environmental, technological, political, and institutional measures:

> However, ignorance still exists on the seismic severity (usually expressed in intensity values) a site may expect in the future as well on the damage a structure may sustain for a given seismic intensity. (Boissonnade and Shah, 1984, p. 233)

And while prediction is "the act of saying what you think will happen in the future: e.g., 'I wouldn't like to make any predictions about the result of this match.'"— even the advanced tools of data analysis may lead to wrong assessments, when inappropriately used to describe the phenomenon under study. A (self-) deceptive conclusion could be avoided by verification of candidate models against (reproducible) experiments on empirical data — and in no other way.

Risk communication in disaster planning

When decisions are made about required actions in response to *prediction* of a disaster, the choices made are usually based on a comparison of expected "black eyes" (risks/costs) and "feathers in caps" (benefits). If the latter exceed the former, it is reasonable to go forward. But each of decision-makers may have rather different opinions on hazards, risks, and outcomes of different decisions and, as it is well-known, even two experts (scientists, in particular) may have three or more opinions!

Therefore, actual decisions sometimes (if not always) are not optimal, especially when there are alternative ways of gaining personal benefits or avoiding personal guilt. In many practical cases, decision makers do not have *any opinion* due to: i) ignorance in *beyond-design* circumstances; ii) denial of hazard and risk — based on misconceptions; and iii) a sense of personal responsibility to an impending disaster when it is too late to take effective countermeasures. As a result, since *Prediction* again is "the act of saying what you think will happen in the future: e.g., 'I wouldn't like to make any predictions about the result of this match.'" — this mimicked view in policy decisions becomes *a common way to avoid responsibility*.

Since there is already a lot of flexibility in common language that justifies the following disclaimer note: "Any opinions in the examples do not represent the opinion of the Cambridge Dictionary editors or of Cambridge University Press or its licensors." — we note that many people, including scientists, do not well distinguish between 'unpredictable', 'random', and 'haphazard', which distinctions are, nevertheless, crucial for scientific reasoning and conclusions. In particular, Stark (2017, 2022) emphasizes that: "'Random' is a very precise statistical term of art" and that notions of *probability* can only apply "if the data have a random component."

Risk Modeling (Michel, 2018) is about the future of Exposure and necessarily convolves Hazard (where possibility now ≈ *likelihood* of an event) with the components of Location, Time, and Vulnerability (Cannon, 1993; McEntire et al., 2002; McEntire, 2004). Fischhof and Kadvany (2011) informatively note that Risk "shows how to evaluate claims about facts (what might happen) and about values (what might matter)", further observing that as was

previously noted with regard to the global COVID-19 pandemic, officially declared 11 Mar 2020 by the World Health Organization (WHO): "societies define themselves by how they define and manage dangers." See also (SISMA-ASI (2009); Kaufmann and Penciakova, 2011; May, 2001; Berke and Beatley, 1992; Scawthorn, 2006; SISMA-ASI (2009); Wang, 2008; Wiggins, 1972; Bolt, 1991; Tierney, 2014).

Thus, an earthquake hazard with a presumed low-likelihood (or low probability) can nevertheless represent a high or even *unacceptable* risk (Berke and Beatley, 1992; May, 2001; Marincioni et al., 2012; Bela, 2014; Tanner et al., 2020), in addition to references cited in previous paragraph — and particularly for those cases noted in "Earthquakes and Sustainable Infrastructure" (Panza et al., 2021), the state-of-the-art approaches are "aimed at the level of natural risks for decision-making in regard to engineering design, insurance, and emergency management".

And while insurance can repair the damage, and while catastrophic reinsurance can even further spread the risk and keep first insurers solvent, *lives* can only be saved and infrastructure installations and public structures can only "resist (or sustain) future strong earthquakes and continue to operate in their original capacity" if they can withstand the shaking. An often unappreciated and complicating factor is that "earthquake risk is characteristically seen as 'remote' "— with naturally rare earthquake events "resulting in low risk awareness and low risk reward (Michel, 2014)."

Volcanic disasters: Nyiragongo and Mt. St. Helens

The recent 22 May 2021 Nyiragongo volcano (DR Congo) flank eruption is tellingly illustrative of a *volcanic* disaster. After just 19 years since the catastrophic January-February 2002 flank eruption, a new flank eruption began on 22 May 2021 (coincidentally on the same date as the Mw 9.5 1960 Chile earthquake, the largest recorded earthquake of the 20th century). As of 27 May 2021 "More than 230,000 displaced people are crowding neighboring towns and villages. Lack of clean water, food and medical supplies, as well as electricity in parts of Goma, are creating catastrophic conditions in many places. To add to all this misery, health authorities are worried about outbreaks of cholera — at least 35 suspected cases have been found so far." (https://www.volcanodiscovery.com/nyira-gongo/eruption-may-2021/activity-update.html).

USGS volcanologist Donald Peterson, who witnessed first-hand the catastrophic 1980 Eruption of Mt. St. Helens in southwestern Washington state, United States, observed in a comprehensive review of "Volcanic Hazards and Public Response" (Peterson, 1988) that "although scientific understanding of volcanoes is advancing, eruptions continue to take a substantial toll of life and property." And although "scientists sometimes tend to feel that the blame for poor decisions in emergency management lies chiefly with officials or journalists because of their failure to understand the threat," he believes otherwise that "however, the underlying problem embraces a set of more complex issues comprising three pervasive factors: 1) the first factor is the volcano: signals given by restless volcanoes are often ambiguous and difficult to interpret, especially at long-quiescent volcanoes; 2) the second factor is people: people confront hazardous volcanoes in widely divergent ways, and many have difficulty in dealing with the uncertainties inherent in volcanic unrest; 3) the third factor is the scientists: volcanologists correctly place their highest priority on monitoring and hazard assessment, but they sometimes fail to explain clearly their *conclusions* to responsible officials and the public, which may lead to inadequate public response." And since "of all groups in society, volcanologists have the clearest understanding of the hazards and vagaries of volcanic activity; they thereby assume an ethical obligation to convey effectively their knowledge to benefit all of society."

Explaining uncertainty; miscommunication and disasters

Common language vocabulary issues aside; "it is not easy to explain the uncertainties of volcanic hazards to people not familiar with volcanoes, and often these difficulties lead to confusion, misunderstanding, and strained relations between scientists and persons responsible for the public welfare, such as civil officials, land managers, and journalists" (Peterson, 1988) — and notably, the fatal 6 April 2009 Mw 6.3 earthquake disaster that occurred in the Abruzzi region of Central Italy, killing more than 300 people and wrecking the medieval heart of the city, is just such a case-in-point: showing that the above *miscommunication* reality will apply *mutatis mutandis* to earthquakes and other hazards. The 2009 L'Aquila earthquake had been preceded by much seismic activity beginning in October 2008, analogous to the preparatory rumblings of an awakening volcano. But even though it occurred in a zone defined at *high seismic hazard*, as charted on a map — high *vulnerabilities* combined with *major failures* in Disaster Risk Mitigation to produce both the *tragic large losses* and an ensuing *legal* prosecution of six scientists and one government official, "the L'Aquila Trial" (See Marincioni et al., 2012; Panza and Bela, 2020 and Supplementary Material therein).

Effective communication

In comprehensively addressing the public response, Peterson "advanced the view that volcanologists should regard the development of effective communications with the public just as important a challenge as that of monitoring and understanding the volcanoes. We must apply the same degree of creativity and innovation to improving public understanding of volcanic hazards," he believed, "as we apply to the problems of volcanic processes. Only then will our full obligation to society be satisfied."

To be creatively most effective, in developing effective communications with the *public* (all people or groups not involved in the scientific study of volcanoes, earthquakes, *etc.*), Peterson offered these insights systematically researched and provided from the *social sciences*, which "deal with the interaction of people with all kinds of hazards."

Sorensen and Mileti (1987), pages 14–53 showed that the response to a warning by a person (Figure 2) or group includes a series of steps that involve hearing a message, understanding it, believing it, personalizing it (that is, being convinced that it really

FIGURE 2
"I want to report an earthquake."

applies to the individual), and finally taking action. Different people and different societies react in individual ways as they progress through these steps. The style of a warning message greatly influences the response it produces, and warnings are most effective if they are specific, consistent, accurate, certain, and clear (Sorensen and Mileti, 1987, page 20). If one or more of these attributes is missing, the message is more likely to be ignored or disbelieved.

What (we think) we know about earthquakes

For a reliable seismic hazard assessment, a specialist must be knowledgeable in understanding seismic effects:

- An earthquake is a sudden movement that generates seismic waves inside the Earth and shakes the ground surface.
- Although historical records on earthquakes are known from 2100 B.C., generally most of the earthquakes before the middle of the 18th century are lacking a reliable description, with a possible exception being the *Catalogo Parametrico dei Terremoti Italiani* (Gasperini et al., 2004) based upon both historical and instrumental data comprising an Italian Earthquakes Catalog more than a thousand years long.
- Earthquakes are complex phenomena. Their extreme catastrophic nature has been known for centuries, due to resulting devastations recorded from many of them.
- Their abruptness, along with their sporadic, irregular and apparently rare occurrences, all facilitate formation of the common perception that earthquakes are *random* and *unpredictable* phenomena.

However, modern advances in seismology prove that this perceived *random* and *unpredictable* behavior is not really the case in a number of important aspects (Kossobokov, 2021).

Nowadays, the location of earthquake-prone sites is accurately mapped (Figure 3) due to rather accurate hypocenter determinations, along with estimates of their source size. The "seismic effects" of earthquakes that are needed for a Seismic Hazard Assessment (SHA) can be characterized from both physically felt and observed effects (Macroseismic Intensity), and also from instrumentally recorded earthquake records: a) seismograms and b) records of the actual ground shaking characterizing acceleration, velocity, and displacement — see chapters in *Encyclopedia of Solid Earth Geophysics* (Gupta, 2020).

A detailed historical review of earliest seismological attempts to quantify sizes of earthquake sources through a measure of their energy radiated into seismic waves, which occurred also in connection with the parallel development of the concept of earthquake magnitude, is supplied by Gutenberg and Richter (1949), Panza and Romanelli (2001), and Okal (2019). Figure 4 illustrates the commonly accepted notation of earthquake magnitude classes.

Ellsworth (1990) offers these important *caveats* whenever performing a systematic SHA: a) "earthquakes are complex physical processes generated by sudden slip on faults, and as such they can only be grossly characterized by simple concepts"; and b) "Magnitude, as commonly used to compare the sizes of different earthquakes, also represents an extreme simplification (cf Felt Intensity: center of energy; Instrumental Seismometer: point of first rupture) of the earthquake process and by itself cannot fully characterize the size of any event. Traditionally, seismologists have developed a suite of magnitude scales, each with its own purpose and range of validity to measure an earthquake. Because no single magnitude scale can be systematically applied to the entire historical record, a summary magnitude, M, is introduced here to facilitate comparisons between events."

Many shaking intensity scales have been developed over a few centuries to measure the damaging results from earthquakes, of which the Modified Mercalli Intensity (MMI) is among the most commonly used. This scale, which maps the center of energy release for pre-instrumental records, classifies *qualitatively* the effects from an earthquake upon the Earth's surface: ranging from "not felt" (intensity I); to "extreme" (intensity X), when most masonry and frame structures are destroyed with foundations; and finally, to "total destruction" (intensity XII on the MMI scale), when rolling waves are seen on the ground surface and objects are thrown upward into the air. We feel worth mentioning here also that, for the Mercalli Cancani Sieberg (MCS) intensity scale, a doubling of Peak Ground Acceleration (PGA) practically corresponds to one unit increment of Macroseismic Intensity (Cancani, 1904).

Numerous approaches to the determination of an earthquake source size have resulted in a number of quantitative determinations of magnitude M based on instrumental, macro-seismic, and other data (Bormann, 2020). Charles Richter (1935) used the physically dimensionless logarithmic scale (because of the very large

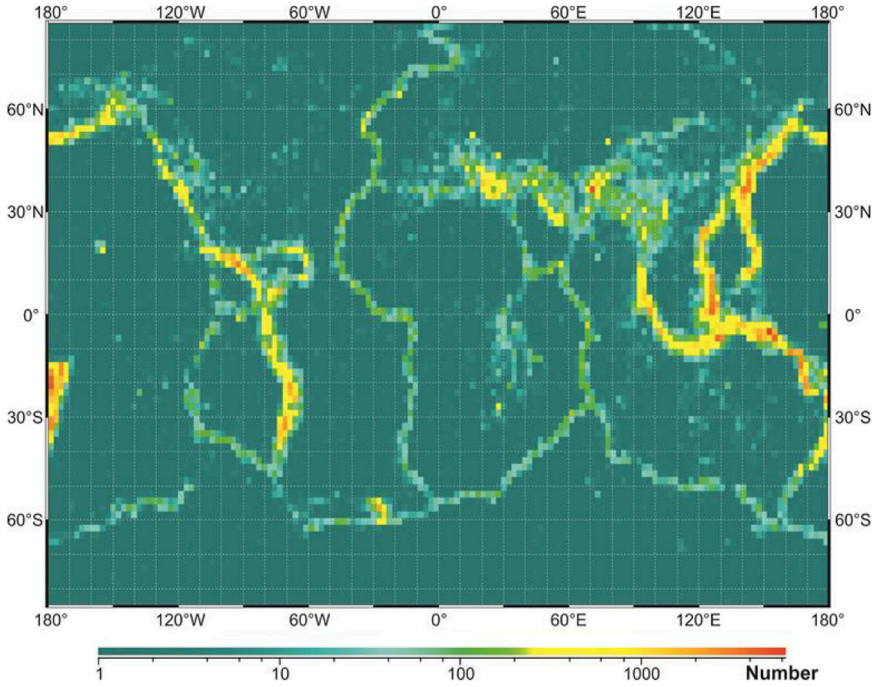

FIGURE 3
Locations of earthquake prone sites: Global map showing the numbers of the M ≥ 4 earthquake epicenters within 2.4°×2.0° grid cells during the period 1963–2020.

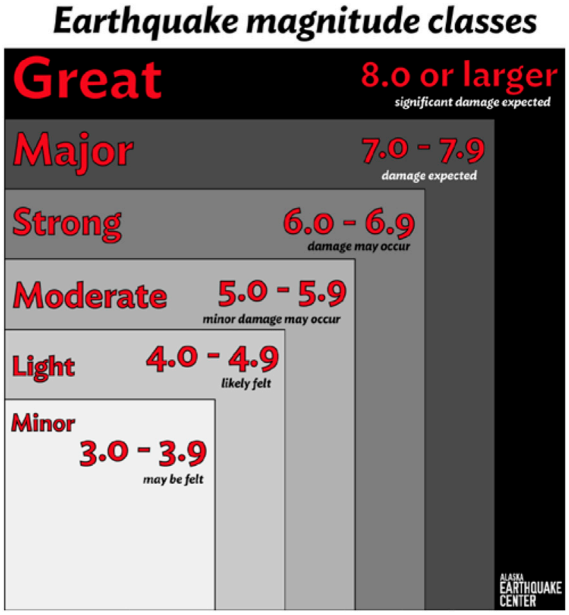

FIGURE 4
Earthquake magnitude classes.

differences in displacement amplitude between different sized events) for his definition of magnitude M — that appears naturally appropriate due to apparent *hierarchical* organization of the lithosphere (which contains mobile blocks ranging from just the size of a grain ~10^{-3} m across — on up to scale of tectonic plates ~10^{6} m). (Keilis-Borok, 1990; Sadovsky, 2004; Ranguelov, 2011; Ranguelov and Ivanov, 2017).

It is not surprising that, for shallow-depth earthquakes, the magnitude M (originally determined by Richter from the ground displacement recorded on a seismogram) is about two-thirds of the MMI intensity at the epicenter I_0, thus $M = ⅔\ I_0 + 1$ (Gutenberg and Richter, 1956). Accordingly, then, a strong (M = 6.0) shallow earthquake may cause only *negligible* damage in buildings of good design and construction near the epicenter, but otherwise *considerable* damage in poorly built or badly designed structures.

Figure 5 illustrates the global magnitude distribution by year for the time period 1963–2020, i.e., after installation of the analog World-Wide Network of Standard Seismograph Stations (WWNSS) https://science.sciencemag.org/content/174/4006/254 (top); and the empirical non-cumulative Gutenberg-Richter plot of N(M) for the entire 58 years of record, with b-value estimated at 0.998 (R^2 = 0.977) for the best fit of $\log_{10}N(M) = a + b \times (8 - M)$ (bottom).

The coastline of Britain and the seismic locus of earthquake epicenters

The set of earthquake epicenters or, in other words, the *seismic locus*, has the same fractal properties as the coastline of Britain. Benoit Mandelbrot (1967) notes: “Geographical curves are so involved in their detail that their lengths are often infinite or, rather, undefinable. However, many are statistically ‘self-

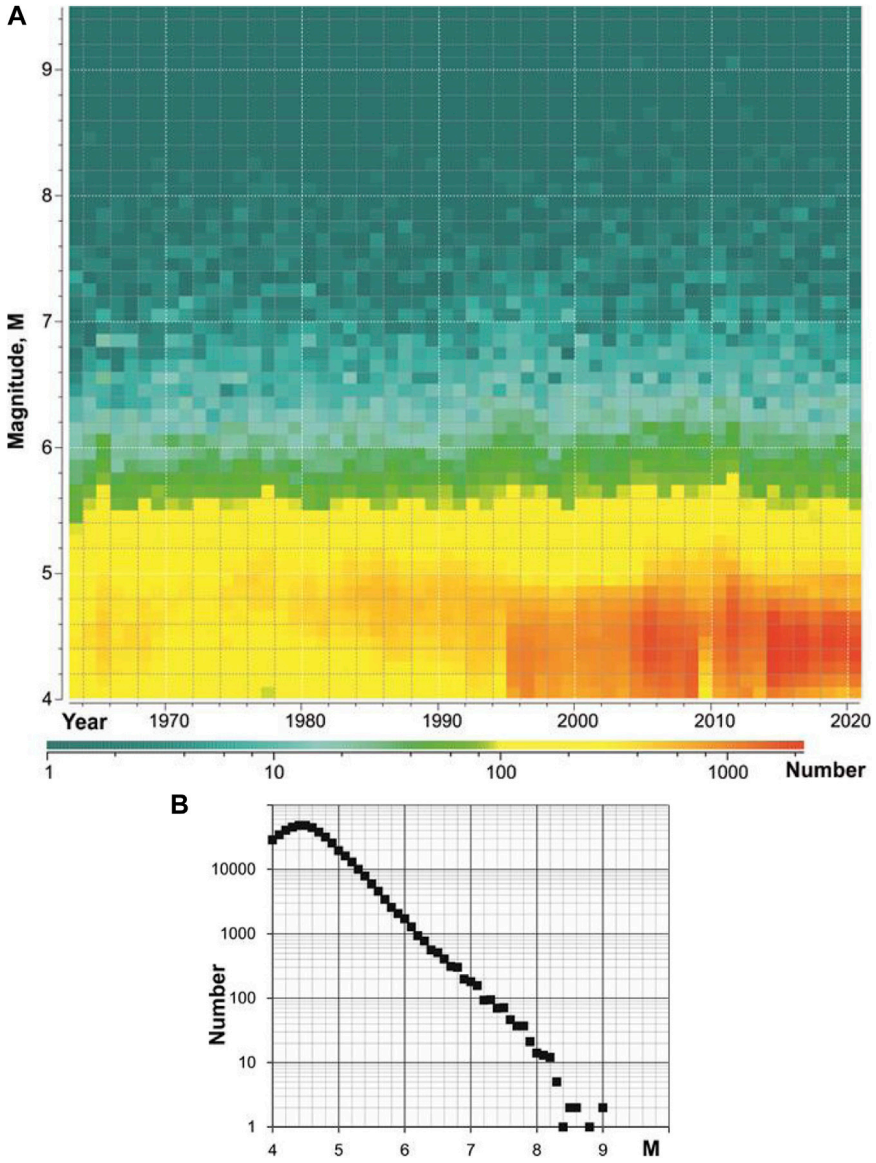

FIGURE 5
The global non-cumulative magnitude distribution by year in 1963–2020 **(A)** and the Gutenberg-Richter plot **(B)**.

similar', meaning that each portion can be considered a reduced-scale image of the whole. Indeed, self-similarity methods are a potent tool in the study of chance phenomena, wherever they appear, from geostatistics to economics and physics. Therefore, scientists ought to consider dimension as a continuous quantity ranging from 0 to infinity."

Following the pioneering works by Mikhail A. Sadovsky (Sadovsky et al., 1982) and Keiiti Aki (Okubo and Aki, 1987), our understanding of the fractal nature of earthquakes and seismic processes has increasingly grown (Kossobokov, 2020) — along with a concomitantly *scientifically revolutionary* better understanding and mapping of both the Earth's interior (Stacey and Davis, 2020), as well as of geophysical aspects of seismic waves propagation (Florsch et al., 1991; Fäh et al., 1993; La Mura et al., 2011; Iturrarán-Viveros and Sánchez-Sesma, 2020).

Naturally, or as might be expected due to hierarchical organization of the lithosphere (referring to the size-related distribution of geographical/seismological phenomena), the number of earthquakes globally, or within a region, is *scaled* by magnitude, according to the Gutenberg-Richter Frequency-Magnitude (FM) relation (Gutenberg and Richter, 1944; 1954). Globally, and for the time period of 58 years shown in Figure 5 the slope (so called b-value) of the plot is about 1, so that each one unit change in magnitude between M = 5 and M = 9 results in approximately a 10-fold change in the number of earthquakes; there were approximately two hundred M = 7 earthquakes compared to about twenty M = 8 and 20,000 M = 5 earthquakes.

The Gutenberg-Richter relation is a *power law* and can be written as $\log_{10} N = a - bM$. As shown in Figure 5, this is also a *Pareto* distribution, or a distribution with "fat" tails, which serves as a reminder that, in SHA, *outliers* always do exist as "possibilities" and must therefore be duly recognized and accounted for in seismic hazard [see e.g., Kanamori (2014; 2021)].

Generalized Gutenberg-Richter relationship and unified scaling law for earthquakes

The Gutenberg-Richter relationship just shown above was further generalized by Kossobokov and Mazhkenov (1988, 1994) to the following fractal form:

$$\log_{10} N(M,L) = A + B \times (5 - M) + C \times \log_{10} L, \quad M_{-} \le M \le M^{-}$$

where: i) *N(M,L)* is the expected annual number of main shocks of magnitude M within an area of linear size L; ii) the similarity coefficients A and B are similar to the *a-* and *b-values* from the classical Gutenberg-Richter law; iii) the newly added similarity coefficient C is the *fractal dimension* (D per Mandelbrot) of the set of epicenters; and iv) $M_{-}$and $M^{-}$are the limits of the *magnitude range* where this relationship holds. The three frequency-magnitude-spatial coefficients provide an insight into *scaling properties* of actual seismicity, and therefore they are of specific interest to seismologists working on seismic zonation and risk assessment.

It was shown that C is significantly different from 2, and that it correlates with the *geometry* of tectonic structures: i) *high values* of C (~1.5) correspond to the regions of complex *dense patterns* of faults of different strikes and *high degrees* of fracturing, whereas; ii) *lower values* of C (~1) are related to regions exhibiting a predominant linear *major fault zone* (which is consistent with rectifiable curves and straight lines, where $D = 1$).

Moreover, for example, in the specific case of the Lake Baikal region in the mountainous Russian region of Siberia, north of the Mongolian border (with area of 1,500,000 km^2 and $C = 1.25$), it was demonstrated (Kossobokov and Mazhkenov, 1988; Kossobokov and Mazhkenov, 1994) that: i) the inclusion of *aseismic* areas leads to *underestimation* of seismic activity in an area of 1,000 km^2 by a factor of 15; and alternatively ii) when a characteristic of seismic activity over 1,000 km^2 is computed for a grid 10 km × 10 km, this leads to *overestimation* by a factor greater than 2.

Earlier, in order to avoid just such *seismic activity bias*, in a pilot study assessing seismic risk for 76 selected Largest Cities of the World in active seismic regions, Keilis-Borok et al. (1984) compared these two integral estimates: 1) the number of cities with population of one million or more affected in 30 years by strong motion of intensity $I \ge$ VIII; and 2) the total population in these cities — with the *actual* aftermaths of these past earthquakes — for reliable "validation of the results" showing specifically that: a) "available data may be sufficient to estimate the seismic risk for a large set of objects, while not for each separate object"; and b) "it indicates, that global seismic risk is rapidly increasing, presenting new unexplored problems."

The Unified Scaling Law for Earthquakes (USLE), got its name later, when Bak et al. (2002) presented an alternative formulation from that above — making use of the *inter-event time* between the earthquake occurrences, instead of their *annual number*. Using the USGS/NEIC Global Hypocenters Data Base, 1964–2001, and a robust box-counting algorithm; Nekrasova and Kossobokov (2002) managed to map the values of A, B, and C in every 1°× 1° box on the Earth marked by record of earthquake occurrence, wherever the catalog of shallow earthquakes of $M \ge 4$ permitted a reliable estimation. The results of this global mapping are available at the data repository of the International Seismological Centre (Nekrasova and Kossobokov, 2019).

The distribution of the number of seismic events by magnitudes — the Gutenberg-Richter frequency magnitude relation — is of paramount importance for seismic hazard assessment of a territory. Accordingly, the *generalization* of the original Gutenberg-Richter relation into the Unified Scaling Law for Earthquakes (USLE) as originally proposed in 1988 makes it possible now to take into account as well the *pattern* of epicentral distribution of seismic events, whenever changing the *spatial scale* of the analysis. This is extremely important for adequate *downscaling* of the frequency-of-occurrence into a smaller target area within any territory under study (e.g., into a megalopolis).

At the time, when Per Bak (Bak et al., 2002) suggested a *dual formulation* of USLE using the time between seismic events, the Institute of Earthquake Prediction Theory and Mathematical Geophysics of the Russian Academy of Sciences developed a modified algorithm for statistically improved, confident Scaling Coefficients Estimation (referred to as SCE) of the USLE parameters to be used for producing *seismic hazard maps* of territories prone to seismic effects. An updated brief review, focused on the use of the USLE approach in relation to assessment of seismic hazard and associated risks, is provided in (Nekrasova et al., 2020).

Multi-scale seismicity model

Complementary to USLE is the Multi-scale Seismicity Model (MSM) by Molchan et al. (1997). For a general use of the classical frequency-magnitude relation in seismic risk assessment, they formulated a *multi-scale seismicity model* that relies on the hypothesis that "only the ensemble of events that are *geometrically small*, compared with the elements of the seismotectonic regionalization, can be described by a log-linear FM relation." It follows then that the *seismic zonation* must be performed at *several scales*, depending upon the *self-similarity* conditions of the seismic events and the *log-linearity* of the frequency-magnitude relation, within the magnitude range of interest. The analysis of worldwide seismicity, using the Global Centroid Moment Tensor (GCMT) Project catalog (where the seismic moment is recorded for the earthquake size) corroborates the idea and observation that a *single* FM relation is not universally applicable. The MSM of the FM relation has been tested in the Italian region, and MSM is one of the considered appropriate ingredients of NDSHA.

Earthquake catalogs evidence clear patterns that there exists a *space-time* energy distribution of seismic events because: i) earthquakes do not happen *everywhere*, but preferentially in

tectonically well-developed highly fractured fault zones within the Earth's lithosphere; ii) earthquake sizes follow the Gutenberg-Richter relationship, which is a surprisingly robust power law (such that, for every magnitude M event, there are ~10 magnitude M − 1 quakes — within an area that is large enough); iii) earthquakes *cluster* in time — in particular, seismologists observe: a) surges and swarms of earthquakes; b) seismically driven *decreasing* cascades of aftershocks; and c) less evident *inverse* cascade (energy *increase*), or *crescendo* of rising activity in foreshocks premonitory to the main shock.

Since earthquake-related observations are generally limited to the recent-most decades (sometimes centuries in just a few rare cases), getting reasonable *confidence limits* on an objective estimate of the *occurrence rate* or inter-event times of a strong earthquake within any particular geographic location necessarily requires a *geologic* span of time that is unfortunately *unreachable* for instrumental, or even historical seismology [see, e.g., (Ellsworth, 1990; Beauval et al., 2008; Stark, 2017; 2022)]. That is why *probability* estimates in Probabilistic Seismic Hazard Analysis (PSHA) remain *subjective* values ranging between 0 and 1, derived from evidently imaginary (but enticingly both *analytically* and *numerically tractable*) unrealistic hypothetical models of seismicity.

Seismic Roulette: Nature spins the wheel!

> "Look deep into nature, and then you will understand everything better".
>
> - Albert Einstein

Regretfully, most, if not all, of earthquake *prediction* claims can be characterized as "invented" windmills, wherein we see the earth "not as it is", but "as it should be" due to very small, if any, samples of clearly defined evidence! Many prediction claims are hampered at their start from the *misuse* of Error Diagram and its analogues — ignoring the evident *heterogeneity* of earthquake distributions in space as well as in time. See e.g. (Bela and Panza, 2021).

A rigorous mathematical formulation of a natural *spatial measure* of seismicity is given in (Kossobokov et al., 1999). This "Seismic Roulette null-hypothesis" (Kossobokov and Shebalin, 2003) (or the hypothesis that *chance* alone in a random process is responsible for the results) is a nice analogy for using the *simple recipe* that accounts for this spatial patternicity (Kossobokov, 2006a) using statistical tools available since Blaise Pascal (1623–1662):

26 consider a *roulette* "wheel" with as many *sectors* as the number of events in the best available catalog of earthquakes, one sector per earthquake epicenter event;
0 make your best bet according to *any* prediction strategy: determining which events are inside a projected space-time "area of alarm" — and then
32 place one chip upon each of the corresponding sectors.

Nature then spins the "wheel", before introducing an energized target-seeking earthquake "ball". If you play seismic roulette *systematically*, then you win and lose systematically (Figure 6). If you are smart enough, and your predictions are effective, the first will outscore the second.

FIGURE 6
Seismic Roulette: Nature spins the wheel!

However, if Seismic Roulette is *not* perfect in confirming your betting strategy (and thus alternatively is *nullifying* your hypothesis), and still you are smart enough to choose an *effective* strategy, then your wins will outscore your losses! And after a while . . . you can then use your best wisdom, or even now an "antipodal strategy", wherein the earthquake "prediction problem" is examined from the standpoint of *decision theory* and goal optimization per Molchan (2003) — so as to win both systematically and statistically *self-similarly* in the future bets!

The results of just such a global "betting" test of the prediction algorithms M8 and MSc did confirm such an "imperfection" of Seismic Roulette (Seismic Roulette is not perfet!) in the recurrence of earthquakes in *Nature* (Ismail-Zadeh and Kossobokov, 2020); but these same results still suggest *placing future bets* can be useful, if used in a *knowledgeable* way for the benefit of the populations exposed to seismic hazard. Their *accuracy* is already enough for undertaking earthquake preparedness measures, which would prevent a considerable part of damage and human loss, although far from the total. And fortunately, the *methodology* linking prediction with disaster management strategies does already exist (Molchan, 1997).

Pattern recognition of earthquake prone areas

In lieu of local seismic observations long enough for trustworthy and reliable SHA, alternatively one may try using Pattern Recognition of Earthquake-Prone Areas (PREPA) based, however, on the appropriate geological and geophysical data sets that are available. This geomorphological *pattern recognition* approach (Gelfand et al., 1972; Kossobokov and Soloviev, 2018) is an especially useful preparedness and mitigation tool in seismic regions that have passed validation: i) first, by exhaustive retrospective testing; and then ii) by the decisive confirmation check afforded by *actual* strong earthquakes that have occurred. Validity of this pattern recognition PREPA methodology has been

proven by the *overall statistics* of strong earthquake occurrences — after numerous publications of pattern recognition results encompassing both many seismic regions and also over many magnitude ranges (see Gorshkov et al., 2003; Gorshkov and Novikova, 2018 and references therein).

Those who can't model are doomed to reality!

One application of PREPA deserves a special comment. Regional pattern recognition problems solved by Gelfand et al. (1976) treated two different sets of natural recognition objects for the two overlapping regions: i) *regularly spaced points* along major strike-slip faults in California; and ii) *intersections* of morphostructural lineaments in California and adjacent territories of Nevada (Figure 7). They then drew from these the qualitative conclusion that areas prone to M ≥ 6.5 are *characterized* by proximity to the ends (or to intersections) of major faults, in association with both: a) *low relief*; and b) often also with some kind of *downward* neotectonic movement expressed in regional topography and geology — with their conclusion further supported by *both* PREPA classifications: i) points; and ii) intersections — wherein the same five groups of earthquake-prone areas show up in both cases. Slight differences are due to the fact that the study of *intersections* covers a larger territory. This supports the idea derived from recognition of points — that strong earthquake-prone *intersections* often associate with neotectonic subsidence on top of a *background* weak uplift.

As evident from Figure 7, the PREPA *termless* prediction for California and Nevada has been statistically justified by the subsequent occurrence of 16 out of 17 magnitude 6.5+ earthquakes within a narrow vicinity of the 73 Dangerous D-intersections of morphostructural lineaments (union of yellow circles in Figure 7) determined by Gelfand et al. (1976) as prone to seismic events that large. The target earthquakes included the recent-most 15 May 2020,

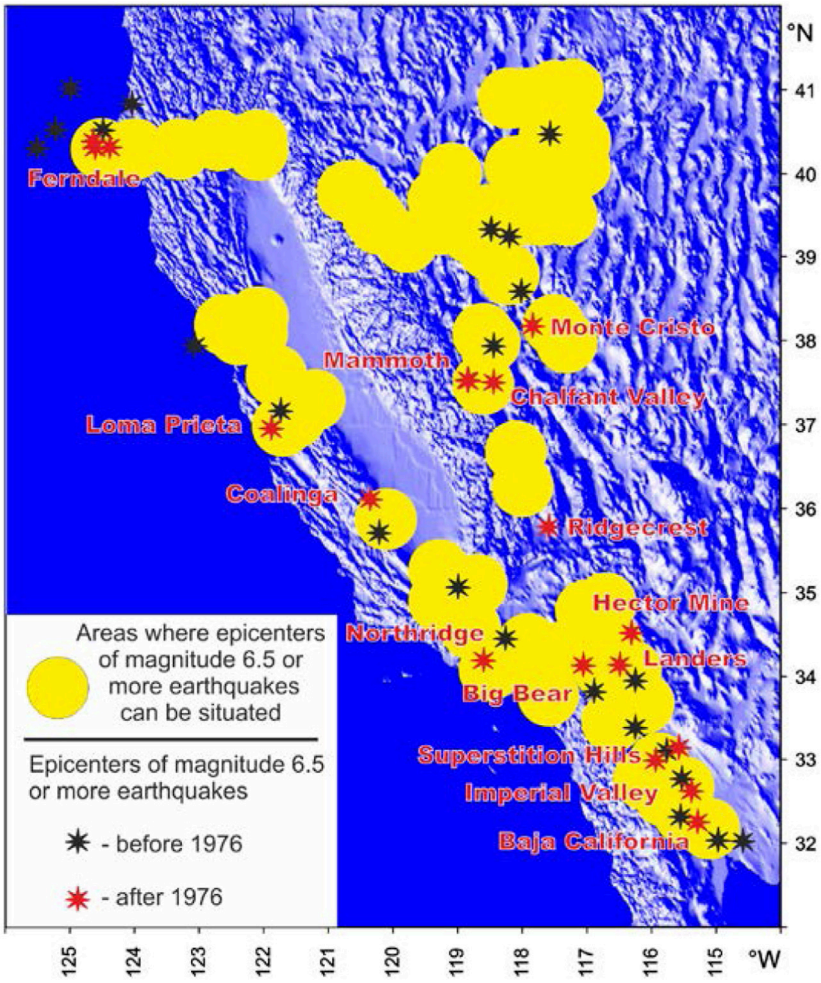

FIGURE 7
Circular 40-km radius outlines of the D-intersections of morphostructural lineaments in California and Nevada and epicenters of magnitude 6.5+ earthquakes before (black stars) and after (red stars with names) publication in 1976 (Gelfand et al., 1976).

M6.5 Monte Cristo Range (NV) earthquake and 6 July 2019, M7.1 Ridgecrest (CA) main shock, i.e., the one exceptional *near-miss* within the study area since 1976. In fact, the first day cascading aftershocks for this event, as well as the entire 2019 Ridgecrest earthquake sequence, extend to the D-intersection. It is also notable that the Puente Hills thrust fault beneath metropolitan Los Angeles *coincides* exactly (Kossobokov, 2013) with the lineament drawn back in 1976, decades in advance of its "rediscovery" by the 1994 Northridge Earthquake (Shaw and Shearer, 1999).

Finally (and importantly for seismic hazard assessment), PREPA is a readily available hazard-related quantity that can be naturally included in NDSHA, while so far, no comparable way exists to formulate a direct use for it within PSHA — wherein earthquake "possibilities" are instead viewed temporally by Senior Seismic Hazard Analysis Committee (SSHAC, 1997) of the United States Nuclear Regulatory Commission as "annual frequencies of exceedance of earthquake-caused ground motions [that, however] can be attained only with significant uncertainty." Therefore, ahem . . . *those who can't model are doomed to reality!*

Seismic hazard and associated risks

> "At half-past two o'clock of a moonlit morning in March, I was awakened by a tremendous earthquake, and though I had never before enjoyed a storm of this sort, the strange thrilling motion could not be mistaken, and I ran out of my cabin, both glad and frightened, shouting, "A noble earthquake! A noble earthquake!" feeling sure I was going to learn something."
>
> John Muir, *The Yosemite, Chapter 4*

Ground shaking may be frightening, but it may not necessarily kill people. For example, the earliest *reported* earthquake in California was on 28 July 1769, and was documented in diaries by the exploring expedition of Gaspar de Portola, enroute from San Diego to chart a land route to Monterey. While camped along the Santa Ana River, about 50 km southeast of Los Angeles, "a sharp earthquake was felt that 'lasted about half-as-long as an *Ave Maria*." Based on descriptions of the quake, it was likely a moderate or strong earthquake. Some described the shaking in expedition diaries as *violent*, and occurring for over the next several days, suggesting aftershocks. Although the magnitude and epicenter are unclear, by comparing these descriptions with more recent events, the quake may have been similar to the M 6.4 1933 Long Beach or the M 5.9 1987 Whittier Narrows earthquake (https://geologycafe.com/california/pp1515/chapter6.html#history).

The exploring party, personally uninjured and unimpeded in this M 5–6 earthquake event, noted *not* that the region portended high *seismic hazard* and *landslide risk*, but instead benignly rather that it appeared to be a good place for *agriculture*!

"Earthquakes do not kill people, buildings do!" is a long-time refrain in the world of seismic hazard preparedness and earthquake engineering or do they? While inadequately designed and poorly constructed buildings, infrastructure and lifeline systems *can* kill people (Gere and Shah, 1984; Bilham, 2009), tsunamis and landslides *are* directly triggered earthquake phenomena that tragically do kill people, as well!

Therefore, for reliably assessing the hazard and estimating the risk that a population is exposed to, one needs to know the possible distribution of earthquakes large enough to produce a primary

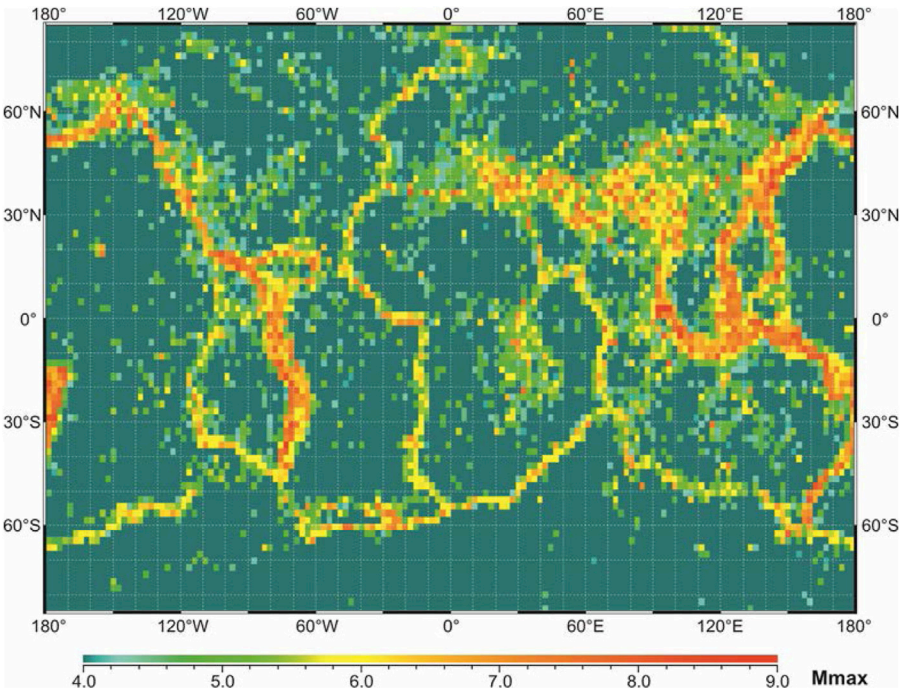

FIGURE 8
The global map of the reported maximal magnitude, Mmax, in 1963–2020.

damage state. The global map of the maximal magnitude (Mmax) observed during the last 57 years, as portrayed within 2.4° × 2.0° grid cells (Figure 8) could be used for this purpose, as a very rough approximation.

Earthquake vulnerability, intensity and disaster

An earthquake of about M ~ 5 (Intensity VI on the MMI scale), may cause slight damage (if any) to an ordinary structure located nearby the epicenter; and therefore, cannot produce any significant loss. On the other hand, a strong earthquake (M 6.0–M 6.9) may result in a real disaster — as has happened on several occasions in the past. See e.g., the M 6.3 L'Aquila Earthquake of 6 April 2009 (Alexander, 2010).

For example, the 21 July 2003, M 6.0 Yunnan (China) earthquake and induced landslides: i) destroyed 264,878 buildings; ii) damaged 1,186,000 houses; iii) killed at least 16 people; and iv) injured 584. Moreover, v) a power station was damaged; vi) roads were blocked; and vii) 1,508 livestock were killed in the province. The resulting damage due to direct and indirect losses (consequences) of this earthquake was estimated at ~ 75 million United States dollars. So, this is a rare case when a shallow M 6 earthquake (one at the fringe of the smallest threshold of potentially hazardous earthquakes) occurred at both a *location* and also at 23:16 local *time* that together unfortunately combined maximum Vulnerability × Exposure of the province (i.e., slopes prone to failure; buildings, houses, *etc.*, that could not withstand the shaking; dense population at home; and livestock still sheltered in their facilities).

Half of a clock face on Modenesi's Towers of Finale Emilia, Ferrara, Italy (Figure 9) — destroyed following an earthquake and aftershocks May 20–29, 2012. Felt Intensities exceeded VII, as depicted on the clock face after the main shock. It was the first strong earthquake "anywhere nearby" since the Ferrara quake of 1570. The relatively *small* number in only 7 fatalities, when a strong and unusually shallow M 6 earthquake struck the Emilia Romagna region of northern Italy, is connected with the event's occurrence time at just after 4 a.m. — fortuitously very early on that Sunday morning 20 May 2012 — on account of the fact that "the affected region is home to countless historic churches, castles, and towers — many of which were damaged or toppled." With so many *vulnerable* churches collapsed or severely damaged, an *origin time* in the late morning might have easily claimed *hundreds* of victims from worshipers participating in religious ceremonies (Panza et al., 2014).

FIGURE 9
Time and earthquake wait for no man.

The world's deadliest earthquakes since 2000

Table 1 lists all eighteen of the World's deadliest earthquakes since the year 2000 — where the number of fatalities in each case exceeded one thousand. Remembering the earlier comment by Ellsworth (1990), i.e., that "earthquakes are complex physical processes generated by sudden slip on faults, and as such they can only be grossly characterized by simple concepts." — we note that the magnitude of any one of these disastrous events has a *poor correlation* with the loss of lives: i) the two deadliest earthquakes, namely, the M 9.0 Indian Ocean disaster of 2004, and the M 7.3 Haiti earthquake of 2010, differ in seismic energy by a factor >350 — but resulted in roughly the same death tolls of above 200,000 people; while ii) the death toll of a later occurring M 9.1 mega-thrust earthquake and tsunami off the coast of Tōhoku (Japan) in 2011 was 2 times lower than that for the strong crustal earthquake of only M 6.6 in Bam (Iran). See also (Bela, 2014) and references therein.

There is one single case showing a negative value ΔI_0 that refers to the smallest of these 18 deadliest earthquakes: the M 6.1 earthquake that struck Hindu Kush (Afghanistan) on 25 March 2002 causing 1,000 + fatalities. A larger M 7.4 deep earthquake (at 200 + km depth) and at distance greater than 150 km, occurred within less than a month on 03.03.2002, causing at least 150 fatalities. The last column in Table 1 shows the difference ΔI_0 between the real Macroseismic Intensity $I_{0\ EVENT}$ and that predicted by the GSHAP Map $I_{0\ GSHAP}$. These computed $\Delta I_0 = I_{0\ EVENT} - I_{0\ GSHAP}$ values are (in all but one case) positive — with their median value of 2.

Seismic hazard mapping

An accurate characterization of seismic hazard at *local scale* requires use of detailed geologic maps of both *active faults* and past earthquake *epicenter* determinations. The typical seismic hazard

TABLE 1 Top deadliest earthquakes since 2000 of at least 1,000+ fatalities including victims of tsunami and other associated effects.

Region	Date	M	Fatalities	ΔI_0
Sumatra-Andaman Islands ("Indian Ocean Disaster")	26 December 2004	9.0	227,898	4
Port-au-Prince (Haiti)	12 January 2010	7.3	222,570	2
Wenchuan (Sichuan, China)	12 May 2008	8.1	87,587	3
Kashmir (northern border India-Pakistan region)	8 October 2005	7.7	87,351	2
Nurdağı (Turkey)	6 February 2023	7.8(8.0)	53,227+	1(2)
Ekinözü (Turkey)		7.5(7.7)		1(2)
Bam (Iran)	26 December 2003	6.6	26,271	0
Bhuj (Gujarat, India)	26 January 2001	8.0	20,085	3
Off the Pacific coast of Tōhoku (Japan)	11 March 2011	9.0	19,759+	3
Bharatpur (Nepal)	25 April 2015	7.8	8,964	2
Yogyakarta (Java, Indonesia)	26 May 2006	6.3	5,782	0
Sulawesi Island (Indonesia)	28 September 2018	7.5	4,340	2
Southern Qinghai (China)	13 April 2010	7.0	2,968	2
Boumerdes (Algeria)	21 May 2003	6.8	2,266	2
Nippes (Haiti)	14 August 2021	7.2	2,248	2
Nias Island (Indonesia)	28 March 2005	8.6	1,313	3
Padang (Southern Sumatra, Indonesia)	30 September 2009	7.5	1,117	1
Hindu Kush (Afghanistan)	25 March 2002	6.1	1,000+	−1

Notes: The data on fatalities in the 2011 Tōhoku mega-earthquake and tsunami include fatalities reported on 13 March 2019 by the Japanese National Police Agency. The data of fatalities of the most recent couple of 06 February 2023 earthquakes in Turkey and Syria keeps growing. $\Delta \boldsymbol{I_0} = I_{0\ EVENT} - I_{0\ GSHAP}$ computed as in Kossobokov and Nekrasova (2010), (2012) and rounded to the closest integer. The list is updated to the present from (https://en.wikipedia.org/wiki/Lists_of_21st-century_earthquakes).

assessment undertaken strives to provide a *preventive* determination of the ground motion characteristics that may be associated with future earthquakes — at regional, local, and even urban scales (Panza et al., 2013).

The first scientific seismic hazard assessment maps were *deterministic* in scope, and they were based on the observations that primary damage: i) decreases generally with the distance away from the earthquake source; and ii) is often correlated with the physical properties of underlying soils at a particular site, e.g., rock and gravel. In the 1970s, after publication of Engineering Seismic Risk Analysis by Alin Cornell (1968), the development of probabilistic seismic hazard maps became *first* fashionable, *then* preferred, and *finally* "required" — so that in the 1990s the *probabilistic* mapping of seismic hazard came to prevail over the heretofore *deterministic* cartography. For a chronologic history (and a Bibliographic Journey of that history), see in particular (Nishioka and Mualchin, 1996; 1997; Hanks, 1997; Bommer and Abrahamson, 2006; McGuire, 2008; Mualchin, 2011; Panza and Bela, 2020, especially Supplementary Material therein).

Global Seismic Hazard Assessment Program (GSHAP) 1992–1999

In particular, a widespread application of PSHA began when the Global Seismic Hazard Assessment Program (GSHAP) was launched three decades ago in 1992 by the International Lithosphere Program (ILP) with the support of the International Council of Scientific Unions (ICSU), and also *endorsed as a demonstration program* within the framework of the United Nations International Decade for Natural Disaster Reduction (UN/IDNDR). The GSHAP project terminated in 1999 (Giardini, 1999) with publication of the final GSHAP Global Seismic Hazard Map (Giardini et al., 1999).

However, following a number of publications critical of the PSHA *technoscience* paradigm, e.g., (Krinitzsky, 1993a; Krinitzsky, 1993b; Krinitzsky, 1995; Castanos and Lomnitz, 2002; Klügel, 2007; see also Udias, 2002), and pivotably the catastrophic 2010 Haiti earthquake, a *systematic comparison* of the GSHAP peak ground acceleration (PGA) estimates with those related to the *actual* earthquakes that had occurred disclosed gross inadequacy of this "probabilistic" product (Kossobokov, 2010a). The discrepancy between: a) the PGA on the GSHAP map; and b) accelerations at epicenters of 1,320 strong ($M \geq 6.0$) earthquakes that happened *after publication* of the 1999 Map appeared to be a disservice to seismic zonation and associated building codes adopted in many countries on both national or regional scale (see Bommer and Abrahamson, 2006 and references therein). For fully half of these earthquakes, the PGA values on the map were surpassed by 1.7 m/s^2 (0.2 g) or more within just 10 years of publication, which fact (of *exceeding* more than 50% of the PSHA hazard map values within just 10 years) evidently *contradicts* the GSHAP predicted "10% chance of

exceedance in 50 years" — for the ground motion contours displayed on the map.

These *problematic* GSHAP results were naturally reported to a wide geophysical community at the Euroscience Open Forum (ESOF 2010) session on "Disaster prediction and management: Breaking a seismo-ill-logical circulus vitiosus", and also at the Union sessions of the Meeting of the Americas and the American Geophysical Union (AGU) 2010 Fall Meeting (Kossobokov, 2010b; Kossobokov, 2010c; Kossobokov and Nekrasova, 2010; Soloviev and Kossobokov, 2010); and later at the EGI Community Forum (EGICF12) by Peresan et al. (2012a). Then, with finally the 11 March 2011, Mw 9.0 Tōhoku mega-earthquake and tsunami disaster, it became absolutely clear that the GSHAP Probabilistic Seismic Hazard Analysis—despite *parascientific apologetics* of its "legacy" advocated by Danciu and Giardini (2015) — is UNACCEPTABLE FOR ANY KIND OF RESPONSIBLE SEISMIC RISK EVALUATION AND KNOWLEDGEABLE DISASTER PREVENTION (Kossobokov and Nekrasova, 2012). See, e.g., (Wyss et al., 2012; Mulargia et al., 2017).

Unsurprising surprises

While, "like Sumatra in 2004, the power of the Tōhoku earthquake in 2011 took us by surprise (Wang, 2012)", and made us question: "After decades of scientific research, how well or how badly are we doing in understanding subduction earthquakes?" ... In *retrospect*, the Tōhoku earthquake and its tsunami were *consistent* with what we had learned from comparative studies of different subduction zones–and therefore, "despite its wrenching pain", the cascading 2011 Tōhoku *Mw 9.0* Megathrust *Earthquake — Tsunami* — Fukushima *Disaster* (from both an earth and tsunami science perspective) was an "Unsurprising Surprise!"

The last column in Table 1 shows the difference ΔI_0 between the real Macroseismic Intensity $I_{0\ EVENT}$ and that predicted by GSHAP $I_{0\ GSHAP}$, which values are *all* (but one case) *positive* with average and median values of about 2! The same holds as well for *all* $M \geq 7.5$ earthquakes, including the most recent 6 February 2023 coupled earthquakes in Turkey. This *underestimation* by two units on MMI scale can mean an event experience of "severe damage in substantial buildings with partial collapse" instead of a GSHAP *forecast "highly likely" intensity* of "slight damage to an ordinary structure."

Moreover, it should be noted that, in *common sense*, such a poor performance of the GSHAP product *could* have already been found at the time of its 1999 publication, and this *should* have been done by the contributors to the Program as the first order *validation* test of the GSHAP final map! The claim of a 10% chance of exceedance in 50 years is violated already in 1990–1999 for more than 40% of 2,200 strong $M \geq 6.0$, for 94% of 242 significant $M \geq 7.0$, and 100% for major $M \geq 7.5$ earthquakes (Kossobokov and Nekrasova, 2012)! Note also that GSHAP directly overlapped the time when it was openly realized and discussed by the earthquake engineering community that "10% probability of exceedance in 50 years was too risky for a life-safety criterion" in the United States Building Codes (Frankel et al., 1996) — because earthquake-resistant design standards, when scaled to 10% in 50 years hazard curve ground motions, were *insufficient* protection when damaging major and great earthquakes did inevitably occur!

Synthetic seismograms: Increasing the reliability of seismic hazard assessment

On the other hand, with our current knowledge of the physical processes of both *earthquake generation* and *seismic wave propagation* in anelastic attenuating media, we can increase the reliability of seismic hazard assessments by basing them instead on computation of *synthetic* seismograms — in terms of a more *realistic* modeling of ground motion (see e.g., Panza, 1985; Fäh et al., 1993; Panza et al., 1996; Panza et al., 2001; Panza and Romanelli, 2001; Paskaleva et al., 2007; Peresan et al., 2012b).

NDSHA, which is immediately *falsifiable* by the occurrence of a damaging event with magnitude exceeding the *predicted threshold*, has so far been validated in all regions where hazard maps prepared under its methodology have existed at the time of later strong or larger occurring earthquakes. PSHA, by providing a *minimum ground motion* that has a commonly 10% or 2% chance of exceedance in 50 years in its hazard model, is therefore not *falsifiable* at the occurrence of *any* single event that far exceeds this *minimum ground motion* value, as shown in Table 1.

Furthermore, such ambiguity (authoritatively calculated and endorsed) also provides a *legal shield* against both "unsurprising surprises", as well as any responsibilities for ensuring satisfactory outcomes to civil populations for any such presumed *unlikely* and *rare* events–on the part of administrators, politicians, engineers and even scientists (e.g., "the L'Aquila Trial," as previously mentioned).

Finally, there are existing algorithms for the diagnosis of "times of increased probability" (TIP) that have also been proven *reliable* in the long-lasting and on-going earthquake prediction experiment that began in 1985 (Kossobokov et al., 1999; Kossobokov and Shebalin, 2003; Kossobokov, 2013) and these can deliver an *intermediate-term Time* and *middle-range Space* component to the newer Neo-Deterministic NDSHA approach in a more targeted public-safety centered evaluation of seismic hazard (Peresan et al., 2011; Peresan et al., 2012a). In some cases, additional geophysical observations can further help in reducing the spatial uncertainty to the narrow-range about tens of kilometers, e.g., (Crespi et al., 2020).

Advanced seismic hazard assessment

The results by Wyss et al. (2012) regarding "Errors in expected human losses due to incorrect seismic hazard estimates" are well in line with the two Topical Volumes *Advanced Seismic Hazard Assessment* edited by Panza et al. (2011), which supply multifaceted information on the modern tools for Seismic Hazard Assessment (SHA).

The contributors to these special issues make clear the significant differences between *hazard*, *risk*, *hazard mitigation*, and *risk reduction* (Klügel, 2011; Peresan et al., 2011; Wang, 2011; Zuccolo et al., 2011), which are of paramount importance as the critical arguments toward revising fundamentally our present existing hazard maps, risk estimates, and engineering practices.

All ideas have consequences. Therefore, any *Standard Method* must be *Reliable* in the first place! That is, it must be: a) good; b) right; and c) true! It must consider: i) the fragility of the local built environment; ii) soil conditions; and iii) furnish now far more informative *risk/resiliency* assessments of cities and metropolitan territories (Paskaleva et al., 2007; Trendafiloski et al., 2009). The consequences of the Maximum Credible Earthquake (MCE) should be the criteria for Reliable Seismic Hazard Assessment (RSHA), because "what can happen" is a more important consideration than "what gets approved" based on a hazard model (see again Kanamori, 2014, 2021). Incidentally, we note that MCE as practiced in NDSHA (per Rugarli et al., 2019) supplies for Japan an enveloping magnitude M 9.3.

Backward into the future!

In spite of both: i) the numerous evidenced shortcomings of PSHA (see Stein et al., 2012; Wyss and Rosset, 2013 for a comprehensive discussion); and ii) its unreliable and poor performances — PSHA (emboldened now by 50 years of *dangerous* "sincere ignorance and conscientious stupidity") is still widely applied at regional and global scale "to continue the vision of a global seismic hazard model" (Danciu and Giardini, 2015; Gerstenberger et al., 2020; Meletti et al., 2021). Regretfully, the Global Earthquake Model project (GEM, http://www.globalquakemodel.org/) is evidently still on the preferred "*circulus vitiosus*" — a situation in which the solution to a problem creates another problem. Recently, the GEM Foundation released Global Seismic Hazard Map (version 2018.1) that depicts the geographic distribution of the PGA "with a 10% probability of being exceeded in 50 years" and makes the same fatal errors of the GSHAP 1999 PSHA map — see also "Development of a global seismic risk model" (Silva et al., 2020).

In the recent AGU *Reviews in Geophysics* article, entitled "Probabilistic Seismic Hazard Analysis at Regional and National Scales: State of the Art and Future Challenges," Gerstenberger et al. (2020): i) keep advocating the *evident misuse of statistics* by attributing any exposure of the fundamental flaws of PSHA (e.g., Castanos and Lomnitz, 2002; Klügel, 2007; Mulargia et al., 2017; Stark, 2017, 2022; Panza and Bela, 2020, *etc.*) to "subjective experts' judgment"; and ii) keep ignoring both — a) the systematic failures-to-predict the magnitude of exceedance (Kossobokov and Nekrasova, 2012; Wyss et al., 2012; Wyss and Rosset, 2013; Wyss, 2015); as well as b) the already two-decades-long *existing* and much more reliable alternative of the *neodeterministic* approach (Panza et al., 2012; Panza et al., 2014; Kossobokov et al., 2015a; Nekrasova et al., 2015a; Kossobokov et al., 2015b).

The PSHA's "State of the Art and Future Challenges" (which more correctly should have been alternatively released under the *technoscience* warning label "Reviews in Risk Modeling for Hazards and Disasters", rather than a true *scientific* oriented "Reviews in Geophysics") purposely "sincerely" missed referencing "NDSHA: A new paradigm for reliable seismic hazard assessment" (Panza and Bela, 2020), published online already about 2 months prior to the Gerstenberger et al. (2020) acceptance date (10 January 2020) and ignored as well *Advanced Seismic Hazard Assessment*, which was published in Pure and Applied Geophysics already 9 years prior (Panza et al., 2011).

Furthermore, Jordan et al. (2014) have *referenced* (Peresan et al., 2012a), which reference fully reveals the qualities, attributes, and applicability of NDSHA to "Operational earthquake forecast/prediction" with direct attention called in the Abstract to the "very unsatisfactory global performance of Probabilistic Seismic Hazard Assessment at the occurrence of most of the recent destructive earthquakes." Peresan et al. (2012a, p. 135) also discuss in detail the "Existing operational practice in Italy," which has been "following an integrated neo-deterministic approach" since 2005.

Supplementary Material in (Panza and Bela, 2020): *Bibliographic Journey To A New Paradigm*, provides detailed references in their chronologically developing order, so that one can see PSHA and NDSHA publications *side-by-side* over now more than two decades — as NDSHA effectively "built a new model that made the existing model obsolete!" Finally, one of just a *few* references *critical* of PSHA that were *surprisingly* included by Gerstenberger et al. (2020) did manage to state with absolute clarity: "Reliance on PSHA for decisions that affect public safety should cease" (Wyss and Rosset, 2013)!

Seismic Roulette is a game of chance

Seismic Roulette is a game of chance! It is true that we gamble against our will, but that does not make it any less of a game! Disastrous earthquakes are *low-probability* events locally; however, in *any* of the earthquake-prone areas worldwide, they reoccur as "unsurprising surprises" with *certainty*, i.e., with 100% probability sooner or later! Should we then synchronize our watches and historic clock towers. And then wait for another *decade*, while "Nature spins the wheel", to find out that GEM is as *wrong* as GSHAP?

The Neo-Deterministic Seismic Hazard Assessment (NDSHA) methodology (Fäh et al., 1993; Panza et al., 2012; Peresan et al., 2012a; Bela and Panza, 2021; Panza and Bela, 2020 and references therein) has demonstrated its abilities to serve as the *Standard Method* for Reliable Seismic Hazard Assessment (RSHA). NDSHA, proposed some 20 years ago (Panza et al., 1996; Panza and Romanelli, 2001), has proven to both reliably and realistically *simulate* comprehensive sets of hazardous earthquake ground motions throughout many regions worldwide. NDSHA, in making use of: i) our present-day comprehensive physical knowledge of seismic source structures and processes; ii) the propagation of earthquake waves in heterogeneous anelastic media; and iii) site conditions — effectively accounts for the complex, essentially *tensor* nature of earthquake ground motions in the affected area. Therefore, NDSHA applications provide realistic synthetic time series of *ground shaking* at a given place, when the best available distribution of the potential earthquake sources can be used for scenario modelling.

Conservative estimates of the maximum credible seismic hazard are obtained when they are based on the actual empirical distribution of earthquake characteristics — supplemented further with i) the existing geologic, tectonic, macro- and paleo-seismic evidence, ii) the results of PREPA, and iii) the implications of USLE, accounting for the local fractal structure of the lithosphere. In fact, USLE allows for a comparison between PSHA and NDSHA by

providing reliable estimates of PGA values associated with model earthquakes of maximal expected magnitude within 50 years (Nekrasova et al., 2014; Parvez et al., 2014; Nekrasova et al., 2015a; Nekrasova et al., 2015b; Kossobokov et al., 2020), it has been comparatively demonstrated that the NDSHA maps that use such estimates *outscore* GSHAP generated PSHA maps in identifying correctly the sites of *moderate*, *strong*, and *significant* earthquakes.

Specifically, the number of unacceptable errors (when PGA on a hazard map at the epicenter of a real earthquake is less, by factor 2 or greater, than PGA attributed to this earthquake) is several times larger for the GSHAP map than for the NDSHA — USLE derived map (e.g., PGA is 11.4, 1.7, and 2.5 times larger for strong earthquakes in Himalayas and surroundings, Lake Baikal region, and Central China, respectively, than on the GSHAP PGA hazard map). This *cannot* be attributed solely to the difference of the empirical probability distributions of the model PGA values within a region, although evidently the USLE model favors larger estimates in the Baikal and Central China regions. Note that at the regional scale of investigation, the GSHAP estimates of seismic hazard can be grossly *underestimated* in the areas of sparse explorations of seismically active faults, such as those to the east of the upper segment of the Baikal rift zone.

Earthquake prediction

> "Science has not yet mastered prophecy. We predict too much for the next year and yet far too little for the next ten."
>
> Neil Armstrong
>
> (Speech to a joint session of Congress, 16 September 1969)

The terms "Earthquake Forecast/Prediction" described in this section are focused primarily on Operational Earthquake Forecasting (OEF) and mean: i) first specifying the *time*, *place*, and *energy* (as a rule in terms of magnitude) of an anticipated seismic event with sufficient accuracy/precision to then ii) provide authoritative warning to those responsible for the undertaking of civil preparedness actions intended to: a) reduce loss-of-life and damage to property; and b) mitigate disruption to life lines and social fabric (i.e., harden community resilience).

Some distinguish forecasting as prediction supplemented with *probability* of occurrence (Allen, 1976; NEPEC, 2016). In common everyday language, however, "forecast" and "prediction" are synonymous to the public when they are referring to earthquake phenomena — at least from a practical awareness and actionable viewpoint. Note, however, that estimates of earthquake *probability* or *likelihood* are the result of one's usually *subjective* deterministic choice of *probability model* — which might *mislead* personal belief away from the *actual* phenomena under study (Gelfand, 1991).

In J.R.R. Tolkien's fantasy adventure "The Hobbit: An Unexpected Journey" — the "necessity of identifying risk in any thorough plans in life" is underscored in making reference to the actual phenomenon: "It does not do to leave a live dragon out of your calculations, if you live near him."

Therefore, earthquake forecast/prediction is neither an easy nor a straight-forward task (but rather an *unexpected journey*) and therefore implies both an informed as well as a delicate application of statistics (Vere-Jones, 2001). Whenever the problems are very broad, as they particularly are here in the earthquake realm of geophysics and the earth sciences — it is always very important to distinguish the *facts* from the *assumptions,* so that one can fully understand the *limitations* of the assumptions, as a scientific safeguard against committing the equivalent of *geophysical* malpractice (see P.B. Stark's "Thoughts on applied statistics" at https://www.stat.berkeley.edu/users/stark/other.htm).

Regretfully, in many cases of Seismic Hazard Assessment (SHA): from i) *time-independent* (term-less); to ii) *time-dependent* probabilistic (PSHA); from iii) *deterministic* (DSHA, NDSHA); to also iv) Short-term Earthquake Forecasting (StEF) — since the claims of a high potential success of the prediction method are based on a *flawed* application of statistics, they are therefore hardly suitable for communication to responsible decision makers.

Making SHA claims (either time-independent or time-dependent) *quantitatively* probabilistic in the "frames" of the most popular objectivists' viewpoint on probability (i.e., *objective chance*) — requires a long series of "yes/no" trials, which however cannot actually be obtained without an *extended* and *rigorous* testing of the method predictions against *real* (live) observations. Moreover, as pointed out by Stark (2017), (2022), the distinction between 'random', 'haphazard', and 'unpredictable' is crucial for scientific inference and applications in practice (see, e.g., Chipangura et al., 2019).

Predicting the unpredictable

By the 1980s, the lithosphere of the Earth was recognized as a *complex hierarchically self-organized non-linear dissipative system,* with critical phase transitions manifested through larger earthquakes (Keilis-Borok, 1990) (see also more recent Wang et al., 2018; Bedford et al., 2020). Mathematically, the characteristics of such *haphazard*, apparently *chaotic* systems are nevertheless *predictable* up to a certain limit, and after substantial averaging (e.g., as in the abovementioned Keilis-Borok et al., 1984). Therefore, a "success" in forecasting disastrous earthquakes necessarily implies a successive step-by-step determination that narrows down the *time interval*, *location area*, and *magnitude range* of any incipient earthquake.

So far, none of the proposed short-term precursory signals have shown sufficient evidence to be used as a reliable precursor ahead of large impending earthquakes (Wyss, 1991; Wyss, 1997; Sornette et al., 2021). For example, when testing the West Pacific short-term forecast of earthquakes with magnitude MwHRV ≥5.8 of Jackson and Kagan (1999) against the catalog of earthquakes in the period from 10 April 2002 through 13 September 2004, the conclusion was drawn by Kossobokov (2006b) that the underlying method could be used for prediction of aftershocks, while it however does not outscore Seismic Roulette *random guessing* — when main shocks are considered. Note that the attribute "short-term" in (Jackson and Kagan, 1999) appears rather misleading, because even for reasonably small values of an alerted space-time volume, some places can remain at "short-term" alert for years.

Short-Term Earthquake Probability (STEP)

The unfortunately *poor performance* of another Short-Term Earthquake Probability (STEP) model (based on earthquake clustering) by Gerstenberger et al. (2005) could have been

anticipated before making operational the United States Geological Survey web site service, as well as the solicited publication announcement in Nature; Kossobokov (2005); Kossobokov (2006a), based on the 15 years of seismic record statistics provided in "Real-time forecasts of tomorrow's earthquakes in California" by Gerstenberger et al., presented a "half-page proof" that suggests *rejecting* with confidence above 97% "the generic California clustering model" used in calculation of forecasts of expected ground shaking for tomorrow. The poor performance of STEP was eventually later further confirmed by Kossobokov (2008), because: in 1,060 days operation of the *real-time* forecasting, the five earthquakes of MMI ≥ VI in California occurred alternatively in the areas of the web-site's *lowest-risk* (about 1/10,000 or less), while the extent of the observed areas of intensity VI for these events (about 100 cells in total) is by far less than the model expected value (about 850 cells). "A website, showing daily ground-shaking probabilities in California, was subsequently removed because of coding problems" (Cartlidge, 2014).

Accuracy of short-term earthquake forecast/prediction tools

Recently Zhang et al. (2021) apply the Error Diagram (Molchan, 1997; Molchan, 2003), weighted by an analogue of Seismic Roulette, to conclude that the correspondence between *earthquakes* and *thermal infrared* (TIR) anomalies, widely observed in decades of satellite imagery, is proven "absent" — because the claims for such are based on a uniform distribution of epicenters that they judge to be inadequate for an appropriate measure of the alarm [see also: Preface; Editors' Introduction discussion on "Statistical Models and Causal Inference" in (Collier et al., 2010)].

In their reviews of the state of knowledge in the field of earthquake forecast/prediction — neither Jordan et al. (2011), nor Sornette et al. (2021) found any reliable methods for a short-term Operational Earthquake Forecasting (OEF) — but acknowledge that the deterministic *pattern recognition* approach is reliably efficient at: i) *intermediate-term time* scale of a few years; and ii) middle-range *distance* encompassing areas of a few target earthquake-source dimensions in *diameter* (see also Kossobokov, 2006a; Kossobokov, 2014; Ismail-Zadeh and Kossobokov, 2020; Kossobokov and Shchepalina, 2020).

For three decades the *deterministic* earthquake prediction algorithms have made use of *clustering* in seismic sequences, observable at different magnitude-space-time scales. For example, the M8 Algorithm (Keilis Borok and Kossobokov, 1990; Healy et al., 1992; Ismail-Zadeh and Kossobokov, 2020) *diagnoses* the "Time of Increased Probability" (TIP) from a multi-parametric analysis of a local system of blocks-and-faults in the traditional "phase space" of *rate* and *rate differential* — supplemented with earthquake-specific measures of earthquake source *concentration* and *clustering*. However, the M8 algorithm does *not* provide probability value, but rather a pattern of its *increase* above the level sufficient for efficient prediction of *target* earthquakes.

After these many decades of rigid *real time* testing of both the validity and reliability of Global M8 predictions (Ismail-Zadeh and Kossobokov, 2020; Kossobokov and Shchepalina, 2020) and Regional CN algorithm predictions for Italy (Peresan et al., 2005) have been confirmed with a high statistical confidence (Peresan, 2018; Kossobokov, 2021).

Therefore, the accuracy of these forecasting/prediction tools is sufficiently proven for efficiently undertaking precautionary civil earthquake preparedness measures. The theoretical framework for optimization of disaster preparedness measures, undertaken in response to reliable earthquake forecast/prediction, was developed under supervision of Leonid V. Kantorovich, the 1975 Nobel Laureate in Economic Sciences (Kantorovich et al., 1974; Kantorovich and Keilis-Borok, 1991).

Davis et al. (2012) have shown further that *prudent* and *cost-effective* actions can be wisely undertaken, *if* the prediction certainty is known but not necessarily high. For example, the huge losses from the 6 Fukushima Nuclear Power Plants were on the order $100 billion, while the *preventive* costs of raising tsunami *wall height*, plus that of *protective housing* for generators to resist the potential flooding, were only about $10 million. As an epilogue (reminiscent of "the L'Aquila Trial"), in 2020 (https://www.theguardian.com/environment/fukushima) a "Japanese court found the government and TEPCO, the operator of the wrecked Fukushima nuclear plants, negligent for failing to take measures to prevent the 2011 nuclear disaster, and ordered them to pay 1 bn yen ($9.5 million) in damages to thousands of residents for their lost livelihoods." Therefore, taking these preventative actions, as detailed by Davis et al. (2012), in response to the *intermediate-term* (Time) and *middle-range* (Space) prediction that was communicated to Japanese authorities in mid-2001 would have been cost-effective for the Fukushima nuclear power plants, even if the prediction had had a whopping 99.99% chance of being false alarm!

Therefore, is a "Likely Impossibility" (or *leaving a live dragon out of your calculations*), a safe bet on which to place chips in Seismic Roulette 00? a) "In court, the government argued it was impossible to predict the tsunami or prevent the subsequent disaster"; and b) "The court said that the government could have taken measures to protect the site, based on expert assessments available in 2002 that indicated the possibility of a tsunami of more than 15 m."

Operational earthquake forecasting

In the Realm of Operational Earthquake Forecasting (OEF), which is "the dissemination of authoritative information about time-dependent earthquake probabilities to help communities prepare for potentially destructive earthquakes" (Jordan et al., 2014), within the broader OEF scheme shown in Figure 10, we believe one should try to use *all* reliable Geophysical Information, including but not limited to: i) Earthquakes; ii) GPS; iii) Gravity; iv) Electro-magnetic; and v) Geochemical input that might be relevant to origination of damaging ground shaking.

This would allow for a true multi-disciplinary forecast/prediction so much needed in practice. Forecasting Information must be reliable, tested, and confirmed by evidence (Allen, 1976; Kossobokov et al., 2015b), such that the heretofore probabilistic-centered models (which have been focused primarily on "expert opinion" and weighting of different subjective "models of seismicity") defer now *rather* to a more collaborative practice of "expert judgement", which is incorporating all of the above forecasting requirements, and as is more simply illustrated

in Figure 11. Ideally, good judgement comes from experience; and not from bad judgement and failed policy disasters, such as experienced at L'Aquila and Fukushima!

Seismology and computer science alone are not enough for a successful collaboration aimed at effective forecasting of larger earthquakes. OEF could be either deterministic, probabilistic, or a combination of both in interaction with user needs within the Realm of Risk Analysis and Mitigation. Naturally, the scheme applies as well to other natural hazards and can be further generalized. Note however, that 'operational' (in everyday language) means *'ready to work correctly'*; hence, it is obvious that SHA belongs to the OEF Realm as, we believe, the most important part of the OEF user interface shown in Figures 10, 11. See (Peresan et al., 2005; Peresan, 2018) for 'operational' forecast/prediction practices in Italy since 2005 and also (Crespi et al., 2020) for a recent example.

Practitioners are positive that any reliable forecasting information can be i) effective, ii) complementary to design and construction of seismically resistant buildings and infrastructure, and iii) well appreciated by the population as a timely precautionary reminder and timely warning (Mileti and Fitzpatrick, 1992; Kossobokov et al., 2015b). Obviously, the spectrum of doable low-key preparedness options increases in the case of *longer* rather than *short-term* warnings. Theoretically speaking, while decision-makers should be aware of the full broad spectrum of possible actions, following general strategies of response to predictions by escalation or de-escalation of safety measures (depending on expected losses and magnitude-space-time accuracy of reliable forecasting), lives can only be saved (and more legal trials avoided) if buildings and infrastructures can withstand the shaking!

Earthquake preparedness should not fluctuate on daily or weekly basis

Therefore, per Wang and Rogers (2014), "Earthquake Preparedness Should Not Fluctuate on a Daily or Weekly Basis" from both public safety, as well as effective public messaging concerns. They say "although fully appreciating the noble intention of OEF and the scientific merits of the seismicity analyses it employs, we are concerned that its wide promotion may lead the public to believe that earthquake preparedness can fluctuate at timescales of days or weeks," and we "question the claim that it should and can be made operational," because:

(1) Where OEF is based largely on *clustering* or potential *foreshock sequences*, it is not reliable, as the "majority of damaging earthquakes are not preceded by anomalous foreshocks."
(2) "The most objective measure of the usefulness of a short-term forecast is whether it can guide pre-seismic evacuation of unsafe buildings."
(3) But providing *probability forecasts* in percentages from very low to even 20% or 40% (and with authoritative uncertainties) may not mean much to a public that only *dichotomizes* Risk: Yes or No! (like "Shall I carry an umbrella today, or not?").
(4) "Crying earthquake is a potent way of blunting earthquake awareness and preparedness," as well as disrupting the economy.

Since the most sensible and reliable way to mitigate the hazard posed by *unsafe* and *killer buildings* requires that the public, the government, and society "make every effort to retrofit or replace an unsafe building to comply with earthquake resistance provisions," while this is not simple, Wang and Rogers believe the scientific community should first and foremost *help* society to deal with these challenges, and not just champion short-term alternatives focusing on evacuations (i.e., "the practice of continual updating and dissemination of physics-based short-term (days) probabilities for the occurrence of damaging earthquakes") to that specific evacuation end.

Reflecting on the damage and fatalities in L'Aquila, they note that the relevant questions to ask regarding reliable mitigation strategies are:

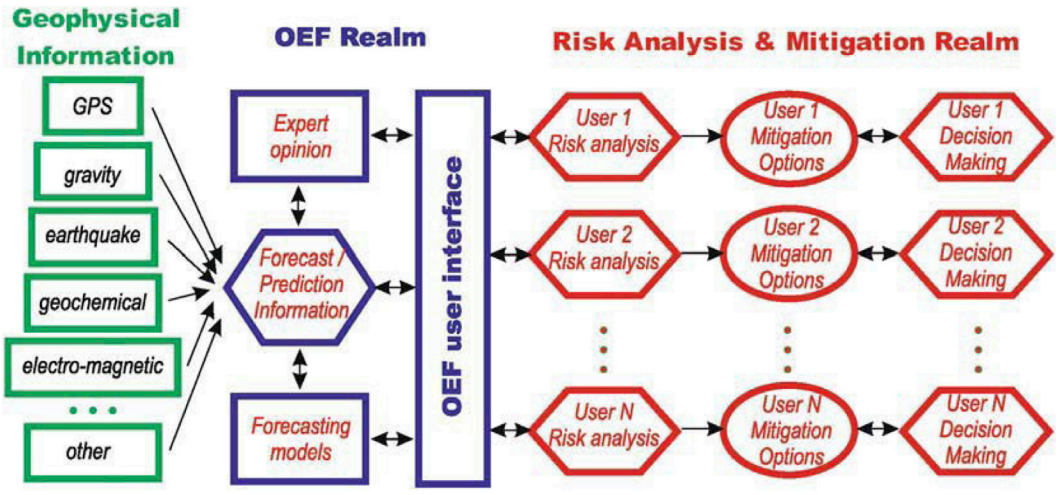

FIGURE 10
Operational Earthquake Forecasting scheme.

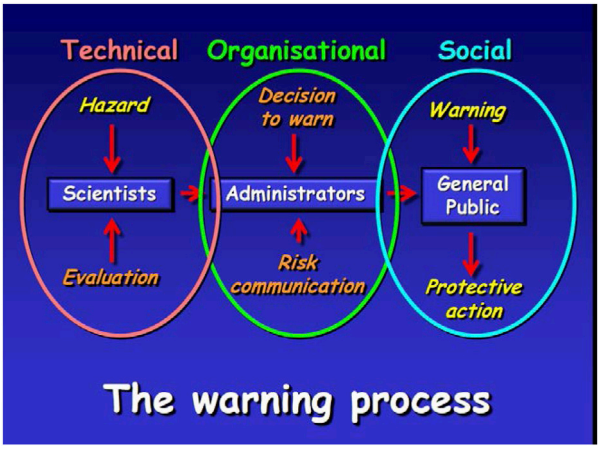

FIGURE 11
The technical NDSHA warning process. *Source* courtesy of David Alexander.

> Why did those buildings collapse? What could have been done better in designing and implementing building codes? How should retrofitting regulations and practices be improved to reduce the vulnerability of old buildings? How can the methods of developing seismic-hazard models be further improved?
>
> .....
>
> During this type of crisis, the scientific community should step up to guide public and government attention to the relevant questions asked above. It is our concern that their attention was guided farther away from these questions by the report of the International Commission on Earthquake Forecasting for Civil Protection (Jordan et al., 2011), which, in our view, incorrectly concludes that the L'Aquila incident demonstrated the need for OEF.

"Society's best strategy against the consequence of earthquakes," they say, "is to focus on making the built environment earthquake resistant." Naturally, when then Nature does *spin the wheel*, you can bet on that!

Earthquake prediction in practice: Success and failure

As an example, the success in predicting in practice the devastating 1975 Haicheng earthquake (Zhang-li et al., 1984) remains the sole case of successful OEF decision-making interaction between scientists and administrators. A "lucky" intermediate-term (Time) guess: i) readied the province for an incipient large earthquake; ii) was followed by an escalation of civil preparedness from low-key actions at low-level alert to short-term monitoring of multidisciplinary observations; and iii) ultimately culminated with "red alert" status! — and *evacuation* of the city of Haicheng was ordered by Chinese officials early in the morning of February 4th — thereby saving most of approximately one million residents from consequences of the devastating M 7.5 shock that hit the area in the evening hours. Although 1,328 people nevertheless died, over 27,000 were injured, and thousands of buildings collapsed, the number of fatalities is just about 1% of the estimate, if the evacuation had *not* taken place.

In deadly contrast, the M 7.8 Great Tangshan Earthquake of 28 July 1976 was sadly "the greatest earthquake disaster in the history of the world", and occurred with *no warning* (Huixian et al., 2002). It was generated by a fault running directly through the middle of the city, which is located in the extreme NE region of China abutting the iconic (and *fractal*) Bohai Bay *indentation* of the Chinese coastline. "Although the building code had seismic design requirements, Tangshan was in a zone requiring no earthquake design." Therefore "red alert" timely evacuation would have been the one-and-only successful action for OEF!

Notably: i) 85% of the buildings in Tangshan either collapsed or were "so seriously damaged as to be unusable;" ii) infrastructure and agriculture were also seriously damaged as well; iii) the shock hit around 4:00 a.m. when the population was mostly at home asleep in vulnerable structures having no earthquake resistance; iv) the extreme intensity XI on MMI scale and subsequent aftershocks caused officially 242,419 victims (Huixian et al., 2002) (this death toll number placing The Great Tangshan Earthquake atop the list of deadliest earthquakes in a century).

Therefore, in contrast to the very successful 1975 Haicheng earthquake forecast/prediction case, The Great Tangshan Earthquake turns out be a "cold shower" of disillusionment on both the Risk Umbrella and the *presumed* reliability of OEF, demonstrating particularly that consideration of MCE as practiced in NDSHA, per Rugarli et al. (2019), has to *envelope* all public safety considerations over and above, we believe, *probability* model perturbations of OEF responses.

It does not do to leave a live dragon out of your calculations

The Caltech EERL 2002–001 Report on The Great Tangshan Earthquake shows *what can happen* when an *unexpected* earthquake strikes an unprepared city, and it makes clear the need for earthquake preparedness even if the (*subjectively* modeled) probability of an earthquake is presumed to be low (Huixian et al., 2002).

Decades later, a golden opportunity was tragically lost to advise the citizens of L'Aquila, Italy on low-key safety measures, when *Commisione Grandi Rischi* (CGR), or Grand Risk Commission, issued their politicized statement on 31 March 2009 — because at this time the situation was favorable for adequate reaction of the public to prudent (*understandable*, *believable*, and *personal*) information on the "increased probability" of an impending strong earthquake (see e.g., Mileti and Fitzpatrick, 1992; Marincioni et al., 2012; Wachinger et al., 2013).

The local authorities and emergency management agencies, in particular, were also *ready* to act in advance, but were advised to the contrary by CGR to *do nothing*! From a strictly scientific viewpoint, an adequate evaluation of the seismic crisis in the

Abruzzo region of Central Italy east of Rome on 31 March 2009 could have actually provided a much more reliable forecast/prediction than the previous and celebratory 1975 Haicheng success story! — if seismological knowledge had not been *misspresented* by CGR:

(I) According to scientific studies by the CGR members (Boschi et al., 1995; Dolce and Martinelli, 2005) L'Aquila was: a) at the highest seismic risk in Italy in the near future; and b) buildings in medieval L'Aquila were extremely vulnerable.

(II) Therefore, given the November 2008 — March 2009 apparently unrelenting seismic activity shaking the Abruzzo region (culminating in March 2009, when over 100 tremors occurred in the vicinity of L'Aquila), any responsible scientific body should *not* have asked local people to "calm down and relax," but should instead have claimed: a) *evident* "increase of seismic risk" within the area; and also advised b) *raising* the "alert level" from background "green" to "yellow", at least, or even "orange". Subsequently it has been shown that this *cluster* of seismic activity that was so alarming to the population was a *foreshock* sequence foreshadowing the M 6.3 L'Aquila main shock (Papadopoulos et al., 2010).

Communicating their already existing scientific knowledge "as is" and *unabridged* could have led to saving the lives of a significant part of the 309 people who perished under the rubbles of the devastating M 6.3 L'Aquila earthquake on 06 April 2009 at 03:32 a.m. Many victims would not have returned back to their homes to sleep, but would have instead remained outside their houses for the rest of the night, following the two premonitory tremors of M3.9 (2009/04/05 22:48 CET) and M3.5 (2009/04/06 00: 39 CET) which preceded the fatal M6.3 (2009/04/06 03:32 CET) main shock by just 3 hours. See in particular '*Voices from the seismic crater in the trial of The Major Risk Committee: a local counternarrative of "the L'Aquila Seven"*' by Pietrucci (2016).

(1) On 22 October 2012 the Court of L'Aquila found all seven CGR members, who had been convened in L'Aquila on 31.03.2009 with "the aim of providing the citizens of Abruzzo with all the information available to the scientific community on the seismic activity of the last few weeks," *guilty* of *negligence, imprudence*, and *inexperience* by their actions in providing incomplete information to the National Department of Civil Protection, to the Abruzzo Region Councilor for Civil Protection, to the Mayor of L'Aquila, and to the citizens of L'Aquila that had resulted in the deaths of people.

Thus, and what was commonly *misunderstood* at the time, the guilty parties were convicted neither for failing to forecast the earthquake, nor for failing to advise evacuation of the city. Rather they were convicted for having provided 'inaccurate, incomplete, and contradictory information' about the ongoing seismic activity and therefore undermining the safety of the population (see e.g., https://www.slideshare.net/dealexander/reflections-on-the-trial-of-the-laquila-seven).

Their providing of this "incomplete information" was as a result of: a) the statements made to the media; and b) the CGR draft report — both of which were: i) imprecise and contradictory on the nature, causes, danger and future developments of the seismic activity in question; ii) also in violation of the general legislation of the Law regarding the "discipline of information and communication" activities of public administrations at the time of said meeting; and iii) only approximate, generic and ineffective in relation to the activities and duties of "forecasting and prevention" (Alexander, 2014). In the Italian three-part legal system, after the Court of L'Aquila guilty verdict 1) above; 2) later the Court of Appeal acquitted six scientists; and 3) the Supreme Court ultimately confirmed this ruling.

It cannot be ruled out, however, that the CGR meeting on 31 March 2009 was convened with the explicit goal to *calm down* the disquieted public from both the ongoing seismic activity, and also the warnings of an amateur earthquake prediction scientist (Alexander, 2014; Imperiale and Vanclay, 2019). And the questions of whether scientists were used or "captured" (allowing their knowledge to be misused) or also complicit (by not taking action to correct misinformation that was the equivalent of *geophysical malpractice*) remains both itchy, as well as worrisome.

More details about so-called "L'Aquila Trial" (or trial of "the L'Aquila Seven"), and the political *crisis in science* it spawned, are given by Panza and Bela (2020) and Supplementary material therein. Information regarding the "AGU Statement: Investigation of Scientists and Officials in L'Aquila, Italy, Is Unfounded" (including Comment and Reply) — are in (Dobran, 2010; Wasserburg, 2010); see also (Stark and Saltelli, 2018).

CN prediction experiment in Italy: 8 target earthquakes

Since the beginning of the real-time CN prediction experiment in Italy in July 2003 (Peresan et al., 2005), only 2 events (out of 8 target earthquakes) were missed. Namely, the 24 November 2004, M 5.5, Salò earthquake in southern Alps, Northern region (Figure 12) and the 6 April 2009, M 6.3, L'Aquila earthquake in the central part of the Apennines, Central region. The L'Aquila earthquake scored as a "failure to predict" just because its epicenter was located about 10 km outside the *alarm territory* of Northern region identified by CN algorithm for the corresponding *time window* (Peresan et al., 2011).

The situation with the Salò earthquake, which again occurred within the Northern Region, was quite different. In fact, fully three target earthquakes hit the same region in a row, respectively those of September 2003 July 2004, and November 2004. Both the first and second earthquakes were correctly predicted by CN algorithm within the alarm window beginning in May 2001, but according to the protocols of the prediction experiment, however, when the *seismic energy release* within the alarm region surpassed the preset sufficiently high threshold after the second, July 2004 earthquake, the alarm was *automatically* terminated — thus resulting in a "failure to predict" for the third November 2004 Salò earthquake (Peresan, 2018).

Discussion and conclusions

> "Nothing is less predictable than the development of an active scientific field."
>
> Charles Francis Richter

Charles Richter, whose critical observation that "only fools and charlatans predict earthquakes" is often cited (see e.g., Hough, 2016),

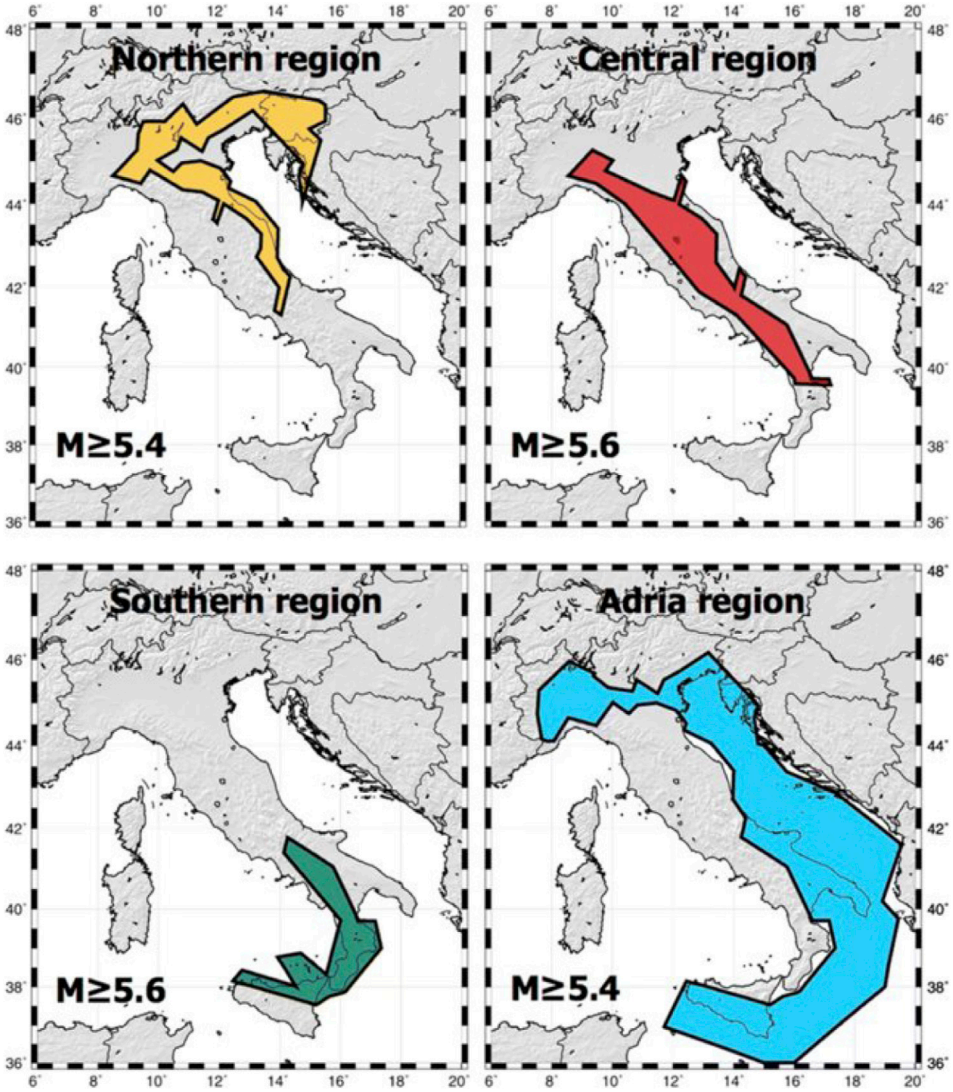

FIGURE 12
Regionalization used in the CN prediction experiment in Italy.

illuminatingly wrote a one-page note (Richter, 1964) next to the article by Russian researchers Vladimir I. Keilis-Borok and Lyudmila N. Malinovskaya that was describing *quantitatively* an observation of a *general increase* in seismic activity in advance of some 20 strong earthquakes (Keylis-Borok and Malinovskaya, 1964). Richter noted: i) that this was "a creditable effort to convert this rather indefinite and elusive phenomenon into a *precisely definable* one"; ii) further marked as important a confirmation of "the necessity of considering a very *extensive* region including the center of the approaching event"; and iii) finally outlined "difficulty and some arbitrariness, as the authors duly point out, in selecting the *area* which is to be included in each individual study." An example of the procedure followed to define the CN-regions in Italy is given by Peresan et al. (2005) and references therein (see also http://www.mitp.ru/en/cn/CN-Italy.html).

As can be judged after reading the most recent review of "The Global Earthquake Forecasting System: Towards Using Non-seismic Precursors for the Prediction of Large Earthquakes" (Sornette et al., 2021), most, if not all, non-seismic "low-hanging fruits" stubbornly remain earthquake precursor candidates unfortunately *lacking* the results of similar credible seismic precursor definition efforts — which results are absolutely required to advance earthquake prediction forward from *challenging* "hindcasting" to a *reliable* "operational forecasting" of earthquake hazard, i.e., ready to be used correctly by both civil protection agencies and populations (Mignan et al., 2021).

One could not realistically or believably challenge that earthquake prediction research *requires* from a scientist both a keen feeling of responsibility, as well as rigid control of all claims and conclusions. Such *responsibility* requires further the highest standards of statistical analysis, because it is well-known that the improper use of statistical methods may lead to *wrong* (although to the user *desirable*) causal inferences. And we were often reminded of this error by Andrei N. Kolmogorov (1903–1987), the famous Russian mathematician known for Probability theory, Topology, Intuitionistic logic, Turbulence and many other studies, who modified for this purpose a famous quotation attributed to Benjamin Disraeli (1804–1881): "There are three kinds of lies: lies, damned lies, and *political* statistics."

It would likewise also be wrong to regard statistics as purely a tool for *exercises in numerology*, by first counting, and then regressing "descriptive" parameters — as proxies for "causal inference" in statistical models (Collier et al., 2010). A main reason is from Albert Einstein's observation that "not everything that can be counted counts, and not everything that counts can be counted." Or, in other words, "as far as the laws of mathematics refer to reality, they are not certain; and as far as they are certain, they do not refer to reality" (Albert Einstein, Geometry and Experience, 27 gennaio 1921).

Furthermore, as one of the highest authorities in modern mathematical sciences, Izrail M. Gelfand (1913–2009) wrote in his Kyoto Prize Commemorative Lecture of the 1989 Laureate in Basic Sciences (Gelfand, 1991): "It is terrible that in our technocratic age we do not doubt the *initial basic principles*. But when these principles become the basis for constructing either a trivial or finely developed model, then the model is viewed as a complete *substitute* for the natural phenomenon itself."

We believe foremostly that PSHA is not "the natural phenomenon itself", and also, per "Cargo-cult statistics and scientific crisis" (Stark and Saltelli, 2018) — that the underlying problem of a widespread pandemic-like *scientific crisis* in many disciplines collaboratively involved in SHA lies squarely in the *misuse* of Statistics far beyond the *possibilities* of its applications (as in the abovementioned GSHAP, STEP, GEM seismic hazard model endeavors) — due primarily to: i) superficial education regarding "initial basic principles"; ii) lots of mechanical application of pretty available software; and our favorite iii) the *questionable* editorial policies of scientific journals, as in (Gerstenberger et al., 2020); see also (Stark, 2018; Stark and Saltelli, 2018; Bela and Panza, 2021).

Regretfully, nowadays for many science has become a "career," rather than a *calling* (Stark and Saltelli, 2018). And for example, in his last appearance of the famous Bertolt Brecht play, Galileo concludes (*in lecture style*) his instructions to a young scholar:

> For a few years I was as strong as the authorities. And yet I handed the powerful my knowledge to use, or not to use, or to misuse as served their purposes. I have betrayed my calling. A man who does what I have done cannot be tolerated in the ranks of science.

Thus, when once again maps are checked "with the actual territory during the journey", the newest GEM global seismic hazard maps based on PSHA are of *deceptive glow* — regrettably the same as the old pretty-shabby ones born of GSHAP, and as a result, therefore, mislead to a disappointing future practice of more unsurprising surprises, when *actual* seismic effects are once again: a) unexpectedly disastrous; as well as b) of unnecessary expenses on earthquake-resistant construction within the essentially aseismic areas.

On the contrary, the three-decades-long physically sound approach of NDSHA models (Fäh et al., 1993; Panza et al., 2013), that predictably outscore comparative PSHA models in efficiency, enables estimating realistically the future magnitude of ground shaking for SHA — with statistically justifiable reliability. Deterministic scenarios of catastrophic earthquakes, which can now be based on the *state-of-the-art* knowledge of the Earth's complex structure and *patterns of seismicity,* provide a much more comprehensive basis for: i) decision-making for land use planning; ii) adjusting building code earthquake-resistant design standards; iii) seismic-related regulations; and iv) operational emergency management.

Today NDSHA is gaining even more momentum in spreading Worldwide a New Paradigm of Reliable Seismic Hazard Assessment, RSHA (Panza and Bela, 2020; Bela and Panza, 2021); and one (see XeRiS - Methodology) that, along with other modern physics-based earthquake scenario modelling platforms, e.g. CyberShake (SCEC, 2018) — should ultimately change the mind-sets of both scientific and engineering communities alike: from a pessimistic disbelief in past forecasting abilities attributable only to "fools and charlatans"... to today's optimistic appreciation of the many challenging issues being addressed by Neo-Deterministic Predictability of Natural Hazards.

Author contributions

JB performed organizational and editing/language tasks related to manuscript. VK wrote initial presentation on Hazards, Risks, and Prediction in the book *Earthquakes and Sustainable Infrastructure* and collaborated on interpretation and manuscript write up. GP helped with overall expanded coverage of topic, provided references, key insights, and editorial managing oversight.

Conflict of interest

The authors declare that the research was conducted in the absence of any commercial or financial relationships that could be construed as a potential conflict of interest.

Publisher's note

All claims expressed in this article are solely those of the authors and do not necessarily represent those of their affiliated organizations, or those of the publisher, the editors and the reviewers. Any product that may be evaluated in this article, or claim that may be made by its manufacturer, is not guaranteed or endorsed by the publisher.

References

Alexander, D. E. (2014). Communicating earthquake risk to the public: The trial of the "L'Aquila seven". *Nat. Hazards* 72 (2), 1159–1173. doi:10.1007/s11069-014-1062-2

Alexander, D. E. (2010). The L'Aquila earthquake of 6 April 2009 and Italian government policy on disaster response. *J. Nat. Resour. Policy Res.* 2 (4), 325–342. doi:10.1080/19390459.2010.511450

Allen, C. R. (1976). Responsibilities in earthquake prediction: To the seismological society of America, delivered in edmonton, Alberta, may 12, 1976. *Bull. Seismol. Soc. Am.* 66 (6), 2069–2074. doi:10.1785/BSSA0660062069

Bak, P., Christensen, K., Danon, L., and Scanlon, T. (2002). Unified scaling law for earthquakes. *Phys. Rev. Lett.* 88 (17), 178501–178504. doi:10.1103/PhysRevLett.88.178501

Beauval, C., Bard, P. Y., Hainzl, S., and Guguen, P. (2008). Can strong motion observations be used to constrain probabilistic seismic hazard estimates? *Bull. Seismol. Soc. Am.* 98 (2), 509–520. doi:10.1785/0120070006

Bedford, J. R., Moreno, M., Deng, Z., Oncken, O., Schurr, B., John, T., et al. (2020). Months-long thousand-kilometre-scale wobbling before great subduction earthquakes. *Nature* 580, 628–635. doi:10.1038/s41586-020-2212-1

Bela, J., and Panza, G. F. (2021). Ndsha - the new paradigm for RSHA - an updated review. *Vietnam J. Earth Sci.* 43 (2), 111–188. doi:10.15625/2615-9783/15925

Bela, J. (2014). Too generous to a fault? Is reliable earthquake safety a lost art? Errors in expected human losses due to incorrect seismic hazard estimates. *Earth's Future* 2, 569–578. doi:10.1002/2013EF000225

Berke, P. R., and Beatley, T. (1992). *Planning for earthquakes: Risk, politics, and policy*. Baltimore, USA: Johns Hopkins Univ. Press, 210. Available at: https://www.amazon.com/Planning-Earthquakes-Risk-Politics-Policy/dp/0801842557.

Bilham, R. (2009). The seismic future of cities. *Bull. Earthq. Eng.* 7, 839–887. doi:10.1007/s10518-009-9147-0

Boissonnade, A. C., and Shah, H. C. (1984). Seismic vulnerability and insurance studies. *Geneva Pap. Risk Insur. - Issues Pract.* 9 (32), 223–254. doi:10.1057/gpp.1984.13

Bolt, B. A. (1991). Balance of risks and benefits in preparation for earthquakes. *Science* 251 (4), 169–174. doi:10.1126/science.251.4990.169

Bommer, J. J., and Abrahamson, N. A. (2006). Why do modern probabilistic seismic-hazard analyses often lead to increased hazard estimates? *Bull. Seismol. Soc. Am.* 96 (6), 1967–1977. doi:10.1785/0120060043

Bormann, P. (2020). "Earthquake, magnitude," in *Encyclopedia of Solid earth geophysics*. Editor H. Gupta (Cham, Switzerland: Springer). doi:10.1007/978-3-030-10475-7_3-1

Boschi, E., Gasperini, P., and Mulargia, F. (1995). Forecasting where larger crustal earthquakes are likely to occur in Italy in the near Future. *Bull. Seismol. Soc. Am.* 85 (5), 1475–1482. doi:10.1785/BSSA0850051475

Box, G. E. P. (1979). "Robustness in the strategy of scientific model building," in *Robustness in statistics*. Editors R. L. Launer and G. N. Wilkinson (New York, USA: Academic Press), 201–236. doi:10.1016/B978-0-12-438150-6.50018-2

Briceño, S. (2014). "The international strategy for disaster reduction and the Hyogo framework for action (2005–2015): Essential tools for meeting the challenges of extreme events," in *Extreme natural hazards, disaster risks and societal implications (special publications of the international union of geodesy and geophysics). Part VII*. Editors A. Ismail-Zadeh, J. U. Fucugauchi, A. Kijko, K. Takeuchi, and I. Zaliapin (Cambridge, UK: Cambridge University Press), 333–347. doi:10.1017/CBO9781139523905.034

Cancani, A. (1904). "Sur l'emploi d'une double échelle sismique des intensités, empirique et absolue," in *Proceedings of the 2nd international conference of seismology. Strasbourg, France, jul 24-28, 1903. Gerlands Beiträge zur Geophysik; Special Volume II, Annexe A-10*. Editor E. Rudolph, 281–283. Available at: https://www.castaliaweb.com/ita/discussioni/PSHA_NDSHA/Cancani1904.pdf.

Cannon, T. (1993). "A hazard need not a disaster make: Vulnerability and the causes of natural disasters natural disasters: Protecting vulnerable communities," in *Proceedings of the conference held in London, 13-15 October 1993*. Editors P. A. Merriman and C. W. A. Browitt (London: Thomas Telford). Available at: https://www.researchgate.net/publication/285133108_A_hazard_need_not_a_disaster_make_Vulnerability_and_the_causes_of_natural_disasters_edited_by_Merriman_Natural_disasters_protecting_vulnerable_communities.

Cartlidge, E. (2014). A dangerous distraction? *Phys. World* 27 (10), 6–7. doi:10.1088/2058-7058/27/10/10

Castanos, H., and Lomnitz, C. (2002). Psha: Is it science? *Eng. Geol.* 66 (3-4), 315–317. doi:10.1016/S0013-7952(02)00039-X

Chipangura, P., Van der Waldt, G., and Van Niekerk, D. (2019). An exploration of the tractability of the objectivist frame of disaster risk in policy implementation in Zimbabwe. *Jàmbá J. Disaster Risk Stud.* 11 (1), 604–610. doi:10.4102/jamba.v11i1.604

Chu, H. Y. (2014). *R. Buckminster Fuller's model of nature: Its Role in his design process and the presentation and Reception of his work*. PhD Thesis (Brighton, UK, Sept 29, 2014: Univ of Brighton), 298. Available at: https://cris.brighton.ac.uk/ws/portalfiles/portal/4754859/Final_Thesis_April+2015.pdf.

Collier, D., Sekhon, J. S., and Stark, P. B. (2010). "Preface, editors' introduction: Inference and shoeleather," in *Statistical models and causal inference: A dialog with the social sciences*. Editors D. Collier, J. S. Sekhon, and P. B. Stark 1st ed./Kindle Ed. (New York, NY, USA: Cambridge University Press), xi-xii–xiii-xvi. Available at: https://www.google.com/books/edition/Statistical_Models_and_Causal_Inference/KfPDgsPIDpsC?hl=en&gbpv=1&printsec=frontcover.

Cornell, C. A. (1968). Engineering seismic risk analysis. *Bull. Seismol. Soc. Am.* 58 (5), 1583–1606. doi:10.1785/BSSA0580051583

Crespi, M. G., Kossobokov, V. G., Panza, G. F., and Peresan, A. (2020). Space-time precursory features within ground velocities and seismicity in North-Central Italy. *Pure Appl. Geophys.* 177, 369–386. doi:10.1007/s00024-019-02297-y

Danciu, L., and Giardini, D. (2015). Global seismic hazard assessment program - GSHAP legacy. *Ann. Geophys.* 58 (1), S0109. doi:10.4401/ag-6734

Davis, C., Keilis-Borok, V., Kossobokov, V., and Soloviev, A. (2012). Advance prediction of the March 11, 2011 great east Japan earthquake: A missed opportunity for disaster preparedness. *Int. J. Disaster Risk Reduct.* 1, 17–32. doi:10.1016/j.ijdrr.2012.03.001

Dobran, F. (2010). Further comment on "AGU statement: Investigation of scientists and officials in L'Aquila, Italy, is unfounded". *Eos, Trans. Am. Geophys. Union (AGU)* 91 (42), 384. doi:10.1029/2010EO420007

Dolce, M., and Martinelli, A. (2005). *Inventario e vulnerabilità degli edifici pubblici e strategici dell'Italia Centro-Meridionale - Vol. II - Analisi di Vulnerabilità e Rischio Sismico*. L'Aquila: Istituto Nazionale di Geofisica e Vulcanologia/Gruppo Nazionale per la Difesa dai Terremoti, 187. Available at: https://emidius.mi.ingv.it/GNDT2/Att_scient/Prodotti_consegnati/Dolce_Zuccaro/Volume%202.pdf.

Ellsworth, W. L. (1990). "Earthquake history, 1769-1989," in *The San Andreas fault system, California. U.S. Geological Survey professional paper 1515 - Chpt 6*. Editor R. E. Wallace, 153–187. Available at: http://pubs.usgs.gov/pp/1990/1515/.

Fäh, D., Iodice, C., Suhadolc, P., and Panza, G. F. (1993). A new method for the realistic estimation of seismic ground motion in megacities: The case of Rome. *Earthq. Spectra* 9 (4), 643–668. doi:10.1193/1.1585735

Fischhoff, B., and Kadvany, J. (2011). *Risk: A very short introduction*. New York, NY, USA: Oxford Uni Press, 185. doi:10.1093/actrade/9780199576203.001.0001

Florsch, N., Fäh, D., Suhadolc, P., and Panza, G. F. (1991). Complete synthetic seismograms for high-frequency multimode SH-waves. *Pure Appl. Geophys. (PAGEOPH)* 136, 529–560. doi:10.1007/BF00878586

Frankel, A., Mueller, C., Barnhard, T., Perkins, D., Leyendecker, E. V., Dickman, N., et al. (1996). National seismic-hazard maps: Documentation june 1996. *U.S. Geol. Surv. Open-File Rep.* 96-532, 110. doi:10.3133/ofr96532

P. Gasperini, R. Camassi, C. Mirto, and M. Stucchi (Editors) (2004). *Parametric catalog of Italian earthquakes. Version 2004 (CPTI04)* (Milan: National Institute of Geophysics and Volcanology). Available at: http://emidius.mi.ingv.it/CPTI/.

Gelfand, I. M., Guberman, S. A., Keilis-Borok, V. I., Knopoff, L., Press, F., Ya Ranzman, E., et al. (1976). Pattern recognition applied to earthquake epicenters in California. *Phys. Earth Planet. Interiors* 11 (3), 227–283. doi:10.1016/0031-9201(76)90067-4

Gelfand, I. M., Guberman, S. I., Izvekova, M. L., Keilis-Borok, V. I., and Ja Ranzman, E. (1972). Criteria of high seismicity determined by pattern recognition. *Dev. Geotect.* 13 (1-4), 415–422. doi:10.1016/B978-0-444-41015-3.50028-8

Gelfand, I. M. (1991). Two archetypes in the psychology of Man. *Nonlinear Sci. Today* 1 (4), 11–16. Available at: https://www.kyotoprize.org/wp-content/uploads/2019/07/1989_B.pdf.

Gere, J. M., and Shah, H. C. (1984). *Terra non Firma: Understanding and preparing for earthquakes*. New York, NY, USA: W. H. Freeman, 203.

Gerstenberger, M. C., Marzocchi, W., Allen, T., Pagani, M., Adams, J., Danciu, L., et al. (2020). Probabilistic seismic hazard analysis at regional and national scales: State of the art and future challenges. *Rev. Geophys.* 58 (2), e2019RG000653. doi:10.1029/2019RG000653

Gerstenberger, M. C., Wiemer, S., Jones, L. M., and Reasenberg, P. A. (2005). Real-time forecasts of tomorrow's earthquakes in California. *Nature* 435, 328–331. doi:10.1038/nature03622

Giardini, D., Grünthal, G., Shedlock, K., and Zhang, P. (1999). The GSHAP global seismic hazard map. *Ann. Geophys.* 42 (6), 1225–1230. doi:10.4401/ag-3784

Giardini, D. (1999). The global seismic hazard assessment program (GSHAP) – 1992/1999. *Ann. Geophys.* 42 (6), 957–974. doi:10.4401/ag-3780

Gorshkov, A., Kossobokov, V., and Soloviev, A. (2003). "Recognition of earthquake-prone areas," in *Nonlinear dynamics of the lithosphere and earthquake prediction. Springer series in synergetics*. Editors V. I. Keilis-Borok and A. A. Soloviev (Berlin, Heidelberg, Germany: Springer), 239–310. Available at: https://www.springer.com/gp/book/9783540435280.

Gorshkov, A., and Novikova, O. (2018). Estimating the validity of the recognition results of earthquake-prone areas using the ArcMap. *Acta Geophys.* 66 (5), 843–853. doi:10.1007/s11600-018-0177-3

H. K. Gupta (Editor) (2020). "Encyclopedia of Solid earth geophysics," *Encyclopedia of earth sciences series*. 2nd ed. (Cham, Switzerland: Springer). doi:10.1007/978-3-030-10475-7

Gutenberg, B., and Richter, C. F. (1956). Earthquake magnitude, intensity, energy, and acceleration: (Second paper). *Bull. Seismol. Soc. Am.* 46 (2), 105–145. doi:10.1785/BSSA0460020105

Gutenberg, B., and Richter, C. F. (1944). Frequency of earthquakes in California. *Bull. Seismol. Soc. Am.* 34 (4), 185–188. doi:10.1785/BSSA0340040185

Gutenberg, B., and Richter, C. F. (1949). *Seismicity of the Earth and associated phenomena*. 1st ed. Princeton, NJ, USA: Princeton Univ. Press, 273. Available at: https://archive.org/details/seismicityofthee009299mbp/page/n7/mode/2up.

Gutenberg, B., and Richter, C. F. (1954). *Seismicity of the Earth and associated phenomena*. 2nd ed. Princeton, NJ, USA: Princeton Univ. Press, 310. doi:10.1111/j.2153-3490.1950.tb00313.x

Hanks, T. C. (1997). Imperfect science, uncertainty, diversity, and experts. *Eos, Trans. Am. Geophys. Union (AGU)* 78 (35), 369–377. doi:10.1029/97EO00236

Healy, J. H., Kossobokov, V. G., and Dewey, J. W. (1992). *A test to evaluate the earthquake prediction algorithm, M8*. U.S. Geological Survey Open-File Report 92-401, pp. 23 with 6 Appendices. doi:10.3133/ofr92401

Hough, S. E. (2016). "Chapter 16. Predicting the unpredictable," in *Richter's scale: Measure of an earthquake, measure of a man* (Princeton, N.J., USA: Princeton University Press), 253–268. doi:10.1515/9781400884445-017

Huixian, L., Housner, G. W., Lili, X., and Duxin, H. (2002). *The great tangshan earthquake of 1976*. Pasadena, CA, USA: California Institute of Technology (Caltech): EERL Report 2002-001 (Unpublished. Available at: https://resolver.caltech.edu/CaltechEERL:EERL.2002.001.

Imperiale, A. J., and Vanclay, F. (2019). Reflections on the L'Aquila trial and the social dimensions of disaster risk. *Disaster Prev. Manag.* 28 (4), 434–445. doi:10.1108/DPM-01-2018-0030

Ismail-Zadeh, A., and Kossobokov, V. (2020). "Earthquake prediction, M8 algorithm," in *Encyclopedia of Solid earth geophysics. Encyclopedia of earth sciences series*. Editor H. Gupta 2nd edition (Cham, Switzerland: Springer). doi:10.1007/978-3-030-10475-7_157-1

Iturrarán-Viveros, U., and Sánchez-Sesma, F. J. (2020). "Seismic wave propagation in real media: Numerical modeling approaches," in *Encyclopedia of Solid earth geophysics. Encyclopedia of earth sciences series*. Editor H. Gupta 2nd edition (Cham, Switzerland: Springer). doi:10.1007/978-3-030-10475-7_6-1

Jackson, D. D., and Kagan, Y. Y. (1999). Testable earthquake forecasts for 1999. *Seismol. Res. Lett.* 70 (4), 393–403. doi:10.1785/gssrl.70.4.393

Jordan, T. H., Chen, Y.-T., Gasparini, P., Madariaga, R., Main, I., Marzocchi, W., et al. (2011). Operational earthquake forecasting: State of knowledge and guidelines for utilization. *Ann. Geophys.* 54 (4), 315–391. doi:10.4401/ag-5350

Jordan, T. H., Marzocchi, W., Michael, A. J., and Gerstenberger, M. C. (2014). Operational earthquake forecasting can enhance earthquake preparedness. *Seismol. Res. Lett.* 85 (4), 955–959. doi:10.1785/0220140143

Kanamori, H. (2021). Rules and outliers in seismology–implications for hazard mitigation plenary; SSA annual meeting. Virtual, April 22, 2021; Abstract. *Seismol. Res. Lett.* 92 (2B), 1215. doi:10.1785/0220210025

Kanamori, H. (2014). The diversity of large earthquakes and its implications for hazard mitigation. *Annu. Rev. Earth Planet. Sci.* 42, 7–26. doi:10.1146/annurev-earth-060313-055034

Kantorovich, L. V., Keilis-Borok, V. I., and Molchan, G. M. (1974). "Seismic risk and principles of seismic zoning," in *Seismic design decision analysis series. Internal report No. 43* (Cambridge, MA, USA: Department of Civil Engineering, MIT), 26. Available at: https://nehrpsearch.nist.gov/static/files/NSF/PB80104813.pdf. See also: Seismic Design Decision Analysis, Report R73-58, Structures Publication No. 381, Jan 1, 1974. https://nehrpsearch.nist.gov/static/files/NSF/PB282979.pdf.

Kantorovich, L. V., and Keilis-Borok, V. I. (1991). "Earthquake prediction and decision-making: Social, economic and civil protection aspects," in *Proceedings of the international conference on earthquake prediction: State-of-the-Art, scientific-technical contributions. Strasbourg, France, 15-18 October 1991, CSEM-EMSC, 586-593. (based on "economics of earthquake prediction". In proceedings of the UNESCO conference on seismic risk, paris, France, 1977)*. Available at: https://www.worldcat.org/title/international-conference-on-earthquake-prediction-state-of-the-art-strasbourg-france-15-18-october-1991-scientific-technical-contributions-reprints/oclc/80533359.

Kaufmann, D., and Penciakova, V. (2011). *Japan's triple disaster: Governance and the earthquake, tsunami and nuclear crises*. Brookings: Op-Ed. Available at: https://www.brookings.edu/opinions/japans-triple-disaster-governance-and-the-earthquake-tsunami-and-nuclear-crises/(Accessed Mar 27, 2022).

Keilis-Borok, V. I., and Kossobokov, V. G. (1990). Premonitory activation of earthquake flow: Algorithm M8. *Phys. Earth Planet. Interiors* 61 (1-2), 73–83. doi:10.1016/0031-9201(90)90096-G

Keilis-Borok, V. I., Kronrod, T. L., and Molchan, G. M. (1984). Seismic risk for the largest cities of the world; intensity VIII or more. *Geneva Pap. Risk Insur. – Issues Pract.* 9 (32), 255–270. doi:10.1057/GPP.1984.14

Keilis-Borok, V. I. (1990). The lithosphere of the Earth as a nonlinear system with implications for earthquake prediction. *Rev. Geophys.* 28 (1), 19–34. doi:10.1029/RG028i001p00019

Keylis-Borok, V. I., and Malinovskaya, L. N. (1964). One regularity in the occurrence of strong earthquakes. *J. Geophys. Res.* 69 (14), 3019–3024. doi:10.1029/JZ069i014p03019

Klügel, J. U. (2007). Error inflation in probabilistic seismic hazard analysis. *Eng. Geol.* 90 (3-4), 186–192. doi:10.1016/j.enggeo.2007.01.003

Klügel, J. U. (2011). Uncertainty analysis and expert judgment in seismic hazard analysis. *Pure Appl. Geophys.* 168 (1), 27–53. doi:10.1007/s00024-010-0155-4

Kossobokov, V. (2008). "Testing earthquake forecast/prediction methods: "Real-time forecasts of tomorrow's earthquakes in California"," in *Abstracts of the contributions of the EGU general Assembly 2008, Vienna, Austria, 13-18 April 2008 (CD-ROM). Geophysical research Abstract 10: EGU2008-A-07826*. Available at: https://www.geophysical-research-abstracts.net/egu2008.html.

Kossobokov, V. (2011). Are mega earthquakes predictable? *Izvestiya, Atmos. Ocean.* 46 (8), 951–961. doi:10.1134/S0001433811080032

Kossobokov, V. G. (2014). "Chapter 18 - times of increased probabilities for occurrence of catastrophic earthquakes: 25 Years of hypothesis testing in real time," in *Earthquake hazard, risk, and disasters*. Editors M. Wyss and J. Shroder, 477–504. doi:10.1016/B978-0-12-394848-9.00018-3

Kossobokov, V. G. (2013). Earthquake prediction: 20 years of global experiment. *Nat. Hazards* 69 (2), 1155–1177. doi:10.1007/s11069-012-0198-1

Kossobokov, V. G. (2021). "Hazards, risks, and predictions," in *Earthquakes and sustainable infrastructure: Neodeterministic (NDSHA) approach guarantees prevention rather than cure*. Editors G. Panza, V. Kossobokov, E. Laor, and B. DeVivo (Amsterdam, Netherlands: Elsevier), 1–25. doi:10.1016/B978-0-12-823503-4.00031-2

Kossobokov, V. G., Keilis-Borok, V. I., and Smith, S. W. (1990). Localization of intermediate term earthquake prediction. *J. Geophys. Res.* 95 (B12), 19763–19772. doi:10.1029/JB095iB12p19763

Kossobokov, V. G., and Mazhkenov, S. A. (1994). "On similarity in the spatial distribution of seismicity computational seismology and geodynamics (volume 1, selected papers from volumes 22 and 23 of Vychislitel'naya seysmologiya," in *Article in computational seismology and geodynamics · March 2013)*. Editors D. K. Chowdhury and N. N. Biswas (Washington DC: AGU, The Union), 6–15. doi:10.1029/CS001p0006

Kossobokov, V. G., and Mazhkenov, S. A. (1988). "Spatial characteristics of similarity for earthquake sequences: Fractality of seismicity," in *Lecture notes of the ICTP workshop on global geophysical informatics with applications to research in earthquake prediction and reduction of seismic risk (trieste, Italy, 15 Nov–16 dec, 1988)*. Available at: http://indico.ictp.it/event/a02153/contribution/3/material/0/0.pdf.

Kossobokov, V. G. (2010c). *Natural hazards at extreme: Predictive understanding versus complex reality*. Abstract in EOS Trans AGU 91(26). Fall Supplement: Abstract NH14A-01. Available at: https://eos.org/current-issues.

Kossobokov, V. G., and Nekrasova, A. K. (2012). Global seismic hazard assessment program maps are erroneous. *Seism. Instrum.* 48 (2), 162–170. doi:10.3103/S0747923912020065

Kossobokov, V. G., and Nekrasova, A. K. (2010). *Global seismic hazard assessment program maps are misleading*. Abstract in EOS Trans AGU 91(52). Fall Meeting of the American Geophysical Union: Abstract U13A-0020.

Kossobokov, V. G. (2006a). Quantitative earthquake prediction on global and regional scales. *AIP Conf. Proc.* 825, 32–50. doi:10.1063/1.2190730

Kossobokov, V. G., Romashkova, L. L., Keilis-Borok, V. I., and Healy, J. H. (1999). Testing earthquake prediction algorithms: Statistically significant advance prediction of the largest earthquakes in the Circum-pacific, 1992–1997. *Phys. Earth Planet. Interiors* 111 (3-4), 187–196. doi:10.1016/S0031-9201(98)00159-9

Kossobokov, V. G. (2010a). "Scaling laws and earthquake predictability," in Assessment of Seismic Risk. Lecture presented at the Advanced Conference on Seismic Risk Mitigation and Sustainable Development. The Abdus Salam International Centre for Theoretical Physics (ICTP), Miramare, Trieste - Italy, 10 - 14 May 2010, 71. doi:10.13140/RG.2.2.32855.09121

Kossobokov, V. G., and Shchepalina, P. D. (2020). Times of increased probabilities for occurrence of world's largest earthquakes: 30 Years hypothesis testing in real time. *Izvestiya, Phys. Solid Earth* 56 (1), 36–44. doi:10.1134/S1069351320010061

Kossobokov, V. G., and Soloviev, A. A. (2018). РасПознавание образов в задачач оценки сейсмической оПасности. *Chebyshevskii Sb.* 19 (4), 55–90. (In Russian with English Abstract). doi:10.22405/2226-8383-2018-19-4-55-90

Kossobokov, V. G. (2010b). "Statistics of extreme seismic events and their predictability," in ESOF 2010 Programme Book. Proceedings of the Euroscience Open Forum, Torino, Italy, 2-7 Jul 2010, 56. Available at: https://www.esof.eu/esof-torino/.

Kossobokov, V. G. (2006b). Testing earthquake prediction methods: «the West Pacific short-term forecast of earthquakes with magnitude MwHRV ≥ 5.8». *Tectonophysics* 413 (1-2), 25–31. doi:10.1016/j.tecto.2005.10.006

Kossobokov, V. G. (2005b). "The 26 december 2004 greatest asian quake: When to expect the next one? Statement," in Special Session on the Indian Ocean Disaster: risk reduction for a safer future, UN World Conference on Disaster Reduction, Kobe, Hyogo, Japan, 18-22 January 2005, 13. doi:10.13140/RG.2.2.11464.14087

Kossobokov, V., Peresan, A., and Panza, G. F. (2015b). On operational earthquake forecast and prediction problems. *Seismol. Res. Lett.* 86 (2), 287–290. doi:10.1785/0220140202

Kossobokov, V., Peresan, A., and Panza, G. F. (2015a). Reality check: Seismic hazard models you can trust. *Eos, Trans. Am. Geophys. Union (AGU)* 96 (13), 9–11. doi:10.1029/2015EO031919

Kossobokov, V. (2005a). "Quantitative earthquake prediction on global and regional scales," in *Quake: Earthquake seminars, 2005 Archives. (December 15, 2005)* (CA, USA: USGS Menlo Park). Available at: http://quake.wr.usgs.gov/resources/seminars.php?show=2005_archives.

Kossobokov, V., and Shebalin, P. (2003). "Earthquake prediction," in *Nonlinear dynamics of the lithosphere and earthquake prediction. Springer series in synergetics*. Editors V. I. Keilis-Borok and A. A. Soloviev (Berlin, Heidelberg, Germany: Springer), 141–207. doi:10.1007/978-3-662-05298-3_4

Kossobokov, V. (2020). "Unified scaling law for earthquakes that generalizes the fundamental gutenberg-richter relationship," in *Encyclopedia of Solid earth geophysics. Encyclopedia of earth sciences series*. Editor H. Gupta 2nd edition (Cham, Switzerland: Springer). doi:10.1007/978-3-030-10475-7_257-1

Krinitzsky, E. L. (1993a). Earthquake probability in engineering. Part 1. The use and misuse of expert opinion. The third Richard H. Jahns distinguished lecture in engineering geology. *Eng. Geol.* 33 (4), 257–288. doi:10.1016/0013-7952(93)90030-G

Krinitzsky, E. L. (1993b). Earthquake probability in engineering—Part 2: Earthquake recurrence and limitations of gutenberg-richter b-values for the engineering of critical structures. *Eng. Geol.* 36 (1-2), 1–52. doi:10.1016/0013-7952(93)90017-7

Krinitzsky, E. L. (1995). Problems with logic trees in earthquake hazard evaluation. *Eng. Geol.* 39 (1-2), 1–3. doi:10.1016/0013-7952(94)00060-F

La Mura, C., Yanovskaya, T. B., Romanelli, F., and Panza, G. F. (2011). Three-dimensional seismic wave propagation by modal summation: Method and validation. *Pure Appl. Geophys.* 168, 201–216. doi:10.1007/s00024-010-0165-2

Lowrance, W. W. (1976). *Of acceptable risk: Science and the determination of safety*. Los Altos, CA, USA: William Kaufmann, 180. Available at: https://eric.ed.gov/?q=ddt&pg=2&id=ED159027.

Mandelbrot, B. B. (1967). How long is the coast of britain? Statistical self-similarity and fractional dimension. *Science* 156 (3775), 636–638. doi:10.1126/science.156.3775.636

Marincioni, F., Appiotti, F., Ferretti, M., Antinori, C., Melonaro, P., Pusceddu, A., et al. (2012). Perception and communication of seismic risk: The 6 April 2009 L'Aquila earthquake case study. *Earthq. Spectra* 28 (1), 159–183. First Published February 1, 2012. doi:10.1193/1.3672928

May, P. J. (2001). Societal perspectives about earthquake performance: The fallacy of "acceptable risk". *Earthq. Spectra* 17 (4), 725–737. doi:10.1193/1.1423904

McEntire, D. A., Fuller, C., Johnston, C. W., and Weber, R. (2002). A comparison of disaster paradigms: The search for a holistic policy guide. *Public Adm. Rev.* 62 (3), 267–281. doi:10.1111/1540-6210.00178

McEntire, D. A. (2004). Tenets of vulnerability: An assessment of a fundamental disaster concept. *J. Emerg. Manag.* 2 (2), 23–29. doi:10.5055/jem.2004.0020

McGuire, R. K. (2008). Probabilistic seismic hazard analysis: Early history. *Earthq. Eng. Struct. Dyn.* 37 (3), 329–338. doi:10.1002/eqe.765

Meletti, C., Marzocchi, W., D'Amico, V., Lanzano, G., Luzi, L., Martinelli, F., et al. (2021). The new Italian seismic hazard model (MPS19). *Ann. Geophys.* 64 (1), SE112. doi:10.4401/ag-8579

G. Michel (Editor) (2018). *Risk modeling for hazards and disasters* (Cambridge, MA, USA: Elsevier), 318. doi:10.1016/C2015-0-01065-6

Mignan, A., Ouillon, G., Sornette, D., and Freund, F. (2021). Global earthquake forecasting system (GEFS): The challenges ahead. *Eur. Phys. J. Special Top.* 230, 473–490. doi:10.1140/epjst/e2020-000261-8

Mileti, D. S., and Fitzpatrick, C. (1992). The causal sequence of risk communication in the parkfield earthquake prediction experiment. *Risk Anal.* 12 (3), 393–400. doi:10.1111/j.1539-6924.1992.tb00691.x

Mitchell, T. (2014). *Seven myths about disasters*. London, UK: Overseas Development Institute ODI. Available at: https://news.trust.org/item/20141103115234-a5v2c/ (Accessed Mar 27, 2022).

Molchan, G., Kronrod, T., and Panza, G. F. (1997). Multi-scale seismicity model for seismic risk. *Bull. Seismol. Soc. Am.* 87 (5), 1220–1229. doi:10.1785/BSSA0870051220

Molchan, G. M. (1997). Earthquake prediction as a decision-making problem. *Pure Appl. Geophys.* 149, 233–247. doi:10.1007/BF00945169

Molchan, G. M. (2003). "Earthquake prediction strategies: A theoretical analysis," in *Nonlinear dynamics of the lithosphere and earthquake prediction. Springer series in synergetics*. Editors V. I. Keilis-Borok and A. A. Soloviev (Berlin, Heidelberg, Germany: Springer), 209–237. doi:10.1007/978-3-662-05298-3_5

Mualchin, L. (2011). "History of modern earthquake hazard mapping and assessment in California using a deterministic or scenario approach," in *Advanced seismic hazard assessment. Topical volume 168, Part II: Regional seismic hazard and seismic microzonation case studies. Pure and applied geophysics (PAGEOPH) SI 168 (II)*. Editors G. Panza, K. Irikura, M. Kouteva, A. Peresan, Z. Wang, and R. Saragoni (Basel, Switzerland: Birkhäuser), 383–407. doi:10.1007/s00024-010-0121-1

Mulargia, F., Stark, P. B., and Geller, R. J. (2017). Why is probabilistic seismic hazard analysis (PSHA) still used? *Phys. Earth Planet. Interiors* 264, 63–75. doi:10.1016/j.pepi.2016.12.002

Nekrasova, A. K., Kossobokov, V. G., Parvez, I. A., and Tao, X. (2020). Unified scaling law for earthquakes as applied to assessment of seismic hazard and associate risks. *Izvestiya, Phys. Solid Earth* 56 (1), 83–94. doi:10.1134/S1069351320010097

Nekrasova, A., and Kossobokov, V. (2002). *Generalizing the Gutenberg-Richter scaling law*. Abstract in EOS Trans AGU 83(47). Fall Meeting of the American Geophysical Union: Abstract NG62B-0958. Available at: https://ui.adsabs.harvard.edu/abs/2002AGUFMNG62B0958N/abstract.

Nekrasova, A., Kossobokov, V., Parvez, I. A., and Tao, X. (2015b). Seismic hazard and risk assessment based on the unified scaling law for earthquakes. *Acta Geod. Geophys.* 50, 21–37. doi:10.1007/s40328-014-0082-4

Nekrasova, A., Kossobokov, V., Peresan, A., and Magrin, A. (2014). The comparison of the NDSHA, PSHA seismic hazard maps and real seismicity for the Italian territory. *Nat. Hazards* 70 (1), 629–641. doi:10.1007/s11069-013-0832-6

Nekrasova, A., and Kossobokov, V. (2019). "Unified scaling law for earthquakes: Global map of parameters," in *ISC seismological dataset repository*. doi:10.31905/XT753V44

Nekrasova, A., Peresan, A., Kossobokov, V. G., and Panza, G. F. (2015a). "A new probabilistic shift away from seismic hazard reality in Italy?," in *Nonlinear mathematical physics and natural hazards. Springer proceedings in physics (SPPHY volume 163)*. Editors B. Aneva and M. Kouteva-Guentcheva (Cham, Switzerland: Springer), 83–103. doi:10.1007/978-3-319-14328-6_7

NEPEC (2016). *Evaluation of earthquake predictions: Recommendations to the USGS earthquake hazards program from the national earthquake prediction evaluation Council (NEPEC), september 2016*, 6. Available at: https://www.usgs.gov/media/files/recommendations-nepec-evaluating-earthquake-predictions.

Nishioka, T., and Mualchin, L. (1997). Deterministic seismic hazard map of Japan from inland maximum credible earthquakes for engineering. *J. Struct. Mech. Earthq. Eng.* 570, 11–19. doi:10.2208/jscej.1997.570_11

Nishioka, T., and Mualchin, L. (1996). *Deterministic seismic hazard map of Japan: Based on inland maximum credible earthquakes*. Sacramento, CA, USA: California Dept. of Transportation, Engineering Service Center, Office of Earthquake Engineering.

Nöggerath, J., Geller, R. J., and Gusiakov, V. K. (2011). Fukushima: The myth of safety, the reality of geoscience. *Bull. Atomic Sci.* 67 (5), 37–46. doi:10.1177/0096340211421607

Okal, E. (2019). Energy and magnitude: A historical perspective. *Pure Appl. Geophys.* 176, 3815–3849. doi:10.1007/s00024-018-1994-7

Okubo, P. G., and Aki, K. (1987). Fractal geometry in the san Andreas fault system. *J. Geophys. Res.* 92 (B1), 345–356. doi:10.1029/JB092iB01p00345

Panza, G. F., and Bela, J. (2020). "Ndsha: A new paradigm for reliable seismic hazard assessment," in *Geo-hazards due to large earthquakes (with contributions from the International Symposium commemorating the 10th anniversary of the 2008 Wenchuan earthquake). Engineering geology SI 275*. Editors T. van Asch, N. Rengers, and Q. Xu (London, UK: Elsevier), 14. Article 105403. doi:10.1016/j.enggeo.2019.105403

Panza, G. F., Kossobokov, V., Peresan, A., and Nekrasova, A. (2014). "Why are the standard probabilistic methods of estimating seismic hazard and risks too often wrong?," in *Earthquake hazard, risk, and disasters*. Editors M. Wyss and J. Shroder (London, UK: Elsevier), 309–357. doi:10.1016/B978-0-12-394848-9.00012-2

Panza, G. F., La Mura, C., Peresan, A., Romanelli, F., and Vaccari, F. (2012). Seismic hazard scenarios as preventive tools for a disaster resilient society. *Adv. Geophys.* 53, 93–165. doi:10.1016/B978-0-12-380938-4.00003-3

Panza, G. F., Peresan, A., and La Mura, C. (2013). "Seismic hazard and strong motion: An operational neodeterministic approach from national to local scale," in *Geophysics and geochemistry, Eds. UNESCO-EOLSS joint committee, in Encyclopedia of life support systems (EOLSS), developed under the Auspices of the UNESCO* (Oxford, UK: Eolss Publishers). Available at: http://www.eolss.net.

Panza, G. F., and Romanelli, F. (2001). Beno Gutenberg contribution to seismic hazard assessment and recent progress in the European–Mediterranean region. *Earth-Science Rev.* 55 (1-2), 165–180. doi:10.1016/S0012-8252(01)00051-4

Panza, G. F., Romanelli, F., and Vaccari, F. (2001). Seismic wave propagation in laterally heterogeneous anelastic media: Theory and applications to seismic zonation. *Adv. Geophys.* 43, 1–95. doi:10.1016/S0065-2687(01)80002-9

Panza, G. F. (1985). Synthetic seismograms: The Rayleigh waves modal summation. *J. Geophys.* 58 (1), 125–145. Available at: https://geophysicsjournal.com/article/67.

Panza, G. F., Vaccari, F., Costa, G., Suhadolc, P., and Fäh, D. (1996). Seismic input modelling for Zoning and microzoning. *Earthq. Spectra* 12 (3), 529–566. doi:10.1193/1.1585896

Panza, G., Irikura, K., Kouteva, M., Peresan, A., Wang, Z., and Saragoni, R. (2011). "Advanced seismic hazard assessment, Preface," in *Advanced seismic hazard assessment. Topical volume 168, Part I: Seismic hazard assessment. Pure and applied geophysics (PAGEOPH) SI 168 (I)*. Editors G. Panza, K. Irikura, M. Kouteva, A. Peresan, Z. Wang, and R. Saragoni (Basel, Switzerland: Birkhäuser), 1–9. doi:10.1007/s00024-010-0179-9

G. Panza, V. Kossobokov, E. Laor, and B. DeVivo (Editors) (2021). *Earthquakes and sustainable infrastructure: Neodeterministic (NDSHA) approach guarantees prevention rather than cure* (Amsterdam, Netherlands: Elsevier), 672. doi:10.1016/C2020-0-00052-6

Papadopoulos, G. A., Charalampakis, M., Fokaefs, A., and Minadakis, G. (2010). Strong foreshock signal preceding the L'Aquila (Italy) earthquake (M_w~6.3) of 6~April~2009. *Nat. Hazards Earth Syst. Sci.* 10 (1), 19–24. doi:10.5194/nhess-10-19-2010

Parvez, I. A., Nekrasova, A., and Kossobokov, V. (2014). Estimation of seismic hazard and risks for the Himalayas and surrounding regions based on Unified Scaling Law for Earthquakes. *Nat. Hazards* 71 (1), 549–562. doi:10.1007/s11069-013-0926-1

Paskaleva, I., Dimova, S., Panza, G. F., and Vaccari, F. (2007). An earthquake scenario for the microzonation of Sofia and the vulnerability of structures designed by use of the Eurocodes. *Soil Dyn. Earthq. Eng.* 27 (11), 1028–1041. doi:10.1016/j.soildyn.2007.03.004

Peresan, A., Kossobokov, V. G., and Panza, G. F. (2012b). Operational earthquake forecast/prediction. *Rend. Fis. Acc. Lincei* 23, 131–138. doi:10.1007/s12210-012-0171-7

Peresan, A., Kossobokov, V. G., Romashkova, L., and Panza, G. F. (2005). Intermediate-term middle-range earthquake predictions in Italy: A review. *Earth-Science Rev.* 69 (1-2), 97–132. doi:10.1016/j.earscirev.2004.07.005

Peresan, A. (2018). "Recent developments in the detection of seismicity patterns for the Italian region," in *Pre-earthquake processes: A multi-disciplinary approach to earthquake prediction studies. AGU geophysical monograph series*. Editors D. Ouzounov, S. Pulinets, K. Hattori, and P. Taylor (New York, NY, USA: Wiley), Vol. 234, 149–172. doi:10.1002/9781119156949.ch9

Peresan, A., Vaccari, F., Magrin, A., Romanelli, F., and Panza, G. F. (2012a). "Ground motion modelling and seismic hazard assessment," in VRCs on EGI and Regional Infrastructures. Proceedings Of Science (POS)EGCIF12-EMITC2)132, EGI Community Forum 2012/EMI Second Technical Conference, ed. F. Ruggieri, 8-9. EGI Community Forum 2012/EMI Second Technical Conference, Munich, Germany, 26-30 Mar, 2012. doi:10.22323/1.162.0132

Peresan, A., Zuccolo, E., Vaccari, F., Gorshkov, A., and Panza, G. F. (2011). "Neo-deterministic seismic hazard and pattern recognition techniques: Time-dependent scenarios for north-eastern Italy," in *Advanced seismic hazard assessment. Topical volume 168, Part II: Regional seismic hazard and seismic microzonation case studies. Pure and applied geophysics (PAGEOPH) SI 168 (II)*. Editors G. Panza, K. Irikura, M. Kouteva, A. Peresan, Z. Wang, and R. Saragoni (Basel, Switzerland: Birkhäuser), 583–607. doi:10.1007/s00024-010-0166-1

Peterson, D. W. (1988). Volcanic hazards and public response. *J. Geophys. Res.* 93 (B5), 4161–4170. doi:10.1029/JB093iB05p04161

Pietrucci, P. (2016). Voices from the seismic crater in the trial of the major risk committee: A local counternarrative of "the L'Aquila seven". *Interface a J. about Soc. movements* 8 (2), 261–285. Available at: http://www.interfacejournal.net/wordpress/wp-content/uploads/2016/12/Interface-8-2-Pietrucci.pdf.

Ranguelo, B. (2011). *Natural Hazards –nonlinearities and assessment*. Sofia, Bulgaria: Acad. Publ. House (BAS, 327.

Ranguelov, B., and Ivanov, Y. (2017). Fractal properties of the elements of PlateTectonics. *J. Min. Geol. Sci.* 60 (1), 83–89.

Richter, C. F. (1935). An instrumental earthquake magnitude scale. *Bull. Seismol. Soc. Am.* 25 (1), 1–32. doi:10.1785/BSSA0250010001

Richter, C. F. (1964). Discussion of paper by V.I. Keylis-Borok and L.N. Malinovskaya, 'One regularity in the occurrence of strong earthquakes. *J. Geophys. Res.* 69 (14), 3025. doi:10.1029/JZ069i014p03025

Rugarli, P., Vaccari, F., and Panza, G. (2019). Seismogenic nodes as a viable alternative to seismogenic zones and observed seismicity for the definition of seismic hazard at regional scale. *Vietnam J. Earth Sci.* 41 (4), 289–304. doi:10.15625/0866-7187/41/4/14233

Sadovsky, M. A., Bolkhovitinov, L. G., and Pisarenko, V. F. (1982). On the property of the discreteness of rocks. Izvestiya of the USSR Academy of Sciences. *Fiz. Zemli* 12, 3–18. (in Russian).

Sadovsky, M. A. (2004). The self similarity of geodynamic processes. Report of Academician M.A. Sadovsky - Laureate of the M.V. *Lomonosov Gold Medal. (in Russ.)* 35, 23–32. Available at: https://www.itpz-ran.ru/wp-content/vs/35/v35_023_Sadovsky.pdf.

Saltelli, A., Dankel, D. J., Di Fiore, M., Holland, N., and Pigeon, M. (2022). Science, the endless frontier of regulatory capture. *Futures* 135, 102860. doi:10.1016/j.futures.2021.102860

Scawthorn, C. (2006). "A brief history of seismic risk assessment," in *Risk assessment, modeling and decision support. Risk, governance and society series*. Editors A. Bostrom, S. French, and S. Gottlieb (Berlin, Heidelberg: Springer), Vol. 14, 5–81. doi:10.1007/978-3-540-71158-2_2

SCEC (2018). The 2018 SCEC annual meeting. Proceedings Volume XXVIII. Available at: https://files.scec.org/s3fs-public/SCEC2018Proceedings.pdf.

Shaw, J. H., and Shearer, P. M. (1999). An elusive blind-thrust fault beneath metropolitan Los Angeles. *Science* 283 (5407), 1516–1518. doi:10.1126/science.283.5407.1516

Silva, V., Amo-Oduro, D., Calderon, A., Costa, C., Dabbeek, J., Despotaki, V., et al. (2020). Development of a global seismic risk model. *Earthq. Spectra* 36 (1), 372–394. doi:10.1177/8755293019899953

SISMA-ASI (2009). "The SISMA project: A pre-operative seismic hazard monitoring system", by Chersich, M., A. Amodio, A. Francia, and C. Sparpaglione, EGU General Assembly, 19-24 April, 2009, Vienna. *Geophys. Res. Abstr.* 11, EGU2009–10946. Available at: http://meetingorganizer.copernicus.org/EGU2009/EGU2009-10946.pdf.

Soloviev, A., and Kossobokov, V. G. (2010). *Seismic hazard and earthquake predictability*. Abstract in EOS Trans AGU 91(26). The Meeting of the Americas: Abstract U13B-08. Available at: https://sciencedocbox.com/Geology/70644784-Seismic-hazard-and-earthquake-predictability.html.

Sorensen, J. H., and Mileti, D. S. (1987). "Public warning needs," in *Proceedings of conference XL: A workshop on the U.S. Geological survey's role in hazards warnings. U.S. Geological Survey open-file report 87-269*, 9–75. Available at: https://www.amazon.com/Proceedings-Conference-XL-Geological-Open-File/dp/1287007430.

Sornette, D., Ouillon, G., Mignan, A., and Freund, F. (2021). Preface to the Global Earthquake Forecasting System (GEFS) special issue: Towards using non-seismic precursors for the prediction of large earthquakes. *Eur. Phys. J. Special Top.* 230, 1–5. doi:10.1140/epjst/e2020-000242-4

SSHAC (1997). "Senior seismic hazard analysis committee Recommendations for probabilistic seismic hazard analysis: Guidance on uncertainty and use of experts," in *NUREG/CR-6372* (Washington DC, USA: US Nuclear Regulatory Commission), Vol. 1, 885–XXI. Appendices: A 72, B 511, C 10, D 7, E 11, F 35, G 97, H 16, I 30, J 64. NUREG/CR-6372, Volume 1 (PDF - 16.4 MB).

Stacey, F. D., and Davis, P. M. (2020). "Earth, density distribution," in *Encyclopedia of Solid earth geophysics. Encyclopedia of earth sciences series*. Editor H. Gupta 2nd edition (Cham, Switzerland: Springer). First Online 22 Jan 2020. doi:10.1007/978-3-030-10475-7_100-1

Stark, P. B. (2018). Before reproducibility must come preproducibility WORLD VIEW: A personal take on events. *Nature* 557, 613. doi:10.1038/d41586-018-05256-0

Stark, P. B. (2017). *Pay No attention to the model behind the curtain*. Berkley, California, USA: University of California at Berkley, 21. Available at: https://www.stat.berkeley.edu/~stark/Preprints/eucCurtain15.pdf (Accessed Mar 27, 2022).

Stark, P. B. (2022). "Pay no attention to the model behind the curtain," in PAGEOPH topical volume 179 (11), Geophysical studies of geodynamics and natural hazards in the northwestern pacific region. Editors A. Soloviev, V. Kossobokov, and J. Eichelberger (Basel, Switzerland: Birkhäuser). 179 (11), 4121–4145. doi:10.1007/s00024-022-03137-2

Stark, P. B., and Saltelli, A. (2018). Cargo-cult statistics and scientific crisis. *Significance* 15 (4), 40–43. doi:10.1111/j.1740-9713.2018.01174.x

Stein, S., Geller, R. J., and Liu, M. (2012). Why earthquake hazard maps often fail and what to do about it. *Tectonophysics* 562-563, 1–25. doi:10.1016/J.TECTO.2012.06.047

Tanner, A., Chang, S. E., and Elwood, K. J. (2020). Incorporating societal expectations into seismic performance objectives in building codes. *Earthq. Spectra* 36 (4), 2165–2176. doi:10.1177/8755293020919417

Tierney, K. (2014). "Communities and societies at risk," in *The social roots of risk: Producing disasters, promoting resilience. High reliability and crisis management series, K. Tierney* (Redwood City, CA, USA: Stanford University Press), 125–159. doi:10.1515/9780804791403

Trendafiloski, G., Rosset, P., Wyss, M., Wiemer, S., Bonjour, C., and Cua, G. (2009). *Estimation of damage and human losses due to earthquakes worldwide - QLARM strategy and experience*. Presentation at EGU General Assembly 2009: 5027. Held 19-24 April, 2009 in Vienna, Austria. Available at: http://meetings.copernicus.org/egu2009.

Udias, A. (2002). Ethical problems in seismology. *Seismol. Res. Lett.* 73 (1), 3–4. doi:10.1785/gssrl.73.1.3

Vaccari, F., and Magrin, A. (2019). "NDSHA computational aspects of the neo-deterministic seismic hazard assessment," in *Resilience and sustainability of cities in hazardous environments*. Editor F. Dobran (Trieste: GVES), 202–212.

Vere-Jones, D. (2001). The marriage of statistics and seismology. *J. Appl. Probab.* 38A, 1–5. doi:10.1017/s0021900200112604

Wang, K., and Rogers, G. C. (2014). Earthquake preparedness should not fluctuate on a daily or weekly basis. *Seismol. Res. Lett.* 85 (3), 569–571. doi:10.1785/0220130195

Wachinger, G., Renn, O., Begg, C., and Kuhlicke, C. (2013). The risk perception paradox—implications for governance and communication of natural hazards. *Risk Anal.* 33 (6), 1049–1065. doi:10.1111/j.1539-6924.2012.01942.x

Wang, K. (2012). "An unsurprising surprise," in *American association for the Advancement of science (AAAS) annual meeting, 16-20 feb, 2012, Vancouver, BC Canada: Abstract 7167*. Available at: https://aaas.confex.com/aaas/2012/webprogram/Paper7167.html.

Wang, K., Sun, T., Brown, L., Hino, R., Tomita, F., Kido, M., et al. (2018). Learning from crustal deformation associated with the M9 2011 Tohoku-oki earthquake. *Geosphere* 14 (2), 552–571. doi:10.1130/GES01531.1

Wang, Z. M. (2011). "Seismic hazard assessment: Issues and alternatives," in *Advanced seismic hazard assessment. Topical volume 168, Part I: Seismic hazard assessment. Pure and applied geophysics (PAGEOPH) SI 168 (I)*. Editors G. Panza, K. Irikura, M. Kouteva, A. Peresan, Z. Wang, and R. Saragoni (Basel, Switzerland: Birkhäuser), 11–25. doi:10.1007/s00024-010-0148-3

Wang, Z. (2008). "Understanding seismic hazard and risk: A gap between engineers and seismologists," in *14th world conference on earthquake engineering, Oct 12–17, 2008, beijing, China, paper S27-001*, 11. Available at: http://invenio.itam.cas.cz/record/12057?ln=en.

Wasserburg, G. J. (2010). Comment on "AGU statement: Investigation of scientists and officials in L'Aquila, Italy, is unfounded". *Eos, Trans. Am. Geophys. Union (AGU)* 91 (42), 384. doi:10.1029/2010EO420006

White, G. F. (2005). Foreword. *Mitig. Adapt. Strategies Glob. Change* 10 (3), 333–334. doi:10.1007/s11027-005-0049-4

Wiggins, J. H. (1972). *The balanced risk concept, new approach to earthquake building codes*. Civil Enginering — ASCE, (August 1972), 55–59.

Wyss, M. (1991). Evaluation of proposed earthquake precursors. *Eos Trans. Am. Geophys. Union* 72 (38), 411. doi:10.1029/90EO10300

Wyss, M., Nekrasova, A., and Kossobokov, V. (2012). Errors in expected human losses due to incorrect seismic hazard estimates. *Nat. Hazards* 62 (3), 927–935. doi:10.1007/s11069-012-0125-5

Wyss, M., and Rosset, P. (2013). Mapping seismic risk: The current crisis. *Nat. Hazards* 68, 49–52. doi:10.1007/s11069-012-0256-8

Wyss, M. (1997). Second round of evaluations of proposed earthquake precursors. *Pure Appl. Geophys.* 149, 3–16. doi:10.1007/BF00945158

Wyss, M. (2015). Testing the basic assumption for probabilistic seismic-hazard assessment: 11 failures. *Seismol. Res. Lett.* 86 (5), 1405–1411. doi:10.1785/0220150014

Zhang, Y., Meng, Q., Ouillon, G., Zhang, L., Hu, D., Ma, W., et al. (2021). Long-term statistical evidence proving the correspondence between tir anomalies and earthquakes is still absent topical collection - the global earthquake forecasting system: Towards using non-seismic precursors for the prediction of large earthquakes. *Eur. Phys. J. Special Top.* 230 (1), 133–150. doi:10.1140/epjst/e2020-000248-4

Zhang-li, C., Pu-xiong, L., De-yu, H., Da-lin, Z., Feng, X., and Zhi-dong, W. (1984). "Characteristics of regional seismicity before major earthquakes,". 1984: UNESCO (063.4)/P2 in *Earthquake prediction: Proceedings of the international symposium on earthquake prediction* (Paris, France: UNESCO), 505–521. Available at: https://digitallibrary.un.org/record/1058?ln=en.

Zuccolo, E., Vaccari, F., Peresan, A., and Panza, G. F. (2011). "Neo-deterministic and probabilistic seismic hazard assessments: A comparison over the Italian territory," in *Advanced seismic hazard assessment. Topical volume 168, Part I: Seismic hazard assessment. Pure and applied geophysics (PAGEOPH) SI 168 (I)*. Editors G. Panza, K. Irikura, M. Kouteva, A. Peresan, Z. Wang, and R. Saragoni (Basel, Switzerland: Birkhäuser), 69–83. doi:10.1007/s00024-010-0151-8

frontiers | Frontiers in Earth Science

TYPE Original Research
PUBLISHED 03 May 2023
DOI 10.3389/feart.2023.1112132

Check for updates

OPEN ACCESS

EDITED BY
Fuqiong Huang,
China Earthquake Networks Center, China

REVIEWED BY
Yong Zheng,
China University of Geosciences Wuhan, China
Ning Gu,
Southern University of Science and Technology, China

*CORRESPONDENCE
Xiaofeng Tian,
tianxf@gec.ac.cn

SPECIALTY SECTION
This article was submitted to Solid Earth Geophysics, a section of the journal Frontiers in Earth Science

RECEIVED 30 November 2022
ACCEPTED 27 March 2023
PUBLISHED 03 May 2023

CITATION
Zhou M, Tian X, Yang Z, Liu Q and Gao Z (2023), The 3-D shallow velocity structure and sedimentary structure of 2017 Ms6.6 Jinghe earthquake source area derived from dense array observations of ambient noise. *Front. Earth Sci.* 11:1112132. doi: 10.3389/feart.2023.1112132

COPYRIGHT
© 2023 Zhou, Tian, Yang, Liu and Gao. This is an open-access article distributed under the terms of the Creative Commons Attribution License (CC BY). The use, distribution or reproduction in other forums is permitted, provided the original author(s) and the copyright owner(s) are credited and that the original publication in this journal is cited, in accordance with accepted academic practice. No use, distribution or reproduction is permitted which does not comply with these terms.

The 3-D shallow velocity structure and sedimentary structure of 2017 Ms6.6 Jinghe earthquake source area derived from dense array observations of ambient noise

Ming Zhou, Xiaofeng Tian*, Zhuoxin Yang, Qiaoxia Liu and Zhanyong Gao

Geophysical Exploration Center, China Earthquake Administration, Zhengzhou, China

To understand the shallow structure and complex sedimentary environment of the 2017 Jinghe Ms6.6 earthquake focal area, we used one mouth of continuous sesimic data from a dense seismic array of 208 short period stations around the earthquake focal area, and applied the ambient noise tomography (ANT) method to image the three-dimensional Shear wave velocity structure at the depth less than 4 km. The shear wave velocity shown clear lateral variations and vertical variations from the surface to the deeper regions and has a tight correlation with surface geological and tectonic features in the study area. Obvious low-velocity anomalies has been presented throughout most of the Jinghe depression, whereas the Borokonu Mountains presented high-velocity anomalies. The thickness of the Cenozoic sedimentary basement in the study area is approximately 1–4 km, and the distribution of thickness is highly uneven. The crystalline basement in the study area has strong bending deformation, and the non-uniform Cenozoic sediments are related to the strong bending deformation of the crystalline basement. The Kusongmuchik piedmont fault is a high-angle thrust fault cutting through the base. There are also many medium low-angle faults, which do not penetrate the surface, which has indicated that they are in a concealed state at present. The results have provided a shallow high-resolution 3D velocity model that can be used in the simulation of strong ground motion and for evaluating potential seismic hazards.

KEYWORDS

Jinghe 2017 Ms6.6 earthquake region, 3-D shear velocity structure, dense array, ambient noise tomography, he Jinghe depression

1 Introduction

On 9 Aug 2017, the Jinghe Ms6.6 earthquake occurred in Jinghe County, Bortala Prefecture, Xinjiang Uygur Autonomous Region (Figure 1). The epicenter was located at 44.27°N and 82.89°E, and the depth was 11 km as measured by China Earthquake Networks Center. Near the epicenter, near the epicenter strong tremors can be felt. Less than a day after the earthquake, a total of 11 aftershocks occurred with M ≥ 3, which affected 33 towns. 32 people were injured, and 142 houses collapsed (Jin et al., 2019; He et al., 2020). One year

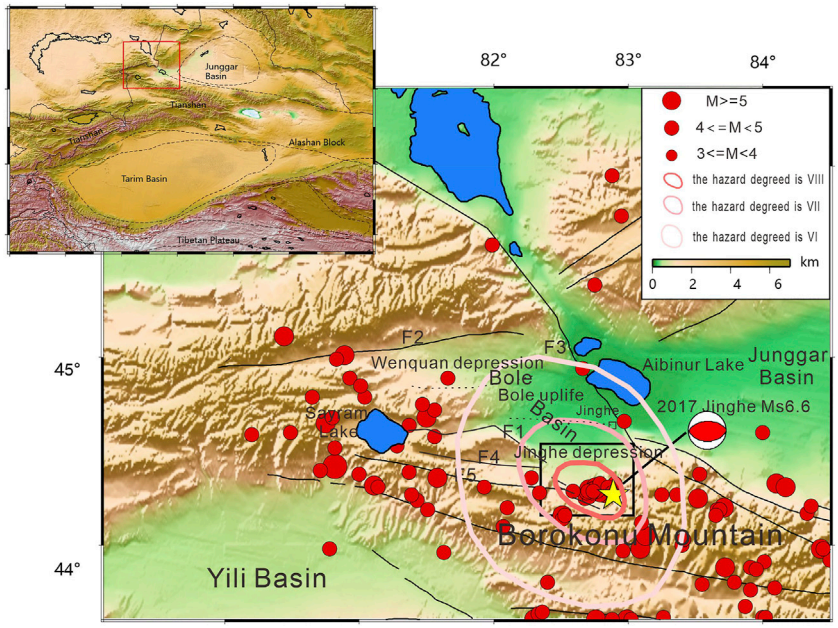

FIGURE 1
Topographic and seismicity maps of the study area.

later, one Ms5.4 earthquake occurred 30 km away to the southwest of the Jinghe Ms6.6 earthquake. Many earthquakes have occurred in this area over a relatively short time, which has resulted in a strong research focus on the seismogenic mechanisms in this area.

Xinjiang is located on the Eurasian seismic belt, where there are many large faults, and earthquakes are active. However, given the wide area, poor surface conditions, and sparse observation stations in Xinjiang, so far, there has been relatively little research on the crust structure in this area. In particular, there is relatively little understanding of the deep and shallow structure of active faults in this area. This affects the understanding of the background around the mechanisms of earthquake generation and their dynamics. After the earthquake, the regional arrays were used to carry out seismic tomography, seismic relocation, and geometric analysis of seismogenic faults in this area (Fu and Wang, 2020; He et al., 2020). However, given the sparse distribution and low resolution of the array, their understanding of the deep seismogenic background in this area has been relatively limited.

The deep crustal structure is closely related to the development of earthquakes, and the structure of the shallow crust is directly related to earthquake disasters. Areas with extensive structural changes such as fault zones are often those with the serious earthquake disasters. Considering that sedimentary structures can amplify seismic signals, it is also likely to increase earthquake damage (Li et al., 2020). Therefore, in the study of earthquake disaster prediction, we should not only pay attention to information on faults but also pay attention to the sedimentary structure of the basin. The Jinghe area is located on thick sedimentary structures, and to reduce the risk of earthquake disasters, it is important to investigate the deep structured and seismogenic background of the fault, as well as determine the sedimentary structure. Studying the sedimentary structure is also play a key role in exploring resource and energy distribution in the shallow crust. This is of considerable importance in the study of the sedimentary environment related to faults, strong earthquake ground motion, and disaster risk prediction.

In recent years, the high-frequency surface wave signal has been obtained using continuous ambient noise data based on the dense seismic array. It is more sensitive to the shallow velocity structure and small-scale ambient noise tomography has been widely used in cities, volcanic activities, metal mines, and other areas (Lin et al., 2013; Fang et al., 2015; Luo et al., 2015; Li et al., 2016; Zhou et al., 2018; Gu et al., 2019; Zellmer et al., 2019; Zulfakriza et al., 2020). A dense seismic array with 208 three component short period seismometers was deployed on 5 July 2018. The range is about 50 km × 50 km with the station spacing being 0.5–5 km (Figure 2). In this study, we determined the 0–4 km three-dimensional (3D) shear wave velocity in the Jinghe area by inverting 1–5 s period dispersions using direct surface wave tomography (Fang et al., 2015).

2 Geological background

The study area was located in the southern of the Bole Basin and the contact part of the Boluokonu Mountain and Kogurqin Mountain (Figure 2A), which form part of the Sayram micro block. The Bole basin is a composite basin of the Upper Paleozoic and Mesozoic Cenozoic, and the Devonian system directly covers the Mesoproterozoic metamorphic rocks. The basin comprises three secondary structures, the Wenquan Depression, Bole Uplift, and the Jinghe Depression. According to the analysis of field outcrops, seismic and drilling data, Devonian, Carboniferous, Permian, Jurassic, Paleogene, Neogene, and Quaternary strata are developed in the basin. The Paleozoic

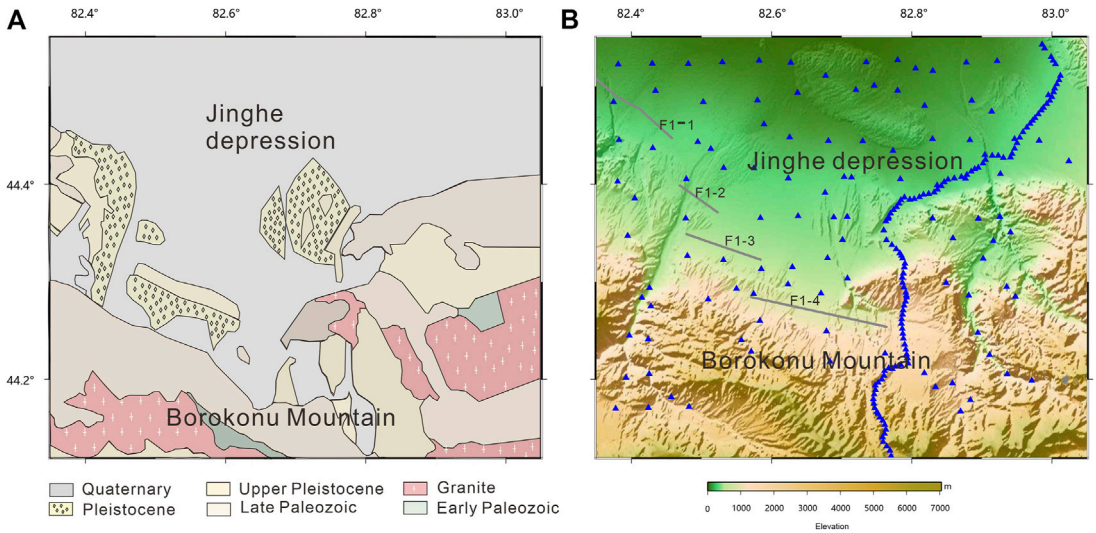

FIGURE 2
(A) Geological map of study area; **(B)** The stations used in this study are shown in the red rectangle in **(A)**, F1 is the Kusongmuchik piedmont fault.

strata is relatively thick, and the Mesozoic Cenozoic strata are relatively thin. Devonian and Carboniferous strata are widely distributed in this area. The Permian system is developed in the west of the Bole uplift, and the entire Triassic system is missing. The Jurassic system is only distributed to the northwest of the Wenquan Depression, and the Tertiary and Quaternary systems are distributed throughout the basin (Sun et al., 1997; Zhang et al., 2017a; Zhang et al., 2017b).

The Borokonu and Kogurqin mountain belts are located in the northern branch of the Western Tianshan Mountains and the northern margin of the Yili Basin. They are characterized by a Paleozoic active continental margin superimposed onto the Precambrian metamorphic crystalline basement (Gao et al., 2009). The Boluoli island arc belt is located in the south and the nappe structure is located in the north. Most of the strata exposures on the Boluokonu Mountain are from the Proterozoic and Paleozoic (Wang et al., 2013), and most of the strata exposed on Kogurqin Mountain are Proterozoic.

The Jinghe earthquake occurred near the eastern section of the Kusongmuchik piedmont fault at the north edge of the Bolokonou Mountain, to the north of Tianshan Mountain, and at the southwest end of the Junggar Basin (Figure 1). The study area was located in the thrust fold tectonic active belt between the Junggar plate and the Tianshan plate. The Kusongmuchick piedmont fault is a newly active fault that has developed on the fold reverse fault zone at the front edge of the Tianshan nappe (Chen et al., 2007). The Kusongmuchik piedmont fault is a Holocene Active fault (Chen et al., 2007), which is a dextral reverse fault that is EW trending. The fault is a boundary fault and regionally active fault located on the north edge of the west end of North Tianshan. According to its activity trends, it is divided into the east, middle, and west segments. Chen et al. (2007) obtained the stratigraphic and structural data from the area through field investigation. It was found that the eastern section of the Kusongmuchick piedmont fault is approximately 50 km long, predominantly composed of four fault oblique columns with a strike of 280°–290°, a length of 9–13 km, with a dip to the south (Figure 2 marked as f2-1, f2-2, f2-3, and f2-4), the dip angle of 40°–60°. Faults and folds have developed in the area where the fault is located, and there is a high level of tectonic activity.

3 Data and methods

From May to July 2018, the Geophysical Exploration Center, China Earthquake Administration deployed a 150 km long linear dense array using the Jinghe County, Nileke County, and Gongliu County of Xinjiang with a NE–SW trend, with an average station spacing of approximately 500 m, comprising 115 stations. The linear array was located through the epicenter area of the Jinghe Ms6.6 earthquake. Meanwhile, a plane dense array was deployed around the epicenter area, with these detector stations spanning an area of 44.16°N–44.54°N and 82.37°–83.04°E, with a total of 115 stations spaced approximately 4 km apart. The original data sampling rate was 200 Hz. The observation instruments used were short-period portable digital seismometers and the corner frequency of the instrument was 5 s. In this study, we used the continuous ambient noise data recorded by the plane dense array and 93 stations of a linear dense array inside the planar array with a total of 208 stations (Figure 2B). This was undertaken to obtain a high-resolution image of the shallow structure beneath the region of the Jinghe Ms6.6 earthquake area. The main fault in the study area was the eastern part of the Kusongmuqike piedmont fault, which is composed of four faults. The trend was 280°–290°, at approximately 50 km, with a dip to the south (Figure 2B marked as F1-1, F1-2, F1-3, F1-4).

The empirical Green's function between station pairs could be derived from the noise cross-correlation function stack over relatively long timescales. In this study, we used the vertical

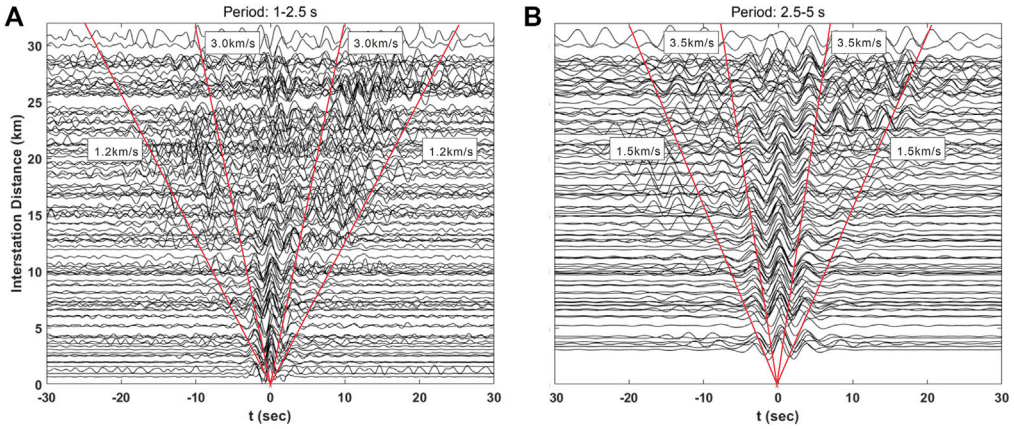

FIGURE 3
(A) A record section of CFs in a period band of 1–2.5 s; **(B)** A record section of CFs in a period band of 2.5–5 s.

component data to calculate the cross-correlation function between stations and extract the Rayleigh surface wave signal. Before using noise data to calculate the cross-correlation function, it is necessary to preprocess single station data, which follows the data processing process for the noise cross-correlation standard (Bensen et al., 2007). The data was reduced to 1 day in length and the original 200 Hz data was downsampled to 50 Hz. We then removed the mean and the trend of the data and band-pass filtered the data in the 0.1–10 s frequency band. To reduce the effect of earthquake signals, we performed spectral whitening and temporal normalization of the data. We performed cross-correlation to obtain the time domain cross-correlation function (CF) for Station Pairs A and B for each set of daily data with a lag time from −100 to 100 s. After preprocessing was complete, the cross-correlation between all the stations could be calculated. All the daily CFs from each station pair was stacked together linearly. A total of 21,528 cross-correlations were obtained in this study. Figure 3 shows an example of noise correlation functions of the vertical–vertical component, based on the long observation time. The CFs of the signal-to-noise ratio (SNR) was relatively high, and we could observe clear surface wave signals in the positive and negative time parts. The surface wave signal was clearly in line with the positive and negative time components. Although the amplitude information was different, the time of arrival of the positive and negative surface waves was consistent.

To improve the cross-correlation SNR, we linearly stacked the positive time and negative time components of Empirical Green's function. The group velocity dispersion curve of the Rayleigh surface wave was automatically extracted using the image analysis method of Yao et al. (2006); Yao et al. (2011). According to the relationship between station spacing and wavelength, we extracted the dispersion curve of 1–5 s, with a sampling interval of 0.1 s. We required the interstation distance to be at least double the wavelength to approximately satisfy the far field approximation of surface wave propagation (Yao et al., 2010), and the SNR ≥5. Using this program, a reliable reference dispersion curve was needed to function. Therefore, 200 dispersion curves were manually identified, and the reference dispersion curve was calculated using these data. A total of 15,700 dispersion curves were extracted using the manually selected dispersion calculation. We controlled the quality of the automatically extracted dispersion curve. According to the reference dispersion curve, the maximum slope of the dispersion curve was 0.5. Therefore, we retained data with a group velocity difference of two adjacent periods less than or equal to 0.05 km/s and then deleted the dispersion curve with less than five points. Therefore, the quality control of the dispersion curve was completed. A total of 5,724 high-quality dispersion curves were retained. According to the dispersion data extracted, statistical information on dispersion quantity over different periods was obtained (Figure 4). In 1–2.8 s with the increase in duration, the number of dispersion increased, and the most number of dispersions occurred over 2.8 s at nearly 3,000. After 2.8 s, with the increase in duration, the number of dispersions gradually decreased to about 1,000.

4 Results

4.1 Inversion method

In this study, we used the direct surface wave tomography method with period-dependent ray tracing method to invert all the dispersive travel-time data simultaneously for the 3D subsurface shear-velocity structure (Fang et al., 2015). This method can be used to avoid the intermediate steps of inversion for phase or group velocity maps and considers ray bending effects on surface-wave tomography in the complex medium. For the forward problem, the fast-matching method was used to compute the surface wave travel times and ray paths between receivers and sources for each period (Rawlinson et al., 2004). The travel-time perturbation at the angular frequency ω concerning a reference model for the path is given by Fang et al. (2015).

$$\delta t_i(\omega) = t_i^{obs}(\omega) - t_i(\omega) \approx -\sum_{k=1}^{K} v_{ik} \frac{\delta C_k(\omega)}{C_k^2(\omega)} \quad (1)$$

in which $t_i^{obs}(\omega)$ is the observed surface wave travel time, $t_i(\omega)$ is the travel time calculated from a reference model that can be updated in

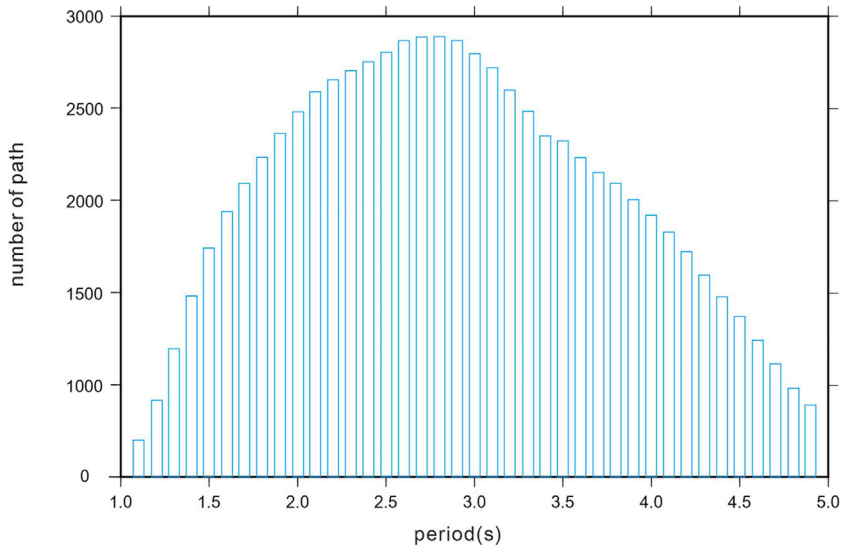

FIGURE 4
The number dispersion at different period.

the inversion, and is the bilinear interpolation coefficients along the ray path associated with the i th travel time data and the phase (or group) velocity $C_k(\omega)$ and its perturbation.

$\delta C_k(\omega)$ of the k th 2D surface grid point at the angular frequency ω. Using the 1D depth kernel of Rayleigh wave phase or group velocity data to compressional velocity (a), shear velocity (β), and density (ρ) at each surface grid node, we can rewrite Eq. 1 as

$$\delta t_i(\omega) = \sum_{k=1}^{k}\left(-\frac{v_{ik}}{C_k^2(\omega)}\right)\sum_{j=1}^{J}\left[R_a(Z_j)\frac{\partial C_k(\omega)}{\partial a_k(z_j)} + R_p(z_j)\frac{\partial C_k(\omega)}{\partial \rho_k(z_j)} + \frac{\partial C_k(\omega)}{\partial \beta_k(z_j)}\right]\Big|_{\Theta_k}\delta\beta_k(z_j) = \sum_{l=1}^{M} G_{il} m_l \tag{2}$$

In which θ_k represents the 1D reference model at the kth surface grid point on the surface, $\alpha_k(z_j)$, $\beta_k(z_j)$, and $\rho_k(z_j)$ are the compression velocity, shear velocity, and mass density at the j th depth grid node, respectively. $R_\alpha^{'}$ and $R_\rho^{'}$ are the scaling factor, J is the number of grid points in the depth direction, and the number of total grid points of the 3D model is M = K × J. We can write (2) as

$$\mathrm{d} = \mathrm{Gm} \tag{3}$$

In which d is the travel time residual, G is the data sensitivity matrix, and M is the model parameter. In the inversion problem, the loss function needs to be minimized to solve formula (3), we can obtain (4)

$$\Phi(\mathrm{m}) = \|d - GM\|_2^2 + \lambda\|LM\|_2^2 \tag{4}$$

Where the first term on the right-hand side gives the l_2-norm data misfit and the second term denotes the l_2-norm model regularization term and the second term is the model regularization term. L is the model smoothing factor; λ is the weight factor of data fitting and model regularization. Therefore, the solution m of formula (3) is

$$\tilde{\mathrm{m}} = \left(G^T\mathrm{G} + \lambda L^T\mathrm{L}\right)^{-1}G^T d \tag{5}$$

Therefore, the inversion problem is transformed into the least square problem in linear inversion (Paige and Saimders, 1982).

4.2 3D model and sensitive kernel

We used direct inversion of 3D S-wave velocity imaging based on independent period ray tracing (Fang et al., 2015) to simultaneously all the dispersions to obtain the S-wave velocity structure of the study area. This includes inversion without the intermediate step of phase- or group-velocity maps and avoids the effect of bending off the great-circle ray in a complex medium.

We used the 1D velocity model of the Tianshan area obtained by Shao. (1996) as the initial velocity model (Figure 5A blue line). The inversion depth was 0–7 km, and there were 14 layers along the depth direction. We calculated the average dispersion curve for all the group dispersion curves. The linear inversion program (Herrman and Ammon, 2004) was used to invert the average dispersion curve to obtain the 1D shear velocity structure (Figure 5A red line). We used the 1D model (Figure 5A red line) to construct the initial three-dimensional inversion model and set the grid spacing to 0.02°, which was equivalent to 30 × 50 = 1,500 horizontal grid points.

We calculated the depth-sensitive kernel function of group velocity with a period of 1–5 s to the S-wave velocity using the 1D model (Figure 5A red line). Figure 6 shows that the maximum sensitive depth of the different Rayleigh waves is approximately 1/2λ (wavelength). According to the sensitive kernel function, the group velocity of 0.5–5 s was mainly sensitive to the depth range of 0–5 km.

4.3 Path coverage and resolution

The resolution of surface wave tomography depended primarily on the coverage and azimuthal distribution of the path. The denser

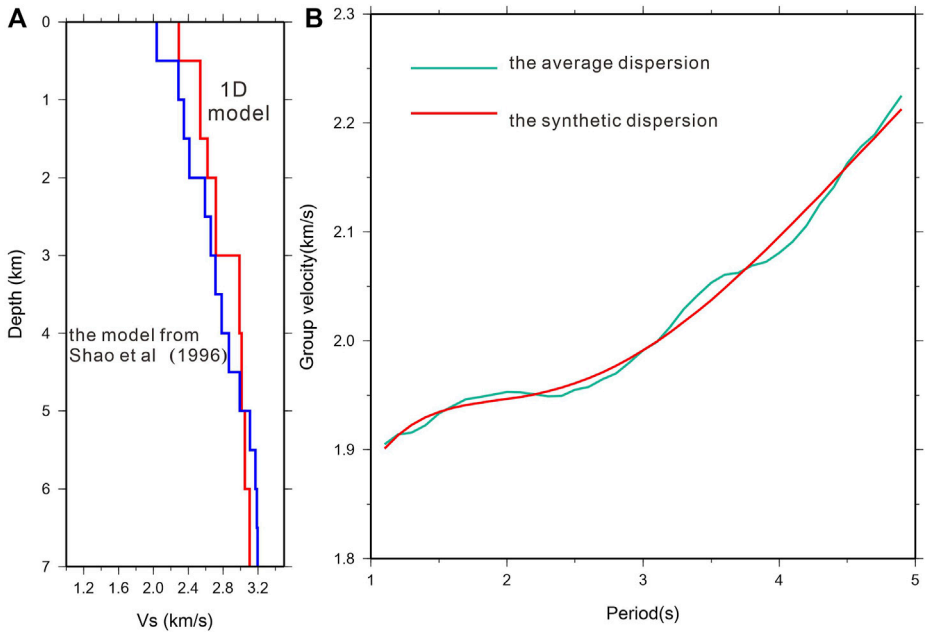

FIGURE 5
(A) The initial model from Shao et al. (1996) (blue line), the 1-D model derived from inverting the measured average group velocity dispersion. **(B)** The green line is the observed average dispersion curve; the red line indicates the dispersion curve obtained by forward calculation using the 1-D average velocity model in FigureA.

the ray path coverage, the higher the resolution; on the contrary, the thinner the path coverage, the lower the resolution. Based on the final inversion, we obtained the path coverage for the group velocity for all periods (Figure 7). The distribution of the ray paths for each period was similar, and the path density in the northwest of the study area was lower than the southeast, due to uneven distribution of stations. With the period increases, the ray coverage density decreases.

We used the checkerboard test to determine which part of the study area should be sufficiently well resolved by our data to justify the inversion of group velocity dispersion curves for the shear wave velocity depth profiles. The checkerboard test uses synthetic data generated on a "checkerboard" velocity structure (Figures 8A–C), using the same station pairs as the observed data. Areas, where the inversion is in line with the original checkerboard pattern, are considered well-resolved. We tried various checkerboard cell sizes of 4.5 × 4.5 km, 6 × 6 km, and 7.5 × 7.5 km throughout 2 s to determine which sizes are well resolved in the study area (Figures 8D–F). Figure 8 shows that the checkerboard test can recover the initial velocity model at 6 × 6 km cell size (Figures 8B, E). The checkerboard test at 6 × 6 km can be recovered effectively in most parts of the study area and was only poor in marginal areas.

To determine the resolution of the 3D shear velocity structures, we used the checkerboard resolution test. The initial velocity model of the checkerboard is the same as the real inversion velocity model. The grid is divided into and the disturbance volume is 27%. Figure 9 shows the checkerboard test results at depths of 0.5, 1.0, 1.5, 2.0, 2.5, and 3.5 km. The resolution is related to the path coverage and, in general. There is dense path coverage; the resolution of the checkerboard resolution test was relatively

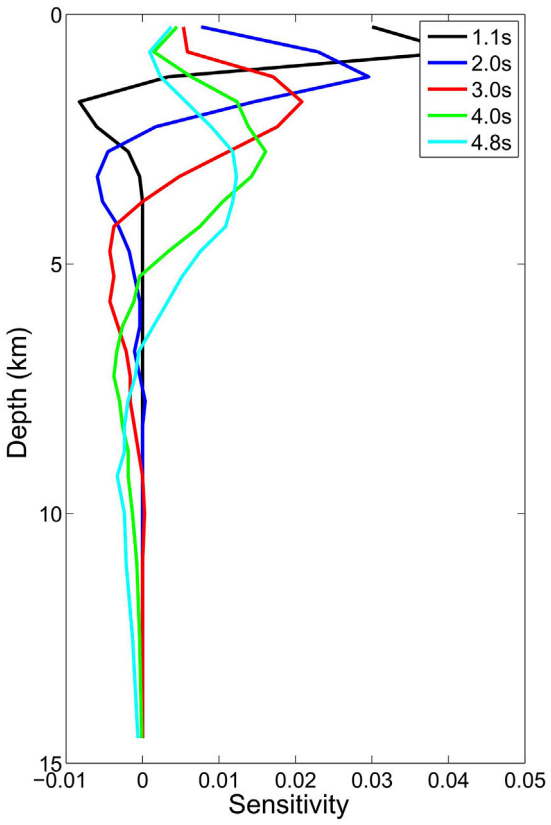

FIGURE 6
Depth sensitivity kernels for group velocity at four periods: 1.1, 2.0, 3.0, 4.0, and 4.8 s.

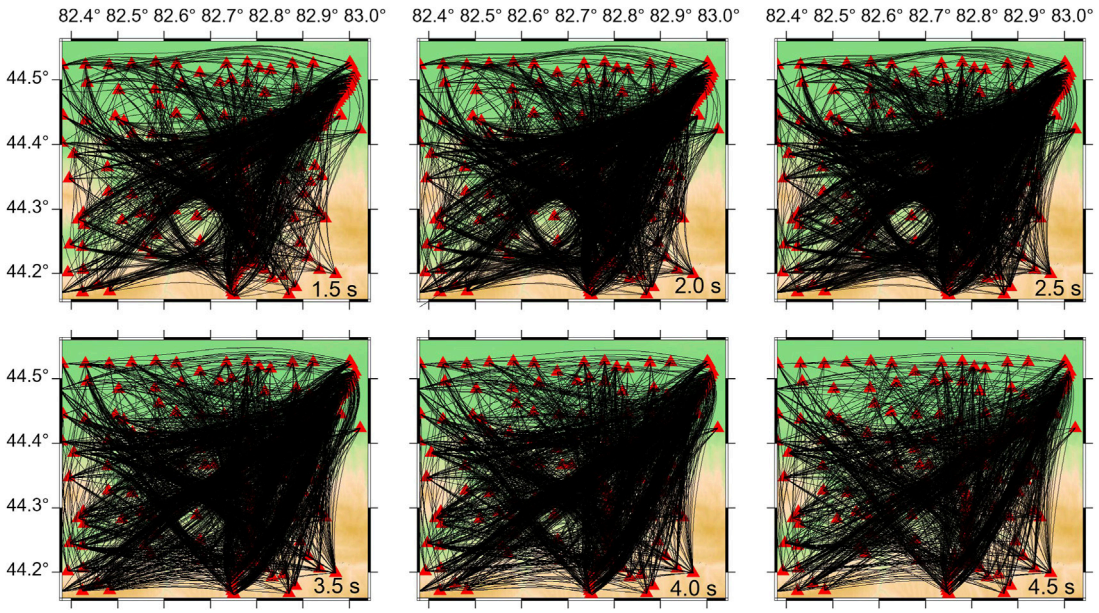

FIGURE 7
The ray paths obtained from the final 3-D model (see Figure 9) at four periods using the fast marching method: 1.5, 2.0, 2.5, 3.5, 4.0, and 4.5 s. The black lines represent the ray paths and the red triangles represent the stations.

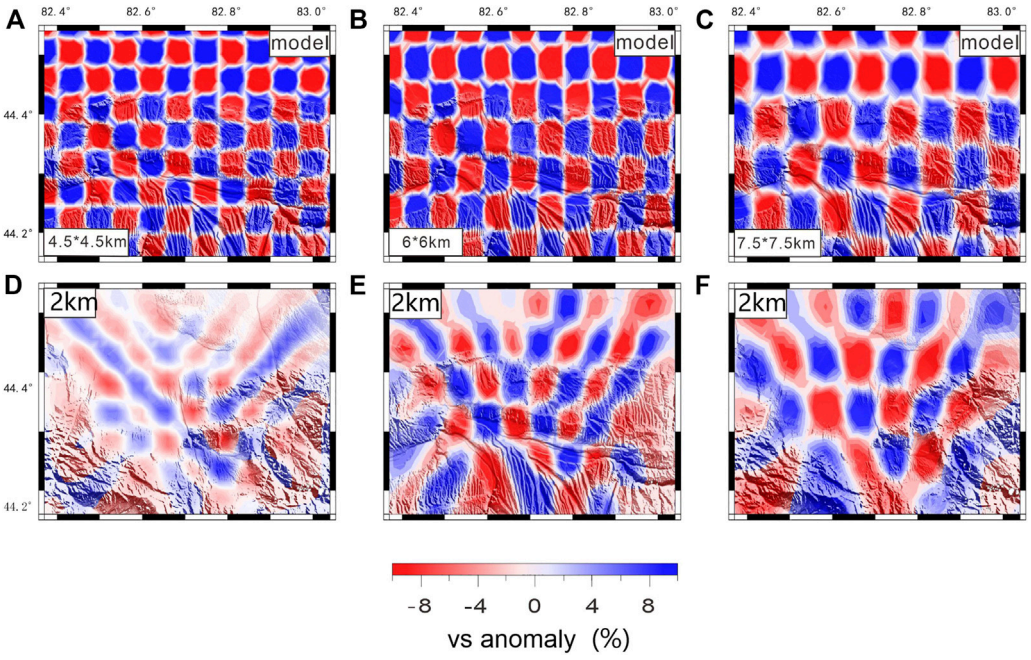

FIGURE 8
The checkboard test by using grid 6*4.5 km, 6*6 km, 7.5*7.5 km for 2 km. **(A–C)** show the initial velocity model and **(D–F)** show the recovery model.

high. At the edge of the study area, where the path coverage becomes sparse, the resolution became relatively low. At a depth of 0.5–2 km, the ray path coverage is relatively dense, and the checkerboard recovery was better. With the increase in depth, the ray path gradually became sparse. The restoration of the checkerboard became worse at the edge of the study area, but it could be restored in the center area. We also obtained the test results of the depth along the longitudinal and latitudinal

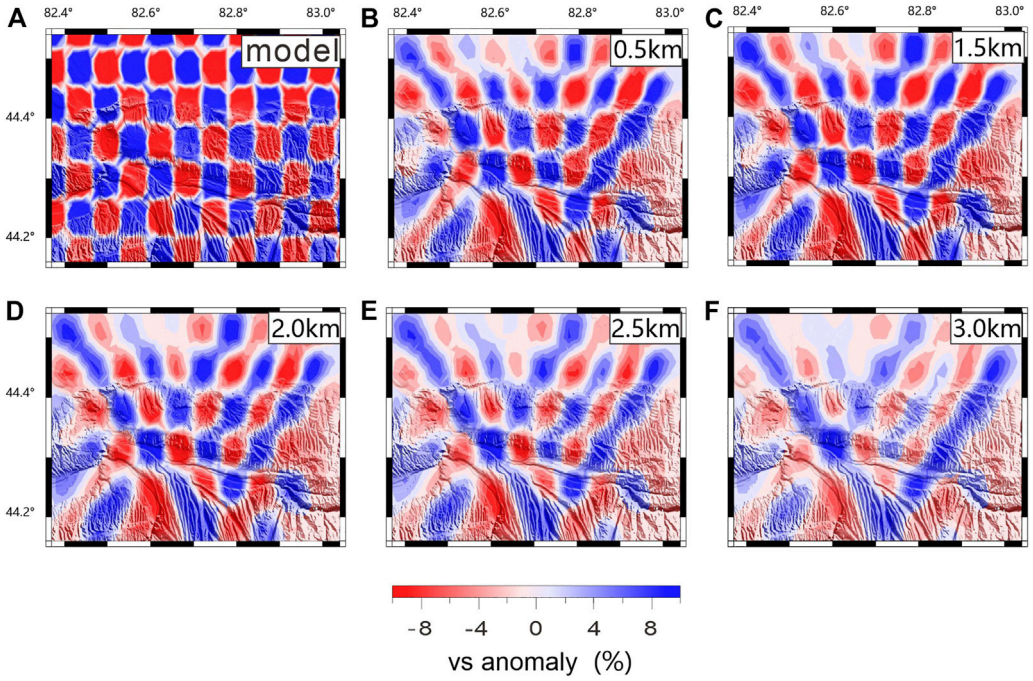

FIGURE 9
Checkerboard resolution tests of the inversion results: **(A)** Checkerboard test model, **(B–F)** different depth of horizontal checkerboard recovery.

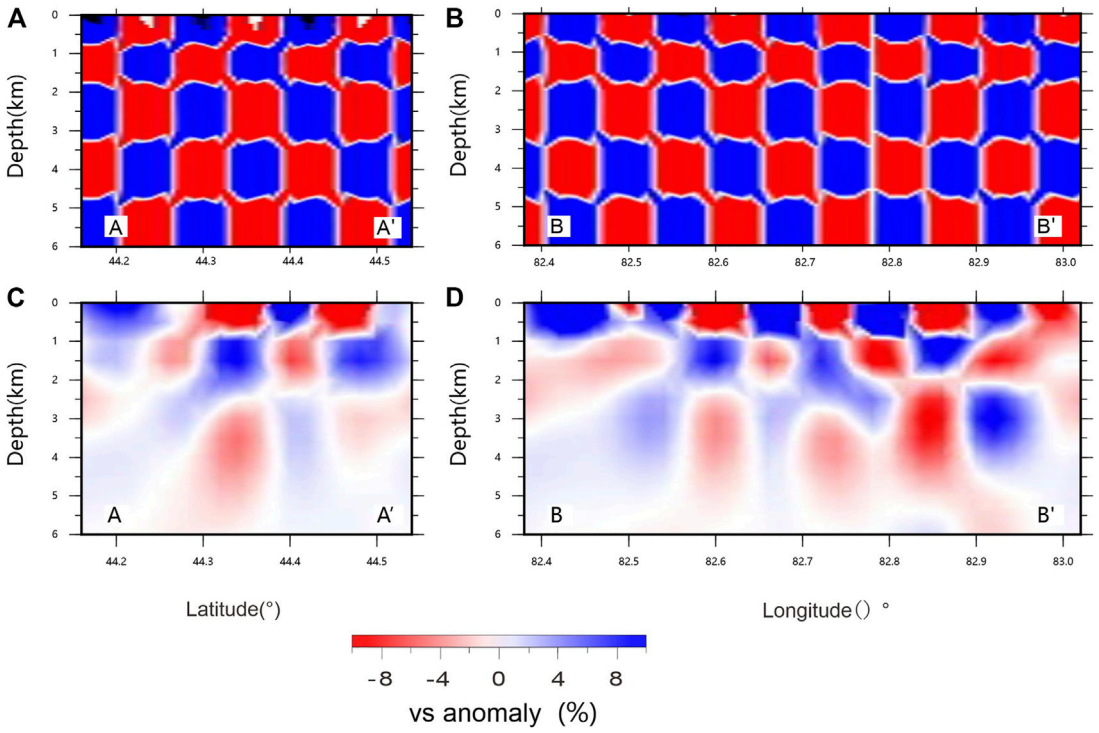

FIGURE 10
Vertical checkerboard test; the location of the profiles show in Figure 12. **(A, B)** are the checkboard theoretical model, **(C, D)** are the vertical chessboard recovery in longitude direction **(D)** vertical chessboard recovery in latitude direction.

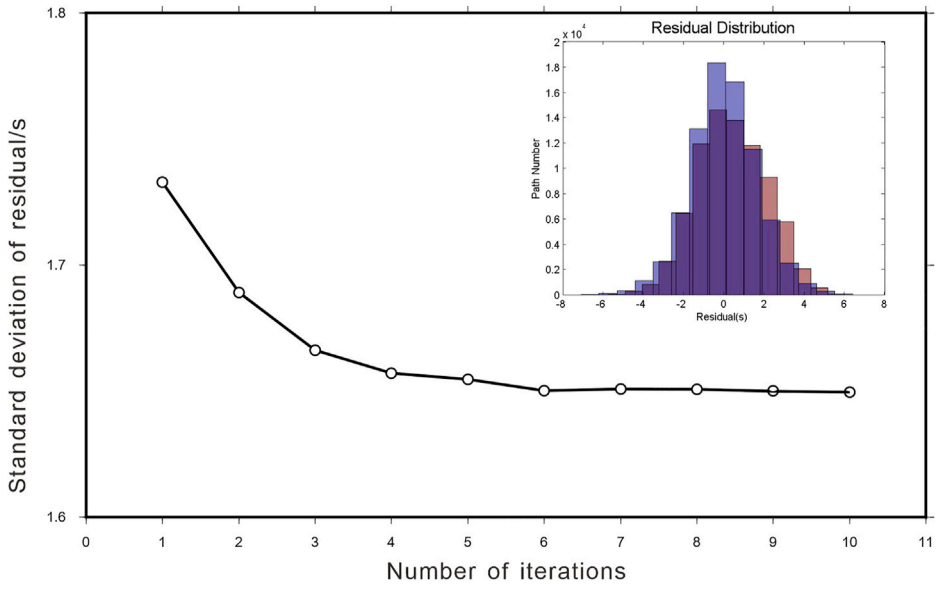

FIGURE 11
Variation of the standard deviation of surface wave travel time residuals with the number of iterations. The histogram of travel time residuals before iteration (red) and after 10 iterations (blue).

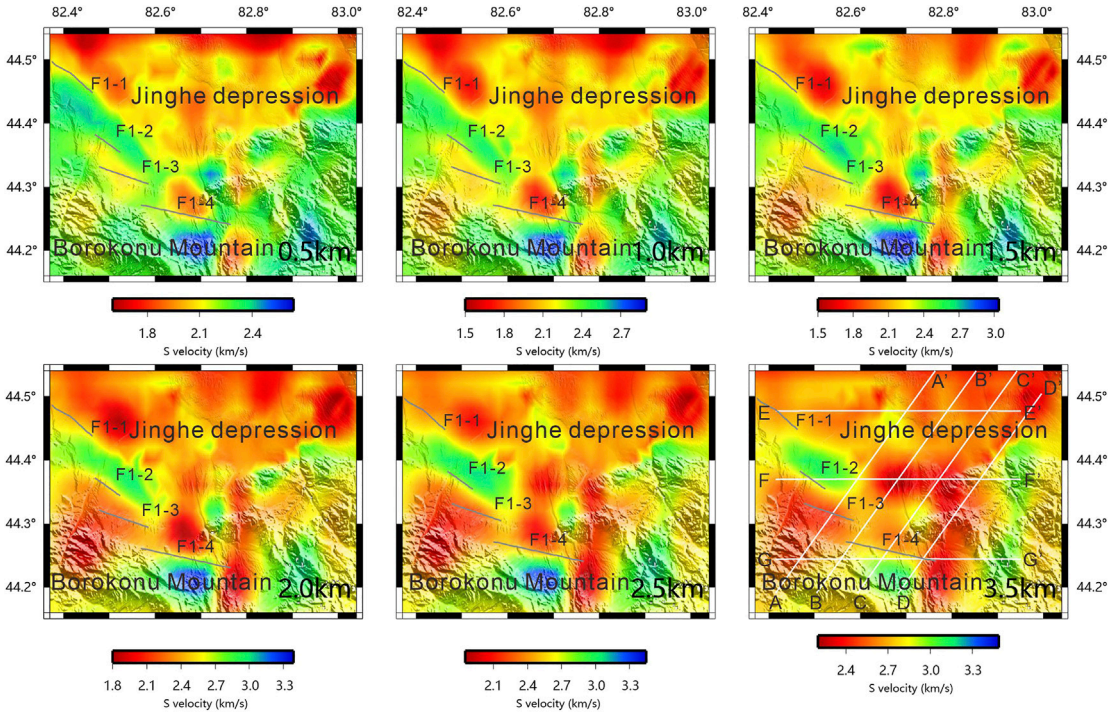

FIGURE 12
S wave velocity distribution at different depths: depth is 0.5, 1.5, 2.5, and 3.5 km.

directions (Figure 10). The grid size of the depth checkerboard test setup gradually increased with increasing depth, with the grid size being 6 km in the horizontal direction. In terms of depth, the shallowest was 600 m with increasing crustal depth, and the grid size gradually increased to 1,500 m. The results have shown that the checkerboard recovery has occurred more successfully in the shallow section with relatively dense dispersion curve coverage. With increasing depth, the dispersion curve coverage was lower,

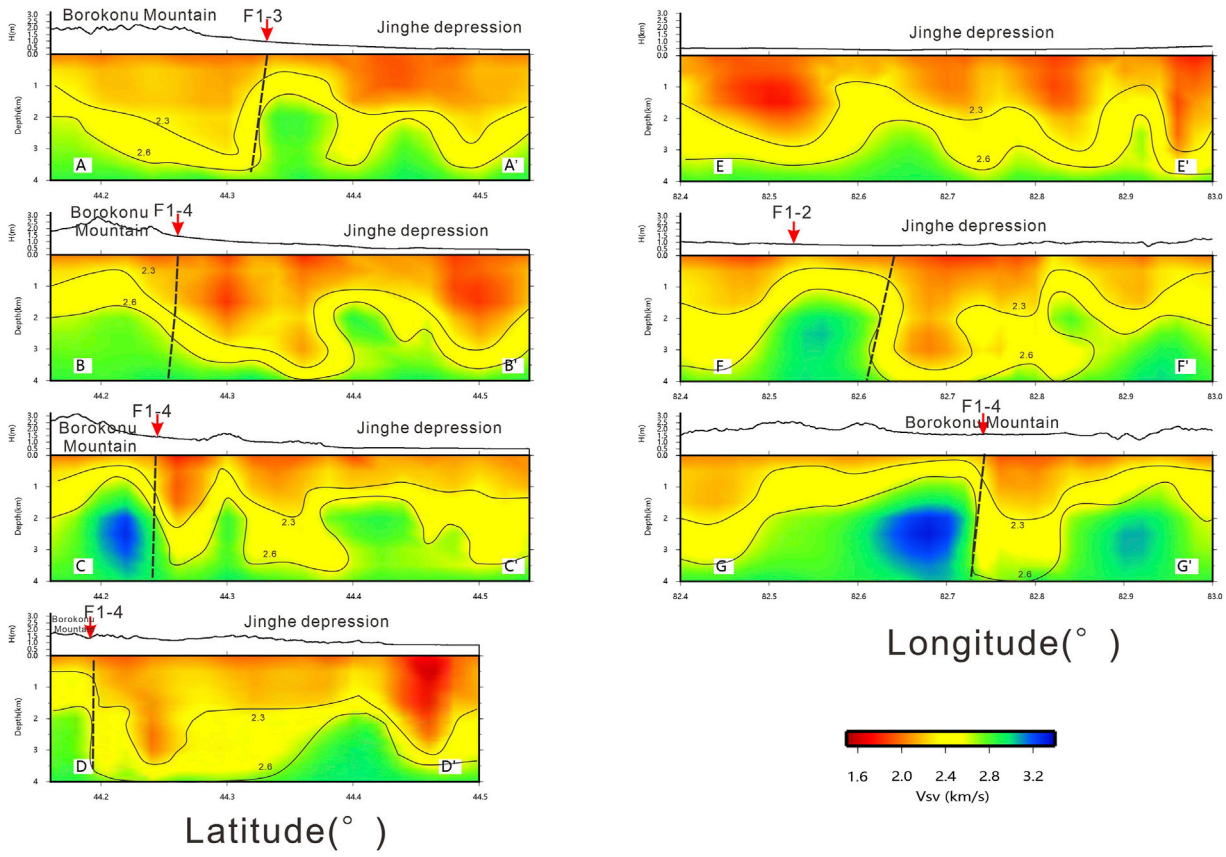

FIGURE 13
The velocity distribution of AA', BB', CC', DD', EE', FF', and GG'.

and the checkerboard recovery gradually became less successful in the edge area.

4.4 3D shear velocity structure

We used all the group velocity dispersions to invert the 3D near-surface shear velocity structure. The standard deviation of travel time residuals decreased from approximately 1.74 s to approximately 1.638 s (10th iteration, see Figure 11). The last travel time residuals were highly concentrated around 0 s (Figure 11, illustration).

Figure 12 shows the shear velocity maps at six depths, that is, 0.5, 1.0, 1.5, 2.0, 2.5, and 3.5 km. The shear velocity maps have shown clear lateral and vertical variations which correlate closely with the main geological structures and tectonic units in the study regions.

The velocity structure characteristics of 0.5, 1 km, and 1.5 km are similar. The Jinghe depression has shown low shear wave velocity; in the valley and the area where the river passes of the Borokonu Mountain shows low velocity, whereas the other region of the Borokonu Mountain has shown high velocity. From near the surface to the deep regions, most of the Jinghe depression with thicker sediments is characterized by low shear wave velocity. Meanwhile, Borokonu Mountain, with its exposed bedrock, is characterized by higher velocities. The location is in the eastern part of Kusongmuqike Piedmont Fault (F1-1) which is the boundary of high and low velocity. The surrounding areas of F1-2 and F1-3 are characterized by high velocity, while the surrounding areas of F1-4 are characterized by low velocity. The results for the shear wave velocity structure have shown a strong correspondence with the geological features of the study area. It indicates that the velocity distribution characteristics in the study area are mainly controlled by regional structures.

Compared with the shallow structure, the velocity structure of 2, 2.5, and 3.5 km are different, with the Jinghe depression still showing a large area of low velocity. In the Borokonu Mountain, the distribution range of low velocity gradually increases, while the distribution range of high velocity gradually decreases. The eastern part of the Songmuqike Piedmont Fault has a high-velocity distribution, but the range of high speed gradually decreases with increasing depth.

We have obtained several profiles, the profiles of AA', BB', CC', and DD' (Figure 13) are near-vertical to the Kusongmuqike piedmont fault with a NE trend. The EE', FF', and GG' are three profiles at the latitudes of 44.22 °N, 44.36 °N, and 44.48 °N. From the four profiles of AA', BB', CC', and DD' (Figure 13), the velocity of the Jinghe depression of the shallow 0–2 km depth range is substantially lower than that of the Boluokonu Mountain. In the range of 2–4 km, the distribution of velocity is relatively complex. From the southwest side to the northeast

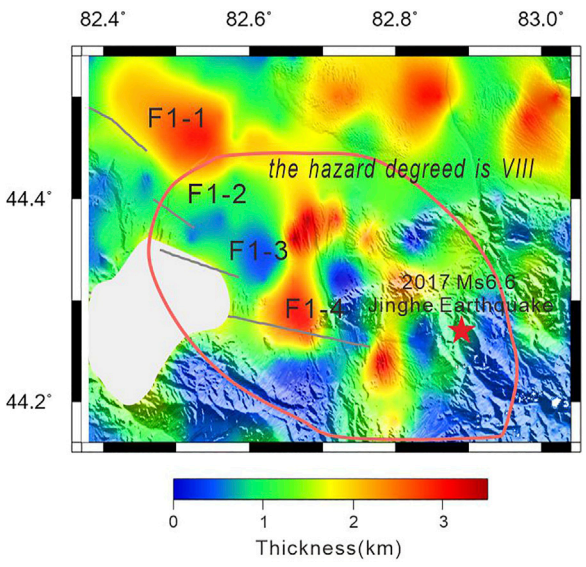

FIGURE 14
The distribution of Cenozoic sedimentary thickness. The red star is the epicenter of the 2017 Ms6.6 Jinghe Earthquake.

side, it is characterized by alternating high and low velocities. The EE's profile along the latitudinal direction traverses the Jinghe depression, showing a low-velocity structure, and the velocity on the west side of the profile is considerably lower than that on the east side. The FF' profile passes through the Boluokonu Mountain, the Jinghe depression, and the Boluokonu Mountain, which has high velocity in the east and west of the profile and low velocity in the middle of the profile. The GG' profile traverses the Borokonou Mountain and has high velocity, but near the Kusongmuqike piedmont fault, it has low velocity.

5 Discussion

The Bole Basin is an intermountain in the Selimu micro block in the western section of the Tianshan Mountains with a Precambrian base, which may be a basin covered by nappes (Sun et al., 1997; Wang et al., 2013; Zhang et al., 2017a). In the early Paleozoic, the northern Tianshan Junggar Ocean in the north of the Selimu micro block began to subduct southward, and the Alatao, Bizhentao, and Kogurqin Mountains began to form. During this period, the Selimu micro block was under the background of uplift. The Bole uplift in the center of the basin divided the basin into Wenquan and Jinghe depressions with the influence of mountain uplift. At this time, the structural styles of two depressions with one uplift were basically formed. In the early Permian, the lake basin declined and generally accepted sedimentation. In addition to Bole uplift, sedimentary structures of deep lake facies and volcanic eruption facies in the upper Permian were formed. From the end of Hercynian period to Indosinian period, the lake basin was uplifted and suffered weathering and denudation, which made the basin generally lack part of the Triassic and Lower Jurassic sediments in this period. At the same time, because the basin was still subject to the uplift and compression of mountains in this period, the tectonic framework of two depressions with one uplift developed by compressional and torsional reverse faults was more obvious. In the middle Yanshan period, the basin declined and entered a stable sedimentary stage; in the late Yanshan period, the basin was always in the uplift stage, and the original subsidence center lifted the fold to form the piedmont fold of Jurassic strata, while the upper Jurassic and Cretaceous sediments were generally absent. During the Himalayan period (the Tianshan Mountains were uplifted again), the orogeny was strong, the basin declined, and huge thickness of Cenozoic alluvial fan and molasse facies debris was deposited. Due to the uplift of the three sides of the mountain, fold structures and contemporaneous and associated faults were well developed, forming the current complex structural pattern (Sun et al., 1997; Wang et al., 2013; Wang et al., 2000; Gao et al., 2016; Zhang et al., 2017a; Zhang et al., 2017b).

Considering that there has been little research in the study region, we found that the Piedmont basement of the North Tianshan Mountains could be divided into two layers according to the results of the geoscience large section (report) basement crossing the three mountains and two basins in the north and south of Xinjiang approximately 200 km away from the east of the study area. The upper layer is composed of lower-velocity Cenozoic sediments; the next layer is composed of Paleozoic sediments with high velocity. According to the result of Wang et al. (2000), the Late Cenozoic sedimentary thickness is approximately 2–4 km, and the P-wave velocity is 3.5–4 km/s. Meanwhile, according to the wave velocity ratio of 1.77 in this area, the S-wave velocity calculated was approximately 1.4–2.3 km/s. This corresponds closely to the S-wave velocity structure obtained from inversion. Therefore, the thickness of the Late Cenozoic sedimentary in this area is calibrated according to the velocity of 2.3 km/s. The thickness of the late Cenozoic sedimentary is shown in Figure 14. The section shows that the thickness of the Late Cenozoic sedimentary basement in the study area is about 1–4 km, that the Late Cenozoic sedimentary basement of Borokonu Mountain is thin, and of Jinghe Depression is thicker. However, there are also pronounced differences in some areas. Sections AA', BB', CC', and DD' are strongly bent and deformed.

According to the evolutionary structure of the area, the Cenozoic sediments covered the Mesozoic strata. In the late Jurassic, the south–north compression activity of the basin was strengthened, the basement was uplifted, and the basin was deposited, resulting in substantial shrinkage of the basin. The profile map has shown that the strata under the Cenozoic sediments have shown strong fold deformation, indicating that the Jinghe Depression was strongly compressed during this period. This result is in line with those of Qi et al. (2008) on tectonic deformation within the transitional belt between Junggar Basin and the northern Tianshan Mountain. Under the influence of the uplift of the Qinghai–Tibet Plateau, the compression in the near north–south region has been

strengthened, and then caused the uplift of the North Tianshan Mountains. Based on the existing faults and weak layers in the sedimentary basin cover, fold structures related to the basement involving thrust faults were formed in the Basin-Mountain transition zone of Junggar, North Tianshan. Our results may also indicate that Jinghe Depression is located in the transitional zone between the Junggar Basin and the Tianshan Mountains. From the Cretaceous to the Paleogene, Junggar Basin continued to develop under the action of isostatic curvature of the crust, and the faulting activity of the basin and its edge weakened. In the Neogene, the Tianshan Mountains began to uplift because of the collision between the Indian plate and the Eurasian plate. The Jinghe Depression formed a piedmont depression that received a substantial thickness of sediments, and the basin fillings were folded and deformed in the late sedimentation period (Wang et al., 2000). This result is also consistent with the thicker Cenozoic sedimentary facies in this area (Figure 12). Stratum bending features are also found in the EE', FF', and GG' profiles, which may indicate that the study area is not only compressed by north–south compressive stress, but also by east–west stress from Kazakhstan on the west side. There are also a series of nappe structures comprising north-dipping faults from north to south on the northern edge of the Bole Basin, indicating that the area has also been compressed from the Alatao Mountain (Sun et al., 1997; Zhang et al., 2017b). This may also indicate differences between the study region and the Basin-Mountain transition zone of Junggar, North Tianshan.

The Basin-Mountain transition zone of Junggar, North Tianshan has developed thrust faults while forming a fold structure from north–south compression. The main fault is a high-angle thrust fault inclined to the basin, and a series of branch thrust faults have developed in the footwall (Qi et al., 2008). The AA', BB', DD', FF', and GG' vertical profiles have shown that there is a substantial difference in velocity on both sides of the fault. The fault is a high-angle thrust fault, which can continue to a depth of 4 km, which indicates that the fault is a fault break-through the basement. In the area of the Piedmont basement fold, there are many medium low-angle faults, which do not break-through the surface, which may indicate that they are in a concealed state at present.

Our results have shown that the thickness of the Cenozoic sediments in Jinghe Depression is approximately 1–4 km, as we know the thicker sediments may contain rich natural resources. Zhang et al. (2017a) concluded that the southwest of Jinghe Depression is an important oil exploration area through the evaluation of the geological conditions of Bole Basin. According to its low speed in the sedimentary basin, when the earthquake propagates to the sedimentary layer, the signal is significantly amplified, which can cause greater seismic damage. After the Jinghe 6.6 earthquake on 9 August 2017, the Xinjiang Earthquake Administration released the hazard degree of the Jinghe M6.6 earthquake (Xinjiang Earthquake Administration, 2018). The hazard degree of the extreme seismic region was VIII, with an area of 979 km^2, a long axis of 44 km, and a short axis of 29 km. Meanwhile, many Level VIIII abnormal points were also found, and Urumqi more than 400 km away, also felt the earthquake. The area of the VIII degree area of the Jinghe earthquake is wider compared to other areas, such as the area of hazard with a degree of VIII from the Jinggu earthquake of M6.6 on 7 October 2014, is 400 km^2 (China Earthquake Administration, 2017a), the area of hazard with a degree of VIII from the Jiuzhaigou earthquake of M7.0 of 8 August 2017, is 778 km^2 (China Earthquake Administration, 2017b), the area of hazard with a degree of VIII of the Milin earthquake of M6.9 of 18 November 2017, is 310 km^2 (China Earthquake Administration, 2014), the area of hazard with a degree of VIII from the Luding M6.8 earthquake on 5 September 2022, is 505 km^2 (Ministry of Emergency management of the People's Republic of China, 2022). Figure 14 shows that the area of the VIII degree of hazard in the Jinghe Depression is substantially larger than that of the Borokonu Mountain. The Jinghe earthquake caused a wider range of disasters that may have been related to the huge Cenozoic sediments in this area. Although Xinjiang is sparsely populated because it is close to the Eurasian seismic belt, the area is seismically active and has a background of earthquakes above magnitude 6.0, so it is urgent to address seismic fortification in this area.

6 Conclusion

Based on the ambient noise data obtained from 208 dense stations deployed in the Jinghe earthquake area, the basic Rayleigh surface wave group velocity dispersion curve with a period of 1–5 s was extracted. We then used the direct surface wave tomographic method with period-dependent ray tracing constrained to invert group dispersion travel time data simultaneously for 3-D shear wave velocity structure. The shear wave velocity model results from 0.5–4 km depths have shown the distribution of buried faults under the study area; the velocity structure anomaly has a strong correlation with regional fault structures and has a strong correlation with the complex sedimentary structure near the surface. From near the surface to the deeper regions, most of the Jinghe depression with thicker sediments is characterized by low shear wave velocity. Meanwhile, the Borokonu Mountains, with their exposed bedrock, are characterized by higher velocities. The thickness of the Cenozoic sedimentary basement in the study area is approximately 1–4 km, and the distribution is highly uneven. The crystalline basement in the study area has strong bending deformation, and the non-uniform Cenozoic sediments are related to the strong bending deformation of the crystalline basement. There is a substantial difference in velocity on both sides of the fault, and the fault can continue to a depth of 4 km, which may indicate that the fault is a fault cutting through the basement. In the area of the Piedmont basement fold, there are many medium low-angle faults, which do not break-through the surface. This may indicate that they are in a concealed state at present. The results have provided a shallow high-resolution 3D velocity model that can be used in the simulation of strong ground motion and for evaluating potential seismic hazards.

Data availability statement

The original contributions presented in the study are included in the article/supplementary material, further inquiries can be directed to the corresponding author.

Author contributions

MZ, XT, ZY, QL, and ZG contributed to the writing of the manuscript. XT led the field work. All authors contributed to giving constructive reviews and suggestions.

Funding

This study was supported by National Natural Science Foundation of China (42074070 and 41774071).

Acknowledgments

We are grateful to Professor Yao Huajian of USTC for providing help in the method and software of DSurfTomo, this work benefited from the thoughtful comments of two anonymous referees. The figures in this work made use of Generic Mapping Tool (GMT; http://gmt.soest.hawaii.edu/) and Seismic Analysis Code (SAC; http://ds.iris.edu/ds/nodes/dmc/software/downloads/sac/) software.

Conflict of interest

The authors declare that the research was conducted in the absence of any commercial or financial relationships that could be construed as a potential conflict of interest.

Publisher's note

All claims expressed in this article are solely those of the authors and do not necessarily represent those of their affiliated organizations, or those of the publisher, the editors and the reviewers. Any product that may be evaluated in this article, or claim that may be made by its manufacturer, is not guaranteed or endorsed by the publisher.

References

Bensen, G. D., Ritzwoller, M. H., Barmin, M. P., Levshin, A. L., Lin, F., Moschetti, M. P., et al. (2007). Processing seismic ambient noise data to obtain reliable broad-band surface wave dispersion measurements. *Geophys. J. Int.* 169 (3), 1239–1260. doi:10.1111/j.1365-246X.2007.03374.x

Chen, J. B., Shen, J., Li, J., Yang, J. L., Hu, W. H., Zhao, X., et al. (2007). Preliminary study on new active characteristics of Kusongmuxieke Mountain front Fault in the west segment of North Tianshan. *Northwestern Seismological Journal* 29 (4), 335–340.

China Earthquake Administration (2017b). Hazard degree map of 18 November 2017 of M6.9 of Milin earthquake. Avaliable At: https://www.cea.gov.cn/cea/dzpd/dzzt/2383773/2383775/3308111/index.html.

China Earthquake Administration (2014). Hazard degree map of the 7 October 2017 M6.8 Jinggu earthquake. Avaliable At: https://www.cea.gov.cn/cea/dzpd/dzzt/370050/370051/5457990/index.html.

China Earthquake Administration (2017a). Hazard degree map of the 8 August 2017 M7.0 Jiuzhaigou earthquake. 2017-08-12. Avaliable At: https://www.cea.gov.cn/cea/dzpd/dzzt/369861/369863/5573795/index.html.

Fang, H. J., Yao, H. J., Zhang, H. J., Huang, Y-C., and van der Hilst, R. D. (2015). Direct inversion of surface wave dispersion for three-dimensional shallow crustal structure based on ray tracing: Methodology and application. *Geophys. J. Int.* 201 (3), 1251–1263. doi:10.1093/gji/ggv080

Fu, G. Y., and Wang, Z. Y. (2020). Crustal structure, isostatic anomaly and flexure mechanism around the Jinghe MS6.6earthquake inXinjiang. *Chin. J.Geophys.* 63 (6), 2221–2229. doi:10.6038/cjg2020N0076

Gao, J., Qian, Q., Long, L. L., Zhang, X., Li, J. L., and Su, W. (2009). Accretionary orogenic process of western tianshan, China. *Geol. Bull. China* 28 (12), 1804–1816.

Gao, Z. Y., Zhou, C. M., Feng, J. R., Wu, H., and Li, W. (2016). Relationship between the tianshan mountains uplift and depositional environment evolution of the basins in Mesozoic-Cenozoic. *Acta sedimentol. sin.* 34 (3), 415–435.

Gu, N., Wang, K. D., Gao, J., Ding, N., Yao, H. J., and Zhang, H. J. (2019). Shallow crustal structure of the tanlu fault zone Near Chao lake in eastern China by direct surface wave tomography from local dense array ambient noise analysis. *Pureand Appl. Geophys.* 176 (3), 1193–1206. doi:10.1007/s00024-018-2041-4

He, X. H., Li, T., Wu, C. Y., Zheng, W. J., and Zhang, P. Z. (2020). Resolving the rupture directivity and seismogenic structure of the 2017Jinghe MS6.6 earthquake with regional seismic waveforms. *Chin. J.Geophys.* 63 (4), 1459–1471. doi:10.6038/cjg2020N0309

Herrmann, R. B., and Ammon, C. J. (2004). "Surface waves receiver functions and crustal structure," in *Computer programs in seismology*. Saint Louis, Madrid: Saint Louis University. Avaliable At: http://www.eas.slu.edu/People/RBHerrmann/CPS330.html.

Jin, H., Zhang, Z. B., Zhao, S. Z., and Yan, X. Y. (2019). Focal Mechanism analysis of Jinghe earthquake with Ms 6.6 on August 9th, 2017. *Inland Earthquake* 33 (3), 209–217.

Li, C., Yao, H. J., Fang, H. J., Huang, X. L., Wan, K. S., Zhang, H. J., et al. (2016). 3D near-surface shear-wave velocity structure from ambient-noise tomography and borehole data in the hefei urban area, China. *Seismol. Res. Lett.* 87 (4), 882–892. doi:10.1785/0220150257

Li, L. L., Huang, X. L., Yao, H. J., Liao, P., Wang, X. L., Bao, Z. W., et al. (2020). Shallow shear wave velocity structure from ambient noise tomography in Hefei city and its implication for urban sedimentary envoirement. *Chin. J.Geophys.* 63 (9), 3307–3323. doi:10.6038/cjg2020O0097

Lin, F. C., Li, D. Z., Clayton, R. W., and Hollis, Dan. (2013). High-resolution 3D shallow crustal structure in Long Beach, California: Application of ambient noise tomography on a dense seismic array. *Geophysics* 78 (4), Q45–Q56. doi:10.1190/geo2012-0453.1

Luo, Y. H., Yang, Y. J., Xu, Y. X., Xu, H. R., Zhao, K. F., and Wang, K. (2015). On the limitations of interstation distances in ambient noise tomography. *Geophys. J. Int.* 201 (2), 652–661. doi:10.1093/gji/ggv043

Ministry of Emergency management of the People's Republic of China (2022). Hazard degree map of the 5 September 2022 M6.8 Luding earthquake. Avaliable At: http://www.mem.gov.cn/xw/yjglbgzdt/202209/t20220911_422190.shtml.

Paige, C., and Sanders, M. A. (1982). Lsqr: An algorithm for sparse linear equations and sparse least squares. *ACM Trans. Math. Softw.* 8, 43–71. doi:10.1145/355984.355989

Qi, J. F., Chen, S. P., Yang, Q., and Yu, F. S. (2008). Characteristics of tectonic deformation within transitional belt between the Junnggar Basin and the northern Tianshan Mountain. *Oil Gas Geol.* 29, 2.

Rawlinson, N., and Sambridge, M. (2004). Wave front evolution in strongly heterogeneous layered media using the fast marching method. *Geophys. J. Int.* 3, 631–647.

Shao, X.Z (1996). crustal structure and tectonics of tianshan orogenic belt: Urumqi-korla deep sounding profile by converted waves of earthquakes. *Chin. J. Geophys.*, 39 (3): 336–346.

Shao, X. Z., Zhang, J. R., Fan, H. J., Zheng, J. D., Xu, Y., Zhang, H. Q., et al. (1996). The crust structures of Tianshan Orogenic belt: a deep sounding work by converted waves of earthquakes along Urumqi-Korla profile. *Acta Geophysica Sinica* 39 (3), 336–345.

Sun, G. L., Wang, K. R., Yang, X. Y., Zhang, Z. F., and Hong, J. A. (1997). The geological and geochemical significance of oil and gas shows in the Bortala Basin, Northern Xinjiang. *Acta Geologica Sinica* 71 (1), 75–85.

Wang, X. L., Gu, X. X., Zhang, Y. M., Peng, Y. W., Zhang, L. Q., Gao, H., et al. (2013). Temporal-spatial distribution, tectonic evolution and metallogenic response of the magmatic rocks in the Boluokenu metallogenic belt, west Tianshan, Xinjiang. *Geol. Bull. China* 32 (5), 774–783.

Wang, Y., Lee, T., Wang, Y. B., and Li, J. C. (2000). Depositional characteristics of late cenozoinc and their tectonic significance of foreland basins at both sides of tianshan mountains in China. *Xingjiang Geol.* 18 (3), 245–250.

Xinjiang Earthquake Administration (2018). Hazard degree map of the 9 August 2017 M6.6 Jinghe earthquake. Avaliable At: http://www.eq-xj.gov.cn/xwdt/hydt/25110.htmxj.gov.cn.

Yao, H., Gouedard, P., McGuire, J., Collins, J., and van der Hilst, R. D. (2011). Structure of young east pacific rise lithosphere from ambient noise correlation analysis

of fundamental- and higher-mode scholte-Rayleigh waves. *Comptes Rendus Geoscience* 343 (8-9), 571–583. doi:10.1016/j.crte.2011.04.004

Yao, H. J., van der Hilst, R. D., and de Hoop, M. V. (2006). Surface-wave array tomography in SE tibet from ambient seismic noise and two-station analysis: I-phase velocity maps. *Geophys. J. Int.* 166 (2), 732–744. doi:10.1111/j.1365-246X.2006.03028.x

Yao, H. J., van der Hilst, R. D., and Montagner, J. P. (2010). Heterogeneity and anisotropy of the lithosphere of SE Tibet from surface wave array tomography. *J. Geophys. Res.* 115, B12307. doi:10.1029/2009JB007142

Zellmer, G. F., Chen, K. X., Gung, Y., Kuo, B. Y., and Yoshida, T. (2019). Magma transfer processes in the NE Japan arc: Insights from crustal ambient noise tomography combined with volcanic eruption records. *Front. Earth Sci.* 7, 40. doi:10.3389/feart.2019.00040

Zhang, M., Mu, Y. Q., Han, L. G., and Liao, H. (2017b). Analysis of tectonic stress field in Bole basin and its surrounding area since Carboniferous. *Petroleum Geol. Eng.* 31 (5), 5–8.

Zhang, M., Xu, T., Mu, Y. Q., Han, L. G., and Liao, H. (2017a). Optimization of favorable exploration zones in Bole Basin. *Petroleum Geol. Eng.* 31 (3), 38–41.

Zhou, M., Tian, X. F., and Wang, F. Y. (2018). Shallow velocity structure of Luoyang basin derive d from dense array observations of urban ambient noise. *Earthq. Sci.* 32, 30–39.

Zulfakriza, Z., Nugraha, A. D., Widiyantoro, S., Cummins, P. R., Sahara, D. P., and Rosalia, S. (2020). Tomographic imaging of the agung-batur volcano complex, bali, Indonesia, from the ambient seismic noise field. *Front. Earth Sci.* 8, 43. doi:10.3389/feart.2020.00043

frontiers | Frontiers in Earth Science

TYPE Original Research
PUBLISHED 09 May 2023
DOI 10.3389/feart.2023.1169877

Check for updates

OPEN ACCESS

EDITED BY
Fuqiong Huang,
China Earthquake Networks Center, China

REVIEWED BY
Zhuowei Xiao,
Chinese Academy of Sciences, China
Chengxin Jiang,
Australian National University, Australia

*CORRESPONDENCE
Hongyi Li,
lih@cugb.edu.cn

RECEIVED 20 February 2023
ACCEPTED 11 April 2023
PUBLISHED 09 May 2023

CITATION
Ma Z, Li H, Liu M, Huang Y, Zhang S and Lv Y (2023), Micro-seismic events detection and its tectonic implications in Northeastern Hainan Province.
Front. Earth Sci. 11:1169877.
doi: 10.3389/feart.2023.1169877

COPYRIGHT
© 2023 Ma, Li, Liu, Huang, Zhang and Lv. This is an open-access article distributed under the terms of the Creative Commons Attribution License (CC BY). The use, distribution or reproduction in other forums is permitted, provided the original author(s) and the copyright owner(s) are credited and that the original publication in this journal is cited, in accordance with accepted academic practice. No use, distribution or reproduction is permitted which does not comply with these terms.

Micro-seismic events detection and its tectonic implications in Northeastern Hainan Province

Zeyu Ma[1], Hongyi Li[1]*, Min Liu[1], Yafen Huang[1], Shengzhong Zhang[2] and Yuejun Lv[3]

[1]School of Geophysics and Information Technology, China University of Geosciences (Beijing), Beijing, China, [2]Network Information Center, China University of Geosciences (Beijing), Beijing, China, [3]National Institute of Natural Hazards, Beijing, China

In this paper, we combine the U-net-based phase picking method (PhaseNet) with Graphics Processing Unit-Based Match and Locate technology (GPU-M&L) and a deep-learning-based seismic signal de-noising method (DeepDenoiser) as a workflow for automatically extracting micro-seismic information from continuous raw seismic data. PhaseNet is first used to detect missed seismic phases by scanning through the 5-year continuous waveform data recorded at five broad-band stations in Hainan province. Then Rapid Earthquake Association and Location method (REAL), VELEST program (1-D inversion of velocities and hypocenter locating) and HypoDD (a double-difference locating method) are applied to associate seismic phases with events and to locate, respectively. This initially established catalogue can be served as the template for the following match-filter work. We choose events with a high signal-to-noise ratio (SNR) as templates and apply GPU-M&L to detect more small earthquakes which are difficult to pick by routine methods due to the low SNR. Then, a deep learning-based noise reduction technique named DeepDenoiser is applied to extract seismic signal from noise to provide a better picking of arrival time and then to improve the relocation effects. Finally, we use HypoDD to relocate these events with P- and S- wave arrival times picked by PhaseNet. Compared with the five events listed in the China Earthquake Networks Center routine catalogue, in this study, we detect and locate 977 earthquakes by following the above procedure. Our relocation results illustrate quite a complex distribution pattern of events due to the complicated fault system in the northeastern part of Hainan Province.

KEYWORDS

seismicity and tectonics, machine learning, seismic signal denoising, phase picking, Hainan (China), fault monitoring and diagnosis

1 Introduction

The identification and location of small earthquakes play a key role in studying the nucleation of large earthquakes, the geometry of fault zones, the monitoring of tremors, low-frequency earthquakes, and micro-earthquakes caused by hydraulic fracturing. However, how to quickly extract small earthquake information from the massive raw continuous waveform data still poses a challenge to seismologists. The traditional phase-picking method is not sufficiently competent in detecting low-magnitude events due to the low signal-to-noise ratio (SNR). In recent years, various techniques for microearthquake detection and phase picking have been proposed, and they can be generally sorted into two main categories: waveform based and pick-based seismic detection.

The operation principle of waveform-based seismic detection is to scan continuous waveforms based on earthquake waveform similarity for finding missing seismic events. For earthquakes with similar focal mechanisms that occurred in adjacent areas, their waveforms show a high degree of similarity. Therefore, using identified seismic events *a priori* as the templates to scan over the continuous waveforms can effectively detect events with low SNR. Matching filter technology (MFT) based on waveform cross-correlation and stacking (Gibbons et al., 2006; Shelly David et al., 2007; Peng and Zhao, 2009), has been proposed and then widely used to detect low-magnitude seismic events. Shelly David et al., 2007 used MFT to detect non-volcanic tremor and low-frequency earthquake swarms and their results reveal the deep structure of seismogenic faults. Meng et al. (2013) applied the MFT method to the 2003 San Simeon earthquake, focusing on aftershock-triggering mechanisms and discussed the subsequent screening principle of the MFT detection events. This technique can detect more seismic events compared with conventional methods, however, its detection performance significantly depends on seismic template events.

In recent years, machine learning, especially deep learning, has been widely used in various scientific fields and has shown great efficiency (Ross et al., 2018; Bergen et al., 2019; Kong et al., 2019; Reichstein et al., 2019; Zhang et al., 2019; Zhou et al., 2019; Zhu and Beroza., 2019; Zhang et al., 2022; Mousavi and Beroza, 2022). Seismologists also apply the deep learning algorithm to the research of earthquake such as event identification, association, and classification. Compared with traditional calculation methods, the deep learning method has the advantages of high efficiency and time and labour saving. Machine learning builds a neural network through a large number of samples, either labelled or not.

Using the deep learning algorithm to identify and associate earthquake phases through the raw continuous waveforms, and then using the MFT algorithm to scan missing events recently has become a highly recognized workflow. Liu et al. (2020a) first combined MFT with deep learning phase-picking methods to construct a high-precision seismic catalogue of the 2019 Ridgecrest earthquake sequence. Zhang et al. (2022) integrated this set of methods into an automatic and pervasive end-to-end workflow (LOC-FLOW). Zhou et al. (2021) have proposed a similar automatic and systematic workflow, PALM, which is also based on different machine learning methods and MFT.

However, both machine learning and MFT techniques may produce false detections since the criteria of picking are based on probability value or cross-correlation threshold which are artificially set and may not be optimal in specific problems. In this study, we propose a new workflow which combines PhaseNet with GPU-M&L technology and DeepDenoiser to extract seismic event signals from continuous raw data. PhaseNet is first used to detect event signals by scanning through raw continuous data . The REAL (Zhang et al., 2019), VELEST (Kissling et al., 1995) and HypoDD (Waldhauser and Ellsworth, 2000) are applied to associate seismic phases with events and locate events, respectively. We select events with a high SNR as templates from the initial catalogue constructed by following the above procedure and apply the GPU-M&L to detect more small earthquakes which are difficult to detect by traditional methods. Then, DeepDenoiser is applied to further confirm the detection of seismic events and simultaneously to provide a better phase picking. Finally, HypoDD is utilized again to relocate these events.

In 1,605, an earthquake of magnitude 7.5 occurred near Haikou in the northeastern part of Hainan Province. This earthquake occurred near the east-west Maniao-Puqian fault system (MPF) and the NNW-trending Puqian-Qinglan fault system (PQF) which are both composed of several faults as shown in Figure 1. These two faults were very active in the Quaternary and controlled the development of the Cenozoic basin and the extent of Quaternary volcanism up to at least the Late Pleistocene (Wang, et al., 2021). The crustal movement in this area has been characterized by strong vertical rise and fall since the Neogene. Uneven subsidence under the control of the NNW trending faults has led to the formation of graben-horst structures. The MPF is a system of deeply extended faults that runs nearly east-west and has been active since the late Cenozoic. The MPF is cut by several NNW-oriented faults, including hidden and exposed faults. Based on the results of gravity measurements and seismic surveys, the faults in the PQF spread horizontally in parallel, in a complex graben-horst configuration. The seismicity of this fault system is weak in the south and strong in the north (Wang et al., 2021). Studying the long-term seismicity of these two faults and their surrounding area can help provide a data basis for analyzing the seismogenic mechanism and tectonic environment of the 1,605 Haikou paleo earthquake.

Based on the results of previous imaging of the subsurface structure in the area, there is a clearly tilted low-velocity anomaly in the crust. This low-velocity anomaly may be associated with the magma and fluids which have a deep root connected with the mantle plume (Lei et al., 2009; Lin et al., 2022). The study of seismic activity in this area will also provide a basis for studying the Hainan hotspot.

In this study, we apply our proposed new workflow to northeast Hainan to study the complex fault system by detecting the seismicity from 2014 to 2018.

2 Methods

The three-component continuous waveform data from January 2014 to December 2018 with a 100 Hz sampling rate recorded by 5 stations are provided by Hainan Earthquake Administration. Only 5 earthquake events are provided from the CENC catalogue around the fault zone area within 5 years.

Firstly we use PhaseNet, an algorithm for identifying seismic phases based on deep learning, to pick up P- and S- phase signals. Secondly, based on the arrival of seismic phases, we use the REAL algorithm to associate them as seismic events. Thirdly, we use the absolute location method VELEST and the double-difference relative location algorithm HypoDD to locate events. Fourthly, we apply GPU-M&L which introduces a weighting factor of SNR on different traces of waveforms, to calculate the cross-correlation coefficient between each template with the 5-year continuous waveform. Fifthly, we use DeepDenoiser, a deep learning denoise algorithm to extract the noise from the signal to further confirm detections. Finally, we use HypoDD again to relocate all the remained earthquakes. The complete workflow is demonstrated in Figure 2 and the principles and technical details of the methods are described.

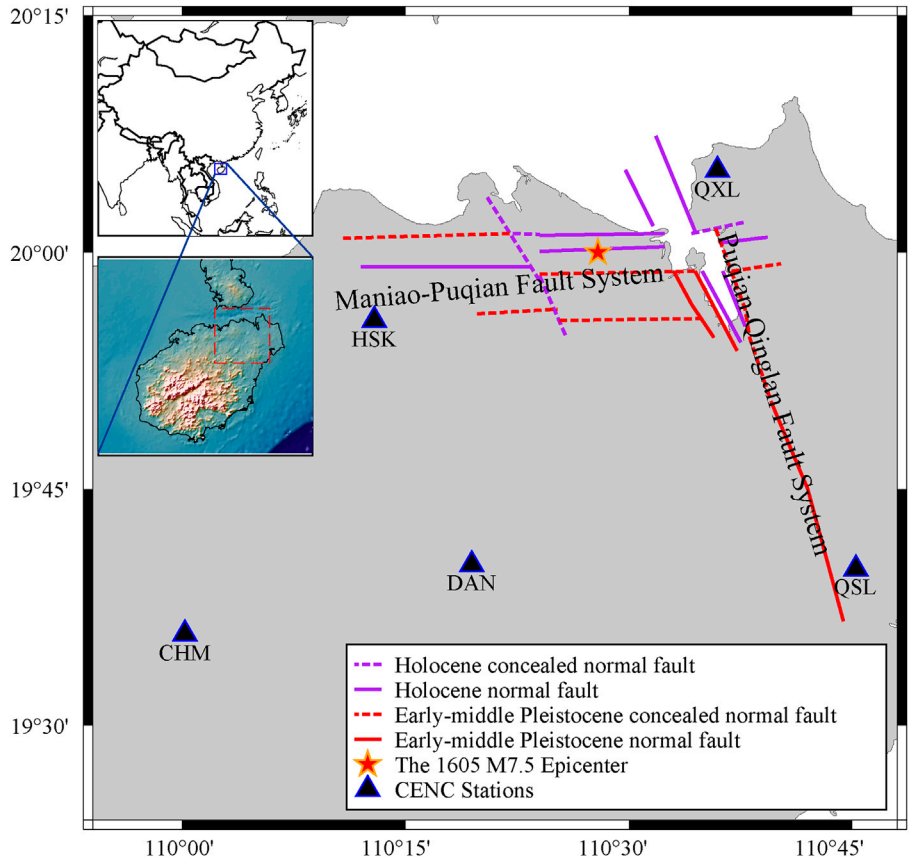

FIGURE 1
Map of the study area and fault systems. The insets in the upper left corner show the study area on a large map of Hainan Province and of China.

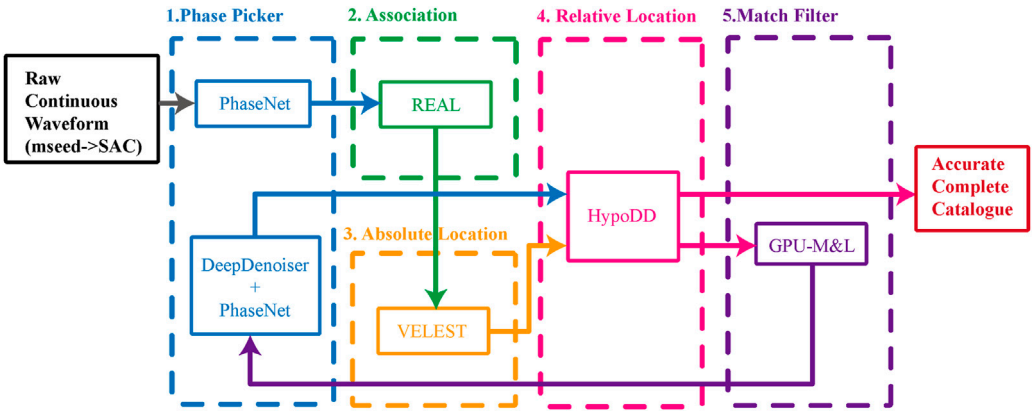

FIGURE 2
Schematic diagram of the workflow.

The phase-picking method based on deep learning - PhaseNet uses a large number of manually labelled seismic waveforms as its training set, providing a model that can label P- and S-wave arrivals with probability peaks. Considering the lack of a large number of seismic events in the Hainan region as training samples for transfer learning, we used the North California model trained by Zhu et al. (2019). This model has been widely applied to different countries and regions and has shown good results. Yen et al. (2021) applied PhaseNet with this model to build a high-resolution catalogue for the central Italy seismic sequence. Li et al. (2023) applied this model

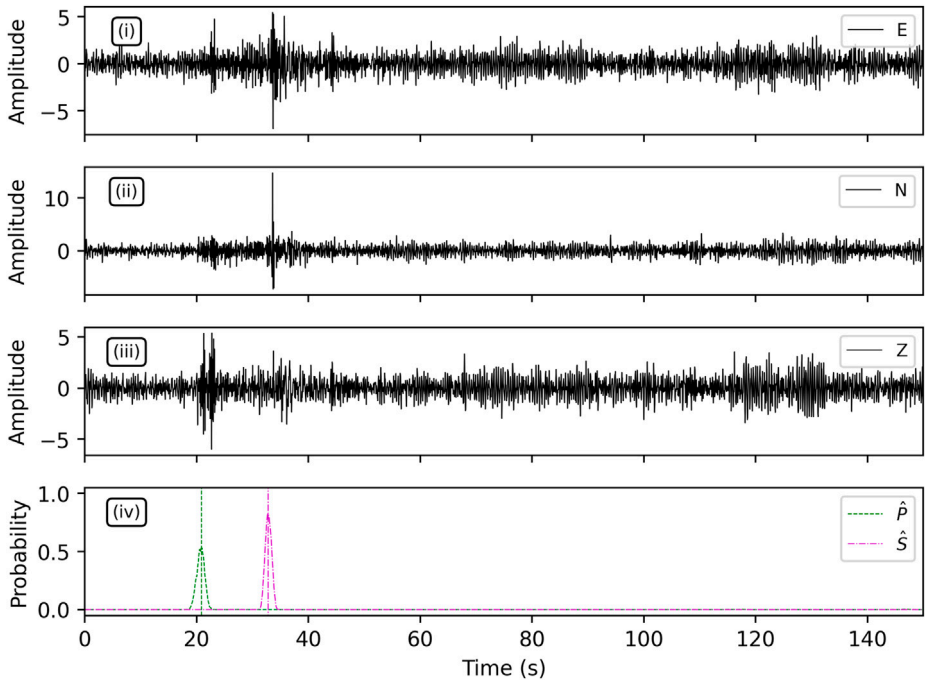

FIGURE 3
PhaseNet picking diagrams showing a new detected event with picked P (green) and S (purple) phases.

in Northeastern China to build a complete small earthquake catalogue to study the Magmatic system and seismicity of the Arxan volcanic group.

The continuous seismic waveform is rearranged as two groups with 15-second-interval and 30-second-long (i.e. 3,000 data points) windows for scanning. Before scanning, to optimize the scanning results and better apply the model, all the original seismic waveforms were temporally normalized without filtering or changing the sampling rate.

It is worth mentioning that we usually set a selection criterion for PhaseNet, which is called the threshold of probability. But this threshold itself does not represent the true positive detection possibility. We regard it as the degree of similarity between the actual processed data and the training set.

The Rapid Earthquake Association and Location technology (REAL) can be used to associate seismic phases and locate seismic events quickly and automatically. Combining the advantages of arrival time picking and waveform-based detection and location methods, the REAL method associates the arrival times of one event from different stations and determines the epicenters by calculating the number of P-wave and S-wave arrival times and travel time residuals.

Based on continuous waveform data recorded by 5 stations in northeast Hainan Province, we used the REAL method to perform association and preliminary location Considering that the 5 fixed stations have a wide distribution range and the average distance between stations is more than 50 km, when at least 5P and 3S phases of a certain earthquake have been recorded, respectively, they will be associated as an event. VELEST, an absolute locating method based on a 1D velocity model and HypoDD, a double-difference locating method were applied to the REAL results to refine the location. VELEST can give an updated 1D velocity model by iteration. Our initial model incorporates previous tomography studies (Lei et al., 2009; Huang, 2014) in the Hainan region and this 1D model is further updated using VELEST to provide better-locating results.

The M&L technology developed by Zhang and Wen. (2015) can give the locations of the events while running the template cross-correlation scanning. While the waveform is being slide-scanned, M&L will search the gridded 3D space in the limited detection area. At each potential position, the travel time difference will be calculated to revise the superimposition result of the cross-correlation waveform. On this basis, Liu et al. (2019) optimized the original M&L program and parallelized processing based on GPU acceleration. The difference between GPU-M&L and M&L is 1) to add a weight factor to each component of the template to improve the detection ability; 2) to implement the M&L method on the GPU to speed up the calculation. The data-trace with a high signal-to-noise ratio will be given higher weight in the step of cross-correlation and superposition.

The operation of the MFT requires that a template is provided and its sensitivity is also highly dependent on the consistency of the waveform between the template and the event to be detected. The application of PhaseNet and REAL to the original waveform can supplement template events for the template matching method, thereby improving the ability to detect missing small earthquake events. In this study, in addition to the earthquake catalogue provided by the Hainan Earthquake Administration, the earthquakes detected by the PhaseNet and REAL methods were also screened and supplemented as template events to improve the detection capabilities of GPU-M&L.

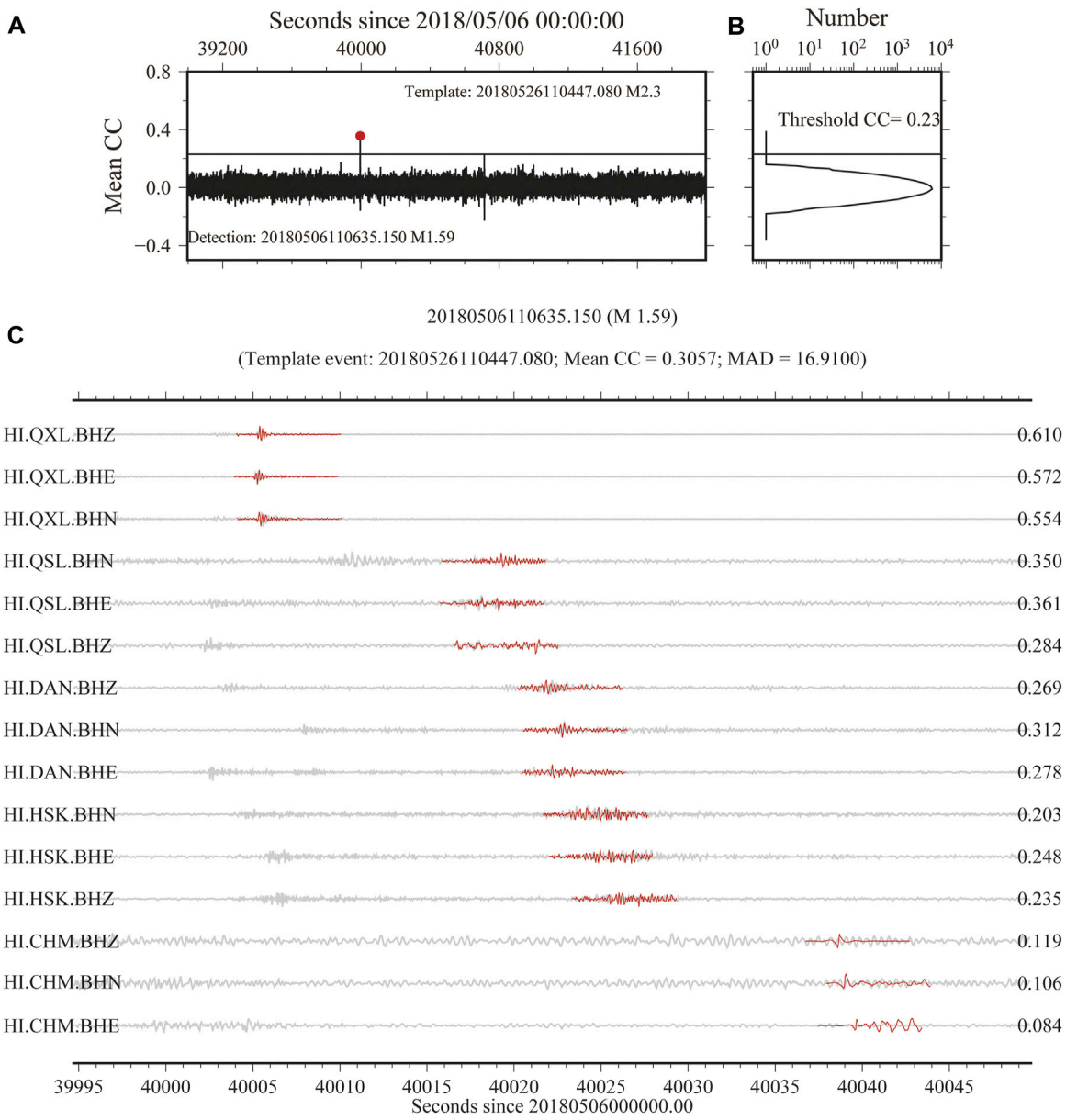

FIGURE 4
An example of template matching scan result. **(A)**. Correlation function for template event with a 3,000-s continuous waveform. **(B)**. A histogram of average correlation values is shown. **(C)**. Continuous waveforms are shown in grey and template event waveforms are in red for each component of 5 CENC stations.

DeepDenoiser is a seismic signal de-noising program developed by Zhu et al. (2019) based on a convolution neural network. After the training of a large number of samples, this program shows good de-noising ability and can perform well in many cases with a low signal-to-noise ratio. DeepDenoiser identifies the time-spectrum image of the input window signal, suppresses the signal which is considered as noise and provides a lossless effective seismic signal. In addition, the event phases after DeepDenoiser are easier to be picked by PhaseNet, so we use PhaseNet to re-mark the de-noised events again. This can provide more accurate and reliable arrival information for event relocation. It is worth mentioning that in previous studies, deep-learning-based frequency-domain seismic signal de-noising usually follows training using specific data (Saad and Chen, 2021; Dahmen et al., 2022; Dong et al., 2022; Yang et al., 2022). The re-trained models have better noise reduction for the data in the specific regions. In our case, we directly use the DeepDenoiser with the North California model without re-training because of the insufficiency of the seismic event data. Since the noise statistics are automatically learned from the data without any assumptions (Zhu et al., 2019), DeepDenoiser can correctly handle various noise signals, hence providing a generalization in the data from different area. It is still recommended to use fine-tuning and re-training models for denoising when sufficient data is available.

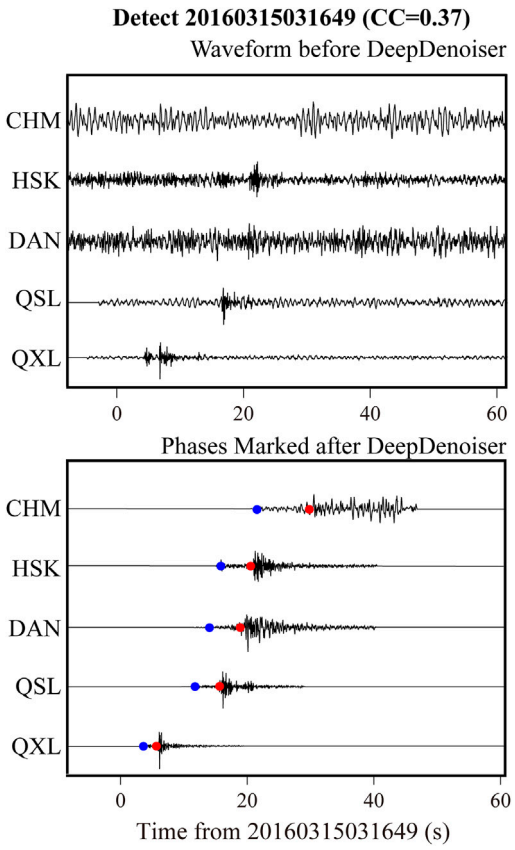

FIGURE 5
An event detected with a CC of 0.37. The arrival time has been revised by DeepDenoiser and Phasenet and the waveform signal is much clearer after de-noising.

3 Results

We applied PhaseNet to scan the 5-year continuous waveforms from 2014 to 2018 at 5 stations in northeast Hainan province to pick the seismic phases. PhaseNet effectively detected the P-wave and S-wave phases in continuous seismic data as shown in Figure 3.

To make the data more suitable for the trained neural network parameter model, we applied the Z-score to normalize the data. The data are rearranged as two groups with 15-second-interval and 30-second-long (i.e. 3,000 data points) windows for scanning. From all continuous waveforms, a total of about 102P-wave and 60 S-wave arrivals have been detected.

The REAL earthquake association and the initial location are then calculated by grid search based on the travel time residual (Zhang et al., 2019). In this study, the horizontal direction of the search area is set to 0.4 × 0.4°with grid size of 0.02 × 0.02, and the depth ranges from 0 to 20 km with a grid size of 2 km. The grid centre is located at the station. Only events associated with over 3P-phases and over 5P- or S- phases will be retained, The selection criterion depends on the number of stations and the quality of the data. Their location will be initially determined on the grid with the largest number of phases. When there are the most identical choices, the grid with the smallest travel time will be selected. Then the absolute locating algorithm VELEST and double-difference relocation method HypoDD is applied to refine the location results.

In the study area, a total of 9 events were scanned and successfully associated. These events include all 5 events recorded in the routine catalogue provided by CENC. 7 of the events detected by the workflow with high SNR and clear phase, whose magnitudes range from 2.3 to 3.4 were relocated and used as template events. The determination of the magnitude of the detected events is calculated based on the widely used relationship between amplitude and local magnitude (Hutton and Boore, 1987).

We then applied the GPU-M&L to the continuous waveform data recorded by the five stations QSL, QXL, DAN, CHM and HSK around the fault. To improve the effect of the template matching process and the reliability of the processing results again, we make certain pre-processing for the waveforms of the continuous waveform and the template event, which includes down-sampling to 20 Hz, de-meaning, de-linearizing trend and filtering to 1–10 Hz. In addition, for the template events, the arrival time information of the P-wave and S-wave is given by the phase information picked up by PhaseNet. Based on this time information marking, the signal-to-noise ratio of each component of the template event is calculated. The data with high SNR are attached to higher weighting factors in the step of template matching, cross-correlation and stacking.

1,450 events have been detected by GPU-M&L with a magnitude larger than −1.0. The events with a weighted average cross-correlation coefficient greater than a threshold are selected as positive detection. Figure 4 shows a schematic diagram of cross-correlation threshold selection.

We first use the conventional Tau-P calculated theoretical arriving time to mark the P- and S- phases on event files. Then we apply DeepDenoiser to extract seismic signals. After that, we update the P- and S- marks with the arrival times provided by PhaseNet (Figure 5). Figure 6 shows the time-magnitude diagram of all the events scanned by GPU-M&L and those further confirmed with DeepDenoiser and PhaseNet.

Then we use HypoDD to constrain and relocate events. In the HypoDD algorithm, we set the weights of the arrival of P waves and S waves as 1.0 and 0.5, respectively. A catalogue of 977 events is finally confirmed with a reliable location. Figure 7 shows the final relocation results of events. A large number of small earthquakes were detected along the boundary of the MPF and PQF zones. 228 out of 977 (23.34%) events of the catalogue are detected by the new template events by PhaseNet. They also fill a large portion of the seismic catalog spatially, providing a big database to delineate the fault feature.

The three-dimensional relocation results of the final complete catalogue show a complex geometry. As we can see, both MPF and PQF are composed of a series of parallel or oblique secondary faults with similar inclinations. We notice that there are inclination differences between the deep and shallow events. Combined with the historical seismic observation records (Wang et al., 2021), it can be inferred that the fault strike in the deep part of the PQF is inconsistent with the shallow part, and it is closer to the north-south direction in the deep. The fault zones in the study area are heterogeneous in seismicity accompanied by complex fault subsidence activity.

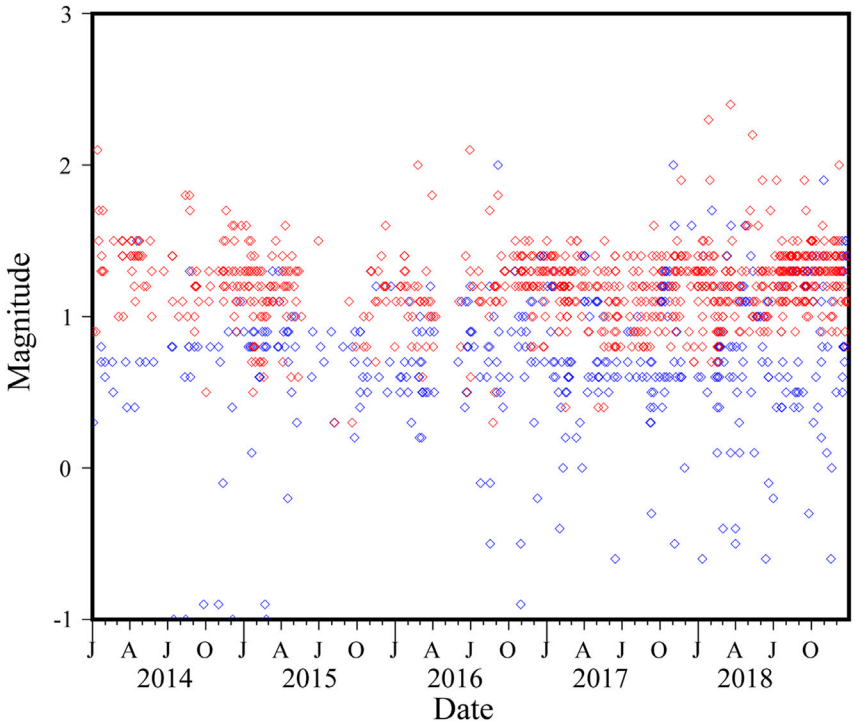

FIGURE 6
Time-magnitude diagram of all the events detected by GPU-M&L (blue) and those confirmed with DeepDenoiser and PhaseNet (red).

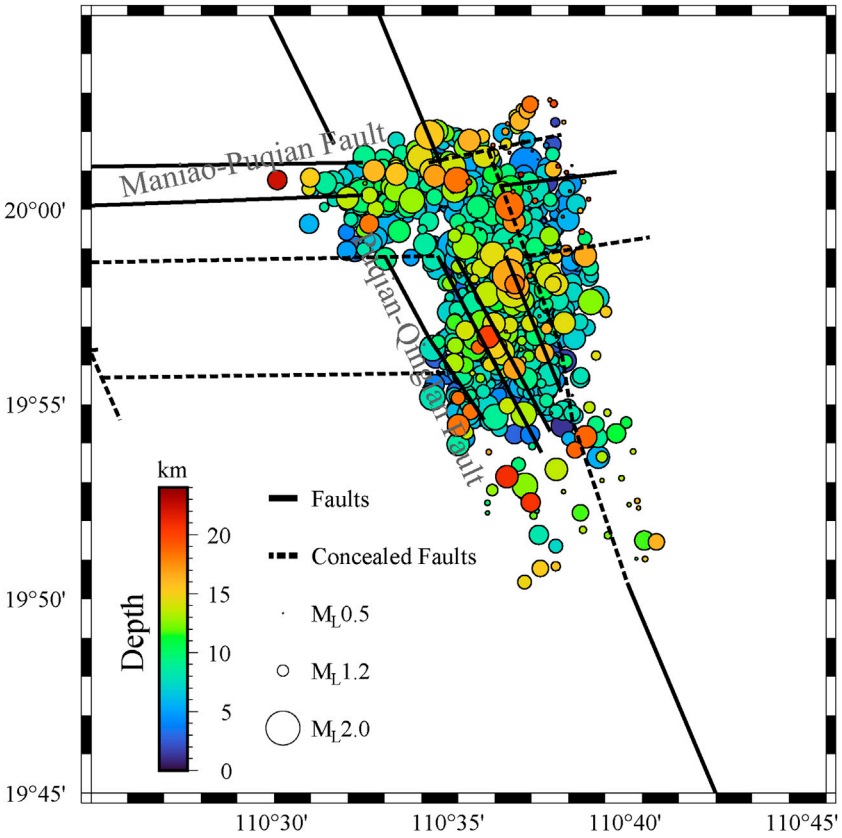

FIGURE 7
Final relocation result of microseismic events. The colour of the circles represents the source depth. And the size of the circles is proportional to the magnitude.

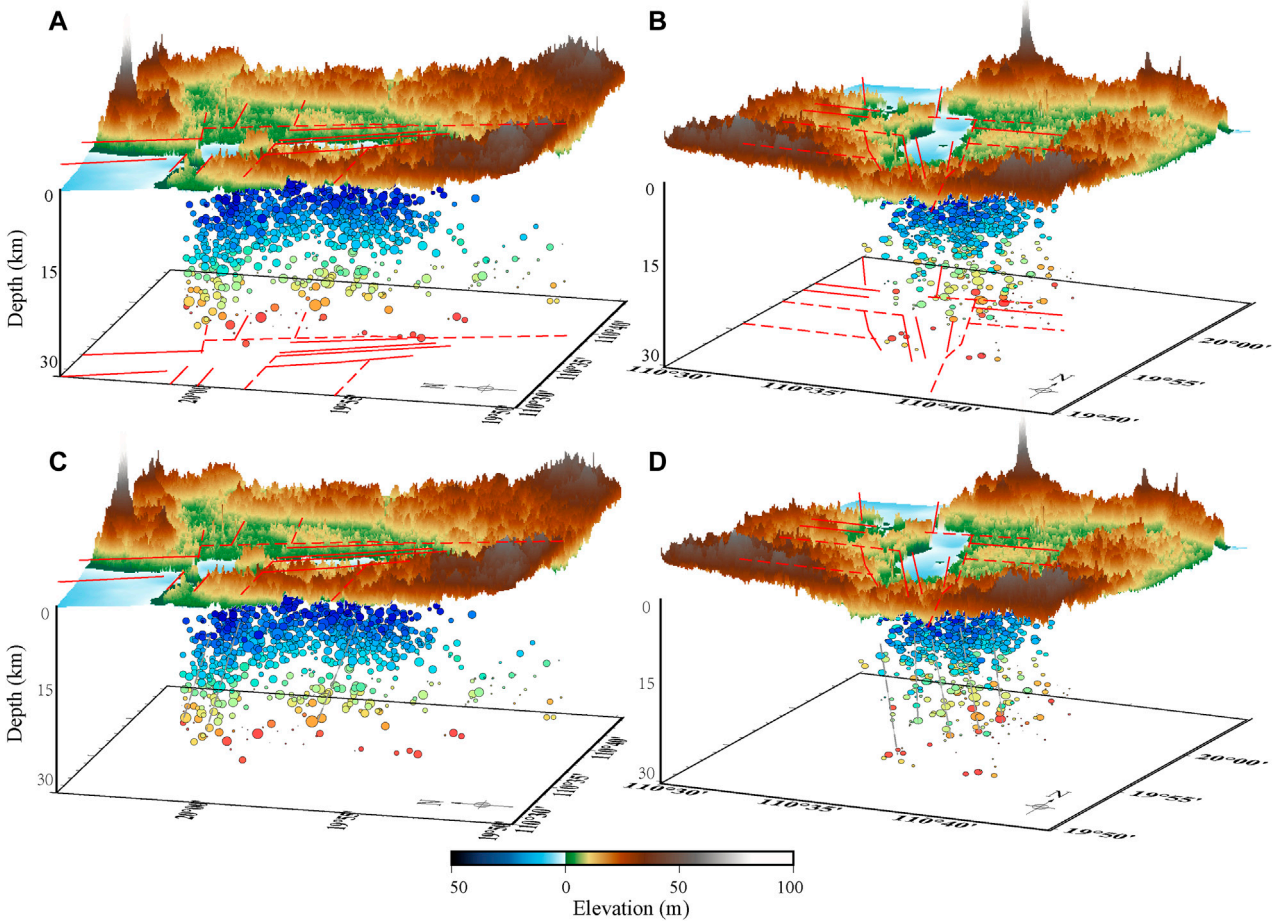

FIGURE 8
Final 3D relocation results of 977 events. The red dash lines indicate the distribution of the fault system. **(A, C)** and **(B, D)** have different viewpoints of the location results. In **(C)** and **(D)**, grey dashed lines are used to indicate the fault position and the dip angles inferred from the fault surface locations and the distribution of the detected events.

4 Discussion and conclusion

A key issue of automated small earthquake identification and detection technology based on machine learning and template matching is how to evaluate its accuracy. The identification performance of MFT for small earthquakes is powerful, but how to ensure that detected events are earthquake events is very important. Most of the constraints on detected events in the past work are limited to the setting of the cross-correlation coefficient threshold and the absolute median deviation threshold. A sufficiently high threshold usually represents higher detection reliability. However, on the other hand, it also means probably more events will be missed due to the high threshold. For different research areas and research purposes, the setting of this threshold is different. Different cross-correlation coefficient thresholds and MAD thresholds have been used in numerous previous works on MFT (Gibbons et al., 2006; Shelly David et al., 2007; Peng and Zhao, 2009; Meng et al., 2013; Liu et al., 2020b; Zhang et al., 2022; Zhou et al., 2021). These adjustments were derived from the experience of the data processors and feedback on the evaluation of the results. This has led to difficulties in establishing a systematic workflow and selecting criteria for specific research questions in specific regions. There have been some previous studies on the confirmation of the accuracy of the template matching results. Liu et al. (2019) used the methods of waveform envelope and spectrum analysis to preliminarily evaluate the robustness of event detection over a period of time. In our research, we used the DeepDenoiser method to de-noise and the PhaseNet method to re-mark, combined with the location process, to finally determine all the detection events. It seems that there is no evidence that events with higher cross-correlation values have higher credibility. The cross-correlation value only makes a certain degree of mathematical judgment on the similarity of signals. Higher than a certain cross-correlation threshold can only indicate that the event is similar to the template event to some extent, instead of proving that the event is more like an earthquake. We found a few false events with high cross-correlation values—many of which are just pulse-shaped noise. This requires us to be vigilant when using technologies like MFT. We still need to consider the application scenarios of various technologies and optimize them.

The mechanism of the Qiongshan M7.5 earthquake and the environment for the formation of the structure has always been a concern of scientists. According to Wang et al. (2021), this paleoseismic event influenced the terrestrial subsidence in northeastern Hainan, which is mainly controlled by the MPF and PQF systems. The tectonic activity of subsidence in this region is heterogeneous, characterized by significant differential lifting and subsidence. Our results show that the spatial distribution of small earthquakes is strongly correlated with these two faults and their secondary branches. As we have seen from our relocation, the network of conjugate faults consisting of the MPF and PQF zones plays a crucial role in the seismic activity which leads to a complex distribution of small earthquakes without a typical linear trend. In addition, the rise of these faults constitute a graben-horst structure, which also makes the distribution of small earthquakes have no dominant focal depth. Earthquakes that occurred on the MPF indicate that the fault system is more active in the eastern section which is influenced by the intersection with the PQF.

Lei et al. (2009) discussed in detail the effects of hot spots on Hainan Island and mantle plume activities. According to the previous subsurface velocity structure tomography (Huang, 2014; Lei et al., 2019; Lin et al., 2022) in the Hainan area, low-velocity anomalies are distributed from the lower mantle to the crust in this area, which is inferred to be related to the mantle plume. As seen in Figure 8, there is a gap zone of small earthquakes along the PQF in the range of 10–20 km. As given in Figure 7, there is a strike difference in the linear distribution of small earthquakes between the deep and shallow parts, that is, the small earthquakes in the deep part (red circles) tend to occur more in the north-south direction. We infer that may be related to fluids which could influence the tectonic activity in this area.

In summary, this study proposes a systematic and automated small earthquake detection and location workflow. We introduce DeepDenoiser into the workflow to improve the reliability of detection which has not been addressed in traditional MFT and machine learning methods for identifying small earthquakes. We applied this method to a set of fault zones in Hainan, and by scanning with only 7 templates we finalized a catalogue of 977 events over a 5-year period. These earthquakes are generally distributed along the strike direction of the MPF and PQF, meanwhile also exhibit some much smaller branch faults which reveal a complex multiple conjugate fault system beneath the study area.

Data availability statement

The raw data is involved with a confidentiality agreement. Requests to access the datasets should be directed to Zeyu Ma, mazy@cugb.edu.cn.

Author contributions

ZM: data curation, methodology, data analysis, visualization and writing; HL: methodoogy, draft review and editing; ML: methodology, software, draft review and editing; YH: methodology, software; SZ: software and data curation; YL: methodoogy and validation.

Funding

This research is co-supported by National Key R&D Program (2022YFF0800701), the National Natural Science Foundation of China (41874063), and Beijing Natural Science Foundation No.8212041.

Acknowledgments

Thanks to the Hainan Earthquake Administration for providing the earthquake catalogue and seismic waveform data. The maps in our paper were made by the Generic Mapping Tools (Wessel et al., 2013) and the Matplotlib (Hunter, 2007). The series of programs we use are open-source by their authors. PhaseNet: https://doi.org/10.1093/gji/ggy423; REAL: https://doi.org/10.1785/0220190052; VELEST: https://www.researchgate.net/publication/240394087_VELEST_user%27%27s_guide-short_introduction; HypoDD: https://doi.org/10.7916/D8SN072H; GPU-M&L: https://doi.org/10.1785/0220190241; DeepDenoiser: https://doi.org/10.1109/TGRS.2019.2926772.

Conflict of interest

The authors declare that the research was conducted in the absence of any commercial or financial relationships that could be construed as a potential conflict of interest.

Publisher's note

All claims expressed in this article are solely those of the authors and do not necessarily represent those of their affiliated organizations, or those of the publisher, the editors and the reviewers. Any product that may be evaluated in this article, or claim that may be made by its manufacturer, is not guaranteed or endorsed by the publisher.

References

Bergen, K. J., Johnson, P. A., de Hoop, M. V., and Beroza, G. C. (2019). Machine learning for data-driven discovery in solid Earth geoscience. *Science* 363 (6433), eaau0323. doi:10.1126/science.aau0323

Dahmen, N. L., Clinton, J. F., Meier, M. A., Stähler, S. C., Ceylan, S., Kim, D., et al. (2022). MarsQuakeNet: A more complete marsquake catalog obtained by deep learning techniques. *J. Geophys. Res. Planets* 127 (11), 7503. doi:10.1029/2022JE007503

Dong, X., Lin, J., Lu, S., Huang, X., Wang, H., and Li, Y. (2022). Seismic shot gather denoising by using a supervised-deep-learning method with weak dependence on real noise data: A solution to the lack of real noise data. *Surv. Geophys* 43, 1363–1394. doi:10.1007/s10712-022-09702-7

Gibbons, S. J., and Ringdal, F. (2006). The detection of low magnitude seismic events using array-based waveform correlation. *Geophysical Journal International* 165 (1), 149–166. doi:10.1111/j.1365-246X.2006.02865.x

Huang, J. (2014). P-and S-wave tomography of the Hainan and surrounding regions: Insight into the Hainan plume. *Tectonophysics* 633, 176–192. doi:10.1016/j.tecto.2014.07.007

Hunter, J. D. (2007). Matplotlib: A 2D graphics environment. *Computing in science and engineering* 9 (3), 90–95. doi:10.1109/MCSE.2007.55

Hutton, L., and Boore, D. M. (1987). The ML scale in Southern California. *Bull. Seismol. Soc. Am.* 77 (6), 2074–2094. doi:10.1785/bssa0770062074

Kissling, E., Kradolfer, U., and Maurer, H. (1995). *Program VELEST user's guide-Short Introduction*. ETH Zurich: Institute of Geophysics.

Kong, Q., Trugman, D. T., Ross, Z. E., Bianco, M. J., Meade, B. J., and Gerstoft, P. (2019). Machine learning in seismology: Turning data into insights. *Seismological Research Letters* 90 (1), 3–14. doi:10.1785/0220180259

Lei, J., Zhao, D., Steinberger, B., Wu, B., Shen, F., and Li, Z. (2009). New seismic constraints on the upper mantle structure of the Hainan plume. *Phys. Earth Planet. Interiors* 173 (1-2), 33–50. doi:10.1016/j.pepi.2008.10.013

Li, J., Tian, Y., Zhao, D., Yan, D., Li, Z., and Li, H. (2023). Magmatic system and seismicity of the Arxan volcanic group in Northeast China. *Geophys. Res. Lett.* 50, e2022GL101105. doi:10.1029/2022GL101105

Lin, J., Xia, S., Wang, X., Zhao, D., and Wang, D. (2022). Seismogenic crustal structure affected by the Hainan mantle plume. *Gondwana Res.* 103, 23–36. doi:10.1016/j.gr.2021.10.029

Liu, M., Li, H., Peng, Z., Ouyang, L., Ma, Y., Ma, J., et al. (2019). Spatial-temporal distribution of early aftershocks following the 2016 Ms 6.4 Menyuan, Qinghai, China Earthquake. *Tectonophysics* Vol. 766, 469–479. doi:10.1016/j.tecto.2019.06.022

Liu, M., Li, H., Zhang, M., and Wang, T. (2020b). Graphics processing unit-based match and locate (GPU-M&L): An improved match and locate method and its application. *Seismol. Res. Lett.* 91 (2A), 1019–1029. doi:10.1785/0220190241

Liu, M., Zhang, M., Zhu, W., Ellsworth, W. L., and Li, H. (2020a). Rapid characterization of the July 2019 Ridgecrest, California, earthquake sequence from raw seismic data using machine-learning phase picker. *Geophys. Res. Lett.* 47, e2019GL086189. doi:10.1029/2019gl086189

Meng, X., Peng, Z., and Hardebeck, J. L. (2013). Seismicity around parkfield correlates with static shear stress changes following the 2003*M_w*6.5 san Simeon earthquake: Stress shadow near parkfield. *J. Geophys. Res. solid earth* 118, 3576–3591. doi:10.1002/jgrb.50271

Mousavi, S. M., and Beroza, G. C. (2022). Deep-learning seismology. *Science* 377 (6607), eabm4470. doi:10.1126/science.abm4470

Peng, Z., and Zhao, P. (2009). Migration of early aftershocks following the 2004 Parkfield earthquake. *Nat. Geosci.* 2 (12), 877–881. doi:10.1038/ngeo697

Reichstein, M., Camps-Valls, G., Stevens, B., Jung, M., Denzler, J., Carvalhais, N., et al. (2019). Deep learning and process understanding for data-driven Earth system science. *Nature* 566 (7743), 195–204. doi:10.1038/s41586-019-0912-1

Ross, Z. E., Meier, M., and Hauksson, E. (2018). P-wave arrival picking and first-motion polarity determination with deep learning. *J. Geophys. Res.* 123 (6), 5120–5129. doi:10.1029/2017jb015251

Saad, O. M., and Chen, Y. (2021). A fully unsupervised and highly generalized deep learning approach for random noise suppression. *Geophys Prospect* 69 (4), 709–726. doi:10.1111/1365-2478.13062

Shelly David, R., Beroza, G. C., and Ide, S. (2007). Non-volcanic tremor and low-frequency earthquake swarms. *Nature* 446 (7133), 305–307. doi:10.1038/nature05666

Waldhauser, F., and Ellsworth, W. L. (2000). A double-difference earthquake location algorithm: Method and application to the northern hayward fault, California. *Bull. Seism. Soc. Am.* 90, 1353–1368. doi:10.1785/0120000006

Wang, C., Jia, L., Hu, D., Zhang, S., and Chen, J. (2021). miR-30b-5p inhibits proliferation, invasion, and migration of papillary thyroid cancer by targeting GALNT7 via the EGFR/PI3K/AKT pathway. *Geol. China* 48 (2), 618–631. doi:10.1186/s12935-021-02323-x

Wessel, P., Smith, W. H., Scharroo, R., Luis, J., and Wobbe, F. (2013). Generic mapping tools: improved version released. *Eos, Transactions American Geophysical Union* 94 (45), 409–410. doi:10.1002/2013EO450001

Yang, L., Liu, X., Zhu, W., Zhao, L., and Beroza, G. C. (2022). Toward improved urban earthquake monitoring through deep-learning-based noise suppression. *Sci. Adv.* 8 (15), eabl3564–10. doi:10.1126/sciadv.abl3564

Yen, F., William, L., Ellsworth, W. L., Zhang, M., Zhu, W., Michele, M., et al. (2021). Machine-learning-based high-resolution earthquake catalog reveals how complex fault structures were activated during the 2016–2017 central Italy sequence, *Seismic Rec.* 1 (1), 11–19. doi:10.1785/0320210001

Zhang, M., Ellsworth, W. L., and Beroza, G. C. (2019). Rapid earthquake association and location. *Seismol. Res. Lett.* 90 (6), 2276–2284. doi:10.1785/0220190052

Zhang, M., Liu, M., Feng, T., Wang, R., and Zhu, W. (2022a). LOC-FLOW: An end-to-end machine learning-based high-precision earthquake location workflow. *Seismol. Soc. Am.* 93 (5), 2426–2438. doi:10.1785/0220220019

Zhang, M., and Wen, L. (2015). An effective method for small event detection: Match and locate (M&L). *Geophys. J. Int.* 200, 1523–1537. doi:10.1093/gji/ggu466

Zhang, Q., Zhang, W., Wu, X., Zhang, J., Kuang, W., and Si, X. (2022b). Deep learning for efficient microseismic location using source migration-based imaging. *J. Geophys. Res. Solid Earth* 127, e2021JB022649. doi:10.1029/2021jb022649

Zhou, Y., Ghosh, A., Fang, L., Yue, H., Zhou, S., and Su, Y. (2021). A high-resolution seismic catalog for the 2021 MS6.4/MW6.1 Yangbi earthquake sequence, Yunnan,China: Application of AI picker and matched filter. *Earthq. Sci.* 34 (5), 390–398. doi:10.29382/eqs-2021-0031

Zhou, Y., Yue, H., Kong, Q., and Zhou, S. (2019). Hybrid event detection and phase-picking algorithm using convolutional and recurrent neural networks. *Seismol. Res. Lett.* 90 (3), 1079–1087. doi:10.1785/0220180319

Zhu, L., Peng, Z., McClellan, J., Li, C., Yao, D., Li, Z., et al. (2019a). Deep learning for seismic phase detection and picking in the aftershock zone of 2008 M7.9 Wenchuan Earthquake. *Phys. Earth Planet. Interiors* 293, 106261. doi:10.1016/j.pepi.2019.05.004

Zhu, W., and Beroza, G. C. (2019). PhaseNet: A deep-neural-network-based seismic arrival-time picking method. *Geophys. J. Interna- tional* 216 (1), 261–273.

Zhu, W., Mousavi, S. M., and Beroza, G. C. (2019b). Seismic signal denoising and decomposition using deep neural networks. *IEEE Trans. Geoscience Remote Sens.* 57 (11), 9476–9488. doi:10.1109/tgrs.2019.2926772

frontiers | Frontiers in Earth Science

TYPE Original Research
PUBLISHED 15 May 2023
DOI 10.3389/feart.2023.1110056

Check for updates

OPEN ACCESS

EDITED BY
Jie Liu,
Sun Yat-sen University, Zhuhai Campus, China

REVIEWED BY
Yongxin Gao,
Hefei University of Technology, China
Hengshan Hu,
Harbin Institute of Technology, China

*CORRESPONDENCE
Wenbao Hu,
hwb@yangtzeu.edu.cn

RECEIVED 28 November 2022
ACCEPTED 25 April 2023
PUBLISHED 15 May 2023

CITATION
Fan Y, Hu W, Han B, Tang J, Wang X and Ye Q (2023), Characteristic identification of seismogenic electromagnetic anomalies based on station electromagnetic impedance. *Front. Earth Sci.* 11:1110056. doi: 10.3389/feart.2023.1110056

COPYRIGHT
© 2023 Fan, Hu, Han, Tang, Wang and Ye. This is an open-access article distributed under the terms of the Creative Commons Attribution License (CC BY). The use, distribution or reproduction in other forums is permitted, provided the original author(s) and the copyright owner(s) are credited and that the original publication in this journal is cited, in accordance with accepted academic practice. No use, distribution or reproduction is permitted which does not comply with these terms.

Characteristic identification of seismogenic electromagnetic anomalies based on station electromagnetic impedance

Ye Fan[1,2], Wenbao Hu[3]*, Bing Han[1], Ji Tang[1], Xiao Wang[2] and Qing Ye[2]

[1]State Key Laboratory of Earthquake Dynamics, Institute of Geology, China Earthquake Administration, Beijing, China, [2]China Earthquake Network Center, Beijing, China, [3]Key Laboratory of Exploration Technologies for Oil and Gas Resources of MOE, Yangtze University, Wuhan, China

The main components of seismo-electromagnetic research are the deep underground electromagnetic seismogenic environment, electromagnetic field changes at different stages of the seismogenic process, and the physical mechanism and change rules of electromagnetic properties of the earth's interior. Traditional electric and magnetic methods mainly analyze the single field change of the geoelectric field, geomagnetic field, or resistivity at frequencies less than 1 Hz. These do not include the extremely low-frequency band that is sensitive to seismic events, so it is difficult to obtain the characteristics of time-spatial variations and propagation characteristics precursors. In comparison, magnetotelluric stations observe magnetotelluric fields containing seismogenic-induced electromagnetic disturbances, and the observation frequency band is wide. In this paper, the three-dimensional numerical simulation method is used to calculate the magnetotelluric apparent resistivity anomaly generated by resistivity changes in the seismogenic zone, and the forward algorithm of arbitrarily orientated dipole source in layered earth is used to simulate the response of low-frequency pre-earthquake electromagnetic radiation. The magnetotelluric response including seismogenic resistivity anomaly and pre-earthquake electromagnetic radiation is obtained using the field component composition method. The frequency characteristics and spatial distribution characteristics of apparent resistivity anomalies are systematically analyzed, and the results are of important significance for the observation, data processing, and identification and analysis of seismic electromagnetic anomalies in different seismogenic processes.

KEYWORDS

seismogenic resistivity anomaly, pre-earthquake electromagnetic emissions, electric dipole source response, magnetotelluric response, apparent resistivity

1 Introduction

Physical quantities that can be related to electromagnetic anomalies in the earthquake developing process mainly include earth resistivity, geomagnetic field, geoelectric field, electromagnetic induction field, and electromagnetic radiation (Zhao et al., 2022). In a deep underground electromagnetic seismogenic environment, changes in the electromagnetic field in the seismogenic process, and the physical mechanism and change characteristics of electromagnetic properties of the earth's interior are the main contents of seismo-

electromagnetic research (Mao, 1986). Since the 1960s, there has been systematic research and observations of seismogenic electromagnetic phenomena in China. Observation stations have been successively set up in key earthquake risk areas for long-term observation of the geomagnetic field, geoelectric field, earth resistivity, magnetotelluric field, and electromagnetic radiation (Pan, 1998), recording a large number of electromagnetic precursors (Huang et al., 2017). In 2018, the experimental satellite *Zhang Heng No.1* was launched for seismic electromagnetic monitoring in China; from this, a space-ground joint seismic electromagnetic monitoring system was established (Zhang et al., 2020). During this period, there has been theoretical and experimental research on the mechanism of earthquake electromagnetic precursors, distribution laws and propagation characteristics, correlation with seismic activity, and information extraction (Huang, 2002; Ma, 2002; Wang et al., 2005; Ding, 2009; Gao and Hu, 2010; Du, 2011; Huang et al., 2015; Ren et al., 2015; 2016; Zhou et al., 2017). These results confirm that the earthquake preparation process does cause electromagnetic anomalies, summarize the characteristics of temporal and spatial variations of seismic electromagnetic anomalies, and use numerical simulations to try to explain the generation mechanism and propagation selective phenomena of seismic electromagnetic signals and focus on numerical simulation research on the mechanism of earthquake electromagnetic co-seismic or post-earthquake attenuation (Gao et al., 2016; Hu et al., 2011), but there is still a lack of strong quantitative explanations for the identification characteristics of electromagnetic anomalies caused by the seismogenesis process.

The early earthquake precursor observation and data analysis methods in China have mainly used traditional electrical and magnetic methods to observe the changes in the geoelectric field, geomagnetic field ($\leq$ 1 Hz), or the earth direct current (DC) resistivity. It is difficult to obtain the time-spatial change and propagation characteristics of seismo-electromagnetic precursor from these observation data including no ultra-low frequency (ULF)/extremely low frequency (ELF) band signals which may be more sensitive to seismic events. At the same time, individual field component is easily affected by the changes in the earth's electromagnetic environment and by human activity. Because these changes and disturbances are random events, they cause great difficulty in the identification of seismic electromagnetic anomalies. During the period 2007–2009, 12 magnetotelluric stations were set to observe the alternating geo-electromagnetic field, the data is mainly used for the study of electromagnetic field background changes (Zhao et al., 2010; Fan et al., 2013), and less for extracting seismic electromagnetic anomaly information (Gao et al., 2010; 2013). During 2011–2015, an ELF electromagnetic observation network for seismic anomaly monitoring has been set up (with the support of major national science and technology infrastructure projects) in the capital circle and the southern section of the North-South Earthquake Belts, which makes it possible to use magnetotelluric impedance for seismic electromagnetic anomaly monitoring. This network can not only observe natural source signals for magnetotelluric sounding, but it can also receive signals of a given frequency regularly sent by a long-distance high-power transmitter to improve the signal-to-noise ratio of the natural source in the low energy window frequency band and reduce the error of the data. Then the apparent resistivity and other observational data will have a higher sensitivity to the anomalies of the underground resistivity structure (Zhao et al., 2012).

The magnetotelluric sounding method based on the principle of electromagnetic induction has the characteristics of the wide frequency band and multi-component observation. Using magnetotelluric data from stations to identify and extract seismic electromagnetic anomaly information has the following advantages. 1) In data processing, the ratio of the mutually orthogonal electric and magnetic field is used to obtain the electromagnetic impedance of the earth and then the apparent resistivity and impedance phase information. This method can automatically eliminate the influence of magnetotelluric field changes of any frequency caused by the change of the earth's electromagnetic environment. 2) Reliable regional background resistivity information at different depths can be obtained from long-term observations by the network, which is convenient for identifying and extracting resistivity anomalies. 3) The seismogenic resistivity anomaly has the characteristic of slow change over a long time, which is easy to distinguish from human activity and local spatial change. 4) Allows for better comprehensive analysis, the electromagnetic impedance anomaly of a magnetotelluric station not only includes the change in the resistivity of the underlying earth formation caused by stress change and fracture development in the adjacent areas but also includes the electromagnetic radiation information generated by pressure in the rock formation.

In many cases, the earth can be represented as a horizontally stratified medium with homogeneous and isotropic properties in each layer (Wait, 1951). In this paper, we introduce a three-dimensional low resistivity anomaly in the horizontally layered stratum model designed to simulate the change of the earth's resistivity in the seismogenic zone, the electromagnetic impedance response in a large spatial range is calculated and its characteristics with frequency and space variation have been analyzed. Assuming that the electromagnetic radiation in the seismogenic region is equivalent to the vector electric dipole radiation source, the electromagnetic impedance response of electric dipole of different orientations is calculated and its characteristics of responses are analyzed. Finally, the dipole source response and magnetotelluric response are synthesized to simulate the observed response of the seismic electromagnetic anomaly by the magnetotelluric stations. From the perspective of 3D numerical simulation, we analyze the characteristics of an electromagnetic anomaly caused by earth resistivity changes and electromagnetic radiation during the pre-seismic period and propose methods to identify and extract different seismic electromagnetic anomalies. This will then provide theoretical support for extremely low-frequency electromagnetic observations used to monitor seismic electromagnetic anomalies.

2 Model design

This study concentrates on observations and processing of magnetotelluric data within a limited spatial area. Based on the one-dimensional (1D) horizontal layered stratum model, the 3D low resistivity anomaly is added to the high resistivity stratum to simulate the resistivity change caused by fracture development in the

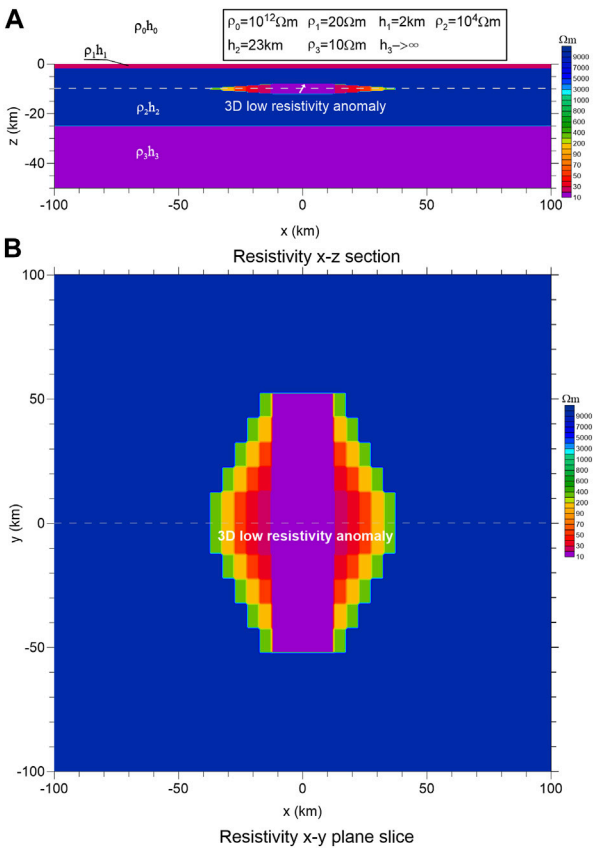

FIGURE 1
Horizontal layered and 3D low resistivity anomaly model using the x-y-z rectangular coordinate system with z=0 at the ground surface and positive upward **(A)** Is the resistivity x-z section, and **(B)** is the resistivity x-y plane slice at a depth of 10 km (z = −10 km).

seismogenic area. The electromagnetic radiation generated by the sudden change of stress in the seismogenic center area before the earthquake is simulated with an inclined electric dipole source at depth.

The designed model structure is shown in Figure 1, where we use the x-y-z rectangular coordinate system with z = 0 at the ground surface and positive upward. Figure 1A shows the x-z resistivity section at y = 0 (shown by the dotted line in Figure 1B) of the horizontally layered model with a 3D low resistivity anomaly. Figure 1B is an x-y slice of resistivity at a depth of 10 km (as shown by the dotted line in Figure 1A), showing the plane structure of the 3D low resistivity anomaly. The top earth layer is a low-resistance cover layer with a thickness of $h_1 = 2km$ and resistivity of $\rho_1 = 20\Omega m$. The second layer is a high resistance intermediate layer, with a thickness of $h_2 = 23km$ and resistivity of $\rho_2 = 10^4\Omega m$. The bottom of the model (lower crust) is a low resistivity half space ($h_3 \rightarrow \infty$) with the resistivity of $\rho_3 = 10\Omega m$. The atmosphere is above the ground surface and its resistivity is set to $\rho_0 = 10^{12}\Omega m$. The embedded 3D low-resistivity anomaly is a flat, low-resistivity wedge-shaped body located in the middle of the high-resistivity layer of the model. The core region of the 3D body is a low resistivity (10 Ωm) cuboid with a length (y-direction) of 105 km, a width (x-direction) of 25 km, and a height (z-direction) of 4 km, centered at (0, 0, −10 km) to simulate the seismogenic core area extending along the fault zone. The resistivity outside the cuboid core increases by 20, 30, 50, 100, and 300 Ωm in steps of 5 km along the x-axis, and the extension range reaches ±37.5 km in the x-direction. The resistivity along the y-axis increases as the same as in the x-direction but by 10 km spatial steps, forming two triangular anomalous bodies whose resistivity gradually increases as distance in the x-direction from the center point in the x-y plane. This structure is used to simulate the change of the formation resistivity near the seismogenic core area. The buried inclined electric dipole (small white arrow in Figure 1A), which simulates the electromagnetic radiation source, is located at (0, 0, −10 km), with an azimuth of θ=0° and inclination of φ=30 °. Unless otherwise specified, the permeability parameter and dielectric constant are set to $\mu_0 = 4\pi \times 10^{-7} H/m$ and $\varepsilon_0 = 8.85418 \times 10^{-12} F/m$, respectively.

3 3D magnetotelluric response simulation

Using 3D simulation software to calculate the magnetotelluric response of the horizontally layered model with the 3D low resistivity anomaly shown in Figure 1, we can obtain the apparent resistivity and phase information of the xy and yx components at the ground observation site. Figure 2 shows contour maps of the apparent resistivity of the two principal component elements with frequencies of 0.1, 0.05, and 0.01 Hz, respectively. Because the model structure is symmetrical, we only show quadrant 1 (with x=0–400 km and y=0–300 km) to investigate the distribution of electromagnetic impedance response. In Figure 2, white ladder lines are used to mark the corresponding positions and boundaries of the 3D low resistivity anomalous body at depth. Different color scales are used in contour maps because the amplitude of different frequency responses varies greatly.

It can be seen from Figure 2 that 1) generally, the existence of a 3D low resistivity anomaly causes the apparent resistivity value above and near the 3D body to be significantly reduced. 2) The amplitude of the apparent resistivity anomaly is largest just above the 3D low resistivity body, and gradually decreases to background value with increasing distance from the boundary of the 3D low resistivity body, and the attenuation distance increases with decreasing frequency. For example, the distance of the ρ_{yx} anomaly decrease to zero on the x-axis is about 80 km when f=0.1 Hz, and about 180 km when f=0.01 Hz 3) The maximum amplitude of the apparent resistivity anomaly occurs at a lower frequency, that because the top surface of the 3D low resistivity anomaly body is buried at a depth of 8 km and has a low-resistivity overburden with a thickness of 2 km, as shown in Figure 1A. 4) Compared with ρ_{xy}; ρ_{yx} has a larger apparent resistivity value, apparent resistivity anomaly amplitude, and anomaly distribution range, which may be because the electrical principal axis of the 3D low resistivity anomaly body is in the y-direction, and ρ_{yx} closer to the response of TM (transverse magnetic) polarization mode. 5) When f=0.05 Hz, the decay rate of ρ_{xy} in the x-direction, outside the 3D low resistivity anomaly, becomes faster and shows a small enhancement (positive anomaly) after attenuating to zero. With the frequency reduced to f=0.01 Hz, the apparent resistivity anomaly outside the 3D low resistivity anomaly has changed from negative to

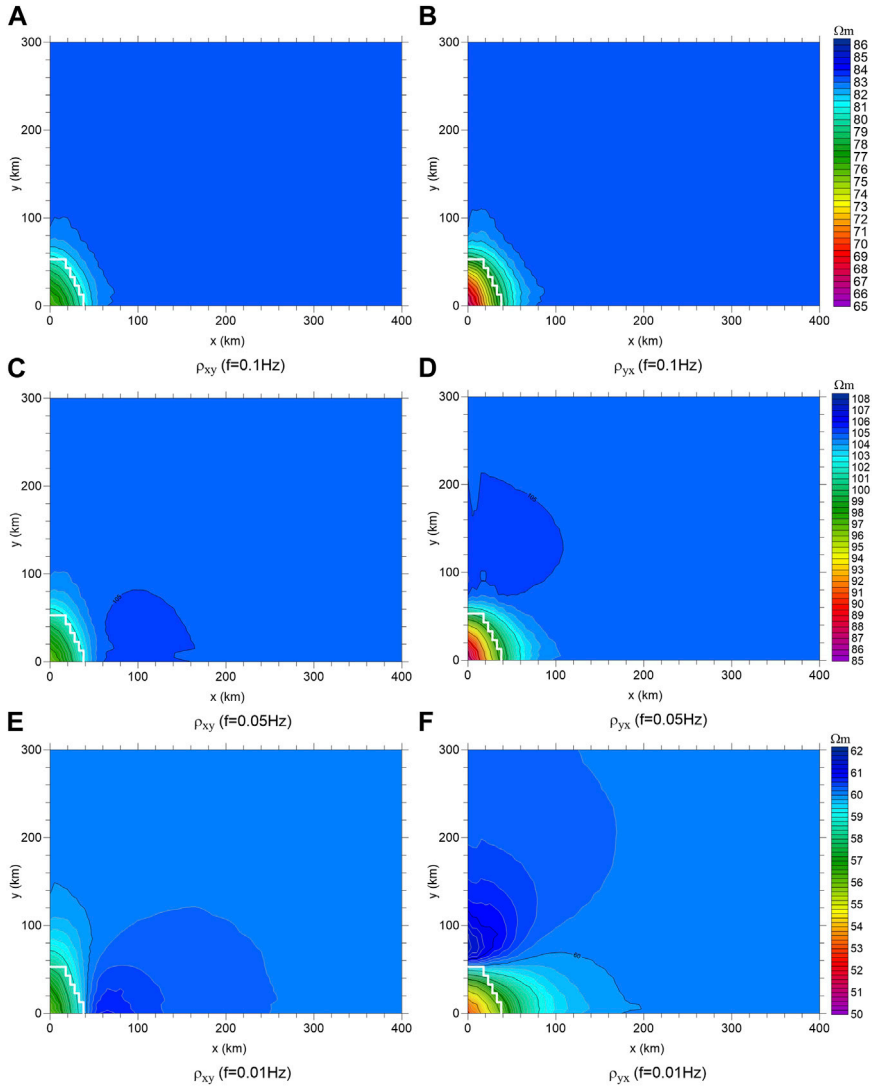

FIGURE 2
Contour maps of the spatial distribution of the apparent resistivity of the two principal components of the 3D model. **(A,C,E)** are the ρ_{xy} at the frequency of 0.1 Hz, 0.05 Hz, 0.01 Hz respectively; **(B,D,F)** are the ρ_{yx} at the frequency of 0.1 Hz, 0.05 Hz, 0.01 Hz respectively.

positive, and the amplitude and extension range of the positive anomaly has increased. Correspondingly, a similar phenomenon occurs in the *y*-direction for ρ_{yx}, and the amplitude and coverage of positive anomalies are larger than that of ρ_{xy}.

To quantitatively evaluate the sensitivity of the magnetotelluric response observed at the stations to the seismogenic resistivity anomaly, Figure 3 shows the ratio curve of the responses of the measuring sites at different offsets along the radial x) direction and axial y) direction of the 3D low resistivity anomaly to the responses of the 1D horizontal layered model of the corresponding measuring sites. The offsets of the measuring sites are 0, 10, 25, 50, 100, 200, and 400 km, respectively. The curve with a ratio of 1 represents the response of a 1D layered model, which is not disturbed by the 3D low resistivity anomaly. If the ratio is larger than 1, the apparent resistivity value increases, making this a positive anomaly. A ratio less than 1 indicates that the apparent resistivity value decreases, that is, a negative anomaly. Because the model contains the 3D low resistivity anomaly, the ratio curve should be dominated by negative anomalies, and how much the ratio deviates from 1 is the amplitude of the anomaly. The apparent resistivity ratio curve in Figure 3 shows that: 1) The influence of 3D low resistivity anomaly begins in the low-frequency band below 5 Hz. 2) In the frequency band of about 1~5 Hz, the apparent resistivity ratio curve shows a positive abnormal overshoot, which is the intrinsic characteristic of the magnetotelluric response. The amplitude of overshoot is largest at zero offsets (up to about 7%) and decreases with an increasing offset; is approaching zero for x offset is greater than or equal to 50 km and while y offset is greater than or equal to 100 km. 3) Generally, in the low-frequency band below 1Hz, the ratio curve is dominated by negative anomalies, and the amplitude of the negative anomaly decreases with increasing offset distance. At the same offset

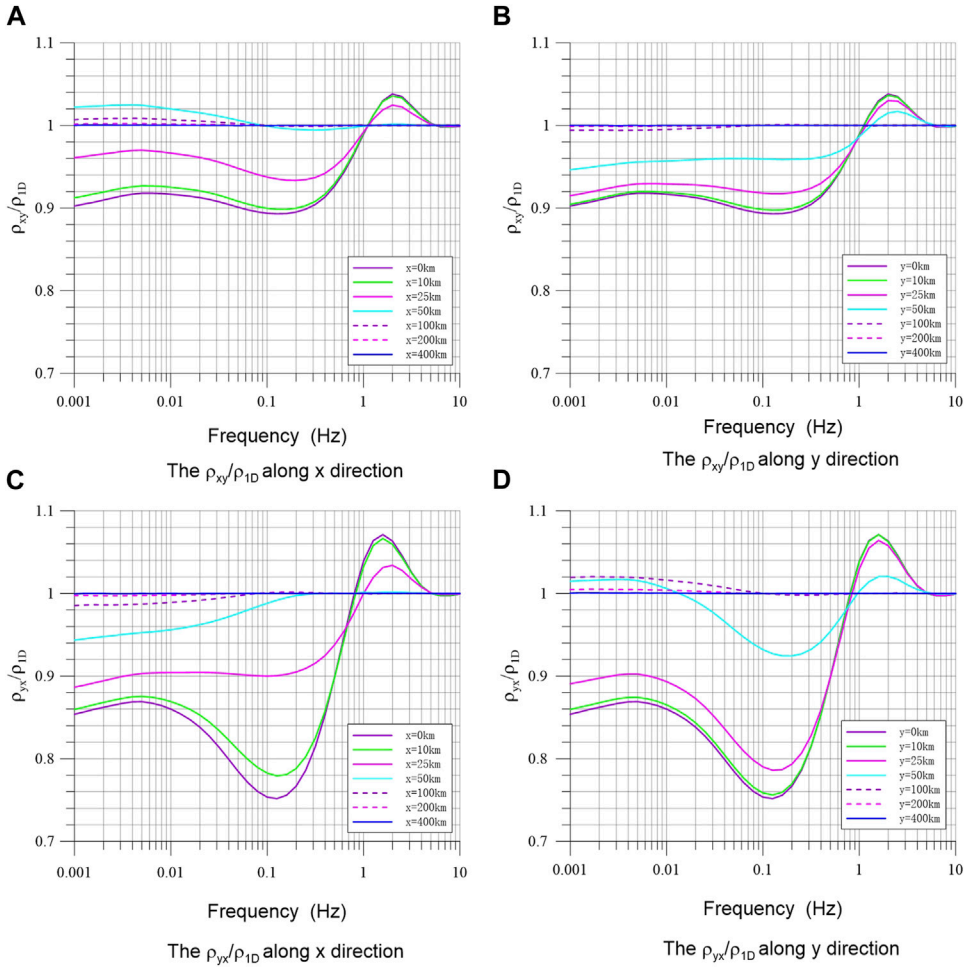

FIGURE 3
Apparent resistivity ratio of the three-dimensional model to one-dimensional layered model for measuring sites of different offsets along x- and *y*-direction. **(A)** and **(B)** are the ρ_{xy}/ρ_{1D} along x and y direction respectively; **(C)** and **(D)** are the ρ_{xy}/ρ_{1D} along x and y direction respectively.

distance, the amplitude of the ρ_{xy}/ρ_{1D} curve is less than the amplitude of the ρ_{yx}/ρ_{1D} curve. For example, at zero offset distance, there is a maximum negative anomaly near the frequency of about 0.13 Hz, the ratio of the ρ_{xy}/ρ_{1D} can reach about −11% and the ratio of the ρ_{yx}/ρ_{1D} can reach about −25%. 4) In the frequency band below 0.1 Hz, the ratio curve of ρ_{xy}/ρ_{1D} with an offset of greater than or equal to 50 km along the *x*-axis shows a small positive anomaly. When the ρ_{xy}/ρ_{1D} offset is 50 km, the maximum positive anomaly reaches about 2.5%, and the positive anomaly amplitude decreases rapidly with the increasing offset. When the ρ_{yx}/ρ_{1D} offset along the *y*-axis is equal to 50 km, a small positive anomaly appears at about 0.013 Hz, and the amplitude is close to 2%. When the offset is equal to 100 km, the ρ_{yx}/ρ_{1D} curve starts to show a positive anomaly at about 0.1 Hz, with an amplitude of about 2%, which decreases rapidly to zero with the further increasing offset. 5) It should be pointed out that the boundaries of the 3D anomalous body are at 37.5 km in the $+x$ direction and 52.5 km in the $+y$ direction, that is, the overshoot anomaly in the frequency band of 1–5 Hz can only be identified within the range of the 3D body; while identifiable weak positive anomalies for the low-frequency band below 0.1 Hz may only appear in the area outside the anomalous body.

The apparent resistivity method is one of the earliest geophysical methods used for earthquake precursor monitoring in China. After years of observation and research, Qian et al. (1982) and Zhang et al. (1996) successively summarized the characteristics of the apparent resistivity anomaly before earthquakes: 1) The apparent resistivity anomaly before earthquakes can be divided into a long-trend anomaly and impending anomaly. 2) Before the earthquake, the apparent resistivity is mostly a decreasing anomaly, though some increasing changes have also been observed. The anomaly amplitude decreases with increasing epicenter distance. 3) Before the earthquake, the long trend anomaly extends outward from the epicenter area, extending out to 150 km. 4) The anomalies are directional. 5) The standard deviation of the monthly average value of the active source apparent resistivity observation method should be less than 0.5%. If the apparent resistivity has a continuous multipoint trend change and the amplitude exceeds 3 times the standard error, it can be identified as the anomaly. Our simulation results described above provide a theoretical basis for the characteristics of the apparent

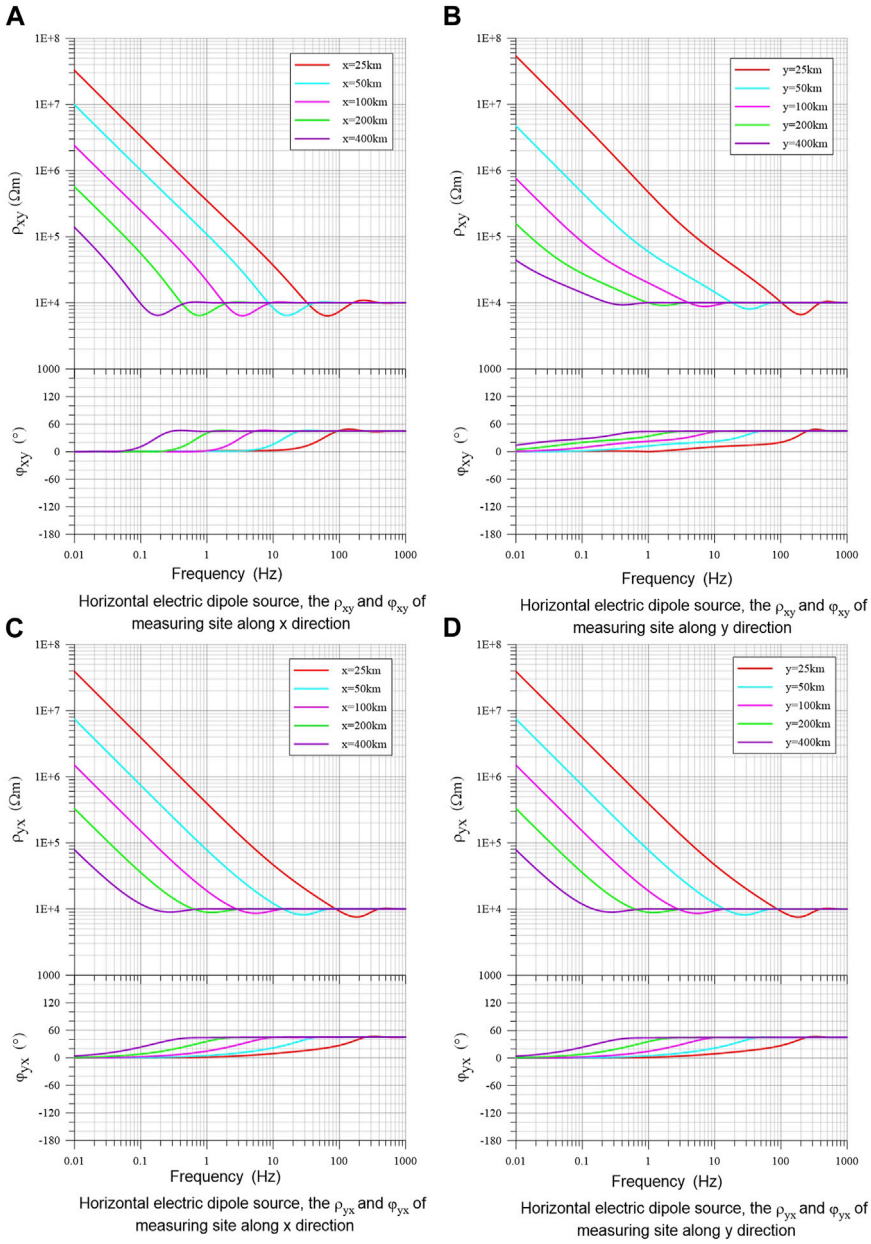

FIGURE 4
Apparent resistivity and phase response of a horizontal dipole source in a homogeneous earth for measuring sites of different offsets along x- and *y*-direction. **(A)** and **(B)** are the ρ_{xy} and φ_{xy} of measuring sites along x and y direction respectively; **(C)** and **(D)** are the ρ_{yx} and φ_{yx} of measuring sites along x and y direction respectively.

resistivity anomaly in the seismogenic area summarized by precursors and verify the identification rule of the resistivity anomaly.

4 Response simulation of electric dipole source in the earth

The electromagnetic responses of the electric dipole source in the horizontally layered earth are calculated using the algorithm by Hu et al. (2023), and the propagation characteristics of the electric dipole source radiation field in earth and its influence on ground observations have been investigated. For comparative studies, the responses of a horizontal and an incline electric dipole in uniform earth and horizontally layered earth are calculated and analyzed respectively.

4.1 Response of an electric dipole source in a uniform earth

An *x*-direction horizontal electric dipole source (azimuth angle θ =0 °, dip angle φ =0 °), and an inclined electric dipole source

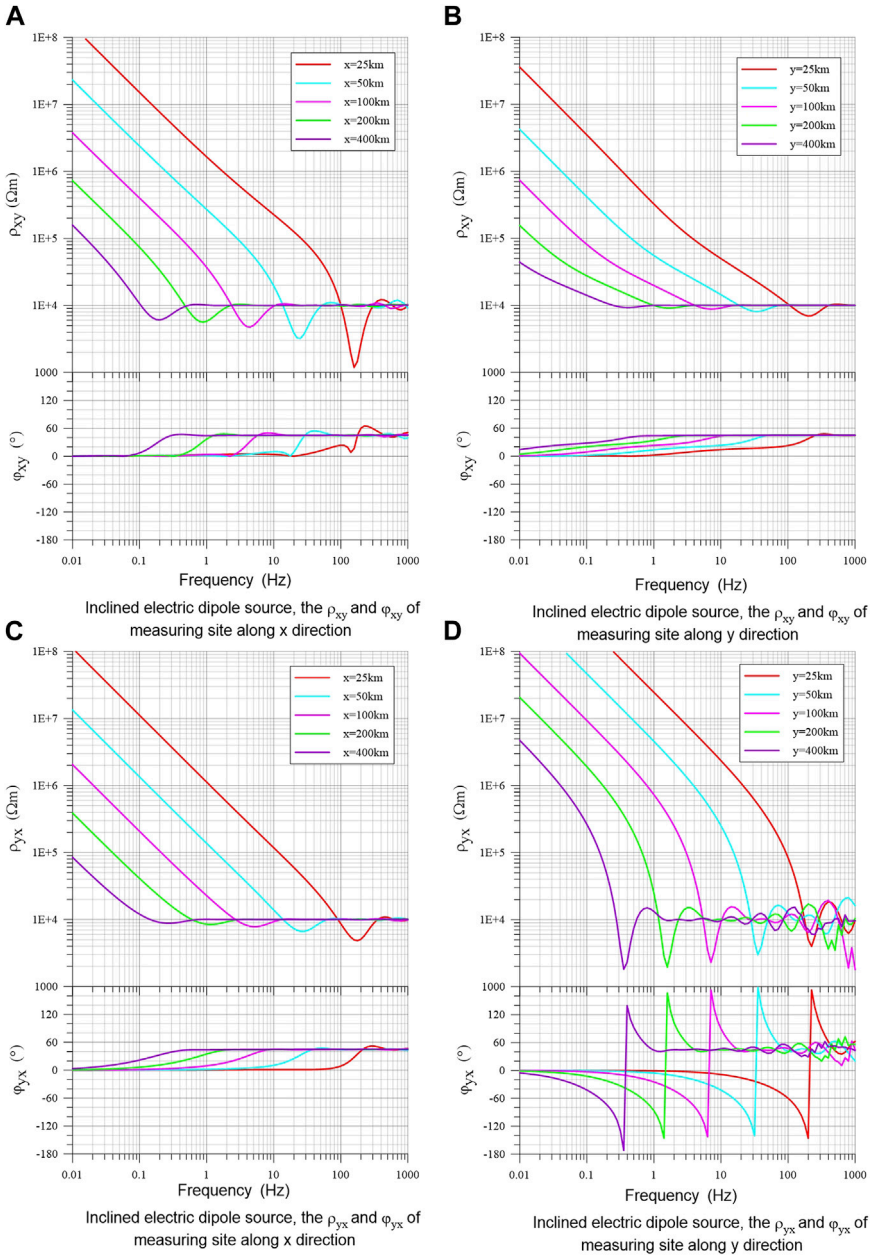

FIGURE 5
Apparent resistivity and phase response of an inclined dipole source in a homogeneous earth for measuring sites of different offsets along x- and *y*-direction. **(A)** and **(B)** are the ρ_{xy} and φ_{xy} of measuring sites along x and y direction respectively; **(C)** and **(D)** are the ρ_{yx} and φ_{yx} of measuring sites along x and y direction respectively.

(azimuth angle θ =0 °, dip angle φ =30 °) are set to located at a depth of 10 km in a uniform earth with the resistivity of 10^4 Ωm. The apparent resistivity and phase are calculated for observation sites at the earth's surface with 25, 50, 100, 200, and 400 km offset in the *x*-direction and *y*-direction respectively. Figure 4 shows the curves of apparent resistivity and phase excited by a horizontal electric dipole source and observed at the earth's surface with different offsets. Figures 4A, B show the apparent resistivity ρ_{xy} (above) and phase φ_{xy} curve (below), and Figures 4C, D show the ρ_{yx} and φ_{yx} with different offsets in the x- and y-directions respectively. In general, all apparent resistivity and phase curves show similar variation patterns with frequency and offset but have slightly different changing rates. When the frequency is high enough, the dipole source field meets the far-field condition, the apparent resistivity value obtained is close to the true resistivity value (10^4 Ωm) of the medium, and the impedance phase is about 45 °, which is a typical plane wave electromagnetic response. When the frequency is low enough, the apparent resistivity and phase of the dipole source field response have typical near-field characteristics, meaning that with decreasing frequency, the apparent resistivity sharply increases, while the

impedance phase correspondingly decreases to zero. Curves of ρ_{yx} and φ_{yx} along the x direction have almost the same pattern and values as curves along the y direction for the corresponding offset, this means the ρ_{yx} and φ_{yx} responses excited by horizontal electric dipole have spatial symmetry in the x-y plane; while the ρ_{xy} and φ_{xy} responses along x direction show slightly different variation rates and frequency feature from responses along the y direction, this indicates the ρ_{xy} and φ_{xy} responses have no symmetry in the x-y plane.

For the field responses of horizontal electric dipole source, the area with an offset greater than $\sqrt{2}\lambda$ (λ-wavelength) can be regarded as the far field, while the area with an offset less than $\lambda/\sqrt{2}$ as the near field. As the frequency decreases, the apparent resistivity starts to deviate from the far-field value at the frequency corresponding to wavelength $\lambda_f \approx d/\sqrt{2}$, where d is the offset along x or y direction; and increases exponentially at the frequency corresponding to wavelength $\lambda_n \approx d\sqrt{2}$, indicating of near field response pattern. The apparent resistivity response at the transition zone between frequencies corresponding to λ_f and λ_n shows somewhat complicated variations, first increasing slightly, and then returning to the far-field value at the frequency corresponding to wavelength $\lambda_t \approx d$, and then decreases slightly. The impedance phase starts to deviate slightly by 45 ° at the frequency corresponding to λ_f, and recovers to the far-field value at the frequency corresponding to λ_t, then decreases slowly to zero as decreasing frequency.

Since the impedance response of the vertical electric dipole source does not have plane wave characteristics as defined by the field responses observed on the ground, it is not presented here. For the field of an inclined dipole source in the earth, the field responses observed on the ground will be affected by the vertical source field, which is much different from the field of a simple horizontal dipole source. Figure 5 shows the curves of apparent resistivity and phase excited by a 30° inclined electric dipole source at 10 km deep from the earth's surface, Figures 5A, B show ρ_{xy} and φ_{xy} curves, and Figures 5C, D show ρ_{yx} and φ_{yx} responses observed at earth surface with different offsets in the x- and y-directions respectively. The basic features of apparent resistivity and phase responses of the inclined dipole mainly follow the typical response patterns of the horizontal dipole with frequencies and offsets. The curves of ρ_{xy}, φ_{xy} along the y-direction, and ρ_{yx}, φ_{yx} along x-direction do not show much effect by vertical dipole responses; while responses of ρ_{xy}, φ_{xy} along x-direction show some effect of vertical dipole especially for small offsets; but responses of ρ_{yx}, φ_{yx} have been severely affected by vertical dipole responses. It can be seen from Figure 5D that the ρ_{yx} and φ_{yx} curves in the y-direction show oscillating feature in the far field zone with decreasing amplitude as frequency. The responses of the horizontal electric dipole source also oscillate, though the amplitude is very small and difficult to identify. Thus one of the effects of the vertical source field is to amplify this oscillation. The apparent resistivity response in the transition zone shows a negative overshot with a large amplitude at the frequency corresponding to λ_t. The impedance phase curve also shows a small amplitude oscillation in the high-frequency band of the far field; starts rising rapidly from close to 45° approaching +180° at the frequency corresponding to λ_f, and drops sharply toward −180° at the frequency corresponding to λ_t; and then rises to zero slowly. It can be seen that the frequency characteristics and spatial distribution characteristics of magnetotelluric responses observed on the ground may become extremely complex if an arbitrarily orientated electric dipole source at depth exists at the same time.

4.2 Response of electric dipole source in the three-layer model.

The frequency characteristics of apparent resistivity and phase response of electric dipole in layered earth medium may become complex due to the difference in sensitivity of different frequencies to different depths. Figure 6 shows the apparent resistivity and phase curves of the horizontal electric dipole source with different offsets along the x - and y-directions in the three-layer earth model. Note that the impedance phases of the two principal component elements have been corrected to the 45 ° baseline. The parameters of the three-layer model are set and described in Figure 1A, and the horizontal dipole source in the x-direction is located at a depth of 10 km. In general, the near- and far-field characteristics of the frequency response excited by the horizontal electric dipole source shown in Figure 6 are still obvious for both apparent resistivity and phase curves. That is, in the high-frequency band, the apparent resistivity value tends to the resistivity of the surface layer, and the impedance phase tends to 45 °; however, in the low-frequency band, the apparent resistivity increases sharply and the phase decreases to zero. The shape of the frequency response curve becomes complex due to the influence of different resistivity layers, especially the conductive cover layer, and it is difficult to define the far/near field transition frequency as well as the oscillation and jump of the phase curve. Figure 6A shows the most complex changes of the ρ_{xy} and φ_{xy} curves in the x-direction. Although the far-field apparent resistivity value is about 20 Ωm, the frequency from the far-field to the transition zone is not much different from the transition frequency as shown in Figure 4 for resistive half-space, especially for large offsets where the resistive layer below the surface has dominant effects. For small offsets (<100 km), the apparent resistivity rises to a certain extent, then starts to decline, and then rises again in the near field zone; this may be a reflection of the layered electrical structure. The smaller the offset, the greater the amplitude of the apparent resistivity rises, with a maximum of about 3000 Ωm which is approaching the resistivity of 10^4 Ωm for the resistive layer. With increasing offset, the amplitude and frequency band of the formation change effect decreases, and the near-field influence characteristics become prominent. The far-field value of φ_{xy} is about 45 °, showing a jump to +180 ° at the transition section, and then gradually return to zero. The jump in corresponding frequency is lower than the phase jump frequency of the uniform high-resistance earth in Figure 4. Figure 6B shows the response of the ρ_{xy} and φ_{xy} in the y-direction. Compared with the ρ_{xy} and φ_{xy} response in the x direction, the apparent resistivity responses have the same variation pattern, but the variation amplitude of the curve is smaller. The change of phase curve is gentle, and shows characteristics of dipole source response; only the curve with an offset of 25 km appears a positive jump at transition frequency. The curves of ρ_{yx} and φ_{yx} in the x- and y-direction as shown in Figures 6C, D reflect the basic characteristics of the dipole source response and again show perfect symmetry. The frequency of the apparent resistivity and phase curves with different offset distances from the

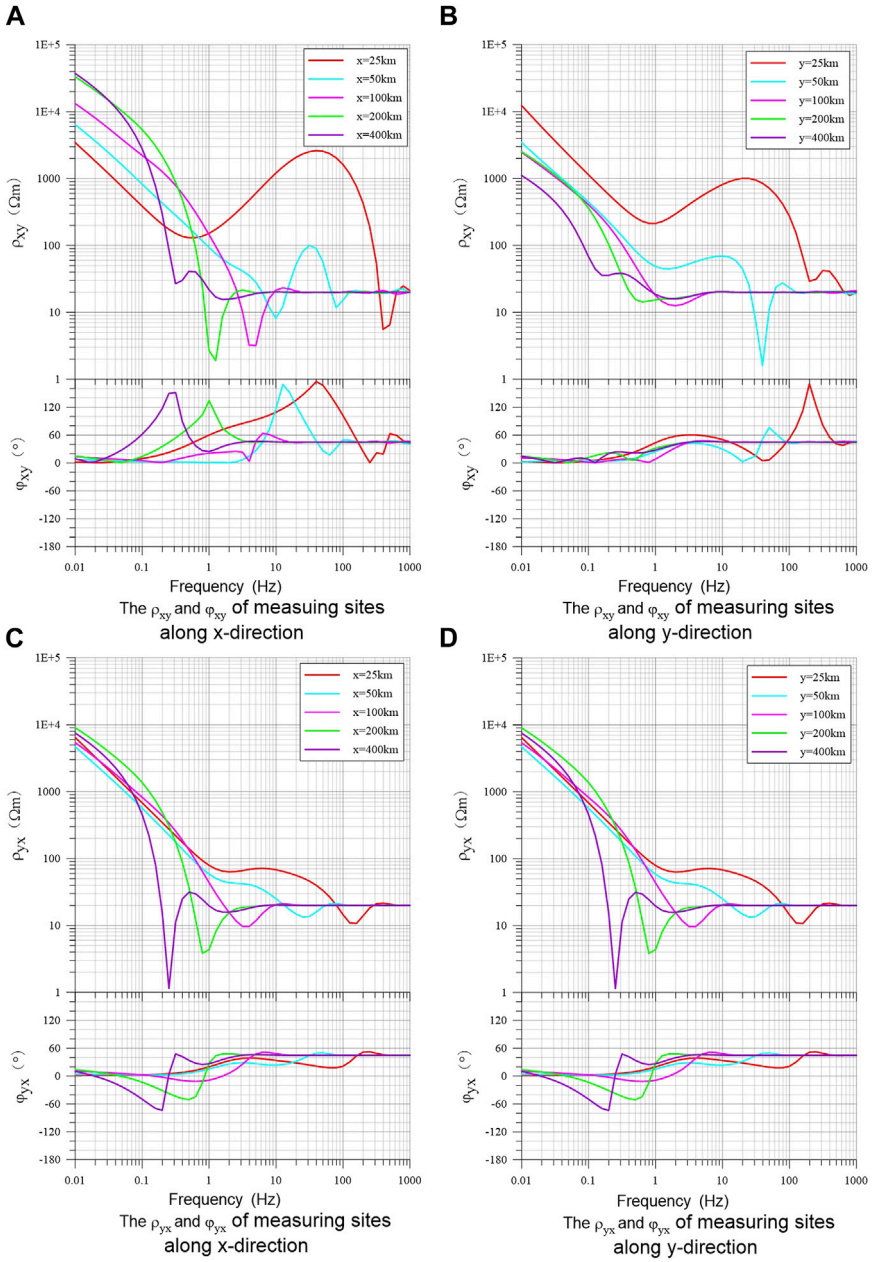

FIGURE 6
Apparent resistivity and phase curves of the horizontal electric dipole source in a three-layer earth model for measuring sites of different offsets along x- and *y*-direction. **(A)** and **(B)** are the ρ_{xy} and φ_{xy} of measuring sites along x and y direction respectively; **(C)** and **(D)** are the ρ_{yx} and φ_{yx} of measuring sites along x and y direction respectively.

far field zone to the transition zone is close to the response of the homogeneous resistive earth as shown in Figure 4. After entering the near-field zone, the apparent resistivity curve rises slowly, and then rises at a similar rate near 1 Hz, approaching 10^4 Ωm for all offsets. When the offset is 400 km, the apparent resistivity shows a large negative overshot and the phase shows a jump in the transition zone.

It can be seen from the above analyses that the electromagnetic response of the horizontal electric dipole source in the layered stratum can reflect the basic characteristics of the dipole source field. However, because of the influence of layered electrical structure, the frequency response curves in different directions, differing offsets, and polarization modes may have complex shapes and variation characteristics. To better understand the spatial distribution characteristics of the electromagnetic response of the horizontal electric dipole source, Figure 7 shows the x-y plane distribution of the apparent resistivity (ρ_{xy} *and* ρ_{yx}) of the horizontal electric dipole source at 100, 10, and 1 Hz, respectively; and the plotting range is the same as in Figure 2. The white arrow in Figure 7 indicates the position of the horizontal electric dipole source in the earth. It can be seen that the spatial

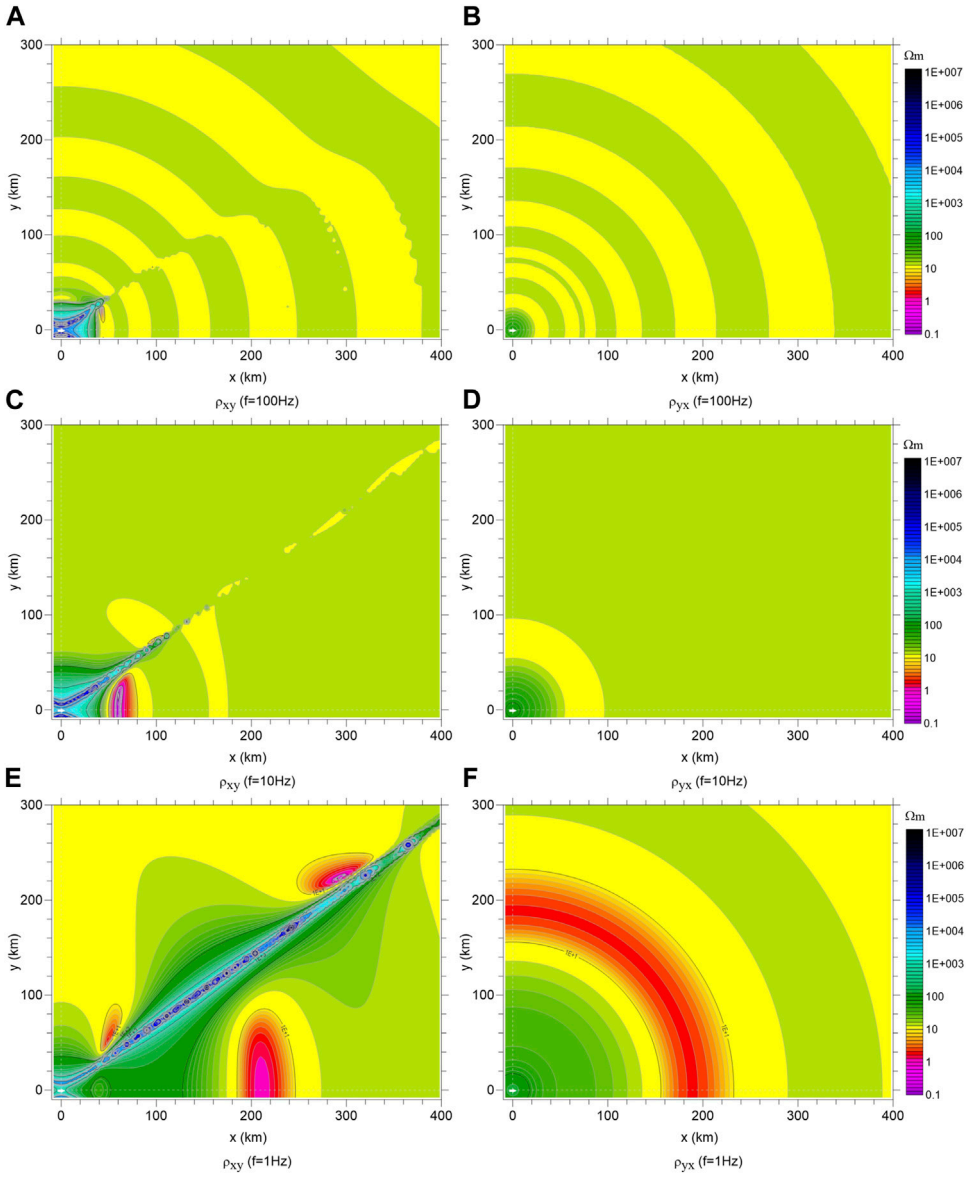

FIGURE 7
Contour plots in the x-y plane of apparent resistivity response of the *x*-direction horizontal electric dipole source in a three-layer earth. **(A,C,E)** are the ρ_{xy} at the frequency of 100 Hz, 10 Hz, 1 Hz respectively; **(B,D,F)** are the ρ_{yx} at the frequency of 100 Hz, 10 Hz, 1 Hz respectively.

distribution form of ρ_{xy} is complex. First, the apparent resistivity in the corresponding rectangular neighborhood above the dipole source increases sharply towards the center of the dipole, and the lower the frequency, the larger the range of resistivity increases. For example, when the frequency is 100 Hz, the range of resistivity increase is a rectangular area composed of $x \approx \pm 35km$ and $y \approx \pm 30km$. However, when the frequency is 1 Hz, it is an area composed of $x \approx \pm 170km$ and $y \approx \pm 90km$, and the shape of the regional boundary is complex. Second, at the periphery of the area with a sharp increase in resistivity, a trough with decreased resistivity appears, corresponding to the negative overshoot of the apparent resistivity curve in Figure 6. The lower the frequency, the wider the wave trough, and, by extension, the greater the reduction in the resistivity value. Moreover, because the Ex and Hy components of the dipole source response have amplitude crossing zero and phase jump from positive to negative (or from negative to positive) at the azimuth of φ =35 °, the resistivity anomaly of ρ_{xy} changes in the vicinity of the line that starts from the center of the dipole source and extends at an azimuth angle of 35 °. From the source center to the outside, the resistivity near the 35 ° line is larger than that of the adjacent area, forming a high resistivity strip extending outward, and the extended distance is far greater than the aforementioned rectangular area scale with sharply increasing resistivity. With further increase in distance, the resistivity near the extension line is slightly smaller than that in the neighborhood. It can be seen from Figure 7C with a frequency of 10 Hz that the x boundary of the rectangular domain with sharply increased resistivity is about x ≈ 50km, and the high resistivity

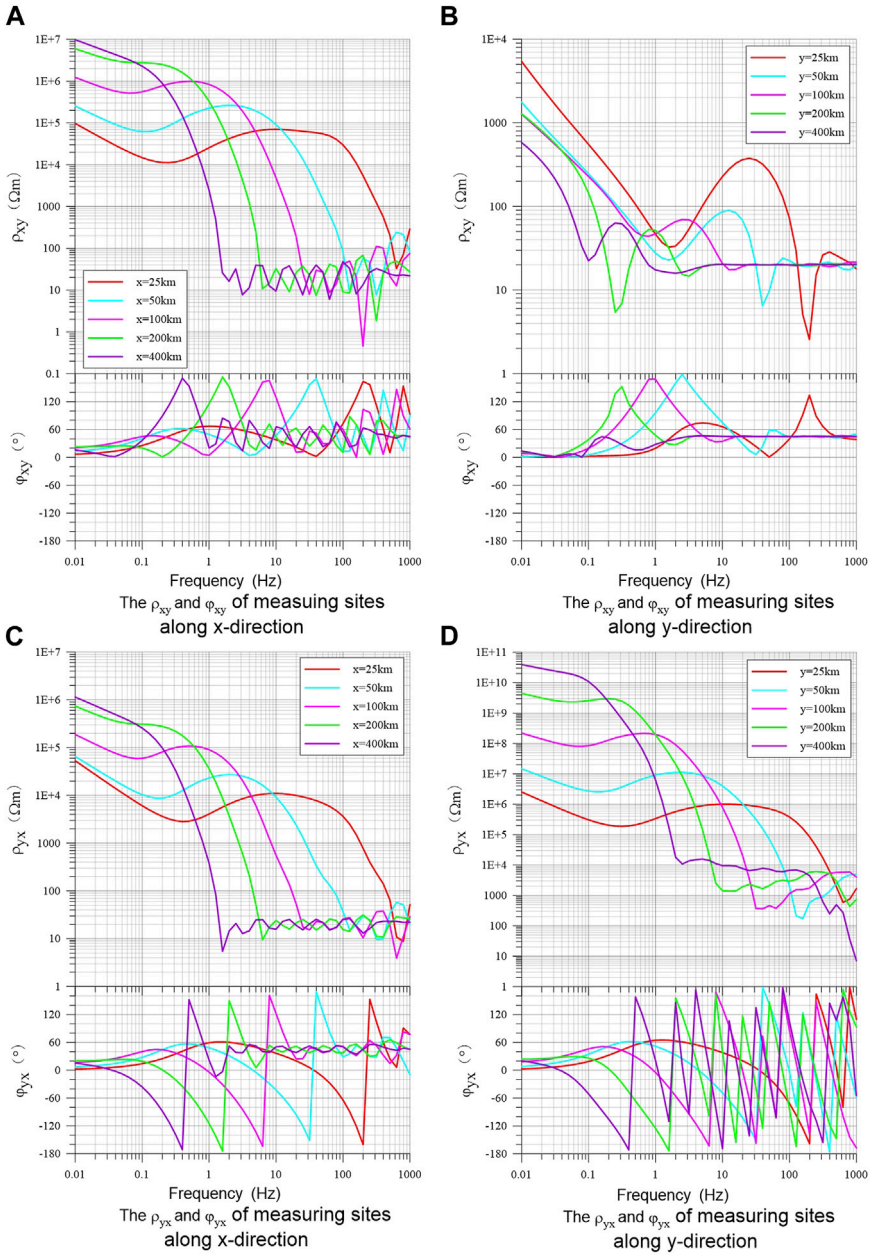

FIGURE 8
Apparent resistivity and phase curves of an inclined electric dipole source in three-layer earth for measuring sites of different offsets along x- and *y*-direction. **(A)** and **(B)** are the ρ_{xy} and φ_{xy} of measuring sites along x and y direction respectively; **(C)** and **(D)** are the ρ_{yx} and φ_{yx} of measuring sites along x and y direction respectively.

anomaly zone along the 35 ° line extends to x ≈ 150 km. Meaning, that if the station is located near the extension line, the electromagnetic anomaly can be observed further away from the seismogenic center. Since the Ey and Hx components of the dipole source response change continuously with the azimuth angle; ρ_{yx} has a simple and symmetrical spatial distribution. The resistivity increases sharply in the circle centered on the dipole source, and the radius of the circle increases with decreasing frequency. Since the earth model is not a homogeneous half-space, it cannot be characterized by the wavelength corresponding to a certain formation resistivity value. From the near source range in Figure 7 that is greater than the surface resistivity value (20 Ωm), it can be seen that the radius is about 23 km when f =100 Hz, 55 km when f = 10 Hz, and 135 km when f = 1 Hz. It can also be seen from Figure 7 that the apparent resistivity ρ_{yx} shows a small change in oscillation amplitude in the far-field area, and the period of the oscillation decreases first and then increases with the increasing offset, which may be caused by a change of apparent resistivity with

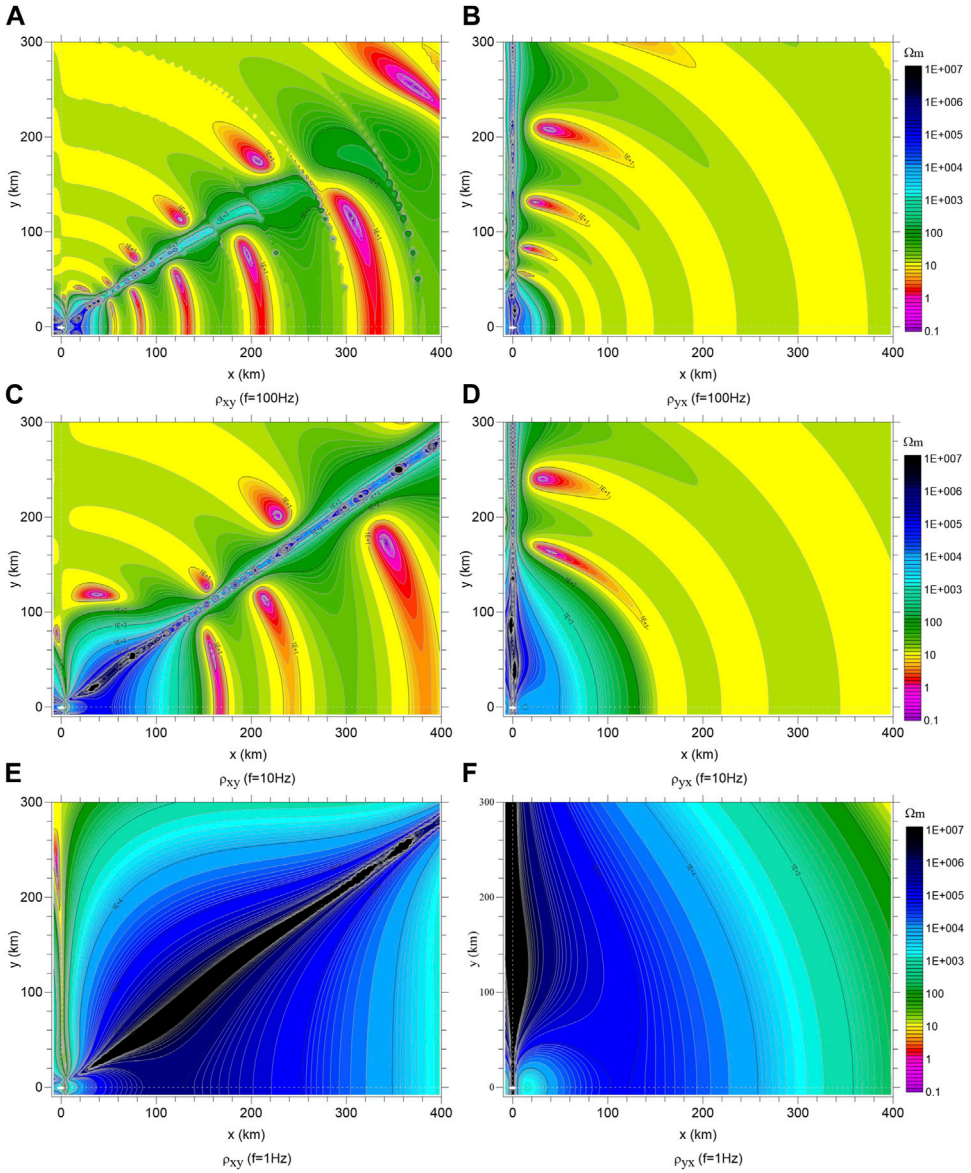

FIGURE 9
Contour plots in the x-y plane of apparent resistivity response of an inclined electric dipole source in a three-layer earth. **(A,C,E)** are the ρ_{xy} at the frequency of 100 Hz, 10 Hz, 1 Hz respectively; **(B,D,F)** are the ρ_{yx} at the frequency of 100 Hz, 10 Hz, 1 Hz respectively.

offset. Because the wavelength becomes longer at low frequencies, it is difficult to identify the oscillation period of the low-frequency response in the displayed space. ρ_{xy} also has similar oscillation characteristics, but the 180 ° shift is generated with the 35 ° line as the boundary; that is, both sides of the 35 ° line correspond to peaks and troughs. The amplitude of the oscillation in the far-field area is not large, which may not be noticed in the processing of actual observation data and anomaly identification.

Figure 8 shows the apparent resistivity and phase curves of the *x*-direction inclined (φ=30 °) dipole in the three-layer earth with different offsets in the x- and y-directions. Compared with the response of the horizontal electric dipole source shown in Figure 6, the response excited by the vertical electric dipole source, except the ρ_{xy} of the *y*-direction, has very different curve shapes and amplitudes in other components. In general, the response curve of a tilted electric dipole source is more complex with frequency. The apparent resistivity response of the tilted dipole source exhibits a large amplitude variation pattern in the near-field zone, first reaching a high value, then decreasing slowly, and finally exhibiting an oscillating pattern with increasing frequency. The near-field maximum amplitude is much higher (at least one to two orders) than the response of the corresponding horizontal electric dipole source. For example, the *x*-direction's ρ_{xy} increase to greater than 10^5 Ωm, the *x*-direction's ρ_{yx} increases to greater than 10^4 Ωm, and the *y*-direction's ρ_{yx} increase to greater than 10^6 Ωm. The turning frequency of the apparent resistivity curve

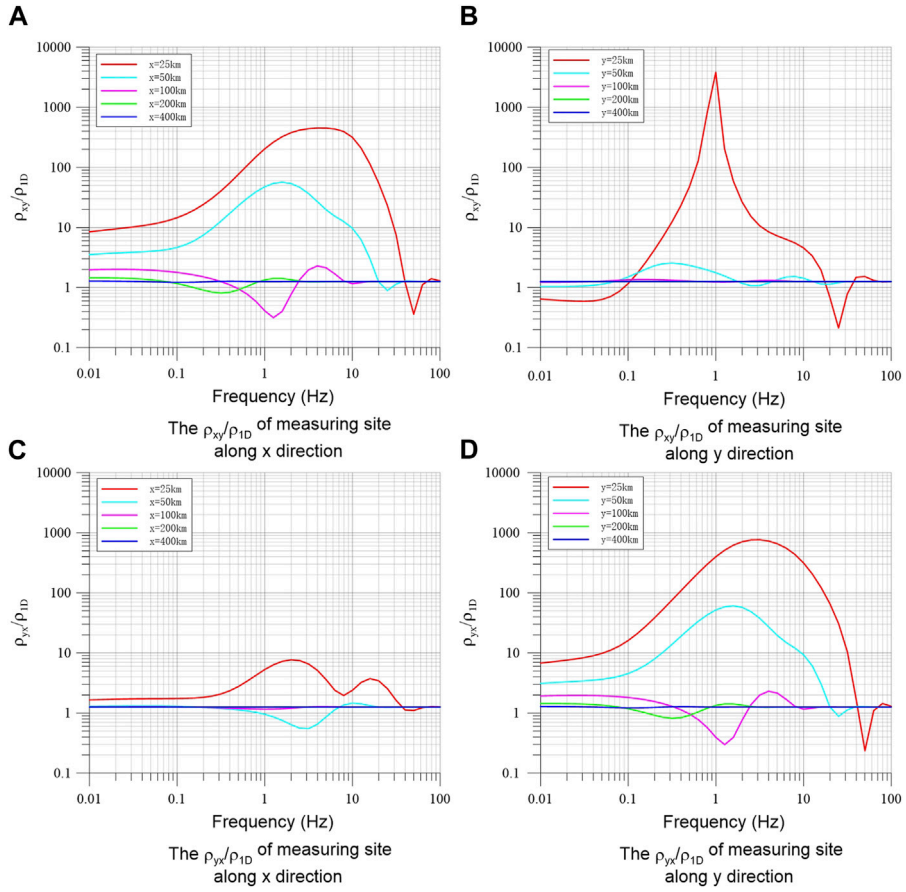

FIGURE 10
Ratio of the apparent resistivity of the 3D anomaly body together with inclined dipole source in the earth to the apparent resistivity of the 1D layered earth model for measuring sites of different offsets along x- and *y*-direction. **(A)** and **(B)** are the ρ_{xy}/ρ_{1D} of measuring sites along x and y direction respectively; **(C)** and **(D)** are the ρ_{yx}/ρ_{1D} of measuring sites along x and y direction respectively.

corresponding to λ_n is about an order of magnitude higher than the turning frequency of the horizontal dipole source. The small amplitude oscillation in the far-field area is more prominent, that is, the amplitude change is greater, and the period is more obvious. The ρ_{yx} value along the *y*-direction in the far-field zone does not reflect the resistivity of the surface layer but is closer to the value of the second layer (10^4 Ωm). The phase curves for φ_{xy} *and* φ_{yx} along the *x*-direction and φ_{xy} along *y*-direction oscillate slightly near the 45 ° line when they are in the far-field area, and when they enter the near-field area, there is a jump of +180 ° to-180 °, and then gradually trend to 0 °. In the far-field region, φ_{yx} along the *y*-direction also oscillates rapidly.

Figure 9 shows the plane distribution of the apparent resistivity of the inclined electric dipole source. To facilitate comparison, the same contour color scale as in Figure 7 is used. Compared with Figure 7, it can be seen that 1) the apparent resistivity of the inclined electric dipole source is much higher than that of the horizontal electric dipole source. 2) The area of near-source area apparent resistivity enhancement is much larger than the response of a simple horizontal dipole source. Taking ρ_{xy} of f = 10 Hz as an example, the boundary in the *x*-direction of the simple horizontal electric dipole source is 50 km, while the boundary of the inclined electric dipole source is 160 km. 3) Because of the effect of vertical electric dipole source response, a resistivity anomaly band is formed for ρ_{yx} response in the *y*-direction; that means the plane distribution of ρ_{yx} for inclined dipole response no longer has simple symmetry. 4) The oscillation amplitude in the far-field area is larger than that of the simple horizontal dipole source, and the oscillation amplitude is even larger near the anomalous extension zone.

It can be seen from the apparent resistivity response of the tilt dipole source in the earth that when the radiation source contains vertical components, the amplitude and spatial range of the apparent resistivity anomaly in the near-field zone are greatly enhanced. Compared with the response of a simple horizontal electric dipole source, the amplitude of the high resistance anomaly is about 2–5 orders of magnitude higher. For the same offset, the frequency of the near-field zone anomaly increases by about an order of magnitude. The spatial range of near-field zone anomaly is about 3 times larger (taking 10 Hz response as an example). It can be seen that the vertical component of seismogenic electromagnetic radiation can greatly increase the detectability of anomalies.

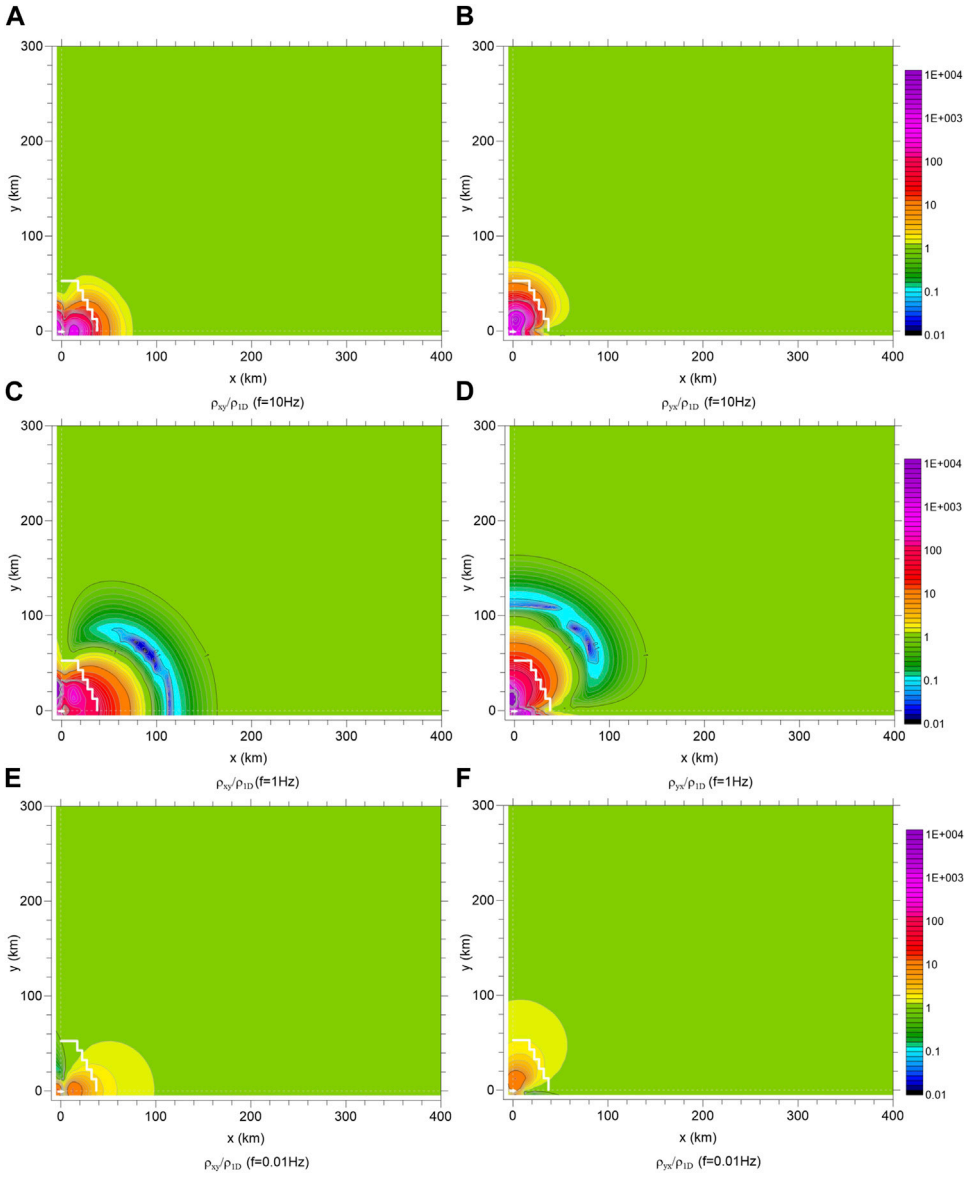

FIGURE 11
Contour plots of the ratio of apparent resistivity with 3D anomaly body together with inclined dipole source to the apparent resistivity of the 1D layered model. **(A,C,E)** are the ρ_{xy}/ρ_{1D} at the frequency of 10 Hz, 1 Hz, 0.01 Hz respectively; **(B,D,F)** are the ρ_{yx}/ρ_{1D} at the frequency of 10 Hz, 1 Hz, 0.01 Hz respectively.

5 Magnetotelluric response with dipole radiation in the earth

The behaviors of the magnetotelluric response of the 3D anomaly of earth resistivity and the dipole response of buried electric dipole radiation source in the seismogenic zone have been presented in previous sections. We now discuss the magnetotelluric responses when the 3D anomalous body and radiation dipole exist at the same time while the magnetotelluric observation is carried on.

In the process of seismogenesis, the formation resistivity in a specific range may be reduced because of the development and expansion of micro-fractures in the earth caused by the accumulation of stress. This earth resistivity change can cause the apparent resistivity decrease in the low-frequency band (less than 1 Hz) and can be observed by magnetotelluric stations in a certain range outside the seismogenic area. As the time of the earthquake approaches, the resistivity anomalies may have the characteristics of gradually enhancing and expanding. The abrupt change of ground stress before an earthquake may also lead to electromagnetic radiation, but the spatial scope will be more limited to the vicinity of the fault. However, only in the short time before an earthquake, the stress is strong enough to generate an anomalous electromagnetic field in the far field (Du et al., 2004). For long-term

monitoring stations, magnetotelluric field changes caused by different types of anomalies may be observed separately or simultaneously in different stages of earthquake preparation. If there is electromagnetic radiation before the earthquake, the field components observed at the station are the superposition of the magnetotelluric field and electromagnetic radiation field components. Because of the randomness of the amplitude and change of the magnetotelluric field, the processing and analysis of single-field data are not practical when processing observational data. Instead, it is mainly through obtaining the power spectrum of each field quantity and defining the ratio of the electromagnetic field quantity, or the impedance element, to characterize the changing relationship of the apparent resistivity with frequency. If low-frequency electromagnetic radiation is generated by the earthquake preparation, the radiation field strength must reach a certain strength before it can have a significant impact on the superimposed total field, which is reflected in the magnetotelluric response where the apparent resistivity systematically deviates from the background value.

To show the influence of the resistivity anomaly and radiation source in the earth on the magnetotelluric response, Figure 10 shows the ratio of the apparent resistivity of the 3D anomaly body and the inclined dipole source to the apparent resistivity of the 1D layered earth model. The structure and parameters of the model are shown in Figure 1. The buried depth of the electric dipole source in the earth is 10 km, the dip angle is 30 °, the source moment (the product of current change and rupture length) is $I \cdot dl$=10^{11}A · m, and the equal source moment is used for all frequencies; Figure 10A shows the ratio curve of the apparent resistivity of the 1D layered model to ρ_{xy} with different offsets along the x-axis: the offsets are x=25, 50, 100, 200, and 400 km, respectively. It can be seen from Figure 10A that the ρ_{xy} response along x direction containing electromagnetic radiation for small offsets (<100 km) presents a positive anomaly with a large amplitude peak (with a maximum of 450) in the medium-frequency band (0.1–50 Hz); small positive and negative variations can be identified at the frequencies (e.g., >40 Hz for the response of 25 km offset) corresponding to the transition zone. As the offset distance increases, the abnormal peak value decreases rapidly and the anomaly of the transition zone shifts to a lower frequency. For the source moment used, the apparent resistivity anomaly with an offset greater than 100 km is weak, and almost no identifiable anomaly for responses of 400 km offset. It can be seen that the influence of the dipole radiation source observed at a magnetotelluric station is more different from the dipole source response itself shown in Figure 8, and cannot be simply identified as the near- or far-field zone for different offsets. Figure 10B shows the ratio curve of ρ_{xy} along the y-direction to the apparent resistivity of the 1D layered model with different offsets. The response of 25 km offset shows a prominent peak of apparent resistivity enhancement with the maximum ratio of 3,800 at about 1Hz, but smoothly reducing to ~0.6 for frequency less than 0.1 Hz. The variation of ratio curves of other offsets is small and difficult to identify for the response of offset greater than 100 km.

Figure 10C shows the ratio curve of ρ_{yx} along the x-axis with different offsets to the apparent resistivity of the 1D layered model. It can be seen that the ρ_{yx} anomaly generated by the electromagnetic radiation source is mainly in the middle-frequency band, but the amplitude is far less than the ρ_{xy} anomaly. It is difficult to identify anomalies in the ratio curve with offsets greater than 50 km. The characteristics of the ρ_{yx} anomaly with differing offsets along the y-direction (Figure 10D) are much similar to those of the ρ_{xy} anomaly along the x-direction (Figure 10A), with only a slight difference in anomaly amplitude, especially for the response of short offset.

Figure 11 shows the spatial distribution of the ratio of the apparent resistivity calculated by superposition of the magnetotelluric response of the 3D low resistance anomaly and the x-direction inclined dipole source response in the layered earth model to the apparent resistivity of the 1D layered earth model, for frequencies of 10, 1 and 0.01 Hz, respectively. The range of the drawings is the same as that in Figure 9. The small white arrows in Figure 11 indicate the position of the electric dipole source in the earth, and the white step lines indicate the boundary of the 3D low resistance anomaly. It can be seen from the plot that the apparent resistivity change caused by the dipole radiation source at depth occurs in the area near the source, and the closer the source, the greater the anomaly. The apparent resistivity far away from the source is almost unchanged (the ratio is equal to 1). The anomaly in the intermediate frequency band has the maximum amplitude enhancement anomaly and a strong reduction anomaly (the ratio is far less than 1). The amplitude of the medium frequency band (f = 1 Hz) anomaly is the largest (0.01–30,000 times), and the expansion range is also large. The anomaly of ρ_{xy} is mainly observed in a sector area in the x direction, and ρ_{yx} in the y direction, with large amplitude enhancement from the dipole center and gradually decay to 1 at the radius of about 100 km and then reduce to a minimum of 0.01 at the radius of about 165 km. The amplitude of the high-frequency band and low-frequency band is relatively small, and the anomalous extension range is also small. The maximum amplitude of f = 10 Hz anomaly (Figures 11A, B) is ~8,000 times, and the sector radius is about 75 km. The maximum amplitude of f = 0.01 Hz anomaly (Figures 11E, F) is ~20 times, and the sector radius is about 95 km.

6 Discussion and conclusion

It can be seen from the analysis of the above simulations that the observational data of magnetotelluric stations may contain seismogenic electromagnetic anomaly information. The characteristics of different types of seismic electromagnetic anomalies in magnetotelluric impedance response can be summarized as follows. In the seismogenic process, the change of formation resistivity (seismogenic resistivity anomaly) can produce a recognizable low-frequency (less than 1 Hz) apparent resistivity anomaly in magnetotelluric data. The anomaly is mainly a reduction of apparent resistivity from the normal value, and small amplitude enhancement anomalies may also be observed at various spatial sites. Although the amplitude of the anomaly is small, it may also be detected hundreds of kilometers (more than 200 km) away from the seismogenic center. However, if there is a low-frequency electromagnetic radiation anomaly at the same time, the influence of seismogenic low resistance anomaly may be completely masked in the low-frequency band due to the strong anomaly generated by dipole radiation in the seismogenic area. The anomaly produced by low-frequency electromagnetic radiation before earthquakes are characterized by a sharp increase of the apparent resistivity in the near-field zone, the phase approaching

zero, and strong amplification of the anomaly by the presence of vertical source dipole components.

The influence of electromagnetic radiation before earthquakes included in magnetotelluric data on apparent resistivity depends on the proportion of each component of the radiation field in the spectral intensity of each component of the corresponding magnetotelluric field and will show different frequency and spatial characteristics from the response of a pure dipole source. For example, the response of a simple dipole source can be simply divided into a far-field zone and a near-filed zone according to frequency or offset, while the response of a dipole source radiation field contained in magnetotelluric data to apparent resistivity shows frequency selectivity, that is, anomalous amplitudes in the high-frequency and low-frequency bands are small, and the abnormal amplitude in the medium frequency band (0.1–50 Hz in this example) is largely due to the weak energy window of magnetotelluric field. In space, the response of the pure dipole source shows a small amplitude oscillation in the far-field area, which is difficult to identify in the magnetotelluric data. The manifestation of electromagnetic radiation in magnetotelluric response before earthquakes are mainly from the apparent resistivity enhancement anomaly with strong amplitude, and the anomaly amplitude decreases with the distance from the radiation source, but the apparent resistivity reduction anomaly with large amplitude may also appear for the data of different observation sites and different frequencies. The magnitude and spatial range of the influence of electromagnetic radiation on apparent resistivity before earthquakes are related to the intensity of the radiation sources. The stronger the radiation field intensity is, the larger the amplitude of apparent resistivity anomaly, and the wider the distribution range of anomaly. The calculation result of the source moment 10^{11}A · m is given in this paper. The actual earthquake case may have even stronger electromagnetic radiation, for example, the Wenchuan earthquake reached 10^{13}A · m (Li et al., 2018), and so the station farther from the seismogenic center can also detect the electromagnetic radiation anomaly.

The algorithm for 3D magnetotelluric modeling has adopted the strategy of magnetic field normalization for field component calculation, and the calculated strength for each field component may be different from the actual spectral intensity of each component measured at the station. However, the basic characteristics of electromagnetic radiation before earthquakes simulated by an electric dipole source in magnetotelluric response are valid.

In summary, electromagnetic impedance responses of a 3D low-resistance anomalous body which is used to simulate the resistivity change of strata in the seismogenic region, and an electric dipole which is used to simulate the seismogenic radiation source in horizontally layered earth model have been calculated, and the characteristics of electromagnetic impedance response with frequency and space over a large area have been analyzed quantitatively. The simulation results show that: 1) Visual resistivity anomalies of the 3D resistivity anomalous body appear in the frequency band below 5 Hz, with negative anomalies dominating in the frequency band below 1 Hz. The amplitude of the negative anomaly decreases with the increase of the offset distance, and the anomaly can be identified over 200 km. The measured data show that the resistivity often presents an abnormal decline feature before the earthquake, and the numerical simulation in this paper provides a theoretical basis for this phenomenon. 2) The vector electric dipole radiation source is equivalent to the electromagnetic radiation in the seismogenic region, and calculating and analyzing the electromagnetic impedance response. It is found that the component of tilted electromagnetic radiation in the *y*-direction will greatly enhance the detectability of electromagnetic anomalies. 3) Considering the electromagnetic radiation and the change of resistivity in the seismogenic area comprehensively, it is found that the medium frequency band (0.1–50 Hz) is the dominant frequency band for seismic electromagnetic anomalies. Around 1 Hz, the anomaly is more obvious and can be detected at a large spatial range.

The obtained results are of great significance for the observation of seismic electromagnetic anomalies, data processing, and analysis of the identification of electromagnetic anomalies in different seismogenic processes. In the future, we can analyze and compare data changes during earthquakes by combining measurement data from 30 ELF stations in the metropolitan area and the North-South seismic zone in China.

Data availability statement

The original contributions presented in the study are included in the article, further inquiries can be directed to the corresponding author.

Author contributions

YF drafted the manuscript and the figures with the guidance of WH. All authors contributed to the completion of procedures, and discussion of this study, and provided feedback on the manuscript.

Funding

This work was supported by the National Natural Science Foundation of China (No. 41574064), Basic Research Funds from the Institute of Geology, China Earthquake Administration (No. IGCEA2002), and the Beijing Natural Science Foundation Project (No. 8212045).

Acknowledgments

The authors would like to express gratitude to EditSprings (https://www.editsprings.cn) for the expert linguistic services. We acknowledge the constructive reviews of the reviewers, and the useful summary and review by the editor JL. We also thank Professor PH (China Earthquake Network Center) for her guidance.

Conflict of interest

The authors declare that the research was conducted in the absence of any commercial or financial relationships that could be construed as a potential conflict of interest.

Publisher's note

All claims expressed in this article are solely those of the authors and do not necessarily represent those of their affiliated organizations, or those of the publisher, the editors and the reviewers. Any product that may be evaluated in this article, or claim that may be made by its manufacturer, is not guaranteed or endorsed by the publisher.

References

Ding, J. H. (2009). *Geomagnetic diurnal earthquake prediction method and earthquake cases*. Beijing: Seismological Press.

Du, A. M., Zhou, Z. J., Xu, W. Y., and Yang, S. F. (2004). Generation mechanisms of ULF electromagnetic emissions before the M_L=7.1 earthquake at Hetan of Xin Jiang. *Chin. J. Geophys.* 47, 832–837. http://www.geophy.cn/article/id/cjg_555.

Du, X. B. (2011). Two types of changes in apparent resistivity in earthquake prediction. *Sci. China Earth Sci.* 54 (1), 145–156. doi:10.1007/s11430-010-4031-y

Fan, Y., Tang, J., Zhao, G. Z., Wang, L. F., Wu, J. X., Li, X. S., et al. (2013). Schumann resonances variation observed from Electromagnetic monitoring stations. *Chin. J. Geophys.* 56, 2369–2377. doi:10.6038/cjg20130723

Gao, S. D., Tang, J., Du, X. B., Liu, X. F., Su, Y. G., Chen, Y. P., et al. (2010). The change characteristics of electromagnetic field before to after Wenchuan Ms8.0 earthquake. *Chin. J. Geophys.* 53, 512–525. doi:10.3969/j.issn.0001-5733.2010.03.005

Gao, S. D., Tang, J., and Sun, W. H. (2013). Electromagnetic anomaly before the Yingjiang M_S5.8 and Myanmar M_S7.2 earthquakes. *Chin. J. Geophys.* 56, 1538–1548. doi:10.6038/cjg20130512

Gao, Y., and Hu, H. (2010). Seismoelectromagnetic waves radiated by a double couple source in a saturated porous medium. *Geophys J. Int.* 181, 873–896. doi:10.1111/j.1365-246x.2010.04526.x

Gao, Y., Harris, M., Wen, J., Huang, Y., Twardzik, C., Chen, X., et al. (2016). Modeling of the coseismic electromagnetic fields observed during the 2004 *Mw* 6.0 Parkfield earthquake. *Geophy. Res. Lett.* 43, 620–627. doi:10.1002/2015GL067183

Hu, H., and Gao, Y. (2011). Electromagnetic field generated by a finite fault due to electrokinetic effect. *J. Geophy. Res.* 116, B08302. doi:10.1029/2010JB007958

Hu, K. Y., Hu, W. B., and Huang, Q. H. (2023). The electromagnetic wave fields induced by dipoles in the horizontally stratified medium. *Chin. J. Geophys.* 8, 1–12. Available at: https://doi.org/10.6038/cjg2023Q0775 (Accessed February 22, 2023). doi:10.6038/cjg2023Q0775

Huang, F. Q., Li, M., Ma, Y. C., Han, Y. Y., Tian, L., Yan, W., et al. (2017). Studies on earthquake precursors in China: A review for recent 50 years. *Geodesy Geodyn.* 8, 1–12. doi:10.1016/j.geog.2016.12.002.geog.2016.12.002

Huang, Q. H. (2002). One possible generation mechanism of co-seismic electric signals. *Proc. Jpn. Acad. Ser. B* 78, 173–178. doi:10.2183/pjab.78.173

Huang, Q. H., Ren, H. X., Zhang, D., and Chen, Y. J. (2015). Medium effect on the characteristics of the coupled seismic and electromagnetic signals. *Proc. Jpn. Acad. Ser. B* 91, 17–24. doi:10.2183/pjab.91.17.91.17

Li, M., Wang, Z. P., Lu, J., Tan, H. D., and Zhang, X. T. (2018). Estimating the equivalent dipole of the 2008 wenchuan M_s8.0 earthquake using observed electromagnetic ground signals. *Earthquake* 38, 49–60. http://dizhen.ief.ac.cn/CN/Y2018/V38/I1/49.

Ma, Q. (2002). The boundary element method for 3-D dc resistivity modeling in layered Earth. *Geophysics* 67, 610–617. doi:10.1190/1.1468622

Mao, T. N. (1986). Present status of electric-magnetic studies in earthquake science in China. *Earthq. Res. China* 30, 31–35. https://www.cnki.com.cn/Article/CJFDTOTAL-ZGZD198603005.htm.

Pan, H. W. (1998). Development and prospects of the earthquake electromagnetic observation system in China. *Earthquake* 18, 115–119. http://dizhen.ief.ac.cn/CN/Y1998/V18/IS1/115.

Qian, F. Y., Zhao, Y. L., Yu, M. M., Wang, Z. X., Liu, X. W., and Chang, S. M. (1982). Anomalous variation of apparent resistivity before earthquakes. *Sci. China Earth Sci.* 9, 831–839. http://www.cnki.com.cn/Article/CJFDTotal-ZBDZ198202004.htm.

Ren, H., Huang, Q., and Chen, X. (2016). Existence of evanescent electromagnetic waves resulting from seismoelectric conversion at a solid–porous interface. *Geophys J. Int.* 204, 147–166. doi:10.1093/gji/ggv400

Ren, H., Wen, J., Huang, Q., and Chen, X. (2015). Electrokinetic effect combined with surface-charge assumption: A possible generation mechanism of coseismic EM signals. *Geophys J. Int.* 200, 837–850. doi:10.1093/gji/ggu435

Wait, J. R. (1951). The magnetic dipole over the horizontally stratified Earth. *Can. J. Phys.* 29, 577–592. doi:10.1139/p51-060

Wang, J. J., Zhao, G. Z., Zhan, Y., Zhuo, X. J., Tang, J., Guan, H. P., et al. (2005). Observations and studies on EM phenomena caused by earthquake in China. *J. Geodesy Geodyn.* 25, 11–21.

Zhang, H. K., Shen, Q. X., Wu, W., Zhao, Y. L., and Mao, T. E. (1996). Research on dynamic prediction method of apparent resistivity in earthquake. *Acta Seismol. Sin.* 18, 340–345. https://www.dzxb.org/article/id/2e00a835-f6c7-47d4-8269-58f665298c71.

Zhang, X. M., Qian, J. D., Sheng, X. H., Liu, J., Wang, Y. L., Huang, J. P., et al. (2020). The seismic application progress in electromagnetic satellite and future development. *Earthquake* 40, 18–37. doi:10.12196/j.ISSN.1000-3274.2020.02.002

Zhao, G. Z., Wang, L. F., Tang, J., Chen, X. B., Zhan, Y., Xiao, Q. B., et al. (2010). New experiments of CSELF electromagnetic method for earthquake monitoring. *Chin. J. Geophys.* 53, 479–486. doi:10.3969/j.issn.0001-5733.2010.03.002

Zhao, G. Z., Wang, L. F., Zhan, Y., Tang, J., Xiao, Q. B., Chen, X. B., et al. (2012). A new electromagnetic technique for Earthquake monitoring CSELF and the first observational network. *Seismol. Geol.* 34, 576–585. doi:10.3969/j.issn.0253-4967.2012.04.004

Zhao, G. Z., Zhang, X. M., Cai, J. T., Zhan, Y., Ma, Q. Z., Tang, J., et al. (2022). A review of seismo-electromagnetic research in China. *Sci. China Earth Sci.* 65, 1229–1246. doi:10.1007/s11430-021-9930-5

Zhou, C., Liu, Y., Zhao, S. F., Liu, J., Zhang, X. M., Huang, J. P., et al. (2017). An electric field penetration model for seismo-ionospheric research. *Adv. Space Res.* 60, 2217–2232. doi:10.1016/j.asr.2017.08.007

frontiers | Frontiers in Earth Science

TYPE Original Research
PUBLISHED 09 June 2023
DOI 10.3389/feart.2023.1213577

Check for updates

OPEN ACCESS

EDITED BY
Giovanni Martinelli,
Section of Palermo, Italy

REVIEWED BY
GuoFu Luo,
Ningxia Meteorological Bureau, China
Fuqiong Huang,
China Earthquake Networks Center, China

*CORRESPONDENCE
Alexandre Canitano,
canitano@earth.sinica.edu.tw

RECEIVED 28 April 2023
ACCEPTED 30 May 2023
PUBLISHED 09 June 2023

CITATION
Canitano A (2023), Sensitivity limits for strain detection of hypothetical remote fluid-induced earthquakes($M_w \geq 4$): a case study in Taiwan.
Front. Earth Sci. 11:1213577.
doi: 10.3389/feart.2023.1213577

COPYRIGHT
© 2023 Canitano. This is an open-access article distributed under the terms of the Creative Commons Attribution License (CC BY). The use, distribution or reproduction in other forums is permitted, provided the original author(s) and the copyright owner(s) are credited and that the original publication in this journal is cited, in accordance with accepted academic practice. No use, distribution or reproduction is permitted which does not comply with these terms.

Sensitivity limits for strain detection of hypothetical remote fluid-induced earthquakes ($M_w \geq 4$): a case study in Taiwan

Alexandre Canitano*

Institute of Earth Sciences, Academia Sinica, Nankang, Taiwan

Capturing and quantifying the timing of remotely triggered earthquakes and understanding the physical processes responsible for this delay represent major challenges in earthquake forecasting. In this study, we propose a physical framework for the integration of borehole strainmeter observations for the investigation of remote triggering of moderate to large earthquakes ($M_w \geq 4$) in Taiwan. Based on the time-delay computation between regional events and global earthquakes, we establish a selection of earthquakes showing fault zone properties (hydraulic diffusivity and nucleation length) that may be compatible with a magnitude-dependent fluid-induced nucleation process. Using theoretical fault zones parameters, we calculate the evolution of fluid pressure transiting along the nucleation region under the assumption of a one-dimensional, homogeneous poroelastic medium. Pore pressure levels reached before earthquake rupture are ranging from about 0.02 kPa to 3 kPa in the case of teleseismic wave-induced elastic pressure ranging from 0.15 kPa to 27.3 kPa. To compute the time-dependent evolution of deformation generated by a remote diffusing pressure front, we model the nucleation region using the analogue volcano source represented by a horizontal circular crack, and calculate synthetic dilatation at the strainmeter location from displacements using a finite-difference approach. In general, predictions are about two to four orders of magnitude smaller than observations (~ 10^{-5} to 10^{-3} nϵ). Therefore, this suggests that detection of pore pressure-related deformation would have required change of volume in the nucleation region that is at least one order of magnitude larger than for the hypothetical cases considered here. The study represents the first attempt to analyze strain time-series for detecting pre-earthquake strain anomalies related to fluid-induced earthquakes and illustrates the challenge for detecting and characterizing intermediate-to far-field earthquake precursors caused by fluid flow in active regions.

KEYWORDS

borehole strainmeter observations, detection limitations, fluid-induced earthquakes, preparatory phase, Taiwan

1 Introduction

Seismic waves from large earthquakes induce ephemeral dynamic stress perturbations over large distances (Huang et al., 2004). Despite leaving no permanent stress changes once they pass, seismic waves are capable of triggering earthquakes at distances far beyond

the aftershock region (Hill, 2008; Brodsky and van der Elst, 2014; Miyazawa et al., 2021). Remote dynamic triggering is a rare (< 2% of the time) (Pankow and Kilb, 2020) but ubiquitous phenomena (Velasco et al., 2008), and the number of evidence keeps growing since the first observations of entensive earthquake triggering in the United States following the 1992 moment magnitude (M_w) 7.3 Landers earthquake (Hill et al., 1993) and the 2002 M_w 7.9 Denali Fault earthquake (Gomberg et al., 2004). In general, dynamically triggered earthquakes occur subsequent to the passage of the surface waves (Hill, 2008; Velasco et al., 2008) with periods of 15–20 s, since they dominate gound motion in the far field (waves with smaller periods tend to be scattered and attenuated) (van der Elst and Brodsky, 2010). However, the optimal conditions for triggering remain unknown and the latter represents likely a complex combination of wave characteristics (e.g., peak amplitude, duration) and local environment (fault types and geometry and wave incidence angle) (Parsons et al., 2014). If long-lasting (hundred of seconds) dynamic perturbations at moderate to high strain level (> 100 nϵ or equivalently ~ 3 kPa) may be an efficient combination for triggering (Pollitz et al., 2012; Johnson and Bürgmann, 2016), peak strain level of teleseismic waves represents a key contribution to long-range triggering (van der Elst and Brodsky, 2010) and critically stressed faults can also rupture under strain level that is near the background noise (~ 2 nϵ) (van der Elst and Brodsky, 2010; Miyazawa et al., 2021) [**Supplementary Figure S1** in the Electronic Supplement shows a case of remote triggering at very low regional strain in Central Greece (Bernard et al., 2006; Canitano et al., 2013)].

Establishing a temporal relationship between two events is simple because seismicity is produced continuously in active tectonic regions. More challenging is to establish temporal and spatial causation between two distant earthquakes. The longer the delay between the mainshock and the posited event, the more difficult to connect them. This delay, which represents a fundamental characteristics of remote triggering, may be difficult to explain by a simple Coulomb failure model only (e.g., Belardinelli et al., 2003). Conversely, a small, or the absence of delay between two events does not necessarily imply remote triggering, as still remains the possibility of coincidental occurrence of events. Indeed, Parsons et al. (2014) found that as many as five earthquakes with $M_w \geq 6$ can occur purely by chance on any given day, for example. Since most of observed remote triggering cases concern microearthquakes and tectonic tremors (Peng et al., 2009; Peng et al., 2011; Gonzalez-Huizar et al., 2012), the magnitude range of the triggered earthquakes is still subject to debate. Many studies report the very rare occurrence of moderate to large earthquakes ($M_w \geq 5$) remotely triggered hours to days following large teleseisms ($M_w \geq 7$) (Parsons and Velasco, 2011; Johnson et al., 2015) while O'Malley et al. (2018) found that higher magnitude earthquakes occur more often than smaller events within 3 days following the passage of seismic waves. In Taiwan, detection of triggered microseismicity and tectonic tremors has also been reported (Chao et al., 2011; Sun et al., 2015), but whether larger events were triggered has not been demonstrated yet. Remote triggering is generally established using statistically significant variations in earthquake rate coincident with the passage of seismic waves (e.g., Johnson and Bürgmann, 2016; Yao et al., 2021). However, going beyond rate changes as the sole indicator for remote triggering (Pankow and Kilb, 2020) is essential for capturing and quantifying the timing of the triggered earthquakes and understanding the physical processes responsible for this delay whose remain major challenges in earthquake forecasting (Brodsky and van der Elst, 2014).

In this study, we propose a physical framework for the integration of borehole strainmeter time-series for the investigation of remote triggering of moderate to large earthquakes ($M_w \geq 4$) in Taiwan. We first analyze the time-delay between any regional event with $M_w \geq 4$ from 2000 to 2022 and the global earthquake with $M_w \geq 7$ that precedes it (**Supplementary Section S1**; **Supplementary Figure S2** in the Electronic Supplement) and then establish a selection of regional earthquakes based on a magnitude-dependent fluid-induced nucleation framework (Parsons et al., 2017). We then investigate pre-earthquake strain signals and propose an approach to compute far-field dilatation induced by an overpressure front diffusing in a fracture. Finally, we discuss the limitations faced for strain detection of the precursory phase related to hypothetical remote fluid-induced earthquakes.

2 Event selection based on a fluid-induced nucleation model

Among the diverse mechanisms proposed to explain delayed remote triggering of earthquakes with all magnitudes (Parsons, 2005; Peng et al., 2011; Shelly et al., 2011), a mechanism in particular shows that delays observed in the case of triggered earthquakes are likely not randomly distributed but are rather proportional to the event magnitudes (Parsons et al., 2017). The mechanism relies on the fact that dynamic straining from seismic waves can break a fluid seal previously blocked into a fault zone (Brodsky et al., 2003) which then releases overpressurized fluid that progressively invades the fault region. Pore fluid infiltration reduces clamping normal stress (strength is reduced with increasing pore pressure) and thus helps promote failure according to the Coulomb failure criteria. Only critically stressed faults are hydraulically conductive (Barton et al., 1995) and thus prone to fluid-induced triggering. As such a process implies fluid flow through a fault zone, a delay is required before failure conditions are met. This fluid transit time increases with earthquake magnitude since the latter is directly proportional to the dimensions of the fault rupture (Kanamori, 1977). Besides, earthquake magnitude also scales with the critical nucleation dimension ($2L_c$, in meter) which represents the size of the smaller asperity where rupture may initiate (Ohnaka, 2000):

$$2L_c = \sqrt[3]{10^{-9} M_0} \tag{1}$$

where M_0 represents the scalar seismic moment (in N.m). The critical nucleation dimension represents the minimum transit distance for a fluid to induce an earthquake of a given magnitude, and measures 0.1 km to about 1.5 km for a magnitude range between 4 and 6.5, for example. Fluid transit from a highly pressurized source through a porous medium follows a diffusion behavior (Malagnini et al., 2012):

$$r = 2.32\sqrt{Dt} \tag{2}$$

where r is the distance from the pressure source, t is time and D is the hydraulic diffusivity.

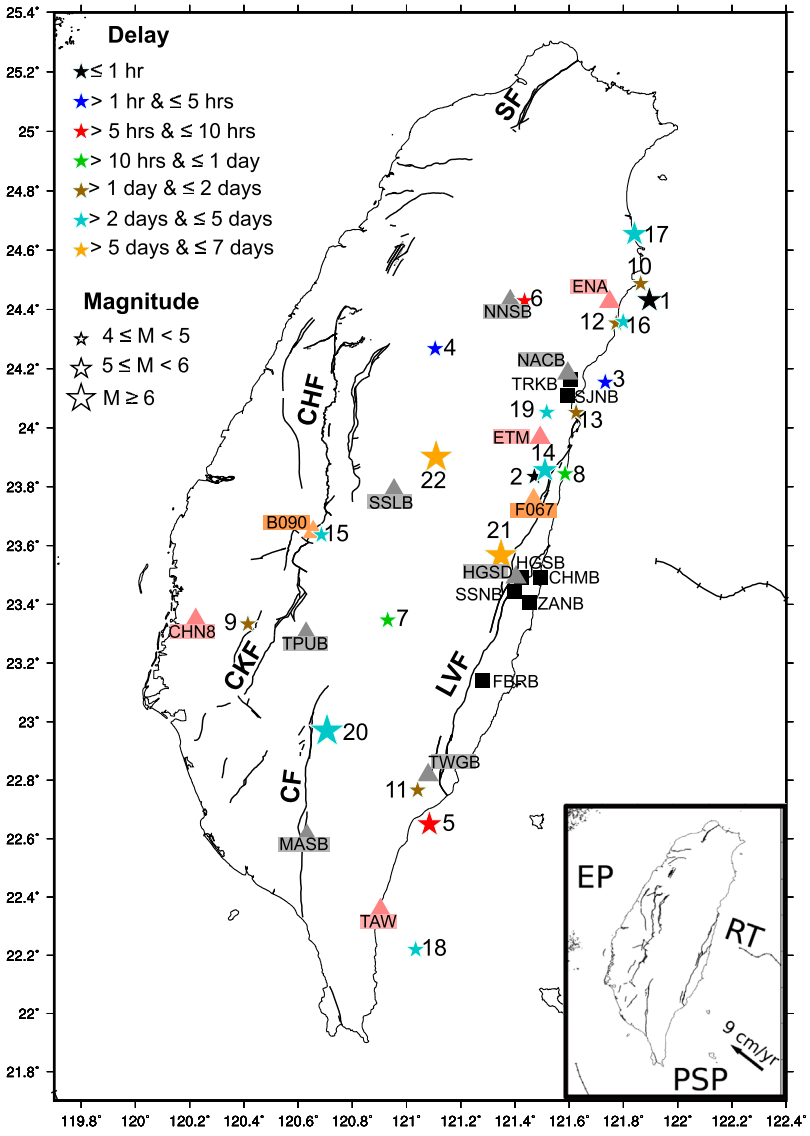

FIGURE 1
Location, magnitude and delay associated with the retained events. Triangles denote strong-motion stations (Broadband Array for Seismology in Taiwan (BATS) Institute of Earth Sciences, Academia Sinica (1996), Taiwan Strong Motion Instrumentation Program (TSMIP) and Central Weather Bureau Seismic Network (CWBSN) are shown in gray, orange and pink, respectively) used for estimating peak dynamic strain and black squares show borehole strainmeters used for analyzing strain changes (11 events). LVF: Longitudinal Valley fault; CF: Chaochou fault; SF: Shanchiao fault; CHF: Chelungpu fault; CKF: Chukou fault. (Inset) Geodynamic framework of Taiwan (RT: Ryukyu trench; EP: Eurasian plate; PSP: Philippine Sea plate). The black arrow indicates the relative motion between the PSP and the EP.

Since the time-delay between a transient stressing of the Earth's crust and the eventual occurrence of remote earthquakes may be diagnostic of their nucleation process (Parsons et al., 2017), we establish a regional earthquake selection that may be compatible with a possible fluid-induced nucleation model. We retain the regional events for which estimated time-delays may be consistent with commonly observed fault zone diffusivity values (typically $D \sim 10^{-2}$ to 10 $m^2.s^{-1}$) (Parsons et al., 2017; Guo et al., 2021). We extend our selection to a delay of approximately 1 week to include some of the largest events ($M_w \geq 6.4$) from the preliminary selection (**Supplementary Section S1**). We estimate maximum trough-to-peak dilatation of the Rayleigh wave using the waveform similarity between dilatation ϵ_v and the vertical component of the seismic acceleration a_z (Canitano, 2020):

$$\epsilon_v = \left(\frac{0.12T_c}{\pi V_r}\right)\left(\frac{1-2\gamma}{\gamma}\right)a_z \quad (3)$$

where T_c is the Rayleigh wave main period (T_c = 15 s), γ denotes the Poisson's ratio (γ = 0.25) and V_r the Rayleigh wave phase velocity (V_r = 4 $km.s^{-1}$). A good waveform coherence is observed between signals (**Supplementary Figure S3**) while amplitude discrepancies (about 10%–15%) may be related to uncertainties in the borehole strainmeter calibration protocol (Canitano et al., 2018). We consider a Rayleigh wave trough-to-peak strain amplitude of 2 nϵ as limit and we adjust the delay

TABLE 1 Characteristics of the mainshocks ($M_w \geq 7$) preceding the retained regional events.

Location	Time	Longitude (°)	Latitude (°)	M_w	Distance (km)	ϵ_m (nϵ)	Ref. regional
Papua	2018-02-25 17:44:44	142.754	−6.070	7.5	4,075	30	1
New Zealand	2009-07-15 09:22:29	166.562	−45.762	7.8	8,976	8	2
Papua	2009-01-03 19:43:50	132.885	−0.414	7.7	2,983	32	3
Bonin Islands	2000-08-06 07:27:12	139.556	28.856	7.4	1,902	24	4
Java	2007-08-08 17:05:04	107.419	−5.859	7.5	3,502	24	5
Indonesia	2015-07-27 21:41:21	138.528	−2.629	7.0	3,528	9	6
Japan	2005-11-14 21:38:51	144.896	38.107	7.0	2,804	36	7
Alaska	2021-07-29 06:15:49	−157.888	55.364	8.2	7,259	15	8
North Sumatra	2012-04-11 08:38:36	93.063	2.327	8.6	3,759	580	9
Indonesia	2000-06-04 16:28:26	102.087	−4.721	7.9	3,889	145	10
E. Sichuan	2008-05-12 06:28:01	103.322	31.002	7.9	1,978	910	11
Philippines	2001-01-01 06:57:04	126.579	6.898	7.5	2,007	23	12
Nicobar Islands	2010-06-12 19:26:50	91.936	7.881	7.5	3,634	52	13
Russia	2020-02-13 10:33:44	148.959	45.616	7.0	3,448	11	14
Japan	2022-03-16 14:36:30	141.579	37.713	7.3	2,531	12	15
Indonesia	2010-09-29 17:11:25	133.760	−4.963	7.0	3,508	5	16
Banda Sea	2005-03-02 10:42:12	129.933	−6.527	7.1	3,575	6	17
Philippines	2012-08-31 12:47:33	126.638	10.811	7.6	1,401	69	18
New Caledonia	2018-12-05 04:18:08	169.427	−21.950	7.5	7,278	9	19
Maule	2010-02-27 06:34:11	−72.898	−36.122	8.8	18,052	61	20
Japan	2013-10-25 17:10:19	144.661	37.156	7.1	2,690	25	21
Indonesia	2000-06-04 16:28:26	102.087	−4.721	7.9	3,792	145	22

by estimating the time-difference between the arrival time of the Rayleigh wave with maximum amplitude at the strong-motion station and the regional event onset (**Figure 1**). Maximum Rayleigh wave amplitude ϵ_m associated with the retained 22 regional events are ranging from 5 nϵ to about 900 nϵ with epicentral distances from about 1,400 km to 18,000 km (**Supplementary Figure S3**; **Table 1**). Regional events are showing delays ranging from about 20 min to 6 days and M_w from 4.12 to 6.80 (**Table 2**). **Figure 2A** presents the retained earthquakes integrated in a magnitude-dependent critical nucleation model.

3 Investigation of pre-earthquake strain anomalies

We investigate pre-earthquake anomalies using *Sacks-Evertson* (Sacks et al., 1971) borehole strainmeter sensors. Given their very high sensitivity at short-to intermediate-period (minutes to weeks), strainmeters represent a powerful tool to search for crustal strain transients, including anomalies preceding earthquakes (Amoruso and Crescentini, 2010; Canitano et al., 2015). We process the 1-min sampling strain time-series [see Canitano et al. (2018); Canitano et al. (2021) for details] for stations located at a maximum distance of about 50 km from our target events (11 events). Other events are either too far from operating stations (> 80 km) or occurred prior to the network deployment. **Figure 3** and **Supplementary Figure S4** present the temporal evolution of dilatation over a time-span of minutes to days preceding regional events.

In general, dilatation level after correction of external perturbations ranges from approximately 10^{-1} to 5.10^{-1} nϵ at the period of minutes to hours and then increases to about 1 nϵ at a daily period to a tens of nanostrain at the period of a few days. For events 1 and 2, which occurred during the passage of surface waves from global earthquakes, we observe no pre-rupture strain variations at remote strainmeters (40 km away). Event 3 (M_w 4.80) possibly represents the most favorable case for detecting subnanometric near-source strain variations (**Figure 3C**). It occurred at shallow depth (7 km), about 14 km away from SJNB station, and 2 h following the Rayleigh wave arrivals of a M_w 7.7 earthquake in Papua. Strain variations are strongly correlated with atmospheric pressure for about 45–50 min after the Rayleigh wave arrivals (15 min after the mainshock origin time), then suddenly the correlation breaks, suggesting the possible detection of an other source of deformation. We observe a gradual expansion starting about 1 h preceding the regional earthquake with a total

TABLE 2 Regional earthquakes ($M_w \geq 4$ with depth ≤25 km) integrated in a fluid-diffusion nucleation model. Events are listed by increasing time-delay.

References	Time	Longitude (°)	Latitude (°)	Depth (km)	M_w	Delay (hour)
1	2018-02-25 18:28:40.89	121.8958	24.4313	22.00	5.23	0.32
2	2009-07-15 10:37:36	121.4718	23.8345	18.50	4.42	0.42
3	2009-01-03 22:04:34.97	121.7331	24.1535	7.46	4.80	2.11
4	2000-08-06 09:51:40.84	121.1055	24.2671	7.44	4.18	2.28
5	2007-08-09 00:55:47.36	121.0845	22.6495	5.51	5.52	7.61
6	2015-07-28 06:59:10.32	121.4355	24.4291	5.98	4.28	9.03
7	2005-11-15 13:41:35.55	120.9303	23.3461	4.65	4.13	15.73
8	2021-07-29 22:55:17.29	121.5850	23.8432	4.78	4.28	15.83
9	2012-04-12 10:39:25.05	120.4148	23.3330	12.80	4.12	25.60
10	2000-06-06 01:49:39.3	121.8635	24.4870	21.55	4.41	32.97
11	2008-05-13 18:27:55.34	121.0410	22.7658	6.97	4.72	35.80
12	2001-01-02 22:54:58.13	121.7736	24.3538	8.46	4.27	39.61
13	2010-06-14 17:17:45.78	121.6258	24.0511	16.40	4.46	45.87
14	2020-02-15 11:00:06.5	121.5107	23.8563	8.32	5.58	48.28
15	2022-03-19 15:23:42.86	120.6862	23.6362	14.62	4.86	72.60
16	2010-10-02 19:23:12.36	121.7991	24.3585	19.38	4.78	73.83
17	2005-03-05 19:06:51.73	121.8408	24.6546	6.39	5.80	80.15
18	2012-09-04 20:00:18.32	121.0336	22.2196	9.91	4.95	103.10
19	2018-12-09 15:15:41.33	121.5170	24.0518	19.68	4.87	106.23
20	2010-03-04 00:18:52.14	120.7066	22.9691	22.64	6.44	111.73
21	2013-10-31 12:02:09.54	121.3485	23.5661	14.98	6.44	138.55
22	2000-06-10 18:23:29.45	121.1091	23.9010	16.21	6.80	141.35

deformation of about -7.10^{-1} nϵ, well above the short-period strain noise of approximately 10^{-1} nϵ. For event 11, large pore pressure variations (> 25 kPa) induced by the intense Rayleigh wave straining in southern LV (about 1 $\mu\epsilon$) following the 2008 Eastern Sichuan earthquake may be expected. However, we find no evidence of pre-earthquake variations, which illustrates the complexity for detecting subnanometric deformation at periods larger than 12–24 h because signals are also impacted by environmental perturbations, especially rainfall (Hsu et al., 2015; Mouyen et al., 2017), and by low tidal strain noise remaining after correction (~ 0.5-1 nϵ) (**Supplementary Figure S4**). Finally, strain contraction of −10 nϵ and −20 nϵ are observed hours to days preceding event 16 and event 21, respectively, and are analyzed in the next section.

4 Connecting strain observations to transient pressure anomalies

To connect the strain observations to potential transient pressure anomalies, we follow a two-step approach. In a first step, we calculate the temporal variation of the theoretical pore pressure induced in the fracture by the passing seismic waves. In a second step, we compute the time-dependent evolution of dilatation generated by a remote diffusing pressure front at the sensor location.

4.1 Theoretical pressure induced in the fracture by elastic waves

The evolution of pore pressure P in the fracture in the case of a one-dimensional (1-D), semi-infinite, isotropic, homogeneous poroelastic medium, is given by (Duoxing et al., 2015):

$$P(x,t) = P_m\left[1 - erf\left(\frac{x}{2\sqrt{Dt}}\right)\right] \quad (4)$$

where P_m represents trough-to-peak stress of seismic waves (obtained through ϵ_m for Hooke's law), *erf* is the error function, x is the distance in the fracture, t is transit time and D is the hydraulic diffusivity. Pore pressure at $x = 0$ (i.e., before fluid initiates transit) is equal to seismic wave elastic pressure ($P(x = 0, t) = P_m$) and estimates range from 0.15 kPa to 27.3 kPa. To estimate the pressure level at the time of the rupture, that is when the fluid has transited along the entire nucleation region ($x = 2L_c$), we estimate the nucleation length for each event (Eq. 1) and then

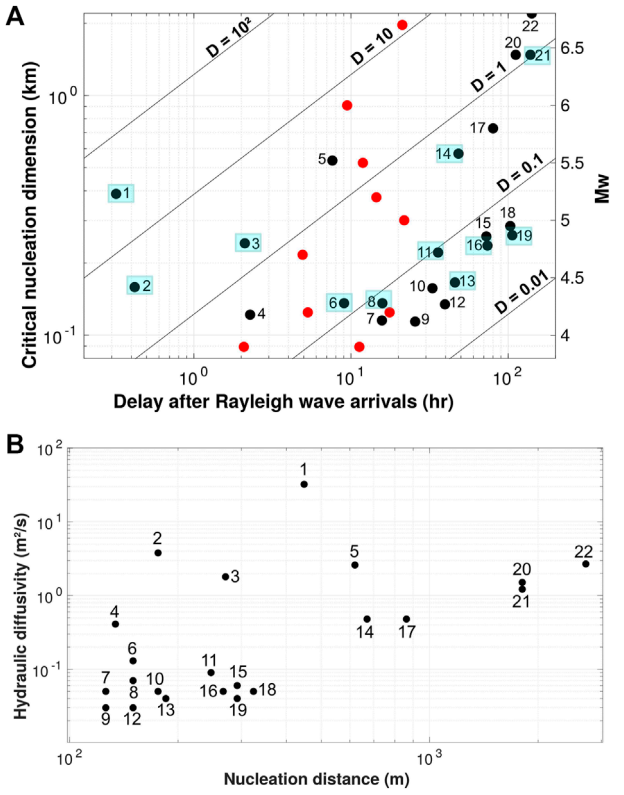

FIGURE 2
(A) Magnitude-dependent nucleation dimension ($2L_c$) versus time-delay for the target earthquakes (black dots). The red dots show remotely triggered earthquakes from *Parsons et al.* (2017). Events for which precursory deformation changes are investigated are outlined by a blue shaded box. Fault zones diffusion rates (Eq. **2**) are plotted for diffusivity values ranging from 10^{-2} to 10^{2} m^2 s^{-1}. **(B)** Theoretical nucleation distance versus fault hydraulic diffusivity for the retained regional earthquakes (**Table 2**).

calculate hydraulic diffusivity using the nucleation length and the estimated time-delay (or transit time) following Eq. **2**. Theoretical diffusivity factors range from 0.03 to 30 $m^2.s^{-1}$ for nucleation distances $2L_c$ of about 0.13–2.7 km (**Figure 2B**) and are generally consistent with estimates from Feng et al. (2021). Pore pressure levels before rupture occurs are ranging from about 0.02 kPa to 3 kPa (**Figure 4**).

4.2 Dilatation computation at strainmeter sites

Full and accurate modeling of crustal deformation induced by a pressure front propagating in an heterogeneous fault zone is a complex problem. To compute the time-dependent evolution of dilatation generated by a remote diffusing pressure front, we adopt some simplifications. We model the nucleation region using the analogue volcano source represented by a horizontal circular crack in a semi-infinite elastic solid. The three dimensional (3-D) displacements generated by a sill-like source in a semi-infinite, elastic half-space subjected to the time-dependent pressure change $P(t)$ (Eq. **4**), are expressed as (Fialko et al., 2001):

$$U_E(t) = a\frac{P(t)}{G}U_r\frac{X}{R}$$
$$U_N(t) = a\frac{P(t)}{G}U_r\frac{Y}{R} \quad (5)$$
$$U_Z(t) = -a\frac{P(t)}{G}U_z$$

where a represents the characteristic crack dimension (here taken as the nucleation distance $2L_c$), G is the half-space rigidity (G = 30 GPa), $X = \frac{x-x_0}{a}$ and $Y = \frac{y-y_0}{a}$ are dimensionless distances with respect to the characteristic crack dimension where (x_0, y_0, z_0) and (x, y, z) are the coordinates of the center of the crack and of the observation point in an E-N-Z referential, respectively, and R ($= \sqrt{X^2+Y^2}$) represents the source-station radial distance. U_r and U_z represent the radial and vertical displacements as detailed in Fialko et al. (2001). We simulate the 3-D displacements using *dMODELS* software (MATLAB-based) (Battaglia et al., 2013) and estimate the temporal evolution of synthetic dilatation at the strainmeter location from displacements using the finite-difference approach proposed by Canitano et al. (2017).

A remarkable property of the 1-D pore pressure equation is that the hydraulic diffusivity represents the only factor that controls the pore pressure dynamics in the fracture (Shapiro et al., 2018). In particular, D controls the pore pressure rise-time (**Figure 4**); the greater the diffusivity, the earlier dilatation changes induced in the crust by a pressure front diffusing in the fracture can be detected. The temporal evolution of the synthetic dilatation generated by a remote overpressure front based on the theoretical parameters related to a fluid-induced nucleation mechanism (**Figure 2B**) is shown in **Figure 5**. In general, predictions underestimate the observations by at least two to four orders of magnitude. Namely, no predicted signal is expected to be $> \sim 10^{-2}$ nϵ which represents the strainmeter nominal resolution. Therefore any precursory signal, if occurred in our earthquake selection, would have remained undetected.

5 Discussion

The detection of crustal strain anomalies and their characterization as earthquake precursors is a complex problem (Bernard, 2001). Although the quality of the data and of the applied corrections play an important role in monitoring strain transients (e.g., the detection level), complexities are mainly related to the transient source characteristics and to the source-station distance (quasi-static deformation decreases with a factor of $1/R^2$). In particular, the detection capability strongly depends of the strength of the source of deformation. Here, the latter is controlled by the size of the nucleation region (which depends of the earthquake magnitude) and by the pressure gradient, which is determined by the fracture hydraulic diffusivity and by the elastic wave pressure. We consider the volume change ΔV in the crack fracture resulting from a uniform pressure gradient ΔP as a proxy for the source strength. For an incompressible fluid, it is expressed as:

$$\Delta V = -4\pi(1-\nu)\frac{\Delta P}{G}a^3\int_0^1 t\phi(t)\,dt \quad (6)$$

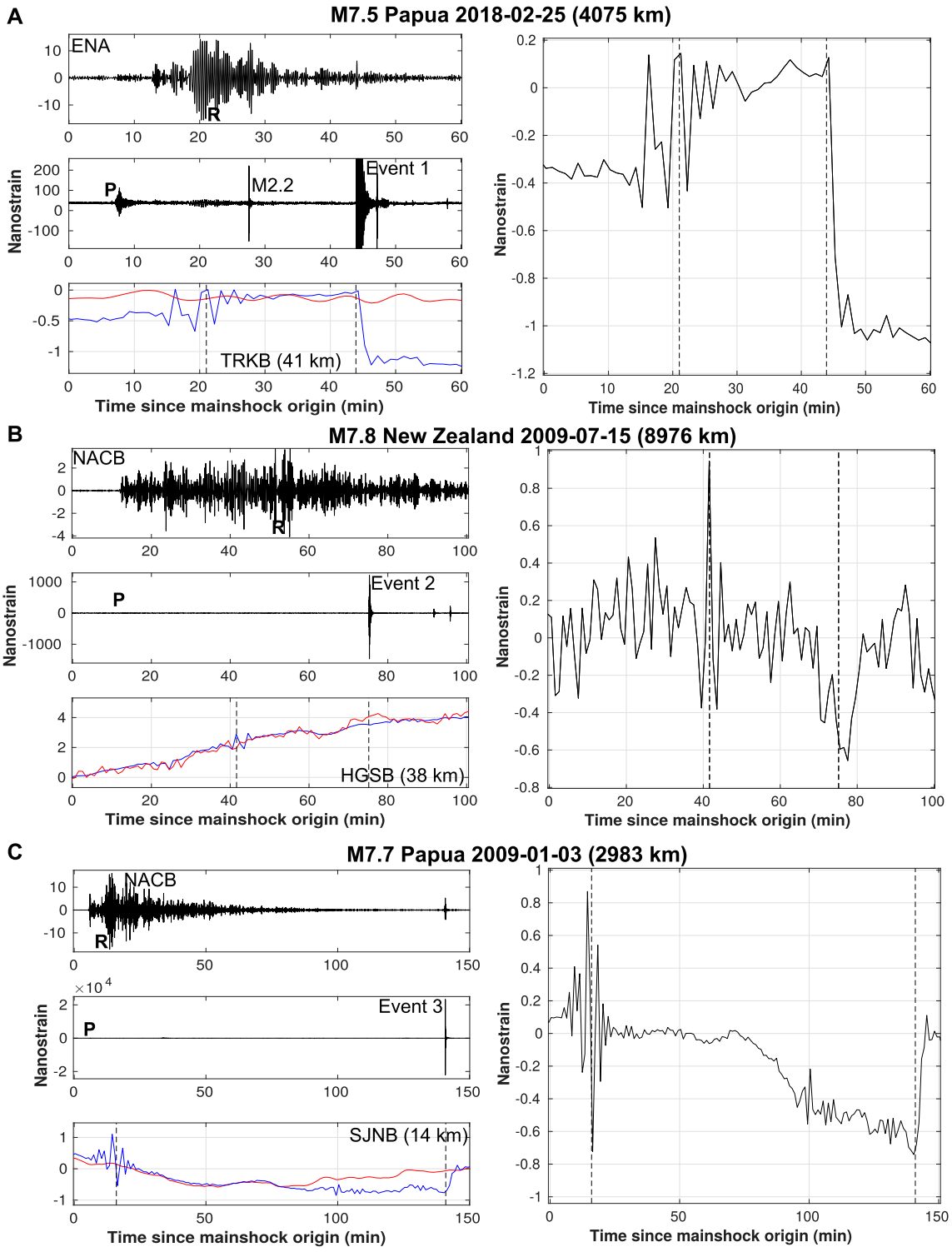

FIGURE 3
Investigation of pre-earthquake anomalies in borehole strain data related to regional earthquakes occurring shortly following the passing of Rayleigh waves (≤2 h) from global events: **(A)** 25 February 2018 M_w 5.23 earthquake (event 1), **(B)** 15 July 2009 M_w 4.42 earthquake (event 2) and **(C)** 3 January 2009 M_w 4.80 earthquake (event 3). (Left) From top to bottom: dilatation estimated from converted vertical seismic acceleration signal bandpassed between 10 and 25 s (*R* denotes Rayleigh waves with maximum amplitude) and raw signal (*P* denotes *P*-wave arrivals), respectively and dilatation recorded by borehole strainmeter (blue curve) and air pressure-induced dilatation (red curve). (Right) Residual dilatation signal (i.e., corrected for air pressure-induced strain). Vertical black dashed lines depict the arrivals of Rayleigh waves with maximum amplitude and the regional event onset, respectively. Strain expansion is positive.

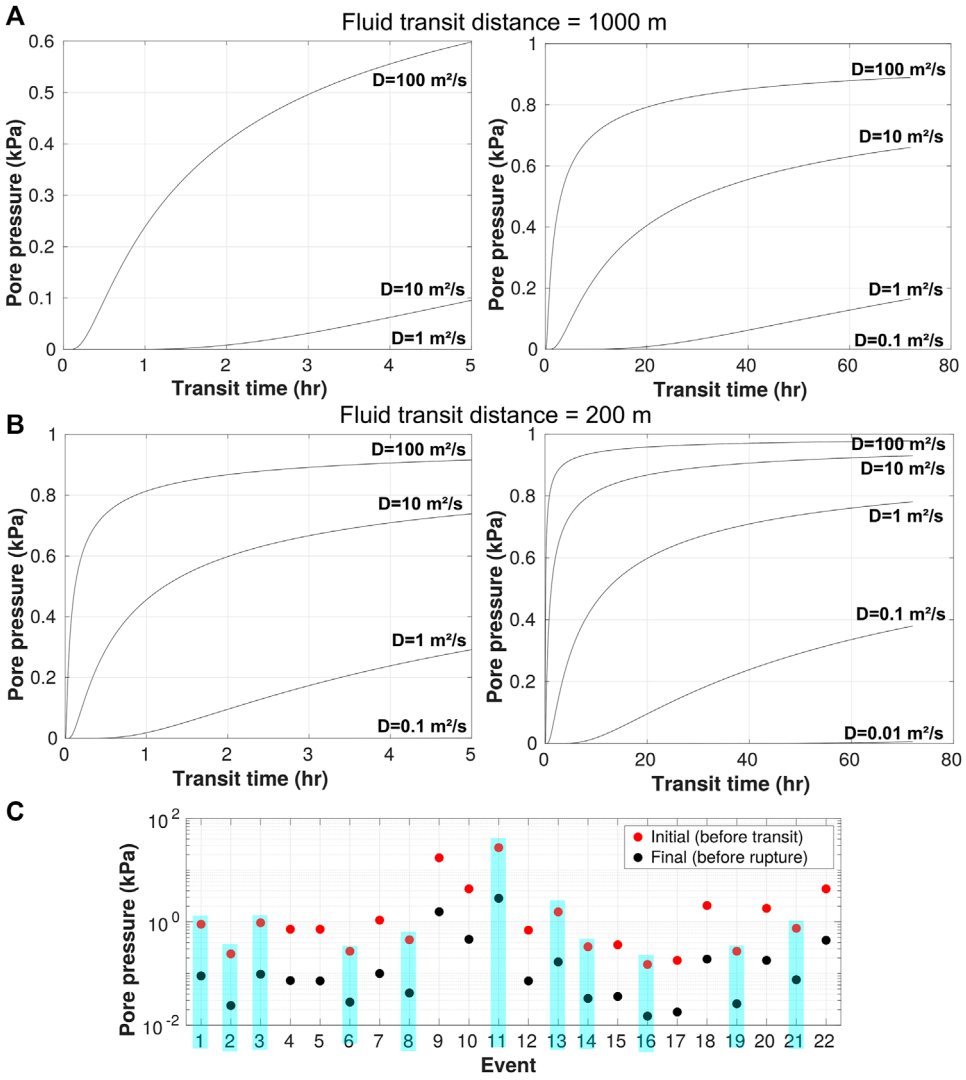

FIGURE 4
Evolution of pore pressure in the fracture resulting from an unitary elastic wave overpressure (1 kPa) as a function of hydraulic diffusivity: **(A)** fluid-transit distance of 1 km and **(B)** fluid-transit distance of 200 m. **(C)** Estimate of initial (before fluid transit) and final (before rupture) pore pressure level in the fracture with respect to the maximum seismic wave elastic pressure for observed time-delays (**Table 2**) and for fluid-transit distances and diffusion factors given by the magnitude-dependent nucleation model (**Figure 2**). Events for which precursory deformation changes are investigated are outlined by a blue shaded box.

where ϕ function is the solution of the Fredholm equation of the second kind (Fialko et al., 2001; Battaglia et al., 2013). **Figure 6** presents the theoretical volume change in the fracture for earthquakes with magnitude ranging from 4 to 7. To detect the precursory phase of a remote fluid-induced earthquake at a subdaily period within a few kilometer radius from the source requires a source volume that is about 5–10 times larger than for the hypothetical cases considered in this study. Since strain measurement noise increases with period (Crescentini et al., 1997), this would require monitoring crustal deformation with a station located near a large regional earthquake that occurred shortly following a large teleseismic event; a configuration that is highly unlikely. Therefore, to improve our understanding of remote earthquake triggering in Taiwan, the protocol adopted here should be combined with a more conservative approach that relies on the search of earthquakes with a wide range of magnitudes following large global events.

Since it controls the dilatation level during computation, the incident-wave strain level may also represent a critical parameter for detection of fluid-induced seismicity. However, the effect of dynamic peak strain on triggered seismicity is not well understood (Brodsky and van der Elst, 2014), and a large strain perturbation doesn't necessarily imply remote triggering, and *vice versa* (Parsons et al., 2014). The 2008 M_w 7.9 Eastern Sichuan earthquake, which generated strong regional ground motions due to pronounced rupture directivity effects (Kurahashi and Irikura, 2010), has induced dynamic stress over Taiwan about twice larger than any other great teleseismic earthquake (e.g., the 2011 M_w 9.0 Tohoku

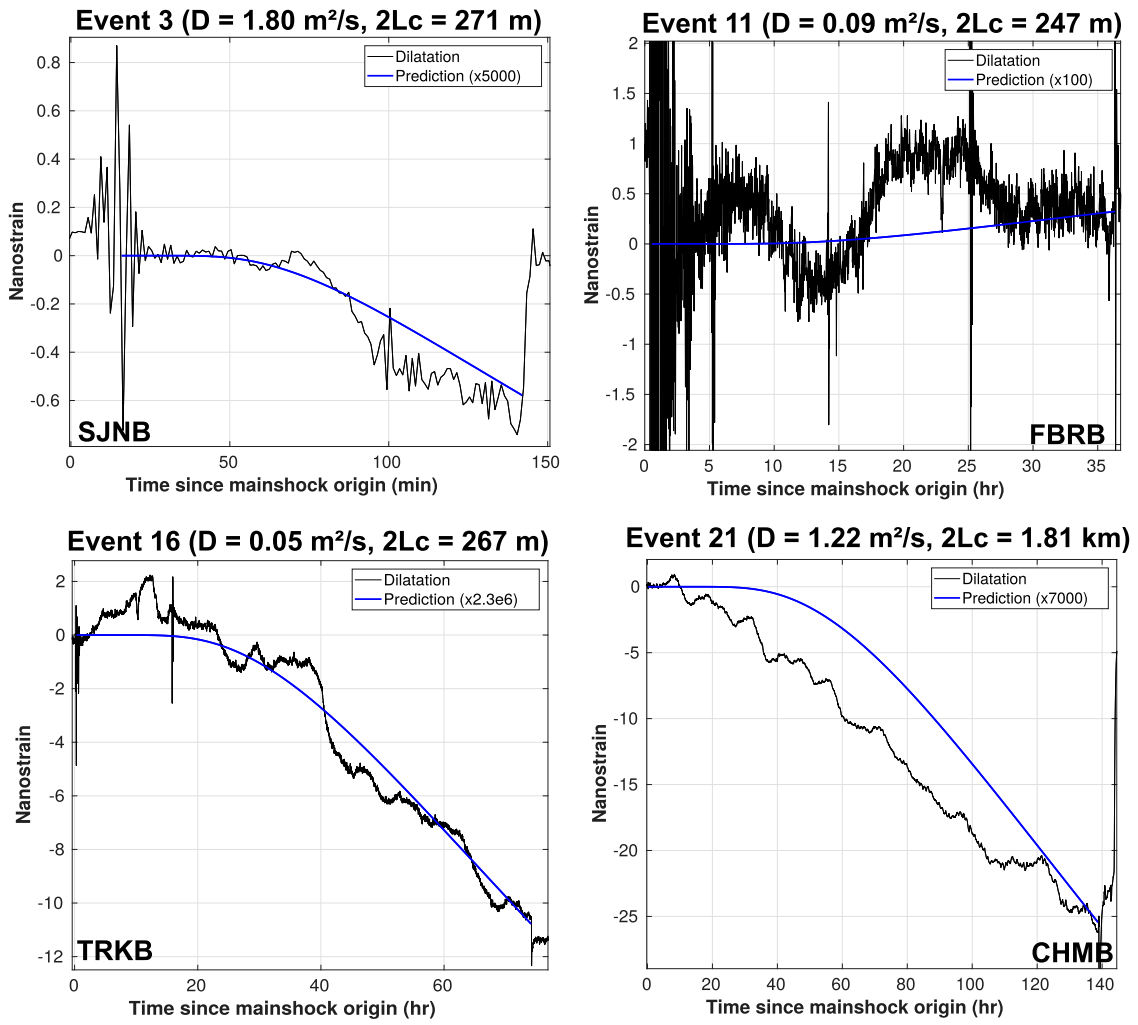

FIGURE 5
Example of temporal evolution of synthetic dilatation at the strainmeter location computed from 3-D displacements generated by a remote overpressure front in a fracture. The onset time of predictions is scaled with the arrival of Rayleigh waves with maximum amplitude at the station. For comparison, amplitude of the predicted signal is magnified to match the strain level observed before rupture.

and the 2012 M_w 8.6 Sumatra events). Although, the event triggered seismicity in northern China (Peng et al., 2010), it had little to no impact on the seismicity in Taiwan (Chao et al., 2011), at least during the first days following the wave passing (**Section 3**). Recently, field (Bonini, 2020) and laboratory (Zheng, 2018; Jin et al., 2021) observations have shown that pore pressure induced in a fluid-filled fracture by a seismic wave can be amplified relative to the incident-wave pressure [up to three orders of magnitude (Zheng, 2018)]. This transient pore fluid amplification would suggest that even seismic waves with insignificant stress levels can induce substantial overpressure in fault zones. Besides, this also implies that fluid level can remain high after transiting in the fracture, therefore favoring nucleation in case of delayed triggering or inducing large normal stress unclamping in case of instantaneous (or nearly-instantaneous) triggering. Such a process may also favor detection at remote distances of transient events that generate little regional deformation, as analyzed here. For example, in the case of event 3 (**Figure 5**), we observe that the pore pressure rise-time and temporal evolution in the fracture is well predicted for station SJNB (nearby station TRKB was shutted off), but the strain level is underestimated by about three orders of magnitude. Although the analyze of a pressure amplification mechanism in the fault zone is beyond the scope of this study, we cannot rule out that such a process may be at play for some cases. On the other hand, moderate strain changes observed for events 16 and 21 are too large to reflect a transient deformation and likely represent the contraction response due to rainfall loading (Canitano et al., 2021), which illustrates the impracticability for detecting precursory strain during environmental disturbances.

Finally, we recognize that our analogue volcano deformation model is by no means complex enough to reflect the far-field deformation caused by fluid flow in active regions, but it provides a preliminary framework for the integration of borehole dilatation observations for the search of precursory signals associated with remote fluid-induced earthquakes (Parsons et al.,

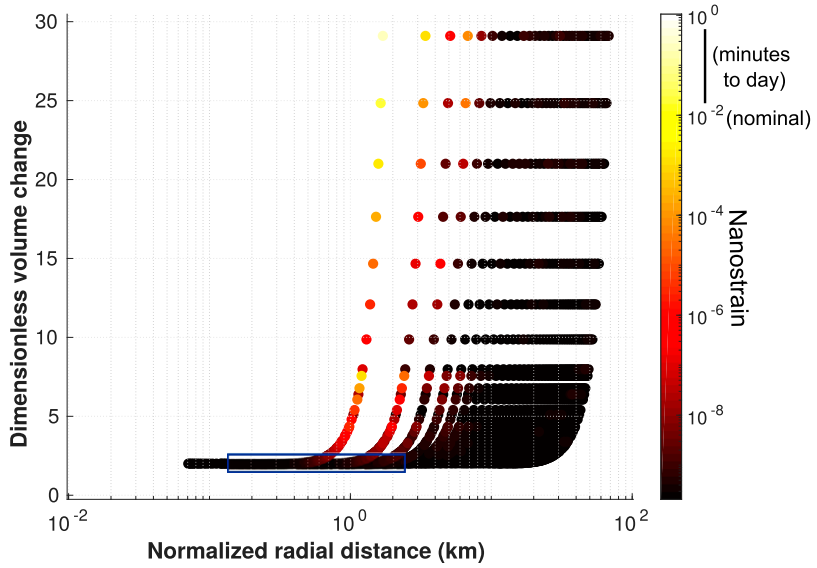

FIGURE 6
Theoretical volume change in the fracture $\Delta V/(a^3 \Delta P/G)$ as a function of the source-station radial distance $R/(z_0/a)$ estimated for earthquakes with magnitude ranging from 4 (a = 0.1 km) to 7 (a = 3 km). The blue region outlines the range where our observations fall. Strain levels associated with the analyzed hypothetical remote fluid-induced earthquakes are at least two to three orders of magnitude lower than the strainmeter nominal resolution (about 10^{-2} nϵ).

2017). A more elaborated model of fault valving (Zhu et al., 2020), integrating fluid-driven aseismic creeep (Shelly et al., 2011; Cebry et al., 2022) and seismicity (Shapiro et al., 2018), combined with a multidisciplinary geophysical monitoring is fundamental for enhancing detection and characterization of precursory phenomena in Taiwan (Fu et al., 2020) or in other active regions (Delorey et al., 2015).

6 Conclusion

We develop a protocol to integrate high-resolution borehole strain measurements for the investigation of remote triggering of moderate to large earthquakes ($M_w \geq 4$) in Taiwan. The physical framework is compatible with a magnitude-dependent fluid-induced nucleation process where the nucleation region is simplified using the analogue volcano source represented by a horizontal circular crack. We observe that theoretical evolution of dilatation generated by a remote diffusing pressure front in a semi-infinite, elastic half-space is two to four orders of magnitude smaller than observations ($\sim 10^{-5}$ to 10^{-3} nϵ). This suggests that detection of pore pressure-related deformation would have required change of volume in the nucleation region that is at least one order of magnitude larger than for the hypothetical cases considered here. The study represents the first attempt to analyze strain time-series for detecting pre-earthquake strain anomalies related to fluid-induced earthquakes and illustrates the challenge for detecting and characterizing intermediate-to far-field earthquake precursors caused by fluid flow in active regions.

Data availability statement

The raw data supporting the conclusion of this article will be made available by the authors, without undue reservation.

Author contributions

The author confirms being the sole contributor of this work and has approved it for publication.

Funding

This research is supported by the Ministry of Science and Technology grant MOST 111-2116-M-001-018.

Acknowledgments

I am thankful to Associate Editor Giovanni Martinelli and two reviewers for their constructive comments allowing to improve the manuscript. I am grateful to Alan Linde, Selwyn Sacks, and the support staff of the Carnegie Institution of Washington for the construction, installation, and maintenance of the dilatometers. I would like to thank Hsin-Ming Lee who has collected the strainmeter data, Ya-Ju Hsu and Zhigang Peng for insightful comments and Pascal Bernard for providing MOK strainmeter data (CRL, Greece). This is the contribution of the Institute of Earth Sciences, Academia Sinica, IESAS2414.

Conflict of interest

The author declares that the research was conducted in the absence of any commercial or financial relationships that could be construed as a potential conflict of interest.

Publisher's note

All claims expressed in this article are solely those of the authors and do not necessarily represent those of their affiliated organizations, or those of the publisher, the editors and the reviewers. Any product that may be evaluated in this article, or claim that may be made by its manufacturer, is not guaranteed or endorsed by the publisher.

Supplementary material

The Supplementary Material for this article can be found online at: https://www.frontiersin.org/articles/10.3389/feart.2023.1213577/full#supplementary-material

References

Amoruso, A., and Crescentini, L. (2010). Limits on earthquake nucleation and other pre-seismic phenomena from continuous strain in the near field of the 2009 L'Aquila earthquake. *Geophys. Res. Lett.* 37. doi:10.1029/2010GL043308

Barton, C. A., Zoback, M. D., and Moos, D. (1995). Fluid flow along potentially active faults in crystalline rock. *Geology* 23 (8), 683–686. doi:10.1130/0091-7613(1995)023<0683:ffapaf>2.3.co;2

Battaglia, M., Cervelli, P. F., and Murray, J. R. (2013). dMODELS: A MATLAB software package for modeling crustal deformation near active faults and volcanic centers. *J. Volcanol. Geotherm. Res.* 254, 1–4. doi:10.1016/j.jvolgeores.2012.12.018

Belardinelli, M. E., Bizzarri, A., and Cocco, M. (2003). Earthquake triggering by static and dynamic stress changes. *J. Geophys. Res.* 108 (B3), 2135. doi:10.1029/2002jb001779

Bernard, P. (2001). From the search of 'precursors' to the research on 'crustal transients. *Tectonophysics* 338, 225–232. doi:10.1016/s0040-1951(01)00078-6

Bernard, P., Lyon-Caen, H., Briole, P., Deschamps, A., Boudin, F., Makropoulos, K., et al. (2006). Seismicity, deformation and seismic hazard in the Western rift of corinth: New insights from the corinth rift laboratory (CRL). *Tectonophysics* 426, 7–30. doi:10.1016/j.tecto.2006.02.012

Bonini, M. (2020). Investigating earthquake triggering of fluid seepage systems by dynamic and static stresses. *Earth Sci. Rev.* 210, 103343. doi:10.1016/j.earscirev.2020.103343

Brodsky, E. E., Roeloffs, E., Woodcock, D., Gall, I., and Manga, M. (2003). A mechanism for sustained groundwater pressure changes induced by distant earthquakes. *J. Geophys. Res.* 108, 2390. doi:10.1029/2002JB002321

Brodsky, E. E., and van der Elst, N. J. (2014). The uses of dynamic earthquake triggering. *Annu. Rev. Earth Planet. Sci.* 42, 317–339. doi:10.1146/annurev-earth-060313-054648

Canitano, A., Bernard, P., Linde, A. T., and Sacks, S. (2013). Analysis of signals of a borehole strainmeter in the Western rift of Corinth, Greece. *J. Geod. Sci.* 3 (1), 63–76. doi:10.2478/jogs-2013-0011

Canitano, A., Hsu, Y. J., Lee, H. M., Linde, A. T., and Sacks, S. (2017). A first modeling of dynamic and static crustal strain field from near-field dilatation measurements: Example of the 2013 M_w 6.2 ruisui earthquake, taiwan. *J. Geod.* 91 (1), 1–8. doi:10.1007/s00190-016-0933-6

Canitano, A., Hsu, Y. J., Lee, H. M., Linde, A. T., and Sacks, S. (2015). Near-field strain observations of the october 2013 ruisui, taiwan, earthquake: Source parameters and limits of very-short term strain detection. *Earth Planets Space* 67, 125. doi:10.1186/s40623-015-0284-1

Canitano, A., Hsu, Y. J., Lee, H. M., T Linde, A., and Sacks, S. (2018). Calibration for the shear strain of 3-component borehole strainmeters in eastern Taiwan through Earth and ocean tidal waveform modeling. *J. Geod.* 92 (3), 223–240. doi:10.1007/s00190-017-1056-4

Canitano, A., Mouyen, M., Hsu, Y. J., Linde, A. T., Sacks, S., and Lee, H. M. (2021). Fifteen years of continuous high-resolution borehole strainmeter measurements in eastern taiwan: An overview and perspectives. *GeoHazards* 2 (3), 172–195. doi:10.3390/geohazards2030010

Canitano, A. (2020). Observation and theory of strain-infrasound coupling during ground-coupled infrasound generated by Rayleigh waves in the Longitudinal Valley (Taiwan). *Bull. Seismol. Soc. Am.* 110 (6), 2991–3003. doi:10.1785/0120200154

Cebry, S. L., Ke, C. Y., Shreedharan, S., Marone, C., Kammer, D. S., and McLaskey, G. C. (2022). Creep fronts and complexity in laboratory earthquake sequences illuminate delayed earthquake triggering. *Nat. Comm.* 13, 6839. doi:10.1038/s41467-022-34397-0

Chao, K., Peng, Z., Wu, C., Tang, C. C., and Lin, C. H. (2011). Remote triggering of non-volcanic tremor around Taiwan. *Geophys. J. Int.* 188 (1), 301–324. doi:10.1111/j.1365-246x.2011.05261.x

Crescentini, L., Amoruso, A., Fiocco, G., and Visconti, G. (1997). Installation of a high-sensitivity laser strainmeter in a tunnel in central Italy. *Rev. Sci. Instru.* 68, 3206–3210. doi:10.1063/1.1148268

Delorey, A. A., Chao, K., Obara, K., and Johnson, P. A. (2015). Cascading elastic perturbation in Japan due to the 2012 M_w 8.6 Indian Ocean earthquake. *Sci. Adv.* 1, e1500468. doi:10.1126/sciadv.1500468

Duoxing, Y., Qi, L., and Lianzhong, Z. (2015). Propagation of pore pressure diffusion waves in saturated porous media. *J. Appl. Phys.* 117, 134902. doi:10.1063/1.4916805

Feng, K. F., Huang, H. H., Hsu, Y. J., and Wu, Y. M. (2021). Controls on seasonal variations of crustal seismic velocity in Taiwan using single-station cross-component analysis of ambient noise interferometry. *J. Geophys. Res. Solid Earth* 126. doi:10.1029/2021JB022650

Fialko, Y., Khazan, Y., and Simons, M. (2001). Deformation due to a pressurized horizontal circular crack in an elastic half-space, with applications to volcano geodesy. *Geophys. J. Int.* 146, 181–190. doi:10.1046/j.1365-246x.2001.00452.x

Fu, C. C., Lee, L. C., Ouzounov, D., and Jan, J. C. (2020). Earth's outgoing longwave radiation variability prior to M ≥ 6.0 earthquakes in the Taiwan area during 2009-2019. *Front. Earth Sci.* 8, 364. doi:10.3389/feart.2020.00364

Gomberg, J., Bodin, P., Larson, K., and Dragert, H. (2004). Earthquake nucleation by transient deformations caused by the M = 7.9 Denali, Alaska, earthquake. *Nature* 427, 621–624. doi:10.1038/nature02335

Gonzalez-Huizar, H., Velasco, A. A., Peng, Z., and Castro, R. (2012). Remote triggered seismicity caused by the 2011, M9.0 Tohoku-Oki, Japan earthquake. *Geophys. Res. Lett.* 39. doi:10.1029/2012GL051015

Guo, H., Brodsky, E. E., Goebel, T. H. W., and Cladouhos, T. T. (2021). Measuring fault zone and host rock hydraulic properties using tidal responses. *Geophys. Res. Lett.* 48 (13). doi:10.1029/2021GL093986

Hill, D. P. (2008). Dynamic stresses, Coulomb failure, and remote triggering. *Bull. Seismol. Soc. Am.* 98, 66–92. doi:10.1785/0120070049

Hill, D. P., Reasenberg, P. A., Michael, A., Arabaz, W. J., Beroza, G., Brumbaugh, D., et al. (1993). Seismicity remotely triggered by the magnitude 7.3 Landers, California, earthquake. *Science* 260 (5114), 1617–1623. doi:10.1126/science.260.5114.1617

Hsu, Y. J., Chang, Y. S., Liu, C. C., Lee, H. M., Linde, A. T., Sacks, S., et al. (2015). Revisiting borehole strain, typhoons, and slow earthquakes using quantitative estimates of precipitation-induced strain changes. *J. Geophys. Res. Solid Earth* 120 (6), 4556–4571. doi:10.1002/2014jb011807

Huang, F., Jian, C., Tang, Y., Xu, G., Deng, Z., and Chi, G. (2004). Response changes of some wells in the mainland subsurface fluid monitoring network of China, due to the September 21, 1999, Ms7.6 Chi-Chi Earthquake. *Tectonophysics* 390, 217–234. doi:10.1016/j.tecto.2004.03.022

Institute of Earth Sciences, Academia Sinica (1996). *Broadband Array in taiwan for Seismology*. Taiwan: Institute of Earth Sciences, Academia Sinica. Other/Seismic Network. doi:10.7914/SN/TW

Jin, Y., Dyaur, N., and Zheng, Y. (2021). Laboratory evidence of transient pressure surge in a fluid-filled fracture as a potential driver of remote dynamic earthquake triggering. *Seismic Rec.* 1, 66–74. doi:10.1785/0320210015

Johnson, C. W., and Bürgmann, R. (2016). Delayed dynamic triggering: Local seismicity leading up to three remote M ≥ 6 aftershocks of the 11 April 2012 M8.6 Indian Ocean earthquake. *J. Geophys. Res. Solid Earth* 121, 134–151. doi:10.1002/2015JB012243

Johnson, C. W., Bürgmann, R., and Pollitz, F. F. (2015). Rare dynamic triggering of remote $M \geq 5.5$ earthquake from global catalog analysis. *J. Geophys. Res. Solid Earth* 120, 1748–1761. doi:10.1002/2014JB011788

Kanamori, H. (1977). The energy release in great earthquakes. *J. Geophys. Res.* 82, 2981–2987. doi:10.1029/jb082i020p02981

Kurahashi, S., and Irikura, K. (2010). Characterized source model for simulating strong ground motions during the 2008 Wenchuan earthquake. *Bull. Seismol. Soc. Am.* 100, 2450–2475. doi:10.1785/0120090308

Malagnini, L., Lucente, F. P., De Gori, P., Akinci, A., and Munafo, I. (2012). Control of pore fluid pressure diffusion on fault failure mode: Insights from the 2009 L'Aquila seismic sequence. *J. Geophys. Res.* 117, B05302. doi:10.1029/2011JB008911

Miyazawa, M., Brodsky, E. E., and Guo, H. (2021). Dynamic earthquake triggering in southern California in high resolution: Intensity, time decay, and regional variability. *AGU Adv.* 2, e2020AV000309. doi:10.1029/2020av000309

Mouyen, M., Canitano, A., Chao, B. F., Hsu, Y. J., Steer, P., Longuevergne, L., et al. (2017). Typhoon-induced ground deformation. *Geophys. Res. Lett.* 44 (21), 11,004–11,011. doi:10.1002/2017gl075615

Ohnaka, M. (2000). A physical scaling relation between the size of an earthquake and its nucleation zone size. *Pure Appl. Geophys.* 157, 2259–2282. doi:10.1007/pl00001084

O'Malley, R. T., Mondal, D., Goldfinger, C., and Behrenfeld, M. J. (2018). Evidence of systematic triggering at teleseismic distances following large earthquakes. *Sci. Rep.* 8, 11611. doi:10.1038/s41598-018-30019-2

Pankow, K. L., and Kilb, D. (2020). Going beyond rate changes as the sole indicator for dynamic triggering of earthquakes. *Sci. Rep.* 10, 4120. doi:10.1038/s41598-020-60988-2

Parsons, T. (2005). A hypothesis for delayed dynamic earthquake triggering. *Geophys. Res. Lett.* 32, L04302. doi:10.1029/2004gl021811

Parsons, T., Malagnini, L., and Akinci, A. (2017). Nucleation speed limit on remote fluid-induced earthquakes. *Sci. Adv.* 3, e1700660. doi:10.1126/sciadv.1700660

Parsons, T., Segou, M., and Marzocchi, W. (2014). The global aftershock zone. *Tectonophysics* 618, 1–34. doi:10.1016/j.tecto.2014.01.038

Parsons, T., and Velasco, A. A. (2011). Absence of remotely triggered large earthquakes beyond the mainshock region. *Nat. Geosci.* 4, 312–316. doi:10.1038/ngeo1110

Peng, Z., Vidale, J. E., Wech, A. G., Nadeau, R. M., and Creager, K. C. (2009). Remote triggering of tremor along the san andreas fault in central California. *J. Geophys. Res.* 114, B00A06. doi:10.1029/2008JB006049

Peng, Z., Wang, W., Chen, Q. F., and Jiang, T. (2010). Remotely triggered seismicity in north China following the 2008 M_w 7.9 Wenchuan earthquake. *Earth Planets Space* 62, 893–898. doi:10.5047/eps.2009.03.006

Peng, Z., Wu, C., and Aiken, C. (2011). Delayed triggering of microearthquakes by multiple surface waves circling the Earth. *Geophys. Res. Lett.* 38, L04306. doi:10.1029/2010gl046373

Pollitz, F. F., Stein, R. S., Sevilgen, V., and Bürgmann, R. (2012). The 11 April 2012 east Indian Ocean earthquake triggered large aftershocks worldwide. *Nature* 490, 250–253. doi:10.1038/nature11504

Sacks, S., Suyehiro, S., Evertson, D. W., and Yamagishi, Y. (1971). Sacks-Evertson strainmeter, its installation in Japan and some preliminary results concerning strain steps. *Pap. Meteorol. Geophys.* 22, 707–712. doi:10.2183/pjab1945.47.707

Shapiro, N. M., Campillo, M., Kaminski, E., Vilotte, J. P., and Jaupart, C. (2018). Low-frequency earthquakes and pore pressure transients in subduction zones. *Geophys. Res. Lett.* 45. doi:10.1029/2018GL079893

Shelly, D. R., Peng, Z., Hill, D. P., and Aiken, C. (2011). Triggered creep as a possible mechanism for delayed dynamic triggering of tremor and earthquakes. *Nat. Geosci.* 4, 384–388. doi:10.1038/ngeo1141

Sun, W. F., Peng, Z., Lin, C. H., and Chao, K. (2015). Detecting deep tectonic tremor in Taiwan with a dense array. *Bull. Seismol. Soc. Am.* 105 (3), 1349–1358. doi:10.1785/0120140258

van der Elst, N. J., and Brodsky, E. E. (2010). Connecting near-field and far-field earthquake triggering to dynamic strain. *J. Geophys. Res.* 115, B07311. doi:10.1029/2009JB006681

Velasco, A. A., Hernandez, S., Parsons, T., and Pankow, K. (2008). Global ubiquity of dynamic earthquake triggering. *Nat. Geosci.* 1, 375–379. doi:10.1038/ngeo204

Wessel, P., and Smith, W. H. F. (1998). New, improved version of generic mapping tools released. *Eos Trans. AGU* 79, 579. doi:10.1029/98EO00426

Yao, D., Peng, Z., Kaneko, Y., Fry, B., and Meng, X. (2021). Dynamic triggering of earthquakes in the North Island of New Zealand following the 2016 M_w 7.8 Kaikoura earthquake. *Earth Planet. Sci. Lett.* 557, 116723. doi:10.1016/j.epsl.2020.116723

Zheng, Y. (2018). Transient pressure surge in a fluid-filled fracture. *Bull. Seismol. Soc. Am.* 108, 1481–1488. doi:10.1785/0120170230

Zhu, W., Allisson, K. L., Dunham, E. M., and Yang, Y. (2020). Fault valving and pore pressure evolution in simulations of earthquake sequences and aseismic slip. *Nat. Comm.* 11, 4883. doi:10.1038/s41467-020-18598-z

frontiers | Frontiers in Earth Science

TYPE Original Research
PUBLISHED 10 August 2023
DOI 10.3389/feart.2023.1082707

Check for updates

OPEN ACCESS

EDITED BY
Mourad Bezzeghoud,
Universidade de Évora, Portugal

REVIEWED BY
Qingyan Meng,
Chinese Academy of Sciences (CAS), China
Yuan Qi,
Central South University, China

*CORRESPONDENCE
Zhihong Zhang,
568950612@qq.com

RECEIVED 28 October 2022
ACCEPTED 20 April 2023
PUBLISHED 10 August 2023

CITATION
Li M, Zhang Z, Yang S, Kong X and Jiao M (2023), Research on thermal infrared anomaly characteristics of moderate strong earthquakes in northeast China. *Front. Earth Sci.* 11:1082707. doi: 10.3389/feart.2023.1082707

COPYRIGHT
© 2023 Li, Zhang, Yang, Kong and Jiao. This is an open-access article distributed under the terms of the Creative Commons Attribution License (CC BY). The use, distribution or reproduction in other forums is permitted, provided the original author(s) and the copyright owner(s) are credited and that the original publication in this journal is cited, in accordance with accepted academic practice. No use, distribution or reproduction is permitted which does not comply with these terms.

Research on thermal infrared anomaly characteristics of moderate strong earthquakes in northeast China

Mengying Li, Zhihong Zhang*, Shichao Yang, Xiangrui Kong and Mingruo Jiao

Liaoning Earthquake Agency, Shenyang, China

In this article, the daily brightness temperature data from January 2006 to May 2020 of China's geostationary meteorological satellite FY-2E/G were used to identify the brightness temperature differences before deep and shallow earthquakes in the study area using wavelet transform and the relative wavelet power spectrum (RWPS) methods. The objective was to explore the characteristics of thermal infrared (TIR) radiation anomaly changes before deep and shallow earthquakes in Northeast China by carrying out anomaly extraction and data analysis. The research has shown that five significant earthquakes experienced TIR radiation anomalies in the vicinity of the epicenter approximately 1–2 months before the event. The amplitude of the anomaly ranged from seven to twenty times higher than average, and the anomaly lasted about 3 months. The infrared radiation anomaly characteristics before the earthquake were especially significant in the case of two earthquakes in the Songyuan area. From the research, it was concluded that the TIR radiation anomaly could act as a short-term precursor for earthquake prediction. The method employed in this study would provide great support for predicting deep and shallow earthquakes in Northeast China using satellite thermal infrared technology.

KEYWORDS

earthquakes, northeast of China, brightness temperature, thermal infrared anomaly, relative wavelet power spectrum

1 Introduction

An earthquake is a seismic and deformation phenomenon that occurs within the earth's crust. Earthquakes not only cause significant losses to human life and property but also have a profound impact on social and economic development and the human living environment. Therefore, earthquake prediction has become a research topic of significant academic and practical value in seismology. With the continuous development of technology, scientists have discovered a close relationship between earthquake activity and thermal infrared (TIR) phenomena. Due to the influence of various geophysical processes, such as underground geothermal flow and fluid movement, on the radiation energy emitted by surface objects in the thermal infrared band, earthquake activity can create abnormal changes in TIR radiation. By observing and analyzing these anomalies, scientists can predict earthquakes (Zhang et al., 2021; Xu et al., 2020; Li et al., 2019; Wang et al., 2018; Dong et al., 2017).

With the development of satellite remote sensing technology, many scientists and research teams have been committed to studying the geothermal precursor phenomena

TABLE 1 Analysis of corresponding TIR anomalies before five earthquakes in the study area.

Date location magnitude	EQ epicenter location	Magnitude (*Ms*)	Depth of earthquake's hypocenter (km)	Abnormal frequency	Abnormal period	Earthquake occurrence after abnormal disappearance	Abnormal duration (d)	Epicenter margin of the earthquake location
2008-05-19	Hunchun, Jilin	6.2	540	5f	Before peak		56	Internal
2008-06-10	Arong Banner, Inner Mongolia	5.2	0	5f	After peak		47	√
2016-01-02	Linkou County, Heilongjiang	6.4	580	5f		√	79	√
2017-07-23	Songyuan, Jilin	4.9	10	5f	After peak		42	√
2018-05-28	Songyuan, Jilin	5.7	13	5f	Before peak		24	√

before earthquakes and corresponding earthquake predictions. Scientists have studied the relationship between satellite TIR remote sensing information and earthquakes since the 1980s (Qiang et al., 1991; Qiang et al., 1998; Zhang et al., 2002). The early reports of temperature changes prior to earthquakes are from ground observations (Asteriadis and Livieratos, 1989; You, 1990). For example, Qiang et al. (1992) believed that the TIR anomaly was the friction between tectonic plates during an earthquake, which caused the greenhouse gases in the rock body to escape along the fractured fissures; they described the phenomenon as "the earth deflates." The inert gas was ionized by the low-altitude electric field to form infrared light of various bands. In recent years, many experts (Kang et al., 2011; Liu et al., 2007; Guo et al., 2014) carried out research in related fields in China and concluded that there were TIR radiation anomalies before earthquakes. Other researchers found significant TIR radiation anomalies before moderate and strong earthquakes in mainland China in recent years (Dai et al., 2016; Xu and Xu, 2013; Zhang et al., 2013; Xie et al., 2015a). The robust satellite technique (RST) method based on statistics was adopted and applied to the Athens *Ms*5.9 earthquake in 1999. The increase in surface temperature in the adjacent area is considered to be a thermal anomaly related to tectonic activities and earthquakes. Tronin et al. (2002) and Lv et al. (2000) studied some earthquakes and found that thermal anomalies on infrared images were related to linear crustal structures and fault zones. Chen et al. (2004)and Chen et al. (2009) proposed and extracted a base field for the annual variation of surface brightness temperature that provided a reference background for extracting crustal activity information using TIR radiation data.

2 Methods

2.1 Thermal infrared brightness temperature data

Satellite TIR remote sensing instruments can directly observe the thermal radiation intensity of ground objects. After calibration and geometric correction, it is called the radiance of the corresponding channel (band). We applied the blackbody radiation formula of Planck's radiation theorem to calculate the radiation temperature (Zhang et al., 2010). The data are from FY-2 Geostationary Meteorological Satellites, and we used the FY-2C/E/G brightness temperature hourly data product to distinguish the true radiation temperature of the object. This is called the brightness temperature. FY-2C was launched on 19 October 2004, FY-2E was launched on 15 June 2008, and FY-2G, a replacement satellite for FY-2E was launched on 31 December 2014. This data product was available from geostationary satellites before infrared remote sensing. Most of the data were polar orbiting satellite data. However, for seismic research, the comparability of data was weak due to the differences between polar orbiting satellite orbits and transit time, and it was difficult to find thermal anomalies before earthquakes. Today, observation data from the FY-2G satellite are commonly used. The orbit of FY-2G is located at 105°E above the equator, 35,000 km from the ground, with an effective observation range of 45°–165°E and 60°S-60°N. The observation range is approximately one-third of the earth's surface. The satellite resolution of brightness temperature observation is 5 km. The FY-2G satellite began to provide valid data service in June 2015. The position of the satellite to each pixel is fixed, so the propagation path of thermal radiation for each pixel from the land surface to the satellite is also almost fixed. Images of brightness temperature and the relative wavelet power spectrum (RWPS) amplitudes can be directly depicted according to the pixel coordinates without the orbit splicing needed for data from polar orbit satellites. The valid data from January 2006 to 1 January 2019 were used to analyze the possible thermal anomalies before earthquake cases. To avoid the impact of direct solar radiation, five real-time observation data collection instances were selected at midnight every day (the data product time interval was taken once an hour), using Beijing time at the 01:00, 02:00, 03:00, 04:00, and 05:00 data points. These observation data points were used to obtain the daily value data that formed the daily brightness temperature data by the window-filling method (Zhang et al., 2010).

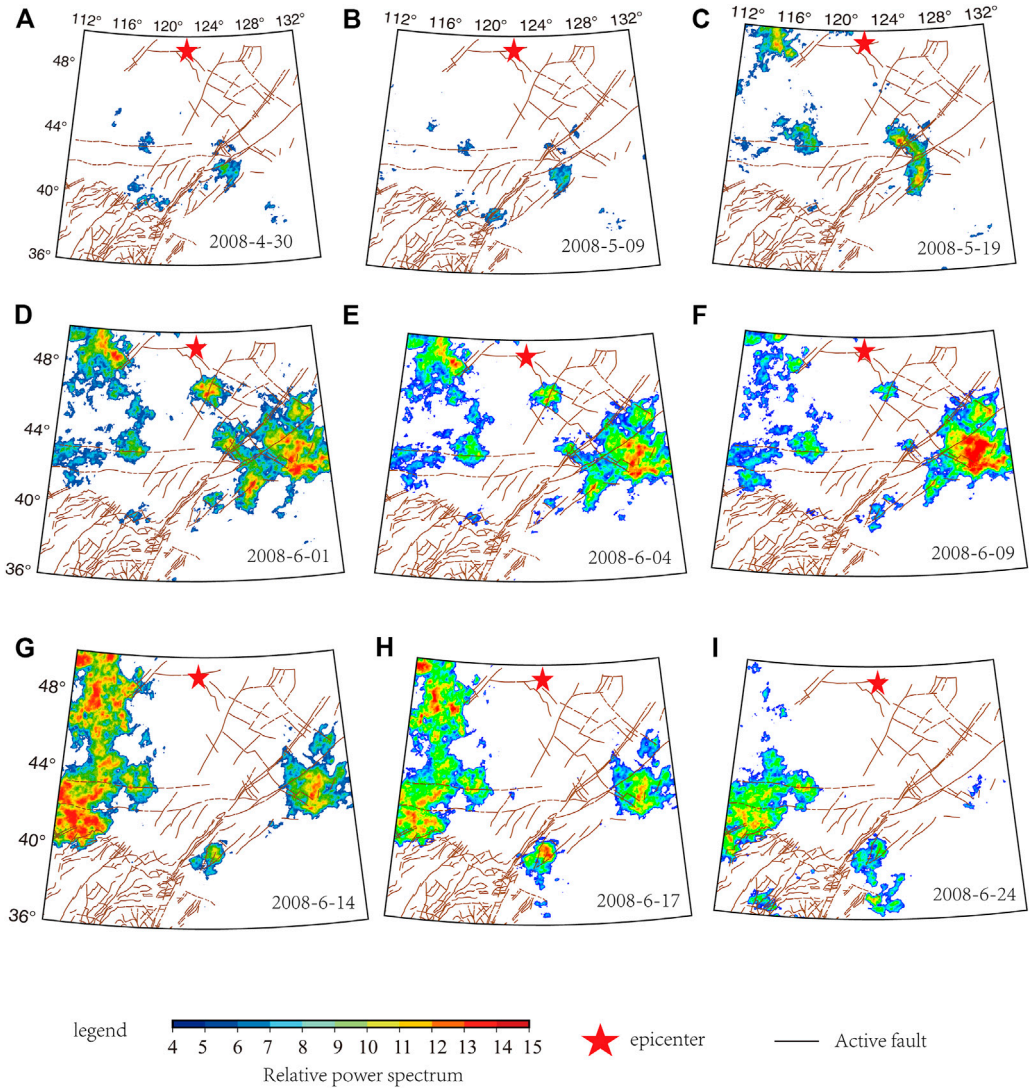

FIGURE 1
Temporal and spatial evolution of the RWPs of the Jilin Hunchun *Ms*6.2 earthquake (red star) on 19 May 2008.

2.2 Wavelet power spectrum technique and data processing

The data processing methods are wavelet transform and RWP estimation. Wavelet transform evolved on the basis of Fourier transform and is an effective method for analyzing unsteady signals. It has been well evolved in the time and frequency domains and has been applied to the fields of geophysics and seismic exploration (Kumar and Foufoula, 1997). The biggest features of wavelet transform technology are self-adaptability and mathematical microscopy. The technology can reconstruct the original signal with almost no loss and focus on any detail of the signal. It is an effective tool for current signal time–frequency analysis. The wavelet transform formula of finite time series is as follows:

$$W_\psi f(a,b) = \frac{1}{\sqrt{a}}\int_{-\infty}^{\infty} f(t)\psi\left(\frac{t-b}{a}\right)\mathrm{d}t. \quad (1)$$

$f(t)$ is the original signal; $W_\psi f(a,b)$ is each frequency band component after wavelet transformation; a is the wavelet scale factor that controls the expansion and contraction of the wavelet function, corresponding to the variable frequency; b is the time shift factor (Torrence and Compo, 1998), which controls the shift of the wavelet function; $\frac{1}{\sqrt{a}}\psi\left(\frac{t-b}{a}\right)$ is a wavelet generating function. The db8 wavelet basis function in the Daubecheies (dbN) wavelet system was used to process the original brightness temperature data by wavelet transform. Power spectrum estimation is divided into classical spectrum estimation and modern spectrum estimation. The classical spectrum estimation mainly has two methods: periodogram and autocorrelation, and the Welch algorithm is improved based on the periodogram method. In this paper, the power spectrum estimation refers to the Welch algorithm. First, the N-length data are divided into L segments, each segment with M points, and then, each data segment is windowed to obtain the Fourier transform, and finally, the average value of each segment of

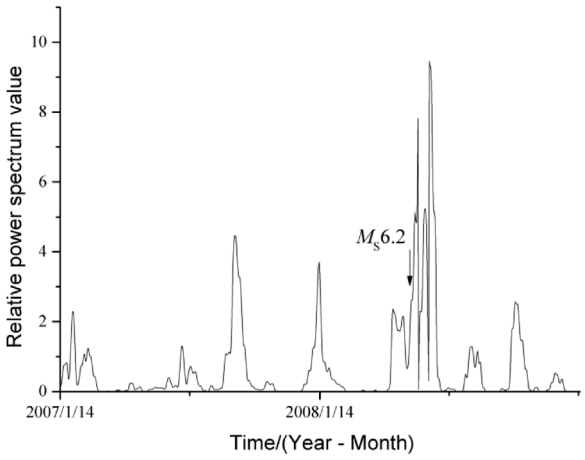

FIGURE 2
Regional mean time sequence diagram of the Hunchun *Ms*6.2 earthquake in Jilin on 19 May 2008.

the power spectrum is calculated (Guo et al., 2010). The calculation formula is as follows:

$$\overline{P_x(w)} = \frac{1}{L}\sum_{i=1}^{L}\frac{1}{MU}\left|\sum_{n=0}^{M-1} x_i(n)w(n)e^{-jwn}\right|^2, i = 1, \cdots L. \quad (2)$$

$U = \frac{1}{M}\sum_{n=0}^{M-1} w^2(n)$ is the normalization factor, $w(n)$ is the window function, and $\overline{P_x(w)}$ is the final calculation result.

By calculating the power spectrum of the aforementioned wavelet transform and the data after removing the influencing factors, considering the mid-short-term earthquakes have a period of occurrence, so taking n = 64 days as the window length and m = 1 day as the sliding window length for Fourier transform, the latest time of the data in the window is considered, and a set of power spectra are obtained by sliding the time history data on each pixel once. Relative amplitude is used to compare the similarities and differences of the power spectra before and after the earthquake. The calculated time and frequency space data are used to scan the whole time and space. The entire frequency band is used to extract and identify the spatiotemporal change characteristics of the abnormal area. The RWP time series value of the region is calculated using a 0.05° × 0.05° unit.

3 Earthquake case analysis and results

In this study, the daily surface brightness temperature data observed by China Geostationary Meteorological Satellite FY-2C/E/G were collected. After spatial correction and calibration, the brightness temperature data in Northeast China (longitude 110°–135°E, latitude 35°–50°N) were selected. A total of 22 earthquakes above magnitude *Ms*4.9 that occurred in the study area since 2006 were analyzed using the RWP analysis method. Among them, five earthquakes showed significant TIR anomalies before their occurrence.

(1) The *Ms*6.2 earthquake occurred in Hunchun, Jilin, on 19 May 2008, with a focal depth of 540 km, which is a deep earthquake. The epicenter of the earthquake is located at the intersection of the Badaogou and Tumenjiang faults, and the focal mechanism solution shows a strike-slip type. Figure 1 shows that the high-value anomaly of the 5th frequency band in the Badaogou fault zone appeared on 30 April, the anomaly area gradually increased on 19 May, the amplitude reached 15, and then, the anomaly area gradually migrated to the southeast. The RWP high value showed a gathering phenomenon, and then, the amplitude and area gradually increased. On 4 June, the high-value areas appeared in a concentrated manner, the amplitude and area reached the maximum and then gradually decreased, and the high-value areas disappeared on 24 June. The abnormality lasted about 56 days.

The *Ms*6.2 earthquake on 19 May was obviously related to the abnormality that had appeared earlier in this position. The change of the abnormality can be summarized as a process of "appearance → enhancement → earthquake → extreme value → attenuation → disappearance." Therefore, it can be inferred that the Huichun *Ms*6.2 earthquake occurred in the range of abnormality on 19 May. The average value in the power spectrum value region of the location was analyzed to visually inspect the changes in the TIR brightness temperature power spectrum before and after the Huichun earthquake in Jilin Province. The relative amplitude time variation sequence showed that from 16 April, the RWP value slowly increased from low to high, then decreased from high to low, and finally increased from low to high, and lasted until 19 May. After the earthquake, the peak value was greatly increased by the abnormality, reaching the maximum value of 9.46 on 16 June (Figure 2). The data difference between each period also reflects the changes before and after the event, showing that the TIR brightness temperature power spectrum has a very significant monitoring value for the earthquake. The aforementioned analysis shows that after the earthquake, the abnormal phenomenon of the TIR brightness temperature power spectrum changed. This phenomenon can accurately reflect the arrival of the earthquake, indicating its value and importance in earthquake monitoring and prediction. Therefore, to more accurately analyze and predict earthquakes, we could make full use of the information on the TIR brightness temperature power spectrum and other related information, effectively coordinate and comprehensively analyze each forecasting means, and then judge the possibility of earthquakes so that it can better cope with natural disasters in the form of earthquakes.

(2) The *Ms*5.2 earthquake occurred in Ayong Banner, Inner Mongolia, on 10 June 2008. It was a deep earthquake. The earthquake was located in the northern section of the Greater Khingan Mountains gradient belt, and the focal mechanism solution showed a right-handed strike-slip type. Figure 3 shows that on 9 May 2008, the 5th frequency band of the main ridge fault of the Great Khingan Mountains showed a high-value anomaly. After 1 June, the anomaly was concentrated in a small area, and its amplitude increased. On 4 June, the anomaly weakened. On 9 June, the anomaly extended southward along the fault of the main ridge of the Great Hinggan Mountains. The anomaly area was concentrated along the fault, and the amplitude of the RWPs reached its maximum. The earthquake occurred on

10.3389/feart.2023.1082707

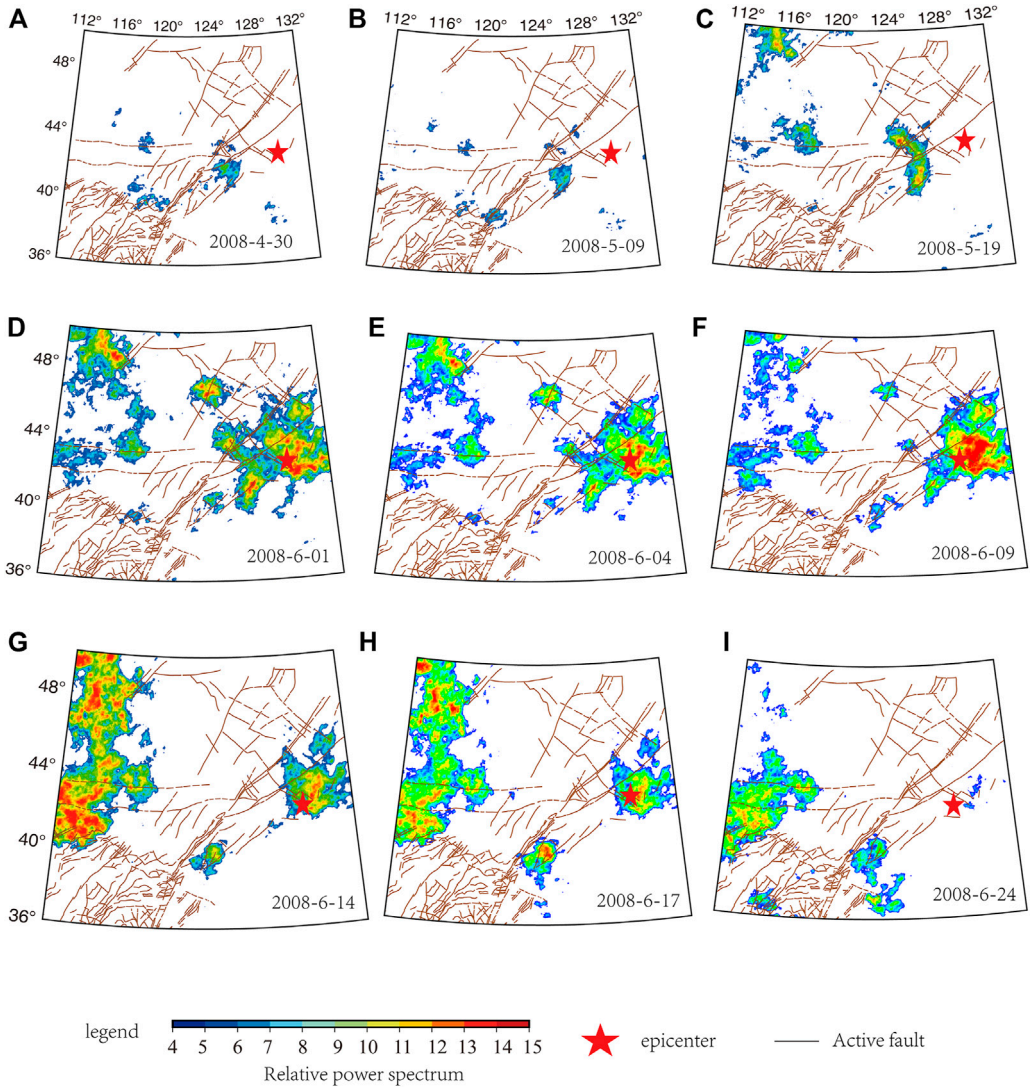

FIGURE 3
Time-space evolution of the RWPs of the *Ms*5.2 earthquake (red star) in Arong Banner, Inner Mongolia, on 10 June 2008.

10 June, with the epicenter at the edge of the anomaly area. On 24 June, the anomaly disappeared and gradually recovered to the normal background value. The time-series curve of RWPs in the high anomaly area is shown in Figure 4. The RWPs gradually "increased → decreased → increased → decreased" on 14 April before the earthquake and reached the peak value of 9.19 on 13 June. Then, after reaching the peak on 10 June, an *Ms*5.2 earthquake occurred. It indicates the obvious changes in the RWPs in the months prior to the earthquake, giving an effective clue for the prediction of the earthquake. Additionally, the changes in the range and value of the fault anomaly area of the main ridge of the Great Khingan before and after the earthquake were noted.

Understanding the genesis of mountain geology can help researchers understand the structural characteristics of the earthquake and better explain the prediction results.

(3) The *Ms*6.4 earthquake that occurred in Linkou County, Heilongjiang Province, on 2 January 2016 had a focal depth of 580 km, making it a deep earthquake. Calculating and scanning the TIR data before the earthquake, Figure 5 shows that the 5th frequency band presented a significantly abnormally high TIR value. The anomaly occurred at the Kubin River fault on 16 October 2015. On 23 October, the amplitude of the RWPs increased in the anomaly area, and then, the anomaly extended southward along the Kubin River fault. The abnormal area and amplitude continued to increase. On 25 October, the abnormal amplitude reached the maximum and then gradually declined until 31 October 2015, when the anomaly disappeared. The duration of the anomaly was 16 days. Sixty-four days later, the *Ms*6.4 earthquake occurred in Linkou County, Heilongjiang Province, with the epicenter at the edge of the abnormal area, near the Muling River segment crack. The time-series curve of RWPs in the high-anomaly area

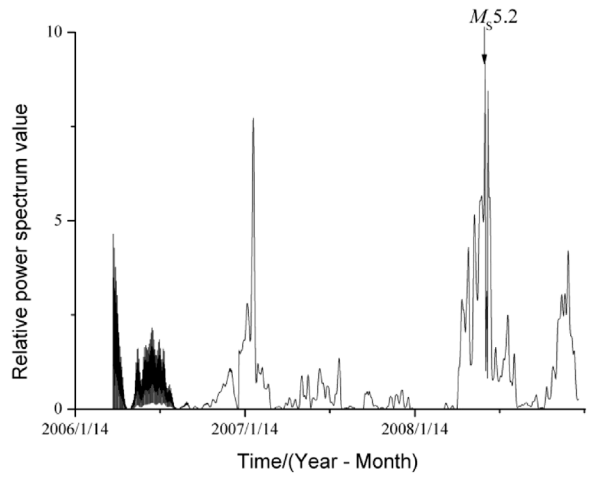

FIGURE 4
Historical time sequence diagram of the regional mean value of the high brightness temperature anomaly of the *Ms*5.2 earthquake in Arong Banner, Inner Mongolia, on 10 June 2008.

is shown in Figure 6. The results showed that there had been four periods of high RWPs in the high-anomaly area since 2011. The high value began to appear at the end of August 2015, before the earthquake, and the RWPs gradually increased → decreased → increased → decreased and reached a peak of 6.21 on 5 June. There was a significant thermal anomaly in the early stage of the *Ms*6.4 earthquake in Linkou County, and it is worth studying the TIR data before the earthquake and the thermal anomaly mechanism during the deep earthquake.

3.1 Geological profile of the Songyuan area and typical cases of Songyuan earthquakes

The Songyuan area is located in the central and western parts of Jilin Province. It is located in the central depression belt and southeast uplift belt in the southern part of the Songliao Fault Basin. The Songliao Basin is the largest Mesozoic and Cenozoic continental sedimentary basin in Northeast China. The direction of the basin basement structure and the neotectonic line is NNE. During the Cenozoic, the internal faults in the basin were still active. The main faults are the second Songhuajiang fault in the northwest direction and the Fuyu–Zhaodong, Yilian–Yitong, and Mishan–Duhua faults in the northeast direction (Figure 7). Those faults are Quaternary active faults. These faults and their intersections are the structural conditions for the occurrence of shallow-source moderate earthquakes in the Songyuan area. The *Ms*4.9 earthquake in 2017, the *Ms*5.7 earthquake in 2018, and the *Ms*5.1 earthquake in 2019 occurred successively in the Songyuan area in recent years. However, before the Songyuan *Ms*5.1 earthquake in 2019, there was no obvious thermal anomaly, suggesting that the greatest amount of greenhouse gases were released in the basin before and after the previous two earthquakes. Based on the aforementioned studies, the TIR of the previous two earthquakes in this area can be researched and analyzed.

3.2 The thermal RWP anomalies associated with the Songyuan *Ms*4.9 and *Ms*5.7 earthquakes

An *Ms*4.9 earthquake occurred in Songyuan on 23 July 2017, with a focal depth of 12 km and an epicenter located at 45.3°N, 124.81°E. Scanning the aforementioned area, we found that the RWPs of the 5-band wavelet (Figure 8) gradually increased before the earthquake after 1 June 2017, and the high-value areas expanded on 20 June. The anomalies of amplitude and area reached a maximum on 5 July, and then gradually attenuated. The earthquake occurred on 23 July, until the high value disappeared on 27 July, and the abnormality lasted for more than a month. Analyzing the temporal and spatial evolution of the TIR anomaly, we found that the RWPs of the TIR brightness temperature data were significantly abnormal, and the abnormal change lasted for some time before and after the earthquake. The TIR anomaly was relatively large, and the shape was more prominent before the earthquake. The whole anomaly evolution followed this process: normal background → anomaly appearance → anomaly enhancement → reaching maximum → anomaly attenuation → earthquake → anomaly disappearance. From Figure 8, it can be clearly seen that the infrared radiation presented little change in the initial stage and slowly increased in the elastic stage. The plastic anomaly gradually returned to the normal background value from the maximum value. The Songyuan *Ms*4.9 earthquake occurred on 23 July, at the edge of the abnormal area on the 18th day after the peak.

In the same area, an *Ms*5.7 earthquake occurred in Songyuan Jilin Province on 28 May 2018. The calculation results showed that 1 week before the earthquake, the RWPs had an abnormal phenomenon around the Jilin-Fengman fault that exceeded the background value. When the time of earthquake occurrence approaches, anomalies expanded along the second Songhuajiang fault in the NW direction, and the anomalies' amplitude gradually increased. After the earthquake occurred, the amplitude and area of the anomaly gradually increased, and in the following month, the anomaly gradually weakened.

The spatiotemporal evolution images of the RWPs in six frequency bands were checked. The 5th frequency band showed significant TIR anomalies before the Songyuan *Ms*5.7 earthquake (Figure 9). Figure 9 shows that in mid-May 2018, the brightness temperature anomalies first appeared in the Jilin–Fengman fault zone. The initial anomaly amplitude was weak, and the anomaly area was small at the beginning. Then, the anomaly area extended along the Tanlu fault zone. The anomaly area gradually enlarged on 27 May. The Songyuan *Ms*5.7 earthquake occurred at a distance of approximately 200 km from the anomaly area on 28 May. After the earthquake, the anomaly area further expanded. The anomaly area and amplitude reached a maximum peak in the area on 12 June and then gradually shrank. The anomaly disappeared on 17 June.

3.3 Time variation characteristics of the average brightness temperature power spectrum in the Songyuan *Ms*4.9 and *Ms*5.7 earthquakes

After the two Songyuan earthquakes occurred in the same abnormally high brightness temperature area, the historical time

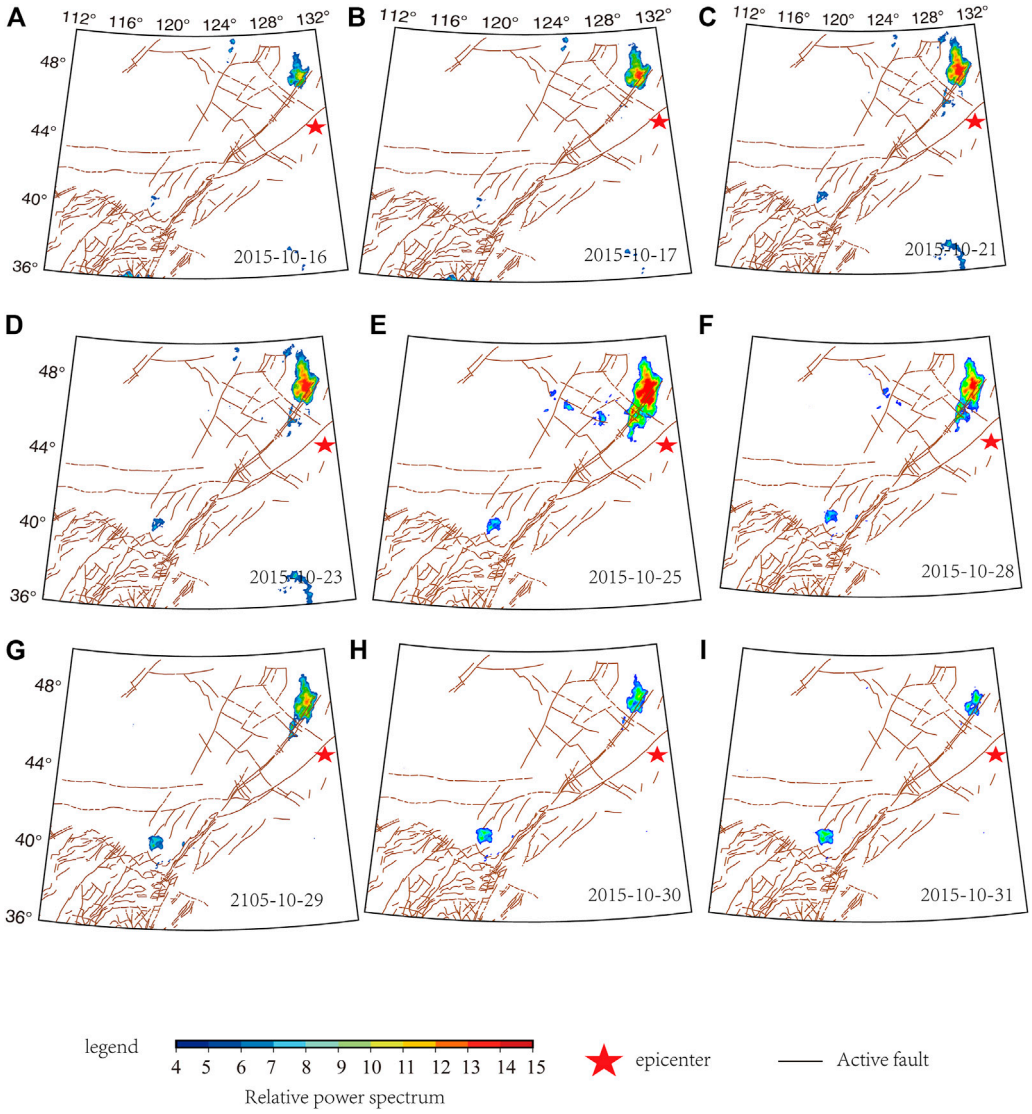

FIGURE 5
Time-space evolution of the RWPs of the Linkou *Ms*6.4 earthquake (red star) in Heilongjiang on 2 January 2016.

sequence diagram of the regional mean value of the high brightness temperature abnormal area was extracted to present the abnormal amplitude more clearly. It can reflect the duration of the anomaly and the relative rate of change. Therefore, the mean value of the RWPs was extracted in the 0.5° × 0.5° range of the significantly abnormal area. The background value and standard deviation of the power spectrum were calculated to form a time-series curve.

In order to analyze the change process of the TIR brightness temperature power spectrum before and after the Songyuan *Ms*4.9 and *Ms*5.7 earthquakes, the average value of the high-value area of the power spectrum was studied. The time sequence of the relative amplitude changes can be seen in Figure 10. Since 2012, the relative amplitude of the average power spectrum of the study area brightness temperature has been higher than six times the mean value (normal background value) five times from 2013 to 2018. For the Songyuan *Ms*4.9 earthquake, the average RWP amplitude of brightness temperature was higher in the significantly abnormal region only from June to July 2017. The RWP amplitude was greater than 4 from 19 June, and the abnormality continued for 32 days. On 21 July, the RWP amplitude dropped to 1.62, and the amplitude was 0.63 on the day of the earthquake on 23 July. After the earthquake, the amplitude returned to the normal background level.

Similarly, the relative amplitude was 4.04 on 26 May 2018 for the Songyuan *Ms*4.9 earthquake, and the relative amplitude reached 6.13 on 27 May. The relative amplitude was 8.22 on 28 May when the earthquake occurred. After the earthquake, the relative amplitude continued to increase. It reached a peak of 12.36 on 12 June, and then, the relative amplitude declined until it returned to 6.01 on 27 June. The Songyuan earthquake occurred in the continuously strengthening stage. There was an obvious anomaly around the Jilin–Fengman fault zone on 25 May 2018. Closer to the time of the earthquake, the anomaly area extended to the epicentral area. The entire anomaly process lasted only 3 days before the

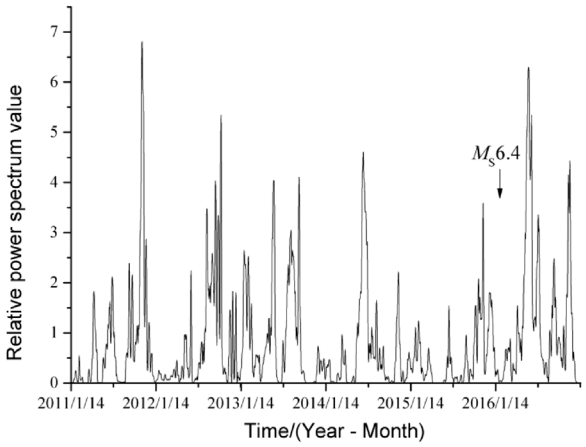

FIGURE 6
Historical time sequence diagram of the regional mean value of the high brightness temperature anomaly in the Linkou *Ms* 6.4 earthquake on 2 January 2016.

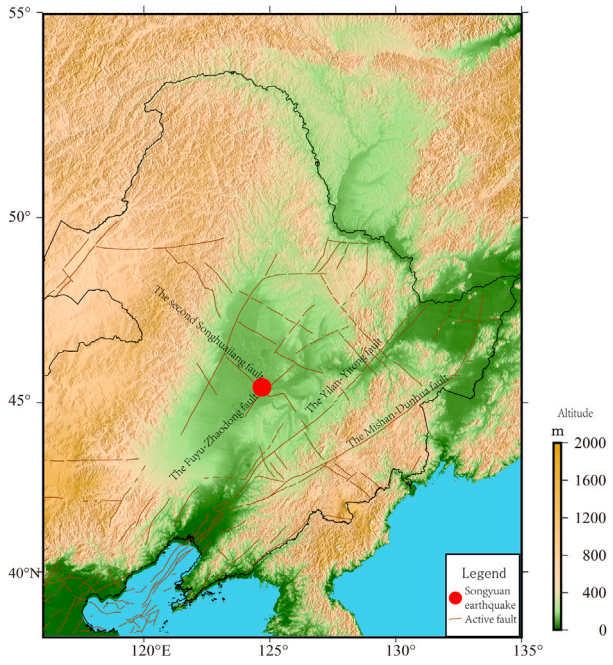

FIGURE 7
Geological structure map of the Songyuan area. The epicenters of the three Songyuan earthquakes (red circles, *Ms*4.9 earthquake in 2017, *Ms*5.7 earthquake in 2018, and *Ms*5.1 earthquake in 2019) and the main active faults in the study area. The black circle represents the Jilin Songyuan Oil and Gas field.

earthquake, but the increased abnormal area and amplitude continued for 1 month, after the earthquake when the abnormality recovered. Based on the previous earthquake example results and experience, the occurrence of two Songyuan earthquakes at different stages of amplitude may be related to the rate of stress accumulation in the epicenter areas.

The overall characteristics of the thermal anomalies of 22 earthquakes with a magnitude above *Ms*4.9 were summarized (Table 1). The spatio-temporal characteristics of thermal anomalies have certain indicative significance, including 1) more than 18% of the examples showed thermal anomalies before and after the earthquake with a missed detection rate of 82% and a total of 38 anomalies since 2006 with a false detection rate of 84%; 2) there are obvious periodicity and amplitude patterns of thermal anomalies before and after earthquakes; 3) there is no corresponding relationship between the size of the thermal anomaly area and the intensity of the earthquake; 4) there is no significant difference between shallow and deep earthquakes in terms of thermal anomalies. In terms of spatial evolution, the probability of earthquake occurrence is higher at the edge of the thermal anomaly area, and the epicenter is often located in the transition zone between the appearance and disappearance of the anomaly. In terms of time series, the duration of earthquake thermal anomalies is between approximately 1 month and half a year. Most earthquakes occurred during the high-value rise or fall stage (turning point signal). The advantages of TIR research for site prediction include fast information acquisition and spatiotemporal dynamic monitoring. Large-scale thermal infrared anomaly scanning can be conducted in the Northeast region, and local areas with high RWP values can be selected for planar scanning.

3.4 The relationship between the basin and seismic thermal radiation

Guo et al. (2010) studied the TIR anomalies in the northwestern edge of the Tarim Basin before the Jiashi-Bachu *Ms*6.8 earthquake in 2003. Xie et al. (2015b) studied the Yutian, Xinjiang *Ms*7.3 earthquake in 2014 and found that anomalies began to appear in the western segment of the western marginal fault zone in the Tarim Basin, and then, the anomaly area further expanded and migrated to the fault zone, eventually formed an abnormal banding area along the fault zone around the Tarim Basin. Zhang et al. (2010) studied the characteristics of the TIR anomalies surrounding the Milin *Ms*6.9 earthquake in Tibet in 2017 and found that this phenomenon was more consistent with the distribution of geothermal resources. Previous studies by experts and scholars have shown that the satellite TIR anomalies before earthquakes are related to the basins rich in geothermal resources. This is a positive answer to the seismic TIR genesis. Therefore, Qiang et al. (2010) proposed the seismic basin effect that clearly supported the earth deflation theory.

The latest theory on the TIR anomaly characteristics of medium-to-strong earthquakes suggests that short-term horizontal strain and vibration within the tectonic fault zone prior to earthquakes can result in the rupture and fragmentation of underground rocks, leading to the release of a large amount of energy and causing changes in surface temperature (Zhang L. F. et al., 2020; Li et al., 2020; Han et al., 2018; Chen et al., 2019; Qin et al., 2019). Furthermore, tectonic activity can cause an increase in the amount of subterranean gas emitted, and the gas can surface and cause an increase in surface temperature, leading to TIR anomalies. Prior to an earthquake, the stresses at the fault zone intensify, and as the stress increases, underground rocks fracture and break, releasing heat and causing changes in surface

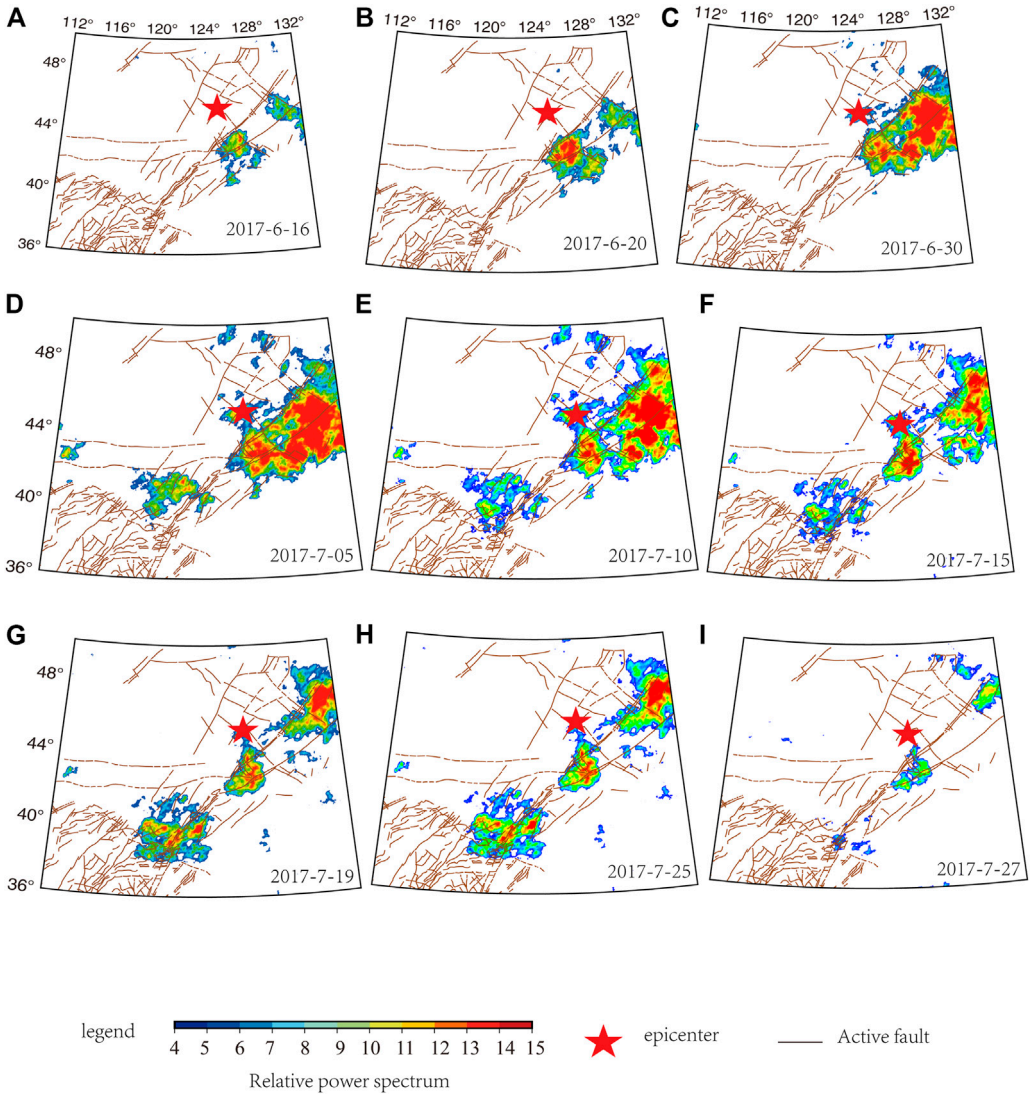

FIGURE 8
Time-space evolution of the 5th frequency band RWP anomalies before the Songyuan *Ms*4.9 earthquake (red star) on 23 July 2017.

temperature. Additionally, as tectonic activity intensifies, the amount of subterranean gas released will also increase, and these gases will spread through the surface, causing thermal infrared anomalies (Zhao et al., 2021; He et al., 2020; Zhou et al., 2019; Xu et al., 2019; Fang et al., 2017). Throughout the entire process of earthquake precursors, the characteristics of TIR anomalies are displayed as a process of "abnormal occurrence → strengthening → peak → weakening → abnormal disappearance → earthquake occurrence." The physical parameters of rocks, such as thermal conductivity, heat capacity, and coefficient of thermal expansion, may also affect the characteristics of TIR anomalies prior to earthquakes. In summary, the TIR anomaly characteristics of medium-to-strong earthquakes are a prognostic manifestation prior to an earthquake, and monitoring and analyzing them can provide valuable information for earthquake prediction. However, it should be noted that TIR anomalies may also be influenced by other factors, such as meteorological factors. Therefore, it is necessary to carefully analyze the possibility of various factors affecting TIR anomalies when monitoring and identifying them to enhance the accuracy and reliability of monitoring.

The Songliao Basin is rich in oil and gas, and the faults around the basin are highly developed. The enhancement of stress is conducive to the acceleration of the gas with relatively high underground temperature along the existing or new fractures, and that gas causes the surface temperature to change. It may be that these factors caused the thermal anomalies distributed along the better-developed Jilin–Fengman fault zone before the Songyuan earthquake. In order to illustrate the possibility of the seismic basin effect, the two earthquakes that occurred in the periphery of the Songliao Basin were analyzed in 2017 and 2018.

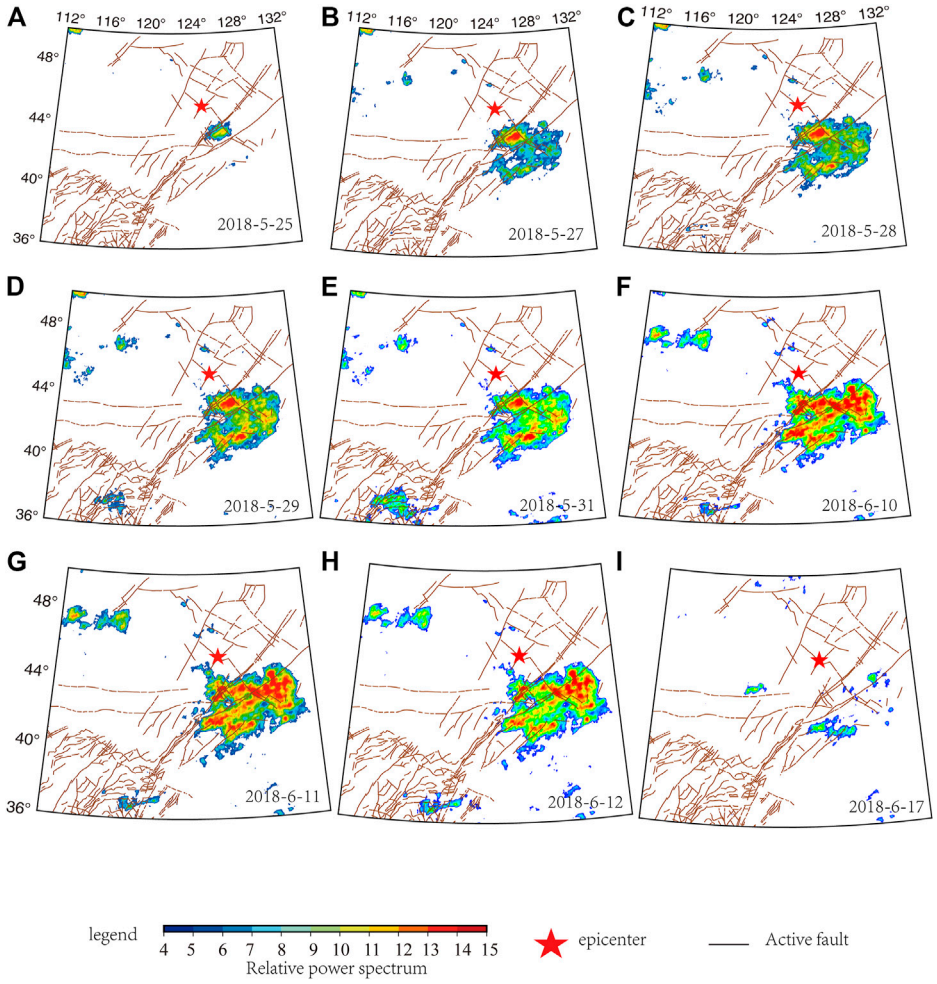

FIGURE 9
Time-space evolution of the 5th frequency band RWP anomalies before the Songyuan *M*s5.7 earthquake (red star) on 28 June 2018.

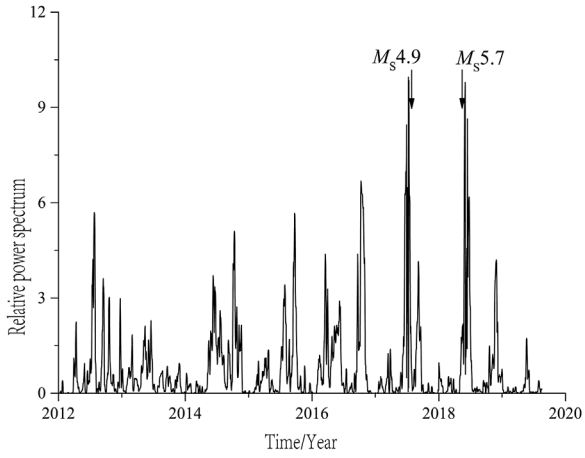

FIGURE 10
Time sequence diagram of regional historical mean value of abnormal high brightness temperature of the two earthquakes in Songyuan, Jilin. (1) Time series curve of mean RWPS in *M*s5.7 Songyuan seismic anomaly area. (2) Time series curve of mean RWPS in *M*s4.9 Songyuan seismic anomaly area.

4 Discussion and conclusion

Before an earthquake, the abnormal temperature increase phenomenon in the epicenter and adjacent areas has been confirmed by many observation results. At the same time, many experts have also found that long-term continuous temperature field changes reflect the activities of faults and large-scale linear structures in the crust (Qu et al., 2006; Ma et al., 2006; Chen et al., 2006; Qiang et al., 2009; Carreno et al., 2001). When the stress approaches the critical state of rock rupture, the number of cracks penetrating the surface increases, and the crustal gas overflows prior to the earthquake. Because of the increase in cracks, the heat convection between the underground rock layer and the surface is strengthened. It may be a combination of these factors that concentrate the TIR anomaly regions before the earthquake near the epicenter and adjacent areas and distribute them along the faults (Qiang et al., 1991; Qiang et al., 1992; Tronin, 1996; Tronin, 2000). Many researchers who have examined these phenomena have pointed out that areas with geothermal and oil and gas enrichment are more prone to thermal anomalies before an earthquake.

This study applied the brightness temperature data of the China Geostationary Meteorological Satellite FY-2C/E/G collected between January 2006 and May 2019 with an effective observation range of 35°–50°N and 110°–135°E. The study used the wavelet transform and RWP methods to analyze and study the brightness temperature data. Based on the analysis of thermal anomalies before and after the two Songyuan earthquakes, the following characteristics are summarized: 1) The RWPs of the brightness temperature data on the two earthquakes were significantly abnormal, and the abnormal initial amplitude and area were small. The anomaly first appeared at the intersection of the Yilan–Yitong and the Mishan–Dunhua faults, and then, the anomaly area gradually expanded, and the overall abnormality showed an increasing trend that was consistent with the distribution of the northern part of the Tanlu fault zone and finally formed an abnormal area distributed in a band. When the abnormal area reached the maximum peak value, it gradually shrank until it disappeared. The abnormal shape was persistent in the time domain and roughly experienced two stages of initial warming and enhanced warming, with a duration of more than 30 days. The abnormal area moved and expanded along the direction of the fault and increased rapidly. The epicenter did not appear in the largest anomaly area but was distributed on the edge of the basin, which might be related to the geological structure and underground environment near the epicenter. 2) The characteristic power spectrum amplitude of the abnormal area was up to 12 times higher than the average value. The abnormal peak value occurred before the earthquake; the earthquake occurred after the abnormal high value decreased. This is the time period when earthquakes are more likely to occur in most earthquake cases. The evolution direction and abnormal peak value characteristics could provide some clues for determining the occurrence time of future earthquakes and tracking the epicenter location.

Therefore, through the analysis of earthquake cases, the overall characteristics of thermal anomalies obtained from the aforementioned earthquakes are summarized. The spatial and temporal characteristics of thermal anomalies are more indicative, showing that there are obvious periods and amplitudes of thermal anomalies before and after earthquakes. There is no correlation between the area of thermal anomaly and its intensity. There is no significant difference between shallow and deep source earthquakes in terms of thermal anomalies. From the spatial evolution characteristics, the seismic probability of the edge of the thermal anomaly area is high. The epicenter is mostly located in the transitional zone between abnormal appearance and disappearance. From the perspective of time series, the duration of seismic thermal anomaly is approximately 1 month to half a year, and the situation is not the same in different regions. Most earthquakes occur in the stage of high-value rising or falling (turning signal).

In a word, TIR precursor anomalies are obviously related to the incubation, occurrence, and development of earthquakes, as well as to the time and location of earthquakes in this area. The abnormal morphological characteristics, evolution processes, and time series curves are all highly representative. We need to continuously improve data processing methods and enhance the accuracy of earthquake predictions in order to achieve greater effectiveness in earthquake prevention and disaster reduction.

Data availability statement

The datasets presented in this study can be found in online repositories. The names of the repository/repositories and accession number(s) can be found at: http://satellite.nsmc.org.cn/portalsite/default.aspx.

Author contributions

ML analyzed these earthquake cases and wrote the manuscript. ZZ is the corresponding author of this article and was responsible for the operation of the processing program and image editing. XK and SY created figures and illustrations. MJ provides guidance on the overall thinking of article writing and the methods and theories used in the article. All authors performed the research, analyzed the results, and approved the manuscript. All authors contributed to the article and approved the submitted version.

Funding

This work was supported by the Science and Technology Project of Liaoning Earthquake Administration (grant number 2022035 and 202218), the China Earthquake Administration Earthquake Tracking Program (grant number 2023010407 and 2023010102), the Special Fund of the Institute of Geophysics, China Earthquake Administration (grant number DQJB21B34), the Special Fund of the National Institute of Natural Hazards, Ministry of Emergency Management of China (grant number ZD2019-16) and Open Fund for Earthquake Forecasting (XM15200700120230188).

Acknowledgments

Part of the geostationary satellite data in this study was provided by the National Satellite Meteorological Center of the China Meteorological Administration, and Yuansheng Zhang, a researcher from the Earthquake Administration of Gansu Province, provided the thermal infrared data analysis and calculation software. The authors would like to express their heartfelt gratitude.

Conflict of interest

The authors declare that the research was conducted in the absence of any commercial or financial relationships that could be construed as a potential conflict of interest.

Publisher's note

All claims expressed in this article are solely those of the authors and do not necessarily represent those of their affiliated organizations, or those of the publisher, the editors, and the reviewers. Any product that may be evaluated in this article, or claim that may be made by its manufacturer, is not guaranteed or endorsed by the publisher.

References

Asteriadis, G., and Livieratos, E. (1989). Pre-seismic responses of underground water level and temperature concerning a 4.8 magnitude earthquake in Greece on october 20, 1988. *Tectonophysics* l70, 165–169. doi:10.1016/0040-1951(89)90111-x

Carreno, E., Capote, R., Yague, A., Tordesillas, J. M., Lopez, M. M., Ardizone, J., et al. (2001). *Observations of thermal anomaly associated to seismic activity from remote sensing*. Portuga1: Genera1 Assembly of European Seismology Commission, 265–269.

Chen, S. Y., Liu, P. X., Liu, L. Q., Ma, J., and Chen, G. Q. (2006). Wavelet analysis of thermal infrared radiation of land surface and its implication in the study of current tectonic activities. *J. Chin. J. Geophys.* 49 (3), 717–723. doi:10.1002/cjg2.886

Chen, S. Y., Ma, J., Liu, P. X., and Liu, L. Q. (2009). A study on the normal annual variation field of land surface temperature in China. *J. Chin. J. Geophys.* 52 (9), 962–971. doi:10.1002/cjg2.1421

Chen, S. Y., Ma, J., Liu, P. X., Liu, L. Q., and Chen, G. Q. (2004). Normal annual variation field of land surface brightness temperature in China. *J. Seismol. Geol.* 26 (3), 528–538.

Chen, X., Li, J., and Guo, N. (2019). Characteristic analysis of satellite thermal infrared anomalies before the Wenchuan Ms8.0 earthquake. *Chin. J. Geophys.* 62 (12), 4900–4911.

Dai, Y., Gao, L. X., Yang, Y. M., Wan, J. Z., Deng, L. L., Zhou, Z. Y., et al. (2016). Chikusetsusaponin V attenuates lipopolysaccharide-induced liver injury in mice. *J. Earthq.* 36 (2), 167–174. doi:10.3109/08923973.2016.1153109

Dong, X. D., Zhu, Z. P., Xu, W., Li, L., and Zhang, H. P. (2017). Thermal infrared remote sensing for earthquake prediction: A case study in south-west China. *J. Geophys. Eng.* 14 (3), 513–523.

Fang, H., Wang, J. P., Huang, X., Zhang, X. L., and Liu, Q. (2017). Statistical analysis of the thermal anomalies detected by satellite sensors before the 2013 Lushan Ms7.0 earthquake in China. *Seismol. Res. Lett.* 88 (1), 197–203.

Guo, X., Zhang, Y. S., Wei, C. X., Zhong, M. J., and Zhang, X. (2014). Medium wave infrared brightness anomalies of wenchuan 8.0 and zhongba 6.8 earthquakes. *J. Acta Geosci. Sin.* 35 (3), 338–344.

Guo, X., Zhang, Y. S., and Zhong, M. J. (2010). Variation characteristics of OLR for the wenchuan earthquake. *J. Chin. J. Geophys.* 53 (11), 2688–2695.

Han, Z., Chen, Y., Zhang, X., Liang, J., Ruthel, G., Berry, C. T., et al. (2018). Host protein BAG3 is a negative regulator of lassa VLP egress. *J. Geophys. Eng.* 15 (1), 64–73. doi:10.3390/diseases6030064

He, Q., Chen, J., Wang, J., Peng, W., and Zhang, P. (2020). Integrated application of multi-source remote sensing data for monitoring pre-earthquake thermal anomalies: A case study of the 2019 M6.0 changning earthquake. *Remote Sens.* 12 (12), 1931.

Kang, C. L., Liu, D. F., Jing, F., Xiong, P., and Cao, Z. Q. (2011). Study on the indication of infrared radiation prior to impending strong earthquakes. *J. Prog. Geophys.* 26 (6), 1897–1905.

Kumar, P., and Foufoula, E. J. (1997). Wavelet analysis for geophysical applications. *J. Rev. Geophy.* 35, 385–412. doi:10.1029/97rg00427

Li, T., Jin, S., Li, X., Zhou, M., and Xiong, C. Y. (2019). Stability analysis of sample data systems with input missing: A hybrid control approach. *J. Earth Sci.* 30 (1), 116–122. doi:10.1016/j.isatra.2019.01.009

Li, Y., Li, W., Shi, Z., Wang, H., and Yang, C. (2020). Investigation of thermal infrared anomaly associated with the Jiuzhaigou Ms7.0 earthquake, China. *Nat. Hazards* 103 (2), 2047–2056.

Liu, S. J., Wu, L. X., Li, J. P., Dong, Y. Q., and Ma, B. D. (2007). Features and mechanisms of the satellite thermal infrared anomaly before hengchun earthquake in taiwan region. *J. Sci. Technol. Rev.* 25 (6), 32–37.

Lv, Q. Q., Ding, J. H., and Cui, C. Y. (2000). Possible satellite thermal infrared anomalies before the Zhangbei M6.2 earthquake on January 10, 1998. *J.Acta Seismol. Sin.* 22 (2), 183–188+219.

Ma, J., Chen, S. Y., Liu, P. X., Wang, Y. P., and Liu, L. Q. (2006). Temporal-spatial variations of associated faulting inferred from satellite infrared information: A case study of the N-S seismo-tectonic zone in China. *J. Chin. J. Geophys.* 49 (3), 707–716. doi:10.1002/cjg2.885

Qiang, Z. J., Kong, L. C., and Wang, G. (1992). Earth gas emis-Sion,Infrared thermo-anomaly and seismicity. *J. Chin. Sci. Bull.* 37 (24), 2259–2262. doi:10.1360/csb1992-37-24-2259

Qiang, Z. J., Lin, C. G., and Li, L. Z. (1998). Brightness temperature anomalies of satellite thermal infrared image: Short-term and impending earthquakes. *J. Sci. China(Series D)* 28 (6), 564–573.

Qiang, Z. J., Ma, G. N., Zeng, Z. X., and Wang, J. (2010). A study of the method of satellite thermal infrared earthquake prediction in imminence. *J. Earth Sci. Front.* (5), 254–262.

Qiang, Z. J., Xu, X. D., and Lin, C. G. (1991). Thermal infrared anomaly precursor of impending earthquake. *J. Sci. Bull. Engl. Version.* 1991 (4), 319–323.

Qiang, Z. J., Yao, Q. L., Wei, L. J., Zeng, Z. X., and Guo, J. F. (2009). The characteristic of current stress hot field by satellite thermal infrared image in China. *J. Acta Geosci. Sin.*, 873–884.

Qin, Y., Zhang, B., and Zhang, L. (2019). Analysis of thermal infrared anomaly characteristics before the Yutian Ms6.3 earthquake on August 8, 2019, Xinjiang, China. *J. Earth Sci.* 30 (6), 1242–1247.

Qu, C. Y., Shan, X. J., and Ma, J. (2006). Formation cause of thermal infrared high temperature belt along honghe fault and its relation to earthquake. *J. Acta Seismol. Sin.* 28 (1), 91–97.

Torrence, C., and Compo, G. P. (1998). A practical guide to wavelet analysis. *J. Bull. Amer. Meteorol. Soc.* 79 (6), 61–78. doi:10.1175/1520-0477(1998)079<0061:apgtwa>2.0.co;2

Tronin, A. A., Hayakawa, M., and Molchanov, O. A. (2002). Thermal IR satellite data application for earthquake research in Japan and China. *J. Geodyn.* 33, 519–534. doi:10.1016/s0264-3707(02)00013-3

Tronin, A. A. (1996). Satellite thermal survey—A new tool for the study of seismoactive regions. *Int. J. Remote Sens.* 17, 1439–1455. doi:10.1080/01431169608948716

Tronin, A. A. (2000). Thermal IR satellite sensor data application for earthquake research in China. *Int. J. Remote Sens.* 21, 3169–3177. doi:10.1080/01431160050145054

Wang, J. P., Zhang, Y. J., Feng, X., Wu, Y., and Wang, Q. Y. (2018). Identification of thermal infrared anomalies before earthquakes based on fuzzy clustering algorithm. *Remote Sens. Lett.* 9 (10), 966–975.

Xie, T., Zheng, X. D., Kang, C. L., Lu, J., and Ma, W. Y. (2015b). Possible thermal brightness temperature anomalies associated with the yutian, Xinjiang MS7.3 earthquake on february 12,2014. *J. Earthq. Res. China* 31 (1), 101–109.

Xie, T., Zheng, X. D., Kang, C. L., Ma, W. Y., and Lu, J. (2015a). Possible thermal brightness temperature anomalies association with the lushan(China) M7.0 earthquake on 20 April 2013. *J. Seismol. Geol.* 37 (1), 149–161.

Xu, X. D., and Xu, B. H. (2013). The infrared warming abnormality analysis of Lushan earthquake. *J. Earth Sci. Front.* 2013 (3), 25–28.

Xu, X., Ruan, X. D., Huang, Y., Ge, X. J., and Zhang, X. L. (2020). Mining thermal anomaly data of active faults from satellite hybrid observations for earthquake prediction. *IEEE Trans. Geoscience Remote Sens.* 58 (2), 963–977.

Xu, X., Ruan, X. D., Huang, Y., Li, L., and Li, L. (2019). Analysis of thermal infrared anomaly characteristics of active faults and fractures on Earth's surface by a new remote sensing model. *IEEE Access* 7, 121491–121500.

You, C. X. (1990). Anomalous variations of ground temperature before Lanchang-Gengma earthquake. *J. Seismol. Res.* 2, 196–202.

Zhang, L. F., Wang, P. L., Zhang, P. T., and Sun, X. H. (2020). Thermal infrared anomalies before Milin MS6.9 earthquake in 2017. *J. China Earthq. Eng. J.* 42 (2), 360–367.

Zhang, X. J., Li, Y., Wang, H. X., Lu, J., and Zhang, Y. B. (2021). Investigation of the relation between the anomaly of active faults and underground water using infrared technology. *J. Appl. Remote Sens.* 15 (1), 016524.

Zhang, X., Zhang, Y. S., Wei, C. X., Tian, X. F., Tang, Q., and Gao, J. (2013). Analysis of thermal infrared anomaly before the lushan Ms7.0 earthquake. *J. China Earthq. Eng. J.* 35 (2), 272–277.

Zhang, Y. S., Guo, X., Zhong, M. J., Shen, W., Li, W., and He, B. (2010). Wenchuan earthquake: Brightness temperature changes from satellite infrared information. *J. Chin. Sci. Bull.* 55 (18), 1917–1924. doi:10.1007/s11434-010-3016-8

Zhang, Y. S., Shen, W. R., and Xu, H. (2002). Satellite thermal infrared anomaly before the xinjiang-qinghai border M8.1 earthquake. *J. Northwest. Seismol. J.* 24 (1), 1–4.

Zhao, B., Li, J., Lin, F., Zhang, L., and Song, C. H. (2021). Thermal infrared anomaly analysis of the 2020 ML 5.8 Qinghai earthquake, China. *Geomatics, Nat. Hazards Risk* 12 (1), 1327–1346.

Zhou, X. B., Chen, Q., Wu, P., Wang, J., and Xiong, Z. X. (2019). Characteristics analysis of thermal infrared radiation anomalies before the Lushan Earthquake. *Infrared Phys. Technol.* 98, 364–372.

frontiers | Frontiers in Earth Science

TYPE Original Research
PUBLISHED 28 August 2023
DOI 10.3389/feart.2023.1201576

Check for updates

OPEN ACCESS

EDITED BY
Fuqiong Huang,
China Earthquake Networks Center,
China

REVIEWED BY
Rosalino Fuenzalida,
Arturo Prat University, Chile
Unger Zoltan,
Eötvös Loránd University, Hungary

*CORRESPONDENCE
Changcheng Li,
1020168681@qq.com

RECEIVED 06 April 2023
ACCEPTED 11 August 2023
PUBLISHED 28 August 2023

CITATION
Li C (2023), Influence of the Yucatan earthquake event.
Front. Earth Sci. 11:1201576.
doi: 10.3389/feart.2023.1201576

COPYRIGHT
© 2023 Li. This is an open-access article distributed under the terms of the Creative Commons Attribution License (CC BY). The use, distribution or reproduction in other forums is permitted, provided the original author(s) and the copyright owner(s) are credited and that the original publication in this journal is cited, in accordance with accepted academic practice. No use, distribution or reproduction is permitted which does not comply with these terms.

Influence of the Yucatan earthquake event

Changcheng Li*

Department of Earth and Space Sciences, Southern University of Science and Technology, Shenzhen, China

In recent years, seismic wave effects caused by meteorite impacts have been widely observed. The meteorite impact event that occurred 66 million years ago is one of the most famous impact events in Earth's history. The influences of the seismic wave field generated by this collision event on the solid Earth itself is worth exploring. Therefore, this study initially estimated the seismic source parameter information based on the multiring structure of the meteorite crater, and then simulates the seismic event. The results of this study provide a possible explanation for the formation of the Earth's tectonic plates. The findings of this study suggest that the seismic wave field generated by the meteorite impact event 66 million years ago may have caused the destruction of the Solid Earth, leading to the formation of the boundary between the Indian Ocean and the Pacific Plate. Simultaneously, this study has important significance for inspiring the development of new geoscientific methods.

KEYWORDS

solid earth, seismology, seismic source, meteorite impact, plate tectonics

1 Introduction

Collisions between objects, such as those that occur in nuclear reactions and due to the generation of gravitational waves, widely occur in nature. Moreover, collisions between meteorites and planets are common in solar systems (Bierhaus et al., 2022; Mark et al., 2022; Kimi and Vijayan, 2023). Among the many previous celestial collision events, the Chicxulub impact event that occurred 66 million years ago has been widely studied (Alvarez et al., 1980; Goderis Steven et al., 2021; Ross et al., 2022; Nixon et al., 2022). The present results show that the main reason for the extinction of dinosaurs is that a change in the Earth's environment was triggered 66 years ago when a meteorite impacted the Earth (Kring, 1997; Schulte et al., 2010; Kunio et al., 2016; Morgan et al., 2022). In addition to causing volcanic eruptions, tsunamis (Hull Pincelli et al., 2020), worldwide wildfires (Venkatesan and Dahl, 1989) and other secondary disasters, this meteorite impact also directly produced strong seismic effects (Kim et al., 2022).

A weak seismic wave field can be used to study the internal structure of a planet (Stahler et al., 2021), while a strong seismic wave field usually results in intense damage (Caglar et al., 2023). The seismic wave field is primarily affected by the physical parameters of the source and the underground medium. For seismic sources, the seismic energy, source type, source direction, depth and source time function are important components to consider.

Regarding the source energy of the Chicxulub event, previous studies have shown that the source energy released by the impact was approximately 5×10^{23} joules (Morgan et al., 1997). Regarding the source direction, numerical experiments show that the meteorite impacted the Yucatan Peninsula at an angle of approximately 45–60 degrees, approaching from the northeast (Collins et al., 2020). However, the source depth and source time function are still unclear.

Nevertheless, the source depth and source time function can be estimated. The method of estimating the seismic time function using near-field seismic waveform information is widely used in the field of seismology (Isadora et al., 2020). For most meteorite impact events, the source time function can normally be approximated as a delta function (Holsapple and Schmidt, 1987). However, due to the seismic wave absorption and attenuation by the existing underground medium, the seismic source time function can generally be approximated as a Ricker wavelet or a triangular function (Ricker, 1977). The dominant frequency of the function is the parameter to be determined. The frequency of large impact events is usually concentrated in low-frequency components (Teanby and Wookey, 2011). To obtain this parameter, we analyzed the multiring structure of the crater and found that this structure reflects a regular ground wave phenomenon due to the presence of excessive energy during the seismic body wave propagation. In this study, two adjacent rings are considered to be the density extremum caused by the same peak frequency. Usually, the corresponding seismic parameters can be determined by solving the body wave equation in the frequency space domain, then setting different parameters, and conducting comparative tests. Basic equations in the field of natural science, such as the acoustic wave equation, light wave equation and seismic body wave equations, they usually have the same form. Li and Chen., 2021 efficiently solved this equation.

After obtaining the above approximate source parameter information, we can conduct research on global seismology to quantitatively explore the influence of the seismic effect generated by this event on both the interior and exterior of the Earth.

2 Data acquisition

An important difficulty in the study of events 66 million years ago is the acquisition of actual data. The direct evidence of meteorite impact mainly comes from meteorite craters.

Since the Chicxulub event occurred, 66 million years have elapsed, and there exists no current seismic data available that can be used to extract the source information from that event. However, geophysical exploration shows that the area retained a multiring structure with a diameter of approximately 180 km (Campos et al., 1997, Morgan et al., 2011; Gulick et al., 2013; Sweeney, 1978). The diameter of the inner ring of the multiring structure is approximately 70 km, and the diameter of the second ring is approximately 100 km at its widest point (Hildebrand et al., 1991). The multiring structure is mainly attributed to variations in the existing medium density caused by the propagation of the compressional wave. The two adjacent peak loops can be regarded as a wave cycle. The exact amplitude of the multiring structure will have changed over 66 million years due to gravity and other effects, but the wavelength information of the multiring structure can be used to estimate the frequency of the seismic source time function of the collision event.

The extraction of data on the multiring structure of meteorite craters in this study are based on previous measurements of gravity data (Hildebrand et al., 1991). The gravity data results mainly reflect changes in the density of the medium. To obtain relatively large amounts of reliable data, this study mined corresponding multiring structures and waveform diagrams from previous articles. Here, the ginput function of MATLAB is Primarily used for data extraction.

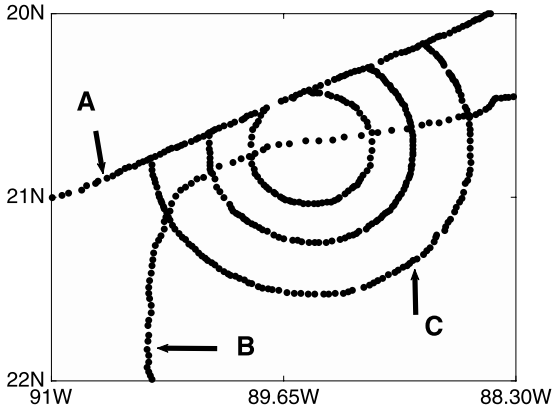

FIGURE 1
Schematic diagram of the crater multi-ring structure of the crater (Hildebrand et al., 1991), in which **(A)** represents the waveform data acquisition system, **(B)** represents the fracture caused by meteorite impact, and **(C)** represents the crater multi-ring structure, there are three multiring structures here, the first ring has a diameter of approximately 70 km, and the second ring has a diameter of approximately 100 km. These two circles represent wave peaks and can be considered as a waveform cycle.

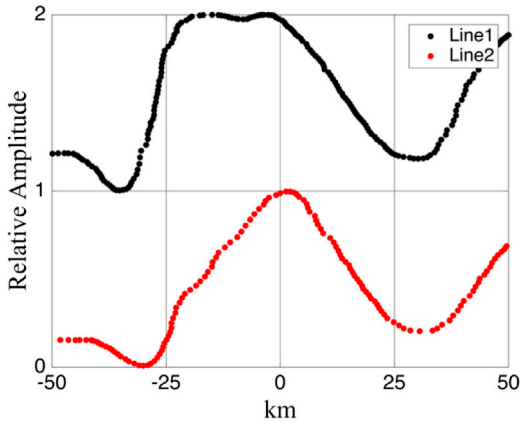

FIGURE 2
Waveform maps of the same region extracted from the survey lines obtained in different articles (Sweeney, 1978; Hildebrand et al., 1991), the wavelength values of Line1 and Line2 are basically the same.

The multiring structure and waveform of the crater are shown in Figures 1, 2.

In addition to the multiring structure of the crater, the waveform results of the crater can also be used as an additional source of information in order to constrain the source information. The waveform results obtained from previous data are as shown in Figure 2.

Based on the above information, we can perform wave field simulations to obtain the source information.

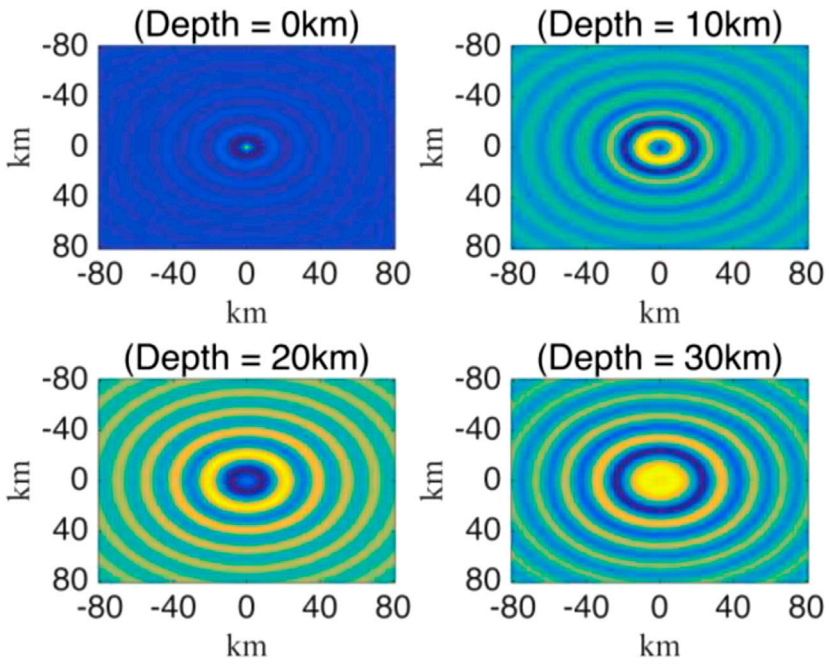

FIGURE 3
Influence of different source depths on multiring structure.

3 Source parameter estimation

Generally, we can use the waveform inversion method to invert the source parameters (Simute et al., 2023). However, due to the limitations of the actual data that is available, and the risk of multiple solutions for parameters with limited data constraints, we use the data fitting method to study this problem. During the data fitting process, the wavelength information of the multiring structure of the meteorite crater is mainly affected by the source depth, dominant frequency, and of the medium wave velocity. The simulation of the multi-ring structure of a meteorite crater is shown below.

Firstly, we can approximate the corresponding wavelength range based on the relationship between wavelength, wave velocity, and frequency as follows.

$$\lambda = v/f,$$

Where λ represents the wavelength information of the multi-ring structure, v represents the wave speed, and f represents the corresponding wave field frequency. The specific results are as follows.

In order to further estimate the relatively accurate source information, we can discuss the results. The rock structure of shallow surface craters is complex (Riller et al., 2018), but this study mainly focuses on low-frequency large-scale structure. To obtain the corresponding source depth. Here, we set the medium velocity to 1,500 m/s and the frequency to 0.1 Hz. Then, set different source depths for calculation. The source depth changes from 0 km to 30 km. The calculation result (Figure 3) shows that when the source is set at the surface, the first ring appears at the source, and as the depth increases, the diameter of the first ring gradually increases. Therefore, we can use the first ring diameter information to constrain the source depth information.

Next, we consider the influence of frequency on the multi-ring structure. At this time, we set the medium velocity to 5,000 m/s, change the frequency from 0.1 Hz to 0.25 Hz, and set the source depth to 20 km. The calculation result (Figure 4) shows that as the calculation frequency gradually increases, the multi-ring structure becomes increasingly dense, which manifests as a shorter wavelength. This information can be used to extract the approximate source dominant frequency information more accurately from the waveform information shown in Figure 2.

Finally, considering the impact of the wave velocity on the circular structure, the dominant frequency was set to 0.1 Hz, and the wave velocity was changed from 1,500 m/s to 3,000 m/s, and the source depth was set to 20 km. The calculation result is shown in Figure 5.

After discussing the influence of different source parameters on the structure of the crater, we compared the crater multiring structure, actual waveform information, and theoretical simulation results. In the actual simulation, the determined medium velocity of the formation was 5 km/s, based on the actual crustal velocity model (Dziewonski and Anderson, 1981). The comparison results are shown in Figure 6. The research results show that when the source depth is 20 km and the calculated frequency is 0.15 Hz, the simulated theoretical wavelength results are closest reconstruction of the actual results. At the same time, some scholars believe that this density change is due to the different thicknesses of the layers of deposited caused by fluctuations in the seismic shear wave, which resulted in a change in density (Morgan et al., 2022). For seismic shear

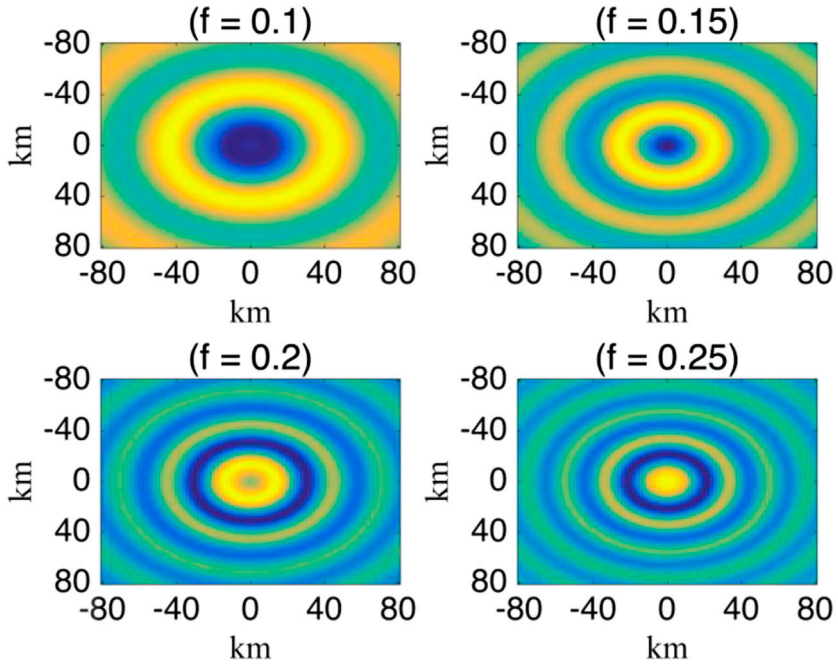

FIGURE 4
The impact of different frequencies on the structure of the multiple circles of the crater.

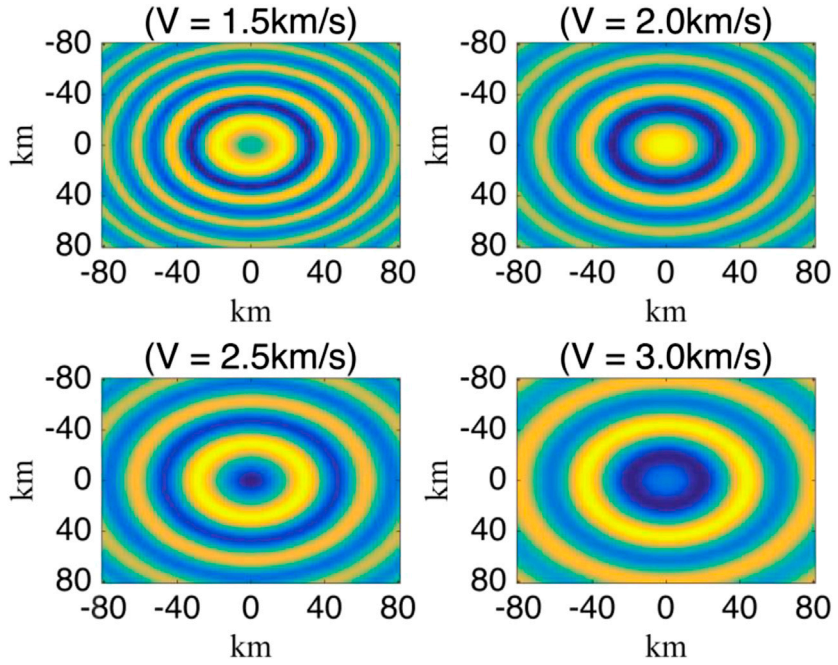

FIGURE 5
Effect of different wave velocities on the multi-ring structure of the crater.

waves, the main difference is that the wave velocity can vary to some extent, but for the simulated global impact of seismic fluctuations caused by meteorite impacts, such as those that are generated from a purely natural phenomena, this source parameter has little influence on the results.

Then, the corresponding source time function can be calculated.

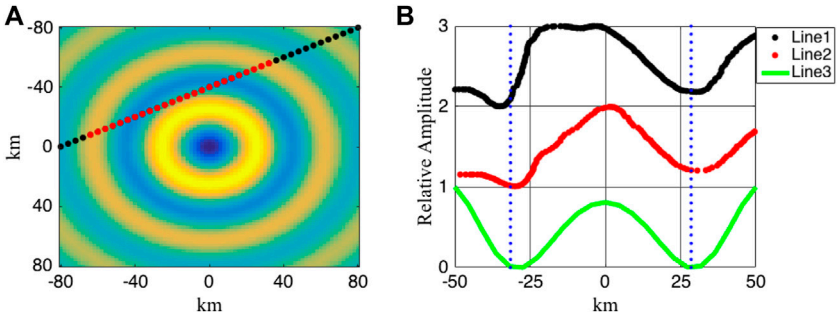

FIGURE 6
(A) Simulated crater multiring structure, **(B)** Simulated waveform, noted as Line3 and the actual waveform comparison results.

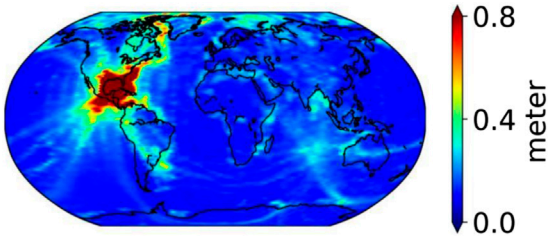

FIGURE 7
Seismic displacement results with receivers set on the surface.

4 Seismic wave effects on the solid earth

To estimate the harm caused by this event, relevant research was conducted on the source. For the meteorite impact process, previous theoretical analysis shows that the process is an external force impact problem (Yang and Chen., 2022). Therefore, the process is discussed first. For a force source, it can be expressed as $\vec{f} = F\overrightarrow{e_f}\delta(x - x_s)S(t)$, where F represents the amplitude, $\overrightarrow{e_f}$ represents the direction of the force, x_s represents the source position, and $S(t)$ is a source time function. The dominant frequency of the earthquake primarily has a specific impact on the amplitude value of the calculated results. The phenomenon of the presence of multiple circular fluctuations in meteorite craters indicates that this problem is a low-frequency seismological problem (Hildebrand et al., 1991). Considering the impact of the actual calculation amount and numerical accuracy, the half duration of the source time function in the following study is 15 s, and the calculated maximum frequency is approximately 0.11 Hz.

For the impact external force impact problem, we can use the impulse theorem to solve it. During the impact process, meteorites are mainly affected by the formation reaction force and the gravitational force of the Earth. The product of the gravitational force and time are negligible relative to the product of the impact velocity and mass of the meteorite, so it is approximately written as follows:

$$\int_0^t F dt = mv,$$

If the Rake wavelet is approximated to a triangular function, the external force is approximately $F = 1.5 \times 10^{19}$ N. After obtaining the source information, we can conduct Seismic wave field simulation (Komatitsch and Tromp, 2002) to estimate the impact of this event on Solid earth.

In the process of using seismological methods to explore the influence of a meteorite impact on solid earth, we accidentally found that the area located beneath the impact of the Hiksurub meteorite would break due to the action of seismic waves, and the break showed clear similarities with the boundary between the Indian plate and the African plate (Figure 7).

As one of the four fundamental theories in the field of natural science in the 20th century, plate tectonics are as important to earth science as the theory of relativity, quantum mechanics, and molecular biology are to the fields of physics and biology (Zheng, 2018). Its development is of great significance to the further development of geology, geochemistry, seismology, geodynamics, rock physics, and other disciplines (Holder et al., 2019). Exploring its initiation mechanism and the timing period of events have always been one of the most innivative of questions to investigate in the field of earth science (Wan et al., 2020).

The theory of plate tectonics originated from the hypothesis of continental drift and the theory of seafloor spreading (Cwojdzinski, 2017). According to the theory of plate tectonics, the lithosphere is rigid relative to the asthenosphere, beneath which lies the low viscosity asthenosphere (Conrad and Lithgow-Bertelloni, 2002). The lithosphere is not a uniform entity, but contains directionally heterogeneous characteristics and is divided into large and small blocks by many active zones, such as mid-ocean ridges, trenches, transform faults, Earth sutures, and continental rifts. The interior of the plates are stable, while the edges and joint zones of the plates are active zones on the Earth's surface, with strong tectonic movement (Ouchi, 1985), magmatic activity (Pilger, 1984), volcanic activity (Canon and Walker, 2004), metamorphic rock (Holder et al., 2019), and seismic activity (Maouche et al., 2019). These active zones are also very favorable mineralization zones (Yang et al., 2022). Second, the lithospheric plates are themselves active. During continental drift, some plates move

away from each other, and some collide with each other to form various geological structures, such as the Mid-Ocean Ridge (Macdonald et al., 1988) and the Alpine Himalayan Fold Belt (Ali et al., 2019). Major volcanic activity zones and major deep seismic zones around the world are also mainly distributed in these plate fractures zones (Barrier et al., 2021).

Plate tectonics are important for the field of seismology. The vast majority of earthquakes in the world are mainly concentrated in the seismic zones. Seismic zones refer to regular banded areas where earthquakes are concentrated, and these seismic zones principally coincide with the tectonic plate edges (Dewey, 1972). There are three main seismic zones on the Earth, namely, the Pacific Rim seismic zone (Yin et al., 2019), the Eurasian seismic zone (Tang et al., 2020), and the oceanic ridge seismic zone (Kagan, 2003). The Pacific Rim seismic belt (Wu et al., 2019) is mainly distributed on the continental margin of the Pacific Ocean. This seismic zone is the primary earthquake area of occurrence area on Earth, where most catastrophic earthquakes with magnitude 8 or above and global earthquakes are concentrated (Yin et al., 2019). In addition, seismic zones are also the main volcanic activity zones in the world. The second largest seismic zone in the world is the Eurasian seismic zone (Wu et al., 2019). There is also much volcanic activity in this area. Historically, many large earthquakes have occurred in this area. This seismic zone is widely distributed and basically covers the Eurasian and African continents. Ocean ridge seismic zones (Wu et al., 2019) are mainly distributed in the Pacific, Atlantic, and Indian oceans, including almost all of the ocean ridge tectonic regions.

Therefore, the theory of plate tectonics involves almost all topics that exist in the field of solid earth science. The plate structure is a sign that the Earth is different from other planets. Due to plate tectonics, materials within the Earth can interact and circulate between circles. This process is beneficial to Earth becoming the current blue livable planet (Stern and Leybourne, 2016). Exploring the initiation mechanisms and timing of events are of great significance to the development of the geosciences.

Regarding the starting time of plate tectonics, based on geological rocks, the possibility that plate tectonics began 4.44 billion to 1 billion years ago has been analyzed (Stern and Leybourne, 2016; Johnson et al., 2017; Weller and Stonge, 2017; Stern, 2018). According to the paleomagnetic evidence, this time period of initiation was advanced to having occurred 800 to 600 million years ago (Piper, 2013). Therefore, it can be considered that the of the global movement plate tectonics do not necessarily start at the same time, and varying start times of different plate tectonic may accompany different time periods of the Earth's evolution. However, there is currently no detailed study on what forces caused the initiation of plate tectonics.

Currently, it is generally believed that there are two possible mechanisms for the initiation of plate tectonics, one is spontaneous generation, and the other is that they were induced by external factors (Zhang, 2022). Regarding spontaneous generation, the possibility of this situation was discussed through numerical simulation experiments (Gerya, 2014). However, this situation needs to reflect the existence of different densities that exist between different plates, and there are also weak zones between plates, which gradually evolve into subduction boundaries.

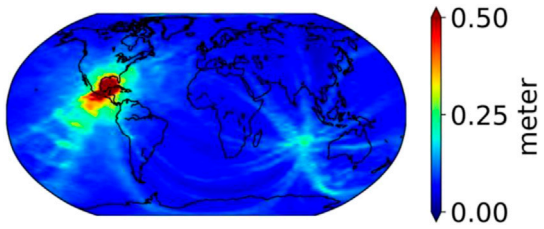

FIGURE 8
Seismic displacement results with receivers set at a depth of 50 km.

Regarding the theory that tectonics were induced by external factors, some scientists have considered the possibility of early meteorite impacts on the Earth leading to meteorite impacts inducing plate tectonics. By explaining the origin of the Tarsi uplift on Mars, they have speculated on the possibility of meteorite impacts leading to the origin of the Earth's plate tectonics (Yin, 2012; Maruyama et al., 2018). However, the above theory lacks quantitative constraints and corresponding direct evidence.

Figure 8 shows that due to the destructive effect of the strong seismic wave field energy on the solid earth, an obvious fault anomaly occurs in the Indian Ocean region, and the location of this fault anomaly is very consistent with the boundary of the earth plate. Therefore, we think that the meteorite impact event 66 million years ago may be the cause of this plate formation. To demonstrate that this fracture affects the entire lithosphere, we calculated seismic displacement results at different depths (Figure 8).

The research results show that this kind of fault has almost spread to the entire lithosphere, which may induce the formation of plates in the region. Of course, in addition to being affected by the seismic source, this calculation result can also be influenced by the Earth model. Here, the S362ANI model is used. Sixty-five million years ago, except for the Atlantic region, the Earth model was basically consistent with the current model (Merdith et al., 2021).

5 Conclution and discussion

Based on seismological methods, this study quantitatively explored the impact of seismic wave effects that were generated by meteorite impacts over 66 million years ago on the solid Earth itself. The research results show that this event promoted the formation of the Indian Ocean plate. This result is of great significance for improving our understanding of spatial distribution patterns of the globe disaster risk from outer space, as well as for the development of plate tectonics theory.

This study has also highlighted some unresolved issues in the field of earth science.

1. In addition to the formation of plate tectonics, meteorite impacts can also form some special internal and external anomalies of the Earth, but existing theories cannot well describe the dynamic formation process of these phenomena. In theory, the best mathematical and physical description method for this study

should be the application of geodynamics, which describe the process of meteorites impacting the Earth from the perspective of earthquake sources and geodynamics, as well as their infulence on the progression of future tectonic changes on Earth. However, the existing geodynamic methods mainly describe the Earth's change process on a large time scale. For the rapid external force effect of meteorite impact, further research may be needed. This method will have an important role in studying the past and present, and predicting the future of the Earth, and can also help us accelerate the evolution of exoplanets to make them more suitable for human beings.

2. The direct evidence for meteorite impacts primarily comes from the multi-ring structure of the crater. This study is generally aimed at extracting source parameter information from the multi-ring structure of a meteorite crater to conduct global seismic wave field simulation, without involving the dynamic formation process of the meteorite crater itself. The further development of elastoplastic wave theory in the future can better help us better understand the formation process of meteorite craters.
3. Among the numerous tectonic plate divisions, the most obvious is the boundary that exists between the American plate and the African plate. The continental drift hypothesis suggests that the two plates originally belonged to the same plate. Based on the comparison of similarities and differences between strata and rocks, it is theoretically possible to predict when the plate split in the past. For the development of the fracture mechanism, concurrent meteorite impacts may further verify this view.

Data availability statement

The original contributions presented in the study are included in the article/Supplementary Material, further inquiries can be directed to the corresponding author.

Author contributions

The author confirms being the sole contributor of this work and has approved it for publication.

Funding

This research was supported by the National Key Research and Development Program of China (No. 2021YFC3000702), and the National Natural Science Foundation of China (Grant Nos. U1901602 and 41790465).

Acknowledgments

We appreciate the invitation from the journal and Huang Fuqiong. We thank the editor and reviewers for their valuable opinions and suggestions during the revision of this article.

Conflict of interest

The author declares that the research was conducted in the absence of any commercial or financial relationships that could be construed as a potential conflict of interest.

Publisher's note

All claims expressed in this article are solely those of the authors and do not necessarily represent those of their affiliated organizations, or those of the publisher, the editors and the reviewers. Any product that may be evaluated in this article, or claim that may be made by its manufacturer, is not guaranteed or endorsed by the publisher.

References

Ali, S. A., Nutman, A. P., Aswad, K. J., and Jones, B. G. (2019). Overview of the tectonic evolution of the Iraqi zagros thrust zone: sixty million years of neotethyan ocean subduction. *J. Geodyn.* 129, 162–177. doi:10.1016/j.jog.2019.03.007

Alvarez, L. W., Alvarez, W., Asaro, F., and Michel, H. V. (1980). Extraterrestrial cause for the Cretaceous/Tertiary extinction. *Science* 208, 1095–1108. doi:10.1126/science.208.4448.1095

Barrier, A., Bischoff, A., Nicol, A., Browne, G. H., and Bassett, K. N. (2021). Relationships between volcanism and plate tectonics: A case-study from the canterbury basin, New Zealand. *Mar. Geol.* 433, 106397. doi:10.1016/j.margeo.2020.106397

Bierhaus, E. B., Trang, D., Daly, R. T., Bennett, C. A., Barnouin, O. S., Walsh, K. J., et al. (2022). Crater population on asteroid (101955) Bennu indicates impact armouring and a young surface. *Nat. Geosci.* 15, 440–446. doi:10.1038/s41561-022-00914-5

Caglar, N., Vural, I., Kirtel, O., Saribiyik, A., and Sumer, Y. (2023). Structural damages observed in buildings after the January 24, 2020 Elazığ-Sivrice earthquake in Türkiye. *Case Stud. Constr. Mater.* 18, e01886. doi:10.1016/j.cscm.2023.e01886

Cañón-Tapia, E., and Walker, G. P. (2004). Global aspects of volcanism: the perspectives of "plate tectonics" and "volcanic systems". *Earth-Science Rev.* 66 (1-2), 163–182. doi:10.1016/j.earscirev.2003.11.001

Collins, G. S., Patel, N., Davison, T. M., Rae, A. S. P., Morgan, J. V., Gulick, S. P. S., et al. (2020). A steeply-inclined trajectory for the Chicxulub impact. *Nat. Commun.* 11, 1480. doi:10.1038/s41467-020-15269-x

Conrad, C. P., and Lithgow-Bertelloni, C. (2002). How mantle slabs drive plate tectonics. *Science* 298 (5591), 207–209. doi:10.1126/science.1074161

Cwojdzinski, S. (2017). History of a discussion: selected aspects of the earth expansion v. plate tectonics theories. *Spec. Publ.* 442 (1), 93–104. doi:10.1144/sp442.24

Dewey, J. F. (1972). Plate tectonics. *Sci. Am.* 226 (5), 56–68. doi:10.1038/scientificamerican0572-56

Dziewonski, A. M., and Anderson, D. L. (1981). Preliminary reference Earth model. *Phys. earth Planet. interiors* 25, 297–356. doi:10.1016/0031-9201(81)90046-7

Gerya, T. (2014). Precambrian geodynamics: concepts and models. *Gondwana Res.* 25 (2), 442–463. doi:10.1016/j.gr.2012.11.008

Goderis, S., Sato, H., Ferrière, L., Schmitz, B., Burney, D., Kaskes, P., et al. (2021). Globally distributed iridium layer preserved within the Chicxulub impact structure. *Sci. Adv.* 7, ABE3647. doi:10.1126/sciadv.abe3647

Gulick, S., Christeson, G., Barton, P., Grieve, R., Morgan, J., and Urrutia-Fucugauchi, J. (2013). Geophysical characterization of the Chicxulub impact crater. *Rev. Geophys.* 51, 31–52. doi:10.1002/rog.20007

Hildebrand, A. R., Penfield, G. T., Kring, D. A., Pilkington, M., Camargo Z., A., Jacobsen, S. B., et al. (1991). Chicxulub Crater: A possible cretaceous/tertiary boundary impact crater on the yucatán Peninsula, Mexico. *Mex.* Geol. 19, 867–871. doi:10.1130/0091-7613(1991)019<0867:ccapct>2.3.co;2

Holder, R. M., Viete, D. R., Brown, M., and Johnson, T. E. (2019). Metamorphism and the evolution of plate tectonics. *Nature* 572 (7769), 378–381. doi:10.1038/s41586-019-1462-2

Holsapple, K. A., and Schmidt, R. M. (1987). Point source solutions and coupling parameters in cratering mechanics. *J. Geophys. Res. Solid Earth* 92 (B7), 6350–6376. doi:10.1029/jb092ib07p06350

Hull Pincelli, M., Bornemann, A., Penman, D. E., Henehan, M. J., Norris, R. D., Wilson, P. A., et al. (2020). On impact and volcanism across the Cretaceous-Paleogene boundary. *Science* 367, 266–272. doi:10.1126/science.aay5055

Isadorade Macedo, A. S., de Figueiredo, J. J. S., de Sousa, M. C., and Nascimento, M. J. (2020). Estimation of the seismic wavelet through homomorphic deconvolution and well log data: application on well-to-seismic tie procedure. *Geophys. Prospect.* 68, 1328–1340. doi:10.1111/1365-2478.12908

Johnson, T. E., Brown, M., Gardiner, N. J., Kirkland, C. L., and Smithies, R. H. (2017). Earth's first stable continents did not form by subduction. *Nature* 543 (7644), 239–242. doi:10.1038/nature21383

Kagan, Y. Y. (2003). Accuracy of modern global earthquake catalogs. *Phys. Earth Planet. Interiors* 135 (2-3), 173–209. doi:10.1016/s0031-9201(02)00214-5

Kim, D., Banerdt, W. B., Ceylan, S., Giardini, D., Lekić, V., Lognonné, P., et al. (2022). Surface waves and crustal structure on Mars. *Science* 378 (6618), 417–421. doi:10.1126/science.abq7157

Kimi, K. B., and Vijayan, S. (2023). Mare filled craters on the Moon. *Icarus* 390, 115298. doi:10.1016/j.icarus.2022.115298

Komatitsch, J. R., and Tromp, J. (2002). The spectral-element method, Beowulf computing, and global seismology. *Science* 298 (5599), 1737–1742. doi:10.1126/science.1076024

Kring, D. A. (1997). Air blast produced by the Meteor Crater impact event and a reconstruction of the affected environment. *Meteorit. Planet. Sci.* 32, 517–530. doi:10.1111/j.1945-5100.1997.tb01297.x

Kunio, K., Oshima, N., Adachi, K., Adachi, Y., Mizukami, T., Fujibayashi, M., et al. (2016). Global climate change driven by soot at the K-Pg boundary as the cause of the mass extinction. *Sci. Rep.* 6, 28427. doi:10.1038/srep28427

Li, C., and Chen, X. (2021). Efficient solution of large scale matrix of acoustic wave equations in 3D frequency domain. *Appl. Geophys.* 18, 299–316. doi:10.1007/s11770-020-0844-4

Macdonald, K. C., Fox, P. J., Perram, L. J., Eisen, M. F., Haymon, R. M., Miller, S. P., et al. (1988). A new view of the mid-ocean ridge from the behaviour of ridge-axis discontinuities. *Nature* 335 (6187), 217–225. doi:10.1038/335217a0

Maouche, S., Bouhadad, Y., Harbi, A., Rouchiche, Y., Ousadou, F., and Ayadi, A. (2019). Active tectonics and seismic hazard in the tell atlas (northern Algeria): A review. *Geol. Arab World-An Overv.*, 381–400. doi:10.1007/978-3-319-96794-3_10

Mark, B., Sholes, S., and Hwang, A. (2022). Impact craters and the observability of ancient martian shorelines[J]. *Icarus* 387. doi:10.1016/j.icarus.2022.115178

Maruyama, S., Santosh, M., and Azuma, S. (2018). Initiation of plate tectonics in the hadean: eclogitization triggered by the ABEL bombardment. *Geosci. Front.* 9 (4), 1033–1048. doi:10.1016/j.gsf.2016.11.009

Merdith, A. S., Williams, S. E., Collins, A. S., Tetley, M. G., Mulder, J. A., Blades, M. L., et al. (2021). Extending full-plate tectonic models into deep time: linking the neoproterozoic and the phanerozoic. *Earth-Science Rev.* 214, 103477. doi:10.1016/j.earscirev.2020.103477

Morgan Joanna, V., Bralower, T. J., Brugger, J., and Wünnemann, K. (2022). The Chicxulub impact and its environmental consequences. *Nat. Rev. Earth Environ.* 3, 338–354. doi:10.1038/s43017-022-00283-y

Morgan, J. V., Warner, M. R., Collins, G. S., Grieve, R. A. F., Christeson, G. L., Gulick, S. P. S., et al. (2011). Full waveform tomographic images of the peak ring at the Chicxulub impact crater. *J. Geophys. Res.* 116, B06303. doi:10.1029/2010jb008015

Morgan, J., Warner, M., Brittan, J., Buffler, R., Camargo, A., Trejo, A., et al. Chicxulub Working Group (1997). Size and morphology of the Chicxulub impact crater. *Nat. Int. Wkly. J. Sci.* 390 (6659), 472–476. doi:10.1038/37291

Nixon, C. G., Schmitt, D. R., Kofman, R., Lofi, J., Gulick, S. P., Saustrup, S., et al. (2022). Borehole seismic observations from the Chicxulub impact drilling: implications for seismic reflectivity and impact damage. *Geochem. Geophys. ,Geosystems* 23 (3), e2021GC009959. doi:10.1029/2021gc009959

Ouchi, S. (1985). Response of alluvial rivers to slow active tectonic movement. *Geol. Soc. Am. Bull.* 96 (4), 504–515. doi:10.1130/0016-7606(1985)96<504:roarts>2.0.co;2

Pilger, R. H., Jr (1984). Cenozoic plate kinematics, subduction and magmatism: south American andes. *J. Geol. Soc.* 141 (5), 793–802. doi:10.1144/gsjgs.141.5.0793

Piper, J. D. A. (2013). A planetary perspective on earth evolution: lid tectonics before plate tectonics. *Tectonophysics* 589, 44–56. doi:10.1016/j.tecto.2012.12.042

Range Molly, M. (2022). The Chicxulub impact produced a powerful global tsunami [J]. *AGU Adv.* 3, e2021AV000629. doi:10.1029/2021AV000627

Ricker, N. H. (1977). *Transient waves in visco-elastic media*. New York: Elsevier.

Riller, U., Poelchau, M. H., Rae, A. S., Schulte, F. M., Collins, G. S., Melosh, H. J., et al. (2018). Rock fluidization during peak-ring formation of large impact structures. *Nature* 562 (7728), 511–518. doi:10.1038/s41586-018-0607-z

Ross, C. H., Stockli, D. F., Rasmussen, C., Gulick, S. P., De Graaff, S. J., Claeys, P., et al. (2022). Evidence of Carboniferous arc magmatism preserved in the Chicxulub impact structure. *GSA Bull.* 134 (1-2), 241–260. doi:10.1130/b35831.1

Schulte, P., Alegret, L., Arenillas, I., Arz, J. A., Barton, P. J., Bown, P. R., et al. (2010). The Chicxulub asteroid impact and mass extinction at the Cretaceous-Paleogene boundary. *Science* 327, 1214–1218. doi:10.1126/science.1177265

Simutė, S., Boehm, C., Krischer, L., Gokhberg, A., Vallée, M., and Fichtner, A. (2023). Bayesian seismic source inversion with a 3-D Earth model of the Japanese Islands. *J. Geophys. Res. Solid Earth* 128 (1), e2022JB024231. doi:10.1029/2022jb024231

Stahler, S. C., Khan, A., Banerdt, W. B., Lognonné, P., Giardini, D., Ceylan, S., et al. (2021). Seismic detection of the martian core. *Science* 373, 443–448. doi:10.1126/science.abi7730

Stern, R. J., Leybourne, M. I., and Tsujimori, T. (2016). Kimberlites and the start of plate tectonics. *Geology* 44, 799–802. doi:10.1130/g38024.1

Stern, R. J. (2018). The evolution of plate tectonics. *Philos. Trans. R. Soc. A* 376, 20170406. doi:10.1098/rsta.2017.0406

Sweeney, J. F. (1978). Gravity study of great impact. *J. Geophys. Res. Solid Earth* 83 (B6), 2809–2815. doi:10.1029/jb083ib06p02809

Tang, Y., Liu, S., Li, X., Fan, Y., Deng, Y., Liu, Y., et al. (2020). Earthquakes spatio–temporal distribution and fractal analysis in the Eurasian seismic belt. *Sci. Fis. Nat.* 31, 203–209. doi:10.1007/s12210-020-00871-4

Teanby, N. A., and Wookey, J. (2011). Seismic detection of meteorite impacts on Mars. *Phys. Earth Planet. Interiors* 186 (1–2), 70–80. doi:10.1016/j.pepi.2011.03.004

Venkatesan, M. I., and Dahl, J. (1989). Organic geochemical evidence for global fires at the Cretaceous/Tertiary boundary. *Nature* 338, 57–60. doi:10.1038/338057a0

Wan, B., Yang, X., Tian, X., Yuan, H., Kirscher, U., and Mitchell, R. N. (2020). Seismological evidence for the earliest global subduction network at 2 Ga ago. *Sci. Adv.* 6 (32), eabc5491. doi:10.1126/sciadv.abc5491

Weller, O. M., and Stonge, M. R. (2017). Record of modern-style plate tectonics in the Palaeoproterozoic Trans-Hudson orogen. *Nat. Geosci.* 10 (4), 305–311. doi:10.1038/ngeo2904

Wu, C., Cui, P., and Li, Y. (2019). "Spatial distribution of coseismic landslides around a UNESCO world heritage site: a case of the 2017 jiuzhaigou earthquake," in *Geophysical research abstracts*, 21.

Yang, S., Wang, Q., Liu, X., Kan, Z., Santosh, M., and Deng, J. (2022). Global spatio-temporal variations and metallogenic diversity of karst bauxites and their tectonic, paleogeographic and paleoclimatic relationship with the Tethyan realm evolution. *Earth-Science Rev.* 233, 104184. doi:10.1016/j.earscirev.2022.104184

Yang, Y., and Chen, X. (2022). A seismic meteor strike on Mars. *Science* 378 (6618), 360–361. doi:10.1126/science.add8574

Yin, A. (2012). An episodic slab-rollback model for the origin of the tharsis rise on Mars: implications for initiation of local plate subduction and final unification of a kinematically linked global plate-tectonic network on earth. *Lithosphere* 4 (6), 553–593. doi:10.1130/l195.1

Yin, L., Li, X., Zheng, W., Yin, Z., Song, L., Ge, L., et al. (2019). Fractal dimension analysis for seismicity spatial and temporal distribution in the circum-Pacific seismic belt. *J. Earth Syst. Sci.* 128, 22–27. doi:10.1007/s12040-018-1040-2

Zhang, S. (2022). When and how plate tectonics begun on earth?. *Earth Sci.* 47 (10), 3806–3815. doi:10.3799/dqkx.2022.817

Zheng, Y. F. (2018). Fifty years of plate tectonics. *Natl. Sci. Rev.* 5 (2), 119. doi:10.1093/nsr/nwy024

frontiers | Frontiers in Earth Science

TYPE Original Research
PUBLISHED 26 September 2023
DOI 10.3389/feart.2023.1260559

Check for updates

OPEN ACCESS

EDITED BY
Giovanni Martinelli,
National Institute of Geophysics and Volcanology, Italy

REVIEWED BY
Xiaocheng Zhou,
China Earthquake Administration, China
Omid Memarian Sorkhabi,
University College Dublin, Ireland
Gaetano De Luca,
National Institute of Geophysics and Volcanology (INGV), Italy

*CORRESPONDENCE
Yuxuan Chen,
cyx630@163.com

RECEIVED 18 July 2023
ACCEPTED 04 September 2023
PUBLISHED 26 September 2023

CITATION
Chen Y and Liu J (2023), Groundwater trace element changes were probably induced by the ML3.3 earthquake in Chaoyang district, Beijing.
Front. Earth Sci. 11:1260559.
doi: 10.3389/feart.2023.1260559

COPYRIGHT
© 2023 Chen and Liu. This is an open-access article distributed under the terms of the Creative Commons Attribution License (CC BY). The use, distribution or reproduction in other forums is permitted, provided the original author(s) and the copyright owner(s) are credited and that the original publication in this journal is cited, in accordance with accepted academic practice. No use, distribution or reproduction is permitted which does not comply with these terms.

Groundwater trace element changes were probably induced by the ML3.3 earthquake in Chaoyang district, Beijing

Yuxuan Chen[1]* and Jianbo Liu[2]

[1]Beijing Earthquake Agency, Beijing, China, [2]Key Laboratory of Orogenic Belts and Crustal Evolution, Ministry of Education, School of Earth and Space Sciences, Peking University, Beijing, China

Geochemical composition changes in groundwater related to earthquakes have been documented in previous studies, and most such studies focused on the changes in major ions, hydrogen, oxygen isotopes, and geochemical gases. Changes in trace elements were suggested to be more sensitive to small earthquakes than the commonly used chemical constituents such as major ions, yet they received less attention. Beijing is located in the Zhangjiakou-Bohai seismic belt and experiences frequent occurrences of small earthquakes. In this paper, we collected groundwater samples from a hot spring in Yanqing district of Beijing weekly from August 2021 to August 2022. Each water sample contained 41 trace chemical compositions. During the sampling, an earthquake with a magnitude of ML3.3 occurred in the Chaoyang district of Beijing on 3 February 2022, so these trace elements changes were systematically monitored before and after the earthquake: Li, Sc, Ti, and Pb elements had upward changes before the earthquake, while Cu, Nb, Th, Zn, Tl, and U elements had downward changes before the earthquake. Eu (rare earth elements) had upward changes after the earthquake. At the same time, the earthquake caused no significant changes in the groundwater level in the seismic monitoring well near the Songshan spring. Such responses indicate that trace elements are likely to be more sensitive to crustal strain than groundwater level. We considered that the earthquake-induced rock cracks before or after the earthquake caused enhancing water-rock interaction and led to the migration of trace elements between the water column and rocks, which is the mechanism to explain the trace elemental changes. This study probably provides a comprehensive assessment of the sensitivity of trace element constituents to the earthquake. Furthermore, we suggest that more long-term continuous monitoring and research of trace elements in Beijing and Zhangjiakou-Bohai Fault Zone should be considered to explore the response mechanism of groundwater geochemistry to earthquakes in the future.

KEYWORDS

Zhangjiakou-bohai fault zone, earthquake monitor, geochemistry, rare earth elements, small earthquake

1 Introduction

As part of the earthquake precursor detection program, changes in groundwater levels, temperatures, and chemical composition related to earthquakes have been documented for decades (Toutain et al., 1997; Roeloffs, 1998; Montgomery and Manga, 2003; Wang and Manga, 2010; Skelton et al., 2014; Manga and Wang, 2015; De Luca et al., 2018; Martinelli, 2020). Because of the feasibility of using automated monitoring systems, earthquake-related changes in water levels, temperatures, and radon concentrations are the most commonly reported responses (King, 1981; Kitagawa et al., 1996; Manga and Wang, 2015; Martinelli, 2020). Hence, these monitoring methods of groundwater also play key roles in precursor detection in China, and a nationwide network of monitoring wells located along strain-sensitive locations has been constructed for this purpose.

In contrast, groundwater geochemical changes induced by earthquakes have been documented relatively rarely (Martinelli, 2020; Shi et al., 2020) because manual sampling and expensive, time-consuming laboratory analyses are required (Wang and Manga, 2010). However, such studies are highly important because earthquake-related chemical changes are considered to be sensitive to crustal stress and to be beneficial for earthquake prediction (Thomas, 1988; Wakita, 1996; Poitrasson et al., 1999; Manga and Wang, 2015; Martinelli and Dadomo, 2017; Shi et al., 2020; Kopylova et al., 2022). For instance, based in part on hundreds of hydrological anomalies including geochemical changes, an imminent prediction was made before the 1975 M 7.3 Haicheng earthquake in China (Wang et al., 2006). Following the 1995 M7.2 Kobe earthquake, several papers reported precursory changes in the concentrations of radon, chlorine, and sulfate ions in groundwater (Igarashi et al., 1995; Igarashi and Wakita, 1995; Tsunogai and Wakita, 1995). Claesson et al. (2004) observed simultaneous changes in trace elements, major elements, and isotopes before and after major earthquakes. Barberio et al. (2017) and Rosen et al. (2018) found that some trace elements exhibited responses to the seismic sequence in central Italy. Skelton et al. (2019) found that changes in major ions and hydrogen and oxygen isotopes were associated with three different earthquakes in Iceland. Shi et al. (2020) found that trace element concentrations showed coseismic decreases following the Tonghai earthquake in the Yunnan Province of China, but no significant changes occurred in major ions and hydrogen and oxygen isotope concentrations.

Overall, according to previous geochemical research, most documented studies investigated the major elements (Tsunogai and Wakita, 1995; Toutain et al., 1997; Kingsley et al., 2001; Woith et al., 2013) and hydrogen and oxygen isotopes related to destructive great earthquakes (Taran et al., 2005; Skelton et al., 2019), and only a few studies focused on trace elements' responses to the earthquake (Rosen et al., 2018; Shi et al., 2020) despite changes in trace elements being more sensitive to small earthquakes than the commonly used chemical constituents. In this paper, we continuously collected 36 water samples of the hot spring from August 2021 to August 2022, and each water sample contained 41 trace elements which contributed to the comparison of the different responses to earthquakes and the discussion on the possible mechanisms and their implications for future seismic monitoring.

2 Background

North China has experienced a period of strong earthquakes frequently over the last few decades. From 1966 to 1998, a series of strong earthquakes occurred, such as the Xingtai M7.2 earthquake in 1966, the Bohai M7.4 earthquake in 1969, the Haicheng M7.3 earthquake in 1975, and the Tangshan M7.8 earthquake in 1976. Since the Zhangbei M6.2 earthquake in 1998, there has been no earthquake above M6 for 20 years. The seismic activity in North China has been relatively quiet, and there would be a potential danger of damaging earthquakes in the next few years.

Zhangjiakou-Bohai Fault Zone is a group of NW-W orderly active fault zones with high seismic activity in North China; the fault zone starting from the northern margin of Taihang Mountain in the west is distributed along the junction area of Yanshan Mountain and the North China Basin and enters the Bohai Sea in the east. In this zone, many violent earthquakes above M6 have occurred (Yang et al., 2022), so it is an important fault zone for earthquake monitoring and research.

Beijing is the capital of China with a large population, and it is located at the intersection of the North China Plain and Zhangjiakou-Bohai seismic belt, where active faults have developed. These faults mainly included the NW orderly Nankou-Sunhe Fault Zone and two groups of NE orderly active fault zones named Huangzhuang-Gaoliying Fault Zone and Shunyi-Liangxiang Fault Zone. All earthquakes occurred along these fault zones or where they intersect (Figure 1), and all these earthquakes were less than M6. Therefore, it is of great scientific and practical significance to carry out small earthquake monitoring and forecasting in the Beijing area.

To better monitor the seismic activity in the capital area, the Chinese Earthquake Administration (CEA) started to deploy the Beijing Metropolitan Digital Seismic Network (BSN) in the late 90s. Currently, the network consists of broadband, borehole, and surface short-period stations that cover Beijing and the surrounding areas densely and uniformly (Jiang et al., 2008; Li and Huang, 2014). Since 2001, 107 stations have been installed in the Chinese capital region, which is the most advanced and densest digital seismic network in Mainland China. A large number of high-quality waveforms have been recorded, which provides an opportunity to improve the location accuracy of small earthquakes in the region (Jiang et al., 2008).

Beijing hosted the 2022 Winter Olympic Games from February 4th to 20th. During this time, continuous monitoring of possible earthquake areas was strengthened. On 3 February 2022, an earthquake with a magnitude of ML3.3 occurred in the Chaoyang district of Beijing (Figure 1). In this study, we conducted the geochemical monitoring study of the Songshan hot spring located in the Yanqing district of Beijing; the spring had an epicentral distance of ~75 km from the Chaoyang earthquake (Figure 1). Geographically, this spring is exposed to the valley of Dahaituo Mountain which is composed of granite with fissure development (Yang et al., 2001), and fault activities were good channels for deep groundwater migration. The groundwater of Songshan spring comes from the granite of Dahaituo Mountain; there is no lake, river, or surface reservoir in the area.

Songshan Spring is an artesian type of rising spring, and the water is from the granite rock body. The spring has 41°C–42°C water

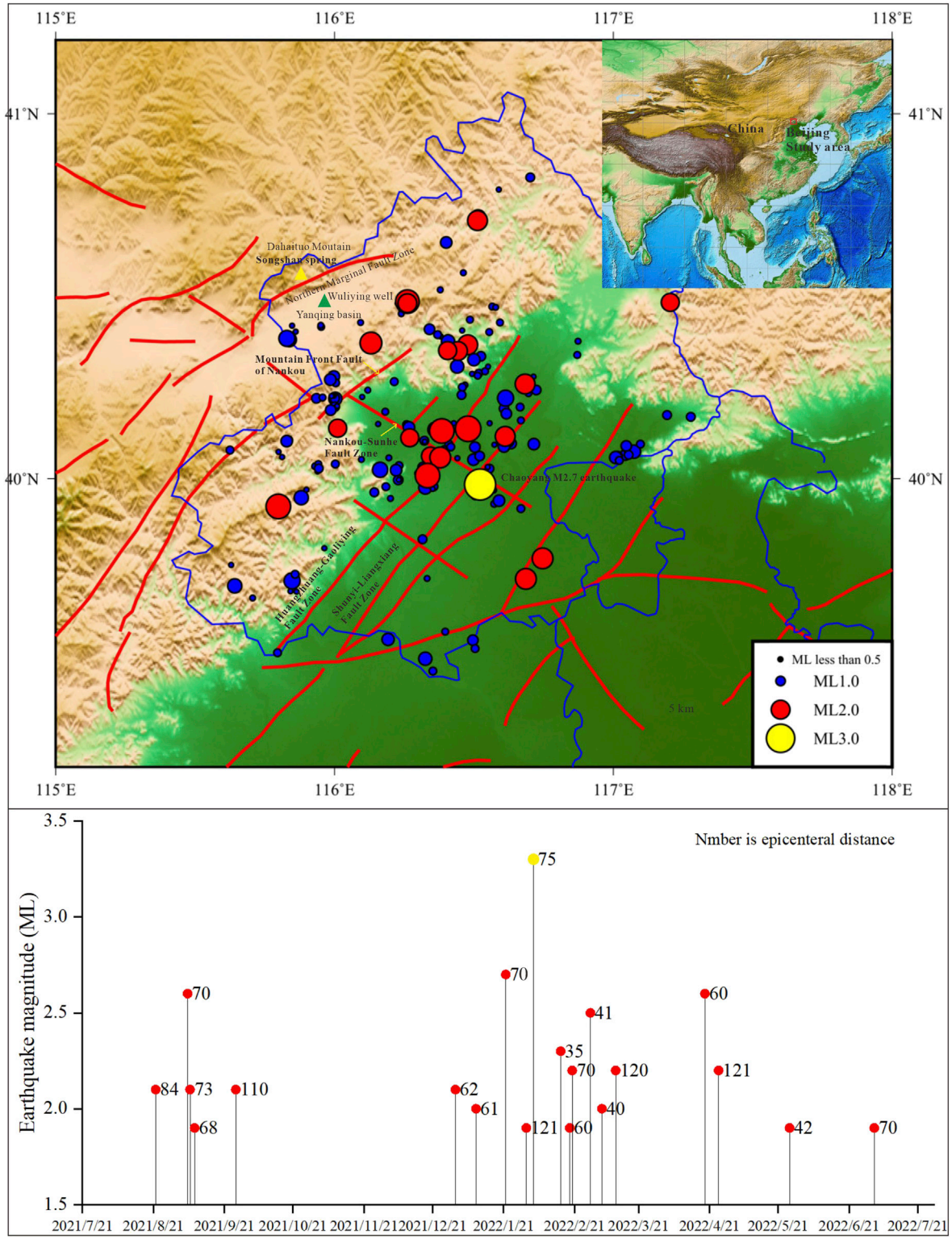

FIGURE 1
Earthquake distribution of the Beijing area from August 2021 to August 2022 and the time sequence of earthquakes above M1.0. The biggest yellow circle is the Chaoyang ML3.3 earthquake, and the yellow and green triangles are the locations of the Songshan hot spring and Wuliying monitoring well, respectively.

temperature, high fluoride content (15.93 mg/L), and high silica content (54 mg/L); the water type is Na-SO4 (Yang et al., 2001). The main observation items of Songshan Spring were water mercury and there were high correspondences between mercury anomalies and earthquakes (Yang et al., 2001).

In addition, a seismic groundwater monitoring well named Wuliying is ~10 km near the Songshan spring. The Wuliying well is located on the subsidence transition zone at the northern edge of the Yanqing Basin, with compressive faults developing around the well area (Gao and Xing, 2011). The groundwater level observation is one of the items of the Wuliying well and is usually recorded at 1-min intervals by a SWY-2 digital instrument developed and produced by the Institute of Crustal Dynamics, China Earthquake Administration. The water-level sensor has a range of 0–50 m, resolution of 1 mm, sampling interval of 1 s, precision of 0.02 percent, and accuracy of 0.05 percent.

3 Methods

3.1 Data collection

Since the Songshan spring belongs to the Yanqing District Earthquake Agency, water samples from the mouth of the fresh spring were collected by the staff working at this station every 7–12 days; the sample collection was from August 2021 to August 2022, and a total of 36 water samples were collected over the monitored period. Each sample was stored in a 200 mL polyethylene bottle. All samples were sent monthly to the Beijing Research Institute of Uranium Geology for 41 trace element constituents analysis, including Li, Ti, Pb, Sc, Ni, Cu, Nb, Th, Zn, Tl, U, Ga, Mo, Ba, Rb, Cs, Sr, Be, Mn, Cr, Co, Y, and Bi as well as rare earth elements (La, Ce, Pr, Nd, Sm, Eu, Gd, Tb, Dy, Y, Ho, Er, Tm, Yb, and Lu) (Supplementary Material,). These trace elements' concentrations were analyzed with the same instrument (An ELEMENT XR mass spectrometer) and the same staff for accuracy. The analytical precision is better than ±2%.

3.2 Statistical analyses

We use 41 trace elemental composition data to calculate a Pearson correlation matrix (r values) that can quantitatively indicate the correlation between each element. The correlation matrix was a visual network by R program to check geochemical elemental clustering and grouping (Figure 4). In the network, each geochemical element is a node and each correlation is an edge in which the width of the edges according to the magnitude of the correlation and the placement of the nodes is a function of the pattern of correlations (Epskamp et al., 2012). This means that stronger correlations have shorter and wider edges and closer placement of nodes (Chen et al., 2021).

Data smoothing methods include LOWESS, rLOWESS, LOESS, and rLOESS using Matlab (Chen, 2023). The LOWESS (Locally Weighted Scatterplot Smoothing) means local regression using weighted linear least squares and a first-degree polynomial model. The rLOWESS means a robust version of LOWESS that assigns lower weight to outliers in the regression. The LOESS means local regression using weighted linear least squares and a second-degree polynomial model. The rLOESS means a robust version of LOESS.

4 Results

Songshan spring has no water level monitoring; we checked water level changes in the Wuliying well near the spring for hydrological responses to earthquakes. The groundwater level in the Wuliying well continuously increased from 1.3 to 1.8 m between July 2021 and August 2021 (Figure 2). No abnormal changes in groundwater level were found related to any earthquakes (Figure 2). The water level change also has no relationship to precipitation as there is only large precipitation during summer (from June to August every year).

The results of analyses of the 36 water samples are listed in the Supplementary Material, (Concentrations of 41 trace elements of each water sample in the Songshan spring). The PAAS-normalized 15 rare earth elements (REE) display remarkable positive Eu anomalies and flat distribution patterns (Figure 3A). Eu concentrations showed a significant increase from 0.002 to 0.007 mg/L from February 2022 to August 2022 (the end of sampling in August) (Figure 3B). These changes were more evident when data smoothing using the mathematic method (rLOWESS, robust Locally Weighted Scatterplot Smoothing) (Figure 3C). Eu had a marked increase after early February.

Apart from REE, the other 26 trace elements show different changes over the monitored period. Based on element correlative clustering, these elements' constitutes can be broadly classified into four groups (Figure 4). The first group consists of Li, Sc, Ti, and Pb elements which cluster each other in the correlation network (pink circles in Figure 4). The second group consists of Cu, Nb, Th, Zn, Tl, and U elements clustering in grey circles in Figure 4. The third group consists of Ga, Mo, Ba, Rb, Cs, and Sr elements clustering in green circles in Figure 4. The fourth group consists of Be, Mn, Cr, Co, Y, Bi, Cd, Sb, Ni, and V elements dispersing in the correlation network (white circles in Figure 4).

The elements of the first group had upward changes (Figure 5): Li, Sc, Ti, and Pb concentrations continued to rise from December 2021 to February 2022 and peak, then remained stable at high values from March to May 2022, and decreased from June to August 2022 (several months after the earthquake). These changes were quite marked when using the smoothing methods (LOWESS, rLOWESS, LOESS, and rLOESS) (Figure 5).

The elements of the second group had significant downward changes (Figure 6): Cu, Nb, Th, Zn, and Tl contents continued to decline from August 2021 to January 2022, then remained stable at minimum values from February to August 2022 (Figure 6). U contents declined from August 2021 to October 2021, then maintained stable values from November 2021 to February 2022, and the last decreased from March to August 2022 (Figure 6).

The elements of the third group had upward and then downward changes (up-convex shape) (Figure 7): elemental concentrations continued to rise from August 2021 to January 2022 and peaked, then remained stable at high values from February to April 2022, and the last decreased from May to August 2022 (Figure 7).

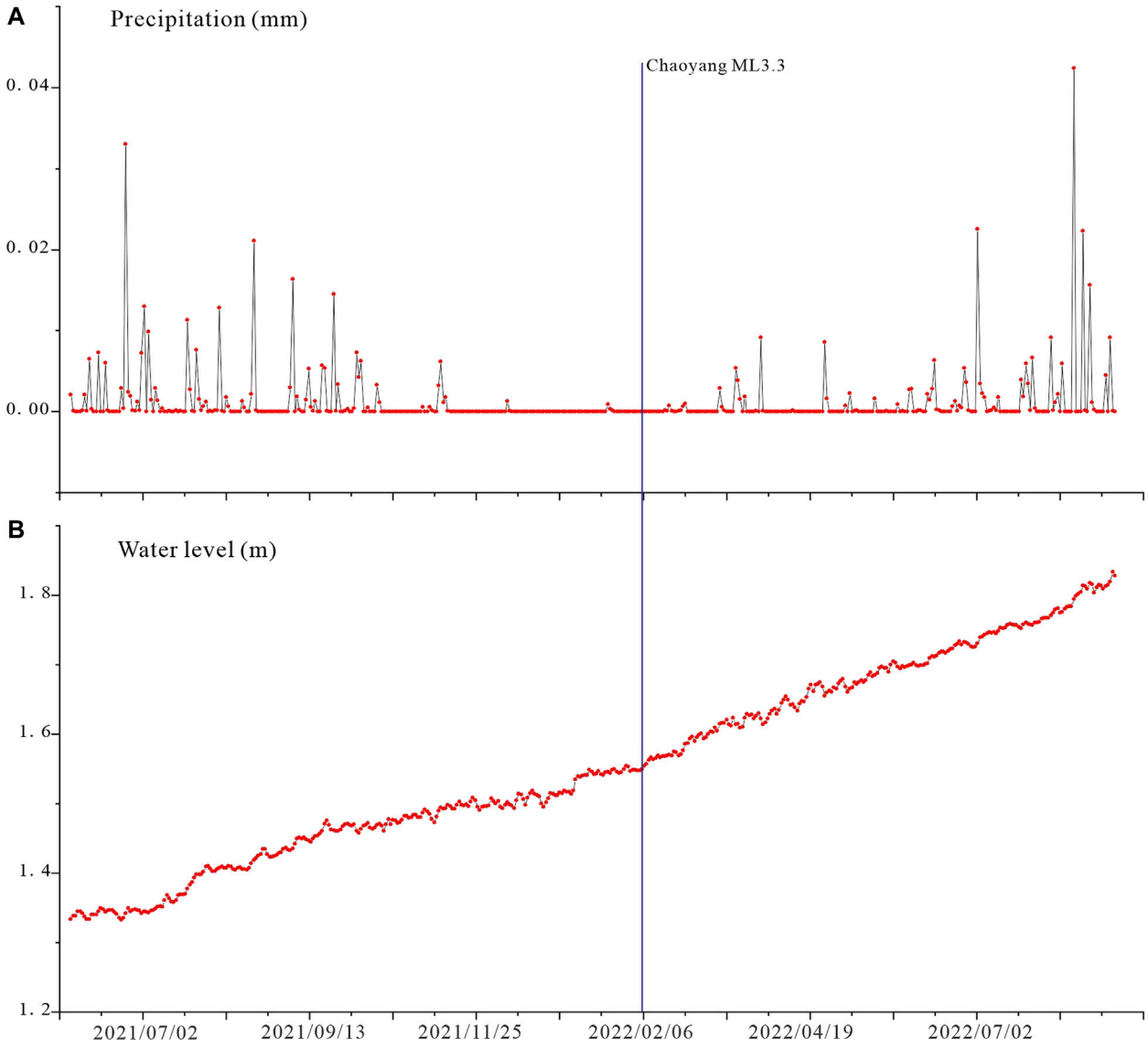

FIGURE 2
Precipitation **(A)** and water level changes **(B)** in the Wuliying well which is ~10 km away from the Songshan hot spring. The blue vertical line shows the time of the Chaoyang ML3.3 earthquake.

The elements of the fourth group had no regular changes, and the relationship with earthquakes was not clear.

5 Discussion

Chaoyang ML3.3 earthquake was an epicentral distance of ~75 km from Songshan hot spring (Figure 1). The seismic energy density produced by this earthquake at the Songshan hot spring was ~0.0019 J/m3 (calculation according to the method by Wang, 2007), which is the same order of magnitude with the minimum energy density (10−4 J/m3) that was required to trigger hydrological responses based on global observations (Wang, 2007). However, there were no changes in the groundwater level of the Wuliying well near the Songshan spring groundwater level to the Chaoyang earthquake, which means that the Chaoyang ML3.3 earthquake might have been too small to cause the hydrological responses of Songshan spring, and no additional water into the wellbore could be expected.

According to the above results, the changes in trace elements have a strong temporal correlation with earthquakes, which means that trace elements were probably sensitive to the small earthquake, but different kinds of trace elements have particular responses to the Chaoyang earthquake, for instance, the Eu element of rare earth elements had obvious upward changes after the Chaoyang earthquake. The first group elements' (Li, Sc, Ti, and Pb) concentrations had upward changes 2 months before the Chaoyang earthquake, then returned to their initial concentration a few months after the earthquake. The second group elements' (Cu, Nb, Th, Zn, Tl, and U) concentrations had downward changes a few months before the Chaoyang earthquake, then maintained stable minimum values until the end of sampling.

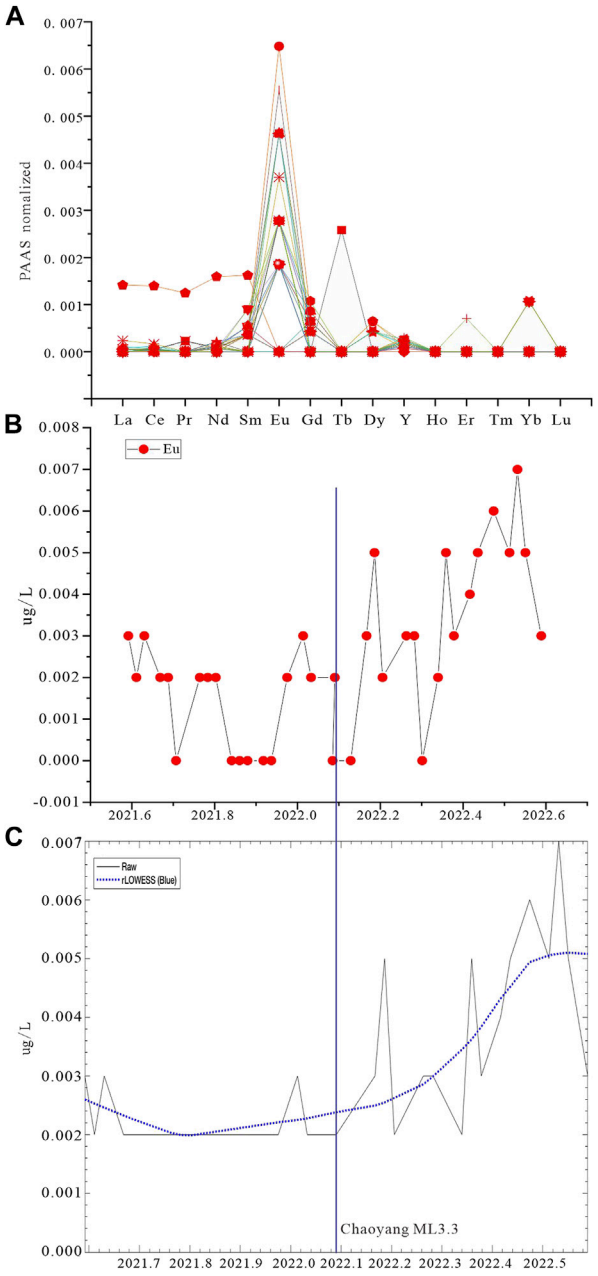

FIGURE 3
PAAS shale-normalized REE patterns **(A)** and variation of Eu element during the study period **(B,C)**. The blue vertical line shows the time of the Chaoyang ML3.3 earthquake.

5.1 Mechanism analysis

What mechanism could explain our observation? The trace elements were not commonly measured in the previous geochemical studies, and only a very limited number of cases could be found (Shi et al., 2020). Many previous studies have documented co-seismic groundwater level changes following earthquakes and have proposed several mechanisms to explain the responses, such as co-seismic static strain-induced dilation and compaction (Ge and Stover, 2000), liquefication or consolidation of sediments (Wang et al., 2001), and permeability changes caused by shaking (Brodsky et al., 2003). However, mechanism explanations for geochemical anomalies are relatively rare and based on co-seismic geochemical changes following the earthquake (Claesson et al., 2007; Shi et al., 2020). For instance, a great part of the geochemical variations in the chemical composition of groundwaters was attributed to aquifer mixing processes (Thomas, 1988). Geochemical gases involved in the Earth's degassing activity are considered responsible for water-gas-rock interaction processes able to induce chemical variations in groundwater composition (King, 1986; Martinelli, 2015). About all geochemical anomalies have been directly or indirectly attributable to deep fluid pressure variations induced by crustal deformative processes since fluid pressure is proportional to stress and volumetric strain (Petrini et al., 2012). In this study, we have examined many trace element constituents' responses to the earthquake in relatively high sample rates and found different constituents obviously increased or decreased changes before or after the Chaoyang earthquake. All trace elements' changes were not co-seismic, so previous mechanisms' explanations might not have been applied to changes in trace elements of our observation.

We considered the previously proposed mechanisms for changes in chemical elements (Claesson et al., 2007; Rosen et al., 2018; Shi et al., 2020). Favara et al. (2001) collected geochemical compositions (Ca, Cl, and SO4) at three thermal springs in the Umbria region of the Central Apennines (Italy) seismic swarm from 1997 to 1998. The authors suggested that the recorded variations actually seem to have been induced by permeability variations related to crustal deformation in the absence of elastic energy release. According to Claesson et al. (2007), the increase in reactive surface area would lead to more extensive water-rock interaction, and increases in concentrations of some dissolved cations would be expected. Rosen et al. (2018) proposed that the changes in trace elements were likely related to the release of groundwater of different residence times from pore spaces or fractures. Shi et al. (2020) suggested that the changes in trace elements were the combined result of the addition of small amounts of water from the reservoirs isolated by the hydraulic barrier and the changes in the physical-chemical environment following the earthquake.

In our study, the Wuliying well near Songshan spring had no groundwater level changes in our case, which indicates that there were no large volumes of chemically distinct groundwater entering the spring and mixing with the original water, so the mechanism of co-seismic strain and permeability changes were excluded. The mechanism of extensive water-rock interaction most likely explained the seismic responses in the Songshan spring as follows (Figure 8).

5.1.1 Mechanism analysis of REE

The Eu element of rare earth elements had obvious upward changes after the Chaoyang earthquake, and the upward pattern of changes was consistent with previous examples. For instance, following the Loma Prieta earthquake in 1989, major ion chemistries (Na, K, Ca, Mg, Cl, SO4, and HCO3) in stream water showed a marked increase in ionic strength, together with the changes in the excess stream discharge (Rojstaczer and Wolf, 1992). Rojstaczer and Wolf (1992) suggested that the additional stream discharge following the Loma Prieta earthquake was derived

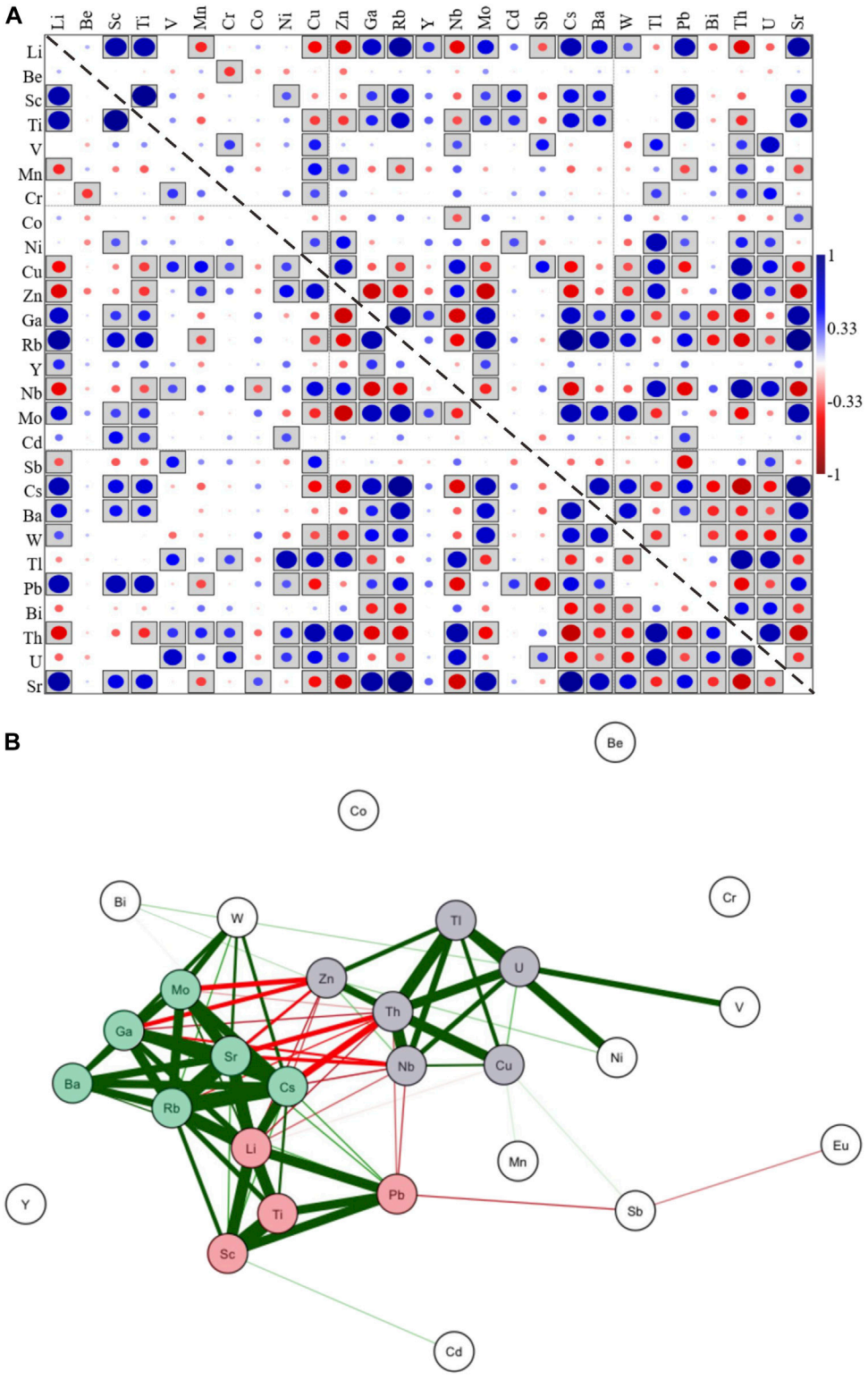

FIGURE 4
Element correlation matrix **(A)** and Elemental correlation cluster **(B)**. Each circle in **(A)** represents the strength of element correlation; the larger the circle, the stronger the correlation and the box shows that the correlation has statistical significance. Network in **(B)** structures based on Pearson correlation matrix of geochemical data. Each geochemical element is a node and each correlation is an edge. Stronger correlations have shorter and wider edges and closer placement of nodes.

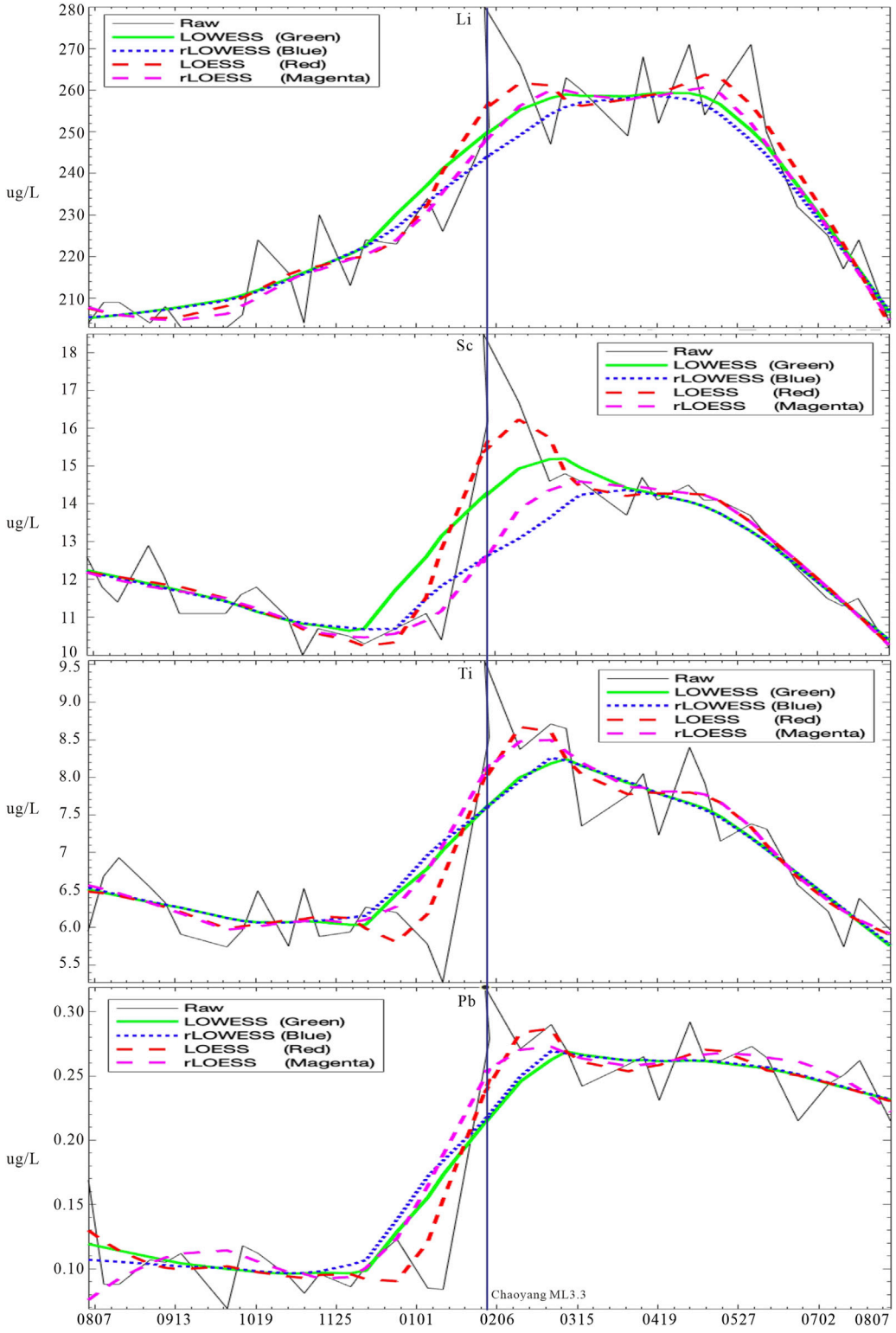

FIGURE 5
Variation of the first group of Li, Sc, Ti, and Pb during the study period (The black line indicates raw data. The green line, blue dotted line, red dashed line, and purple dashed line indicate the LOWESS, rLOWESS, LOESS, and rLOESS fitting methods, respectively). The blue vertical line shows the time of the Chaoyang ML3.3 earthquake.

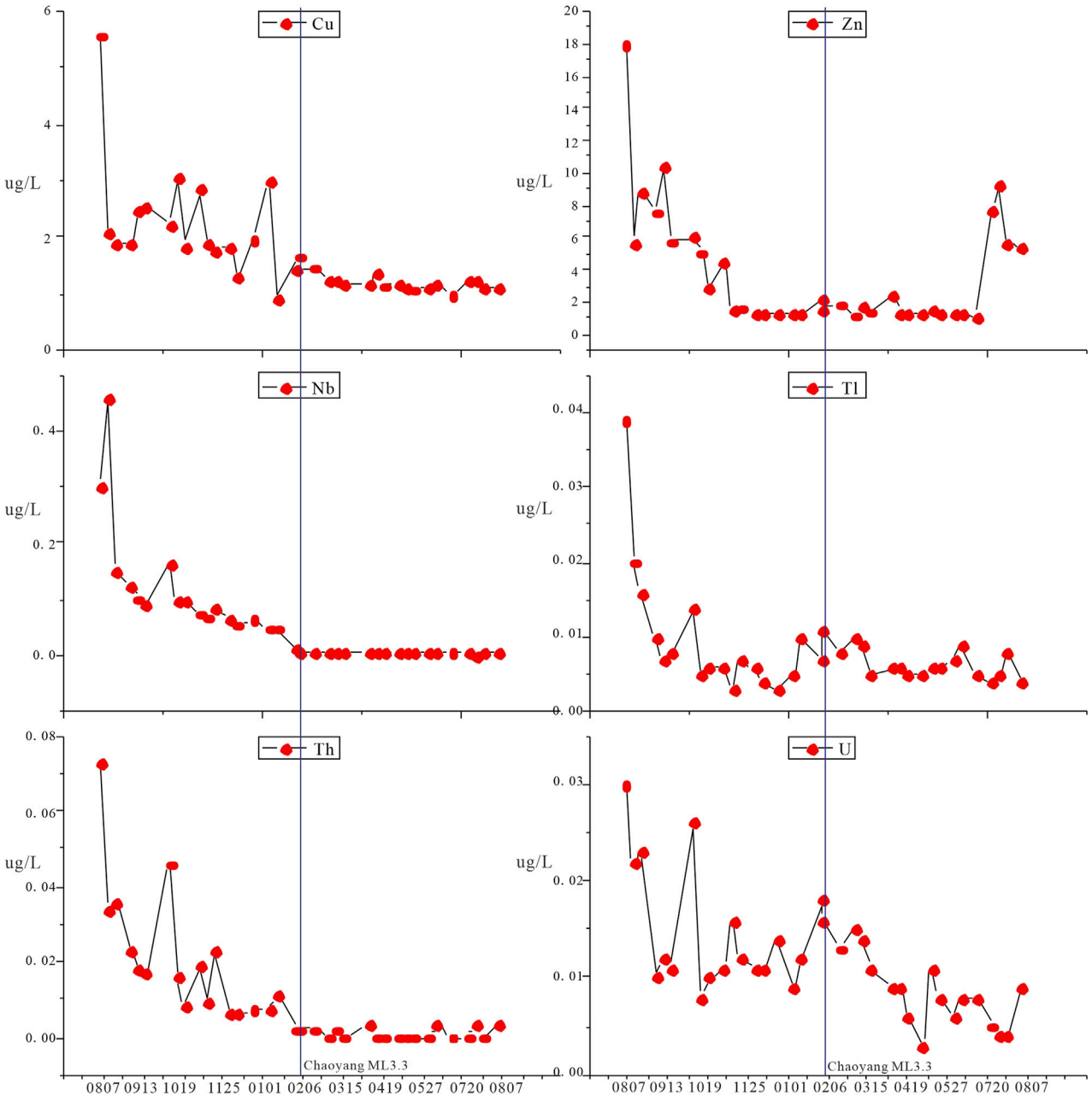

FIGURE 6
Variation of the second group of Cu, Nb, Th, Zn, Tl, and U during the study period. The blue vertical line shows the time of the Chaoyang ML3.3 earthquake.

from groundwater from the surrounding highlands of the drainage basin.

In our case, Songshan spring displayed remarkable positive Eu anomalies of REE (3A), which coincided with petrological evidence because the bedrock of Songshan spring is granite containing a large amount of feldspar minerals, which commonly became Eu-enriched during crystallization owing to the ready substitution of Eu2+ for Ca2+ (Taylor and McLennan, 1985; Chen et al., 2021). Eu concentrations showed obvious upward changes before the Chaoyang earthquake. The most likely mechanism was intensive water-rock interaction. The probable scenario was that rock ruptures after the earthquake increased the reactive surface area between rocks and groundwater, exposing more feldspar minerals to water, and leading to increased Eu concentrations in the water column (Figure 8).

5.1.2 Mechanism analysis of the first group trace elements

The first group of Li, Sc, Ti, and Pb elements increased before the earthquake then decreased significantly over a period of several months after the earthquake until it approached the pre-earthquake conditions. The type of changes were consistent with the previous

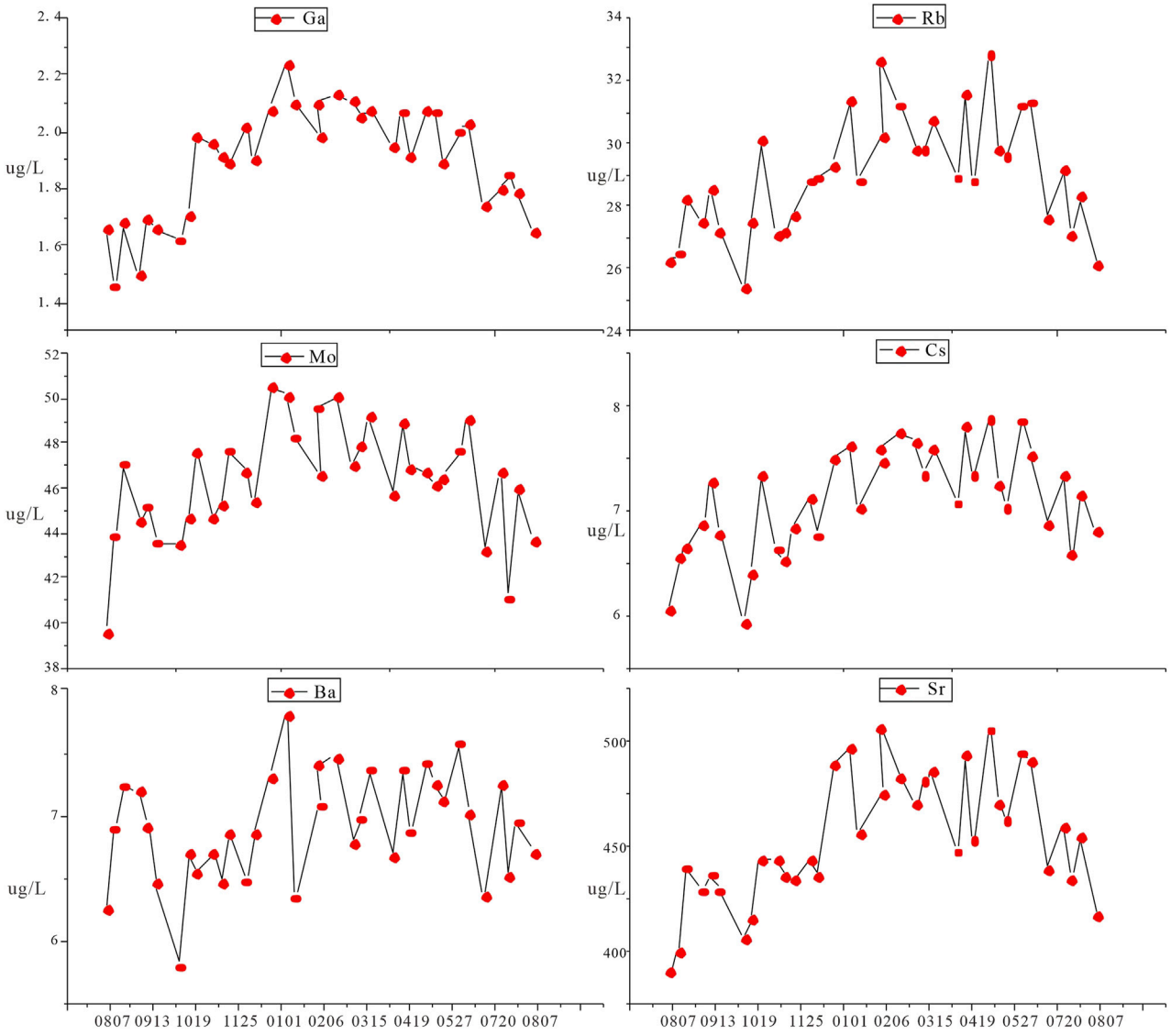

FIGURE 7
Variation of the third group of Ga, Mo, Ba, Rb, Cs, and Sr during the study period.

few cases. For instance, before the 1995 M 7.2 Kobe earthquake, chloride concentration gradually increased (Tsunogai and Wakita, 1995). The chloride changes were considered to be consistent with a 'drastic' increase in strain (Tsunogai and Wakita, 1995). The mechanism of extensive water-rock interaction can also explain the response that the first group elements rise rapidly before the earthquake.

Songshan spring came from granite, which is rich in these elements, for instance, Li is a typical lithophile and often enriched in mica and other silicate minerals and easy to hydrolyze. Sc has a very high partition coefficient in granites, Ti is high content in quartz, and Pb can replace K+ and Ca2+ in rock-forming minerals with isomorphism (Mou, 1999). Hence, the most likely scenario was that local stresses might create granite microcracks before the earthquake, exposing more fresh minerals to water, enhancing water-rock interaction, releasing more elements into the water column, and causing the rise response (Figure 8). Following the earthquake, microcracks may merge to form large-scale ruptures (Lockner and Beeler, 2002), the elements would accelerate into the water column, and the element concentrations would further rise until saturation. Several months after the earthquake, the stress would be redistributed, the fractures would no longer develop or partially fault-reseal (Claesson et al., 2007), and the elemental contents in the water column would decline.

5.1.3 Mechanism analysis of the second group trace elements

The second group of Cu, Nb, Th, Zn, Tl, and U elements concentrations had downward changes during a few months before the Chaoyang earthquake, then maintained stable minimum values until the end of sampling, and the pattern of changes was similar to the previous few examples. Claesson et al. (2004) reported pre-seismic rapid decreasing anomalies in the concentrations of Cr and Fe before the Mw 5.8 earthquake on

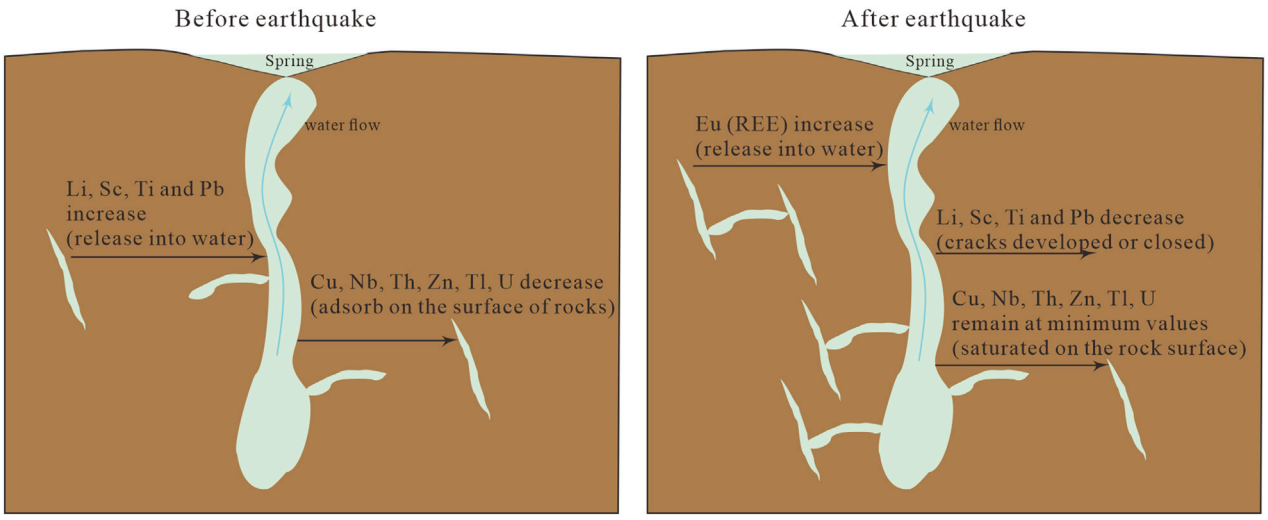

FIGURE 8
Concept model of earthquake-induced trace elements changes in Songshan spring. Microcracks led to intensive water-rock interaction before the earthquake, and Li, Sc, Ti, and Pb were released into water, and Cu, Nb, Th, Zn, Tl, and U adsorbed on the surface of rocks. After the earthquake, Eu (REE) was released into the water.

16 September 2002. The authors interpreted that the earthquake ruptured a hydrological barrier, permitting a rapid influx of water from other aquifers.

In our case, the second group elements declined before the earthquake with no addition of distinct additional water. Thus, the most likely mechanism was also intensive water-rock interaction. The pattern of falling changes in the second group elements was completely contrary to the pattern of rising changes in the first group elements. Because second group elements have large proton numbers and mass, and the elements with large mass mostly exist in minerals by the mechanism of adsorption (Mou, 1999), enhanced rock ruptures would result in the increase of the mineral surface area, and the increase of these elements adsorbed on the surface of minerals, leading to the decrease of the concentration of these elements in the water column (Figure 8). Due to the different adsorption and desorption capacity of different elements, the decline rate was inconsistent (Figure 6). These elements' concentrations decreased in groundwater further until the element contents were saturated on the rock surface.

5.1.4 Mechanism analysis of the third group trace elements

The third group of Ga, Mo, Ba, Rb, Cs, and Sr elements had upward and then downward changes (up-convex shape), and these elements were likely to be related to the season but not to the earthquake. These elements are closely located in the periodic table near the Ca element, indicating these elements have very similar chemical properties to Ca. According to petrology, elements of Ba, Rb, Cs, and Sr often replace Ca in the mineral with isomorphism (Mou, 1999). The solubility of Ca in water decreases with the increase in temperature; when the temperature is high in summer, these elements' concentrations decrease in the water, and when the temperature is low in winter, these elements' concentrations increase in the water.

Besides the mechanism of intensive water-rock interaction, slight changes in the physical-chemical or oxidation-deoxidation environment would cause changes in trace element concentrations. Thus, the changes in trace elements in the Songshan spring were mainly caused by the result of the water-rock interaction combined with the changes in the physical-chemical environment caused by the earthquake.

5.2 Relationship between trace elements and seismic activities

There were approximately 400 earthquakes occurring in the Beijing area during sampling (from August 2021 to August 2022) (Figure 1); only 22 of them were above M1.0, and the Chaoyang ML3.3 earthquake was the biggest one, which means that seismic activities in Beijing were dominated by frequent small earthquakes. In terms of the spatial distribution of earthquakes, these earthquakes mainly occurred in two groups of NE orderly active fault zones and one NW orderly Nankou-Sunhe Fault Zone which was controlled by the large-scale Zhangjiakou-Bohai Fault Zones in the northwest direction. The Chaoyang ML3.3 earthquake and Songshan hot spring were located in the northwest direction and were consistent with the distribution direction of Zhangjiakou-Bohai Fault Zones, so they had a strong spatial correlation.

From a time series perspective, trace elements of different groups had significant upward or downward changes before or after February. Coincidentally, the biggest Chaoyang earthquake occurred on February 3, so they had a strong temporally relationship. In addition to the Chaoyang earthquake, there were 10 earthquakes above M1.0 densely occurring from December 2021 to March 2022 (Figure 1); the swarm of earthquakes might be temporally related to changes in trace elements, but the spatial distribution of these earthquakes was not clustered and spread along a northwest direction which was also consistent with the distribution direction of Zhangjiakou-Bohai Fault Zones. Hence, a group of small earthquakes above M1.0, which is mainly the biggest Chaoyang

earthquake, indicates that the Zhangjiakou-Bohai seismic zones were strongly active in February, which probably caused the abnormal changes in trace elements.

On a regional scale, there were three earthquakes above M1.0 during sampling in the Yanqing district, and the three earthquakes occurred near the Mountain Front Fault of Nankou (Figure 1) which was far away from Songshan spring. At the same time, no earthquakes above M1.0 occurred during sampling in the Northern Marginal Fault Zones of the Yanqing basin which is closest to Songshan spring.

Above all, the Chaoyang earthquake had a small magnitude and longer epicenter distance, and trace elements had the potential to be more sensitive in detecting small changes caused by minor crustal strain. Hence, the monitoring of trace elements had temporal-spatial significance in the Beijing area where small earthquakes occurred frequently.

Notably, different geological and hydrogeological settings may show distinct sensitivities to trace element constitutes, thus sensitive trace elements to seismic activities are determined by the aquifer lithology and physical-chemical conditions for specific sites. In the Songshan spring aquifer system, Li, Sc, Ti, Pb, Cu, Nb, Th, Zn, Tl, U, and REEs were sensitive to earthquake stress and would be good candidates for monitoring earthquake activities. Furthermore, we propose to comparatively investigate the sensitivity of trace element composition in the Beijing area even in the Zhangjiakou-Bohai Fault Zone. Additionally, we do not know the changes in major ions and isotopes in Songshan spring, so more comprehensive geochemical composition should be provided in future research, providing additional useful information to deepen the understanding of the mechanism of geochemistry changes to earthquake stress.

6 Conclusion

This study has the following three conclusions.

1. Although the Chaoyang ML3.3 earthquake had a small magnitude and longer epicenter distance, some trace elements in Songshan spring are likely to be sensitive to crustal minor strain by the earthquake. The Eu element of rare earth elements had obvious upward changes after the earthquake. The first group consisting of Li, Sc, Ti, and Pb elements had significantly upward changes, and the second group consisting of Cu, Nb, Th, Zn, Tl, and U elements had downward changes before the earthquake.
2. The changes in trace elements in the Songshan spring were mainly caused by the result of the water-rock interaction.
3. The monitoring of trace elements had temporal-spatial significance in the Beijing area where small earthquakes occurred frequently. Furthermore, we proposed to comparatively investigate the sensitivity of trace element composition in the Zhangjiakou-Bohai Fault Zone.

Data availability statement

The original contributions presented in the study are included in the article/Supplementary Material, further inquiries can be directed to the corresponding author.

Author contributions

YC: Conceptualization, Investigation, Writing–original draft. JL: Writing–review and editing, Conceptualization, Investigation.

Funding

This work was supported by grants from the National Natural Science Foundation of China (41972027) and the Project of Monitoring, Forecasting, and Research of China Earthquake Administration (3JH-202201057).

Acknowledgments

We express our sincere thanks to two reviewers and Dr. Gaetano De Luca for valuable constructive comments on this manuscript that greatly enhanced the clarity and improved this work.

Conflict of interest

The authors declare that the research was conducted in the absence of any commercial or financial relationships that could be construed as a potential conflict of interest.

Publisher's note

All claims expressed in this article are solely those of the authors and do not necessarily represent those of their affiliated organizations, or those of the publisher, the editors and the reviewers. Any product that may be evaluated in this article, or claim that may be made by its manufacturer, is not guaranteed or endorsed by the publisher.

Supplementary material

The Supplementary Material for this article can be found online at: https://www.frontiersin.org/articles/10.3389/feart.2023.1260559/full#supplementary-material

References

Barberio, M. D., Barbieri, M., Billi, A., Doglioni, C., and Petitta, M. (2017). Hydrogeochemical changes before and during the 2016 Amatrice-Norcia seismic sequence (central Italy). *Sci. Rep.* 7 (1), 11735. doi:10.1038/s41598-017-11990-8

Brodsky, E. E., Roeloffs, E., Woodcock, D., Gall, I., and Manga, M. (2003). A mechanism for sustained groundwater pressure changes induced by distant earthquakes. *J. Geophys. Res.* 108 (B8), 2390. doi:10.1029/2002JB002321

Chen, Y. (2023). Time-frequency characteristics of groundwater in Wuliying monitoring well, Yanqing, Beijing and its relationship with regional seismic activity [J]. *North China Earthquake Sci.* 41 (2), 1–12. doi:10.3969/j.issn.1003–1375.2023.02.000

Chen, Y., Liu, J., Shen, B., Wang, Y., Wu, R., and Zhan, R. (2021). Geochemistry of lower ordovician microbialites on the yangtze platform, south China: implications for oceanic oxygenation at the onset of the GOBE. *Palaeogeogr. Palaeoclimatol. Palaeoecol.* 578, 110564. doi:10.1016/j.palaeo.2021.110564

Claesson, L., Skelton, A., Graham, C., Dietl, C., Mörth, M., Torssander, P., et al. (2004). Hydrogeochemical changes before and after a major earthquake. *Geology* 32 (8), 641–644. doi:10.1130/g20542.1

Claesson, L., Skelton, A., Graham, C., and Mörth, C. M. (2007). The timescale and mechanisms of fault sealing and water-rock interaction after an earthquake. *Geofluids* 7 (4), 427–440. doi:10.1111/j.1468-8123.2007.00197.x

De Luca, G., Di Carlo, G., and Tallini, M. (2018). A record of changes in the Gran Sasso groundwater before, during and after the 2016 Amatrice earthquake, central Italy. *Sci. Rep.* 8, 15982. doi:10.1038/s41598-018-34444-1

Epskamp, S., Cramer, A., Waldorp, L., Schmittmann, V., and Borsboom, D. (2012). Qgraph: network visualizations of relationships in psychometric data. *J. Stat. Softw.* 48, 1–18. doi:10.18637/jss.v048.i04

Favara, R., Italiano, F., and Martinelli, G. (2001). Earthquake-induced chemical changes in the thermal waters of the Umbria region during the 1997-1998 seismic swarm. *Terra nova.* 13 (3), 227–233. doi:10.1046/j.1365-3121.2001.00347.x

Gao, L., and Xing, C. Q. (2011). Two abnormalities in fluid precursor observation in beijing wuliying well and related discussion (in Chinese). *Northwest. Seismol. J.* 33 (3), 644–652. doi:10.3969/j.issn.0253-4967.2011.03.013

Ge, S., and Stover, S. C. (2000). Hydrodynamic response to strike-and dip-slip faulting in a halfspace. *J. Geophys. Res.* 105 (B11), 25513–25524. doi:10.1029/2000JB900233

Igarashi, G., Saeki, S., Takahata, N., Sumikawa, K., Tasaka, S., Sasaki, Y., et al. (1995). Groundwater radon anomaly before the Kobe earthquake in Japan. *Science* 269, 60–61. doi:10.1126/science.269.5220.60

Igarashi, G., and Wakita, H. (1995). Geochemical and hydrological observations for earthquake prediction in Japan. *J. Phys. Earth* 43, 585–598. doi:10.4294/jpe1952.43.585

Jiang, C. S., Wu, Z. L., and Li, Y. T. (2008). Estimating the location accuracy of the Beijing Capital Digital Seismograph Network using repeating events. *Chin. J. Geophys.* 51 (3), 817–827.

King, C. Y. (1981). Do radon anomalies predict earthquakes? *Nature* 262. doi:10.1038/293262a0

King, C. Y. (1986). Gas geochemistry applied to earthquake prediction: an overview. *J. Geophys. Res. Solid Earth* 91 (B12), 12269–12281. doi:10.1029/jb091ib12p12269

Kingsley, S., Biagi, P., Piccolo, R., Capozzi, V., Ermini, A., Khatkevich, Y., et al. (2001). Hydrogeochemical precursors of strong earthquakes: A realistic possibility in kamchatka. *Part C. Sol. Terr. Planet. Sci.* 26, 769–774. doi:10.1016/s1464-1917(01)95023-8

Kitagawa, Y., Koizumi, N., and Tsukuda, T. (1996). Comparison of postseismic groundwater temperature changes with earthquake-induced volumetric strain release: yudani Hot Spring, Japan. *Jpn. Geophys Res. Lett.* 23 (22), 3147–3150. doi:10.1029/96gl02517

Kopylova, G. N., Boldina, S. V., and Serafimova, Y. K. (2022). Earthquake precursors in the ionic and gas composition of groundwater: A review of world data. *Geochem. Int.* 60 (10), 928–946. doi:10.1134/s0016702922100056

Li, Z. C., and Huang, Q. H. (2014). Assessment of detectability of the Capital circle Seismic Network by using the probability-based magnitude of completeness (PMC) method. *Chin. J. Geophys.* 57 (8), 2584–2593. doi:10.6038/cjg20140818

Lockner, D. A., and Beeler, N. M. (2002). Rock failure and earthquakes, in *International handbook of earthquake and engineering seismology*. Editor W. H. K. Lee, et al. (San Diego: Academic Press), 505–537.

Manga, M., and Wang, C.-Y. (2015). *Earthquake hydrology, treatise on geophysics*. Amsterdam: Elsevier.

Martinelli, G., and Dadomo, A. (2017). Factors constraining the geographic distribution of earthquake geochemical and fluid-related precursors. *Chem. Geol.* 469, 176–184. doi:10.1016/j.chemgeo.2017.01.006

Martinelli, G. (2015). Hydrogeologic and geochemical precursors of earthquakes: an assessment for possible applications. *Boll. Geofis. Teor. Appl.* 56, 83–94. doi:10.4430/bgta0146

Martinelli, G. (2020). Previous, current, and future trends in research into earthquake precursors in geofluids. *Geosciences* 10, 189. doi:10.3390/geosciences10050189

Montgomery, D. R., and Manga, M. (2003). Streamflow and water well responses to earthquakes. *Science* 300, 2047–2049. doi:10.1126/science.1082980

Mou, B. L. (1999). *Elements in geochmistry*. Beijing: Peking University Press.

Petrini, R., Italiano, F., Riggio, A., Slejko, F. F., Santulin, M., Buccianti, A., et al. (2012). Coupling geochemical and geophysical signatures to constrain strain changes along thrust faults. *Boll. Geof. Teor. Appl.* 53, 113–134. doi:10.4430/bgta0017

Poitrasson, F., Dundas, S. H., Toutain, J.-P., Munoz, M., and Rigo, A. (1999). Earthquake-related elemental and isotopic lead anomaly in a springwater. *Earth. Planet. Sci. Lett.* 169 (3), 269–276. doi:10.1016/s0012-821x(99)00085-0

Roeloffs, E. A. (1998). Persistent water level changes in a well near Parkfield, California, due to local and distant earthquakes. *J. Geophys. Res.* 103 (B1), 869–889. doi:10.1029/97JB02335

Rojstaczer, S., and Wolf, S. (1992). Permeability changes associated with large earthquakes:An example from Loma Prieta, California. *Geology* 20 (3), 211–214. doi:10.1130/0091-7613(1992)020<0211:pcawle>2.3.co;2

Rosen, M. R., Binda, G., Archer, C., Pozzi, A., Michetti, A. M., and Noble, P. J. (2018). Mechanisms of earthquake-induced chemical and fluid transport to carbonate groundwater springs after earthquakes. *Water. Resour. Res.* 54 (8), 5225–5244. doi:10.1029/2017wr022097

Shi, Z. M., Zhang, H., and Wang, G. C. (2020). Groundwater trace elements change induced by M5.0 earthquake in Yunnan. *J. Hydrology* 581, 124424. doi:10.1016/j.jhydrol.2019.124424

Skelton, A., Andrén, M., Kristmannsdóttir, H., Stockmann, G., Mörth, C. M., Sveinbjörnsdóttir, Á., et al. (2014). Changes in groundwater chemistry before two consecutive earthquakes in Iceland. *Nat. Geosci.* 7, 752–756. doi:10.1038/ngeo2250

Skelton, A., Liljedahl-Claesson, L., Wästeby, N., Andrén, M., Stockmann, G., Sturkell, E., et al. (2019). Hydrochemical changes before and after earthquakes based on long-term measurements of multiple parameters at two sites in northern Iceland—a review. *J. Geophys. Res. SolidEarth(ja)* 124, 2702–2720. doi:10.1029/2018JB016757

Taran, Y. A., Ramirez-Guzman, A., Bernard, R., Cienfuegos, E., and Morales, P. (2005). Seismic-related variations in the chemical and isotopic composition of thermal springs near Acapulco, Guerrero, Mexico. *Geophys. Res. Lett.* 32 (14). doi:10.1029/2005gl022726

Taylor, S. R., and McLennan, S. M. (1985). *The continental crust: Its composition and evolution*. Oxford: Blackwell.

Thomas, D. (1988). Geochemical precursors to seismic activity. *Pure. Appl. Geophys.* 126 (2–4), 241–266. doi:10.1007/bf00878998

Toutain, J., Munoz, M., Poitrasson, F., and Lienard, A. (1997). Springwater chloride ion anomaly prior to a M L = 5.2 Pyrenean earthquake. *Earth. Planet. Sci. Lett.* 149 (1), 113–119. doi:10.1016/s0012-821x(97)00066-6

Tsunogai, U., and Wakita, H. (1995). Precursory chemical changes in ground water: kobe earthquake, Japan. *Jpn. Sci.* 269, 61–63. doi:10.1126/science.269.5220.61

Wakita, H. (1996). Geochemical challenge to earthquake prediction. *PNAS* 93 (9), 3781–3786. doi:10.1073/pnas.93.9.3781

Wang, C-Y. (2007). Liquefaction beyond the near field. *Seismol. Res. Lett.* 78, 512–517. doi:10.1785/gssrl.78.5.512

Wang, C.-Y., Cheng, L. H., Chin, C. V., and Yu, S. B. (2001). Coseismic hydrologic response of an alluvial fan to the 1999 Chi-Chi earthquake, Taiwan. *Taiwan. Geol.* 29 (9), 831–834. doi:10.1130/0091-7613(2001)029<0831:chroaa>2.0.co;2

Wang, C. Y., and Manga, M. (2010). *Earthquakes and water*. Berlin Heidelberg: Springer-Verlag.

Wang, K., Chen, Q.-F., Sun, S., and Wong, A. (2006). Predicting the 1975 Haicheng earthquake. *Bull. Seism. Soc. Am.* 96, 757–795. doi:10.1785/0120050191

Woith, H., Wang, R., Maiwald, U., Pekdeger, A., and Zschau, J. (2013). On the origin of geochemical anomalies in groundwaters induced by the Adana 1998 earthquake. *Chem. Geol.* 339, 177–186. doi:10.1016/j.chemgeo.2012.10.012

Yang, M., Liu, G., Liu, Z., Ma, J., Li, L., Wang, Z., et al. (2022). Geochemical characteristics of geothermal and hot spring gases in Beijing and Zhangjiakou Bohai fault zone. *Front. Earth Sci.* 10, 933066. doi:10.3389/feart.2022.933066

Yang, M., Wu, P., Wang, L., Fan, Z., and Liu, Y. (2001). A study on effect reflecting earthquake of mercury anomaly of songshan spring of yanqing county.beijing city (in Chinese). *Northwest. Seismol. J.* 23 (2), 120–124.

frontiers | Frontiers in Earth Science

TYPE Brief Research Report
PUBLISHED 02 November 2023
DOI 10.3389/feart.2023.1286817

Check for updates

OPEN ACCESS

EDITED BY
Paolo Capuano,
University of Salerno, Italy

REVIEWED BY
Simona Gabrielli,
National Institute of Geophysics and Volcanology (INGV), Italy
Boyko Ranguelov,
University of Mining and Geology "Saint Ivan Rilski", Bulgaria

*CORRESPONDENCE
Lisa Pierotti,
l.pierotti@igg.cnr.it

RECEIVED 31 August 2023
ACCEPTED 12 October 2023
PUBLISHED 02 November 2023

CITATION
Martinelli G, Pierotti L, Facca G and Gherardi F (2023), Geofluids as a possible unconventional tool for seismic hazard assessment.
Front. Earth Sci. 11:1286817.
doi: 10.3389/feart.2023.1286817

COPYRIGHT
© 2023 Martinelli, Pierotti, Facca and Gherardi. This is an open-access article distributed under the terms of the Creative Commons Attribution License (CC BY). The use, distribution or reproduction in other forums is permitted, provided the original author(s) and the copyright owner(s) are credited and that the original publication in this journal is cited, in accordance with accepted academic practice. No use, distribution or reproduction is permitted which does not comply with these terms.

Geofluids as a possible unconventional tool for seismic hazard assessment

Giovanni Martinelli[1,2,3], Lisa Pierotti[4]*, Gianluca Facca[4] and Fabrizio Gherardi[4]

[1]Istituto Nazionale di Geofisica e Vulcanologia (INGV), Palermo, Italy, [2]Institute of Eco-Environment and Resources, Chinese Academy of Sciences (CAS), Lanzhou, China, [3]Laboratory of Petroleum Resources Research, Institute of Geology and Geophysics, Chinese Academy of Sciences (CAS), Lanzhou, China, [4]Consiglio Nazionale Delle Ricerche (CNR), Istituto di Geoscienze e Georisorse (IGG), Pisa, Italy

In recent decades, phenomenological methods known as Recognition of Earthquake-Prone Areas (REPA) were set up for identifying potential sites of powerful earthquakes. The information on potential earthquake sources provided by the REPA method is an essential part of seismic hazard assessment methodology. For the first time, we have combined global-scale information on the geographic occurrence of geofluids with global-scale information on earthquake occurrence, heat flow distribution, and S-wave dispersion, to gain insights into the evolution of local stress-strain fields. We focused on areas characterized by the occurrence of thermal waters and/or by the release of deep-seated gases, as traced by the isotope composition of associated helium. We noticed that the geographic distribution of these geofluids could serve as an indirect indicator of crustal permeability anomalies generated by crustal deformation procedures. This study proposes adding geofluids to the list of fundamental geological parameters to be considered in hazard assessment research.

KEYWORDS

seismic hazard, thermal waters, helium isotopes, heat flow distribution, S-wave dispersion

1 Introduction

The development of a culture of preventative measures including seismic hazard assessment, micro zonation studies, and proper building rules, can reduce the severity of the damage caused by earthquakes. In this framework, the Probabilistic Seismic Hazard Assessment (PSHA) approach has become the most prevalent and standard method for addressing seismic hazard assessment (e.g., Giardini et al., 2003). The PSHA is based on the use of probability distributions for magnitudes and source site distances recorded in earthquake catalogs, as originally proposed by Cornell (1968). The most relevant weakness of the PSHA is the dependence of the probability theory on the Gutenberg-Richter magnitude and on the completeness of available earthquake catalogs (e.g., Krinitzsky, 1995). Petersen et al. (2014) proposed to improve the PSHA by incorporating GPS and further geodetic data. Furthermore, various countries with consistent gaps in their earthquake catalogs have adopted Deterministic Seismic Hazard Assessment (DSHA) techniques (e.g., Kramer, 1996). An accurate definition of earthquake sources plays a prominent role in developing a seismic hazard assessment strategy, regardless of the applied methodology, either probabilistic or deterministic. To this purpose, a phenomenological approach for identifying possible locations of strong earthquakes was

established, known as the Recognition of Earthquake-Prone Areas (REPA) method (Gelfand et al., 1976 and references therein). The information on potential earthquake sources delivered by the REPA is an important component of the seismic hazard assessment, as envisioned by the more recent neo-deterministic seismic hazard assessment (NDSHA) methodology (Panza et al., 2012; and references therein). It combines a morpho-structural zoning method, which defines the locations of nodes over the study region, and a pattern recognition technique, which divides all the nodes into seismogenic and non-seismogenic ones to a specific cutoff of magnitude (Zhang et al., 2021; and references therein). The approach assumes that strong earthquakes are correlated with the nodes formed around intersections of lineaments. The nodes are delineated by the morpho-structural zoning method (MSZ), which is based on geomorphologic and geological data and does not rely on a knowledge of past seismicity (Gorshkov et al., 2003; Gorshkov and Soloviev, 2021). The seismogenic nodes defined by pattern recognition provide first-order systematic information that may significantly contribute to a reliable seismic hazard assessment. The information on the possible locations of strong earthquakes provided by the methodology can be directly incorporated into the neo-deterministic procedure (NDSHA) for seismic hazard assessment, filling in possible gaps in known seismicity (Panza et al., 2012). One of the main advantages of the MSZ is that it does not require prior knowledge of the regional seismicity of the studied region since it is based on the analysis of the available topographic, tectonic, and geological data, whereas paleoseismological studies require information about past seismic activity. Newer applications named Neo-Deterministic Seismic Hazard Assessment (NDSHA) proposed by Zhang et al. (2021) also take into account morpho-structural zoning, which in turn takes into account nodes (fractured areas), lineaments, and topographical features, such as the highest and lowest elevations of the studied area. The steepness of topographic surfaces and the sharpness of morphostructural parameter fluctuations, among other parameters, may indicate high tectonic activity. This paper underlines that the location of deep-seated geofluids' natural emissions is globally tied to different classes of tectonic activity because these features bring information on processes that largely occur in the lower crust. This in turn allows for identifying the surface projection of normally hidden discontinuities that influence geometry and patterns of seismic release. Thus, the geographic distribution of geofluids could be utilized as an indirect indicator of different classes of crustal permeability anomalies eventually generated by crustal deformation processes (e.g., Tamburello et al., 2018; Tamburello et al., 2022 and references therein). Moving on these grounds, this work aims to identify possible interrelations between areas of active seismicity, the location of thermal springs, and mantle-derived fluid emissions, as revealed by their $^3He/^4He$ signature, and additional geophysical parameters, such as heat flow, and S-wave distribution, in order to identify general criteria to relate seismic events and deep-seated geofluids.

2 Material and methods

We exploited the concept widely consolidated in the literature that fluid dynamics and rock deformation processes are strongly linked, to search for possible global correlations between seismicity, and a number of geophysical and geochemical parameters measurable at/from the surface. The justification for this approach stems from the fact that several authors have already highlighted a correlation between the occurrence of significant earthquakes and anomalous fluids (Irwin and Barnes, 1980; Gold and Soter, 1984; Manga et al., 2012; Chiodini et al., 2020). It is well-established that earthquakes have the potential to favor the onset of new, underground fluid flow regimes when they are capable of causing significant shaking and permanent strains in large rock volumes. Significant volumes of fluids can be permanently displaced when rocks, even with reduced initial permeability, are pervasively fractured by the upward propagation of seismogenic faults. Suitable conditions for the expulsion of thermal waters can be achieved along seismogenic faults (Curewitz and Karson, 1997; Vannoli et al., 2021; Wu et al., 2023). Geofluids can be displaced over large distances and for long times, possibly until the surface, through zones of enhanced permeability in the Earth's crust, under the effect of pressure gradients (Gleeson and Ingebritsen, 2017). Heat generation, crustal deformation, gravity effects due to the topographic relief, diagenetic processes, and overpressuring due to circulating fluids are effective mechanisms generating fundamental pressure forces at mid-crustal depth, up to the Earth's surface (Bredehoeft and Norton, 1990). On these grounds, we tried to match the information contained in a number of global, georeferenced compilations now available in the literature, to highlight possible relationships between different parameters and seismicity. In particular, we considered the following datasets: i) carbon dioxide emissions (Irwin and Barnes, 1980; Tamburello et al., 2018); ii) heat flow (Lucazeau, 2019); iii) S-wave dispersion (Debayle et al., 2016; Hasterok et al., 2022) and we updated datasets of thermal springs (Waring, 1965; Tamburello et al., 2022) and isotope composition of helium (Abedini et al., 2006). By taking advantage of recently computerized catalogs of seismicity (Storchak et al., 2013), we followed the same approach already utilized in the literature about the investigation of the spatial relationships between the distribution of earthquakes (Figure 1), and the location of anomalous fluid emissions (e.g., Kuz'mina and Novopashina, 2018; Tamburello et at., 2018), to identify areas potentially capable of hosting future strong earthquakes (M>6). A specific advancement of this work was the critical re-evaluation of the helium database by Abedini et al. (2006), and its extension via the addition of present-day geofluids data published until 2022. The largest volcanic calderas on Earth commonly extend over areas of 10–500 km^2 (Mason et al., 2004). These areas are characterized by gaseous emissions of predominant volcanic origin that are not of interest to the present treatment. Therefore, in order to filter out purely volcanic gases from our database, we decided to consider only gas emissions located beyond a prudential radius of 30 km from the main volcanic edifices worldwide.

2.1 World thermal springs dataset

In 1965, Waring compiled one of the most comprehensive available data sets about the distribution of thermal springs worldwide (Waring, 1965). More than 6,000 sites, with one or more springs for each site, were identified in more than 100 countries. Tamburello et al. (2022) digitized and enlarged

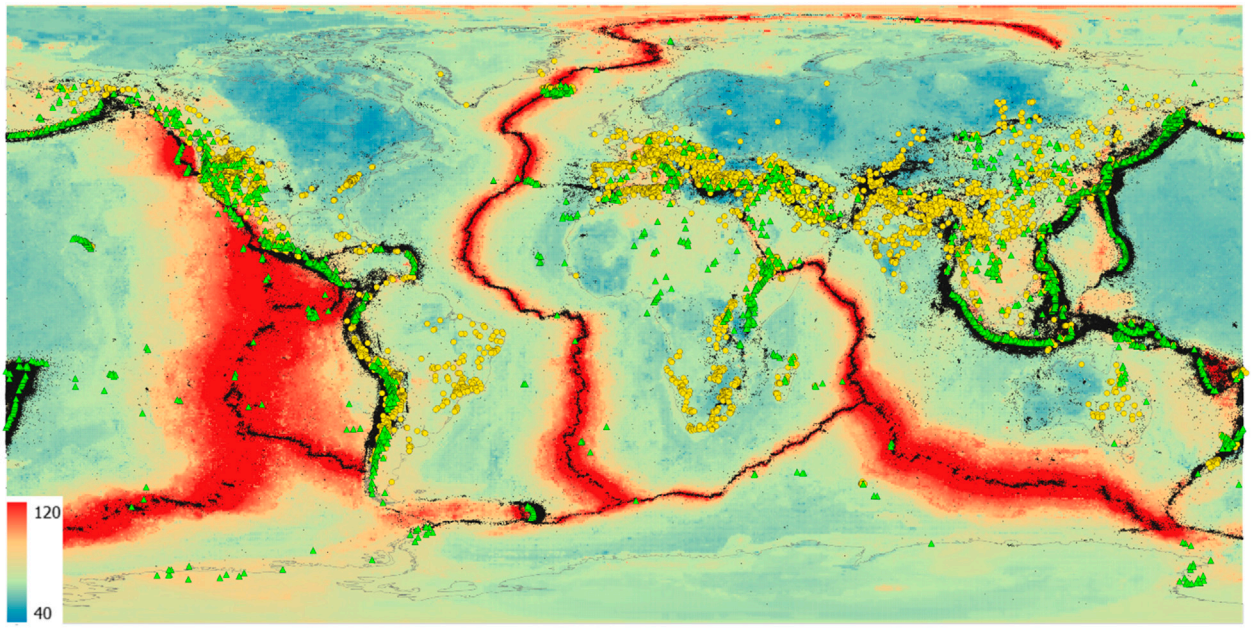

FIGURE 1
Heat flow map (Lucazeau, 2019) with location of (1) thermal springs (yellow dots; after Waring, 1965; Wexsteen, et al., 1988; Ciezkowski et al., 1992; Pesce, 2005; Wang, 2008; Lahsen et al., 2010; Yousefi et al., 2010; Chandrasekharam et al., 2015), (2) Holocenic and Pleistocenic volcanoes (green triangles; Global Volcanism Program, 2013), (3) 4<M<9.2 earthquakes (black dots; Storchak et al., 2013; http://www.isc.ac.uk/iscgem/accessed on 20 July 2023).

this data set with Supplementary Data S1 from recent literature, including additional information on geographical coordinates, temperatures, and flow rates. These data have been statistically processed and visualized with machine-learning algorithms, in a GIS environment (Graser, 2013). In order to integrate the dataset with further thermal springs in areas where possible lack of recent data was qualitatively observed such as Argentina (Pesce, 2005), Chile (Lahsen et al., 2010), China (Wang, 2008), Iran (Yousefi et al., 2010) Poland (Ciezkowski et al., 1992), Switzerland (Wexsteen, et al., 1988) and Yemen (Chandrasekharam et al., 2015), their geographic location having been georeferenced using the QGIS software (http://www.qgis.org).

2.2 World helium dataset

Helium (hereafter He) is the lightest of the noble gases, and because of its low atomic mass, is affected by strong fugacity values. He exists on Earth as two isotopes, ^3He and ^4He, with the former being primarily primordial and stored in the mantle and the latter being continuously produced in the Earth's interior by Uranium and Thorium decay (Ozima and Podosek, 2004). The radiogenic ^4He produced in the crust dominates the He flux in stable continental regions (mantle He 1%). The primordial ^3He, on the other hand, escapes into the atmosphere primarily from volcanoes and active tectonic regions (from extensive to compressive), making the He isotopic ratio ($^3He/^4He$) a powerful tool for recognizing mantle-crust tectonics also in the absence of volcanic evidence (e.g., O'nions and Oxburgh, 1983; Lupton, 1983). We consider the database compiled by Abedini et al. (2006) as a background document. In its original version (Version 1.0), this database was an MS Excel file with more than 5,000 entries on noble gas concentrations and isotopic ratios published until 2003. Data refer to geofluids and rocks from different geological and geotectonic environments. In this work, we only focus on present-day fluids discharged from springs, wells, mofetes, and fumaroles, and we complemented the dataset with additional $^3He/^4He$ analyses on geofluids published until 2022. Criteria for the selection of new data include the availability of full geographical coordinates, and/or sufficiently accurate location maps in the original manuscripts, to extract approximate information at least on the coordinates of the sampling points.

3 Discussion

3.1 Thermal springs, geodynamic and seismicity

Most of the areas hosting thermal springs overlap earthquake distribution and/or are located frequently within a radius of 30 Km from the main volcanic edifices. Further thermal springs are located outside volcanic areas in faulted zones (Figure 1).

About 60% of hydrothermal fluids recorded in the world are in the range 30°C–70°C, corresponding to the reservoir's depths in the range of 2–3 km, depending on local/regional geothermal gradients, and on the specific geometry and recharge mechanisms of the underground circulation paths. Below this range of depths, the weight of the overlying rocks significantly decreases porosity and permeability, hindering the onset of well-extended, and spatially

continuous hydrothermal circuits (Twiss and Moores, 1997). A broad literature also confirmed that vertical permeability may significantly change under the effect of tectonic activity (e.g., among many others, Wang et al., 2016; Brogi et al., 2021): faulting induced by seismic events has been effective in generating thermal springs emissions belonging to hydrothermal systems due to rock fracturing and the availability of feeding groundwaters. Wang and Manga (2015) and Sato et al. (2020) reported detailed descriptions of the opening or re-opening phases of ephemeral or permanent warm water springs related to significant local seismic events. According to Tamburello et al. (2022) thermal springs belonging to hydrothermal circuits are chiefly located in extensional faulted areas characterized by the occurrence of earthquakes above magnitude 4. Faults are characterized, among other parameters, by a length and by a width usually obtained by aftershock distribution (Wells and Coppersmith, 1994). In turn, length and width are roughly proportional to the magnitude of mainshocks capable of inducing faulting effects (Leonard, 2010). Seismic events below magnitude 4 are generally considered not to have sufficient energy to generate highly faulted areas, and/or faults of sufficient length and width to sustain hydrothermal circulation (Wells and Coppersmith, 1994). On the reverse, earthquakes in the magnitude range of 4–6 are believed to generate fault lengths in the range of 1–30 km (Wells and Coppersmith, 1994). Most earthquakes occur in the crust, in the depth range of 10–40 km (e.g., Maggi et al., 2000), which implies that earthquakes below magnitude 6 do not have the energy to generate faults capable of deepening from the surface down to the bottom of the Earth's crust. Conversely, moderate and strong seismic events (M>6.5) can maintain relatively high values of crustal permeability during geological time allowing for the emission of mantle-derived geofluids (Figure 1). Faulting induced by seismic events of the considered catalog has been effective in generating thermal springs emissions belonging to hydrothermal systems due to rock fracturing and the availability of feeding groundwaters. In order to better understand the effects of tectonic and possible geothermal anomalies on thermal spring distribution the heat flow map compiled by Lucazeau (2019) has been considered (Figure 1). Thermal springs appear mostly related to seismic activity that occurred in areas characterized by relatively recent (0.2 Ma) orogenetic phases (Hasterok et al., 2022) while a further group of thermal springs is located in areas not affected by volcanic activity or by significant seismic activity. In these areas, possible effects of palaeotectonic activity belonging to orogenetic phases of the first Quaternary period (1–2 Ma) (Hasterok et al., 2022) probably survived during geological time. This is the case in Brazil.

3.2 Helium, geodynamic, and seismicity

Noble gases and He isotope ratios in particular, can be used as effective tools (e.g., Mamyrin and Tolstikhin, 1984; Porcelli et al., 2002; Ozima and Podosek, 2004; Burnard, 2013; Sano et al., 2014; Sano et al., 2015; Liu et al., 2023) to study the origin of deep (crustal or mantle) degassing in active tectonic regions, and are deemed capable of providing information on the presence of faults of considerable extension and depth produced by recent and past M>6 earthquakes. Figure 2 shows the R/Ra values for all the helium isotope data available in Abedini et al. (2006) and updated in this work, with respect to the earthquake distribution deduced from the databases described by Storchak et al. (2013); http://www.isc.ac.uk/iscgem/ accessed on 20 July 2023) and with respect to volcanic edifice distribution (Hasterok et al., 2022 and references therein).

We consider the highest $^3He/^4He$ value as representative of the region of provenance when multiple analyses are available. Where available, the $^3He/^4He$ values normalized to air and corrected for air contamination (R_C) are preferred to air-normalized values (R_A), to exclude helium isotope data possibly affected by the entrainment of air-derived helium (e.g., Craig et al., 1978; $R_A = (^3He/^4He)_m/(^3He/^4He)_{air}$). Typical crustal values are about 0.02 R_A, due to relatively high ^4He continental abundances generated via $U-Th$ decay (e.g., Mamyrin and Tolstikhin, 1984; Andrews, 1985). Mantle values are 6–8 R_A for the old subcontinental lithospheric mantle (SCLM) and mid-ocean ridge basalts (MORB), respectively (e.g., Kurz et al., 1982; Dunai and Baur, 1995; Gautheron and Moreira, 2002). Taking these end-members as reference, we tentatively consider a threshold of $R_C > 1.22\,R_A$ to clearly identify geofluids with a high mantle component. The $R_C = 1.22\,R_A$ value corresponds to a mantle contribution of 15% (MORB) to 20% (SLCM), depending on the geotectonic environment. An even higher contribution of about 22.3% can be estimated in subduction zones, where the mantle component is characterized by an average value of 5.4 ± 1.9 R_A (e.g., Hilton et al., 2002). Interestingly, a different threshold than the relatively conservative value of $R_C > 1.22\,R_A$ selected here could be used to trace unequivocally mantle contribution in surficial fluids. For example, a threshold value of 1 R_A would indicate the presence of a magmatic or mantle helium contribution of up to 12.3%, based on a MORB-type signature of the local mantle component, in the case where atmospheric contamination and/or contribution may be waived based on checking of $^4He/^{20}Ne$ values (e.g., Craig et al., 1978). In the absence of information on $^4He/^{20}Ne$, in our analysis we adopted the conservative approach of considering only $^3He/^4He$ significantly higher than the atmospheric ratio ($> 1.22\,R_A$).

Most frequent values (about 43% of the considered database) are below the threshold of 1.22 Ra. The highest values are found close to volcanic areas, in rifted geological environments, and in anomalously high heat flow areas, with maxima recorded in Iceland (e.g., Hilton et al., 1990; Poreda et al., 1992), where a mantle plume reaches the earth's surface.

One of the primary objectives of seismology is to accurately delineate and analyze the diverse physical characteristics of the Earth, including but not limited to temperature, composition, volatile content, and the existence of partial melt. Over the past 2 decades, there has been a significant enhancement in the resolution of global S wave upper mantle tomographic models. The primary factor contributing to this phenomenon is the expansion of accessible data and the advancement of automated methodologies capable of analyzing a substantial volume of surface wave seismograms. In particular, Lebedev and van der Hilst (2008) observed that low-Sv-velocity anomalies beneath mid-ocean ridges extend down to ~100 km depth. Pronounced seismic lithosphere beneath cratons extends down to ~200 km. Low-velocity zones are weak or absent beneath most cratons. Debayle et al. (2016 and references therein) discovered a notable azimuthal anisotropy inside

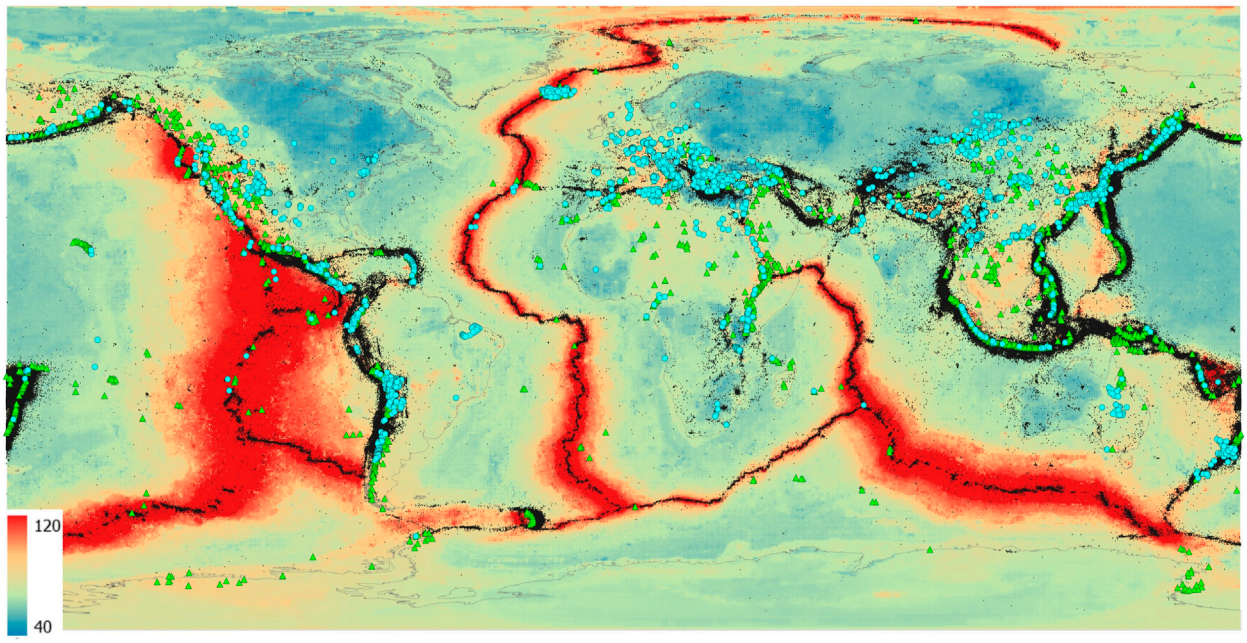

FIGURE 2
Heat flow map (Lucazeau, 2019) with location of (1) geofluids analyzed for helium isotope composition (blue dots; Abedini et al., 2006; revised and updated), (2) Holocenic and Pleistocenic volcanoes (green triangles; Global Volcanism Program, 2013), (3) 4<M<9.2 earthquakes (black dots; Storchak et al., 2013; http://www.isc.ac.uk/iscgem/ accessed on 20 July 2023).

the first 200 km of the Earth's mantle. Importantly, their findings indicate that this anisotropy does not exhibit a greater extent beneath continents compared to oceans. In their study, Adenis et al. (2017) presented also a comprehensive model of shear wave attenuation in the upper mantle on a global scale. The findings of their research demonstrate a notable association between surface tectonics and shear wave attenuation, specifically up to a depth of 200 km. The model reveals that regions underlying continents exhibit lower levels of attenuation, whilst regions underlying oceans display higher levels of attenuation. Anomalies that exhibit attenuation are observed beneath mid-ocean ridges at depths reaching 150 km, as well as beneath the majority of Pacific hot spots spanning from the lithosphere to the transition zone. The existence of extensive attenuating anomalies observed at a depth of 150 km in the Pacific Ocean indicates the presence of many thermal plumes situated within the asthenosphere. Montagner et al. (2007) provided pieces of evidence to support the existence of a direct correlation between the inferred mantle depth origin based on seismic tomography and the $^3He/^4He$ ratios observed in erupted magmas on a continental scale. The utilization of surface wave dispersion measurements and seismic tomography has provided insights into the relationship between tectonic settings and lithospheric seismic velocities. It has been observed that old cratons exhibit the highest seismic velocities, whereas tectonically active places tend to have relatively lower velocities. These findings could be better constrained by $^3He/^4He$ data and by heat flux data.

Considering the dispersion of S-waves (Debayle et al., 2016; Hasterok et al., 2022; see Figure 4), it was observed that most of anomalous ^3He areas are located above rock volumes affected by significantly low Vs. values.

Low Vs. values at depths in the order of 70 km are routinely interpreted as areas where partial melting processes are active (the phenomenon that occurs when a rock is subjected to temperatures high enough to cause certain minerals to melt, but not all of them). Therefore, under such conditions, the presence of fluids cannot be excluded, actually, it is very likely. S-wave dispersion may indicate, among others, the occurrence of deep-seated geofluids (Shito et al., 2006; Anderson, 2007; Unsworth and Rondenay, 2013). The obtained map of Helium 3 values has been compared with earthquake distribution deduced by databases described by Storchak et al. (2013); http://www.isc.ac.uk/iscgem/ accessed on 20 July 2023). High ^3He values recorded in high heat flow areas affected by deep geofluid feeding may be considered within tectonically active areas considered by the scientific literature currently available (e.g., Torgersen, 1993; Ballentine and Burnard, 2002; Polyak et al., 2020).

4 Selected candidate areas prone to significant next earthquakes

Figure 3 shows the correlation between heat flow and S-wave negative velocity perturbations for those areas where non-volcanic geofluids issue at the surface. In particular, this diagram only includes geofluids with an approximate minimum mantle contribution of 15%, as indicated by their $^3He/^4He > 1.22$ Ra. The top-left corner of Figure 4 shows regions characterized by relatively high heat flow values (Lucazeau, 2019) that are significantly affected by negative velocity perturbations (Debayle et al., 2016; Hasterok et al., 2022). This feature is typically associated with regions of major degassing, possibly linked to hidden magmatic bodies, or mantle

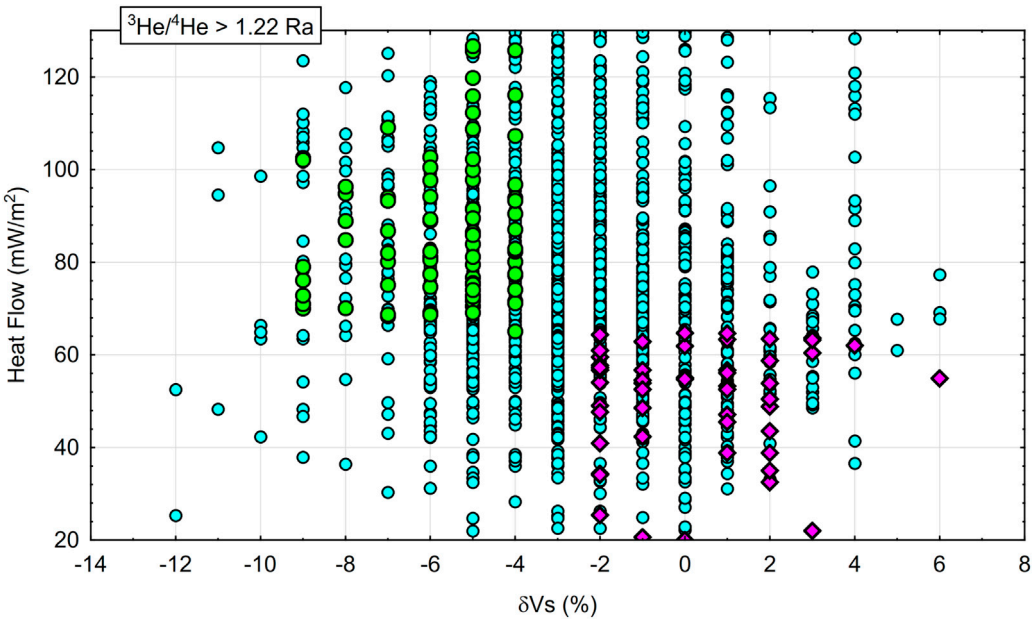

FIGURE 3
Heat flow vs. δVs (%) correlation plot for non-volcanic geofluids with $^3He/^4He$ > 1.22 Ra (after Abedini et al., 2006, modified and updated). Within this framework, we consider as "non-volcanic" those geofluids that emerge at the Earth surface at a minimum distance of 30 km from main volcanic edifices (see text). Green dots: geofluids collected in high heat flow areas (Lucazeau, 2019), characterized by negative δVs (%) perturbations (Debayle et al., 2016; Hasterok et al., 2022). Purple diamonds: geofluids collected in low heat flow areas (i.e., heat flow below the average value of continental areas; Lucazeau, 2019), scarcely or unaffected by negative δVs (%) perturbations (Debayle et al., 2016; Hasterok et al., 2022).

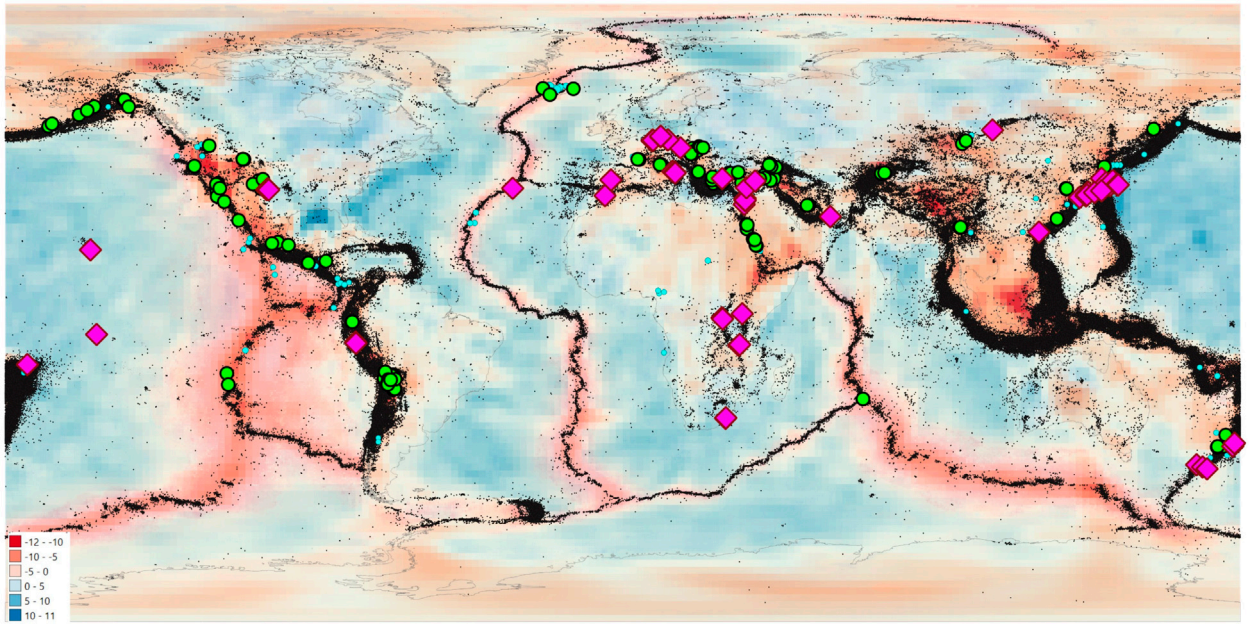

FIGURE 4
S-wave Dispersion map (Debayle et al., 2016; Hasterok et al., 2022) with location of non-volcanic fluid emissions (i.e., minimum distance of 30 km from main volcanic edifices, see text) characterized by R >1.22 Ra. Green dots: high heat flow areas (Lucazeau, 2019), significantly affected by negative δVs (%) values (Debayle et al., 2016; Hasterok et al., 2022). Purple diamonds: low heat flow areas (Lucazeau, 2019) scarcely affected, or unaffected, by significant δVs (%) values (Debayle et al., 2016; Hasterok et al., 2022). Black dots - 4<M<9.2 earthquakes (Storchak et al., 2013; http://www.isc.ac.uk/iscgem/ accessed on 20 July 2023).

plumes capable of conveying mantle fluids up to the surface, as occurs in Iceland (e.g., Samuel and Farnetani, 2003; Jackson et al., 2017). The low-right portion of the graph contains representative points from areas characterized by heat flow values below the average continental value (Lucazeau, 2019), which are scarcely affected, or unaffected, by significant S-wave negative velocity perturbations (Debayle et al., 2016; Hasterok et al., 2022 – see also Supplementary Figure S1). The latter areas, albeit apparently not always affected by frequent recent earthquakes recorded in seismic catalogs, have probably been affected by tectonic activities in the past capable of inducing faulting processes which reach the mantle or the lower crust like seismic events characterized by $M \geq 6.5$.

In areas identified by purple diamonds (Figure 4) and characterized by seismicity values that often do not coincide with the maximum magnitude values recorded in the world, relatively low heat flow, lack of close volcanic edifices, non-significant S-wave negative velocity perturbations values, possible deep-rooted faults, did not close during the geological time and were poorly affected by self-sealing phenomena, thus revealing possible still active tectonic strains capable of increasing crustal permeability, as observed by other authors in selected areas where noble gas prospections were carried out for different research purposes (e.g., Italiano et al., 2000; Italiano et al., 2001; Caracausi and Sulli, 2019; Caracausi et al., 2022; Liu et al., 2023).

These findings allow us to not exclude, in principle, the possible occurrence of any future strong seismic events in the identified faulted areas due to the eventual long recurrence time of seismic events. Further unexpected areas could be in similar conditions, because the current, preliminary version of the graph, is capable of identifying only the most relevant end-members.

Further to this, because the here considered databases could be inherently incomplete, we cannot exclude that other regions around the world in addition to those identified in this manuscript are in similar conditions Supplementary Figure S2. An obvious outcome of this work is the recommendation to test the method again as soon as new and more extensive data are available.

5 Conclusion

Areas affected by significant tectonic activity have been identified by the mapping of thermal springs. In principle, all the areas where significant tectonic activity is superimposed upon areas that host thermal springs should continue over time to host seismic events until large-scale geodynamic events modify present-day global tectonic activity. Anomalous geofluid locations emitting mantle-derived significant components have been found also outside of known seismically active areas, particularly in areas affected by anomalous heat flow and by the possibly anomalous dispersion of S wave values. After excluding the existence of magma-related local geological disturbances, the identified mantle-derived geofluid emissions could be affected, in principle, by moderate and strong seismic events ($M>6$) which maintained relatively high crustal permeability values during geological time, in spite of the lack of a relatively high frequency of earthquakes in catalogs which consider only the last 6 decades, the lack of volcanic vents, the lack of anomalous heat flow and the lack of enhanced values of negative S wave perturbation. The existence of geofluid emissions in the form of thermal springs shows that there is a first quantum value in crustal permeability, and is determined by the occurrence of seismic events characterized by magnitude values of 4 ± 0.5 and 6 ± 0.5. There is also a second quantum value in the crustal permeability evidenced by a significant presence of Helium 3 in geofluids and is determined by the occurrence of seismic events characterized between 6 ± 0.5 and 9.2. The identified sites should be considered in pattern recognition studies that accompany NDSHA. In the recent past, flaws in seismic hazard evaluations have been reported by various Authors (Kossobokov and Nekrasova, 2012; Wyss et al., 2012, etc.). The incompleteness of seismic catalogs could be considered, among others, responsible for possible seismic hazard underevaluation in various sites on Earth. The identified procedures, in principle, could help to better identify areas in which deep faults capable of reaching the upper mantle layers permanently remain affected by increased values of crustal permeability, probably due to unrevealed or undetected slight crustal strain phenomena. We have set up a procedure to preliminarily identify potential earthquake-prone areas in unexpected sites of the world. The adopted procedures may be further improved by considering less conservative filters or by means of further sampling and analysis of local geofluids. Detailed site-by-site studies will better clarify the identified features of unexpected potentially tectonically active areas. Geofluids have been confirmed to be powerful tools capable of contributing to a better description of future seismic hazard evolutive trends. Recent Seismic Hazard Assessment methods take into account morpho-structural zoning, which in turn takes into account nodes (fractured areas), lineaments, and topographical features such as the highest and lowest elevations of the studied area. The present work added geofluids to the previously known list of geological parameters useful for Seismic Hazard Assessment.

Data availability statement

The databases used in this work for thermal waters, seismic events and selected superficial manifestations with He isotope signature $R > 1.22$ Ra are available upon request from the corresponding author.

Author contributions

GM: Conceptualization, Methodology, Supervision, Writing–original draft. LP: Conceptualization, Data curation, Methodology, Visualization, Writing–review and editing. GF: Data curation, Software, Supervision, Validation, Writing–review and editing. FG: Conceptualization, Data curation, Investigation, Methodology, Supervision, Validation, Writing–review and editing.

Funding

The author(s) declare that no financial support was received for the research, authorship, and/or publication of this article.

Acknowledgments

The authors warmly acknowledge the two reviewers for their constructive criticisms, and P. Capuano for his editorial supervision.

GM carried out present research activity within the frame of project proposal IGCP-724, Fluid Geochemistry and Earthquake Forecasting. Part of present paper has been presented during AOGS 2023.

Conflict of interest

The authors declare that the research was conducted in the absence of any commercial or financial relationships that could be construed as a potential conflict of interest.

The author(s) declared that they were an editorial board member of Frontiers, at the time of submission. This had no impact on the peer review process and the final decision.

Publisher's note

All claims expressed in this article are solely those of the authors and do not necessarily represent those of their affiliated organizations, or those of the publisher, the editors and the reviewers. Any product that may be evaluated in this article, or claim that may be made by its manufacturer, is not guaranteed or endorsed by the publisher.

Supplementary material

The Supplementary Material for this article can be found online at: https://www.frontiersin.org/articles/10.3389/feart.2023.1286817/full#supplementary-material

References

Abedini, A. A., Hurwitz, S., and Evans, W. C. (2006). *USGS-NoGaDat-A global dataset of noble gas concentrations and their isotopic ratios in volcanic systems (No. 202)*. Reston, Virginia: US Geological Survey.

Adenis, A., Debayle, E., and Ricard, Y. (2017). Attenuation tomography of the upper mantle. *Geophys. Res. Lett.* 44 (15), 7715–7724. doi:10.1002/2017gl073751

Anderson, D. L. (2007). *New theory of the earth*. Cambridge: Cambridge University Press, 384.

Andrews, J. N. (1985). The isotopic composition of radiogenic helium and its use to study groundwater movement in confined aquifers. *Chem. Geol.* 49 (1-3), 339–351. doi:10.1016/0009-2541(85)90166-4

Ballentine, C. J., and Burnard, P. G. (2002). Production, release and transport of noble gases in the continental crust. *Rev. Mineralogy Geochem.* 47 (1), 481–538. doi:10.2138/rmg.2002.47.12

Bredehoeft, J. D., and Norton, D. L. (1990). "Mass and energy transport in a deforming Earth's crust," in *The role of fluids in crustal processes* (Washington, D.C: National Academies Press), 27–41.

Brogi, A., Alçiçek, M. C., Liotta, D., Capezzuoli, E., Zucchi, M., and Matera, P. F. (2021). Step-over fault zones controlling geothermal fluid-flow and travertine formation (Denizli Basin, Turkey). *Geothermics* 89, 101941. doi:10.1016/j.geothermics.2020.101941

P. Burnard (Editor) (2013). *The noble gases as geochemical tracers* (Berlin Heidelberg: Springer). doi:10.1007/978-3-642-28836-4

Caracausi, A., Buttitta, D., Picozzi, M., Paternoster, M., and Stabile, T. A. (2022). Earthquakes control the impulsive nature of crustal helium degassing to the atmosphere. *Commun. Earth Environ.* 3, 224. doi:10.1038/s43247-022-00549-9

Caracausi, A., and Sulli, A. (2019). Outgassing of mantle volatiles in compressional tectonic regime away from volcanism: the role of continental delamination. *Geochem. Geophys. Geosyst.* 20, 2007–2020. doi:10.1029/2018gc008046

Chandrasekharam, D., Lashin, A., Al Arifi, N., Al Bassam, A. A., and Varun, C. (2015). Evolution of geothermal systems around the Red Sea. *Environ. Earth Sci.* 73, 4215–4236. doi:10.1007/s12665-014-3710-y

Chiodini, G., Cardellini, C., Di Luccio, F., Selva, J., Frondini, F., Caliro, S., et al. (2020). Correlation between tectonic CO2 Earth degassing and seismicity is revealed by a 10-year record in the Apennines, Italy. *Sci. Adv.* 6 (35), eabc2938. doi:10.1126/sciadv.abc2938

Ciezkowski, W., Gröning, M., Leśniak, P. M., Weise, S. M., and Zuber, A. (1992). Origin and age of thermal waters in Cieplice Spa, Sudeten, Poland, inferred from isotope, chemical and noble gas data. *J. Hydrology* 140 (1-4), 89–117. doi:10.1016/0022-1694(92)90236-o

Cornell, C. A. (1968). Engineering seismic risk analysis. *Bull. Seismol. Soc. Am.* 58, 1583–1606. doi:10.1785/bssa0580051583

Craig, H., Lupton, J. E., and Horibe, Y. (1978). "A mantle helium component in circum-Pacific volcanic gases: hakone, the Marianas, and Mt. Lassen," in *Terrestrial rare gases. 16*. Editors E. C. Alexander and M. Ozima (Tokyo: Center for Academic Press), 3.

Curewitz, D., and Karson, J. A. (1997). Structural settings of hydrothermal outflow: fracture permeability maintained by fault propagation and interaction. *J. Volcanol. Geotherm. Res.* 79, 149–168. doi:10.1016/S0377-0273(97)00027-9

D. Porcelli, R. Ballentine, and R. Wieler (Editors) (2002). *Noble gases in Geochemistry and cosmochemistry, vol. 47* (Washington DC: Mineralogical Society of America).

Debayle, E., Dubuffet, F., and Durand, S. (2016). An automatically updated S-wave model of the upper mantle and the depth extent of azimuthal anisotropy. *Geophys. Res. Lett.* 43, 674–682. doi:10.1002/2015gl067329

Dunai, T. J., and Baur, H. (1995). Helium, neon and argon systematics of the european subcontinental mantle:implications for its geochemical evolution. *Geochimica Cosmochimica Acta* 59, 2767–2783. doi:10.1016/0016-7037(95)00172-v

Gautheron, C., and Moreira, M. (2002). Helium signature of the subcontinental lithospheric mantle. *Earth Planet. Sci. Lett.* 199, 39–47. doi:10.1016/s0012-821x(02)00563-0

Gelfand, I. M., Guberman, S. A., Keilis-Borok, V. I., Knopoff, L., Press, F., Ranzman, I. Y., et al. (1976). Pattern recognition applied to earthquake epicenters in California. *Phys.Earth Planet. Inter.* 11, 227–283. doi:10.1016/0031-9201(76)90067-4

Giardini, D., Grünthal, G., Shedlock, K. M., and Zhang, P. (2003). "The GSHAP global seismic hazard map. In international," in *Handbook of earthquake and engineering seismology*. Editors W. Lee, H. Kanamori, P. Jennings, and C. Kisslinger (Amsterdam, Netherlands: Academic Press), 1233–1239.

Gleeson, T., and Ingebritsen, S. (2017). *Crustal permeability*. Chichester: Wiley-Blackwell. ISBN 9781119166566 p 451.

Gold, T., and Soter, S. (1984). Fluid ascent through the solid lithosphere and its relation to earthquakes. *Pure Appl. Geophys.* 122, 492–530. doi:10.1007/bf00874614

Gorshkov, A., and Soloviev, A. (2021). "Morphostructural zoning for identifying earthquake-prone areas," in *Earthquakes and sustainable infrastructure: neodeterministic (NDSHA) approach guarantees prevention rather than cure*. Editors G. F. Panza, V. G. Kossobokov, E. Laor, and B. De Vivo (Elsevier), 135–149.

Gorshkov, A. I., Kossoboko, V., and Soloviev, A. A. (2003). "Recognition of earthquake prone areas," in *Nonlinear dynamics of the lithosphere and earthquake prediction*. Editors V. Keilis-Bork, and A. A. Soloviev (Heidelberg: Springer), 235–320.

Graser, A. (2013). *Learning QGIS 2.0*. Birmingham: Packt Publishing.

Hasterok, D., Halpin, J. A., Collins, A. S., Hand, M., Kreemer, C., Gard, M. G., et al. (2022). New maps of global geological provinces and tectonic plates. *Earth-Science Rev.* 231, 104069. doi:10.1016/j.earscirev.2022.104069

Hilton, D. R., Fischer, T. P., and Marty, B. (2002). Noble gases and volatile recycling at subduction zones. *Rev. Mineralogy Geochem.* 47, 319–370. doi:10.2138/rmg.2002.47.9

Hilton, D. R., Grönvold, K., O'Nions, R. K., and Oxburgh, E. R. (1990). Regional distribution of 3He anomalies in the Icelandic crust. *Chem. Geol.* 88 (1-2), 53–67. doi:10.1016/0009-2541(90)90103-e

Irwin, W. P., and Barnes, I. (1980). Tectonic relations of carbon dioxide discharges and earthquakes. *J. Geophys. Res. Solid Earth* 85 (B6), 3115–3121. doi:10.1029/jb085ib06p03115

Italiano, F., Martelli, M., Martinelli, G., and Nuccio, P. M. (2000). Geochemical evidence of melt intrusions along lithospheric faults of the southern Apennines (Italy): geodynamic and seismogenic implications. *J. Geophys. Res.* 106, 13569–13578. doi:10.1029/2000jb900047

Italiano, F., Martinelli, G., and Nuccio, P. M. (2001). Anomalies of mantle-derived helium during the 1997–1998 seismic swarm of Umbria–Marche, Italy. *Geophys. Res. Lett.* 28, 839–842. doi:10.1029/2000gl012059

Jackson, M. G., Konter, J. G., and Becker, T. W. (2017). Primordial helium entrained by the hottest mantle plumes. *Nature* 542 (7641), 340–343. doi:10.1038/nature21023

Kossobokov, V. G., and Nekrasova, A. K. (2012). Global seismic hazard assessment Program maps are erroneous. *Seism. Instrum.* 48 (2), 162–170. doi:10.3103/s0747923912020065

Kramer, S. L. (1996). *Geotechnical earthquake engineering*. Pearson Education India. ISBN-10: 8131707180.

Krinitzsky, E. L. (1995). Deterministic versus probabilistic seismic hazard analysis for critical structures. *Eng. Geol.* 40, 1–7. doi:10.1016/0013-7952(95)00031-3

Kurz, M. D., Jenkins, W. J., and Hart, S. R. (1982). Helium isotopic systematics of oceanic islands and mantle heterogeneity. *Nature* 297, 43–47. doi:10.1038/297043a0

Kuz'mina, E. A., and Novopashina, A. V. (2018). Groundwater outflows and fault density spatial relation in the Baikal rift system (Russia). *Acque Sotterranee-Italian J. Groundw.* 7 (1). doi:10.7343/as-2018-317

Lahsen, A., Muñoz, N., and Parada, M. A. (2010). "Geothermal development in Chile," in Proceedings World Geothermal Congress (Vol. 25, p. 7), Bali, Indonesia, April 25-30, 2010.

Lebedev, S., and Van Der Hilst, R. D. (2008). Global upper-mantle tomography with the automated multimode inversion of surface and S-wave forms. *Geophys. J. Int.* 173 (2), 505–518. doi:10.1111/j.1365-246x.2008.03721.x

Leonard, M. (2010). Earthquake fault scaling: self-consistent relating of rupture length, width, average displacement, and moment release. *Bull. Seismol. Soc. Am.* 100, 1971–1988. doi:10.1785/0120090189

Liu, W., Zhang, M., Chen, B., Liu, Y., Cao, C., Xu, W., et al. (2023). Hydrothermal He and CO_2 degassing from a Y-shaped active fault system in eastern Tibetan Plateau with implications for seismogenic processes. *J. Hydrology* 620, 129482. doi:10.1016/j.jhydrol.2023.129482

Lucazeau, F. (2019). Analysis and mapping of an updated terrestrial heat flow data set. *Geochem. Geophys. Geosys.* 20, 4001–4024. doi:10.1029/2019gc008389

Lupton, J. E. (1983). TERRESTRIAL INERT GASES: isotope tracer studies and clues to primordial components in the mantle. *Ann. Rev. Earth Planet Sci.* 11, 371–414. doi:10.1146/annurev.ea.11.050183.002103

Maggi, A., Jackson, J. A., McKenzie, D., and Priestley, K. (2000). Earthquake focal depths, effective elastic thickness, and the strength of the continental lithosphere. *Geology* 28, 495–498. doi:10.1130/0091-7613(2000)28<495:efdeet>2.0.co;2

Manga, M., Beresnev, I., Brodsky, E. E., Elkhoury, J. E., Elsworth, D., Ingebritsen, S. E., et al. (2012). Changes in permeability caused by transient stresses: field observations, experiments, and mechanisms. *Rev. Geophys.* 50 (2). doi:10.1029/2011rg000382

Mason, B. G., Pyle, D. M., and Oppenheimer, C. (2004). The size and frequency of the largest explosive eruptions on Earth. *Bull. Volcanol.* 66 (8), 735–748. doi:10.1007/s00445-004-0355-9

Montagner, J. P., Marty, B., Stutzmann, E., Sicilia, D., Cara, M., Pik, R., et al. (2007). Mantle upwellings and convective instabilities revealed by seismic tomography and helium isotope geochemistry beneath eastern Africa. *Geophys. Res. Lett.* 34 (21), L21303. doi:10.1029/2007gl031098

O'nions, R. K., and Oxburgh, E. R. (1983). Heat and helium in the earth. *Nature* 306 (5942), 429–431. doi:10.1038/306429a0

Ozima, M., and Podosek, F. A. (2004). *Noble gas Geochemistry*. 2nd edition. Cambridge: Cambridge University Press, 286.

Panza, G. F., La Mura, C., Peresan, A., Romanelli, F., and Vaccari, F. (2012). Seismic hazard scenarios as preventive tools for a disaster resilient society. *Adv. Geophys.* 53, 93–165. Elsevier. doi:10.1016/B978-0-12-380938-4.00003-3

Pesce, A. H. (2005). "Argentina country update," in *Proceedings world geothermal congress 2005 antalya* (Turkey: International Geothermal Association).

Petersen, M. D., Zeng, Y., Haller, K. M., McCaffrey, R., Hammond, W. C., Bird, P., et al. (2014). *Geodesy- and geology-based slip rate models for the Western United States (excluding California) national seismic hazard maps*. Open-File Report 2013–1293. Reston, VA: U.S. Geological Survey, 80. doi:10.3133/ofr20131293

Polyak, B. G., Tolstikhin, I. N., and Khutorskoi, M. D. (2020). Ascending heat and mass flow in continental crust: on the problem of driving forces of tectogenesis. *Izvestiya, Phys. Solid Earth* 56 (4), 490–510. doi:10.1134/s1069351320030088

Poreda, R. J., Craig, H., Arnorsson, S., and Welhan, J. A. (1992). Helium isotopes in Icelandic geothermal systems: I. ^{3}He, gas chemistry, and ^{13}C relations. *Geochimica Cosmochimica Acta* 56 (12), 4221–4228. doi:10.1016/0016-7037(92)90262-h

Samuel, H., and Farnetani, C. G. (2003). Thermochemical convection and helium concentrations in mantle plumes. *Earth Planet. Sci. Lett.* 207 (1-4), 39–56. doi:10.1016/s0012-821x(02)01125-1

Sano, Y., Hara, T., Takahata, N., Kawagucci, S., Honda, M., Nishio, Y., et al. (2014). Helium anomalies suggest a fluid pathway from mantle to trench during the 2011 Tohoku-Oki earthquake. *Nat. Commun.* 5, 3084. doi:10.1038/ncomms4084

Sano, Y., Kagoshima, T., Takahata, N., Nishio, Y., Roulleau, E., Pinti, D. L., et al. (2015). Ten-year helium anomaly prior to the 2014 Mt Ontake eruption. *Sci. Rep.* 5, 13069. doi:10.1038/srep13069

Sato, T., Kazahaya, K., Matsumoto, N., and Takahashi, M. (2020). Deep groundwater discharge after the 2011 Mw 6.6 Iwaki earthquake, Japan. *Earth Planets Space* 72, 54. doi:10.1186/s40623-020-01181-7

Shito, A., Karato, S.-I., Matsukage, K. N., Nishihara, Y., Jacobse, S., and Van Der Lee, S. (2006). *Towards mapping the three-dimensional distribution of water in the upper mantle from velocity and attenuation tomography*. Washington D.C.: Geophysical Monograph-American Geophysical Union, 225–236.

Storchak, D. A., Di Giacomo, D., Bondár, I., Engdahl, E. R., Harris, J., Lee, W. H., et al. (2013). Public release of the ISC–GEM global instrumental earthquake catalogue (1900–2009). *Seismol. Res. Lett.* 845, 810–815. doi:10.1785/0220130034

Tamburello, G., Chiodini, G., Ciotoli, G., Procesi, M., Rouwet, D., Sandri, L., et al. (2022). Global thermal spring distribution and relationship to endogenous and exogenous factors. *Nat. Commun.* 13 (1), 6378. doi:10.1038/s41467-022-34115-w

Tamburello, G., Pondrelli, S., Chiodini, G., and Rouwet, D. (2018). Global-scale control of extensional tectonics on CO2 earth degassing. *Nat. Commun.* 9 (1), 4608. doi:10.1038/s41467-018-07087-z

Torgersen, T. (1993). Defining the role of magmatism in extensional tectonics: helium 3 fluxes in extensional basins. *J. Geophys. Res. Solid Earth* 98 (9), 16257–16269. doi:10.1029/93jb00891

Twiss, R. J., and Moores, E. M. (1997). *Structural geology*. 2nd Ed. San Francisco, 73 CA: Freeman and Company, 736.

Unsworth, M., and Rondenay, S. (2013). "Mapping the distribution of fluids in the crust and lithospheric mantle utilizing geophysical methods," in *Metasomatism and the chemical transformation of rock* (Berlin, Heidelberg: Springer), 535–598. doi:10.1007/978-3-642-28394-9_133-642-28394-9_13

Vannoli, P., Martinelli, G., and Valensise, G. (2021). The seismotectonic significance of geofluids in Italy. *Front. Earth Sci.* 9, 579390. doi:10.3389/feart.2021.579390

Wang, C.-Y., Liao, X., Wang, L.-P., Wang, C.-H., and Manga, M. (2016). Large earthquakes create vertical permeability by breaching aquitards. *Water Resour. Res.* 52, 5923–5937. doi:10.1002/2016WR018893

Wang, C.-Y., and Manga, M. (2015). New streams and springs after the 2014 Mw 6.0 South Napa earthquake. *Nat. Commun.* 6, 7597. doi:10.1038/ncomms8597

Wang, K. (2008). *The types, distribution and basic characteristics of geothermal areas in China*. Geothermal Training Programme: Lectures on Geothermal areas in China Lecture 1. Orkustofnun, Grensásvegur 9, Reports 2008 IS-108 Reykjavík, Iceland Number 7.

Waring, G. A. (1965). Thermal springs of the United States and other countries of the world - a Summary. *U. S. Geol. Surv. Prof. Pap.* 492, 383.

Wells, D. L., and Coppersmith, K. J. (1994). New empirical relationships among magnitude, rupture length, rupture width, rupture area, and surface displacement. *Bull. Seism. Soc. Am.* 84, 974–1002. doi:10.1785/BSSA0840040974

Wexsteen, P., Jaffé, F. C., and Mazor, E. (1988). Geochemistry of cold CO2-rich springs of the scuol-tarasp region, lower engadine, Swiss alps. *J. Hydrology* 104 (1-4), 77–92. doi:10.1016/0022-1694(88)90158-8

Wu, Y., Zhou, X., Zhuo, L., Guangbin, T., Ma, J., and Wang, Y. (2023). Structural controls of the northern Red River Fault Zone on the intensity of hydrothermal activity and distribution of hot springs in the Yunnan-Tibet geothermal belt. *Geothermics* 109, 102641. doi:10.1016/j.geothermics.2022.102641

Wyss, M., Nekraskova, A., and Kossobokov, V. (2012). Errors in expected human losses due to incorrect seismic hazard estimates. *Nat. Hazards* 62, 927–935. doi:10.1007/s11069-012-0125-5

Yousefi, H., Noorollahi, Y., Ehara, S., Itoi, R., Yousefi, A., Fujimitsu, Y., et al. (2010). Developing the geothermal resources map of Iran. *Geothermics* 39 (2), 140–151. doi:10.1016/j.geothermics.2009.11.001

Zhang, Y., Romanelli, F., Vaccari, F., Peresan, A., Jiang, C., Wu, Z., et al. (2021). Seismic hazard maps based on neo-deterministic seismic hazard assessment for China seismic experimental site and adjacent areas. *Eng. Geol.* 291, 106208. doi:10.1016/j.enggeo.2021.106208

frontiers | Frontiers in Earth Science

TYPE Original Research
PUBLISHED 28 December 2023
DOI 10.3389/feart.2023.1245677

Check for updates

OPEN ACCESS

EDITED BY
Jie Liu,
Sun Yat-sen University, China

REVIEWED BY
Huilin Wang,
Huazhong University of Science and Technology, China
Wanpeng Feng,
Sun Yat-sen University, China

*CORRESPONDENCE
Caibo Hu,
hucb@ucas.ac.cn

RECEIVED 23 June 2023
ACCEPTED 17 November 2023
PUBLISHED 28 December 2023

CITATION
Shi M, Meng S, Hu C and Shi Y (2023), Crustal heterogeneity effects on coseismic deformation: numerical simulation of the 2008 M_W 7.9 Wenchuan earthquake. *Front. Earth Sci.* 11:1245677. doi: 10.3389/feart.2023.1245677

COPYRIGHT
© 2023 Shi, Meng, Hu and Shi. This is an open-access article distributed under the terms of the Creative Commons Attribution License (CC BY). The use, distribution or reproduction in other forums is permitted, provided the original author(s) and the copyright owner(s) are credited and that the original publication in this journal is cited, in accordance with accepted academic practice. No use, distribution or reproduction is permitted which does not comply with these terms.

Crustal heterogeneity effects on coseismic deformation: numerical simulation of the 2008 M_W 7.9 Wenchuan earthquake

Mingqian Shi[1,2], Sichen Meng[1,2], Caibo Hu[1,2]* and Yaolin Shi[1,2]

[1]College of Earth and Planetary Sciences, University of Chinese Academy of Sciences, Beijing, China, [2]The Key Laboratory of Computational Geodynamics, Chinese Academy of Sciences, Beijing, China

Coseismic deformation of large earthquakes causes significant property damages and fatalities, which requires quantitative research of multiple disciplines such as geodesy, geological investigation, seismic tomography, and seismic dislocation theory. The finite element method accounts for material heterogeneity and geometric complexity, making it suitable for studying the coseismic deformation of large earthquakes. This paper develops a parallel elastic finite element program that utilizes split nodes and high-performance parallel computing technology on the FELAC software platform to study the coseismic deformation of large earthquakes. We verify the accuracy of the parallel elastic finite element program by comparing its results with the analytical solutions from seismic dislocation theory for four ideal earthquake cases. Finally, we established parallel elastic finite element models to study the coseismic deformation of the 2008 Wenchuan earthquake. The simulation results are consistent with the GPS and InSAR data. Coseismic surface deformation results are significantly influenced by medium regional heterogeneity with different layered structures besides the Longmenshan fault. The finite element program lay the foundation for the inversion of the coseismic fault rupture process based on the heterogeneous medium model and complex geometric model.

KEYWORDS

coseismic deformation, finite element model, seismic dislocation theory, Wenchuan earthquake, GPS, InSAR

1 Introduction

Coseismic deformation by large earthquakes offers insights into the elastic properties of Earth's medium. It arises from the sudden release and modification of strain energy along the fault, causing significant losses in terms of property and human lives. The complexity of coseismic deformation induced by the 2008 M_W 7.9 Wenchuan earthquake has been accurately captured through Global Positioning System (GPS) and Interferometric Synthetic Aperture Radar (InSAR) data. This study employs a series of parallel elastic finite element models to examine the influence of crustal medium variations on the coseismic deformation caused by the Wenchuan earthquake.

The study of coseismic deformation has matured, with well-established theoretical frameworks providing analytical and semi-analytical solutions rooted in seismic dislocation theory. Steketee (1958) initially proposed analytical dislocation solutions in semi-infinite elastic space, which were later extended by Okada (1985, 1992) to include both surface and internal coseismic deformation in three-dimensional semi-infinite elastic space. Sun et al. (1996, 2009) made significant advancements in coseismic dislocation theory specifically for the spherical layered earth

model. Wang et al. (2003) developed the program EDGRN/EDCMP for coseismic deformation calculation in elastic or layered elastic Earth media. Additionally, USGS introduced the Coulomb 3.3 software (Toda et al., 2011) based on seismic dislocation theory in homogenous semi-infinite elastic space, which was widely applied in the calculation of coseismic deformation and the analysis of seismic hazard change. While commonly employed for forward calculation of coseismic deformation, the accuracy of the calculation results strongly depends on simple geometry and material model, which hinders the accurate acquisition of coseismic deformation calculations for complex geometric and material cases. Large earthquakes frequently occur at plate boundaries and interplate block edges, characterized by significant lateral variations in the medium. Practical scenarios necessitate the development of numerical simulation methods that account for the complex geometry and transverse heterogeneity of materials in coseismic deformation calculation.

Satellite geodesy, facilitated by recent advancements in space observation technology, has proven pivotal in observing and documenting surface deformation caused by large earthquakes, both coseismic and postseismic. Massonet et al. (1993) conducted a pioneering study using InSAR data to capture the coseismic deformation of the M_W 7.3 Landers earthquake in Southern California. GPS and InSAR technologies have become prevalent tools to observe crustal deformation by large earthquakes. Numerous studies have employed a combination of InSAR and GPS data to investigate coseismic and postseismic deformation resulting from various earthquakes, such as the 2001 Ms 8.1 eastern Kunlun earthquake (Wan et al., 2008), the 2001 M_W 7.8 Kokoxili earthquake (Tu et al., 2016; Zhao et al., 2018), the 2008 M_W 7.9 Wenchuan earthquake (Wan et al., 2017), the 2011 M_W 9.0 Tohoku-Oki earthquake (Wang M. et al., 2011), and the M_W 7.8 Gorkha, Nepal earthquake (Sreejith et al., 2016). Previous studies have employed geodetic inversion techniques to estimate interseismic and coseismic slips for various seismic events (Tong et al., 2010; Ozawa et al., 2012). While image processing techniques effectively extract deformation characteristics from observed data, these interpretations primarily offer insights into observation results and do not comprehensively reveal specific earthquake mechanisms.

The finite element method (FEM) is extensively employed for numerical analysis of coseismic deformation. Freed and Lin (2001) utilized a viscoelastic finite element model to calculate coseismic and postseismic Coulomb stress changes associated with the 1992 Landers earthquake sequence, providing a valuable understanding of the delayed triggering of the 1999 Hector Mine earthquake. Zhang et al. (2015) employed a 3D finite element program based on the equivalent physical force method of seismic dislocation to investigate coseismic deformation in a spherical Earth model. Hu et al. (2012) and Wang et al. (2021) adopted the finite element method to analyze both coseismic and postseismic deformation of the 2008 Wenchuan earthquake. In addition, Hu et al. (2004) investigated postseismic deformation using a 3D viscoelastic Burgers FEM model for notable earthquakes, including the 1960 giant Chile earthquake, the 2004 giant Sumatra earthquake (Hu and Wang, 2012), and the 2012 M_W 8.6 Indian Ocean earthquake (Hu et al., 2016). Luo and Liu (2010, 2018) utilized a three-dimensional viscoelastoplastic finite element model to calculate coseismic and postseismic Coulomb stress changes caused by the 2008 Wenchuan earthquake. Viscoelastic element models have also been applied to significant earthquakes, such as the 2004 M_W 9.2 Sumatra–Andaman, 2005 M_W 8.7 Nias, and 2007 M_W 8.4 Bengkulu earthquakes (Wiseman et al., 2015), as well as the 1964 M_W 9.2 Alaska earthquake (Suito and Freymueller, 2009). Numerical methods offer valuable tools for constructing realistic models of complex problems, allowing for scientific explanations grounded in mechanical mechanisms.

In this study, we developed a parallel finite element program based on the PFELAC 2.2 software platform (Element Computing Technology Co., Ltd, 2018a; Element Computing Technology Co., Ltd, 2018b; Xu et al., 2022) to precisely simulate coseismic displacement and stress fields associated with large earthquakes. To achieve this, we employed the split nodes technique (Melosh and Raefsky, 1981) and high-performance parallel computing technology. The surface coseismic displacement field and stress field at a half fault depth were validated against analytical or semi-analytical solutions provided by EDGRN/EDCMP (Wang et al., 2003) and Coulomb 3.3 (Toda et al., 2011) for four fault models: pure strike-slip, normal, reverse, and oblique thrust faults. Furthermore, by manipulating the transverse elastic moduli of the model, we quantitatively assessed the effects of medium heterogeneity on coseismic deformation. We calculated the coseismic deformation of the 2008 Wenchuan earthquake using the finite fault inversion model proposed by Wan et al. (2017) and compared it with observed geodetic GPS and InSAR data. The developed model captures the impact of crustal heterogeneity on the coseismic deformation of the 2008 Wenchuan earthquake.

2 Method and model

2.1 Elastic finite element formula

Formula (1) represents the virtual work principle in the 3D elastic finite element method, stating that the strain energy's virtual work is the sum of the virtual work of the body force and the virtual work of the traction force (Hu, 2009; Hu et al., 2009; 2012).

$$\int_V \delta\boldsymbol{\varepsilon}^{\mathrm{T}} \cdot \boldsymbol{\sigma} dV = \int_V \delta\boldsymbol{u}^{\mathrm{T}} \cdot \boldsymbol{f} dV + \int_\Gamma \delta\boldsymbol{u}^{\mathrm{T}} \cdot \boldsymbol{T} \mathrm{d}\Gamma \tag{1}$$

where $\boldsymbol{\sigma}$ and $\boldsymbol{\varepsilon}$ represent the column vector form of stress and strain tensors, respectively, with $\boldsymbol{\sigma} = \{\sigma_{xx}\ \sigma_{yy}\ \sigma_{zz}\ \sigma_{yz}\ \sigma_{xz}\ \sigma_{xy}\}^{\mathrm{T}}$ and $\boldsymbol{\varepsilon} = \{\varepsilon_{xx}\ \varepsilon_{yy}\ \varepsilon_{zz}\ \gamma_{yz}\ \gamma_{xz}\ \gamma_{xy}\}^{\mathrm{T}}$ (engineering strain). The column vectors $\boldsymbol{f} = \{f_x\ f_y\ f_z\}^{\mathrm{T}}$ and $\boldsymbol{T} = \{T_x\ T_y\ T_z\}^{\mathrm{T}}$ represent the body force in the study area V and traction force on the boundary Γ, respectively. $\delta\boldsymbol{u} = \{\delta\mathrm{u}\ \delta\mathrm{v}\ \delta\mathrm{w}\}^{\mathrm{T}}$ denotes the virtual displacement, and $\delta\boldsymbol{\varepsilon} = \{\delta\varepsilon_{xx}\ \delta\varepsilon_{yy}\ \delta\varepsilon_{zz}\ \delta\gamma_{yz}\ \delta\gamma_{xz}\ \delta\gamma_{xy}\}^{\mathrm{T}}$ represents the virtual strain.

The 3D elastic constitutive equation is given by (Hu, 2009; Hu et al., 2009; 2012)

$$\boldsymbol{\sigma} = \boldsymbol{D}\boldsymbol{\varepsilon} \tag{2}$$

The elastic matrix **D** can be expressed as

$$\boldsymbol{D} = fact* \begin{bmatrix} 1-p\nu & p\nu & p\nu & 0 & 0 & 0 \\ p\nu & 1-p\nu & p\nu & 0 & 0 & 0 \\ p\nu & p\nu & 1-p\nu & 0 & 0 & 0 \\ 0 & 0 & 0 & 0.5-p\nu & 0 & 0 \\ 0 & 0 & 0 & 0 & 0.5-p\nu & 0 \\ 0 & 0 & 0 & 0 & 0 & 0.5-p\nu \end{bmatrix} \tag{3}$$

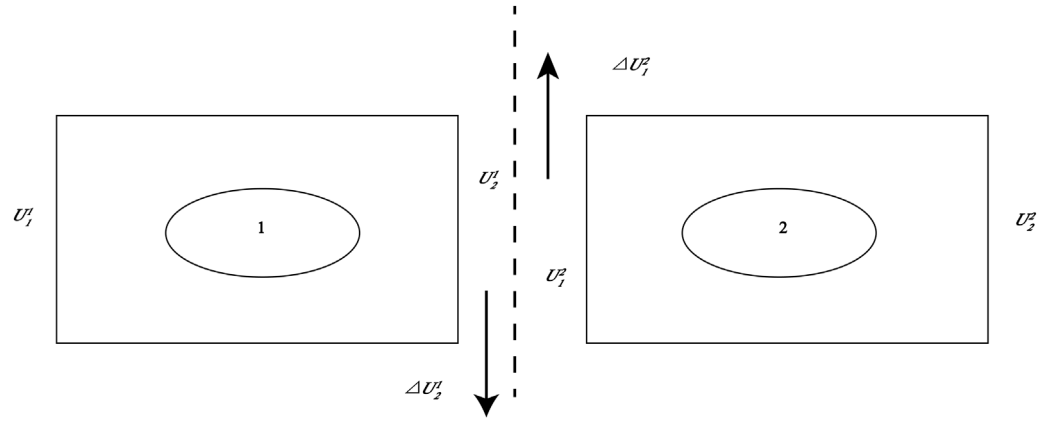

FIGURE 1
One-dimensional fault model illustrating the splitting nodes technique (adapted from Melosh and Raefsky, 1981). Elements 1 and 2, with U as the displacement, are positioned adjacent to the seismogenic fault. The superscript denotes the element number, while the subscript indicates the node number of the element. ΔU represents the total dislocation of an earthquake.

where $fact = \frac{pe}{(1+p\nu)(1-2*p\nu)}$. The parameters pe and pν correspond to Young's modulus and Poisson's ratio, respectively.

To calculate coseismic displacement and stress, we employ the splitting nodes technique to convert coseismic dislocation on faults into a load vector. In this case, there are no body forces ($\boldsymbol{f} = \{f_x\, f_y\, f_z\}^{\mathrm{T}}$) or traction forces ($\boldsymbol{T} = \{T_x\, T_y\, T_z\}^{\mathrm{T}}$). Instead, we introduce the initial strain $\boldsymbol{\varepsilon}_0 = \{\varepsilon_{xx0}\, \varepsilon_{yy0}\, \varepsilon_{zz0}\, \gamma_{yz0}\, \gamma_{xz0}\, \gamma_{xy0}\}^{\mathrm{T}}$, obtained from the splitting coseismic dislocation on faults. Consequently, we derive the finite element formula (4) as follows (Hu, 2009; Hu et al., 2009; 2012):

$$\int_V \delta\boldsymbol{\varepsilon}^{\mathrm{T}} \cdot \boldsymbol{\sigma} dV = \int_V \delta\boldsymbol{\varepsilon}^{\mathrm{T}} \cdot \boldsymbol{\sigma}_0 dV \tag{4}$$

Expanding Formula (4), we have (Hu, 2009; Hu et al., 2009; 2012):

$$\begin{aligned}
&\int_V (fact*(1-p\nu)*\varepsilon_{xx}\delta\varepsilon_{xx} + fact*p\nu*\varepsilon_{yy}\delta\varepsilon_{xx} + fact*p\nu*\varepsilon_{zz}\delta\varepsilon_{xx} \\
&+ fact*p\nu*\varepsilon_{xx}\delta\varepsilon_{yy} + fact*(1-p\nu)*\varepsilon_{yy}\delta\varepsilon_{yy} + fact*p\nu*\varepsilon_{zz}\delta\varepsilon_{yy} \\
&+ fact*p\nu*\varepsilon_{xx}\delta\varepsilon_{zz} + fact*p\nu*\varepsilon_{yy}\delta\varepsilon_{zz} + fact*(1-p\nu)*\varepsilon_{zz}\delta\varepsilon_{zz} \\
&+ shear*fact*\gamma_{yz}\delta\gamma_{yz} + shear*fact*\gamma_{xz}\delta\gamma_{xz} \\
&+ shear*fact*\gamma_{xy}\delta\gamma_{xy})dV \\
&= \int_V (fact*(1-p\nu)*\varepsilon_{xx0}\delta\varepsilon_{xx} + fact*p\nu*\varepsilon_{yy0}\delta\varepsilon_{xx} \\
&\quad + fact*p\nu*\varepsilon_{zz0}\delta\varepsilon_{xx} + fact*p\nu*\varepsilon_{xx0}\delta\varepsilon_{yy} \\
&\quad + fact*(1-p\nu)*\varepsilon_{yy0}\delta\varepsilon_{yy} + fact*p\nu*\varepsilon_{zz0}\delta\varepsilon_{yy} \\
&\quad + fact*p\nu*\varepsilon_{xx0}\delta\varepsilon_{zz} + fact*p\nu*\varepsilon_{yy0}\delta\varepsilon_{zz} \\
&\quad + fact*(1-p\nu)*\varepsilon_{zz0}\delta\varepsilon_{zz} + shear*fact*\gamma_{yz0}\delta\gamma_{yz} \\
&\quad + shear*fact*\gamma_{xz0}\delta\gamma_{xz} + shear*fact*\gamma_{xy0}\delta\gamma_{xy})dV
\end{aligned} \tag{5}$$

where $shear = 0.5 - p\nu$. In the subsequent section, we will discuss the computation of the initial strain $\boldsymbol{\varepsilon}_0 = \{\varepsilon_{xx0}\, \varepsilon_{yy0}\, \varepsilon_{zz0}\, \gamma_{yz0}\, \gamma_{xz0}\, \gamma_{xy0}\}^{\mathrm{T}}$, obtained from the distribution of coseismic dislocation $\Delta\boldsymbol{U} = \{\Delta U \Delta V \Delta W\}^{\mathrm{T}}$ on seismogenic faults using the splitting nodes technique.

2.2 Splitting nodes technique

The splitting nodes technique, pioneered by Melosh and Raefsky (1981), offers a straightforward approach to calculate coseismic displacement and stress, as outlined in formulas (4) and (5). The underlying principle of the splitting nodes technique is depicted in Figure 1 (Melosh and Raefsky, 1981).

The relationship between the nodal displacement of the element and the global nodal displacement is given by (Melosh and Raefsky, 1981):

$$U_1^1 = U_1, U_2^1 = U_1^2 = U_2, U_2^2 = U_3 \tag{6}$$

where the displacement $U_2^1 = U_1^2 = U_2$ consists of two components: the average displacement $\bar{U}$ and the half dislocation $\Delta U/2 = \Delta U_2^1 = -\Delta U_1^2$.

The global finite element equations of elements 1 and 2 are expressed as follows (Melosh and Raefsky, 1981):

$$\begin{bmatrix} K_{11}^1 & K_{12}^1 & 0 \\ K_{21}^1 & K_{22}^1 + K_{11}^2 & K_{12}^2 \\ 0 & K_{21}^2 & K_{22}^2 \end{bmatrix} \begin{bmatrix} U_1 \\ U_2 \\ U_3 \end{bmatrix} = \begin{bmatrix} F_1 - K_{12}^1 \Delta U_2^1 \\ F_2 - K_{22}^1 \Delta U_2^1 - K_{11}^2 \Delta U_1^2 \\ F_3 - K_{21}^2 \Delta U_1^2 \end{bmatrix} \tag{7}$$

The term [K] represents the global stiffness matrix, [U] denotes the global nodal displacement vector, while [F] corresponds to the global load vector.

Formula (7) expresses the determination of the coseismic load vector, which is caused by the three-dimensional coseismic dislocation $\Delta\boldsymbol{U} = \{\Delta u\, \Delta v\, \Delta w\}^{\mathrm{T}}$ on the seismogenic faults.

2.3 Parallel technology

We developed a parallel elastic finite element program based on the virtual work principle (formulas (4), (5)) and the splitting nodes technique (formula (7)), utilizing the PFELAC 2.2 software platform (Element Computing Technology Co., Ltd., 2018a, 2018b; Xu et al., 2022). The parallel computation employed the domain

TABLE 1 The geometry and material parameters of four earthquake fault models.

Model	Type	Young's modulus E/GPa	Possion's ratio ν	Strikeslip direction/°	Fault length /km	Fault width /km	Dip angle /°	Rake angle /°
1	strikeslip	81	0.25	180	20	10	80	0
2	normal	81	0.25	180	20	10	65	90
3	thrust	81	0.25	180	20	10	35	90
4	oblique thrust	81	0.25	180	20	10	35	45

decomposition method, consisting of a master process and a series of sub-processes. The master process is responsible for the assembling of the global stiffness matrix and global load vector, as well as the parallel solution of the system of super-sized linear equations. The subprocesses calculated the element stiffness matrix and element load vector. This research analyzed coseismic deformations by four different-type earthquakes using parallel finite element programs. The developed finite element programs were validated with results from Coulomb 3.3 and EDGRN/EDCMP to assess their accuracy.

3 Program testing

To validate our 3D elastic parallel finite element method (FEM) programs, we tested with four ideal earthquake models: pure strike-slip, normal, thrust, and oblique thrust faults, and compared the results with analytical solutions. The parameters for each model are listed in Table 1. Our finite element model has dimensions of 200 km × 200 km × 50 km, adequately encompassing the fault dimensions. The seismogenic fault is positioned at the center of the model and has a length of 20 km and a width of 10 km, extending to the surface. The FEM model employed a homogeneous, elastic, and isotropic material, with a uniform dislocation of 1 m assigned to the pure strike-slip, normal, and thrust faults, respectively. In the FEM model of the oblique thrust fault, the strike-slip and thrust dislocation components were both $\sqrt{2}/2$ m. We compared the coseismic displacements and stresses obtained from our FEM models with those from the Coulomb 3.3 and EDGRN/EDCMP programs to validate our 3D elastic parallel finite element method (FEM) programs. This study focuses on comparing the FEM simulations and the results by EDGRN/EDCMP and Coulomb 3.3 specifically for Model 4 (oblique thrust fault). The comparison for Models 1, 2, and 3 (pure strike-slip, normal, and thrust faults) is available in the Appendix.

Figure 2 compares surface coseismic displacement fields (u, v, w) of Model 4 (oblique thrust fault) with those by the Coulomb 3.3 program. The horizontal surface coseismic displacement (u, v) and vertical surface coseismic displacement (w) exhibit an asymmetric pattern for both the FEM model and the Coulomb 3.3 program. The overall patterns of the three coseismic surface displacement components are highly similar between the FEM model and the Coulomb 3.3 program.

Figure 3 illustrates the coseismic stress field $(\sigma_{xx}, \sigma_{yy}, \sigma_{zz}, \sigma_{xy}, \sigma_{yz}, \sigma_{xz})$ at the half fault depth between the FEM model and the Coulomb 3.3 program for Model 4 (oblique thrust fault). The left column shows the FEM results, while the right column displays the results from the Coulomb 3.3 program. Both normal stresses $(\sigma_{xx}, \sigma_{yy}, \sigma_{zz})$and shear stresses $(\sigma_{xy}, \sigma_{yz}, \sigma_{xz})$ exhibit asymmetry. The patterns of six coseismic stress components by the FEM and the program Coulomb 3.3 are highly similar.

In Figure 4, we compare the surface coseismic displacements along a profile, passing the midpoint of the surface trace of the fault outcrop, perpendicular to the strike-slip direction using the FEM model, Coulomb 3.3, and EDGRN/EDCMP programs for Model 4 (oblique thrust). The three components exhibit highly similar patterns, with minor discrepancies that could be attributed to the sparse mesh grid of the FEM model.

By comparing the coseismic surface displacement (Figures 2, 4) and coseismic stress (Figure 3) of Model 4, we have validated the accuracy and reliability of our 3D elastic parallel FEM programs. Additionally, in the Appendix section, we have conducted similar tests for the remaining three models (pure strike-slip, normal, and thrust faults).

In this paper, a set of parallel finite element programs to study the coseismic deformation of large earthquakes is developed on the PFELAC software platform based on the domain decomposition parallel finite element technique and the split node method. This parallel finite element program can take into account the complex geometry of the originating faults, the complexity of the coseismic rupture process, the strong topographic relief, and the material inhomogeneity of the Earth's medium in the transverse and longitudinal directions. Due to the use of the domain decomposition parallel finite element technique, the node number of finite element meshes can reach ten million, which guarantees the calculation accuracy of the coseismic displacement and stress fields in the study area. On this basis, we can also calculate the coseismic Coulomb stress changes on the major faults around a large earthquake based on this parallel finite element program, which can be used to evaluate the seismic hazard changes on the major faults after a large earthquake. We can also quantitatively analyze the inhomogeneous distribution of coseismic stress drop on the main earthquake fault plane, which can be used to judge the range of aftershock distribution on the main earthquake fault plane.

4 Case study: the coseismic deformation of the 2008 M_W 7.9 Wenchuan earthquake

The 2008 M_W 7.9 Wenchuan earthquake occurred in the Longmen Shan fault zones, which include the Beichuan fault, the

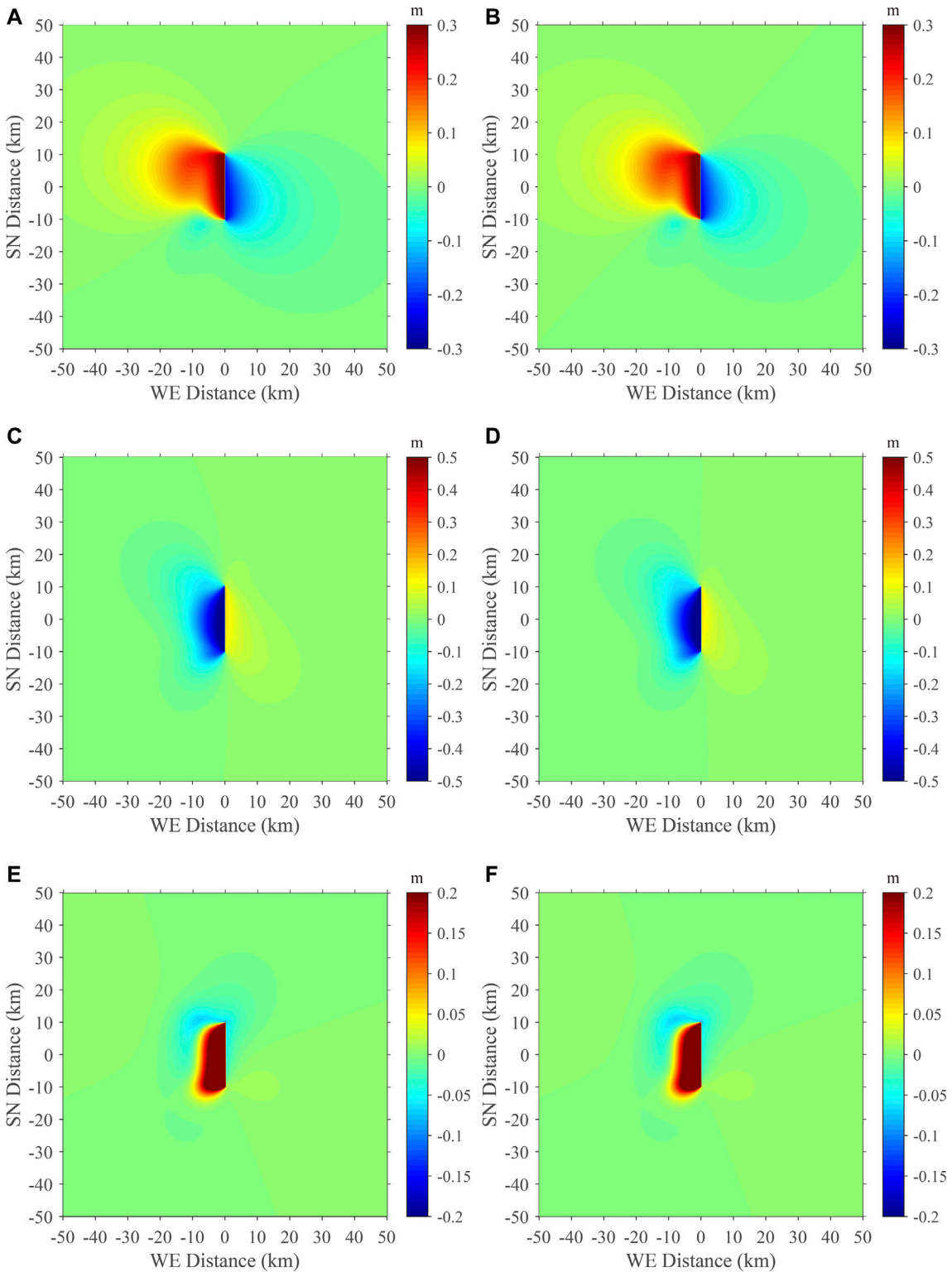

FIGURE 2
Comparison of the coseismic surface displacements Model 4 (oblique thrust fault) between the FEM model and Coulomb 3.3 program. Left column: u, v, and w components by the FEM (panels **A, C, E**). Right column: u, v, and w components by Coulomb 3.3 program (panels **B, D, F**).

Wenchuan-Maowen fault, and the Pengguan fault (Shen et al., 2009; Figure 5). The Longmen Shan fault zones, with a length of >300 km, predominantly strike in the NE-SW direction. Their well-constrained geometry is based on geological surveys (Xu et al., 2008), precise aftershock positioning (Huang et al., 2008; Liu et al., 2019), seismic tomography (Lei and Zhao, 2009; Liu et al., 2009), and deep seismic

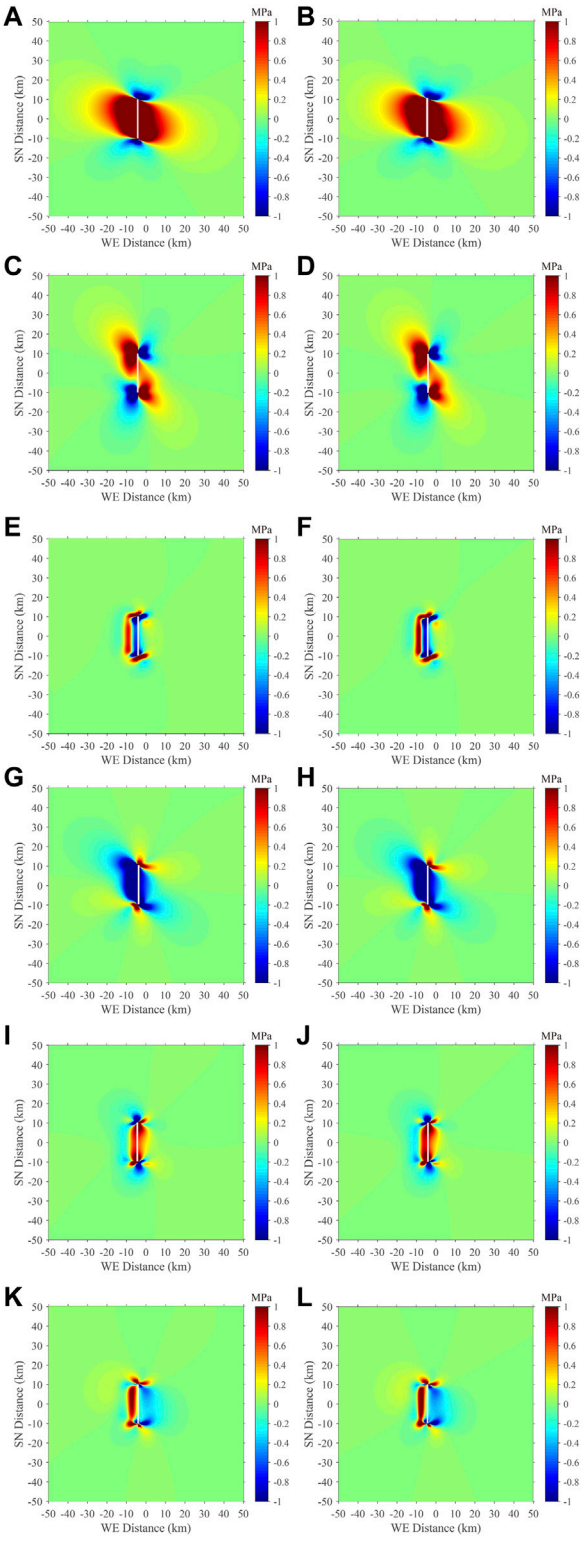

FIGURE 3
Comparison of coseismic stress at half fault depth between the FEM and Coulomb 3.3 program. Left column: FEM results for $\sigma_{xx}, \sigma_{yy}, \sigma_{zz}, \sigma_{xy}, \sigma_{yz}, \sigma_{xz}$. Right column: Coulomb 3.3 program results for $\sigma_{xx}, \sigma_{yy}, \sigma_{zz}, \sigma_{xy}, \sigma_{yz}, \sigma_{xz}$., The x-axis label represents the eastward direction, while the y-axis label represents the northward direction.

reflection profiles (Guo et al., 2013). The Longmen Shan fault zones are one of the longest rupture zones observed in interplate thrust earthquakes (Xu et al., 2008). The Longmen Shan fault zones exhibit significant variations in topography and crustal structure, with an elevation difference of around 4 km between the Qinghai-Tibetan Plateau and the Sichuan Basin, and variations in crustal thickness by

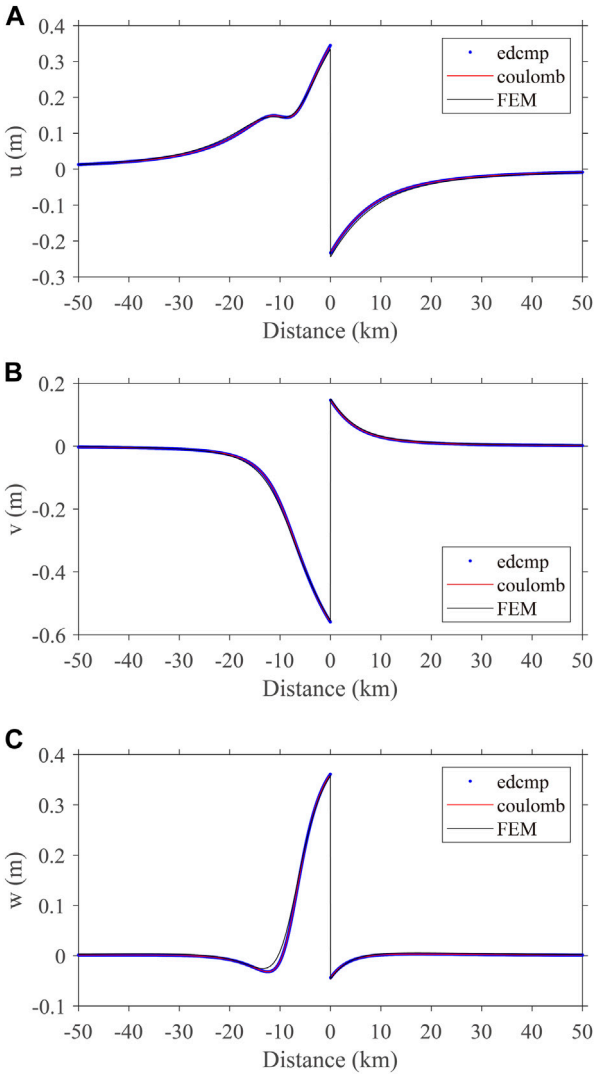

FIGURE 4
Comparison of surface coseismic displacement along a profile, passing the midpoint of the surface trace of the fault outcrop, perpendicular to the strike-slip direction using the FEM model, Coulomb 3.3, and EDGRN/EDCMP programs for Model 4 (oblique thrust fault). The x-axis represents the eastward direction, and the y-axis represents the displacement components.

tens of kilometers (Liu et al., 2015; 2018). Tomographic studies reveal significant structural differences in the media on both sides of the Longmen Shan fault zones (Lei and Zhao, 2016), providing direct evidence of medium heterogeneity within and around the fault zones through observed variations in seismic velocities. The jelly sandwich model of the Qinghai-Tibet Plateau (Bürgmann and Dresen, 2008) implies vertical stratification, indicating significant medium heterogeneity in the adjacent regions to the fault zones. We will introduce the 3D parallel elastic finite element models to provide valuable insights into the impact of medium heterogeneity on the coseismic deformation of the 2008 M_W 7.9 Wenchuan earthquake.

The steep slopes surrounding the Longmen Shan fault zones limit the number of GPS observation points. After the 2008 Wenchuan earthquake, the China Crustal Observation Network project team initially provided data from 122 GPS observation points, which was later increased to 158 points by Shen et al. (2009). Wang Q. et al. (2011) contributed additional coseismic and postseismic deformation data. Wang et al. (2021) conducted an analysis of long-term deformation observations and identified a deceleration trend in the GPS velocity field from northwest to southeast when using the fault zones as a boundary. The strain rate field exhibited significant variations across the fault zones in the presence of continuous deformation fields obtained through GPS velocity interpolation. Localized abrupt changes in strain rate along the Longmen Shan fault zones can be attributed to significant variations in medium properties, corresponding to complex stress distribution. The Japan Aerospace Exploration Agency (JAXA) and the European Space Agency (ESA), using GPS and InSAR data revealed that the 2008 M_W 7.9 Wenchuan earthquake predominantly involved thrust-slip motion, with a moderate strike-slip component. The coseismic deformation of the 2008 Wenchuan earthquake reflects the opposing displacements on either side of the fault zones and the consequent shortening of the crust. The observed coseismic displacements were comparatively larger in the Songpan-Ganzi region than those in the Sichuan Basin. The difference can be explained by theoretical models indicating a weaker crustal medium in the Qinghai-Tibet Plateau than that in the Sichuan Basin and the special geometry of the fault zones. In our numerical simulation, we employed seismic tomography (Lei and Zhao, 2009; Liu et al., 2009) and deep seismic reflection profiles (Guo et al., 2013) to construct a finite element model of the coseismic deformation induced by the 2008 Wenchuan earthquake.

The coseismic vertical displacement of the 2008 Wenchuan earthquake is significant, yet direct measurements of this component remain limited. Based on direct topographic measurements, previous studies revealed the following coseismic vertical displacement patterns during the 2008 Wenchuan earthquake: (1) The Yingxiu-Beichuan rupture zone experienced vertical displacements ranging from 0.2 to 11 m, with an average of 2–4 m. The maximum displacement of 11 m occurred on the eastern side of Beichuan town, marking the highest coseismic vertical displacement within the surface rupture zone (Li et al., 2008; Dong and Chen, 2009). (2) The Hanwang rupture zone exhibited vertical displacements ranging from 0.5 to 4 m, with the highest point at Shaba Village, Jiulong Town, Mianzhu City, reaching approximately 4 m (Li et al., 2008). (3) The Xiaoyudong rupture zone demonstrated vertical displacements ranging from 0.2 to 3 m, with an average of 1–1.5 m (Li et al., 2008). Previous studies utilized first-class precision level measurement to determine the coseismic vertical displacement components of the Wenchuan earthquake along specific level routes. The findings revealed that: (1) The western hanging wall of the main rupture zone in the Longmen Shan Central Rupture predominantly experienced significant coseismic uplift. The vertical displacement decreases rapidly with distance from the fault. The highest uplift, approximately 4.7 m, was observed at the Beiyun 1 level point in Beichuan town. (2) The maximum vertical sinking occurred within the Beichuan-Guixi fault valley, with a coseismic sinking of approximately 0.6 m (Wang et al., 2010; Dong et al., 2012).

Several research teams have focused on surface rupture and quantified the coseismic dislocation distribution of the 2008 Wenchuan earthquake (Xu et al., 2010; Zhang et al., 2011;

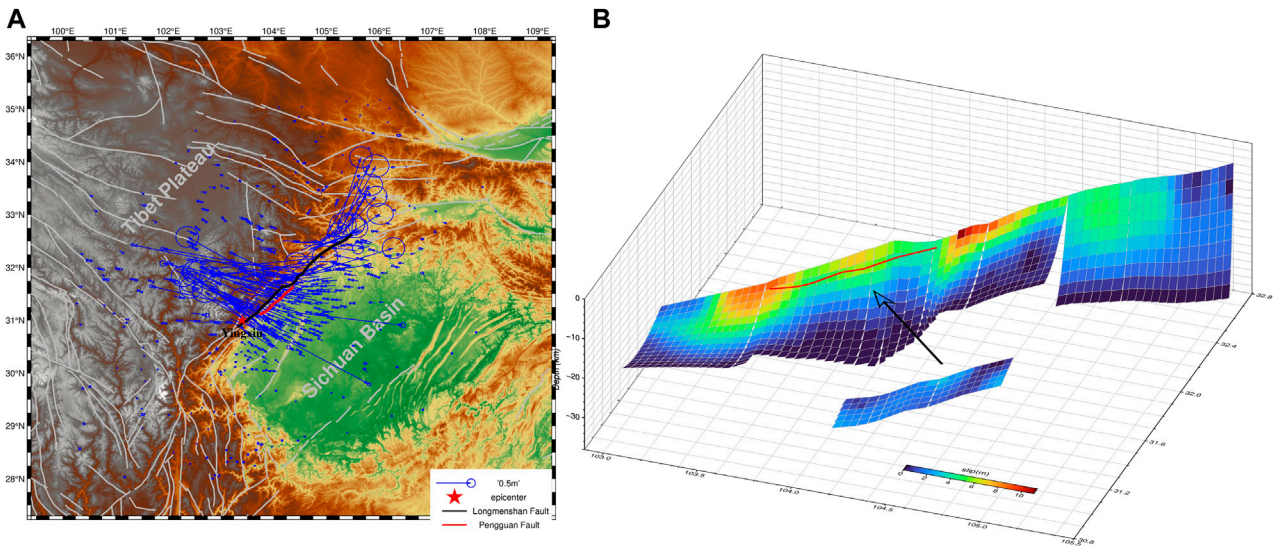

FIGURE 5
The tectonic background and coseismic dislocation distribution of the 2008 M_W 7.9 Wenchuan earthquake. **(A)** Tectonic background: blue arrows denote coseismic GPS data, gray lines represent the main active faults, black and red lines denote the Beichuan fault, the Wenchuan-Maowen fault, and the Pengguan fault. The red star denotes the epicenter of the 2008 Wenchuan earthquake. **(B)** Coseismic dislocation distribution of the 2008 M_W 7.9 Wenchuan earthquake (Wan et al., 2017).

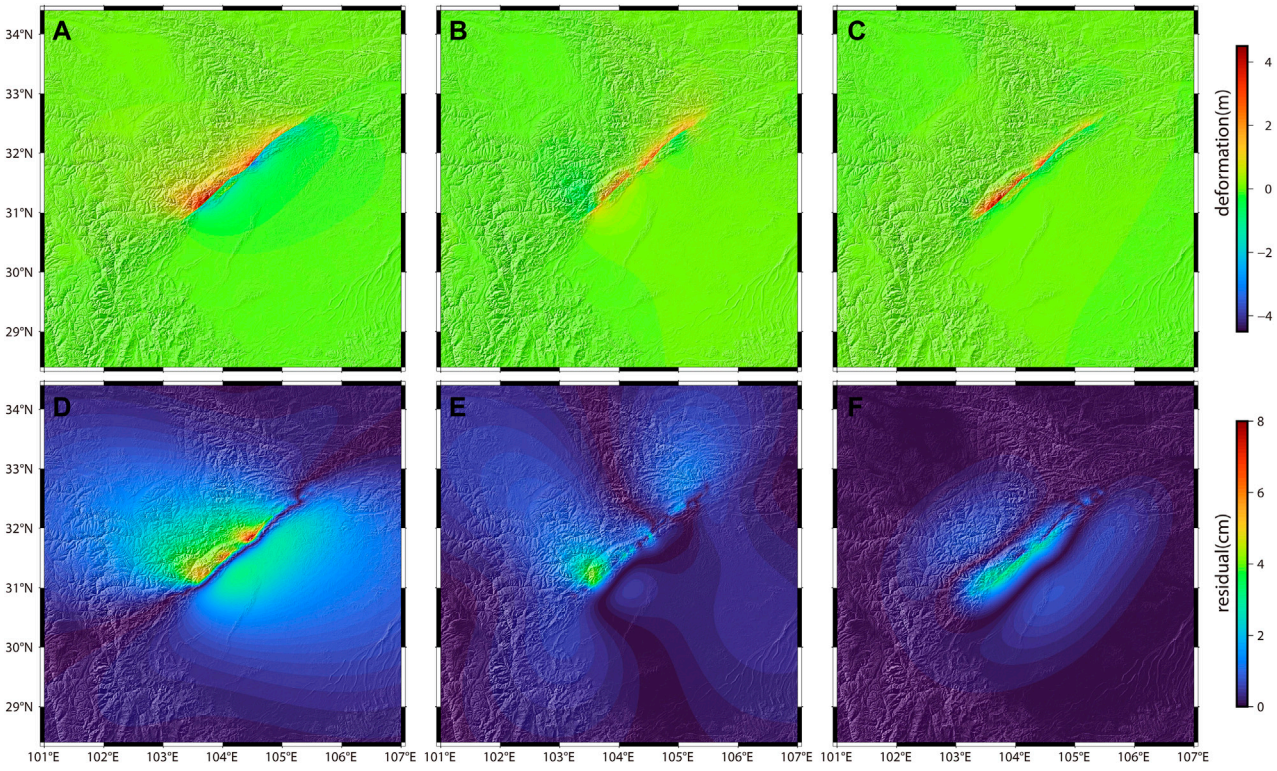

FIGURE 6
The coseismic surface displacements of Model B and the absolute residuals of the coseismic surface displacements by Model A and Model **(B)**. Panels **(A-C)** represent the u, v, w components of the coseismic surface displacements of Model B, respectively. Panels **(D-F)** show the absolute residuals of the coseismic surface displacements (u, v, w) by Model A and Model **(B)**.

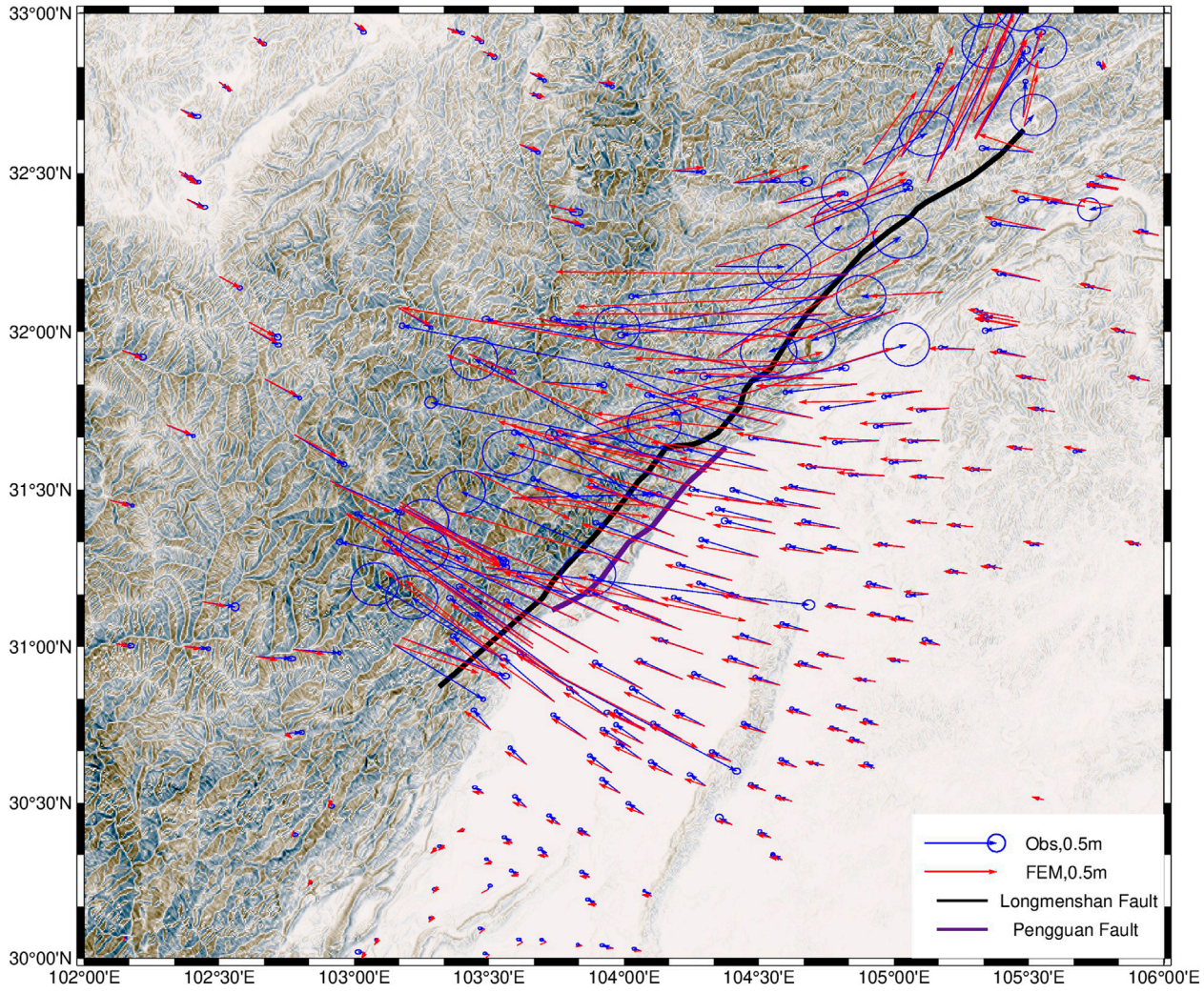

FIGURE 7
A comparison between the coseismic surface deformation predicted by Model B and the corresponding GPS data.

Tan et al., 2015). Previous studies employed various approaches, such as joint inversion of InSAR and GPS data (Tong et al., 2010; Xu et al., 2010) and Okada's static elastic dislocation model (Bai et al., 2012), to characterize the fault's coseismic rupture. However, these models have limitations in accounting for the heterogeneity of the medium in the Longmen Shan fault zones. To overcome this limitation, we adopted Wan's (2017) coseismic rupture model, which incorporates the layered structure of the medium and the spatial complexity of the fault rupture plane.

In this study, we utilized a large finite element model with dimensions of 1,000 km*1,000 km*100 km to comprehensively compare with fault sizes. Two parallel finite element models, Model A and Model B, were constructed based on the coseismic dislocation inversion model proposed by Wan et al. (2017). Model A represents a uniform medium with Young's modulus of 8.1E10 Pa and Poisson's ratio of 0.25. Conversely, Model B incorporates heterogeneity by including different material properties in seven vertically divided layers, as derived from Wan et al. (2017). Furthermore, there are significant horizontal variations in the medium on both sides of the fault zones.

Figure 6 illustrates the coseismic surface displacements of Model B and the absolute residuals of the coseismic surface displacements by Model A and Model B, respectively. The results confirm that the 2008 Wenchuan earthquake is predominantly characterized by thrust slip, with a moderate component of strike-slip motion. The simulated coseismic vertical displacements reveal significant uplift exceeding 4 m in the western hanging wall of the Longmen Shan fault zones, consistent with the first-class precision level measurements (Figure 6C; Wang et al., 2010; Dong et al., 2012). These simulated vertical displacements align with findings from first-class precision level and direct topographic measurements, indicating a sharp decrease with increasing distance from the fault (Figure 6C; Li et al., 2008; Dong and Chen, 2009; Wang et al., 2010; Dong et al., 2012). The absolute residuals of Models A and B exceed 8 cm, highlighting the significance of accounting for the vertical and transverse heterogeneity of the medium. The comparison of simulated coseismic horizontal displacements and GPS data is shown in Figure 7.

Figure 7 compares the coseismic surface deformation by Model B with GPS observation data. The root mean square error (RMSE)

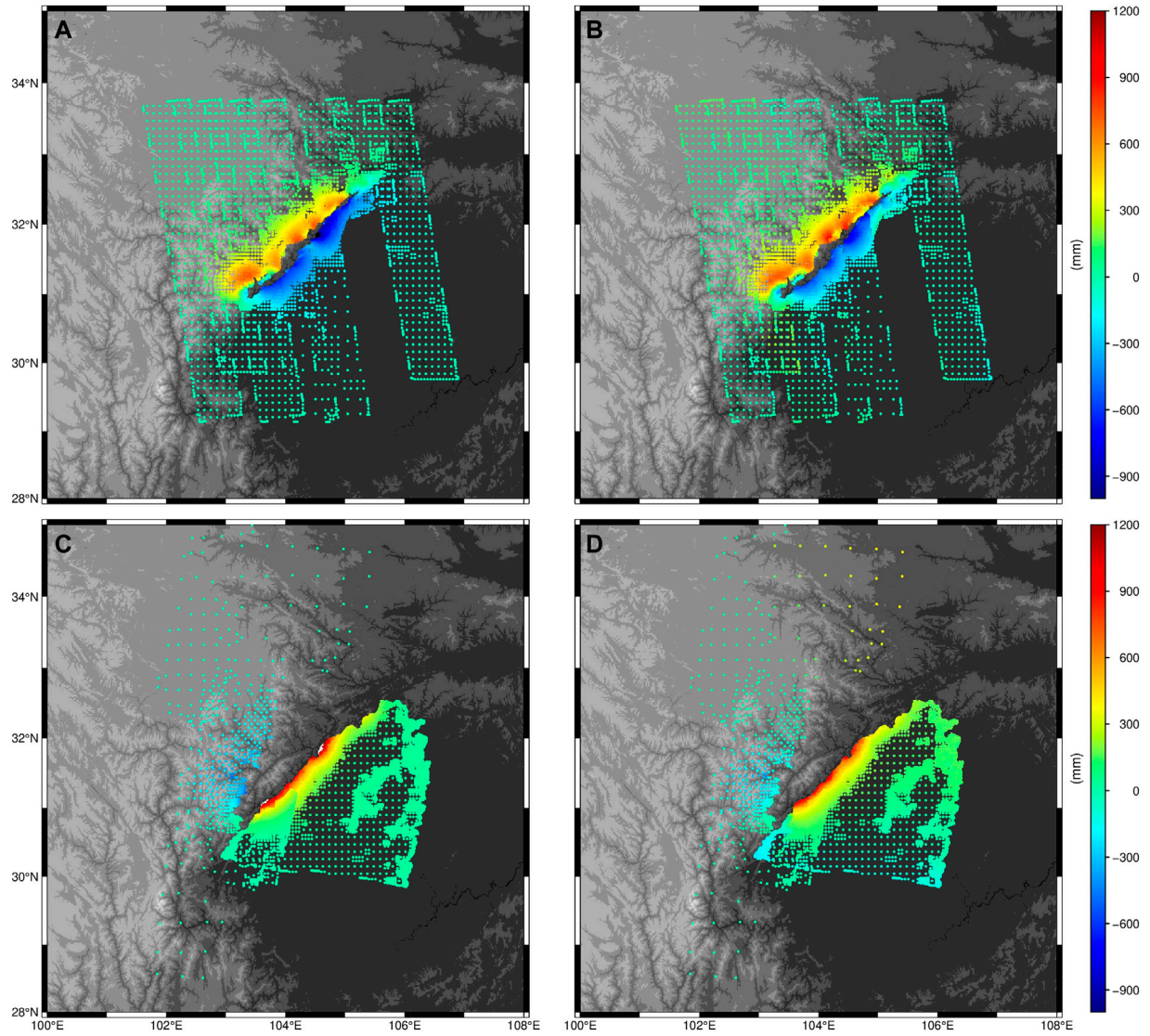

FIGURE 8
A comparison of the coseismic surface deformation by Model B and InSAR data. **(A)** LOS ascending displacement by Model B; **(B)** LOS ascending displacement by InSAR data; **(C)** LOS descending removal by Model B; **(D)** LOS descending displacement by InSAR data.

between the east component of the finite element model and GPS data is 7.98 cm, while for the north component, it is 5.61 cm. The GPS observation data uncertainty is quantified by RMSE values of 1.56 cm (east component) and 1.81 cm (north component). The finite element computation results demonstrate coherence with the actual characteristics of coseismic surface deformation.

Figure 8 compares the coseismic deformation between Model B and InSAR data. The left column represents the results of Model B, while the right column shows the InSAR data. Figures 8A, B present the ascending Line Of Sight (LOS) displacement with a root mean square error (RMSE) of 11.0 cm. Figures 8C, D display the descending LOS displacement with an RMSE of 9.11 cm. By employing the complex rupture model proposed by Wan et al. (2017), Model B demonstrates consistency with both GPS and InSAR data.

5 Discussion

We have developed a parallel elastic finite element program with the splitting nodes technique for accurate computation of coseismic displacement and stress fields by large earthquakes. To validate the effectiveness and accuracy of our FEM program, we conducted a comparative analysis of four earthquake cases using results from programs EDGRN/EDCMP and Coulomb 3.3 based on seismic dislocation theory. The parallel elastic finite element method offers advantages in handling geometric complexity, material heterogeneity, and complex boundary conditions. Utilizing this method, we can calculate Coulomb stress changes (ΔCFS) on major fault planes our parallel elastic finite element method to determine coseismic displacement and stress fields, to assess the alteration in seismic hazard following significant earthquakes (Toda et al., 2008).

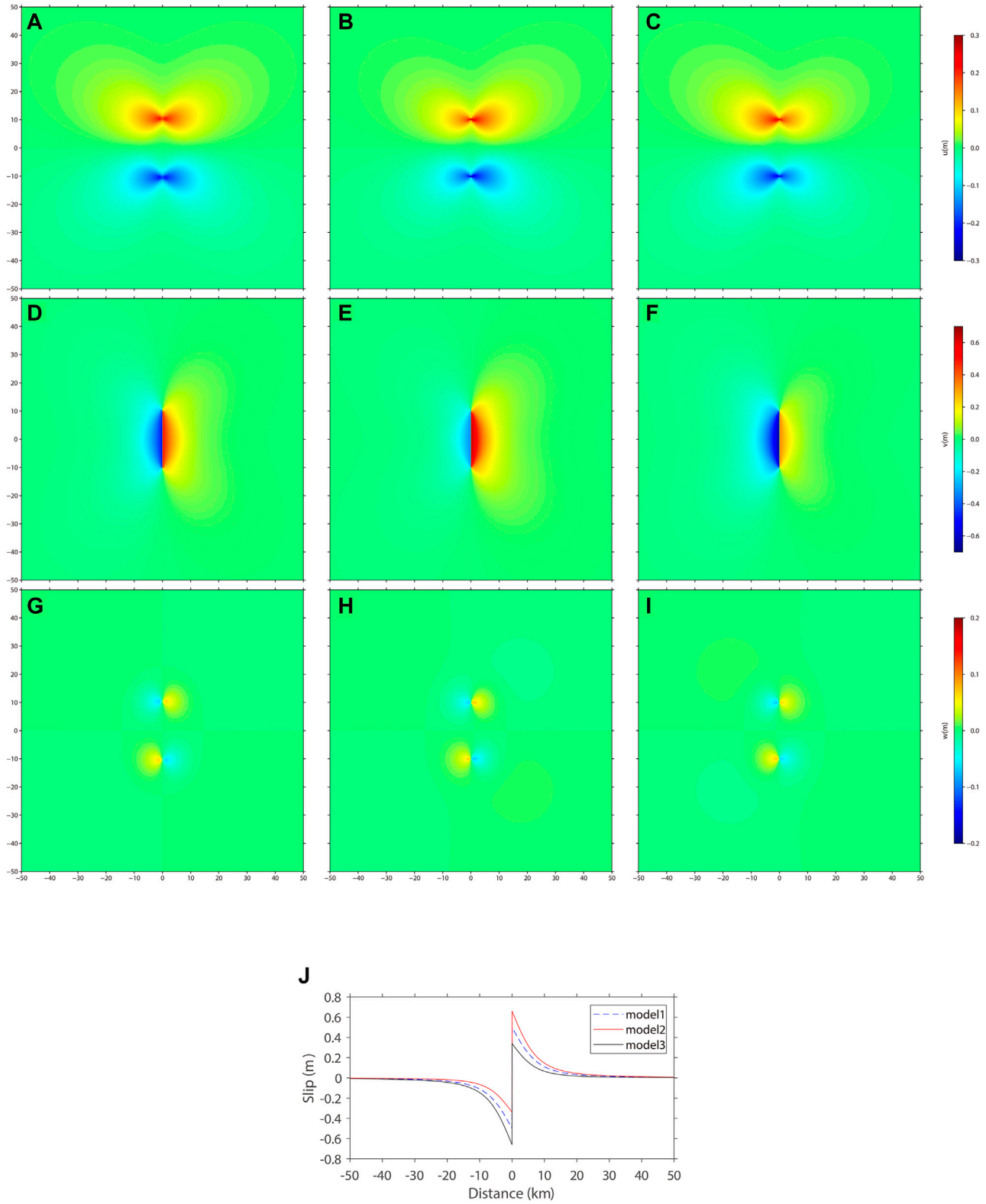

FIGURE 9
Comparison of the surface coseismic deformation results for the three theoretical models. **(A, D, G)**: u v w by Model 1; **(B, E, H)**: u v w by Model 2; **(C, F, I)**: u v w by Model 3; **(J)**: displacement component v comparison along a surface profile by Model 1, 2, and 3.

Three theoretical models (Model 1, Model 2, and Model 3) were developed to quantitatively investigate the impact of different medium variations on the distribution of coseismic deformation. In all models, a vertical complete strike-slip fault with a 1 m pure strike-slip dislocation is present at the center. The Poisson's ratio is uniformly set to 0.25 for all three models. The Young's modulus values on the left and right sides of the fault are described as Ea and Eb, respectively. The sum of Ea and Eb remains constant throughout the models, with specific values assigned as follows: Ea=Eb=8.1E10 Pa (Model 1); Ea=2 Eb=10.8E10 Pa (Model 2); Eb=2Ea=10.8E10 Pa (Model 3). Figure 9 presents the coseismic surface deformations of the three models. The results demonstrate that in Model 1, where Young's modulus of the media on both sides of the fault is equal (Model 1), strict symmetry is observed in the surface coseismic displacements on both sides of the fault. However, in models (Model 2 and Model 3) with a doubling difference in Young's modulus of the media on each side of the fault, the symmetry of the surface coseismic displacements between the two fault segments is lost. The segment with a lower Young's modulus exhibits larger assigned displacement, while the segment with a higher Young's modulus has smaller assigned displacement. Nevertheless, the overall distribution characteristics of total deformation remain unaffected. Li and Huang (2011) conducted numerical simulations and found a positive correlation between the vertical component of the seismic coseismic displacement field and the shear modulus, while the horizontal component showed a negative correlation. This indicates the importance of considering lateral variations in the medium, which can be determined quantitatively through seismic tomography imaging and deep seismic reflection profiles when analyzing the coseismic deformation of major earthquakes.

The asymmetry of the surface coseismic distribution of an ideal fault may be caused both by the inhomogeneity of the material on both sides of the fault (Figure 9) and by the geometric complexity of the fault. The Longmen Shan faults exhibit a spade-like structure. Xu and Xu (2015) investigated models with different dip angles and material parameters, revealing greater coseismic deformation in the hanging wall than in the foot wall Quantitative analysis is required to understand the influence of fault morphology on coseismic deformation. Our findings inform future inversion studies in the coseismic rupture of large earthquakes, highlighting the importance of considering fault geometry and media differences on the inversion results.

6 Conclusion

We have developed a 3D parallel elastic finite element program using split nodes and high-performance parallel computing. To validate its accuracy, we compared the program's results for four ideal earthquake cases with analytical solutions from seismic dislocation theory. Our program investigates the media inhomogeneity in the lateral and depth directions on both sides of the main fault, complementing existing homogeneous models. This development lays the groundwork for future inversion studies of coseismic fracture processes based on inhomogeneous models. Using the program, we analyzed the coseismic deformation of the 2008 Wenchuan earthquake, obtaining results consistent with previous research and GPS data. This demonstrates the program's suitability for complex geometry and inhomogeneous media in coseismic deformation analysis.

Data availability statement

The original contributions presented in the study are included in the article/Supplementary Material, further inquiries can be directed to the corresponding author.

Author contributions

MS: Conceptualization, Methodology, Visualization, Formal analysis, Writing–original draft, Writing–review and editing. SM: Writing–original draft, Writing–review and editing. CH: Conceptualization, Methodology, Supurvision, Writing–review and editing, Funding acquision, Project administration. YS: Conceptualization, Formal analysis, Writing–original draft, Writing–review and editing.

Funding

This research was supported by the National Science Foundation of China (42074117) and the Fundamental Research Funds for the Central Universities (E2ET0413X2).

Acknowledgments

Professors Yongen Cai, Yuanze Zhou, and Pengpeng Huangfu gave some constructive suggestions on the numerical simulations. Dr. Bojing Zhu and Dunyu Liu polished the manuscript. The finite element modeling was carried out by the software PFELAC of version 2.2.

Conflict of interest

The authors declare that the research was conducted in the absence of any commercial or financial relationships that could be construed as a potential conflict of interest.

Publisher's note

All claims expressed in this article are solely those of the authors and do not necessarily represent those of their affiliated organizations, or those of the publisher, the editors and the reviewers. Any product that may be evaluated in this article, or claim that may be made by its manufacturer, is not guaranteed or endorsed by the publisher.

Supplementary material

The Supplementary Material for this article can be found online at: https://www.frontiersin.org/articles/10.3389/feart.2023.1245677/full#supplementary-material

References

Bai, Y., Xu, X.-W., Xu, J., and Zhou, B. (2012). The spatial distribution of displacement fields in 2008 Wenchuan earthquake. *Prog. Geophys. (in Chinese)* 27 (1), 29–31. doi:10.6038/j.issn.1004-2903.2012.01.004

Bürgmann, R., and Dresen, G. (2008). Rheology of the lower crust and upper mantle: evidence from rock mechanics, geodesy and field observations. *Annual Review of Earth and Planetary Sciences* 36 (1), 531–567. doi:10.1146/annurev.earth.36.031207.124326

Dong, Y., and Chen, C. (2009). Character of coesimic vertical displacement near Beichuan during Wenchuan MS 8.0 earthquake. *Journal of Geodesy and Geodynamics (in Chinese)* 29 (6), 28–31. doi:10.14075/j.jgg.2009.06.017

Dong, Y., Luo, S., Han, Y., and Chen, C. (2012). Co- and post-seismic vertical displacements of Wenchuan M_S 8.0 earthquake near Beichuan. *Acta Seismologica Sinica (in Chinese)* 34 (5), 611–620. doi:10.3724/SP.J.1246.2011.00029

Element Computing Technology Co. Ltd (2018b). *Parallel architecture of FELAC (in Chinese)*, 8–14.

Element Computing Technology Co., Ltd (2018a). *Fundamentals and applications of finite element analysis of FELAC*, 48–59. *(in Chinese)*.

Freed, A. M., and Lin, J. (2001). Delayed triggering of the 1999 Hector Mine earthquake by viscoelastic stress transfer. *Nature* 411, 180–183. doi:10.1038/35075548

Guo, X., Gao, R., Randy Keller, G., Xu, X., Wang, H., and Li, W. (2013). Imaging the crustal structure beneath the eastern Tibetan Plateau and implications for the uplift of the Longmen Shan range. *Earth and Planetary Science Letters* 379, 72–80. doi:10.1016/j.epsl.2013.08.005

Hu, C. (2009). *A new method to study earthquake triggering and continuous evolution of stress field*. Beijing: Ph.D. Dissertation: Peking University.

Hu, C., Cai, Y., and Wang, Z. (2012). Effects of large historical earthquakes, viscous relaxation, and tectonic loading on the 2008 Wenchuan earthquake. *Journal of Geophysical Research Solid Earth* 117 (B06410). doi:10.1029/2011jb009046

Hu, C., Zhou, Y., Cai, Y., and Wang, C. (2009). Study of earthquake triggering in a heterogeneous crust using a new finite element model. *Seismological Research Letters* 80 (5), 799–807. doi:10.1785/gssrl.80.5.799

Hu, Y., Bürgmann, R., Banerjee, P., Feng, L., Hill, E. M., Ito, T., et al. (2016). Asthenosphere rheology inferred from observations of the 2012 Indian Ocean earthquake. *Nature* 538, 368–372. doi:10.1038/nature19787

Hu, Y., and Wang, K. (2012). Spherical-earth finite element model of short-term postseismic deformation following the 2004 Sumatra earthquake. *Journal of Geophysical Research Solid Earth* 117 (B05404). doi:10.1029/2012jb009153

Hu, Y., Wang, K., He, J., Klotz, J., and Khazaradze, G. (2004). Three-dimensional viscoelastic finite element model for postseismic deformation of the great 1960 Chile earthquake. *Journal of Geophysical Research* 109 (B12403). doi:10.1029/2004jb003163

Huang, Y., Wu, J. P., Zhang, T. Z., and Zhang, D. N. (2008). Relocation of the *M*8.0 Wenchuan earthquake and its aftershock sequence. *Science in China Series D Earth Sciences* 51 (12), 1703–1711. doi:10.1007/s11430-008-0135-z

Huang, Z., Su, W., Peng, Y., Zheng, Y., and Li, H. (2003). Rayleigh wave tomography of China and adjacent regions. *Journal of Geophysical Research Solid Earth* 108 (B2), 2073. doi:10.1029/2001jb001696

Lei, J., and Zhao, D. (2009). Structural heterogeneity of the longmenshan fault zone and the mechanism of the 2008 wenchuan earthquake (M_S 8.0). *Geochemistry, Geophysics, Geosystems* 10, Q10010. doi:10.1029/2009gc002590

Lei, J., and Zhao, D. (2016). Teleseismic p-wave tomography and mantle dynamics beneath Eastern Tibet. *Geochemistry, Geophysics, Geosystems* 17, 1861–1884. doi:10.1002/2016gc006262

Li, F., and Huang, J. (2011). Numerical simulation of influences of medium heterogeneity and dip of fault on coseismic displacement. *Journal of Geodesy and Geodynamics (in Chinese)* 31 (5), 52–60. doi:10.3969/j.issn.1671-5942.2011.05.012

Li, H., Fu, X., Woerd, J., Si, J., Wang, Z., Hou, L., et al. (2008). Co-seisimic surface rupture and dextra-slip oblique thrusting of the M_S 8.0 Wenchuan Earthquake. *Acta Geologica Sinica (in Chinese)* 82 (12), 1623–1643. doi:10.3321/j.issn:0001-5717.2008.12.002

Liu, C., Dong, P., Zhu, B., and Shi, Y. (2018). Stress shadow on the southwest portion of the Longmen Shan Fault impacted the 2008 Wenchuan earthquake rupture. *Journal of Geophysical Research Solid Earth* 123, 9963–9981. doi:10.1029/2018jb015633

Liu, C., Zhu, B.-J., Yang, X.-L., and Shi, Y.-L. (2015). Crustal rheology control on earthquake activity across the eastern margin of the Tibetan Plateau: insights from numerical modelling. *Journal of Asian Earth Sciences* 100, 20–30. doi:10.1016/j.jseaes.2015.01.001

Liu, Q., Li, Y., Chen, J., Guo, B., Li, S., Wang, J., et al. (2009). Wenchuan M_S 8.0 earthquake: preliminary study of the S-wave velocity structure of the crust and upper mantle. *Chinese Journal of Geophysics (in Chinese)* 52 (2), 309–319. doi:10.6038/j.issn.0001-5733.2012.08.008

Liu, X., Wu, J., Liang, C., Qian, Q., and Du, P. (2019). The latest seismicity characteristics and significance in Longmenshan Fault Zone. *Chinese Journal of Geophysics (in Chinese)* 62 (4), 1312–1322. doi:10.6038/cjg2019M0283

Luo, G., and Liu, M. (2010). Stress evolution and fault interactions before and after the 2008 great Wenchuan earthquake. *Tectonophysics* 491, 127–140. doi:10.1016/j.tecto.2009.12.019

Luo, G., and Liu, M. (2018). Stressing rates and seismicity on the major faults in eastern Tibetan Plateau. *Journal of Geophysical Research Solid Earth* 123 (10), 968–986. doi:10.1029/2018jb015532

Massonnet, D., Rossi, M., Carmona, C., Adragna, F., Peltzer, G., Feigl, K., et al. (1993). The displacement field of the Landers earthquake mapped by radar interferometry. *Nature* 364, 138–142. doi:10.1038/364138a0

Melosh, H. J., and Raefsky, A. (1981). A simple and efficient method for introducing faults into finite element computations. *Bulletin of the Seismological Society of America* 71 (5), 1391–1400. doi:10.1785/bssa0710051391

Okada, Y. (1985). Surface deformation due to shear and tensile faults in a half-space. *Bulletin of the Seismological Society of America* 75 (4), 1135–1154. doi:10.1785/bssa0750041135

Okada, Y. (1992). Internal deformation due to shear and tensile faults in a half-space. *Bulletin of the Seismological Society of America* 82 (2), 1018–1040. doi:10.1785/bssa0820021018

Ozawa, S., Nishimura, T., Munekane, H., Suito, H., Kobayashi, T., Tobita, M., et al. (2012). Preceding, coseismic, and postseismic slips of the 2011 Tohoku earthquake, Japan. *Journal of Geophysical Research Solid Earth* 117, B07404. doi:10.1029/2011jb009120

Shen, Z.-K., Sun, J., Zhang, P., Wan, Y., Wang, M., Bürgmann, R., et al. (2009). Slip Maxima at fault junctions and rupturing of barriers during the 2008 Wenchuan earthquake. *Nature Geoscience* 2, 718–724. doi:10.1038/ngeo636

Sreejith, K. M., Sunil, P. S., Agrawal, R., Saji, A. P., Ramesh, D. S., and Rajawat, A. S. (2016). Coseismic and early postseismic deformation due to the 25 April 2015, M_W 7.8 Gorkha, Nepal, earthquake from InSAR and GPS measurements. *Geophysical Research Letters* 43, 3160–3168. doi:10.1002/2016gl067907

Steketee, J. A. (1958). On Volterra's dislocations in a semi-infinite elastic medium. *Canadian Journal of Physics* 36, 192–205. doi:10.1139/p58-024

Suito, H., and Freymueller, J. T. (2009). A viscoelastic and afterslip postseismic deformation model for the 1964 Alaska earthquake. *Journal of Geophysical Research Solid Earth* 114 (B11404). doi:10.1029/2008jb005954

Sun, W., Okubo, S., Fu, G., and Araya, A. (2009). General formulations of global co-seismic deformations caused by an arbitrary dislocation in a spherically symmetric Earth model-applicable to deformed earth surface and space-fixed point. *Geophysical Journal International* 177, 817–833. doi:10.1111/j.1365-246x.2009.04113.x

Sun, W., Okubo, S., and Vaníček, P. (1996). Global displacements caused by point dislocations in a realistic Earth model. *Journal of Geophysical Research Solid Earth* 101 (B4), 8561–8577. doi:10.1029/95jb03536

Tan, H., Wu, G., Xuan, S., Yang, G., Fan, W., and Shen, C. (2015). Wenchuan M_S 8.0 earthquake coseismic slip distribution inversion. *Geodesy and Geodynamics* 6 (3), 173–179. doi:10.1016/j.geog.2015.05.001

Toda, S., Lin, J., Meghraoui, M., and Stein, R. S. (2008). 12 May 2008 M = 7.9 Wenchuan, China, earthquake calculated to increase failure stress and seismicity rate on three major fault systems. *Geophysical Research Letters* 35 (L17305). doi:10.1029/2008gl034903

Toda, S., Stein, R. S., Sevilgen, V., and Lin, J. (2011). *Coulomb 3.3 graphic-rich deformation and stress-change software for earthquake, tectonic, and Volcano Research and teaching-user guide*. Open-File Report. doi:10.3133/ofr20111060

Tong, X., Sandwell, D. T., and Fialko, Y. (2010). Coseismic slip model of the 2008 Wenchuan earthquake derived from joint inversion of interferometric synthetic aperture radar, GPS, and field data. *Journal of Geophysical Research* 115, B04314. doi:10.1029/2009jb006625

Tu, H.-W., Wang, R.-J., Diao, F.-Q., Zhang, Y., Wan, Y.-G., and Jin, M.-P. (2016). Slip model of the 2001 Kunlun mountain M_S 8.1 earthquake by SDM: joint inversion from GPS and InSAR Data. *Chinese Journal of Geophysics (in Chinese)* 59 (6), 404–413. doi:10.1002/cjg2.20245

Wan, Y., Shen, Z.-K., Bürgmann, R., Sun, J., and Wang, M. (2017). Fault geometry and slip distribution of the 2008 M_W 7.9 Wenchuan, China earthquake, inferred from GPS and insar measurements. *Geophysical Journal International* 208, 748–766. doi:10.1093/gji/ggw421

Wan, Y., Shen, Z.-K., W, M., Zhang, Z.-S., Gan, W.-J., Wang, Q.-L., et al. (2008). Coseismic slip distribution of the 2001 Kunlun mountain pass west earthquake constrained by GPS and InSAR data. *Chinese Journal of Geophysics* 51, 753–764. doi:10.1002/cjg2.1268

Wang, M., Li, Q., Wang, F., Zhang, R., Wang, Y. Z., Shi, H. B., et al. (2011a). Far-field coseismic displacements associated with the 2011 Tohoku-Oki earthquake in Japan observed by Global Positioning System. *Chinese Science Bulletin* 56 (23), 2419–2424. doi:10.1007/s11434-011-4588-7

Wang, M., Shen, Z. K., Wang, Y. Z., Bürgmann, R., Wang, F., Zhang, P. Z., et al. (2021). Postseismic deformation of the 2008 Wenchuan earthquake illuminates

lithospheric rheological structure and dynamics of Eastern Tibet. *Journal of Geophysical Research Solid Earth* 126. doi:10.1029/2021jb022399

Wang, Q., Qiao, X., Lan, Q., Freymueller, J., Yang, S., Xu, C., et al. (2011b). Rupture of deep faults in the 2008 Wenchuan earthquake and uplift of the Longmen Shan. *Nature Geoscience* 4, 634–640. doi:10.1038/ngeo1210

Wang, Q., Cui, D., Zhang, X., Wang, W., and Liu, J. (2010). Studies on surface vertical deformation of the Longmenshan and the Wenchuan M_S 8.0 earthquake. *Recent Developments in World Seismology (in Chinese)* 6, 11–12. doi:10.3969/jissn.0235-4975.2010.06.010

Wang, R., Martin, F. L., and Roth, F. (2003). Computation of deformation induced by earthquakes in a multi-layered elastic crust—fortran programs EDGRN/EDCMP. *Computers and Geosciences* 29, 195–207. doi:10.1016/s0098-3004(02)00111-5

Wiseman, K., Bürgmann, R., Freed, A. M., and Banerjee, P. (2015). Viscoelastic relaxation in a heterogeneous earth following the 2004 sumatra–andaman earthquake. *Earth and Planetary Science Letters* 431, 308–317. doi:10.1016/j.epsl.2015.09.024

Working Group of the Crustal Motion Observation Network of China Project (2008). Coseismic displacement field of the 2008 *Ms* 8.0 Wenchuan earthquake determined by GPS. *Sci. China (Ser. D) (in Chinese)* 38 (10), 1195–1206. doi:10.3321/j.issn:1006-9267.2008.10.003

Xu, B., and Xu, C. (2015). Numerical simulation of influences of the Earth Medium's lateral heterogeneity on co- and post-seismic deformation. *Geodesy and Geodynamics* 6 (1), 46–54. doi:10.1016/j.geog.2014.11.001

Xu, C., Liu, Y., Wen, Y., and Wang, R. (2010). Coseismic slip distribution of the 2008 M_W 7.9 Wenchuan earthquake from joint inversion of GPS and InSAR Data. *Bulletin of the Seismological Society of America* 100, 2736–2749. doi:10.1785/0120090253

Xu, M., Li, H., Song, Z., Xu, Q., Zhang, X., Fu, P., et al. (2022). *An electric-thermal-solid physical fields coupling calculation based on FELAC platform*, 2022. IEEE 5th International Conference on Electronics Technology, 532–536. doi:10.1109/ICET55676.2022.9825404

Xu, X., Wen, X., Ye, J., Ma, B., Chen, J., Zhou, R., et al. (2008). The M_S 8.0 Wenchuan earthquake surface ruptures and seismogenic structure. *Seismology and Geology (in Chinese)* 30 (3), 597–629. doi:10.3969/j.issn.0253-4967.2008.03.003

Zhang, B., Zhang, H., and Shi, Y. (2015). Equivalent-body force approach on modeling elastic dislocation problem using finite method. *Chinese Journal of Geophysics (in Chinese)* 58 (05), 1666–1674. doi:10.6038/cjg20150518

Zhang, G., Qu, C., Shan, X., Song, X., Zhang, G., Wang, C., et al. (2011). Slip distribution of the 2008 Wenchuan M_S 7.9 earthquake by joint inversion from GPS and InSAR measurements: a resolution test study. *Geophysical Journal International* 186, 207–220. doi:10.1111/j.1365-246x.2011.05039.x

Zhao, D., Qu, C., Shan, X., Bürgmann, R., Gong, W., and Zhang, G. (2018). Spatiotemporal evolution of postseismic deformation following the 2001 M_W 7.8 Kokoxili, China, earthquake from 7 years of Insar Observations. *Remote Sensing* 10, 1988. doi:10.3390/rs10121988

frontiers | Frontiers in Earth Science

TYPE Original Research
PUBLISHED 28 December 2023
DOI 10.3389/feart.2023.1285136

Check for updates

OPEN ACCESS

EDITED BY
Giovanni Martinelli,
National Institute of Geophysics and Volcanology, Italy

REVIEWED BY
Xiaocheng Zhou,
China Earthquake Administration, China
Liu Wei,
Tianjin University, China
Guangcai Wang,
China University of Geosciences, China

*CORRESPONDENCE
Le Hu,
hulecugb@126.com

RECEIVED 29 August 2023
ACCEPTED 17 November 2023
PUBLISHED 28 December 2023

CITATION
Bao Z, Hu L, Xiao J, Zha X, Lv J and Zhao Y (2023), Stable isotopes and hydrogeochemical evolutions of groundwater from a typical seismic fault zone in the Mt. Lushan region, Eastern China.
Front. Earth Sci. 11:1285136.
doi: 10.3389/feart.2023.1285136

COPYRIGHT
© 2023 Bao, Hu, Xiao, Zha, Lv and Zhao. This is an open-access article distributed under the terms of the Creative Commons Attribution License (CC BY). The use, distribution or reproduction in other forums is permitted, provided the original author(s) and the copyright owner(s) are credited and that the original publication in this journal is cited, in accordance with accepted academic practice. No use, distribution or reproduction is permitted which does not comply with these terms.

Stable isotopes and hydrogeochemical evolutions of groundwater from a typical seismic fault zone in the Mt. Lushan region, Eastern China

Zhicheng Bao[1], Le Hu[2]*, Jian Xiao[1], Xiaohui Zha[1], Jian Lv[1] and Ying Zhao[1]

[1]Jiangxi Earthquake Angecy, Nanchang, China, [2]Institute of Earthquake Forecasting, China Earthquake Administration, Beijing, China

We analyzed the major chemical components, hydrogen (δD) and oxygen isotopes (δ^{18}O), and tritium activity in groundwater from Jiujiang well number 2 (JJ2) as well as atmospheric precipitation and water from the Maweishui spring and Tianhuajing reservoir in the Mt. Lushan region, Eastern China. The results show that the water in JJ2 is of the HCO_3-Ca·Mg type, with ionic components mainly arising from calcite and dolomite mineral dissolution. According to the δD and δ^{18}O data, the groundwater of JJ2 mainly comes from atmospheric precipitation, and the recharge elevation is 554 m. Results for tritium activity indicate that JJ2 is fed by both an ancient water supply and a new water supply within a period of 10 years. These results demonstrate that JJ2 has characteristics of both shallow and deep circulating water, which implies that aquifers involving two different recharge sources rise to the well surface via different circulation paths. That is exactly why JJ2 is tectonically sensitive and could display a remarkable gas radon anomaly before the Ruichang-Yangxin M_L 5.0 earthquake in 2011. Our results also indicate that ascertaining the hydrological characteristics and cycling process of groundwater are crucial for understanding the earthquake anomalies and judging whether a seismic groundwater monitoring well is reliable or not.

KEYWORDS

hydrogeochemistry, stable isotope, tritium activity, geochemical characteristics, radon anomaly

1 Introduction

Underground fluid is proved to be an important carrier for transmitting information of geological evolution within the Earth and thus its geochemical characteristics and genesis are widely studied (Zhang, 1992; Che et al., 1998; Du and Kang, 2000; Liu, 2006; Li et al., 2022; 2023). Detailed researches involving the relationship between groundwater and surface runoff (Grasby et al., 1999; Su et al., 2009; Gu et al., 2017), the circulation process and water-rock interactions (He and Singh, 2019; Hosono and Masaki, 2020; Hosono et al., 2019; Nakagawa et al., 2020; Shi et al., 2020; Barberio et al., 2017; Skelton et al., 2014; Barberioet al., 2017; Zhou et al., 2020; Chen et al., 2015; Li et al., 2021; Martinelli and Dadomo, 2017; Skelton et al., 2019; Li et al., 2017; Bao et al., 2019; Du and Liu, 2003; Sun et al., 2016; Zhou et al., 2022; Tian et al., 2021; Song et al., 2006), the changes of chemical compositions before

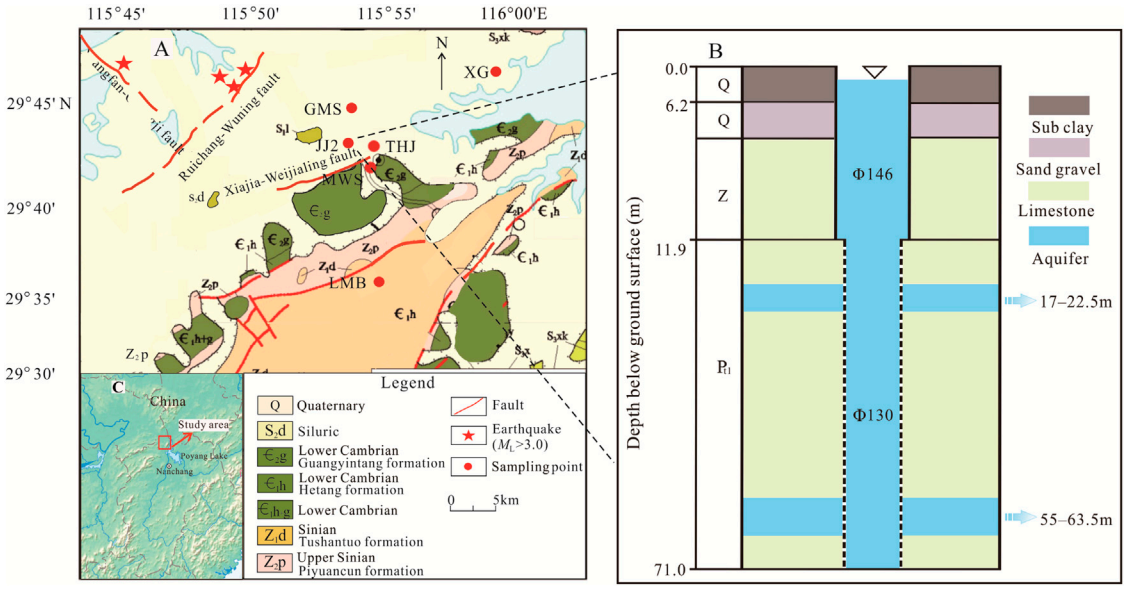

FIGURE 1
(A) Structural geological map of the study area. **(B)** Schematic diagram of well structure and aquifers of JJ2. **(C)** Location of the study area.

and after earthquakes (Tsunogai and Wakita, 1995; Claesson et al., 2004; Reddy and Nagabhushanam, 2011; Reddy et al., 2011; He and Singh, 2019; Hosono and Masaki, 2020; Hosono et al., 2019; Nakagawa et al., 2020; Shi et al., 2020; Barberio et al., 2017; Skelton et al., 2014; Barberioet al., 2017; Zhou et al., 2020; Chen et al., 2015; Zhao et al., 2023), and the earthquake anomaly verification (Liu and Ren, 2009; Zhang et al., 2014; Zhang et al., 2016; Zhou et al., 2021). All these studies demonstrated that making clear the origin and forming process of underground fluid is the prerequisite for identifying earthquake precursors (Li et al., 2022; 2023).

Ruichang-Yangxin M_L 5.0 earthquake, occurred on 10 September 2011, is one of the large earthquakes occurred in the central and eastern regions of China in recent years. About 1 month before the earthquake, radon in groundwater from Jiujiang well number 2 (herein after JJ2) increased rapidly, showing a remarkably high value anomaly. The reason that JJ2 can exhibit such anomaly could be the fact that JJ2 is a cold spring located on the fault zone with a moderate groundwater age as there is a hypothesis that neither young and old groundwater can reflect the change of the geochemical environment in the crust effectively while groundwater with moderate age is more able to show relatively complete abnormal forms before earthquakes (Pan and Gao, 2001). But to better understand the cause of this radon anomaly, more detailed works need to be done on the groundwater characteristics in the JJ2. Therefore, this paper attempts to give a reasonable explanation to the seismic hydrogeochemical characteristics of the well and the causes of the pre-earthquake anomaly of gas radon through the analysis results of hydrochemical composition, hydrogen and oxygen isotopes and well water dating. This would provide a scientific basis for further understanding the recharge cycle and anomaly formation in shallow wells on the fault zone and exploring the formation mechanism of gas radon anomaly in areas with few earthquakes and weak earthquakes and its response relationship with regional tectonic activities.

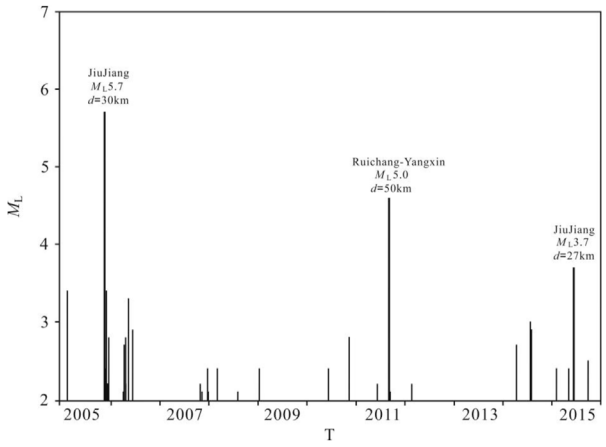

FIGURE 2
Time-series map of earthquakes above M_L 2.0 within 150 km of the Jiujiang seismic station.

2 Geological setting

The JJ2 is a typical well at the Jiujiang Seismic Monitoring Centre station (JJS) (29.65°N, 115.33°E, 110 m) which is located in the northwestern side of Lushan Mount (Mt Lushan) in the north of Jiangxi province and tectonically belongs to the junction zone of Yangtze block (Jiangnan ancient land) and Dabie Mountain block (Lv et al., 2008). The climate here is subtropical monsoon, with annual average temperature of 16.7°C and average annual precipitation of 1,300 mm. Active faults are well developed in the

area including the NE-trending Tanlu Fault, the NW-trending Xiangfan-Guangji Fault, and the NEE trending Xiajia-Weijialing Fault (Figure 1). The Xiajia-Weijialing fault near the JJ2 is a left strike-slip fault on the edge of the northwestern margin of Lushan Mountain. The fault extends for about 8 km wide and about 11.5 km long, with a general tendency 320°–330° and an inclination of 60~70°. The study area is seismically active, within which three earthquakes with magnitude above 3.0 have occurred since 2005, including the Jiujiang-Ruichang M_L 5.7 earthquake in 2005, the Ruichang-Yangxin M_L 5.0 earthquake in 2011, and the Jiujiang M_L 3.7 earthquake in 2015 (Figure 2).

JJ2 is a structurally confined artesian well started running since 2008. The well has the depth of 71 m and the casing of 11.9 m. From the surface to 6.2 m, it is composed of loam and gravel of Lianwei Formation of Quaternary; 6.2–11.9 m is composed of strongly weathered carbonaceous limestone of Piyuancun Formation of Sinian; and 11.9–71 m is composed of Lower Proterozoic carbonaceous limestone (Figure 1). The well has two aquifers at 17–22.5 m and 55–63.5 m respectively, and the current daily discharge is approximately 300 tons. There is a reservoir about 1 km away and a river about 50 m away which comes from the Maweishui (MWS) spring in the Mt Lushan.

3 Sampling and analyzing methods

Atmospheric precipitations from the courtyard of JSS (JIJ), Guomiansichang (GMS), Xingang (XG), and Lushan Meteorological Bureau (LMB) were collected for δD and $\delta^{18}O$ analysis. Water samples from the JJ2, MWS spring, and Tianhuajing reservoir (THJ) were collected for δD, $\delta^{18}O$ and chemical analysis. The sampling bottle was high density polyethylene (HDPE) screw cap bottle with a thin neck. In order to avoid contamination of samples, sampling bottle was cleaned with deionized water before collecting samples, and then with the collected water sample for three times. By overflow method, the bottle was capped immediately after filling, and the mouth wrapped with parafilm. Two samples were collected at each sampling point. A total of 239 effective water samples were obtained, of which 198 were obtained from atmospheric precipitation, and 41 from JJ2, THJ reservoir and MWS spring water. The collection method was to connect a sampling bottle under the rain gauge. In order to prevent sundries from entering the sampling bottle, a ping-pong ball was placed in the rain gauge. Effective precipitation with long rainfall duration was used for test and analysis. Water samples from JJ2, which was used for hydrogen and oxygen isotope testing, were collected once every 2 weeks, and water samples from four different seasons were selected for hydrochemical composition analysis. The water from THJ reservoir and MWS spring were collected once for hydrogen and oxygen isotope and water chemical composition analysis. All samples were filtered through a 0.22 μm membrane before measurement.

Water temperature, pH value, and total dissolved solids (TDS) were recorded in the sampling point, and each parameter was measured thrice continuously and averaged. The hydrochemical components and hydrogen and oxygen isotope analysis of the samples were completed in the Key Laboratory of Crustal Dynamics (Underground Fluid Dynamics Laboratory Unit) of

TABLE 1 Summary of stable isotopes and chemical compositions of different water bodies in the Lushan regions ["-" represents no text data, "*" represents data from Bao et al. (2022)].

NO	Sample type	Longitude& altitude	Altitude (m)	temperature (°C)	TDS mg/L	pH	$\delta^{18}O$ (‰)	δD (‰)	d (‰)	Na^+	K^+	Mg^{2+}	Ca^{2+}	F^-	Cl^-	SO_4^{2-}	HCO_3^-	NO_3^-	Classify
JJ2	Well water	29.65°N,115.33°E	110	18.4	247.07~258.15	7.3	−7.42~−6.09	−43.87~−39.69	9.03~15.93	1.32~2.26	1.32~1.94	13.39~14.86	35.84~43.26	0.18~0.52	0.38~2.35	4.97~9.38	177.34~194.16	0.11~1.67	HCO_3-Ca-Mg
JJJ	Precipitation	29.65°N,115.33°E	110	--	15.96~20.70	--	−12.45~−1.26	−90.30~−4.74	1.83~26.39	0.1~0.42	0.01~0.22	0.04~0.08	0.30~0.81	0.02~0.15	0.28~0.75	1.44~2.70	6.10~20.99	1.13~5.61	--
GMS	Precipitation	29.70°N,115.34°E	68	--	18.08~39.55	--	−10.65~−2.5	−65.4~−3.04	7.14~23.32	0.12~0.53	0.16~0.53	0.03~0.11	0.44~2.07	0.02~0.17	0.39~1.51	1.92~9.57	2.97~13.04	12.20	--
LMB	Precipitation	29.59°N,115.35°E	1325	--	--	--	−15.97~0.48	−126.77~22.11	−26.42~25.53	--	--	--	--	--	--	--	--	--	--
XG	Precipitation	29.78°N,115.98°E	60	--	--	--	−13.00~−6.22	−96.13~−38.34	3.85~11.65	--	--	--	--	--	--	--	--	--	--
THJ*	Surface water	29.66°N,115.34°E	138	22.8	46.8	7.1	−5.66	−33.36	11.92	1.45	0.55	0.95	9.00	0.13	1.55	8.11	38.44	11.43	HCO_3-Ca
MWS*	Spring	29.66°N,115.33°E	569	17.3	42.9	5.7	−7.53	−44.25	15.99	94.44	3.29	0.19	3.84	16.99	5.97	18.00	27.46	1.18	HCO_3-Na

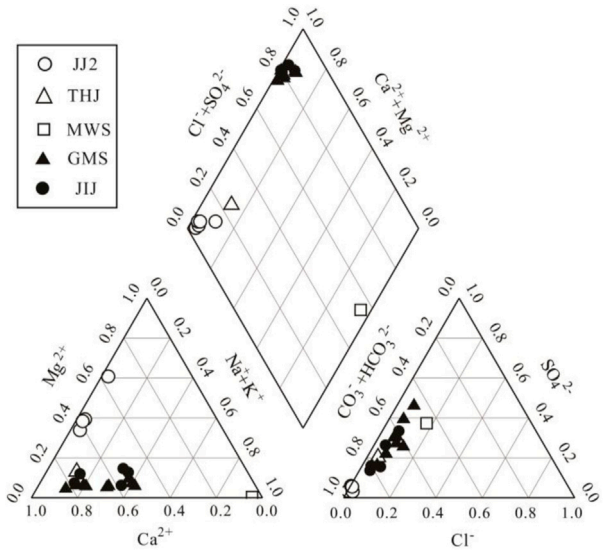

FIGURE 3
Piper diagram of chemical macronutrients.

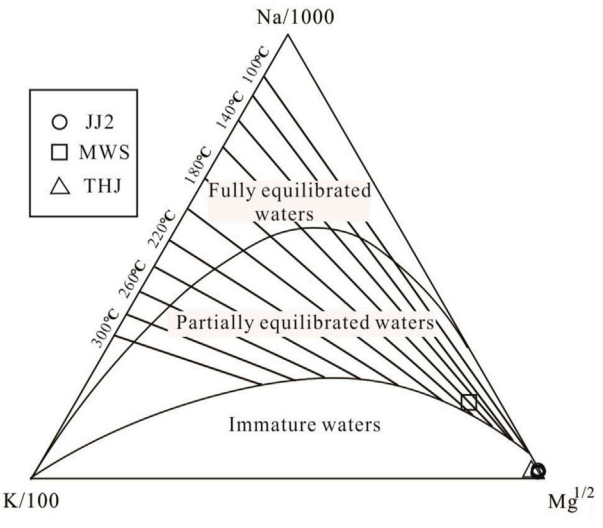

FIGURE 5
Na-K-Mg diagram and partial enlargement of water sample.

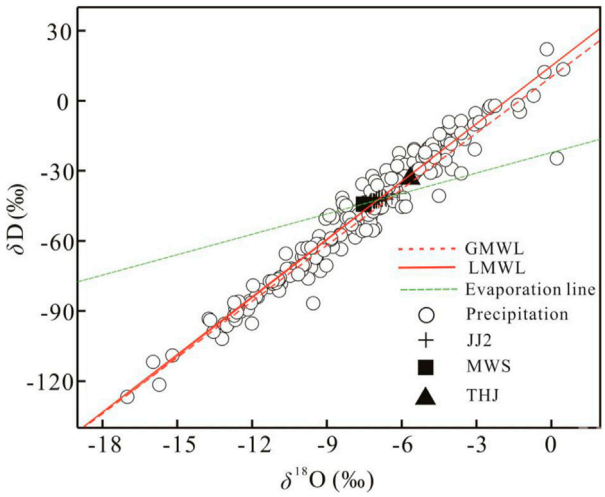

FIGURE 4
Distribution chart of δD and $\delta^{18}O$ in the water sample.

China Earthquake Administration, where major element analysis equipment used was ICS-2100 ion chromatograph (flow accuracy <0.1%). Oxygen isotope analysis equipment used was Picarro liquid water isotope analyzer (L2130-i type, United States of America), and the results of stable isotopes of hydrogen and oxygen were expressed in thousandths difference relative to Vienna standard mean marine water (VSMOW):

$$\delta = \left(R_{sample} - R_{s\tan dard}\right) \Big/ R_{s\tan dard} \times 1000 \quad (1)$$

Here, R_{sample} represents the ratio of $^{18}O/^{16}O$ (D/H) in the samples; $R_{standard}$ represents the ratio of $^{18}O/^{16}O$ (D/H) in VSMOW. The accuracy of the tests conducted was determined to be $\delta^{18}O < 0.05‰$ and $\delta D < 0.5‰$. The tritium isotope radioactivity of the samples was tested at the Institute of Hydrogeology and Environmental Geology, Chinese Academy of Geological Sciences, using a Quantulus-1220 ultra-low background liquid scintillation spectrometer. Liquid scintillation counting was employed as the analytical method.

SD-3A Intelligent Digital Radon Meter operates based on the flashing light method. When radon gas enters the scintillation chamber, the α particles emitted from the decay of radon and its progeny cause the "fluorescent body" on the wall of the sampler in the scintillation chamber, which is made of ZnS (Ag), to emit weak flashes of light. The photomultiplier inside the instrument then detects and converts these flashes of light into electrical impulses. These electrical impulses are further amplified by the electronic circuits, and finally, the processor records the corresponding electrical impulse signals. Subsequently, the processor calculates the radon content (concentration) in the measured gas (or soil) using the principle of pulse count rate, which is determined by the number of electric pulses recorded per unit time.

4 Results

4.1 Hydrochemical characteristics

The main analytical phases of hydrochemistry in the study area (pH, TDS, Ca^{2+}, Mg^{2+}, Na^{+}, K^{+}, F^{-}, Cl^{-}, SO_4^{2-}, and HCO_3^{-}) are shown in Table 1. Generally, the pH values of groundwater and surface water were weakly alkaline, while that of MWS Spring was acidic. The TDS of JJ2 water, THJ water, and MWS water were 247.07~258.15 mg/L, 46.80 mg/L, and 42.90 mg/L respectively. The TDS of groundwater was higher than that of surface water. As can be seen in Piper's three-line diagram, the main positive ions include Ca^{2+}, Mg^{2+}, and Na^{+}, and the main negative ions are HCO_3^{-} and Cl^{-}. In the piper chart, the water samples are mainly distributed in three zones (Figure 3). Among them, the water samples on the first zone (JJ2 and THJ) belongs to the HCO_3–Ca·Mg type.

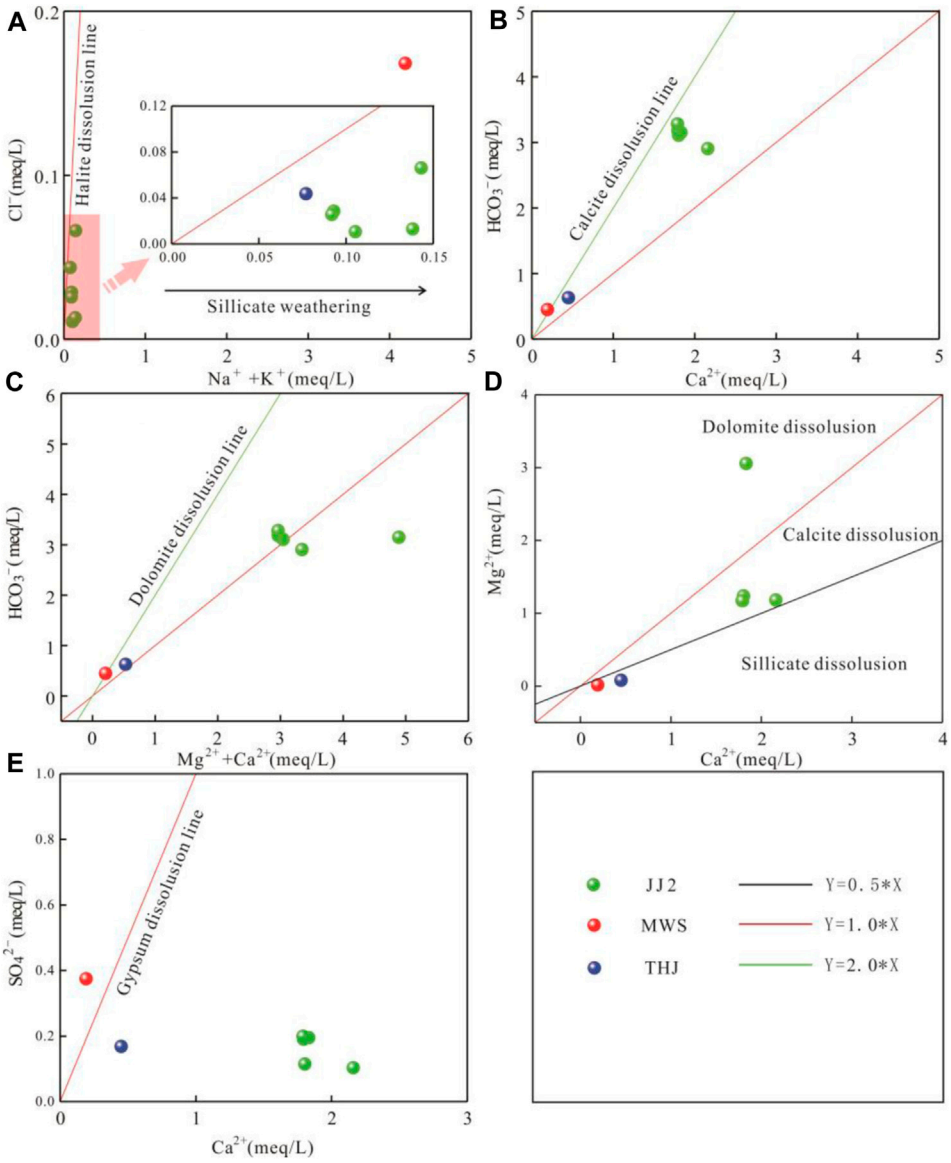

FIGURE 6
(A) Relationships between $Na^+ + K^+$ and Cl^- of JJ2. **(B)** Relationships between Ca^{2+} and HCO_3^- of JJ2. **(C)** Relationships between $Mg^{2+} + Ca^{2+}$ and HCO_3^- of JJ2. **(D)** Relationships between Ca^{2+} and $Mg^{2+}$of JJ2. **(E)** Relationships between Ca^{2+} and $SO_4^{2-}$of JJ2.

Atmospheric precipitations (JIJ and GMS) in the second zone belongs to the Cl–Na type. Other water samples are located in the third zone of the piper diamond graph that belong to the HCO_3–Na type.

4.2 Characteristics of hydrogen and oxygen isotope composition

The measured values of hydrogen isotope (δD) and oxygen isotope isotopic composition ($\delta^{18}O$) in JJ2 was −43.87‰~-39.69‰ and −7.42‰~-6.09‰, respectively. The mean values of $\delta^{18}O$ and δD for the JJ2 are −6.99‰ and −42.55‰ respectively. The measured value of δD and $\delta^{18}O$ in atmospheric precipitation was −126.77‰ ~22.11‰ and-15.97‰~0.48‰, respectively. The mean values of $\delta^{18}O$ and δD for the atmospheric precipitation are −7.67‰ and −48.68‰ respectively. According to the measured values of hydrogen and oxygen isotopes of atmospheric precipitation, the local atmospheric precipitation line was: $\delta D = 8.6\ \delta^{18}O + 18.8$ (r=0.97, n= 198), and the slope and intercept were roughly the same as those in Nanjing (Wang et al., 2013; Liu et al., 2014). According to the δD and $\delta^{18}O$ of groundwater in JJ2, the evaporation line of groundwater at JJS was fitted as: $\delta D = 3.0\ \delta^{18}O - 21.9$ (r=0.86, n=34). Moreover, it could be observed that δD and $\delta^{18}O$ of the JJ2 water are mainly distributed near the meteoric water line (Figure 4). Compared with the local precipitation line and the global atmospheric precipitation line, the slope and intercept of the fitted evaporation line were obviously smaller, which indicates that the whole water belongs to the atmospheric genetic type and experienced certain evaporation before the atmospheric precipitation is replenished (Craig, 1961; Giggenbach, 1992).

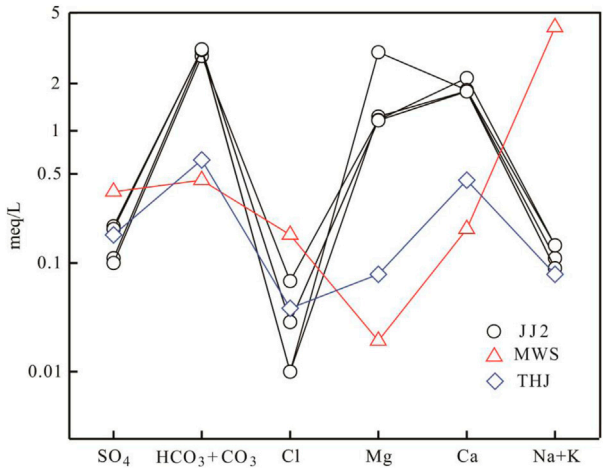

FIGURE 7
Scherer diagrams shows the characteristics of constant components.

4.3 Gas radon concentrations

The intelligent digital radon-detectors (SD-3A) samples once every hour. This paper provides the observed gas radon data time series from January to December 2011 (Figure 9C). It can be seen that the normal background values are varying in range of 0.3 Bq/L to 2.0 Bq/L. However, the value began to rise rapidly since 12th of August 2011 and reach a maximum value of 28.5Bq/L on 30th of August. After that, the value began to decline. During the process, the Ruichang-Yangxin M_L5.0 earthquake occurred on 11 September, which is about 27 km away from the JJ2.

5 Discussion

5.1 Groundwater circulation depth

Groundwater geochemical evolution is mainly controlled by various chemical reactions between water and rock, and identifying these reactions is the basis of groundwater geochemical evolution research (Giggenbach, 1988). In this paper, Na-K-Mg triangle graphic method is utilized to analyze the chemical equilibrium reaction characteristics and cycle depth of groundwater components. The Na–K–Mg triangular plot (Figure 5) shows the sample of JJ2 and THJ are in immature water zone, indicating that they are not fully equilibrated with the reservoir rocks. The sample of MWS plot in the partial equilibrated water zone, which show that part of water-rock interaction had reached equilibrium, the circulating depth of underground water was deep.

Cation geothermometers can be used to estimate approximate reservoir temperatures. In this study, the Na-K-Mg triangulation based on Na-K and K-Mg geothermometers were used to assess the thermal storage temperature of underground water samples. According to the temperature marking in Figure 5, the reservoir temperatures of groundwater in JJ2 was about 60~80 °C, and the MWS sample was about 160°C.

According to the reservoir temperature, the circulated depth calculation formula shown as follows is adopted

$$Z = Z_0 + (T - T_0)/T_{grad} \quad (2)$$

Here, Z represents the circulation depth (km); Z_0 represents the depth of the constant temperature zone (km); T represents the reservoir temperature (°C); T_0 represents the temperature of the constant temperature zone (°C), namely, the local average temperature; Tgrad represents the geothermal gradient (°C/km) reflecting the geothermal change per kilometer of the place below the constant temperature zone (Xiong et al., 1990). Based on the previous studies on groundwater in the study area, we selected the geothermal gradient Tgrad of 21.3°C/km (Wang et al., 2023a), the annual mean temperature T_0 in the Jiujiang is 17.5°C, and the Z_0 is 20 m. The circulation depth of the JJ2 and MWS are about 2015~2,954 m and 6710 m respectively, which implies that the circulating path of groundwater in MWS spring was different from that in JJ2. The circulation depth and the reservoir temperature of the JJ2 and MWS are positive-related. Cool waters are likely involved during the long circulation pathways between the reservoir and the spring vent.

5.2 Recharge elevation

The linear regression between different elevations and their hydrogen and oxygen isotope ratios could fit the elevation gradient of oxygen isotopes in the study area. When studying the groundwater recharge elevation, "isotope elevation gradient" can be used in a local area. According to previous research results (Ou et al., 2011), the elevation gradient of $\delta^{18}O$ and δD in Lushan area is 0.188‰/100 m and 0.0138‰/100 m respectively. The recharge elevation of groundwater in the study area can be estimated by using the elevation gradient value, and its calculation formula is as follows:

$$H = \frac{(\delta G - \delta P)}{K} + h \quad (3)$$

Here, H represents the recharge elevation (m), h represents the sampling point elevation (m); δ_G represents the isotopic composition of underground water (‰), δ_P represents the atmospheric precipitation near the sampling point (‰); K represents the isotopic altitude gradient (‰/100 m). Considering the probably oxygen drift caused by water-carbonate rock interaction (Pang et al., 2017), $K_{\delta D}$ = 0.0138‰/100 m was used in this study. So, the calculated recharge elevation calculated is 554 m.

5.3 Groundwater age

Tritium is a radioactive isotope of hydrogen, with a half-life of 12.43 a (Lucas and Unterweger, 2000), which can be subdivided into natural tritium and artificial tritium according to its origin. Natural tritium mainly comes from cosmic rays, and artificial tritium mainly comes from human activities such as nuclear experiments. Tritium is released during the month of precipitation, surface water, and groundwater, and is not easy to react with environmental media along with hydrogeological and other processes for life, but only follows the radioactive law, with the change being quite independent (Wang, 1991). Based on the inherent characteristics of tritium, it

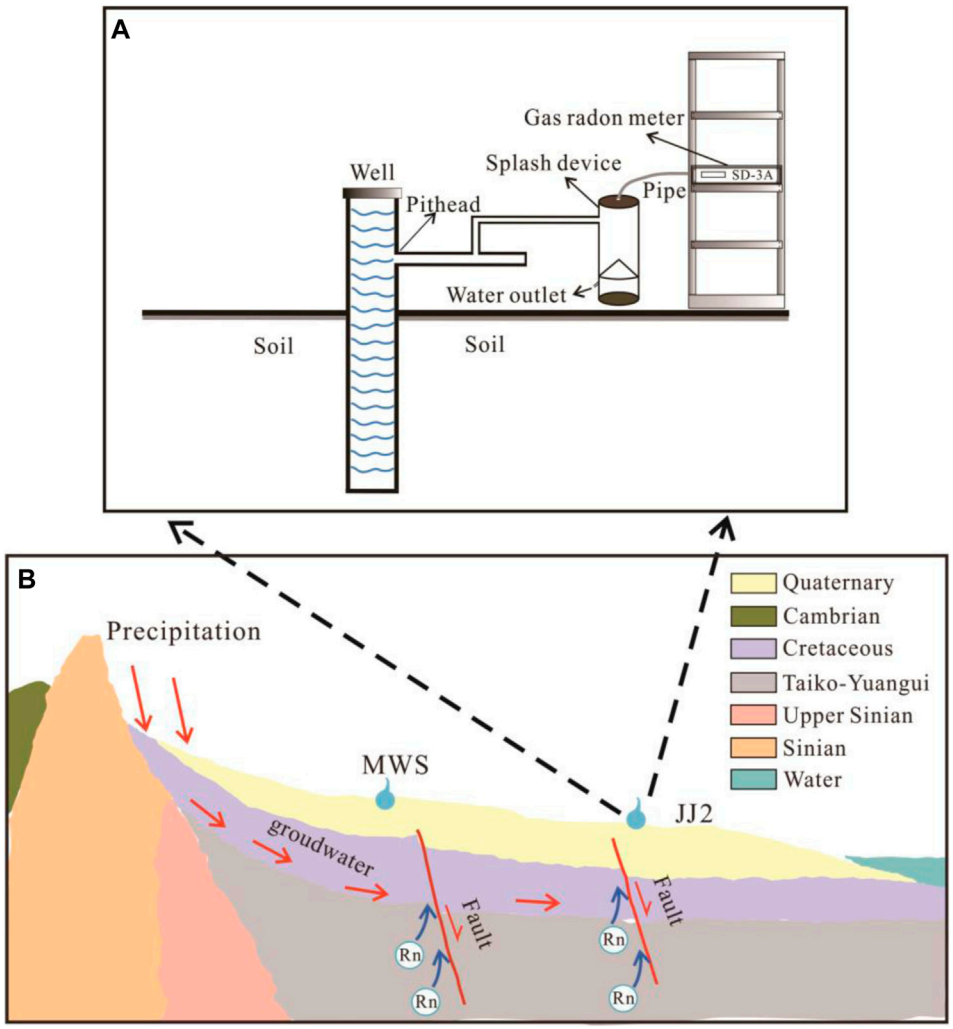

FIGURE 8
(A) Schematic diagram of the observation well. **(B)** The source of escaping gas radon.

tends to estimate the age of groundwater and discriminate the source of recharge. The tritium content in the natural state is very low (<0.5). According to previous studies (Gu, 2011), when the activity is less than 1.0 Tritium Unit (TU), the old water was replenished before 1953, 1~3 TU, old water mixed with new water for nearly 10 years. According to recent study, the tritium activity of JJ2 is 1.6 ± 0.6TU (Bao et al., 2022), which indicated that the JJ2 has both old water supply and nearly 10 years new water supply, the groundwater was of moderate age and had the conditions to reflect the dynamic changes of medium and environment in the fault zone (Zhang et al., 2019). It also implied that the two aquifers in JJ2 have different circulation paths and recharge sources.

5.4 Petrographic compositions involved in dissolution and hydraulic relationship

The ratio of ion molar concentrations in groundwater is often used to discriminate the source of dissolved ionic minerals in the water samples (Su et al., 2022). γCl/γNa+K ratios of most waters fall below 1:1 ratio line (Figure 6A), implying that cation exchange and weathering of silicates ($NaAlSi_3O_8+8H_2O \rightarrow Na^+ + Al(OH)_4 + 3H_4SiO_4$) may be significant processes along the JJ2 (Xiao et al., 2022; Wang et al., 2023b). As shown in Figures 6B, C, $\gamma HCO_3/\gamma Ca$ in the waters of JJ2 fall in the zone between lines 1:1 and 1:2, and the ratio of $\gamma HCO_3/\gamma Mg+Ca$ in all waters of JJ2 mostly fall along the line 1:1, combined with the chemical types of HCO_3-Ca·Mg in JJ2, suggesting that the dissolution of calcite and dolomite are relevant to the lixiviation of carbonate. This phenomenon is also consistent with the lithological characteristics of the strata around JJ2. As shown in Figure 1, the stratigraphic lithology around the aquifer of JJ2 consists of carbonaceous greywacke, siliceous greywacke and sandstone, constituted mainly by calcites, dolomites, quartz, feldspars and clay minerals. So, Ca^{2+} and Mg^{2+} mainly originate from the dissolution of carbonates (calcites and dolomites), as well as some silicate minerals such as feldspars, which is further evidenced by the results in Figure 6D where the JJ2 samples fall mainly in the calcite dissolution zone, and occasionally in the dolomite dissolution zone.

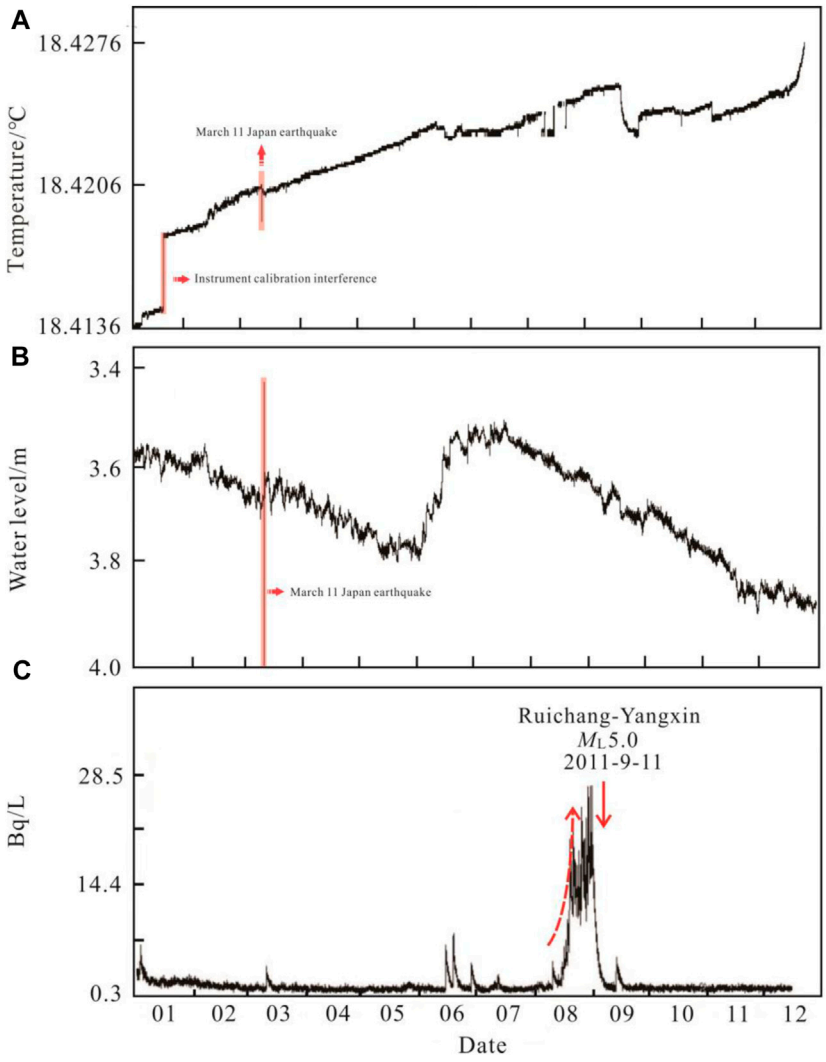

FIGURE 9
(A) Time series diagram of water temperature from JJ2. **(B)** Time series diagram of water level from JJ2. **(C)** Time series diagram of gas radon concentration from JJ2.

Scherer diagram can intuitively reflect the chemical characteristics of different water bodies. It is generally believed that waters with strong morphological consistency may have similar sources and circulation processes. Therefore, Scherer diagrams are often used to distinguish the hydraulic relationships of different water bodies. (Craig, 1961; Zhang et al., 2019). As shown in Figure 7, it can be found that the ion sources of MWS and THJ are more complex compared to JJ2, in which MWS mainly includes calcite, dolomite, silicate and gypsum, while THJ mainly include calcite, dolomite, silicate, gypsum and Halite. The ion content curves of MWS and JJ2 are significantly different from each other, suggesting that they are not hydraulically connected. In the piper diagrams (Figure 3), the water of JJ2 and MWS belong to different water chemistry types, which further implies that they have different origins. Although the hydrochemistry types of JJ2 and THJ are the same, the morphology of their ion content curves are still very different, so it is discriminate that they are weakly hydraulically connected to each other. This is similar to the results reflected in Figure 6.

5.5 Response of observation well to seismic activity

The evolution of *d* excess of groundwater is mainly controlled by surrounding rocks, oxygen-bearing components, lithology and aquifer sealing conditions, water retention time, and physical and chemical properties of water. The *d* value of JJ2 was 9.03~15.93, with the mean value of 13.40, which belongs to modern circulating leaching water (Bao et al., 2021). This is consistent with the fact that JJ2 samples are located in the immature area of the Na-K-Mg block, and have a shallow recharging elevation. That is to say, JJ2's aquifer cycle

recharge faster and do not react adequately with the surrounding rocks. The δD and $\delta^{18}O$ compositions indicates that the source of water in JJ2 is of the atmospheric precipitation genesis type, so the main recharge source of water in the aquifer in JJ2 is the atmospheric precipitation via infiltration through the rock fissures (Figure 8C). However, some deep-derived fluids may also get involved as evidenced by the results of the tritium activity analysis.

Radon, as an earthquake-sensitive component of subsurface fluids, is one of the longest observed and most widely used monitoring items in the field of earthquake forecasting. Abundant studies have proved that there are significant Rn anomalies before the occurrence of earthquakes (Igarashi et al., 1995; Sugisaki et al., 1996; Liu and Ren, 2009; Muto et al., 2021). One month before the Ruichang-Yangxin M_L 5.0 earthquake (<50 km), escaping radon in JJ2 showed significant high value anomalies (Figure 9C). Based on the results above, we think that there are two reasons resulting such sensitive response. Firstly, the JJ2 is located right on the fault, so its aquifer is connected well to the fault fracture zone which provides abundant pathways for circulation of substances in the underground fluid in the preparation process of earthquakes (Figure 8A); Secondly, the JJ2 is fed by moderate aged water, which can promptly reflect the changes in the geochemical environment within the earth's crust and show a more complete pattern of anomaly before the earthquake. In addition, the water level and water temperature measurements in the observation wells did not observe obvious precursor anomalies before the earthquakes (Figures 9A, B), indicating that the hydrophysical observations were not sensitive or the sensitivity of the instruments was not enough to capture the significant anomalies.

6 Conclusion

In this study, the water samples from the JJ2 well, THJ reservoir, MWS spring, and local atmospheric precipitations were collected and analyzed, based on which responding mechanism of water in JJ2 to tectonic activities were discussed. Main conclusions were obtained as follows:

(1) The water type of the JJ2 and THJ is HCO_3-Ca-Mg type, and of MWS spring is HCO_3-Na type. The JJ2 water experienced weak water-rock interactions and belongs to the immature water, with the circulating depth of 2015~2,954 m. MWS spring water experienced relative more intense water-rock interactions and is close to the partially equilibrated water, having the circulating depth about 6710 m. In addition, the waters from the JJ2, MWS spring, and THJ reservoir are not hydraulically connected.
(2) The JJ2 water is mainly a modern leaching water of atmospheric origin, with recharge elevation of about 554 m, and partially exchanged with fluids from deep parts of the fault.
(3) Due to the JJ2 is located right on the fault and has characteristics of both shallow and deep circulating water, JJ2 water can respond to regional tectonic activities sensitively as evidenced by the Radon anomaly before the Ruichang-Yangxin M_L 5.0 earthquake in 2011.

Data availability statement

The original contributions presented in the study are included in the article/supplementary material, further inquiries can be directed to the corresponding author.

Author contributions

ZB: Investigation, Methodology, Writing–original draft. LH: Conceptualization, Funding acquisition, Writing–review and editing. JX: Investigation, Writing–original draft. XZ: Investigation, Methodology, Writing–original draft. JL: Data curation, Investigation, Writing–original draft. YZ: Investigation, Writing–original draft.

Funding

The author(s) declare financial support was received for the research, authorship, and/or publication of this article. This study was funded by Open Fund from Engineering Research Center for Seismic Disaster Prevention and Engineering Geological Disaster Detection of Jiangxi Province (No. SDGD202215), the National Natural Science Foundation of China, China (No. 41861022), and the Spark Program of Earthquake Technology of CEA (No. XH18024Y). This study is a contribution of IGCP-724 project.

Acknowledgments

The authors are grateful to the Editor and reviewers for their constructive comments and suggestions. We thank Xiaobin Ou and Rengui Huang for handling earthquake data, and International Science Editing Company for polishing the language.

Conflict of interest

The authors declare that the research was conducted in the absence of any commercial or financial relationships that could be construed as a potential conflict of interest.

The reviewer XZ declared a shared affiliation with the author LH to the handling editor at time of review.

Publisher's note

All claims expressed in this article are solely those of the authors and do not necessarily represent those of their affiliated organizations, or those of the publisher, the editors and the reviewers. Any product that may be evaluated in this article, or claim that may be made by its manufacturer, is not guaranteed or endorsed by the publisher.

References

Bao, Z., Gao, X., Zhang, L., Zhao, Y., Zha, X., Xiang, Y., et al. (2019). Hydrogen and oxygen isotope characteristics and significance of groundwater from Jiu-jiang seismic station. *Earthq. Res. China* 35, 499–508. (In Chinese).

Bao, Z., Zha, X., Gao, X., Zhao, Y., Zhao, A., Xu, Z., et al. (2022). Hydrogeochemincal characteristics and genesis for jiujiang NO.2 well in Jiangxi Province. *China Earthq. Eng. J.* 44, 920–928. (In Chinese). doi:10.20000/j.1000-0844.20210201001

Bao, Z., Zha, X., Zhao, Y., Zhao, A., Xiang, Y., and Jiang, Y. (2021). Hydrogeochemical characteristics and genesis of groundwater in Lushan area of Jiujiang. *J. Geodesy Geodynameics* 41, 471–477. (In Chinese). doi:10.14075/j.jgg.2021.05.006

Barberio, M. D., Barbieri, M., Billi, A., Doglioni, C., and Petitta, M. (2017). Hydrogeochemical changes before and during the 2016 Amatrice-Norcia seismic sequence (central Italy). *Sci. Rep.* 7, 11735. doi:10.1038/s41598-017-11990-8

Che, Y., Liu, W., and Yu, J. (1998). The relationship between crustal fluids and major earthquakes and its implications for earthquake prediction. *Seismol. Geol.* 20, 431–436. (In Chinese). doi:10.1088/0256-307X/16/9/027

Chen, Z., Zhou, X., Du, J., Xie, C., Liu, L., Li, Y., et al. (2015). Hydrochemical characteristics of hot spring waters in the Kangding district related to the Lushan <i>M</i>_S = 7.0 earthquake in Sichuan, China. *Nat. Hazards Earth Syst. Sci.* 15, 1149–1156. doi:10.5194/nhess-15-1149-2015

Claesson, L., Skelton, A., Graham, C., Dietl, C., Mörth, M., Torssander, P., et al. (2004). Hydrogeochemical changes before and after a major earthquake. *Geology* 32, 641–644. doi:10.1130/g20542.1

Craig, H. (1961). Isotopic variations in meteoric waters. *Science* 133, 1702–1703. doi:10.1126/science.133.3465.1702

Du, J., and Kang, C. (2000). Characteristics of earthquake precursors and its geological significance. *Earthquake* 20, 95–101. (In Chinese). doi:10.3969/j.issn.1000-3274.2000.03.015

Du, J., and Liu, C. (2003). Isotopic-geochemical application to earthquake predicition. *Earthquake* 23, 274–279. (In Chinese). doi:10.3969/j.issn.1000-3274.2003.02.012

Giggenbach, W. F. (1988). Geothermal solute equilibria:Derivation of Na-K-Mg-Ca geoindicators. *Geochim. A. T. Cosmochim. Acta* 52, 2749–2765. doi:10.1016/0016-7037(88)90143-3

Giggenbach, W. F. (1992). Isotopic shifts in waters from geothermal and volcanic systems along convergent plate boundaries and their origin. *Earth Planet. Sci. Lett.* 113, 495–510. doi:10.1016/0012-821x(92)90127-h

Grasby, S. E., Hutcheon, L., and McFarland, L. (1999). Surface-water-groundwater interaction and the influence of ion exchange reactions on river chemistry. *Geology* 27, 223–226. doi:10.1130/0091-7613(1999)027<0223:swgiat>2.3.co;2

Gu, H., Chi, B., Wang, H., Zhang, Y., and Wang, M. (2017). Relationship between surface water and groundwater in the Liujiang Basin—hydrochemical constrains basin-hydrochemical Constrains. *Adv. Earth Sci.* 32, 789–799. (In Chinese). doi:10.11867/j.issn.1001-8166.2017.08.0789

Gu, W. (2011). *Isotope hydrology*. Beijing, China: Science Press. (In Chinese).

He, A., and Singh, R. P. (2019). Coseismic groundwater temperature response associated with the wenchuan earthquake. *Pure Appl.Geophys.* 177, 109–120. doi:10.1007/s00024-019-02097-4

Hosono, T., and Masaki, Y. (2020). Post-seismic hydrochemical changes in regional groundwater flow systems in response to the 2016 Mw 7.0 Kumamoto earthquake. *J. Hydrol.* 582, 124340. doi:10.1016/j.jhydrol.2019.124340

Hosono, T., Yamada, C., Shibata, T., Tawara, Y., Wang, C. Y., Manga, M., et al. (2019). Coseismic groundwater drawdown along crustal ruptures during the 2016 Mw 7.0 Kumamoto earthquake. *Water Resour. Res.* 55, 5891–5903. doi:10.1029/2019wr024871

Igarashi, G., Saeki, S., Takahata, N., Sumikawa, K., Tasaka, S., Sasaki, Y., et al. (1995). Ground-water radon anomaly before the kobe earthquake in Japan. *Science* 269 (5220), 60–61. doi:10.1126/science.269.5220.60

Li, C., Zhou, X., Yan, Y., Quyang, S., and Liu, F. (2021). Hydrogeochemical characteristics of hot springs and their short-term seismic precursor anomalies along the xiaojiang fault zone, southeast tibet plateau. *Water* 13, 2638. doi:10.3390/w13192638

Li, J., Li, Y., Lu, L., Sun, F., Xie, C., and Cui, Y. (2017). Geochemistry of sping water in the liupan mountain area. *Earthquake* 37, 61–72. (In Chinese). doi:10.3969/j.issn.1000-3274.2017.01.007

Li, Y., Chen, Z., Hu, L., Su, S., Zheng, C., Liu, Z., et al. (2022). Advances in seismic fluid geochemistry and its application in earthquake forecasing. *Chin. Sci. Bull.* 67, 1404–1420. (In Chinese). doi:10.1360/TB-2021-0955

Li, Y., Fang, Z., Zhang, C., Li, J., Bao, Z., Zhang, X., et al. (2023). Research progress and prospect of seismic fluid geochemistry in short-imminent earthquake prediction. *Seismol. Geol.* 45 (3), 593621. (In Chinese). doi:10.3969/j.issn.0253-4967.2023.03.001

Liu, J., Song, X., Yuan, G., Sun, X., and Yang, L. (2014). Stable isotopic compositions of precipitation in China. *Tellus Ser. B-Chemical Phys. Meteorology* 66, 22567. doi:10.3402/tellusb.v66.22567

Liu, L., Chen, H., Yang, Y., and Wang, J. (2008). Characteristics and genesis of rNa/rCl in shallow groundwater in the Suzhou-Wuxi-Changzhou region. *Geol. China* 35, 117–122. (In Chinese). doi:10.3969/j.issn.1000-3657.2008.01.012

Liu, Y. (2006). Review of the research progress on the seismological science of underground fluid in China during Last 40 Years. *Earthq. Res. China* 22, 222–235. (In Chinese). doi:10.3969/j.issn.1001-4683.2006.03.002

Liu, Y., and Ren, H. (2009). Preliminary analysis of the characteristics of post-seismic effect of radon after the wenchuan 8 .0 earthquake. *Earthquake* 29 (1), 12–131. (In Chinese). doi:10.3969/j.issn.1000-3274.2009.01.016

Liu, Y., Ren, H., and Wang, B. (2009). Application prospect of environmental isotopes and tracing techniques for earthquake prediction. *Earth Sci. Front.* 16, 369–377. (In Chinese). doi:10.1016/s1872-5791(08)60076-7

Lucas, L., and Unterweger, M. (2000). Comprehensive review and critical evaluation of the half-life of tritium. *J. Res. Natl. Inst. Stand. Technol.* 105, 541–549. doi:10.6028/jres.105.043

Lv, J., Zheng, Y., Ni, S., and Gao, J. (2008). Focal mechanisms and seismogenic structures of the M_S 5.7 and M_S 4.8 Jiujiang-Ruichang earthquakes of Nov. 26, 2005. *Chin. J. Geophys.* 51, 158–164. (In Chinese). doi:10.3321/j.issn:0001-5733.2008.01.020

Martinelli, G., and Dadomo, A. (2017). Factors constraining the geographic distribution of earthquake geochemical and fluid-related precursors. *Chem. Geol.* 469, 176–184. doi:10.1016/j.chemgeo.2017.01.006

Muto, J., Yasuoka, Y., Miura, N., Iwata, D., Nagahama, H., Hirano, M., et al. (2021). Preseismic atmospheric radon anomaly associated with 2018 Northern Osaka earthquake. *Sci. Rep.* 11 (1), 7451. doi:10.1038/s41598-021-86777-z

Nakagawa, K., Yu, Z. Q., Berndtsson, R., and Hosono, T. (2020). Temporal characteristics of groundwater chemistry affected by the 2016 Kumamoto earthquake using self-organizing maps. *J. Hydrol.* 582, 124519. doi:10.1016/j.jhydrol.2019.124519

Ou, Y., Zhong, J., Liao, J., Yu, M., and Yin, R. (2011). Discussion on geothermal water in lushan xingzi hot spring. *J. East China Inst. Technol.* 34, 81–85. (In Chinese). doi:10.3969/j.issn.1674-3504.2011.01.013

Pan, S., and Gao, A. (2001). A preliminary study on the relation between reflecting earthquake ability of spring and groundwater age and its application in earthquake prediction. *Northwest. Seismol. J.* 23, 189–193. (In Chinese). doi:10.3969/j.issn.1000-0844.2001.02.017

Pang, Z., Kong, Y., Li, J., and Tian, J. (2017). An isotopic geoindicator in the hydrological cycle. *Procedia Earth and Planetary Science* 17, 534–537. doi:10.1016/j.proeps.2016.12.135

Qiu, X., Wang, Y., Wang, Z., Regenauer-Lieb, K., Zhang, K., and Liu, J. (2018). Determining the origin, circulation path and residence time of geothermal groundwater using multiple isotopic techniques in the Heyuan Fault Zone of Southern China. *J. Hydrology* 567, 339–350. doi:10.1016/j.jhydrol.2018.10.010

Reddy, D., and Nagabhushanam, P. (2011). Groundwater electrical conductivity and soil radon gas monitoring for earthquake precursory studies in Koyna, India. *Appl. Geochmistry* 26, 731–737. doi:10.1016/j.apgeochem.2011.01.031

Reddy, D., Nagabhushanam, P., and Sukhija, B. S. (2011). Earthquake (M_S 5.1) induced hydrogeochemical and $\delta^{18}O$ changes: validation of aquifer breaching-mixing model in koyna, India. *Geophys. J. Int.* 184, 359–370. doi:10.1111/j.1365-246x.2010.04838.x

Shi, Z., Zhang, H., and Wang, G. (2020). Groundwater trace elements change induced by M5.0 earthquake in Yunnan. *J. Hydrol.* 581, 124424. doi:10.1016/j.jhydrol.2019.124424

Skelton, A., Andrén, M., Kristmannsdóttir, H., Stockmann, G., Mörth, C. M., Sveinbjörnsdóttir, Á., et al. (2014). Changes in groundwater chemistry before two consecutive earthquakes in Iceland. *Nat. Geosci.* 7, 752–756. doi:10.1038/ngeo2250

Skelton, A., Claesson, L. L., Wästeby, N., Andrén, M., Stockmann, G., Sturkell, E., et al. (2019). Hydrochemical changes before and after earthquakes based on long-term measurements of multiple parameters at two sites in northern Iceland—a review. *J. Geophys. Res. Solid Earth.* 124, 2702–2720. doi:10.1029/2018jb016757

Song, S., Ku, W., Chen, Y., Liu, C., Chen, H., Chan, P., et al. (2006). Hydrogeochemical anomalies in the springs of the chiayi area in west-central taiwan as possible precursors to earthquakes. *Pure Appl. Geoghysics* 163, 675–691. doi:10.1007/s00024-006-0046-x

Su, C., Nie, F., Zou, S., Zhao, G., Lu, F., Huang, Q., et al. (2018). Hydrochemical characteristics and formation mechanism of strontium-rich groundwater in xintian county, hunan province. *Geoscience* 32, 554–564. (In Chinese). doi:10.19657/j.geoscience.1000-8527.2018.03.13

Su, S., Li, Y., Chen, Z., Chen, Q., Liu, Z., Lu, C., et al. (2022). Geochemistry of geothermal fluids in the zhangjiakou-penglai fault zone, north China: implications for structural segmentation. *J. Asian Earth Sci.* 230, 105218. doi:10.1016/j.jseaes.2022.105218

Su, X., Wan, Y., Dong, W., and Hou, G. (2009). Hydraulic relationship between malianhe river and groundwater: hydrogeochemical and isotopic evidences. J. Jilin

Univ. (Earth Sci. Ed. 39, 1087–1094. (In Chinese). doi:10.3969/j.issn.1671-5888.2009.06.017

Sugisaki, R., Takamoriito, I., Nagamine, K., and Kawabe, I. (1996). Gas geochemical changes at mineral springs associated with the 1995 southern Hyogo earthquake (M = 7.2), Japan. *Jpn. Earth Planet. Sci. Lett.* 139, 239–249. doi:10.1016/0012-821x(96)00007-6

Sun, X., Wang, G., Shao, Z., and Si, X. (2016). Geochemical characteristics of emergent gas and groundwater in Haiyuan fault zone. *Earth Sci. Front.* 23, 140–150. (In Chinese). doi:10.13745/j.esf.2016.03.018

Tian, J., Li, Y., Zhou, X., Peng, Z., Li, L., Xing, L., et al. (2021). Geochemical characteristics of hydrothermal volatiles from southeast China and their implications on the tectonic structure controlling heat convection. *Front. Earth Sci.* 9, 786051. doi:10.3389/feart.2021.786051

Tsunogai, U., and Wakita, H. (1995). Precursory chemical changes in groundwater: kobe earthquake, Japan. *Science* 269, 61–63. doi:10.1126/science.269.5220.61

Wang, A., Sun, Z., Lan, W., Yang, N., Ye, H., Tong, Y., et al. (2023a). Occurrence features of geothermal resources and geothermal potential assessment of Jiangxi Province. https://kns.cnki.net/kcms2/detail/11.1167.P.20230728.1454.002.html.

Wang, H. (1991). *Introduction to isotope hydrogeology*. Peking: Geological Publishing House, 30–50.

Wang, T., Zhang, J., Liu, X., and Yao, L. (2013). Variation of stable isotopes in precipiation and water vapor sources in Nanjin Area. *J. China Hydrology* 33, 25–31. (In Chinese). doi:10.3969/j.issn.1000-0852.2013.04.005

Wang, Y., Yuang, X., Zhang, Y., Zhang, X., Xiao, Y., Duo, J., et al. (2023b). Hydrochemical, D–O–Sr isotopic and electromagnetic characteristics of geothermal waters from the Erdaoqiao area, SW China: insights into genetic mechanism and scaling potential. *Ore Geol. Rev.* 158, 105486. doi:10.1016/j.oregeorev.2023.105486

Xiao, Y., Liu, K., Hao, Q., Xiao, D., Zhu, C., Yin, S. Y., et al. (2022). Hydrogeochemical insights into the signatures, genesis and sustainable perspective of nitrate enriched groundwater in the piedmont of Hutuo watershed, China. *Catena* 212, 106020. doi:10.1016/j.catena.2022.106020

Xiong, L., Wang, J., and Pang, Z. (1990). Circulation depth of the thermal water in Zhangzhou geothermal fifield. *Sci. Geol. Sin.* 4, 377–384. (In Chinese).

Zhang, G., Deng, W., He, Y., and Ramsis, S. (2006). Hydrochemical characteristics and evolution laws of groundwater in Songnen Plain, Northeast China. *Adv. water Sci.* 17, 20–28. (In Chinese). doi:10.3321/j.issn:1001-6791.2006.01.004

Zhang, L., Liu, Y., Ren, H., and Guo, L. (2016). Application of Stable oxygen and hydrogen isotopes to the verification of Groundwater anomalies. *Seismol. Geol.* 38, 721–731. (In Chinese). doi:10.3969/j.issn.0253-4967.2016.03.017

Zhang, L., Liu, Y., Ren, H., and Ke, Y. (2019). Application of hydrochemistry to the verification of groundwater anomalies. *Earthquke* 39, 29–38. (In Chinese). doi:10.3969/j.issn.1000-3274.2019.01.004

Zhang, L., Liu, Y., Sun, X., and Fang, Z. (2014). A study of water level anomalies using hydrochemical and physical methods. *Seismol. Geol.* 36, 513–522. (In Chinese). doi:10.3969/j.issn.0253-4967.2014.02.019

Zhang, W. (1992). *Observation and prediction of hydrogeochemical earthquake precursors*. Beijing, China: Seismological Pres. (In Chinese).

Zhao, D., Zhou, X., Zhang, Y., He, M., Tian, J., Shen, J., et al. (2023). Hydrogeochemical study of hot springs along the tingri–nyima rift: relationship between fluids and earthquakes. *Water* 15, 1634. doi:10.3390/w15081634

Zhou, R., Zhou, X., Li, Y., He, M., Li, J., Dong, J., et al. (2022). Hydrogeochemical and isotopic characteristics of the hot springs in the litang fault zone, southeast qinghai–tibet plateau. *Water* 14, 1496. doi:10.3390/w14091496

Zhou, Z., Tian, L., Zhao, J., Wang, H., and Liu, J. (2020). Stress-Related pre-seismic water radon concentration variations in the panjin observation well, China (1994–2020). *Front. Earth Sci.* 8, 596283. doi:10.3389/feart.2020.596283

Zhou, Z., Zhong, J., Zhao, J., Yan, R., Tian, L., and Fu, H. (2021). Two mechanisms of earthquake-induced hydrochemical variations in an observation well. *Water* 13, 2385. doi:10.3390/w13172385

frontiers | Frontiers in Earth Science

TYPE Original Research
PUBLISHED 27 February 2024
DOI 10.3389/feart.2024.1269753

Check for updates

OPEN ACCESS

EDITED BY
Giovanni Martinelli,
National Institute of Geophysics and Volcanology, Italy

REVIEWED BY
Huai Zhang,
University of Chinese Academy of Sciences, China
Caibo Hu,
University of Chinese Academy of Sciences, China

*CORRESPONDENCE
Guofu Luo,
luoguofu_05@163.com

RECEIVED 30 July 2023
ACCEPTED 09 February 2024
PUBLISHED 27 February 2024

CITATION
Luo G, Xu Y, Luo H, Ding F and Li W (2024), Spatio-temporal characteristics of seismic strain anomalies reveal seismic risk zones along the Longmenshan fault zone and adjacent areas.
Front. Earth Sci. 12:1269753.
doi: 10.3389/feart.2024.1269753

COPYRIGHT
© 2024 Luo, Xu, Luo, Ding and Li. This is an open-access article distributed under the terms of the Creative Commons Attribution License (CC BY). The use, distribution or reproduction in other forums is permitted, provided the original author(s) and the copyright owner(s) are credited and that the original publication in this journal is cited, in accordance with accepted academic practice. No use, distribution or reproduction is permitted which does not comply with these terms.

Spatio-temporal characteristics of seismic strain anomalies reveal seismic risk zones along the Longmenshan fault zone and adjacent areas

Guofu Luo*, Yingcai Xu, Hengzhi Luo, Fenghe Ding and Wenjun Li

Seismological Bureau of Ningxia Hui Autonomous Region, Yinchuan, China

Introduction: Identifying and quantifying earthquake precursors, and analyzing their physical mechanisms, continues to be a challenge for earthquake forecasting. In this study, orthogonal functions were developed to effectively identify precursor anomalies, thereby improving the forecasting of strong earthquakes.

Methods: To study the spatio-temporal contour anomalies in seismic strain fields, we assessed them for seismic activity variables and natural orthogonal function expansion, in six strong earthquakes near the Longmenshan Fault Zone, China, that have occurred since 2008.

Results: We observed that, prior to these earthquakes, the temporal factor (the time variation characteristics of the strain field) displayed anomalies with high/low values exceeding the mean square error within a stable context. The anomalies exhibited multi-component characteristics and were primarily concentrated in the first four-strain fields. Short-term and impending-earthquake anomalies were observed in the temporal factor before the 2008 Wenchuan (*M*8.0) and 2013 Lushan (*M*7.0) earthquakes, while medium-term and long-term anomalies appeared before the other four strong earthquakes, without notable short-term anomalies. The temporal evolution of strain field contour anomalies, and the strain contours positive and negative intersection, showed that central areas surrounded by multiple strain field contour anomalies were potential locations for strong earthquakes. This suggests a potential approach for earthquake location forecasting. Since 2009, there have been five strong earthquakes, each affected to varying degrees by anomalous strain fields from the 2008 Wenchuan (*M*8.0) earthquake.

Conclusion: The results of this study corroborate the findings of the focal mechanism's node shear stress, indicating significant physical implications of the anomalies and the reliability of these conclusion.

KEYWORDS

Longmenshan fault zone, natural orthogonal function, seismic strain anomalies, temporal and spatial characteristics, shear stress results of focal mechanism

1 Introduction

The Longmenshan Fault Zone (LFZ) is situated in Sichuan Province, western China, where the eastern edge of the Tibetan Plateau converges with the Sichuan Basin. It has an approximate northeast (NE)–southwest (SW) orientation, spanning 500 km in length and 30–50 km in width. The NE end intersects with the Qinling Fault Zone, while the SW section obliquely intersects the Xianshuihe Fault Zone. The LFZ boasts a complex geological structure, comprising four main faults; the Houshan, Zhongyang, Qianshan, and Shanqianyinfu faults, and the associated thrusts (Chen et al., 2007; Li et al., 2008; Yi et al., 2012; Chen et al., 2013; Yang et al., 2021). The LFZ is bounded by the Bayankala block in the west and the Sichuan Basin in the east. The landform contrast between the mountains and basin is strong, and the topographic elevation difference within 50 km is approximately 4,000 m is an orogenic belt with obvious variation of terrain gradient and tectonic stress concentration (Deng et al., 1994; Fu et al., 2008; Yan et al., 2014; Shi and Gao, 2010); however, the average shortening rate under long-term evolution is not significant (Clark and Royden, 2000; Burchfield et al., 2008; Wang et al., 2017). Owing to the collision and extrusion of the Eurasian and Indian Ocean plates have led to an arc-shaped Himalayan orogeny thrusting into the northeastern margin of the Tibetan Plateau (Molnar and Tapponnier, 1975; England and Houseman, 1986; England and Houseman, 1988; Harrison et al., 1992; Fu et al., 2008; Luo et al., 2019). This resulted in an eastward drift of the Tibetan Plateau, which encounters substantial obstruction from the South China Block (Teng et al., 2014), leading to intense activity and deformation of LFZ structure and Bayan Har Block (Xu et al., 2008; Xu et al., 2013), consequently generating multiple strong earthquakes (Deng et al., 1994; Yang et al., 1999). The LFZ has therefore emerged as a significant focal point for research.

Before 2008, there were few earthquakes with a magnitude of *M*7 or higher on the LFZ, and the intensity of seismic activity was significantly lower than that of the Xianshuihe Fault Zone (towards the west) and the Minjiang Fault Zone (towards the north). However, on 12 May 2008, the Wenchuan earthquake (*M*8.0) took place in the midsection of LFZ, which was historically recognized for its lower seismic intensity (Yi et al., 2012; Gong et al., 2020). This earthquake caused a unilateral rupture in the northeast direction (Xu et al., 2008; Xu et al., 2009; Xu et al., 2010), with an approximate length of 340 km along the Zhongyang and Shanqian faults (Zhang et al., 2009).

Several studies have investigated patterns in the crustal strain field based on drilling experiments in seismogenic structures to provide different explanations for the generation and interaction of the Wenchuan (*M*8.0) earthquake (Zhang et al., 2008; Chen et al., 2013; Li et al., 2013; Wu et al., 2015; Li et al., 2016; Ye et al., 2017; Zheng et al., 2017; Li et al., 2018; Xu et al., 2018). Subsequently, on 20 April 2013, 5 years after the Wenchuan earthquake, the Lushan (*M*7.0) earthquake occurred on a blind thrust fault of southern LFZ (Xu et al., 2013; Li et al., 2014). This earthquake caused a rupture that was approximately 30 km long (Xie et al., 2018). The aftershock sequence of the Lushan earthquake (Zhao et al., 2013; Liu et al., 2019) and stress field inversion of the focal mechanism (Ma et al., 2021) provided evidence for the process of surface rupture. Many seismologists believe that the 2008 Wenchuan (*M*8.0) earthquake influenced the subsequent Lushan (*M*7.0) earthquake (Du et al., 2013; Wang et al., 2013; Yi et al., 2016; Jia and Zhou, 2018; Duan et al., 2020), and there has been extensive debate regarding the possibility of strong earthquakes occurring in a 50–60-km seismic gap between the area of influence of the two earthquakes (Wan et al., 2017; Diao et al., 2018; Guo et al., 2020; Li et al., 2022). In addition, a *M*6.6 earthquake occurred on the Lintan–Tanchang Fault, at the junction of Min and Zhang Counties in Gansu Province, which may have also been affected by the Wenchuan (*M*8.0) earthquake in 2008 (Ge, 2013; Huang et al., 2019). On 22 November 2014, the Kangding (*M*6.3) earthquake occurred in the southern Xianshuihe Fault Zone at the intersection with LFZ (Yi et al., 2015), which was triggered by Wenchuan (*M*8.0) and Lushan (*M*7.0) earthquakes (Wang et al., 2016). On 8 August 2017, the Jiuzhaigou (*M*7.0) earthquake occurred between the Minjiang and Tazang faults in the Shuzheng Fault Zone which lies north of LFZ. Research on the seismogenic fault, coseismic deformation field, and stress and strain states of the Jiuzhaigou earthquake (Shan et al., 2017; Xu et al., 2017; Cheng et al., 2018; Jin et al., 2019) explains the influence of the Wenchuan (*M*8.0) earthquake (Huang et al., 2019). After the Jiuzhaigou (*M*7.0) earthquake, stress in the vicinity of LFZ was effectively alleviated; however, stress in the Xianshuihe Fault Zone became acutely concentrated, resulting in a heightened possibility of strong earthquakes (Li et al., 2018). Consequently, the *M*6.8 Luding earthquake occurred in the Xianshuihe Fault Zone on 5 September 2022 (Li et al., 2022).

In summary, the Wenchuan (*M*8.0) earthquake led to changes in the stress state near LFZ, which affected seismic activity in the region. Over a span of 15 years, the 6 significant earthquakes described above occurred in the vicinity of LFZ. This study investigates the mutual interactions and influences between these strong earthquakes, focusing on the stresses released by each seismic event.

Several methods have been employed to investigate the interactions among strong earthquakes near LFZ. These methods can be categorized as follows: 1) Coulomb stress transfer analysis, which examines stress changes in different media or faults induced by strong earthquakes (Wan et al., 2009; Wang et al., 2014; Wang et al., 2014; Jin et al., 2019; Jia, 2020); 2) numerical simulations that model regional stress changes based on various hypocenter models (Toda et al., 2008; Shi and Cao, 2010; Yi et al., 2013); 3) focal mechanism solutions, in association with GPS and InSAR inversion, to assess regional stress variations (Yi et al., 2012; 2015; 2017; Jiang et al., 2014; Huang et al., 2019; Meng et al., 2022); and 4) calculation of regional stress changes by analyzing the stress and strain fields released during earthquakes (Luo et al., 2011; Yang and Ma, 2011; Yang and Ma, 2012; Luo et al., 2014; Luo et al., 2015; Yang et al., 2017; Luo et al., 2019; Luo et al., 2023).

The first three methods involve inversion models for computing regional stress changes. While these methods are well-established, they rely on various assumptions that can yield inconsistent results regarding stress effects. Consequently, their effectiveness continues to be a controversial topic. In contrast, the fourth method is a relatively recent development with fewer documented applications. In the present study, this fourth method was applied, utilizing the stress released by earthquakes in the vicinity of LFZ as the independent variable. Additionally, the natural orthogonal function (Neha and Pasari, 2022) was applied to investigate the

spatio-temporal variations in the regional strain field prior to the six powerful earthquakes with magnitudes ≥ $M6.3$ that have occurred since 2008. By identifying anomalous seismic activity preceding these events and analyzing the interactions and mutual influence among the earthquakes, this study offers new seismological insights into the seismic hazard and dynamic mechanisms of LFZ.

2 Methods and data

2.1 Methods

The natural orthogonal function (NOF) method is considered a cutting-edge tool for predicting, evaluating, and detecting small-scale, short-term, and long-term changes in datasets. This method is widely used in crustal deformation analysis and dimensionality reduction of data sets in seismological, climatic, and atmospheric sciences. Neha and Pasari, (2022) discusses the basic principles of the natural orthogonal function (EOF) method and its applications in various industries. Herein, we focus on how to use the natural orthogonal function method to extract temporal and spatial anomalies of seismic strain field before strong earthquakes.

The seismic strain field S, also called the natural orthogonal function expansion approach, was used to break down seismic strain (a random variable) into temporal and spatial functions (Luo et al., 2023). According to the intensity of seismic activity in the area, the strain field was constructed using the grid method for a particular study region.

The area was divided into n equal-area elements $\Delta S = \Delta x \times \Delta y$, with center coordinates of $\left(x_j, y_j\right)(j = 1, 2, ...n)$, and time interval Δt was selected. The observation time was divided into several m periods $t_i = \Delta t \times i(i = 1, 2, ...m)$. The derived and used as field function values reflecting the spatio-temporal coordinates $\left(x_i, y_i, t_j\right)(i, j = 1, 2, ...n)$ were set as the observed values for each area element in each time-period S_{ij}.

The release of seismic energy was symbolized by E. We considered the proportionality of the square root of seismic energy to seismic strain, i.e., $\sqrt{E} = c\varepsilon$ (Yang and Zhao, 2004), where c is the focal-related parameter of the earthquake in the study region and ε is the seismic focal region cumulative strain parameter, where both parameters reflect changes in the focal region's strain field. Following an evaluation of the area, the matrix form of the strain field function was established through $S = \sum_i \sqrt{E_i}$ (Yang and Ma, 2016) and expressed as follows:

$$\boldsymbol{S} = \begin{bmatrix} S_{11} & S_{12} & \cdots & S_{1m} \\ S_{21} & S_{22} & \cdots & S_{2m} \\ \vdots & \vdots & \vdots & \vdots \\ S_{n1} & S_{n2} & \cdots & S_{nm} \end{bmatrix} \tag{1}$$

Similar seismic blocks were present in the Longmenshan fault zone, and the seismic focal-related parameter c was almost constant. The seismic strain filed, also called the field function, where S_{ji} $(j = 1, 2, \ldots n, i = 1, 2, \ldots m)$ is the j-th time-period and i-th grid of the cumulative seismic strain value. The natural orthogonal function expansion approach was conducted by dividing the matrix S into the summation of the products of orthogonal spatial function X and orthogonal temporal function T (Yang and Ma, 2016):

$$S_{ji} = \sum_{k=1}^{n} T_{jk} X_{ki} \begin{cases} j = 1, 2, \cdots, n \\ i = 1, 2, \cdots, m \end{cases} \tag{2}$$

where X_{ki} is a spatial function that does not change with time and T_{jk} is a function of time that does not change in space. They satisfy the orthogonal and normalization conditions, respectively, as follows (Yang and Ma, 2016):

$$\sum_{i=1}^{m} X_{ki} X_{li} \begin{cases} 0 & k \neq l \\ 1 & k = l \end{cases} \tag{3}$$

$$\sum_{j=1}^{n} T_{jk} T_{jl} \begin{cases} 0 & k \neq l \\ 1 & k = l \end{cases} \tag{4}$$

The corresponding covariance matrix $R = S'S$ (Yang et al., 2017) characteristic equation is as follows:

$$\begin{bmatrix} R_{11} & R_{12} & \cdots & R_{1n} \\ R_{21} & R_{22} & \cdots & R_{2n} \\ \vdots & \vdots & \vdots & \vdots \\ R_{n1} & R_{n2} & \cdots & R_{nn} \end{bmatrix} \begin{bmatrix} x_1 \\ x_2 \\ \vdots \\ x_n \end{bmatrix} = \lambda \begin{bmatrix} x_1 \\ x_2 \\ \vdots \\ x_n \end{bmatrix} \tag{5}$$

The eigenvectors $\vec{x}_p$ and eigenvalues λ_p $(p = 1, 2, \ldots n)$ were obtained. Because the covariance matrix R is a real symmetric matrix, n eigenvalues are solved as positive real numbers. The physical meaning of the eigenvalues in this paper is to obtain the main strain field in the study area through a series of solutions. n eigenvalues correspond to n eigenvectors, which reflect the spatial characteristics of the strain field and are only spatial functions. The time factor of the strain field can be solved by the feature vector and the strain field, and the time-related anomalies of the seismic activity in the study area can be extracted by projection of the characteristics of the strain field over time.

The temporal factor of the strain field was expressed as (Yang and Ma, 2016):

$$\overrightarrow{T_p} = S\vec{x}_p \; p = 1, 2, \ldots n \tag{6}$$

The strain fields of eigenvectors $\vec{x}_p$ represent the spatial distribution of seismic strain constituting the field, and the temporal factor $\vec{T}_p$ represents the dynamic characteristics of the strain fields at different times. Due to the symmetry of the matrix, the eigenvalues obtained were positive real numbers, the eigenvalues were arranged from large to small, and the eigenvectors corresponding to t eigenvalues satisfy the accuracy of fitting the total strain field, indicating that the first t spatio-temporal variables of the strain field as the research object represent the spatio-temporal characteristics of the total strain field in the study area (the manuscript is the Longmenshan fault zone and its adjacent areas). The fitting accuracy of the first t eigenvalues was:

$$\eta = \frac{\sum_{p=1}^{t} \lambda_p}{\sum_{p=1}^{n} \lambda_p} \tag{7}$$

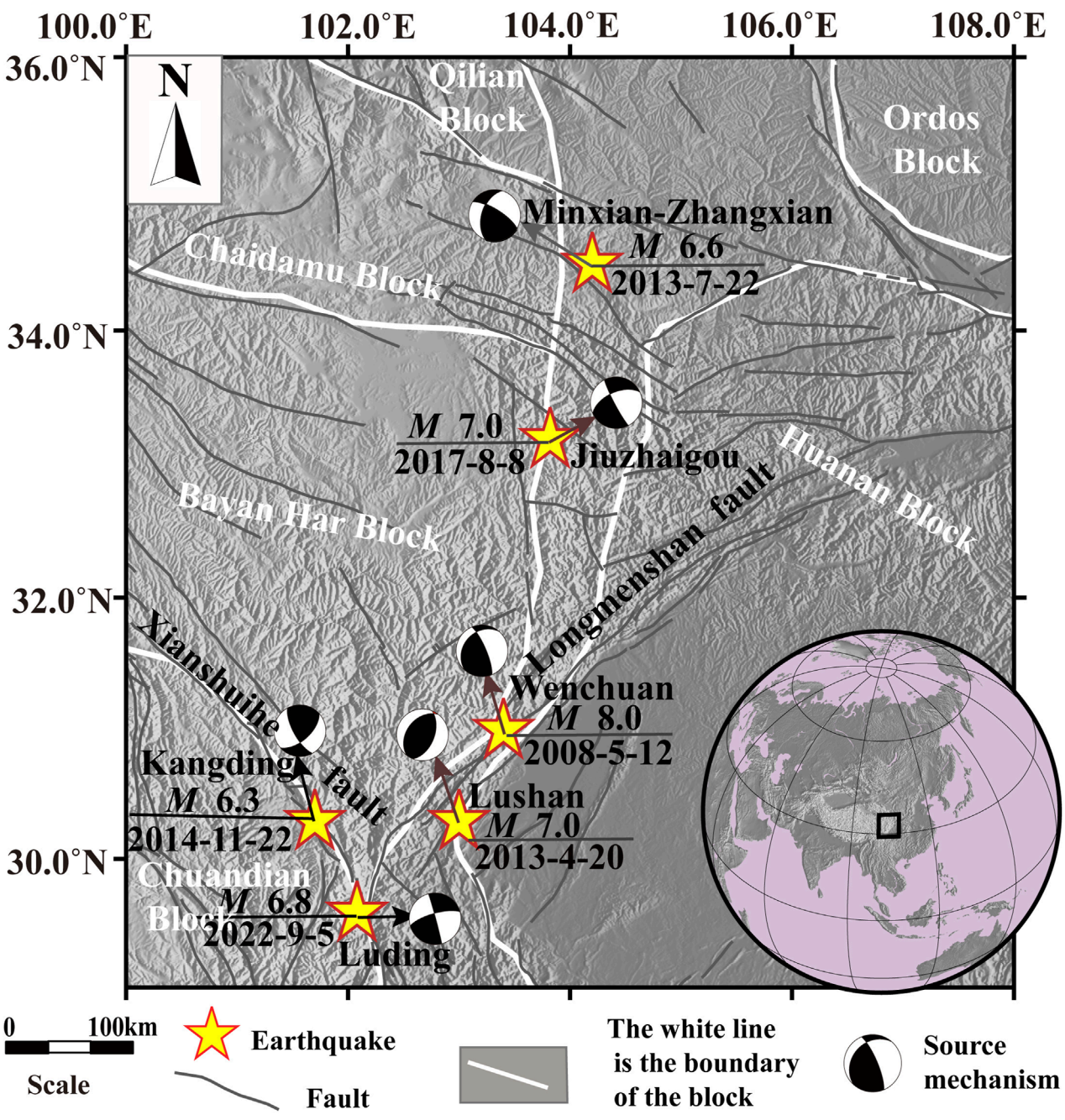

FIGURE 1
Distribution of epicentre and mechanism of $M \geq 6.3$ earthquakes around the Longmenshan fault zone since 2008. Black lines represent fault. The white lines represent the boundary of the block, including the Qilian block, Ordos block, Chaidamu block, Bayan Har block, Chuandain block and Huanan block. The black circle in the lower right corner is the world topographic map. The yellow stars represent the epicentres of six earthquakes of magnitude $M \geq 6.3$, according to data from the China Earthquake Networks Center (CENC). Black source mechanism data from the United States Geological Survey (USGS).

where η (Yang and Ma, 2016) represents the fitting acuracy of the strain field.

The biggest advantage of natural orthogonal function method was that it can extract the main strain fields with anomalies in the study area, which was equivalent to concentrating the main information of the strain fields in the study area in the first t strain fields, focusing on the study of the spatio-temporal anomalies of the first t strain fields, and eliminating the strain fields with no abnormalities or no obvious abnormal changes. The spatiotemporal anomalies of t main strain fields were studied to simplify complex problems.

2.2 Study objects and data sources

This study focused on six strong earthquakes that occurred in the vicinity of LFZ since 2008: the 2008 Wenchuan (*M*8.0) earthquake, 2013 Lushan (*M*7.0) earthquake, 2013 Min County–Zhang County (*M*6.6) earthquake, 2014 Kangding (*M*6.3) earthquake, 2017 Jiuzhaigou (*M*7.0) earthquake, and 2022 Luding (*M*6.8) earthquake (Figure 1). The focal mechanism solution data for these six earthquakes were mainly supplied by the US Geological Survey (USGS), and the earthquake catalog data for the study area were provided by the China Earthquake Networks Center (CENC). Since 1995, the b-values of small and medium earthquakes in the study area have been calculated, and the minimum complete magnitude was determined to be *M*2.0 (Yang et al., 2017; Luo et al., 2019). Considering that the probability of moderate or stronger earthquakes occurring is generally very low, and the release of seismic strain has a significant impact on the study area, a lower limit of *M*2.0 and an upper limit of *M*5.0 were selected for the earthquake magnitude range to ensure that the selected data fully reflected the contextual seismic activity in the region and the development of strong earthquake sources (Table 1). In principle, aftershocks were not deleted; however, for overlapping areas of impact between strong earthquakes, it was necessary to delete the aftershocks of the previous six earthquakes to avoid affecting the subsequent strong earthquake. For example, the study areas of the 2008 Wenchuan (*M*8.0) earthquake and 2013 Lushan (*M*7.0) earthquake partially overlapped; therefore, to study the seismic strain field before the Lushan earthquake, it employed the K-K theory (Luo et al., 2019) to delete the aftershocks of the Wenchuan (*M*8.0) earthquake.

2.3 Spatio-temporal extent of selected data

Two spatial statistical scales were selected for the six earthquakes. The first scale was for seismically active areas related to the strong earthquake hypocenters, referred to as the research area and set to be no less than 3° × 3° (Yang et al., 2017; Luo et al., 2023). The second scale was a smaller statistical unit used for calculating anomalies, known as the grid; its size was set at 0.5° × 0.5°. The rationale for selecting these two spatial regions was as follows. First, the statistical areas of different focal scales are associated with the size of the seismogenic structure. Mei, S. R. (1997) studied the long-term anomaly evolution process before three earthquakes of ≥ *M*7 in the North China Plain. They estimated the seismically active area to be within 400–500 km and found that it gradually reduced during the evolution process. They stated that the extent of the seismically active area in the 10 years before the earthquake was approximately 3°–4°. Based on this, a range of approximately 3° longitude and latitude around the epicenter of six earthquakes were selected as different study areas, making adjustments considering factors such as earthquake magnitude, the scale of the seismogenic structure, and the distribution of seismic activity. This selected range included both the stages of strengthening and weakening of seismic activity before an earthquake. When calculating the strain field of strong earthquakes, grids with equal intervals are utilized, and the grid size needs to reflect the anomaly characteristics of the regional strain field. If the grid is too dense, the distribution of the strain field will become fragmented, making it difficult to discern the main characteristics. Conversely, if the grid is too sparse, the anomaly characteristics of seismic activity will not be well reflected, leading to weakened anomaly differences and the loss of important anomaly information. Therefore, based on previous research (Luo et al., 2023), a grid unit of 0.5° × 0.5° was selected.

2.4 Computation procedure

The procedure for calculating the seismic strain field was as follows. Firstly, the area was divided into grid units of 0.5° × 0.5°. A time interval of a year and a sliding step of a month were used, ensuring that there was a minimum of 10 years' worth of seismic data in the area. Secondly, the seismic strain field matrix $\boldsymbol{S}$ was constructed, and the covariance matrix $\boldsymbol{R}$ was solved to obtain the eigenvalues of the main strain field. Finally, using the aforementioned research method, the temporal factor and contours of the main strain field corresponding to the eigenvalues were calculated to analyze the relationships between anomalies and strong earthquakes.

3 Results

3.1 Strain field temporal factor variation

In this study, the natural orthogonal function was used to calculate the strain field of the six strong earthquakes in the vicinity of LFZ that have occurred since 2008. When t is equal to 4, the first 4 strain fields have exceeded 80% of the total strain field. Before the 2013 Lushan (*M*7.0) earthquake, the strain field exceeded 92%, indicating that the anomaly information of the regional strain fields before these six strong earthquakes was concentrated in the first 4 main strain fields.

Table 2 shows the seismic strain field temporal factor before the six strong earthquakes, including calculation grids and time interval, time of anomaly for the first 4 strain field temporal factors, type of anomaly, mean-square-error, and accuracy as a proportion of the total fields. When the strain field temporal factor exceeded the mean square error before a strong earthquake, it was considered an anomaly (Luo et al., 2023). Anomalies were divided into long-term (2–10 years before the earthquake), medium-term (from 3 months to 2 years before the earthquake), short-term (1–3 months before the earthquake), and impending (several days before the earthquake).

Figure 2 shows the temporal factors of the seismic strain before the six strong earthquakes in the vicinity of LFZ. The results show whether the increase or decrease in the temporal factors of the strain fields exceeded the mean square error. Before the 2008 Wenchuan (*M*8.0) earthquake, 2013 Lushan (*M*7.0) earthquake, and 2022 Luding (*M*6.8) earthquake, the regional strain field showed obvious short-term anomalies. Impending-earthquake anomalies appeared in the main strain field (T3) of the Wenchuan (*M*8.0) earthquake and the main strain field (T1) of the Lushan (*M*7.0) earthquake (Table 2). In 2013, before the Zhang County–Min County (*M*6.6) earthquake, there were medium-term anomalies in the strain field. Except for T4, the other three strain field anomalies were affected by the relatively large strain field anomaly of the Wenchuan (*M*8.0)

TABLE 1 Seismic data of six strong earthquakes around the Longmenshan fault zone since 2008.

No.	Earthquake	Coordinates of the study area [lat. (º) and long. (º)]	Time span of the data	Focal mechanism solution nodal section I (º)			Focal mechanism solution nodal section II (º)			Data source
				Strike	dip	rake	Strike	dip	rake	
1	2008-05-12 Wenchuan (Sichuan), M_s 8.0	30.0°–33.5° 101.5°–106°	1995-01–2008-04	222	29	152	336	79	63	USGS
2	2013-04-20 Lushan (Sichuan), M_s 7.0	29.5°–31.5° 102.5°–105.5°	2000-01–2013-03	218	39	103	21	52	79	USGS
3	2013-07-22 Minxian-Zhangxian (Gansu),M_s 6.6	33.0°–36.5° 103.0°–106.5°	2000-01–2013-06	302	73	41	197	51	157	USGS
4	2014-11-22 Kangding (Sichuan), M_s 6.3	28.5°–32.0° 100.5°–103.0°	2000-01–2014-10	151	70	33	48	59	156	USGS
5	2017-08-08 Jiiuzhaigou (Sichuan), M_s 7.0	32.0°–34.5° 102.5°–105.0°	2000–01–2017–07	246	57	−173	152	84	−33	USGS
6	2022-09-05 Luding (Sichuan), M_s 6.8	28.0°–31.0° 100.5°–103.5°	2014-01–2022-08	345	88	17	254	73	177	USGS

Note: The time of the earthquake is Beijing time, and the earthquake directory is from China Earthquake Networks Center. Additional data for columns 5 through 10 are primarily from the United States Geological Survey.

10.3389/feart.2024.1269753

10.3389/feart.2024.1269753

TABLE 2 Parameters of the strain field temporal factors of 6 *Ms* ≥6.3 earthquakes around the Longmenshan fault zone since 2008.

No.	Earthquake	Grids (n, m)	Anomaly centroid (°N, °E)	Temp-oral factor	Time of anomaly (year-month)	Mean square error	Type of anomaly	Accura-cy *r*
1	2008-05-12 Wenchuan Ms 8.0	(63,158)	32.3,101.7	T1	2006-05–11	±2.0	Medium term	0.86
			33.0,104.7	T2	2005-07–12	±1.2	Long-to-medium term	
			30.2,103.2	T3	2008-02–04	±1.0	Short-to-imminent term	
				T4	2007-04–06	±0.8	Medium term	
2	2013-04-20 Lushan Ms 7.0	(24,157)	30.5,102.5 31.5,103.6 29.5,105.5	T1	2013-02–03	±1.4	Short-to-imminent term	0.92
				T2	2012-01–03	±1.3	Medium term	
				T3	2012-10–12	±0.5	Medium term	
				T4	2012-02–09	±0.4	Medium term	
3	2013-07-22 Minxian-Zhangxian Ms 6.6	(49,160)	34.5,104.3	T1	2003-08–10	±2.5	Long term	0.86
				T2	2006-08–09[a]	±2.1	Long term	
				T3	2005-04–06[a]	±1.1	Long term	
				T4	2011-10–12	±0.8	Medium term	
4	2014-11-22 Kangding Ms 6.3	(35,176)	30.5,102.5 29.8,101.5	T1	2008-02–05[a] 2011-03-05	±1.0	Long term	0.83
				T2	2008-02–05[a] 2011-03-05	±1.0	Long term	
				T3	2003-10–12 2008-02–05[a]	±0.7	Long term	
				T4	2008-05–07[a]	±0.7	Long term	
5	2017-08-08 Jiiuzhaigou Ms 7.0	(16,209)	32.5,104.6 34.2,102.2	T1	2006-04–06	±1.8	Long term	0.80
				T2	2008-03–05[a]	±1.4	Long term	
				T3	2005-05–2006-04	±0.9	Long term	
				T4	2013-05–11	±0.7	Long term	
6	2022-09-05 Luding Ms 6.8	(36,102)	28.5,103.5 29.6,102.2	T1	2014-11–2015-03	±2.6	Long term	0.88
				T_2	2018-03–07 2022-04-07	±2.4	Long and short term	
				T_3	2018-03–07 2022-03–07	±2.2	Long and short term	
				T_4	2021-05–09 2022-06-08	±1.8	Medium and short term	

Note: n, number of grids; m, time interval. T_k is the *k*th (1–4) strain-field time factor.

[a]Indicates that the period was affected by the *M*s 8.0 wenchuan earthquake.

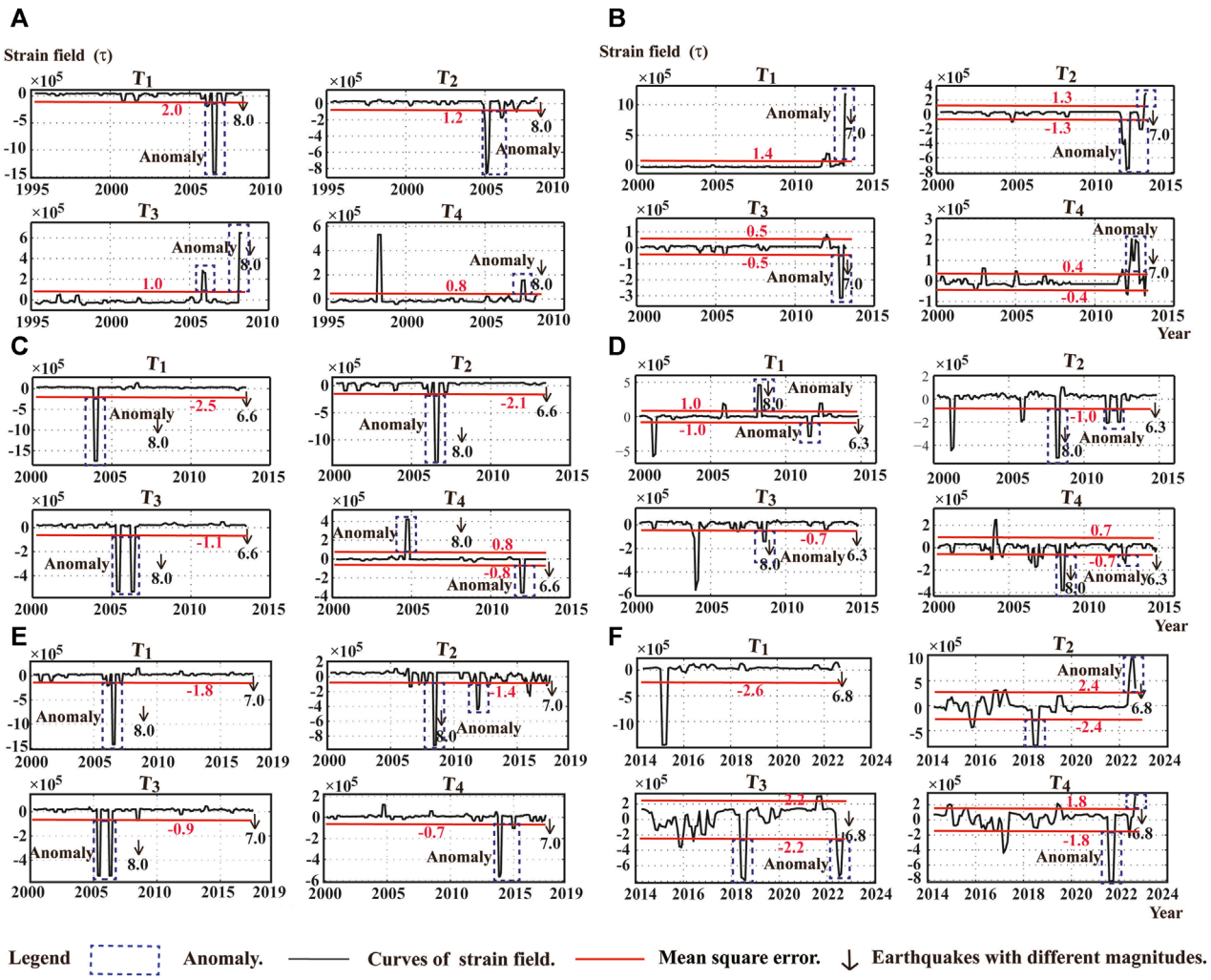

FIGURE 2
Temporal factors of the first 4 strain fields of 6 $M \geq 6.3$ earthquakes around the Longmenshan fault zone since 2008. The green dotted line represents the anomaly, the red line is the mean square error, the black arrow represents the magnitude of a $M \geq 6.3$ earthquake. **(A)** 2008 Wenchuan (*M*8.0) earthquake; **(B)** 2013 Lushan (*M*7.0) earthquake; **(C)** 2013 Minxian-Zhangxian (*M*6.6) earthquake; **(D)** 2014 Kangding (*M*6.3) earthquake; **(E)** 2017 Jiuzhaigou (*M*7.0) earthquake; **(F)** 2022 Luding (*M*6.8) earthquake.

earthquake. There were no short-term anomalies in the strain field before the 2014 Kangding (*M*6.3) earthquake or 2017 Jiuzhaigou (*M*7.0) earthquake. Medium-term anomalies were also affected by the Wenchuan (*M*8.0) earthquake.

3.2 Interactions between strong earthquakes in the southern LFZ

According to Table 1, the study area of the 2008 Wenchuan (*M*8.0) earthquake was 30°–33.5°N and 101.5°–106.0°E; that of the 2013 Lushan (*M*7.0) earthquake was 29.5°–31.5°N N and 101.5°–106.0°E. These two study areas partially overlapped, but their temporal factor anomaly curves were different. Therefore, it was necessary to compare the differences in the strain field temporal factors between the two, and to determine whether there was any mutual influence between the earthquakes. A study area was selected to include both earthquakes (29.5°–33.5°N, 101.5°–106.5°E). The area of a strain field with a contour value (or absolute value) greater than 0.05×10^5 before a strong earthquake is considered to be an anomaly area (Luo, et al., 2019). Positive contours represent released strain and negative contours represent accumulated strain. Points where positive and negative contours intersect along large active faults are often the locations of future strong earthquakes (Luo, et al., 2023).

Figure 3A shows the strain field contour distribution before the 2008 Wenchuan (*M*8.0) earthquake (1 January 2000, to 11 May 2008). The anomaly areas were concentrated at 31.7°–32.7°N & 101.5°–102.3°E and 32.7°–33.5°N & 104.3°–105.3°E. These two areas were outside of the study area forthe Lushan (*M*7.0) earthquake, confirming that the four strain field temporal factor anomalies before the Lushan earthquake were not affected by the Wenchuan (*M*8.0) earthquake. The LFZ did not have notable contour anomalies, but the Wenchuan (*M*8.0) earthquake still

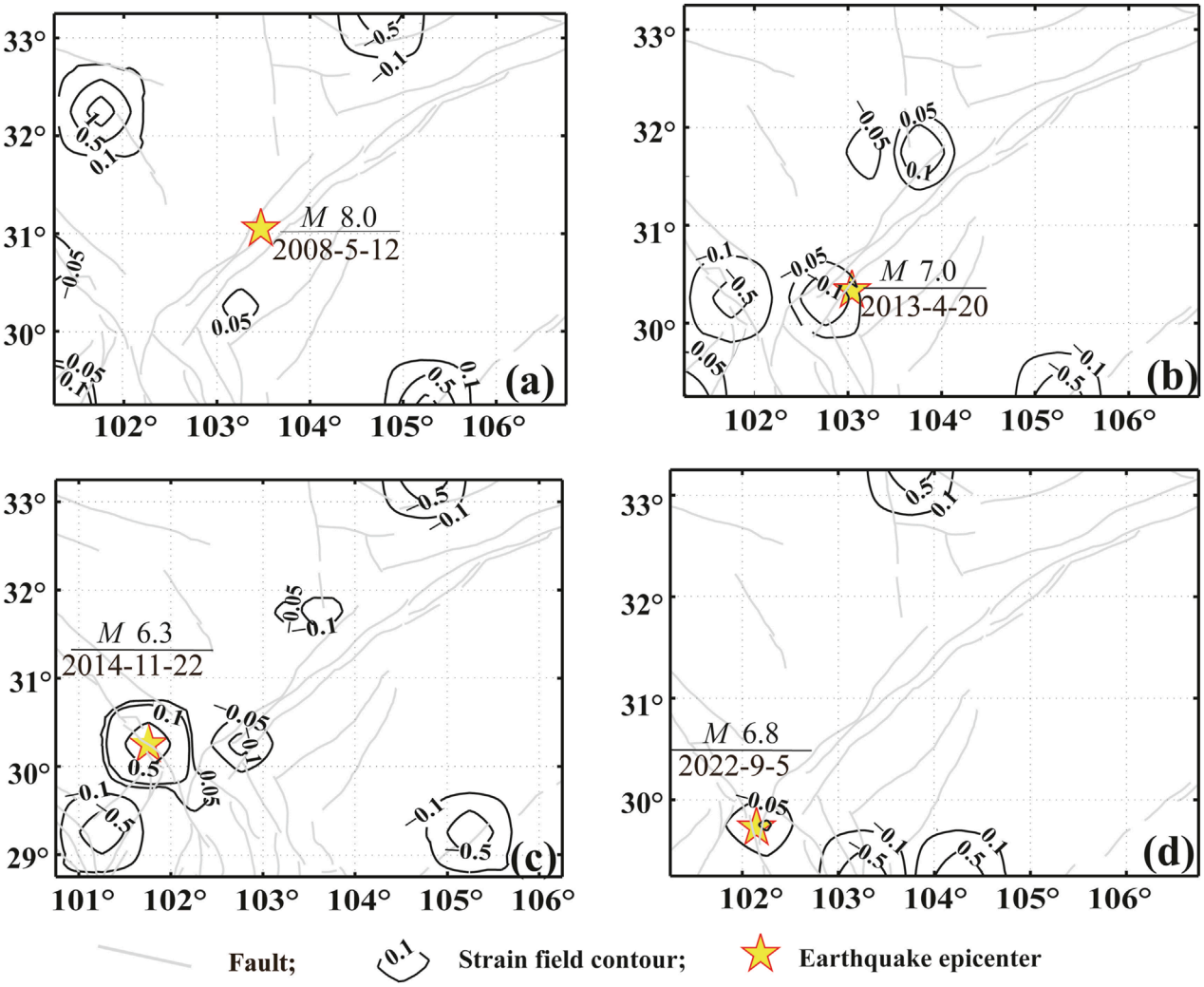

FIGURE 3
Spatial isoline distribution of strain field before Wenchuan, Lushan, Kangding and Luding earthquakes. The gray line is the fault, the black line is the strain field contour line, negative value represents the accumulated strain and the positive value represents the released strain, the isoline value 0.1 represents 0.1 times 10^5. The yellow stars represents the epicenter of strong earthquake. **(A)** Strain field from 1 January 2000 to 11 May 2008; **(B)** Strain field from 1 January 2009 to 19 April 2013; **(C)** Strain field from 1 January 2009 to 21 November 2014; **(D)** Strain field from 1 January 2015 to 4 September 2022.

occurred. Figure 3B shows the evolution of the strain field contours before the 2013 Lushan (*M*7.0) earthquake (1 January 2009, to 19 April 2013). The anomaly areas were concentrated at 29.5°–30.7°N & 101.5°–103.3°E and 31.5°–32.2°N & 103.3°–104.3°E. The 2013 Lushan (*M*7.0) earthquake occurred on the edge of the former anomaly area. Figure 3C shows the anomaly areas of the strain field spatial equivalent before the 2014 Kangding (*M*6.3) earthquake (1 January 2009, to 21 November 2014). After the Wenchuan (*M*8.0) and Lushan (*M*7.0) earthquakes, the area of strain field anomalies in the vicinity of where the Xianshuihe Fault Zone intersects with the LFZ increased, and the 2014 Kangding (*M*6.3) earthquake occurred in the high-value anomaly area. Figure 3D shows the contours of the strain field before the 2022 Luding (*M*6.8) earthquake (1 December 2014, to 4 September 2022). The anomaly areas are mainly concentrated at 29.5°–30.0°N and 102.0°–104.5°E. The Luding (*M*6.8) earthquake occurred on the edge of the anomaly area.

These results indicate that since 2009, the southern section of LFZ, where it intersects with the Xianshuihe Fault Zone, has experienced high-value anomalies. The 2013 Lushan (*M*7.0) earthquake, 2014 Kangding (*M*6.3) earthquake, and 2022 Luding (*M*6.8) earthquake all occurred in this vicinity and were all affected by the 2008 Wenchuan (*M*8.0) earthquake.

3.3 Interactions among strong earthquakes in the northern LFZ

As shown in Table 1, the study areas of the Wenchuan, Min-Zhang, and Jiuzhaigou earthquakes are different, but with small overlaps. A study area containing all three strong earthquakes (30.0°–36.5°N, 101.5°–106.5°E) was chosen to analyze the spatial evolution of seismic strain field anomalies.

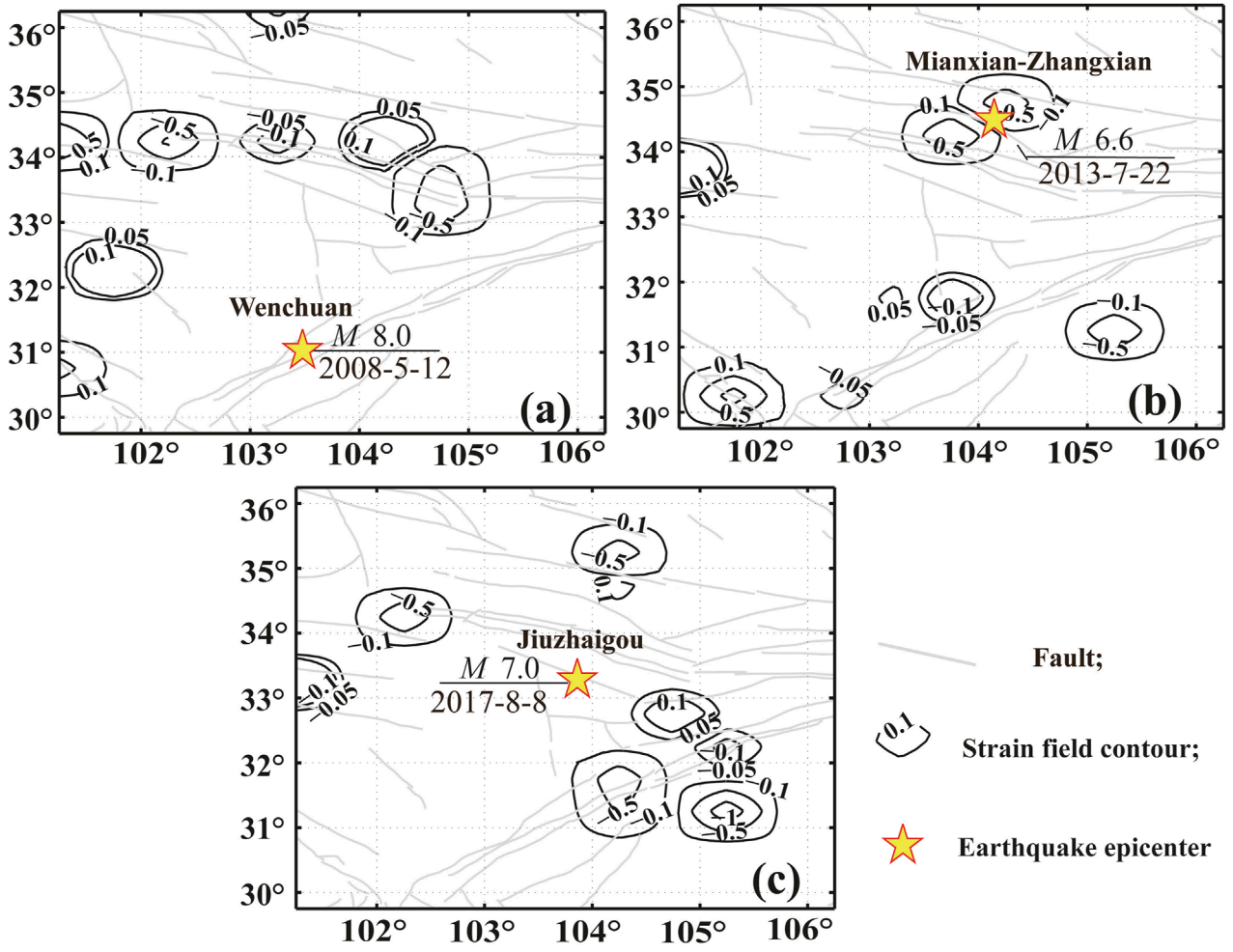

FIGURE 4
Spatial isoline distribution of strain field before Wenchuan, Minxian-Zhangxian and Jiuzhaigou earthquakes. The gray line is the fault, the black line is the strain field contour line, negative value represents the accumulated strain and the positive value represents the released strain, the isoline value 0.1 represents 0.1 times 10^5. The yellow stars represents the epicenter of strong earthquake. **(A)** Strain field from 1 January 2000 to 11 May 2008; **(B)** Strain field from 1 January 2009 to 2 July 2013; **(C)** Strain field from 22 July 2013 to August 2017.

Figure 4A shows that in the period before the 2008 Wenchuan (*M*8.0) earthquake (1 January 2000, to 11 May 2008); seismic strain field contour anomalies were mainly concentrated in the eastern Kunlun Fault, with anomalies distributed in patches around the 34° north line. Special anomalies were concentrated at 33.0°–34.7°N and 103.8°–105.3°E, in the vicinity of the epicenters of the 2013 Min County–Zhang County (*M*6.6) and 2017 Jiuzhaigou (*M*7.0) earthquakes, indicating that anomalies formed decades before these strong earthquakes. There were no anomalies in the epicentral area of the Wenchuan (*M*8.0) earthquake, which is consistent with the results in Figure 4A.

Figure 4B were the contour distribution of the strain field in the period before the 2013 Min County–Zhang County (*M*6.6) earthquake (1 January 2009, to 21 July 2013). It shows that the strain field anomalies after the Wenchuan earthquake were mainly concentrated in the area of 33.8°–35.2°N and 103.3°–104.7°E, except for LFZ. This area is also in the vicinity of the epicenters of 2013 Min County–Zhang County (*M*6.6) and 2017 Jiuzhaigou (*M*7.0) earthquakes. Before the Wenchuan earthquake, an anomaly area formed in this region. After the Wenchuan earthquake, anomalies increased significantly in this area. The more northerly location of the anomalies further indicated that the Wenchuan earthquake had a certain influence on the Min County–Zhang County and Jiuzhaigou earthquakes. Figure 4C shows the strain field contours before the 2017 Jiuzhaigou (*M*7.0) earthquake (22 July 2013, to 7 August 2017). After the 2013 Min County–Zhang County (*M*6.6) earthquake, regional strain field anomalies were mainly distributed in the northern central parts of LFZ and could have been related to the 2017 Jiuzhaigou (*M*7.0) earthquake. Comparing Figures 4A–C, the Wenchuan and Jiuzhaigou earthquakes were found to occur at the center of a ring of anomalies in the seismic strain field, with no anomalies in the vicinity of the epicenters, while the Min County–Zhang County earthquake occurred in the strain field anomaly area.

In summary, by studying the spatio-temporal evolution of the strain fields of six earthquakes in the vicinity of LFZ, the seismic

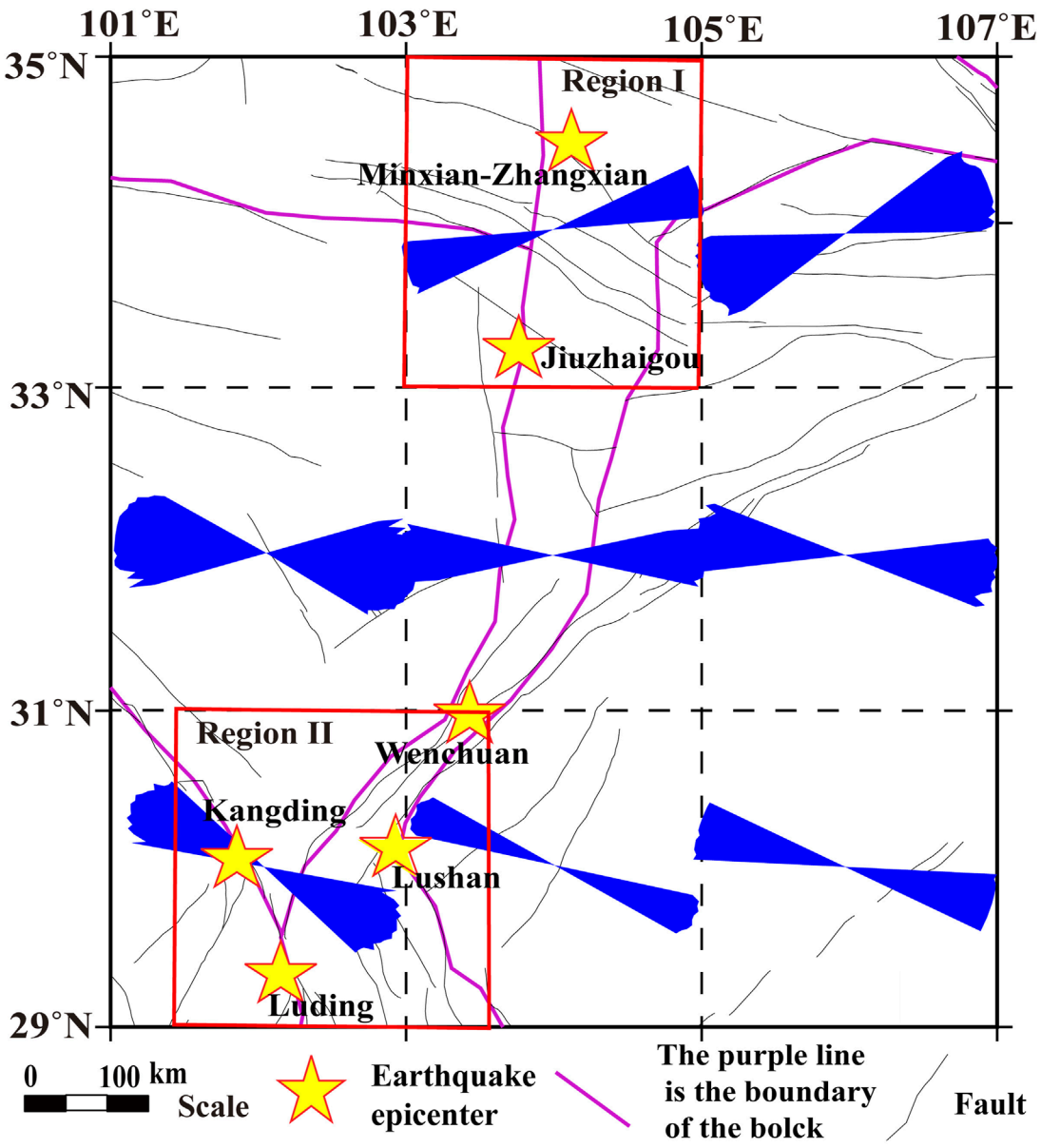

FIGURE 5
Zoning results of seismic tectonic stress field around the Longmenshan fault zone (Wang et al., 2015). The blue rose leaves represent the direction of the principal compressive stress in the 2° × 2° region. The red line frame represents the study area, where regionIcontains the Minxian-Zhangxian *M*6.6 earthquake and the Jiugouzhai (*M*7.0) earthquake, and region II contains the Wenchuan (*M*8.0) earthquake, Lushan (*M*7.0) earthquake, Kangding (*M*6.3) earthquake and Luding (*M*6.8) earthquake. The yellow stars represent the epicenters of six earthquakes. Black lines show major faults. The purple lines represent the boundary of the block.

strain field temporal factor anomalies were found to be closely related to contour anomalies. Controlled by regional tectonics and stress fields, seismic strain in fault zones is accumulated or released, resulting in changes in seismic strain field anomalies over time. The southern region of LFZ intersects with the Xianshuihe Fault Zone. The development and occurrence of the 2008 *M*8.0 Wenchuan and 2013 Lushan (*M*7.0) earthquakes inevitably restrained the Xianshuihe Fault Zone. This also explains the 2014 *M*6.3 Kangding and 2022 Luding (*M*6.8) earthquakes. The northern section of LFZ intersects with the Minjiang Fault, Huya Fault, and Wenxian Fault. The development of strong earthquakes on these faults will inevitably be mutually restraining and regulating, which explains the mutual influences of the 2008 Wenchuan (*M*8.0) earthquake, 2013 Min County–Zhang County (*M*6.6) earthquake, and 2017 Jiuzhaigou (*M*7.0) earthquake. This result is consistent with the *b*-value method (Yi et al., 2013; Liu and Pei, 2017) and Benioff strain method (Li et al., 2022) study the influence of stress and strain changes on strong earthquakes

10.3389/feart.2024.1269753

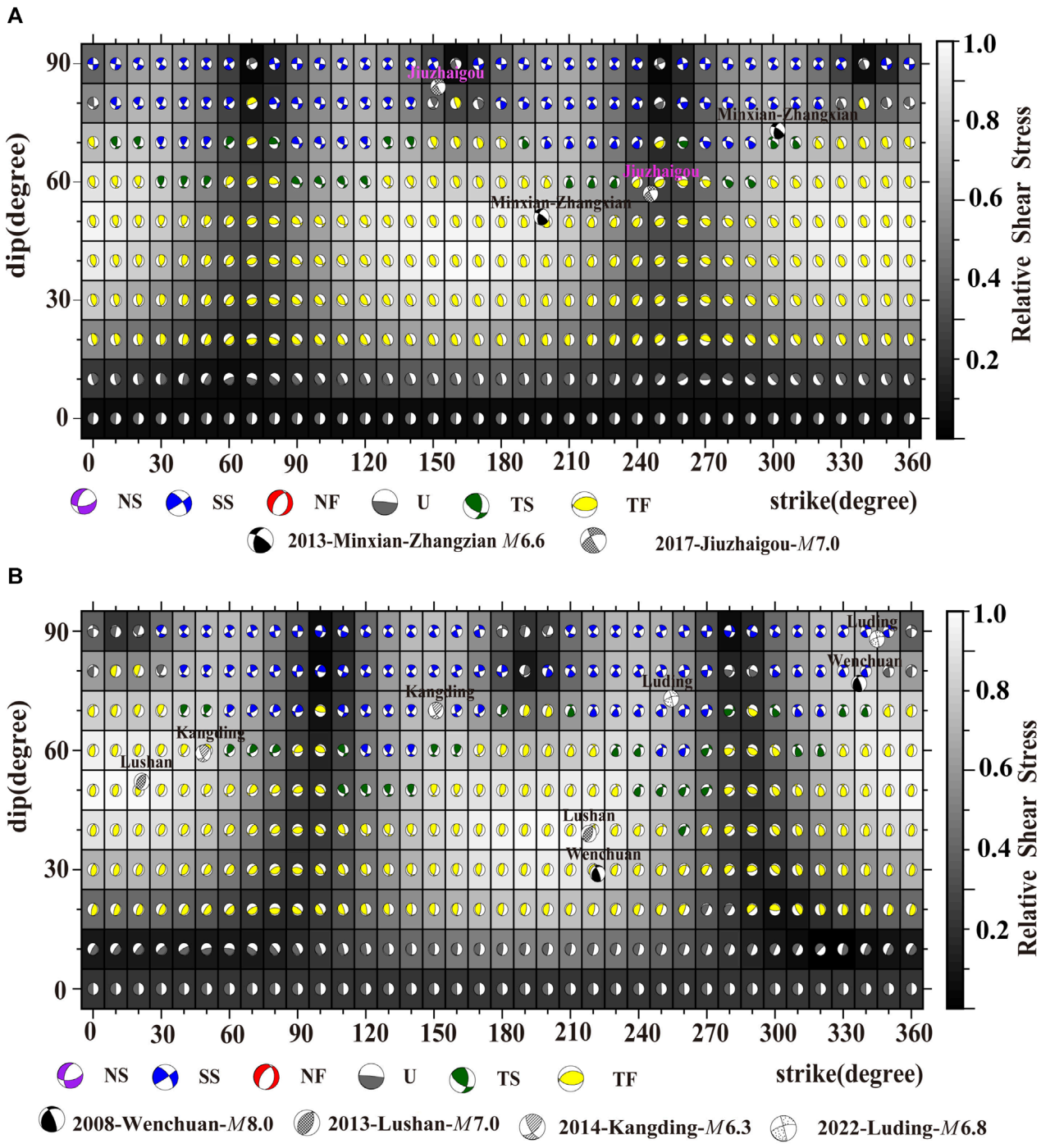

FIGURE 6
The shear stress result of the tectonic stress field around Longmen Mountain fault at the focal plane of strong earthquake. The abscissa is the strike of the focal mechanism, and the ordinate is the dip Angle. With 10° as the step length for both horizontal and vertical coordinates, theoretical numerical simulation focal mechanism solutions of different node surface shapes were divided. NS represented positive fault-and-strike slip type, SS represented strike slip type, NF represented positive fault-and-strike slip type, TS represented reverse fault-and-strike slip type, TF represented reverse fault-and-strike type, and U represented uncertain focal mechanism solutions. The background colors of the grid squares from black, grey to white represent the shear stress from small to large under the stress system. **(A)** The focal mechanism joint shear stress results in region I are compared with the USGS focal mechanism solutions for the Minxian-Zhangxian earthquake and the Jiuzhaigou earthquake. **(B)** The nodal shear stress results of the theoretical focal mechanism solution for region II are compared with those of the USGS Wenchuan, Lushan, Kangding and Luding earthquakes.

in the LFZ. Strong earthquakes occur around low *b* value and high stress, after strong earthquakes, the *b* value of the region recovers obviously and gradually increases. On the Benioff strain curve, the cumulative strain in the region rises obviously and the slope of the curve becomes larger within 1 year after the earthquake.

10.3389/feart.2024.1269753

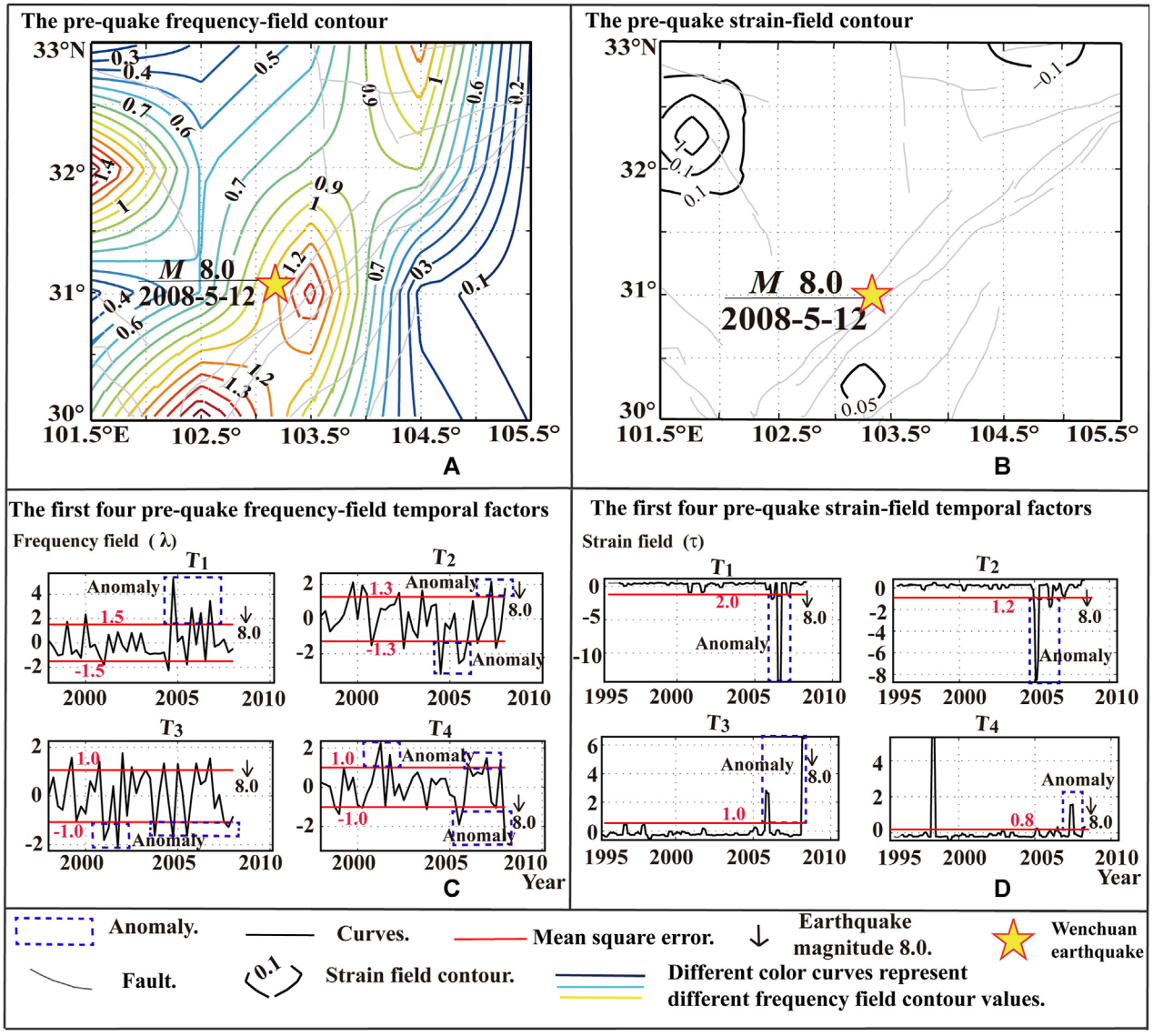

FIGURE 7
Temporal and spatial anomalies of frequency field and strain field before the 2008 Wenchuan (*M*8.0) earthquake. The pre-quake frequency-field of spatial contour anomalies distribution **(A)**; The pre-quake strain-field of spatial contour anomalies distribution **(B)**; The first 4 pre-quake frequency-field of temporal factors anomalies distribution **(C)**; The first 4 pre-quake strain-field of temporal factors anomalies distribution **(D)**.

3.4 Comparison of NOF results with shear stress results of focal mechanism node

Based on previous research reports (Wang et al., 2015) on the zoning of the tectonic stress system in the vicinity of LFZ (Figure 5), the principal compressive stress direction in region I was northeastern, and the stress field parameters were compressive axis strike of 72°, inclination angle of 2°, long-axis strike of 304°, plunge of 87°, and stress shape factor R-value of 0.68. The principal compressive stress direction of region II was northwesterly, and the stress field parameters were a final axis strike of 103°, inclination angle of 8°, long-axis strike of 226°, plunge of 82°, and stress shape factor R-value of 0.76. Based on the stress field parameters of the two regions, and using focal mechanism and shear stress Method in Regional tectonic Stress Field (Wan, 2020), the relative shear stress of the two nodal planes of the focal mechanism solutions (from the USGS) of the 2013 Min County–Zhang County (*M*6.6) earthquake and 2017 Jiuzhaigou (*M*7.0) earthquake in region I were calculated (Figure 6A). The results show that the relative shear stress of the Min County–Zhang County earthquake was large, and the seismic stress was fully released; whereas, that of the Jiuzhaigou earthquake was small, and the seismic stress was not fully released. The relative shear stress of the two nodal planes of the focal mechanism solutions (from USGS) of the 2008 Wenchuan (*M*8.0) earthquake, 2013 Lushan (*M*7.0) earthquake, 2014 Kangding (M6.3) earthquake, and 2022 Luding (*M*6.8) earthquake in region II were calculated (Figure 6B). The results show that the relative shear stress of the Wenchuan and Lushan earthquakes were larger, and the seismic stress was fully released; as such, the risk of powerful earthquakes in LFZ was low. However, the relative shear stresses of the Kangding

TABLE 3 Temporal and spatial anomalies of strain field and frequency field before the 2008 Wenchuan *Ms* 8.0 earthquake.

Earthquake	Seismic field	Temporal factor anomaly			Spatial contour anomaly		
		Time of anomaly (ear-month)	Temporal factor	Type of anomaly	Anomaly centroid [° N, °E)]	Anomaly radiu (km)	Distance between anomaly center and earthquake (km)
2008–05-12 Wenchuan M_s 8.0	Frequency field	2004-07–12	T_1, T_2	Long-to-med-ium term	32.1,101.5	56	210
		2005-07–12	T_2, T_3	Long-to-med-ium term	33.0,104.5	42	245
		2006-10–12	T_1	Medium term	30.0,102.5	34	140
		2008-01–04	T_4	Short-to-Immin-ent term	31.0,103.6	26	0
	Strain field	2005-07–12	T_2, T_3	Long-to-med-ium term	32.3,101.7	39	213
		2006-05–11	T_1	Medium term	33.0,104.7	27	252
		2007-04–06	T_4	Medium term	30.2,103.2	21	100
		2008-01–04	T_3	Short-to-immi-nent term			

Note: T_k is the *k*th (1–4) strain-field time factor.

and Luding earthquakes were smaller, and the seismic stress was not fully released, resulting in an elevated risk of future events; 7 years after the Kangding (*M*6.3) earthquake, the 2022 Luding (*M*6.8) earthquake occurred ~85 km away.

In the vicinity of LFZ, the results of strain field obtained by natural orthogonal function (EOF) method are basically consistent with the results of shear stress generated by regional tectonic stress field at focal mechanism node. The 2008 Wenchuan (*M*8.0) earthquake and 2013 Lushan (*M*7.0) earthquake had larger shear stresses, and the seismic stress was fully released, which had significant impacts on surrounding tectonic fault stress. There were also notable medium-term and short-term temporal factor anomalies in the strain fields, and the contour anomaly areas were relatively large. Conversely, theKangding (*M*6.3) earthquake, Jiuzhaigou (*M*7.0) earthquake, and Luding (*M*6.8) earthquake had relatively smaller shear stresses, and the seismic stress was not fully released, creating a small impact on the surrounding tectonic fault stress. There were few short-term temporal factor anomalies, and the contour anomaly areas were relatively small.

4 Discussion

4.1 Spatio-temporal anomalies of strain and frequency fields

The results of this study were compared with previous research on the frequency field of LFZ (Luo et al., 2023) to identify differences in spatial and temporal anomalies of the frequency and strain fields. Taking the 2008 Wenchuan (*M*8.0) earthquake as an example (Figure 7), the time intervals of the first 4 temporal factor anomalies were the same between the studies. The distribution of the temporal factors (i.e., which temporal factor the anomalies are distributed in) was the key difference. The central area of contour anomalies was largely similar, but the number of anomalies differs (Table 3). Before the 2008 Wenchuan (*M*8.0) earthquake, there were four central areas of high-value frequency field contour anomalies (Luo et al., 2023) and three centers of strain field contour anomalies. These three anomaly locations were all approximately the same distance from the center of the Wenchuan earthquake. The difference is that there was an anomaly area in the frequency field in the vicinity of the Wenchuan epicenter, but not in the strain field. In summary, a comparison of the spatial anomalies of the frequency and strain fields showed that they were largely consistent. However, temporal factor anomalies were easily identifiable in the strain field, and contour anomaly information was more comprehensive in the frequency field.

4.2 Reasons for anomalies

By comparing the frequency and strain fields (Figure 7), and searching the seismic catalog in the study area, the factors affecting spatio-temporal anomalies in the two fields were discovered to be different. Frequency field temporal factor changes fluctuated considerably, and anomalies were complex. The contour anomalies mainly had high gradients and dense distributions. This may be because the spatial and temporal anomalies in the frequency field

were primarily affected by the occurrence of minor earthquakes in the region. Nevertheless, changes in the temporal factors of the strain fields were relatively systematic, with prominent anomalies. High-value strain field spatial and temporal anomalies were relatively sporadic. This may be because spatial and temporal anomalies in the strain field were primarily affected by moderate earthquakes. In summary, in this region, the frequency field was primarily affected by the frequency of *M*2–3 earthquakes, and the strain field was mainly affected by *M*4–5 foreshocks.

4.3 Orthogonal function as a forecasting tool

The identification of earthquake precursors is of great significance to earthquake forecasting. This study used the orthogonal function, which is commonly used in atmospheric and climate science (Lorenz, 1956; Obukhov, 1960), to identify strong earthquake precursors in the vicinity of LFZ for earthquake forecasting. Earthquake forecasting remains a contentious scientific issue. However, recently, significant progress is seen in medium-term and short-term seismicity-based forecasting techniques. The approaches can be divided into 7 physical process-based models and 10 smoothed seismicity-based models (Tiampo and Shcherbakov, 2012). The natural orthogonal function becomes 11 techniques to use the smoothed seismicity-based model. More earthquake forecasting information is provided in the spatially and temporally of strain field, but it is limited by the relatively short time of earthquake catalogs data. In order to evaluate the application of orthogonal function in earthquake prediction, it is necessary to accumulate seismic observation data over a long period.

5 Conclusion

In this study, the spatio-temporal anomalies of seismic strain fields were investigated before and after six strong earthquakes that have occurred since 2008 in the LFZ. Temporal factor anomalies were mainly concentrated in the first 4 strain fields. All the first 4 strain fields had medium- and long-term anomalies that was over the mean square error, and some temporal factors had short-term anomalies (For example, the Wenchuan *M*8.0 and Lushan *M*7.0 earthquakes). More anomaly components produced more reliable results. Areas at intersections of strain accumulation and strain release, or central areas surrounded by multiple high-value strain field anomalies, are often places where powerful earthquakes subsequently occur. The high value anomaly of strain contour is basically consistent with the high value of shear stress of regional tectonic stress field at the focal mechanism plane, which indicates that the orthogonal function method is more reliable in identifying anomalies before strong earthquakes.

Temporal factor anomalies in the strain fields appeared around 2008, and the strong earthquakes occurred several years later in the anomaly area of strain field contours. This indicates that the spatio-temporal anomalies in seismic strain fields of some strong earthquakes in the vicinity of LFZ were affected by the 2008 Wenchuan (*M*8.0) earthquake. Future research should analyze the impact of interactions in strain fields between powerful earthquakes.

Data availability statement

The datasets presented in this study can be found in online repositories. The names of the repository/repositories and accession number(s) can be found in the article/Supplementary material.

Author contributions

GL: Writing–original draft, Formal Analysis, Funding acquisition, Methodology, Software. YX: Conceptualization, Writing–original draft. HL: Data curation, Writing–original draft. FD: Data curation, Writing–original draft. WL: Methodology, Writing–original draft.

Funding

The author(s) declare financial support was received for the research, authorship, and/or publication of this article. This work has been supported by the Ningxia Natural Science Foundation Project (Grant number 2021AAC03483; 2022AAC03687, and 2022AAC03695).

Acknowledgments

Seismic data used in this study were obtained from the Sichuan Earthquake Administration and the China Earthquake Networks Center (CENC). The focal mechanism solution data for these six earthquakes mainly came from the US Geological Survey (USGS).

Conflict of interest

The authors declare that the research was conducted in the absence of any commercial or financial relationships that could be construed as a potential conflict of interest.

Publisher's note

All claims expressed in this article are solely those of the authors and do not necessarily represent those of their affiliated organizations, or those of the publisher, the editors and the reviewers. Any product that may be evaluated in this article, or claim that may be made by its manufacturer, is not guaranteed or endorsed by the publisher.

References

Burchfiel, B. C., Royden, L. H., Hilst, R. D. V. D., Hanger, B. H., Chen, Z., King, R. W., et al. (2008). A geological and geophysical context for the Wenchuan earthquake of 12 May 2008, Sichuan, *People's Republic of China*. *GSA Today* 18 (7), 4–11. doi:10.1130/GSATG18A.1

Chen, C. Y., Ren, J. W., Meng, G. J., Yang, P. X., and Su, J. F. (2013). Division, deformation and tectonic implication of active blocks in the eastern segment of Bayan Har block. *Chin. J. Geophys.* 56 (12), 4125–4141. doi:10.6038/cjg20131217

Chen, G. G., Ji, F. J., Zhou, R. J., Xu, J., and Ye, Y. Q. (2007). Primary research of activity segmentation of Longmenshan fault zone since Late-Quaternary. *Seismol. Geol. (in Chinese)* 29 (3), 657–673. doi:10.1016/S1872-5791(07)6004-X

Chen, L. C., Ran, Y. K., Wang, H., Li, Y. B., and Ma, X. Q. (2013). The Lushan *M*s7.0 earthquake and activity of the southern segment of the Longmenshan fault zone. *Chin. Sci.Bull.* 58 (28-29), 3475–3482. doi:10.1007/s11434-013-6009-6

Cheng, J., Yao, S. H., Liu, J., Yao, Q., Gong, H. L., and Long, H. Y. (2018). Visoelastic coulomb stress of historical earthquake on the 2017 Jiuzhaigou earthquake and the subsequent influence on the seismic hazards of adjacent faults. *Chinese J. Geophys. (in Chinese)* 61 (5), 2133–2151. doi:10.6038/cjg2018L0609

Clark, M. K., and Royden, L. H. (2000). Topographic ooze: building the eastern margin of Tibet by lower crustal flow. *Geology* 28 (8), 703–706. doi:10.1130/0091-7613(2000)028<0703:tobtem>2.3.co;2

Deng, Q. D., Chen, S. F., and Zhao, X. L. (1994). Tectonics, seismicity and dynamics of longmenshan mountains and its adjacent regions. *seismology and Geology* 16 (4), 389–403. (in Chinese).

Diao, F. Q., Wang, R. J., Wang, Y. B., Xiong, X., and Walter, T. R. (2018). Fault behavior and lower crustal rheology inferred from the first seven years of postseismic GPS data after the 2008 Wenchuan earthquake. *Earth and Planetary Science Letters* 495, 202–212. doi:10.1016/j.epsl.2018.05.020

Du, F., Long, F., Xiang, R., Yi, G. X., Gong, Y., Zhao, M., et al. (2013). The *M*7.0 Lushan earthquake and the relationship with the *M*8.0 Wenchuan earthquake in Sichuan, China. *Chinese J. Geophys.* 56 (5), 1772–1873. (in Chinese). doi:10.6038/cjg20130535

Duan, H. R., Zhou, S. Y., Li, R., Chen, S. L., and Yan, Q. C. (2020). Relationship between the slip distribution of the Lushan earthquake fault and the Wenchuan earthquake fault. *Chinese J. Geophys. (in Chinese)* 63 (1), 210–222. doi:10.6038/cjg2020N0042

England, P., and Houseman, G. (1986). Finite strain calculations of continental deformation: 2. comparison with the India-Asia collision zone. *Journal of Geophysical Research Solid Earth* 91 (B3), 3664–3676. doi:10.1029/jb091ib03p03664

England, P. C., and Houseman, G. A. (1988). The mechanics of the Tibetan plateau. *Phil. Trans. R. Soc. Lod. A* 326 (1589), 301–320. doi:10.1098/rsta.1988.0089

Fu, B. H., Shi, P. L., and Zhang, Z. W. (2008). Spatial characteristics of the surface rupture by the *M*s8.0 Wenchuan earthquake using high-resolution remote sensing imagery. *Acta Geological Sinica (in Chinese)* 82 (12), 1679–1683.

Ge, W. P. (2013). Discussion on the relationship between regional landform and seismogenic structure of the MinxianZhangxian *M*s6.6 earthquake. *China earthquake engineering journal* 35 (4), 840–847. (in Chinese).

Gong, M., Xu, X. W., and Li, K. (2020). Fault geometry responsible for the initial rupture process of Wenchuan earthquake. *Chinese J. Geophys.* 63 (3), 1224–1234. (in Chinese). doi:10.6038/cjg2020N0255

Guo, R. M., Zheng, Y., and Xu, J. (2020). Stress modulation of the seismic gap between the 2008 *M*s8.0 Wenchuan earthquake and the 2013 *M*s7.0 Lushan earthquake and implications for seismic hazard. *Geophysical Journal International* 221 (3), 2113–2125. doi:10.1093/gji/ggaa143

Harrison, T. M., Copeland, P., Kidd, W. S. F., and Yin, A. (1992). Raising tibet. *Science* 255 (5052), 1663–1670. doi:10.1126/science.255.5052.1663

Huang, L. Y., Cheng, H. H., Zhang, H., Gao, Y., and Shi, Y. L. (2019). Coseismic and postseismic stress evolution caused by the 2008 Wenchuan earthquake and its effects on the 2017 *M*s7.0 Jiuzhaigou earthquake. *Chinese J. Geophys* 62 (4), 1268–1281. doi:10.6038/cjg2019L0545

Jia, K. (2020). Modeling the spatiotemporal seismicity patterns of the longmen Shan Fault zone based on the coulomb rate and state model. *Seismol. Res. lett.* 1, 275–286. –12. doi:10.1785/0220200088

Jia, K., and Zhou, S. Y. (2018). Triggering relationship in strong earthquake sequence around the Bayan Har block and its tectonic significance based on Coulomb stress changes and seismicity. *Acta Seismologica Sinica (in Chinese)* 40 (3), 291–303. doi:10.11939/jass.20170201

Jiang, Z. S., Wang, M., Wang, Y. Z., Wu, Y. Q., Che, S., Shen, Z. K., et al. (2014). GPS constrained coseismic source and slip distribution of the 2013 *M*w 6.6 Lushan, China, earthquake and its tectonic implications. *Geophys. Res. lett.* 41 (2), 407–413. doi:10.1002/2013GL058812

Jin, Z. T., Wan, Y. G., Liu, Z. C., Huang, J. C., Li, Y., and Yang, F. (2019). The static stress triggering influences of the 2017 *M*s7.0 Jiuzhaigou earthquake on neighboring areas. *Chinese J. Geophys.* 62 (4), 1282–1299. doi:10.6038/cjg2019L0675

Li, B., Xie, F. R., Huang, J. S., Xu, X. W., Guo, Q. L., Zhang, G. W., et al. (2022). *In situ* stress state and seismic hazard in the Dayi seismic gap of the Longmenshan thrust belt. *Science China (Earth Sciences)* 65 (7), 1388–1398. doi:10.1007/s11430-021-9915-4

Li, C. Y., Sun, K., Ma, J., Li, J. J., Liang, M. J., and Fang, L. H. (2022). The 2022 *M*6.8 Luding earthquake: a complicated event by faulting of the Moxi segment of the Xianshuihe fault zone. *Seismology and Geology* 44 (6), 1648–1666. doi:10.3969/j.issn.0253-4967.2022.06.017

Li, H., Wang, H., Xu, X. Q., Si, J., Pei, J., Li, T., et al. (2013). Characteristics of the fault-related rocks, fault zones and the principal slip zone in the wenchuan earthquake fault scientific drilling project hole-1 (WFSD-1). *Tectonophysics* 584, 23–42. doi:10.1016/j.tecto.2012.08.021

Li, H. B., Wang, H., Yang, G., Xu, Z. Q., Zhang, J. J., Si, J., et al. (2016). Lithological and structural characterization of the Longmenshan fault belt from the 3rd hole of the Wenchuan earthquake fault scientific drilling project (wfsd -3). *International Journal of Earth Sciences* 105 (8), 2253–2272. doi:10.1007/s00531-015-1285-9

Li, H. B., Xu, Z. Q., Wang, H., Zhang, L., He, X. L., Si, J. L., et al. (2018). Fault behavior, physical properties and seismic activity of the Wenchuan earthquake fault zone: evidences from the Wenchuan earthquake fault scientific drilling project (wfsd). *Chinese J. Geophys* 61 (5), 1680–1697. doi:10.6038/cjg2018M0257

Li, Y., Gao, Y. G., Wang, W. H., and Xu, Y. K. (2022). Benioff strain anyalysis of the Longmenshan fault zone. *China Earthquake Engineering Journal* 44 (4), 896–900. doi:10.20000/j.1000-0844.20210330001

Li, Y. Q., Jia, D., Wang, M. M., Shaw, J. H., He, J., Lin, A., et al. (2014). Structural geometry of the source region for the 2013 *M*w6.6 Lushan earthquake: implication for earthquake hazard assessment along the Longmenshan. *Earth planet. Sci. Lett.* 390, 275–286. doi:10.1016/j.epsl.2014.01.018

Li, Z. W., Liu, S. G., Chen, H. D., Liu, S., Guo, B., and Tian, X. B. (2008). Structural segmentation and zonation and differential deformation across and along the Longmen thrust belt, west Sichuan, China. *Journal of Chendu University of Technology (Science and Technology Edition)* 35 (4), 440–454.

Lin, A., Gang, R., and Bing, Y. (2012). Field evidence of rupture of the Qingchuan Fault during the 2008 *M*w7.9 Wenchuan earthquake, northeastern segment of the Longmen Shan thrust belt, China. *Tectonophysics* 522-523, 243–252. doi:10.1016/j.tecto.2011.12.012

Liu, X. M., Wu, J., Liang, C. T., Qian, Q. W., and Du, P. X. (2019). The latest seismicity characteristics and significance in Longmenshan Fault Zone. *Chinese J. Geophys* 62 (4), 1312–1322. doi:10.6038/cjg2019M0283

Liu, Y. B., and Pei, S. P. (2017). Temporal and spatial variation of *b*-value before and after Wenchuan earthquake and its tectonic implication. *Chinese J. Geophys* 60 (6), 2104–2112. doi:10.6038/cjg20170607

Lorenz, E. N. (1956). Empirical orthogonal function and statistical weather prediction. science report 1, statistical forecasting project, department of meteorology, MIT. *NTIS. AD* 110268, 1–49.

Luo, G. F., Ding, F. H., Ma, H. Q., and Yang, M. Z. (2023). Pre-quake frequency characteristics of *M*s ≥7.0 earthquake in mainland China. *Front. Earth Sci.* 10, 10–992858. doi:10.3389/feart.2022.992858

Luo, G. F., Ding, F. H., Xu, Y. C., Luo, H. Z., and Li, W. J. (2023). Strain fields of *m*s >6.0 earthquakes in menyuan, qinghai, China. *Front. Earth Sci.* 11, 1152348. doi:10.3389/feart.2023.1152348

Luo, G. F., Liu, Z. W., Luo, H. Z., and Ding, F. H. (2019). Effect of the strain field of Wenchuan 8 earthquake on the strong earthquake around the epicenter. *Progress in Geophysics (in Chinese)* 34 (3), 0908. doi:10.6038/pg2019CC0454

Luo, G. F., Ma, X. J., Ma, H. Q., and Yang, M. Z. (2015). Analysis of regional seismic energy field before Lushan *M*s7.0 earthquake. *Journal of disaster prevention and reduction (in Chinese)* 31 (1), 54–58.

Luo, G. F., Yang, M. Z., Ma, H. Q., and Xu, X. Q. (2011). Intermediate and short-term anomalies of seismic activity energy field before the Wenchuan *M*8.0 earthquake. *Earthquake(in Chinese)* 31 (3), 135–142.

Luo, G. F., Zeng, Z. W., Ma, H. Q., and Yang, M. Z. (2014). Analysis of energy field of seismic activity before the Minxian-Zhangxian *M*s6.6 Earthquake. *China earthquake engineering journal (in Chinese)* 36 (2), 314–319. doi:10.3969/j.issn.1000-0844.2014.02.0314

Luo, Y., Zhao, L., and Tian, J. H. (2019). Spatial and temporal variations of stress field in the Longmenshan fault zone after the 2008 Wenchuan, China earthquake. *Tectonophysics* 767, 228172–228213. doi:10.1016/j.tecto.2019.228172

Ma, C. H., Qian, F., and Zhang, H. M. (2021). Similation of rupture process and its influence factors of the 2013 *M*s7.0 Lushan earthquake. *Chinese J. Geophys.* 64 (1), 170–181. (in Chinese). doi:10.6038/cjg2021O0114

Mei, S. R. (1997). *General characteristics of long term evolution of seismicity before strong earthquakes in North China//Theory and method of short impending earthquake prediction*. China: Beijing Press Seismological.

Meng, W., Guo, X. Y., Li, Y. H., Han, L. B., and Zhang, C. Y. (2022). Tectonic stress field and dynamic characteristics in the northeastern margin of the Tibetan Plateau. *Chinese J. Geophys.* 65 (9), 3229–3251. (in Chinese). doi:10.6038/cjg2022P0236

Molnar, P., and Tapponnier, P. (1975). Cenozoic Tectonics of Asia: effects of a Continental Collision: features of recent continental tectonics in Asia can be interpreted as results of the India-Eurasia collision. *Science* 189 (4201), 419–426. doi:10.1126/science.189.4201.419

Neha, and Pasari, S. (2022). A review of empirical orthogonal function (eof) with an emphasis on the co-seismic crustal deformation analysis. *Nat. Hazards.* 110, 29–56. doi:10.1007/s11069-021-04967-4

Obukhov, A. M. (1960). The statistically orthogonal expansion of empirical functions. bulletin of the academy of sciences of the USSR. *Geophys Ser* 1, 288–291.

Shan, X. J., Qu, C. Y., Gong, W. Y., Zhao, D. Z., Zhang, Y. F., Zhang, G. F., et al. (2017). Coseismic deformation field of the Jiuzhaigou *Ms*7.0 earthquake form Sentinel-1A InSAR data and fault slip inversion. *Chinese J. Geophys. (in Chinese)* 60 (12), 4527–4536. doi:10.6038/cjg20171201

Shi, Y. L., and Cao, J. L. (2010). Some aspects in static stress change calculation case study on Wenchuan earthquake. *Chinese Journal of Geophysics (in Chinese)* 51 (1), 102–110. doi:10.3969/j.issn.0001-5733.2010.01.011

Teng, J. W., Pi, J. L., Yang, H., Yan, Y. F., Zhang, Y. Q., Yuan, X. M., et al. (2014). Wenchuan-Yingxiu *Ms*8.0 earthquake seismogenic fault and deep dynamic response. *Chinese J. Geophys* 57 (2), 392–403. doi:10.6038/cjg20140604

Tiampo, K. F., and Shcherbakov, R. (2012). Seismicity-based earthquake forecasting techniques: ten years of progress. *Tectonophysics* 522–523, 89–121. doi:10.1016/j.tecto.2011.08.019

Toda, S., Lin, J., Meghraoui, M., and Stein, R. (2008). 12 May 2008 *M*7.9 Wenchuan, China, earthquake calculated to increase failure stress and seismicity rate on three major fault systems, *Geophys. Res. Lett.* 35, 1–6. doi:10.1029/2008GL034903

Wan, Y. G. (2020). Simulation on relationship between stress and mechanisms of earthquake. *Chinese Journal of Geophysics* 63 (6), 2281–2296. doi:10.6038/cjg2023Q0093

Wan, Y. G., Shen, Z. K., Sheng, S. Z., and Xu, X. F. (2009). The influence of 2008 Wenchuan earthquake on surrounding faults. *Acta Seismologica Sinica (in Chinese)* 31 (2), 128–139.

Wan, Y. R., Shen, Z. K., Bvrgmann, R., Sun, J. B., and Wang, M. (2017). Fault geometry and slip distribution of the 2008 *M*w7.9 Wenchuan, China earthquake, inferred from GPS and InSAR measurements. *Geophys. J. Int.* 208 (2), 748–766. doi:10.1093/gji/ggw421

Wang, J. J., Xu, C. J., Freymueller, J. T., Li, Z. H., and Shen, W. B. (2014). Sensitivity of coulomb stress change to the parameters of the coulomb failure model: a case study using the 2008 *M*w7.9 Wenchuan earthquake. *J. Geophys. Res. Solid Earth.* 119 (4), 3371–3392. doi:10.1002/2012jb009860

Wang, W. M., Hao, J. L., and Yao, Z. X. (2013). Preliminary result for rupture process of Apr. 20,2013,Lushan earthquake,Sichuan, China. *Chinese J. Geophys.* 56 (4), 1412–1417. (in Chinese). doi:10.6038/cjg20130436

Wang, X. F., Xiao, J., Xu, H. H., and He, J. K. (2016). Dynamic responses of the Xianshuihe and Longmenshan fault zones to regional tectonic loading. *Chinese J. Geophys. (in Chinese)* 59 (4), 1403–1413. doi:10.6038/cjg20160421

Wang, X. S., Lu, J., Xie, Z. J., Long, F., Zhao, X. Y., and Zheng, Y. (2015). Focal mechanisms and tectonic stress field in the north-south seismic Belt of China. *Chinese J. Geophys* 58 (11), 4149–4162. (in Chinese). doi:10.6038/cjg20151122

Wang, Y. Z., Wang, F., Wang, M., Shen, Z. K., and Wan, Y. G. (2014). Coulomb stress change and evolution induced by the 2008 Wenchuan earthquake and its delayed triggering of the 2013 *M*w 6.6 Lushan earthquake. *Seismol. Res. Lett.* 85 (1), 52–59. doi:10.1785/0220130111

Wang, Z., Wang, X. B., Huang, R. Q., and Liu, G. N. (2017). Deep structre imaging of multi-geophysical parameters and seismogenesis in the Longmenshan fault zone. *Chinese J. Geophys.* 60 (6), 2068–2079. (in Chinese). doi:10.6038/cjg20170604

Wu, Y. Q., Jiang, Z. S., Zhao, J., Liu, X. X., Wei, W. X., Liu, Q., et al. (2015). Crustal deformation before the 2008 Wenchuan *Ms*8.0 earthquanke studied using GPS data. *J. Geodyn.* 85, 11–23. doi:10.1016/j.jog.2014.12.002

Xie, J. J., Li, X. J., Wen, Z. P., and Zou, B. (2018). Variation of near-fault strong ground motion with directions during the 2013 Lushan *Ms*7.0 earthquake. *Chinese J. Geophys. (in Chinese)* 61 (4), 1266–1280. doi:10.6038/cjg2018K0686

Xu, X. W., Chen, G. H., Wang, Q. X., Chen, L. C., Ren, Z. S., and Xu, C. (2017). Discussion on seismogenic structure of Jiuzhaigou earthquake and its implication for current strain state in southeastern Qinghai-Tibet Plateau. *Chinese J. Geophys. (in Chinese)* 60 (10), 4018–4026. doi:10.6038/cjg20171028

Xu, X. W., Chen, G. H., Yu, G. H., Sun, X. J., Tan, X. B., and Chen, L. C. (2010). Reevaluation of surface rupture parameters of the 5·12 Wenchuan earthquake and its tectonic implication for Tibetan uplift. *Chinese Journal of Geophysics (in Chinese)* 53 (10), 2321–2336. doi:10.3969/j.issn.0001-5733.2010.10.006

Xu, X. W., Wen, X. Z., Han, Z. J., Chen, G. H., Li, C. Y., Zhen, W. J., et al. (2013). Lushan *Ms*7.0 earthquake: a blind reserve-fault event. *Chinese Sci. Bull.* 58 (28), 3437–3443. doi:10.1007/s11434–013–5999–4

Xu, X. W., Wen, X. Z., Ye, J. Q., Ma, B. Q., Chen, J., Zhou, R. J., et al. (2008). The *M*s8.0 Wenchuan earthquake surface ruptures and its seismogenic structure. *Seismology and Geology (in Chinese)* 30 (3), 597–629.

Xu, X. W., Wen, X. Z., Yu, G. H., Chen, G. H., Klinger, Y., Hubbard, J., et al. (2009). Coseismal reverse and oblique-slip surface faulting generated by the 2008 *M*w7.9 Wenchuan earthquake, China. *Grology* 37 (6), 515–518. doi:10.1130/G25462A.1

Xu, Z. Q., Wu, Z. L., Li, H. B., and Li, L. (2018). The most rapid respond to a large earthquake—the Wenchuan earthquake fault scientific drilling project. *Chinese J. Geophys.* 61 (5), 1666–1679. doi:10.6038/cjg2018M0256

Yan, Z. K., Li, Y., Zhao, G. H., Zhou, R. J., Li, J. B., Zhang, W., et al. (2014). The relationship between Lushan earthquake and Wenchuan earthquake by segmentation of geology and geomorphology of LongmenShan. *Chinese Journal of Nature (in Chinese)* 36 (1), 51–58.

Yang, M. Z., and Ma, H. Q. (2011). Variation of energy field of Longmenshan fault zone before the Wenchuan *Ms*8.0 earthquake. *Earthquake Research in China (in Chinese)* 27 (3), 260–267.

Yang, M. Z., and Ma, H. Q. (2012). Analysis of regional seismic energy field before Wenchuan *Ms*8.0 earthquake. *Progress in Geophysics (in Chinese)* 27 (3), 872–877. doi:10.6038/j.issn.1004-2903.2012.03.006

Yang, M. Z., and Ma, H. Q. (2016). Seismic active field theory and anomaly analysis method. *Beijing Press Seismological*, 23–39.

Yang, M. Z., Ma, H. Q., Luo, G. F., and Xu, X. Q. (2017). Research on the seismic strain field before strong earthquakes above *M*6 in Chinese mainland. *Chinese J. Geophys. (in Chinese)* 60 (10), 3804–3814. doi:10.6038/cjg20171010

Yang, M. Z., and Zhao, W. M. (2004). Statistical analysis of seismic activity energy field in Ningxia and its adjacent areas. *Journal of Earthquake (in Chinese)* 26 (5), 571–577.

Yang, X. P., Jiang, P., Song, F. M., Liang, X. H., and Chen, X. C. (1999). The evidence of the south Longmenshan Fault zones cuting late Quaternary stratum. *Seismology and Geology (in Chinese)* 21 (4), 341–345.

Yang, Y. H., Zhang, X. M., Hua, Q., Sou, L. N., Feng, C. J., Qiu, Y. R., et al. (2021). Segmentation characteristics of the Longmenshan fault—constrained from dense focal mechanism data. *Chinese J. Geophys.* 64 (4), 1181–1205. doi:10.6038/cjg2021O0286

Ye, Q. D., Ding, Z. F., Wang, S. W., Yu, D. X., and Zhen, C. (2017). Determining the source parameters of the micro earthquakes near the third borehole of the Wenchuan Earthquake Fault Scientific (wfsd-3) and its implications. *Chinese J. Geophys. (in Chinese)* 60 (7), 2716–2732. doi:10.6038/cjg20170718

Yi, G. X., Long, F., Liang, M. J., Zhang, H. P., Zhao, M., and Ye, Y. Q. (2017). Focal mechanism solution and seismogenic structure of the 8 August 2017 Jiuzhaigou (*M*7.0) earthquake and its aftershocks, northern Sichuan. *Chinese J. Geophys.* 60 (10), 4083–4097. doi:10.6038/cjg20171033

Yi, G. X., Long, F., Vallage, A., Klinger, Y., Liang, M. J., and Wang, S. W. (2016). Focal mechanism and tectonic deformation in the seismogenic area of the 2013 Lushan earthquake sequence southwestern China. *Chinese J. Geophys.* 59 (10), 3711–3731. doi:10.6038/cjg20161017

Yi, G. X., Long, F., Wen, X. Z., Liang, M. J., and Wang, S. W. (2015). Seismogenic structure of the *M*6.3 kangding earthquake sequence on 22 nov. 2014, southwestern China. *Chinese J. Geophys.* 58 (4), 1205–1219. doi:10.6038/cjg20150410

Yi, G. X., Long, F., and Zhang, Z. W. (2012). Spatial and temporal variation of focal mechanisms for aftershocks of the 2008 *Ms*8.0 Wenchuan earthquake. *Chinese J. Geophys.* 55 (4), 1213–1227. doi:10.6038/j.issn.0001-5733.2012.04.017

Yi, G. X., Wen, X. Z., Xin, H., Qiao, H. Z., Wang, S. W., and Gong, Y. (2013). Stress state and major earthquake risk on the southern segment of the Longmen Shan fault zone. *Chinese Journal of geophysics Chinese edition* 56 (4), 1112–1120. doi:10.6038/cjg20130407

Zhang, P. Z., Wen, X. Z., Shen, Z. K., and Chen, J. H. (2008). Oblique, high-angle, listric-reverse faulting and associated development of strain: the Wenchuan earthquake of May 12, 2008, Sichuan, China. *Annu. Rev.Earth Planet* 38, 353–382. doi:10.1146/annurev-earth-040809-152602

Zhang, P. Z., Wen, X. Z., Xu, X. W., Zhang, P., Wen, X., Huang, Y., et al. (2009). Multi-unit combination model of the 2008 Wenchuan magnitude 8.0 earthquake. *Chin. Sci. Bull. (in Chinese)* 54 (7), 944–953. doi:10.1360/csb2009-54-7-944

Zhao, B., Gao, Y., Huang, Z. B., Zhao, X., and Li, D. (2013). Double difference relocation, focal mechanism and stress inversion of Lushan *Ms*7.0 earthquake sequence. *Chinese J. Geophys. (in Chinese)* 56 (10), 3385–3395. doi:10.6038/cjg20131014

Zheng, T., Ding, Z. F., Chang, L. J., Zhen, C., Zhang, H., and Li, D. F. (2017). *S*-ware slitting in upper crust near the scientific drilling wfsd-3 at the Wenchuan earthquake fault zone. *Chinese J. Geophys* 60 (5), 1690–1702. (in Chinese). doi:10.6038/cjg20170507

Frontiers in Earth Science

Investigates the processes operating within the major spheres of our planet

Advances our understanding across the earth sciences, providing a theoretical background for better use of our planet's resources and equipping us to face major environmental challenges.

Discover the latest Research Topics

See more →

Frontiers

Avenue du Tribunal-Fédéral 34
1005 Lausanne, Switzerland
frontiersin.org

Contact us

+41 (0)21 510 17 00
frontiersin.org/about/contact